Transactions of the ASME

HEAT TRANSFER DIVISION
Chairman, R. J. SIMONEAU
Secretary, F. A. KULACKI
Senior Technical Editor, G. M. FAETH
Technical Editor, I. CATTON
Technical Editor, R. GREIF
Technical Editor, P. J. MARTO
Technical Editor, R. H. PLETCHER
Technical Editor, R. K. SHAH
Technical Editor, R. VISKANTA
Technical Editor, M. M. YOVANOVICH

BOARD ON COMMUNICATIONS
Chairman and Vice President
K. N. REID, JR.

Members-at-Large
W. BEGELL
J. T. COKONIS
W. G. GOTTENBERG
F. LANDIS
J. R. LLOYD
R. E. NICKELL
J. E. ORTLOFF
C. F. PHILLIPS
R. E. REDER

President, L. S. FLETCHER
Executive Director,
PAUL ALLMENDINGER
Treasurer,
ROBERT A. BENNETT

PUBLISHING STAFF
Mng. Dir., Publ., J. J. FREY
Dep. Mng. Dir., Pub.,
JOS. SANSONE
Managing Editor,
CORNELIA MONAHAN
Production Editor,
VALERIE WINTERS
Editorial Prod. Asst.,
MARISOL ANDINO

The Journal of Heat Transfer (ISSN 0022-1481) is published quarterly for $100 per year by The American Society of Mechanical Engineers, 345 East 47th Street, New York, N Y 10017. Second class postage paid at New York, NY and additional mailing offices. POSTMASTER: Send address changes to The Journal of Heat Transfer, c/o THE AMERICAN SOCIETY OF MECHANICAL ENGINEERS, 22 Law Drive, Box 2300, Fairfield, NJ 07007-2300.
CHANGES OF ADDRESS must be received at Society headquarters seven weeks before they are to be effective. Please send old label and new address.
PRICES: To members, $24.00, annually; to nonmembers, $100.00.
Add $6.00 for postage to countries outside the United States and Canada.
STATEMENT from By-Laws. The Society shall not be responsible for statements or opinions advanced in papers or . . . printed in its publications (B7.1, para. 3).

INDEXED by the Engineering Index, Inc.

Journal of Heat Transfer

Published Quarterly by The American Society of Mechanical Engineers

VOLUME 107 • NUMBER 3 • AUGUST 1985

ANNOUNCEMENTS

TECHNICAL PAPERS

TECHNICAL NOTES

DISCUSSION

Optimization of Thermal Conductivities of Isotropic and Orthotropic Solids

R. A. Meric
Applied Mathematics Department,
Research Institute for Basic
Sciences, TUBITAK,
Gebze, Kocaeli, Turkey

Optimization of thermal conductivities of isotropic and orthotropic solids is treated as a steady-state optimal control problem. Nonlinear necessary optimum conditions are first derived for the so-called material optimization problem, and a general numerical method of solution is then proposed. The iterative numerical procedure solves the linearized state and co-state equations by the finite element method and minimizes the performance index by the conjugate gradient method. Numerical solutions, checked with exact results when possible, are given for an isotropic infinite plate and a cylinder.

1.0 Introduction

Much literature is available on control systems described by linear differential equations. However, if the control (or design) characteristics to be selected appear in the coefficients of the otherwise linear differential equations the system equations become nonlinear when taken as equations involving both state and control variables. One field in which such nonlinearities are encountered is material optimization.

In a steady-state optimization or open-loop control problem, control variables may represent various types of physical quantities and then lead to different optimization problems. Generally speaking, we may be interested in (*a*) shape, (*b*) load, or (*c*) material optimization.

For a shape optimization problem in heat transfer, optimization of circular fins with heat generation for minimum weight was achieved by Razani and Ahmadi [1]. Recently, the present author has investigated various load optimization problems in heat transfer and thermoelasticity, where the control loads specifically represented heat fluxes or sources, and surface tractions [2–8]. As for a material optimization problem, Lurie [9] investigated the problem of distributed control over the conductivity of the working fluid in magnetohydrodynamic channel flow and estimated the advantages in power generation gained from it.

In this paper, optimization of thermal conductivities of isotropic and orthotropic solids is investigated as a material optimization problem. The present analysis is one of the few studies on optimization of material properties which appear as coefficients of the state variables in heat transfer. The problem formulation and its overall solution procedure is, however, applicable to a wide variety of problems. Another material optimization problem which can be solved in a similar fashion would be that of optimizing heat transfer coefficients and/or insulation material thicknesses for a convection type of boundary condition. In that case, it is noted that control variables would appear as coefficients of the state variables, not in the heat conduction equation, but in the boundary condition only.

In the present investigation, the necessary conditions of optimality are first derived for an isotropic body by using calculus of variations and a Lagrange multiplier function. A numerical method of solution is then proposed in which the finite element and conjugate gradient methods are utilized for a mathematical programming approach. Numerical results are given for two one-dimensional problems involving an infinite plate and an infinite cylinder, both of which are composed of uniform material layers.

Contributed by the Heat Transfer Division for publication in the JOURNAL OF HEAT TRANSFER. Manuscript received by the Heat Transfer Division May 3, 1984.

The orthotropic material case is treated in the Appendix, where only the problem formulation and necessary optimum conditions are provided for brevity.

2.0 Problem Formulation

Consider an isotropic solid body of arbitrary geometry with nonhomogeneous thermal conductivity k in three dimensions. A similar problem formulation with orthotropic thermal conductivity is treated in the Appendix. The steady-state heat conduction in the body is governed by the following equations

$$\text{in } D: \ \nabla\cdot(k\nabla T)+Q=0 \tag{1}$$

$$\text{on } S_1: \ T=\bar{T} \tag{2}$$

$$\text{on } S_2: \ kT'+q+\alpha(T-T_\infty)=0 \tag{3}$$

where D denotes the physical domain of interest with the boundary $S = S_1 + S_2$; T is the temperature; Q and q are the heat source and boundary heat flux, respectively; $\bar{T}$ is the prescribed temperature; α denotes the heat transfer coefficient; T_∞ is the ambient temperature and T' represents the gradient of T normal to the surface.

All the quantities in equations (1–3) are assumed to be known except for the distribution of k which is not given a priori in the problem. The thermal conductivity k will play the role of control function in an optimization problem, controlling the system state (i.e., the temperature in the body) such that some physical objectives are achieved. In practice, this type of optimization of thermal conductivities might be needed for designing composite structures of various material layers. Insulation designs of heat systems, such as heating pipes, might also require optimization of thermal conductivities or other physical quantities (such as insulation thicknesses) leading to similar optimization problems.

The aim of the present optimization problem is to find the optimal k in the nonhomogeneous body, satisfying the condition that k and T distributions will be as close as possible to (desired) k_0 and T_0, respectively. By working in the space of square-integrable functions (and thus excluding point functions), the so-called performance index J of the optimization problem can thus be defined as follows

$$J[k,T]=\frac{1}{2}\int_D [(T-T_0)^2+\beta(k-k_0)^2]dD \tag{4}$$

where β is a given weighting parameter. There are actually two physical goals inherent in the problem. These are simply stated as (*a*) $T\to T_0$, and (*b*) $k\to k_0$. The weighting parameter β simply weighs these objectives in a linear combination. In other words, increased values of β decrease the achievement of the first objective, while increasing the achievement of the

second objective. We also set the value of β according to our needs and resources (i.e., availability of high or low conductivity materials).

The static optimization problem of optimal thermal conductivity may formally be described as a steady-state optimal control problem governed by an elliptic partial differential equation [10]. By adopting control problem terminology it can be stated as follows:

Find the optimal control function k such that the performance index $J[k, T]$ is minimized under the state equation constraint (1) and the boundary constraints (2–3).

By noting the fact that each term of $J[k, T]$ is defined in D, the control problem is classified as a domain control–domain observation problem. The unknowns are the control function k and the corresponding state function T. It may also be noted that the state equation (1) is a nonlinear (bilinear) equation when taken in terms of the control and state functions. Hence, a nonlinear optimization problem is at hand.

3.0 Necessary Optimum Conditions

The present optimization problem has been stated as a control problem under the system equation constraint (1). It is possible, however, to adjoin this constraint with $J[k, T]$ by means of a Lagrange multiplier function λ, obtaining a modified (or augmented) performance index J^*, i.e.,

$$J^*[k,T,\lambda] = J[k,T] + \int_D \lambda[\nabla\cdot(k\nabla T) + Q]dD \tag{5}$$

The necessary condition for J^* to be stationary is that its first variation should be equal to zero for permissible values of δk, δT, and $\delta\lambda$, hence

$$\delta J^*[k,T,\lambda] = 0 \tag{6}$$

By substituting equation (4) into (5) and then taking the first variation, δJ^* may be written as [11]

$$\delta J^* = \int_D \{(T-T_0)\delta T + \beta(k-k_0)\delta k + \delta\lambda[\nabla\cdot(k\nabla T)+Q] + \lambda[\nabla\cdot(\delta k\nabla T + k\nabla\delta T)]\}dD \tag{7}$$

The Green's generalized first and second identities may be given in terms of three scalar functions u, v, and w as follows

$$\int_D [w\nabla u\cdot\nabla v + u\nabla\cdot(w\nabla v)]dD = \int_S wuv'dS \tag{8}$$

and

$$\int_D [u\nabla\cdot(w\nabla v) - v\nabla\cdot(w\nabla u)]dD = \int_S w(uv' - vu')dS \tag{9}$$

The last two integral terms in equation (7) may then be expanded by using equations (8) and (9), respectively, as

$$\int_D \lambda\nabla\cdot(\delta k\nabla T)dD = -\int_D \delta k\nabla\lambda\cdot\nabla T dD + \int_S \delta k\lambda T'dS \tag{10}$$

and

$$\int_D \lambda\nabla\cdot(k\nabla\delta T)dD = \int_D \delta T\nabla\cdot(k\nabla\lambda)dD + \int_S k(\lambda\delta T' - \lambda'\delta T)dS \tag{11}$$

Introducing equations (10) and (11) into (7) and rearranging terms, δJ^* may be written as the summation of the domain integral part, δJ_D^*, and the boundary integral part, δJ_S^*, as

$$\delta J^* = \delta J_D^* + \delta J_S^* \tag{12}$$

where

$$\delta J_D^* = \int_D \{[\nabla\cdot(k\nabla T)+Q]\delta\lambda + [\nabla\cdot(k\nabla\lambda)+T-T_0]\delta T + [\beta(k-k_0) - \nabla\lambda\cdot\nabla T]\delta k\}dD \tag{13}$$

and

$$\delta J_S^* = \int_S [\lambda\delta(kT') - k\lambda'\delta T]dS \tag{14}$$

The first variational forms of the boundary conditions (2) and (3) are simply given as

$$\text{on } S_1 \ : \ \delta T = 0 \tag{15}$$

$$\text{on } S_2 \ : \ \delta(kT') + \alpha\delta T = 0 \tag{16}$$

It is now possible to introduce the above equations into δJ_S^*, where, for convenience, the boundary integral on S is first decomposed into two boundary integrals defined on S_1 and S_2. Thus, it may easily be shown that δJ_S^* takes the following form:

$$\delta J_S^* = \int_{S_1} \lambda\delta(kT')dS + \int_{S_2} (k\lambda' + \alpha\lambda)\delta T dS \tag{17}$$

Combining equations (6), (12), (13), and (17) finally gives the unconstrained variational form of the performance index as

$$\delta J^* = \int_D \{[\nabla\cdot(k\nabla T)+Q]\delta\lambda + [\nabla\cdot(k\nabla\lambda)+T-T_0]\delta T + [\beta(k-k_0) - \nabla\lambda\cdot\nabla T]\delta T\}dD + \int_{S_1} \lambda\delta(kT')dS + \int_{S_2} (k\lambda' + \alpha\lambda)\delta T dS = 0 \tag{18}$$

It may be noted that all the system state and boundary constraints have been incorporated into δJ^*. The variations δk, δT, and $\delta\lambda$ are now independent of each other, thus their coefficients may be set equal to zero separately in order to

Nomenclature

$[B]$ = gradient matrix
D = physical domain
J = performance index
J^* = modified performance index
k = isotropic thermal conductivity
k_1, k_2 = orthotropic thermal conductivities
$\{N\}$ = shape function vector
n = number of layers or finite elements
n_x, n_y = direction cosines
Q = distributed heat source
q = boundary heat flux
S = domain boundary
S_1, S_2 = parts of S
T = temperature
$\bar{T}$ = prescribed temperature
T_∞ = ambient temperature
$\{T\}$ = nodal temperature vector
u, v, w = dummy scalar functions
x, y = Cartesian coordinates
α = heat transfer coefficient
β, β_1, β_2 = weighting parameters
δ = variational operator
∇ = gradient vector
λ = Lagrange multiplier function
$\{\lambda\}$ = nodal values of λ

Subscripts

S = that of boundary S
D = that of domain D
0 = desired level

Superscripts

e = finite element e
T = transpose
$(\cdot)'$ = normal gradient of $(\cdot)$

satisfy equation (6) [11]. This yields the stationary conditions of J^* (i.e., the Euler-Lagrange equations of calculus of variations), which may be written along with the essential boundary conditions (2-3) as follows

The T-problem:

$$\text{in } D : \nabla\cdot(k\nabla T)+Q=0 \tag{19}$$

$$\text{on } S_1 : T=\bar{T} \tag{20}$$

$$\text{on } S_2 : kT'+q+\alpha(T-T_\infty)=0 \tag{21}$$

The λ-problem:

$$\text{in } D : \nabla\cdot(k\nabla\lambda)+T-T_0=0 \tag{22}$$

$$\text{on } S_1 : \lambda=0 \tag{23}$$

$$\text{on } S_2 : k\lambda'+\alpha\lambda=0 \tag{24}$$

The gradient condition:

$$\text{in } D : \beta(k-k_0)-\nabla\lambda\cdot\nabla T=0 \tag{25}$$

It may be noted that equations (19-25) have artificially been divided into groups headed by "the T-problem," etc. Although these equations are a complete set and form the necessary conditions for optimum performance index J subject to equations (1-3), their superficial grouping will help in explaining an iterative method of solution which will be adopted in the next section.

The necessary optimum conditions constitute a nonlinear boundary value problem (BVP) in mathematical physics in terms of the unknown functions k, T, and λ. Similar optimum conditions are given for an orthotropic solid body in the Appendix. Since the equations are nonlinear a solution method will unavoidably be iterative.

4.0 Method of Solution

The present iterative solution procedure can be simply explained as follows: By taking an initial guess for the control function k, the T and λ problems, each of which describes a linear BVP in terms of the current k, can be solved consecutively by an appropriate method (e.g., the finite element method). Updating the control can then be achieved via optimization techniques by minimizing the modified performance index J^* using the available information about its gradient with respect to k. The iterative procedure continues until a given tolerance is reached in the convergence of successive solutions of k.

In the next subsections, the space discretization and minimization techniques used in the overall iterative procedure are outlined.

4.1 Finite Element Method. Since the system state T, costate λ, and control k variables are space dependent, the T- and λ-problems have to be discretized in space by using discretization techniques, such as the finite element method (FEM) for a numerical solution at each iteration step. The FEM is a well-known method for solving elliptic problems such as the steady-state heat conduction problem [12, 13]. In this method, numerical solutions are found at discrete nodal points in the domain and on the boundary by first assuming interpolations of functions within each subdomain (or finite element).

In the present material optimization problem the FEM is chosen since the nonhomogeneous thermal conductivity is most easily handled by this method, while another technique such as the boundary element method (BEM) may prove itself more efficient for load optimization problems [5-7].

The FEM solutions of the T and λ problems require C^0 continuous elements, i.e., element interpolation functions must be such that T and λ become continuous between the elements [13]. On the other hand, the distribution of k may be piecewise uniform over the elements, i.e., a different constant in each element.

If piecewise uniform conductivities are adopted over the finite elements, incomplete element "conductivity matrices" [13] may first be stored for the T and λ problems. Complete element conductivity matrices can then be obtained by simply multiplying each incomplete matrix with the current value of the element conductivity, thus saving computer execution times.

Through the space discretizations of the variables the optimal control problem has been transformed into a so-called "reduced order optimization" problem. Thus, the problem can be treated as a mathematical programming (i.e., finite dimensional optimization) problem in which the function to be minimized is given by the discretized J^*.

4.2 Conjugate Gradient Method. Starting with an initial guess for the uniform conductivity over each finite element, the corresponding nodal values of T and λ are thus found by using the FEM. In each iteration step, the improvement of control values can then be achieved by the minimization of the modified performance index J^* using either the discretized J^* only (i.e., a zeroth-order method) or its gradient with respect to the discrete controls (thermal conductivities) as well (i.e., a first-order method). Since the gradient condition (25) already provides us with the required information, a first-order method, which is much more efficient in finding a local minimum of a function of several variables, can be effectively utilized.

It is noted that in an iteration step, the modified performance index J^* is simply given by equation (4) (compare with equation (5)) since the heat conduction equation (19) has already been satisfied by the FEM. Thus, for each finite element with a uniform k, it may be shown that

$$J^{*e}=\frac{1}{2}\int_{D^e}\{[\{N\}^T\{T\}^e-T_0]^2+\beta(k^e-k_0)^2\}dD \tag{26}$$

where $\{N\}$ is the usual "shape function vector" of the FEM [13]; the nodal temperature values are stored in the vector $\{T\}^e$, and the superscripts e and T denote the element number and transpose of a matrix, respectively.

In each element, the gradient of J^{*e} with respect to k^e (the required information for a first-order minimization algorithm) is provided by the following expression using the gradient condition (25) in integral form:

$$\frac{\partial J^{*e}}{\partial k^e}=\int_{D^e}\{\beta(k^e-k_0)-\{T\}^{eT}[B]^T[B]\{\lambda\}^e\}dD \tag{27}$$

where $[B]$ is the "gradient matrix" of the FEM. In the above equation the second term on the RHS represents the scalar product of the gradients of λ and T in an element.

The function J^* can now be minimized with respect to the discrete element conductivities by using any first-order unconstrained optimization technique. The conjugate gradient method (CGM) of Fletcher and Reeves [14] is adopted in the present study since the computer storage requirement for the method is relatively low [15]. A computer program in FORTRAN is also available for the CGM in the literature [16].

The CGM provides "better" element conductivities at each iteration level of the numerical method. It is noted that conductivities are updated automatically through the algorithm [15, 16].

The outlined general iterative procedure, which at each iteration step involves the solution of two potential problems by the FEM and updating element conductivities by the CGM, is continued until a specified tolerance is reached in the convergence of conductivities.

5.0 Numerical Results and Discussion

Numerical results have been obtained for an isotropic infinite plate and infinite cylinder, which are composed of

uniform material layers. Although these simple geometries are essentially one-dimensional, two-dimensional isotropic quadratic quadrilateral elements with eight nodes have been utilized for the FEM solution of both the T- and λ-problems (see Fig. 1).

Some of the parameters of the optimization problem were fixed as follows: $\bar{T} = T_0 = k_0 = 1$, $Q = 0.1$ and $q = T_\infty = 0$. The number of finite elements n, hence the number of uniform thermal conductivity layers, was varied, as well as the heat transfer coefficient α and the weighting parameter β. The temperature boundary conditions are indicated in Fig. 1.

During the iterative solution procedure several initial guesses were tried to make sure of a global minimum. Computations were performed on a VAX-11/780 computer system. The numerical procedure has typically taken ten iterations for convergence.

It was possible to obtain an exact solution for the infinite plate with a single material layer. In Table 1, numerical results are shown to be in excellent agreement with the exact results when $\alpha = 0.5$. The weighting parameter β plays an important role in the problem. It can be said that taking a smaller value for β would result in the temperature T getting closer to the desired level T_0 (albeit with high-conductivity values). Nevertheless, if high-conductivity materials are not available one might not choose a very small value for β. On the other extreme, by taking a very large value for β we would indicate our desire of using k close to k_0, sacrificing in $T \rightarrow T_0$. Thus, the value of β is chosen by us according to the relative importance we give to the attainment of $T \rightarrow T_0$ versus $k \rightarrow k_0$.

The weighting parameter β is set as 10^{-6} for all the remaining numerical results. In Table 2, the average optimal thermal conductivity, averaged over the finite elements, is given when the infinite plate was composed of different number of layers, i.e., for various n. Increasing n, one would have more degrees of freedom (and ability) to achieve desired distributions of temperature throughout the solid body.

For the remaining two figures n was set as 10. In Fig. 2, optimal thermal conductivity k which is piecewise constant in each finite element (or layer) is shown as a function of x with solid constant line segments when α, the heat transfer coefficient, takes on various numerical values for the infinite plate. Smoothed-out thermal conductivities are also depicted by the dashed lines in the figure. As the type of boundary condition (21) changes its character (with $q = 0$) as α becomes zero or infinitely large, the value of this parameter greatly affects the optimum thermal conductivity values. It may be seen from the figure that (with $\bar{T}$ and T_0 each set equal to 1) larger values of α necessitate higher optimal conductivities to be able to conduct heat from the prescribed temperature boundary at $x = 0$ to the convective boundary at $x = 1$ with $T_\infty = 0$.

The last figure, Fig. 3, shows the optimal thermal con-

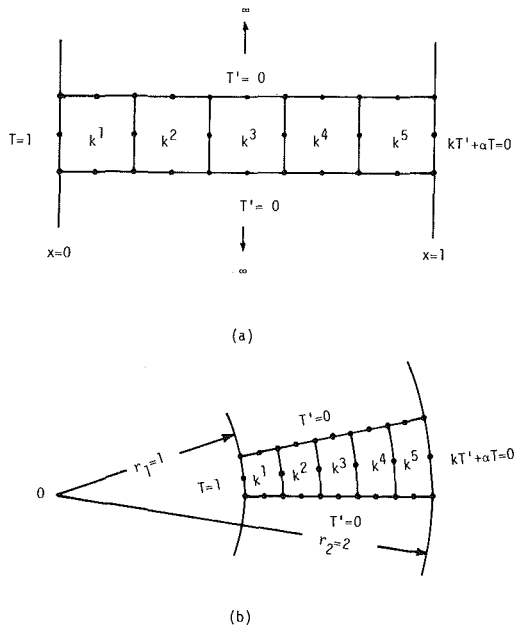

Fig. 1 Problem geometry, finite elements, and temperature boundary conditions for (a) infinite plate and (b) infinite cylinder

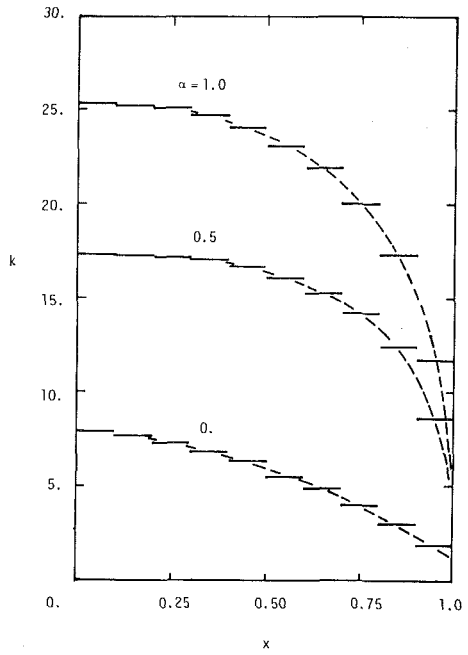

Fig. 2 Optimal thermal conductivities for infinite plate

Table 1 Exact and numerical optimal k for the infinite plate with $n = 1$ and $\alpha = 0.5$

β	Exact	Numerical
10^{-6}	15.773037	15.773382
10^{-3}	2.7800291	2.7800304
10^{0}	1.0174046	1.0174046
10^{3}	1.0000180	1.0000180

Table 2 Optimal thermal conductivities for the infinite plate

Number of layers	Heat transfer coefficient		
n	$\alpha = 0$	$\alpha = 0.5$	$\alpha = 1.0$
1	6.3099	15.7733	22.7719
2	5.8207	15.5362	22.3549
5	5.5889	15.3077	21.9912
10	5.5246	15.2260	21.8462

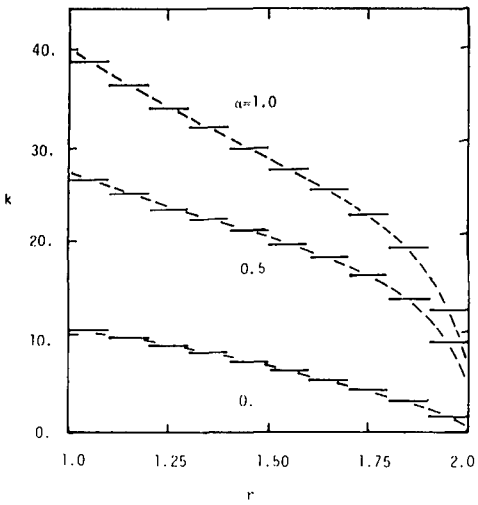

Fig. 3 Optimal thermal conductivities for infinite cylinder

ductivity k as a function of the radial distance r for the infinite cylinder. Similar trends, but with larger magnitudes for k, have been observed for the cylinder as in the case of the plate.

6.0 Conclusions

In the present analysis, optimization of thermal conductivities of solids has been investigated as a material optimization problem. The necessary optimum conditions, which are described by nonlinear PDE's, are derived for both isotropic and orthotropic solids, although numerical results are provided only for the isotropic case.

The proposed iterative numerical method of solution, which utilizes the FEM in solving the state and co-state equations and the CGM in minimizing the performance index, is general for all types of material properties. On the other hand, larger computer execution times would be needed for orthotropic materials, as the "conductivity matrix" in the FEM will have to be reevaluated fully at each iteration level.

The state PDE, i.e., the heat conduction equation, is formally bilinear in terms of the state (temperature) and control (thermal conductivity) functions. Thus, for guess values of discrete thermal conductivities the equation is effectively linearized when solved for the state variable by the FEM, requiring no inner iterations. The co-state equation enjoys similar characteristics.

It may be noted that if there are any constraints on the thermal conductivity, such as upper and/or lower bounds, different minimization techniques must be used, as the CGM is an unconstrained method. Quasi- or modified-Newton routines for the minimization of a function with constraints on the variables are, however, available in the NAG Library [15].

References

1 Razani, A., and Ahmadi, G., "On Optimization of Circular Fins With Heat Generation," *J. The Franklin Institute*, Vol. 303, 1977, pp. 211-218.

2 Meric, R. A., "Finite Element Methods for an Optimal Steady-State Control Problem," *Int. J. Numer. Meths. Engn.*, Vol. 12, 1978, pp. 1375-1382.

3 Meric, R. A., "Finite Element and Conjugate Gradient Methods for a Nonlinear Optimal Heat Transfer Control Problem," *Int. J. Numer. Meths. Engn.*, Vol. 14, 1979, pp. 1851-1863.

4 Meric, R. A., "Finite Element Analysis of Optimal Heating of a Slab With Temperature Dependent Thermal Conductivity," *Int. J. Heat Mass Transfer*, Vol. 22, 1979, pp. 1347-1353.

5 Meric, R. A., "Boundary Integral Equation and Conjugate Gradient Methods for Optimal Boundary Heating of Solids," *Int. J. Heat Transfer*, Vol. 26, 1983, pp. 261-267.

6 Meric, R. A., "Boundary Element Methods for Optimization of Distributed Systems," *Int. J. Numer. Meths. Engn.*, Vol. 20, 1984, pp. 1291-1306.

7 Meric, R. A., "Boundary Elements for Static Optimal Heating of Solids," ASME JOURNAL OF HEAT TRANSFER, Vol. 106, No. 4, Nov. 1984, pp. 876-880.

8 Meric, R. A., "Optimal Boundary Tractions for Solids With Initial Thermal Strains," ASME *Journal of Applied Mechanics*, Vol. 52, 1985.

9 Lurie, K. A., "The Mayer-Bolza Problem for Multiple Integrals: Some Optimum Problems for Elliptic Differential Equations Arising in Magnetohydrodynamics," *Topics in Optimization*, edited by G. Leitmann, Academic Press, New York, 1967.

10 Lions, J. L., "Optimal Control of Systems Governed by Partial Differential Equations," Springer-Verlag, Berlin, 1971.

11 Gelfand, I. M., and Fomin, S. V., *Calculus of Variations*, Prentice-Hall, Englewood Cliffs, NJ, 1963.

12 Wilson, E. L., and Nickell, R. E., "Application of the Finite Element Method to Heat Conduction Analysis," *Nucl. Eng. Design*, Vol. 4, 1966, pp. 276-286.

13 Hinton, E., and Owen, D. R. J., *Finite Element Programming*, Academic Press, New York, 1977.

14 Fletcher, R., and Reeves, C. M., "Function Minimization by Conjugate Gradients," *Computer J.*, Vol. 7, 1964, pp. 149-154.

15 NAG Library, Numerical Algorithms Group, Oxford, England.

16 Kuester, J. L., and Mize, J. H., *Optimization Techniques with FORTRAN*, McGraw-Hill, New York, 1973.

APPENDIX

Optimization of Orthotropic Thermal Conductivities

Problem Formulation. For convenience, only a two-dimensional formulation is given. The optimization problem may be stated as finding the orthotropic thermal conductivities k_1 and k_2 in the x and y directions, respectively, such that the following equations are satisfied.

The T-problem:

$$\text{in } D: \frac{\partial}{\partial x}\left(k_1 \frac{\partial T}{\partial x}\right) + \frac{\partial}{\partial y}\left(k_2 \frac{\partial T}{\partial y}\right) + Q = 0 \tag{A1}$$

$$\text{on } S_1: T = \bar{T} \tag{A2}$$

$$\text{on } S_2: k_1 \frac{\partial T}{\partial x} n_x + k_2 \frac{\partial T}{\partial y} n_y + q + \alpha(T - T_\infty) = 0 \tag{A3}$$

and the following performance index J is minimized

$$J = \frac{1}{2} \int_D [(T - T_0)^2 + \beta_1 (k_1 - k_{01})^2 + \beta_2 (k_2 - k_{02})^2] dD \tag{A4}$$

where β_1 and β_2 are weighting parameters; k_{01} and k_{02} are the desired levels of k_1 and k_2, respectively, and n_x and n_y are the direction cosines.

Necessary Conditions of Optimality. By using calculus of variations the necessary optimum conditions can be derived similar to the isotropic case. Together with the T-problem (equations (A1-A3)) these optimum conditions are given as follows.

The λ-problem:

$$\text{in } D: \frac{\partial}{\partial x}\left(k_1 \frac{\partial \lambda}{\partial x}\right) + \frac{\partial}{\partial y}\left(k_2 \frac{\partial \lambda}{\partial y}\right) + T - T_0 = 0 \tag{A5}$$

$$\text{on } S_1: \lambda = 0$$

$$\text{on } S_2: k_1 \frac{\partial \lambda}{\partial x} n_x + k_2 \frac{\partial \lambda}{\partial y} n_y + \alpha \lambda = 0 \tag{A7}$$

The gradient conditions:

$$\text{in } D: \beta_1 (k_1 - k_{01}) - \frac{\partial \lambda}{\partial x} \frac{\partial T}{\partial x} = 0 \tag{A8}$$

$$\text{in } D: \beta_2 (k_2 - k_{02}) - \frac{\partial \lambda}{\partial y} \frac{\partial T}{\partial y} = 0 \tag{A9}$$

It may be noted that since there are two control functions k_1 and k_2 there exist two gradient conditions (A8) and (A9), which indicate the sensitivities of J with respect to k_1 and k_2, respectively.

V. W. Antonetti
Manager,
Advanced Thermal Laboratory,
International Business Machines Corporation,
Data Systems Division,
Poughkeepsie, N.Y.
Mem. ASME

M. M. Yovanovich
Professor,
Department of Mechanical Engineering,
Thermal Engineering Group,
University of Waterloo,
Ontario, Canada
Mem. ASME

Enhancement of Thermal Contact Conductance by Metallic Coatings: Theory and Experiment

A thermomechanical model for nominally flat, rough contacting surfaces coated with a metallic layer is developed. The model is shown to agree quite well with thermal test data obtained using nickel specimens, with one side of the contact coated with silver and the other side glass-bead blasted. In addition, it is demonstrated that a coated joint can be reduced to an equivalent bare joint by employing an effective hardness and an effective thermal conductivity. Using this technique, 61 coated test points were correlated, with an RMS difference of ±12.6 percent between the data and a correlation which had previously been used only for bare contacts.

Introduction

The success of a thermal design often requires that the heat transfer coefficient across an interface be enhanced, that is, improved over the bare joint situation. Techniques commonly employed include the application of a thermal grease to the contacting surfaces [1, 2], insertion of a soft metal foil at the interface [3, 4], and coating one or both of the contacting surfaces with a relatively soft metal [2, 5, 6].

Metallic coatings are an important enhancement alternative because a user can avoid the handling problem often associated with soft foils, and the contamination problem which often makes chemically active thermal greases objectionable. Despite the importance of metallic coatings, however, the only attempt to develop an overall thermomechanical model is by O'Callaghan et al. [5]. They also conducted experiments on abutting stainless steel specimens, where one side of the interface was coated with tin. Because their test apparatus was severely underpowered, the reported interface temperature differences were extremely small, casting doubt on the reliability of the data. Furthermore, the model of O'Callaghan et al. does not predict their own data very well.

A solution for only the *thermal portion* of a coated contact, albeit with different boundary conditions, has been described in [7, 8]. The constriction resistance was determined for a finite cylindrical flux tube with a hot spot located on a layer and a Robin condition specified at the end opposite the contact. However, the complications introduced by the boundary condition of the third kind are not required in the present application, and therefore, the thermal problem remains to be solved using more appropriate boundary conditions.

With regard to the *mechanical portion*, thermal contact resistance correlations for bare surfaces, for example [9], require as input the microhardness of the softer material. It is reasonable to assume in enhancement situations that the softer of the two contacting surfaces will be the metallic layer. Clearly, when the layer is very thick the microhardness to employ would be that of the layer. As the layer thickness decreases it is equally clear that the microhardness will increase, approaching the microhardness of the substrate as the layer thickness approaches zero. But what of the intermediate condition? Although analytical studies have been done regarding elastic contact stress in layers [10], no relevant analysis could be found relating to the equivalent plastic situation.

Contributed by the Heat Transfer Division for publication in the JOURNAL OF HEAT TRANSFER. Manuscript recevied by the Heat Transfer Division March 1, 1984.

The purpose of the present work, therefore, is to develop a thermomechanical model for the prediction of the contact conductance of nominally flat, rough surfaces enhanced with a metallic coating, and to verify the theory by experiment.

Theoretical Analysis

Before beginning, it is appropriate to state the assumptions inherent in the analysis that will follow:

1 Contacting surfaces are clean, free of oxides, etc., and contact occurs in a vacuum. Radiation across the interface and conduction across the interstitial gaps are negligible.

2 Contacting surfaces are microscopically rough but macroscopically flat and have a Gaussian height distribution.

3 In general, the real pressure between contacting surfaces is equal to the microhardness of the softer material. When either of the contacting surfaces is coated with a soft metal, the real pressure between the surfaces is equal to the "effective microhardness" of the layer-substrate combination. (More will be said of this later.)

4 The real contact area consists of circular, isothermal, microcontact spots which are distributed uniformly over the apparent area. When a layer is present, the contact is also assumed to be a circular spot, but now residing on the top of the layer. In other words, penetration of the harder surface into the layer, which undoubtedly occurs to some extent, is ignored to simplify the subsequent thermal analysis. This is at least partially justifiable on the basis of [11] wherein solutions were obtained for the constriction resistance of numerous symmetric and nonsymmetric, singly connected, planar geometries. The conclusion of the latter study was that the constriction resistance of an arbitrary contact was approximately equal to a circular contact of equal area. It is assumed that this conclusion would also apply to arbitrary contact shapes on a layer.

5 The contact between the layer and the substrate is "perfect." It has been shown [12] that the resistance of a so-called perfect joint is about two orders of magnitude less than the constriction resistance expected here.

6 When a surface is coated, the surface characteristics are the same as the underlying substrate [6].

Uncoated Contacting Surfaces. Clearly the development of a predictive model for coated contacts will be based, in large measure, on what is known about bare contacts. With the assumptions already made, the heat transfer across a bare joint will be confined to the discrete microcontacts formed by the contacting asperities. If a total of N circular microcontacts, having a mean radius a, are distributed over the apparent contact area, we can write the joint resistance as [9]

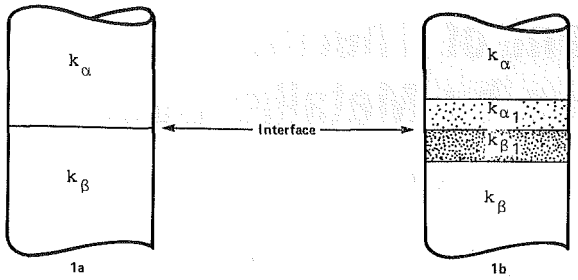

Fig. 1 Contact of bare and coated joint

$$R_j = \frac{1}{N}\left[\frac{\psi(\epsilon)}{4k_\alpha a} + \frac{\psi(\epsilon)}{4k_\beta a}\right] \tag{1}$$

where k_α and k_β are the thermal conductivities of the contacting surfaces shown in Fig. 1(*a*).

The constriction parameter $\psi(\epsilon)$ has been evaluated by several authors [13–16]. In [17] it was shown that the constriction parameter can also be approximated by the following power law correlation

$$\psi(\epsilon) = 0.76\left(\frac{P}{H}\right)^{-0.027} \tag{2}$$

where the error is ±1 percent in the range $10^{-4} \le P/H \le 10^{-2}$. An expression for the mean contact spot radius was derived in [16], which, as shown in [17], can be approximated using the following power law correlation

$$a = 0.77\left(\frac{\sigma}{m}\right)\left(\frac{P}{H}\right)^{0.097} \tag{3}$$

where the error is ±4.5 percent in the range $10^{-4} \le P/H \le 10^{-2}$. A simple force balance at the contacting surface can be used to determine the total number of microcontacts per unit area as

$$\frac{N}{A_a} = \frac{1}{\pi a^2}\left(\frac{P}{H}\right) \tag{4}$$

By substituting equation (4) into equation (1), and noting that the resistance is the reciprocal of the product of the joint conductance and the apparent contact area, the general expression for the thermal conductance across a bare interface becomes

$$\frac{1}{h_j} = \frac{\pi a}{4}\left(\frac{H}{P}\right)\left[\frac{\psi(\epsilon)}{k_\alpha} + \frac{\psi(\epsilon)}{k_\beta}\right] \tag{5}$$

Coated Contacting Surfaces. When a joint is coated, the effective microhardness H' of the layer-substrate combination will, of course, be different from that of a bare joint. This results in a change in the total number of microcontact spots needed to support the load, in a different contact spot radius a', and a different constriction parameter $\psi(\epsilon', \phi_n)$. In this case, the constriction parameter not only depends upon the relative mean contact spot size ϵ', but also upon a modification factor ϕ_n, which is some function of the relative layer thickness τ and substrate-to-layer thermal conductivity ratio K.

By referring to Fig. 1(*b*), an expression for the thermal contact conductance across a joint with a layer on both sides of the contact can be obtained by rewriting equation (5) as

$$\frac{1}{h_j'} = \frac{\pi a'}{4}\left(\frac{H'}{P}\right)\left[\frac{\psi(\epsilon', \phi_{n_\alpha})}{k_\alpha} + \frac{\psi(\epsilon', \phi_{n_\beta})}{k_\beta}\right] \tag{6}$$

Equation (6) can be cast in a more convenient form by introducing a constriction parameter correction factor defined as the ratio of the constriction parameter with a layer to that without a layer, for the same value of the relative contact radius, that is $C = \psi(\epsilon', \phi_n)/\psi(\epsilon')$. Then equation (6) becomes

$$\frac{1}{h_j'} = \frac{\pi a'}{4}\left(\frac{H'}{P}\right)\psi(\epsilon')\left[\frac{C_\alpha}{k_\alpha} + \frac{C_\beta}{k_\beta}\right] \tag{7}$$

Using the approximation for the constriction parameter given by equation (2), and the approximate expression for the contact spot radius equation (3), we obtain the following ratios:

$$\frac{\psi(\epsilon)}{\psi(\epsilon')} = \left(\frac{H}{H'}\right)^{0.027} \tag{8}$$

and

$$\frac{a}{a'} = \left(\frac{H'}{H}\right)^{0.097} \tag{9}$$

Now, we divide equation (5) by equation (7), and substitute into the resulting expression equations (8) and (9). After rearrangement this yields

$$h_j' = h_j\left(\frac{H}{H'}\right)^{0.93}\left[\frac{k_\alpha + k_\beta}{C_\alpha k_\beta + C_\beta k_\alpha}\right] \tag{10}$$

Inspection of equation (10) reveals that the contact conductance of a joint with a layer on both sides of an interface is equal to the bare joint conductance multiplied by two terms: The first term will be defined as a mechanical augmentation factor, and the second as a thermal augmentation factor.

Coated Contacting Surfaces (Alternate Analyis). Referring again to Fig. 1(*b*), we can also obtain the thermal contact resistance for a joint when a layer is presented by rewriting equation (1), with the primed quantities being associated with

Nomenclature

a = contact spot radius
A = area
b = flux tube radius
C = constriction parameter correction factor
d = equivalent Vickers indentation depth
H = Vickers microhardness
H' = effective microhardness of soft layer on harder substrate
h = thermal contact conductance
J_n = Bessel function, first kind, order n
K = thermal conductivity ratio (substrate to layer)
k = thermal conductivity
k' = effective thermal conductivity
m = combined average absolute asperity slope = $\sqrt{m_\alpha^2 + m_\beta^2}$
N = number of contact spots in apparent area A_a
P = apparent contact pressure
R = thermal resistance
t = layer thickness
γ_n = constriction parameter modification factor attributable to contact temperature basis
λ_n = eigenvalues
ϵ = relative mean contact spot radius = $a/b = \sqrt{P/H}$
δ_n = roots of $J_1(\delta_n) = 0$
ρ_n = constriction parameter modification factor attributable to heat flux distribution
σ = combined RMS roughness = $\sqrt{\sigma_\alpha^2 + \sigma_\beta^2}$
τ = relative layer thickness = (t/a)
ϕ_n = constriction parameter modification factor attributable to the layer
$\psi(\epsilon)$ = constriction parameter

Superscripts

$'$ = layer

Subscripts

a = apparent
c = contact or constriction
j = joint
L = layer
s = substrate
v = Vickers
α = one side of contact
β = other side of contact

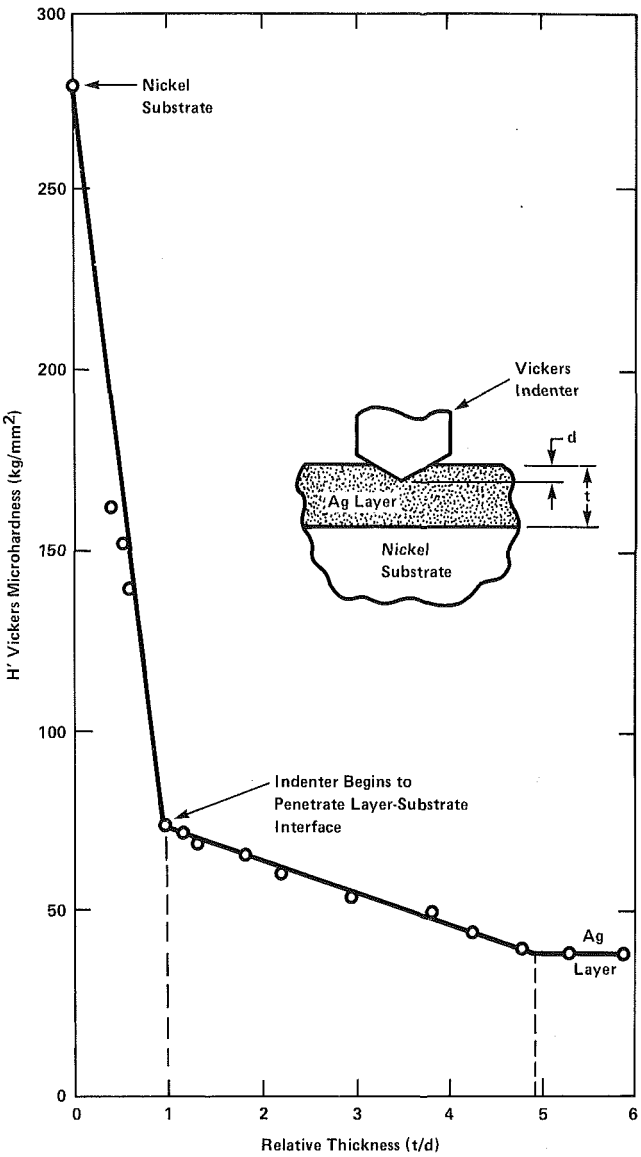

Fig. 2 Vickers microhardness of silver layer on nickel substrate

the layers. When the definition of the constriction parameter correction factor is accounted for, the result is

$$R_j' = \frac{\psi(\epsilon')}{4N'a'}\left[\frac{C_\alpha}{k_\alpha} + \frac{C_\beta}{k_\beta}\right] \tag{11}$$

Now an effective thermal conductivity is defined as

$$k' = \frac{2k_\alpha k_\beta}{C_\alpha k_\beta + C_\beta k_\alpha} \tag{12}$$

Then the contact resistance for a coated joint reduces to

$$R_j' = \frac{\psi(\epsilon')}{2a'N'k'} \tag{13}$$

where a' is given by equation (3) and N' by equation (4). Note that both quantities depend on the effective microhardness H'.

Equation (13) yields numerical results identical to equation (10), but has the same algebraic form as the equivalent expression for the contact resistance of a bare joint. This has the advantage of allowing a direct numerical comparison of the parameters that contribute to the contact resistance for both the bare and coated cases.

Regardless of which of the two previous analytical approaches is used, in order to determine the theoretical contact conductance for a coated joint, the effective microhardness of the particular layer–substrate combination being considered must be evaluated by mechanical analysis or by experimental means, and a thermal analysis must be performed to determine the constriction parameter correction factor due to the layer.

Thermal Analysis of a Coated Contact. The thermal portion of the analysis requires the solution of Laplace's equation for heat flow from a single concentric circular hot spot residing on a layer at the end of an infinite right circular cylinder whose walls are adiabatic. The complete solution is presented in [17]. In summary, the constriction parameter (for example on the α side) is first defined as

$$\psi(\epsilon', \phi_n) = 4k_\alpha a' R_c' \tag{14}$$

Then, after determining the constriction resistanace R_c', using an approach similar to [7, 8], the constriction parameter for a coated contact is shown to be

$$\psi(\epsilon', \phi_n) = \frac{16}{\pi\epsilon'} \sum_{n=1}^{\infty} \frac{J_1^2(\delta_n'\epsilon')}{(\delta_n')^3 J_0^2(\delta_n')} \phi_n \cdot \gamma_n \cdot \rho_n \tag{15}$$

Equation (15) is nothing more than the expression for the dimensionless constriction parameter for a bare contact, with a uniform heat flux at the contact and the resistance based on the average contact temperature, as derived in [15], multiplied by three modification factors.

The first modification factor ϕ_n accounts for the influence of the layer; the second γ_n accounts for the contact temperature basis used in determining the constriction resistance (average, isothermal or centroidal); and the third ρ_n accounts for the contact heat flux distribution assumed.

For abutting surfaces, it is usual to assume that the contact spots are isothermal. The modification factors in this case are $\gamma_n = 1$, and

$$\phi_n = K\left[\frac{(1+K) + (1-K)\exp(-2\delta_n'\epsilon'\tau')}{(1+K) - (1-K)\exp(-2\delta_n'\epsilon'\tau')}\right] \tag{16}$$

and

$$\rho_n = \frac{\sin(\delta_n'\epsilon')}{2J_1(\delta_n'\epsilon')} \tag{17}$$

The constriction parameter correction factor is now obtained by dividing the constriction parameter with a layer present, that is equation (15), by an expression for the constriction parameter without a layer, that is equation (15) with $\phi_n = 1$. The reader is referred to [17] for a tabulation of numerical values.

Mechanical Analysis of a Coated Joint. In the following discussion, a methodology is outlined which allows the determination of the effective microhardness H' of a soft metallic layer on a harder substrate. The approach is semiempirical.

Vickers Microhardness Distribution. Figure 2 shows the results of Vickers microhardness measurements performed on Nickel 200 specimens with differing vapor-deposited silver coating thickness. (This is the layer–substrate combination used in the thermal tests described in the next section.) Several other layer–substrate combinations were tested as well, and all exhibited similar characteristic curves. The results are contained in [17].

The open literature reveals no similar research in this area. The search for a physical explanation of observed results leads to the work of Mulhearn [18]. By plotting equal strain contours under indenters, Mulhearn showed that material is displaced radially outward from the indentation. This suggests the following interpretation of the microhardness data from the present study. By referring to Fig. 2, it can be seen that in the region $t/d > 4.9$, the effective microhardness equals the layer microhardness. In this case, the indenter and the elastic–plastic boundary are wholly within the layer. In the intermediate region $1.0 \leq t/d \leq 4.9$, the indenter is still

totally within the layer but the elastic-plastic boundary has expanded to the point where it is distorted by the underlying harder substrate, and because of this the effective microhardness gradually increases. At $t/d = 1.0$, the indenter has penetrated the layer and is influenced directly by the underlying substrate. As a consequence, the slope of the curve changes abruptly and the effective microhardness increases until it reaches the substrate microhardness value at $t/d = 0$.

Effective Microhardness. Rather than a single indenter, let us now consider a multiplicity of indenters, as when a hard, rough surface is put in contact with a softer layer. What is proposed here is that the effective microhardness for this situation can be determined from a Vickers microhardness curve appropriate for the materials combination, such as for silver on nickel, as shown in Fig. 2. With this assumption, the following effective microhardness equations are obtained from Fig. 2. In the region $t/d < 1.0$

$$H' = H_s\left(1 - \frac{t}{d}\right) + 1.81\, H_L\left(\frac{t}{d}\right) \tag{18}$$

and in the region $1.0 \le t/d \le 4.9$

$$H' = 1.81\, H_L - 0.208\, H_L\left(\frac{t}{d} - 1\right) \tag{19}$$

When $t/d > 4.90$ the effective microhardness equals the layer microhardness.

In equations (18) and (19), d is the equivalent Vickers indentation depth of the harder contacting surface. In order to determine d, it is necessary to understand how a Vickers indentation is determined from microhardness measurements.

When a Vickers indenter is pressed into a surface it leaves a square indentation. By geometry the indentation depth is equal to the measured half-diagonal a_v multiplied by the slope of the Vickers indenter m_v, i.e., $d = m_v a_v$. But the asperities of an actual indenting hard, rough surface have an average asperity radius a and an average slope m. So in order to use Fig. 2 the average asperity indentation depth must be adjusted to an equivalent Vickers depth. This is accomplished by first setting the cross-sectional area of the contacting asperity equal to the projected area of a Vickers indentation; that is $a_v = a\sqrt{\pi/2}$. Now, combining the simple relationships immediately preceding, and substituting equation (3) for the asperity contact radius yields

$$d = 0.77\sqrt{\frac{\pi}{2}}\left(\frac{m_v}{m}\right)\sigma\left(\frac{P}{H'}\right)^{0.097} \tag{20}$$

Next, one has a choice of letting the asperity slope m in equation (20) remain a variable, or of fixing it at the Vickers value of 0.286. (The asperity slopes for the experimental portion of this work ranged from 0.129 to 0.350.) The thermomechanical model was compared to experimental data using both alternatives. Since neither of the alternatives consistently predicted the data better than the other, it was decided to fix the slope at the Vickers value because this minimized the overall RMS difference between the model and the data. This is equivalent to assuming, in equation (20), that $m_v/m = 1.0$. Implicit in this assumption is that Vickers indenters with slopes in the range cited will produce an effective microhardness curve identical to Fig. 2. With this assumption, equation (20) becomes

$$d = 0.97\,\sigma\left(\frac{P}{H'}\right)^{0.097} \tag{21}$$

It is interesting to note that the indentation depth is primarily dependent on the RMS roughness of the indenting surface and is a weak function of P/H'. In addition, because the indentation depth depends upon the effective microhardness, and the depth must be known to determine the effective microhardness, an iterative approach is required. Convergence is very rapid, however, because the indentation depth is such a weak function of the effective microhardness.

Table 1 Test specimen characteristics

Series	Specimens	Bare σ	Bare m	Coated σ	Coated m	t
A	08/09	4.29	0.239	0.16	0.025	0.0
	10/11	4.27	0.236	0.17	0.024	0.0
	12/13	4.06	0.231	0.19	0.030	1.4
	14/15	4.24	0.233	0.20	0.031	5.1
	16/17	4.45	0.252	0.27	0.038	39.5
	18/19	4.38	0.232	0.14	0.022	0.81
	22/23	4.19	0.224	0.21	0.027	1.2
	Average	4.26	0.234	0.19	0.028	
	Series A combined values: $\sigma = 4.27$, $m = 0.236$					
B	24/25	1.24	0.129	0.17	0.025	1.2
	26/27	1.21	0.137	0.19	0.024	0.0
	36/37	1.30	0.140	0.14	0.018	6.3
	Average	1.27	0.135	0.155	0.022	
	Series B combined values: $\sigma = 1.28$, $m = 0.137$					
C	28/29	8.62	0.350	0.14	0.018	2.4
	30/31	8.31	0.338	0.17	0.025	7.2
	32/33	8.03	0.348	0.19	0.024	18.0
	34/35	8.48	0.344	0.14	0.018	0.0
	Average	8.32	0.345	0.17	0.022	
	Series C combined values: $\sigma = 8.32$, $m = 0.346$					

Specimen material: Nickel 200
Cross-sectional area: 0.000641 m^2
σ = RMS roughness, μm
m = average absolute asperity slope, radians
t = coating thickness, μm

Averages consider only coated specimen pairs.
Combined values are for an equivalent rough surface against a perfect smooth.

Regarding the substrate microhardness H_S in equation (18) it should be noted that manufacturing processes such as lapping produce a surface microhardness layer. In these cases, it has been demonstrated [19, 20] that the use of the bulk microhardness for predicting contact conductance is incorrect. Instead, the method outlined in [19, 20] should be used to determine an appropriate microhardness value for the substrate.

Application of Theoretical Model. The reader is referred to [21] where the utility of the model developed here is illustrated by using it to analyze a common electronics packaging problem: heat transfer across a coated aluminum joint.

Experimental Program

Coated contact resistance test data in the open literature were found to be either unreliable [5], or to have inadequate test specimen surface characterization [2, 6]. An experimental program was undertaken, therefore, in order to generate test data against which to compare the theoretical model.

Specimens, Properties, and Test Parameters. Test specimens, fabricated from a single Nickel 200 rod, were finished to 28.6 mm diameter by 31.8 mm long, with both ends lapped smooth to a flatness deviation less than 1 μm. The specimens were tested in pairs, with one of the pair treated further by glass-bead blasting one end to a specified roughness. The other specimen was either left bare or had a layer of silver vapor deposited on one end. The characteristics of the test specimens are shown in Table 1. As shown in Table 1, three groups of test specimens were tested. The first, designated Series A, had a combined (or equivalent) surface roughness of 4.27 μm. Series B had a combined roughness of 1.28 μm, and the final group, Series C, had a combined roughness of 8.32 μm.

Details of the contact resistance test apparatus and the test procedure have been fully described elsewhere [17, 20]. In brief, contact resistance measurements were made in a vacuum chamber. The direction of heat flow was from the

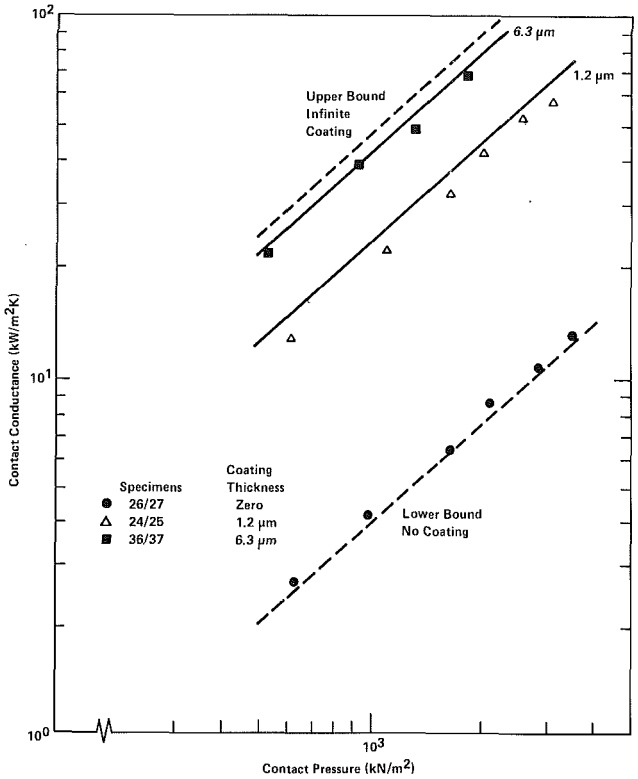

Fig. 3 Test results: contact conductance versus pressure (σ = 1.28 μm)

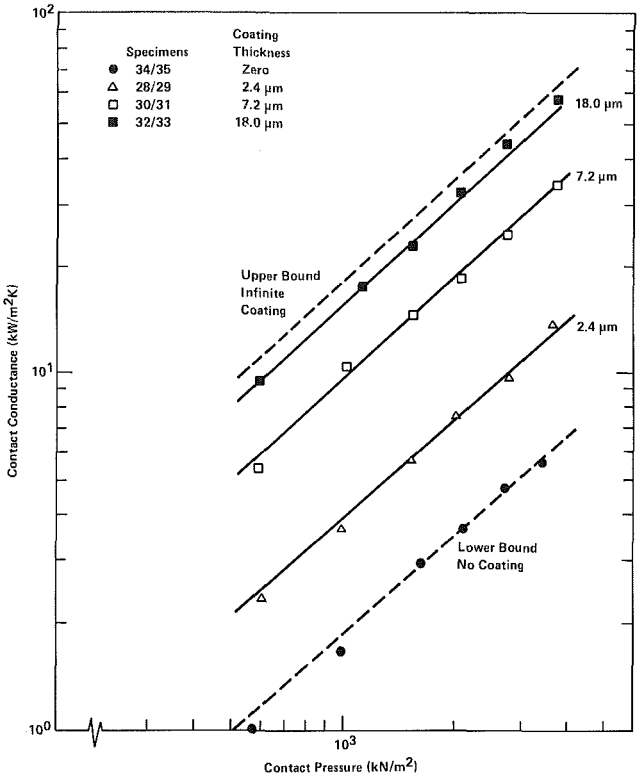

Fig. 5 Test results: contact conductance versus pressure (σ = 8.32 μm)

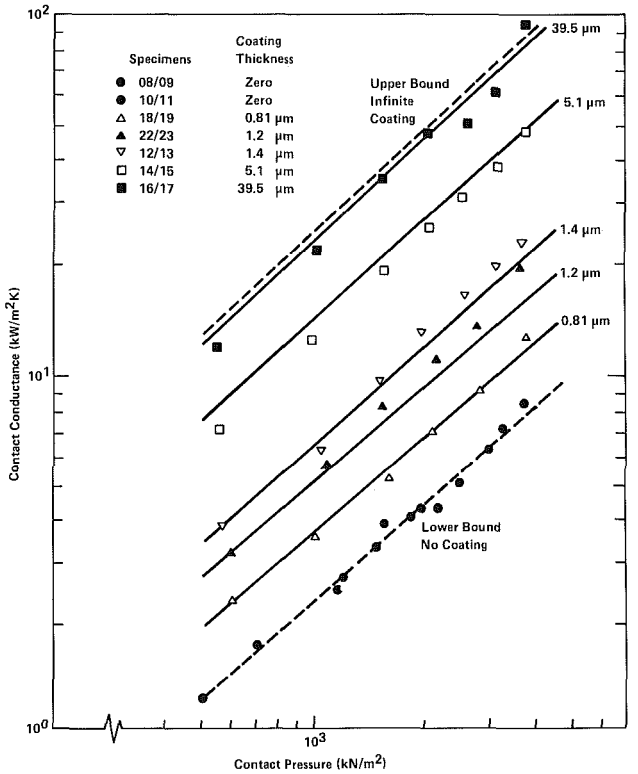

Fig. 4 Test results: contact conductance versus pressure (σ = 4.27 μm)

bare, glass-bead-blasted upper specimen to the silver-coated lower specimen. The range of the experimental parameters was approximately as follows: The heat flux varied from 2000 to 7000 kW/m^2; the contact pressure from 500 to 3700 kN/m^2; the interfacial temperature differences from 1.7 to 50°C (it should be noted that the majority of the temperature differences were greater than 10°C); and the mean interface temperature varied from 85 to 206°C. The experimental error in the test setup was estimated to be ±4.5 percent.

Initially, thermal tests were conducted on the bare specimens, which can be considered the zero layer thickness case, or in other words the lower bound on the coated contact conductance. The test results for the bare joints have been previously reported in [21]. In summary, the agreement between the bare joint test data and Yovanovich's correlation [9] was excellent, with the RMS difference being only ±5.6 percent, provided the appropriate effective surface microhardness for the lapped surface is employed in the relative load expression.

Comparison of Coated Specimen Data Versus Model. For the coated test specimens, test results are compared to the proposed thermomechanical model, given by equation (10), in Figs. 3–5. It should be noted that the line representing the predicted performance for each specimen pair was computed using thermophysical properties determined as follows: First, contact temperatures for a given upper and lower specimen pair were determined at each test point. Next, average contact temperatures were calculated using the test data for all the runs experienced by the specimen pair. Then, based on these average contact temperatures, the thermal conductivity for the nickel substrates of the upper and lower specimens and for the silver layer were determined. The effective microhardness, on the other hand, was based on room temperature Vickers microhardness measurements. This is justified by test data [17, 22] which indicated that significant softening of the silver layer did not occur at the contact temperature levels in the present experiment.

The RMS difference between the theoretical model and the experimental results is as follows: Series A: ±11.3 percent, Series B: ±7.5 percent, and Series C: ±6.9 percent.

Figure 3 presents a plot of the contact conductance versus test pressure for Series B experiments, that is for the set of specimens with a combined surface roughness of 1.28 μm. As can be seen from Fig. 3, the coated contact conductance is

Table 2 Summary of calculated theoretical parameters and contact resistances for specimens at test pressure of approximately 2000 kN/m²

	P	t	t/d	H'	$\psi(\epsilon')$	C	k'	a'	N'	R'
Series B: Average Roughness = 1.28 μm										
26/27	2105	0.0	0.0	360.0	0.9636	1.000	64.5	3.3	11200	0.2025
24/25	2032	1.2	1.77	65.9	0.9171	0.428	87.7	4.2	36500	0.0342
36/37	1817	6.3	9.40	40.0	0.8996	0.198	103.9	4.3	52900	0.0194
Series A: Average roughness = 4.27 μm										
08/09	1925	0.0	0.0	300.0	0.9619	1.000	67.2	6.8	2930	0.3619
18/19	2055	0.8	0.38	214.0	0.9534	0.644	80.5	7.4	3660	0.2189
22/23	2107	1.2	0.57	169.9	0.9471	0.565	84.0	7.5	4600	0.1636
12/13	1922	1.4	0.68	144.2	0.9452	0.518	84.7	7.1	5530	0.1424
14/15	2005	5.1	2.19	62.4	0.9154	0.291	97.4	8.0	10500	0.0561
16/17	1990	39.5	17.10	40.0	0.8951	0.159	107.2	8.1	15900	0.0325
Series C: Average roughness = 8.32 μm										
34/35	2080	0.0	0.0	280.0	0.9590	1.000	67.1	9.4	1730	0.4364
28/29	1990	2.4	0.55	164.8	0.9478	0.480	86.9	9.9	2540	0.2145
30/31	2023	7.2	1.58	67.5	0.9182	0.287	97.7	10.8	5380	0.0811
32/33	2027	18.0	3.96	47.8	0.9030	0.190	105.1	10.5	8070	0.0509

Note: P = pressure, kN/m²
t = layer thickness, μm
t/d = dimensionless indentation depth
H' = effective hardness, kg/mm²
$\psi(\epsilon')$ = constriction parameter
C = constriction parameter correction factor
k' = effective thermal conductivity, W/m K
a' = contact spot radius, μm
N' = total number of microcontacts
R' = theoretical contact resistance, K/W

bounded by the bare joint, or zero layer thickness line (the lower bound), and by the infinitely thick silver layer case (the upper bound). There is approximately one order of magnitude between the two bounds.

Figure 4 is for Series A experiments, that is for the set of specimens with a combined surface roughness of 4.27 μm. In this case, a 1.2-μm layer thickness is seen to improve the contact conductance to a much lesser degree than for the comparable layer thickness in Fig. 3. Indeed, the relative enhancement effect for all the specimens tested in this series is not as pronounced as for those tested against the smoother surfaces in Fig. 3.

As can be seen in Fig. 5 (Series C: 8.32 μm combined roughness), the general tendency is the same, that is for a given layer thickness the relative improvement is less than is observed for the smoother 1.28 and 4.27-μm cases. This is attributed to the fact that a rough surface penetrates the layer more deeply than would a smoother contacting surface, and hence is more affected by the harder substrate under the layer, which results in a higher effective microhardness and, in turn, a lower contact conductance. This leads to the general conclusion that a given layer thickness will have more of an enhancement effect as the roughness of the bare contacting surface is decreased.

It is interesting to examine the parameters involved in the calculation of the theoretical contact resistance for all the specimens tested. Table 2 summarizes the results of such a calculation. Since all the computations were performed at the same approximate test pressure, the test specimen pairs differ only in the texture of the bare contacting surface and in the thickness of the metallic layer. From the table, it is seen that the effective microhardness H' diminishes quite rapidly as the layer thickness increases. As expected, for a given layer thickness, the lowest effective microhardness value occurs when the layer is in contact with the smoothest abutting surface. Table 2 also shows that the contact spot radius a' is determined primarily by the surface texture and influenced in only a minor way by the layer thickness. Since the mechanical load is about the same for all the specimens, as the contact

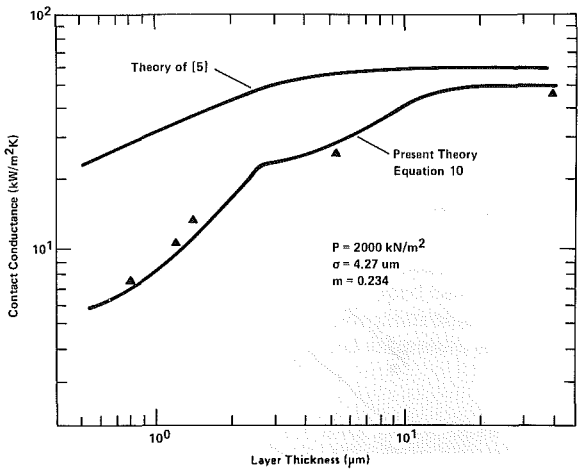

Fig. 6 Comparison of present theory and experimental data with theory of O'Callaghan et al. [5]

spot size decreases the number of contacts must increase in order to support the load. Further inspection of Table 2 reveals that the constriction parameter correction factor C and the resulting effective thermal conductivity k' are strongly dependent on the layer thickness, with only a slight dependence on the surface texture.

As mentioned previously, the only other model available against which the test results from this study can be compared is that of O'Callaghan et al. [5]. Figure 6 shows that the present theory predicts the test data from this work far better than the O'Callaghan et al. model.

Contact Correlation of Coated Specimen Test Data. The contact correlation for coated contacting surfaces is developed as follows. The bare contact conductance from Yovanovich's correlation [9] is substituted into equation (10) yielding

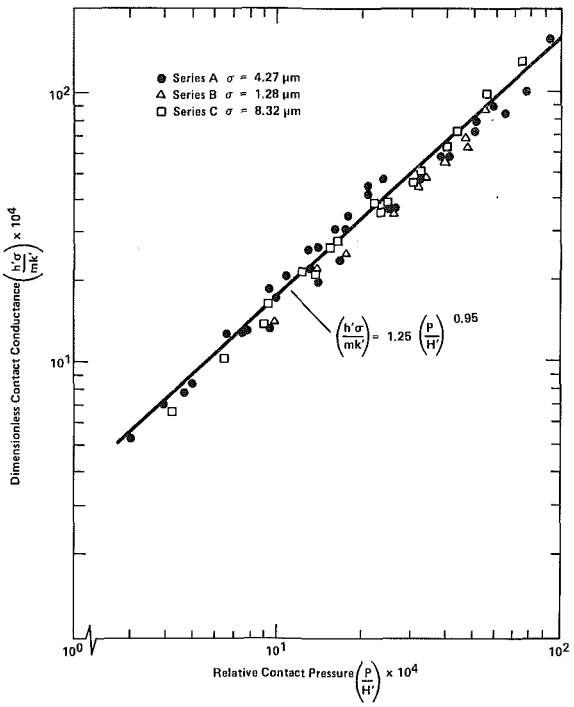

Fig. 7 Test results: dimensionless conductance versus relative pressure for coated contacting surfaces

$$h_j' = \left[1.25\left(\frac{m}{\sigma}\right)\left(\frac{2k_\alpha k_\beta}{k_\alpha + k_\beta}\right)\left(\frac{P}{H}\right)^{0.95}\right]\cdot \left(\frac{H}{H'}\right)^{0.93}\left(\frac{k_\alpha + k_\beta}{C_\alpha k_\beta + C_\beta k_\alpha}\right) \tag{22}$$

which reduces to

$$h_j' = 1.25\left(\frac{m}{\sigma}\right)\left(\frac{P}{H'}\right)^{0.95}\left(\frac{H'}{H}\right)^{0.02} k' \tag{23}$$

Now $(H'/H)^{0.02}$ is set equal to unity, essentially neglecting this term on the basis that the error introduced will be minimal. Equation (23) then simplifies to

$$\frac{h_j'\sigma}{mk'} = 1.25\left(\frac{P}{H'}\right)^{0.95} \tag{24}$$

Equation (24) for coated contacts is identical to the correlation for bare contacts given in [9], except that an effective thermal conductivity and an effective microhardness have replaced the usual values used for a bare joint.

Figure 7 shows that all coated test data correlate very well using equation (24). The overall RMS error for all coated data points is ±12.6 percent. In other words, using an effective microhardness and an effective thermal conductivity, the coated test data were correlated by [9] which had previously been used only for bare contacts. The implication is that a coated joint can be reduced to an equivalent bare joint by employing an effective microhardness and an effective thermal conductivity.

Conclusions

Based on this research, the major conclusions reached are: The thermomechanical model developed herein predicts the thermal contact conductance of the silver-coated contacting surfaces tested quite well; that a coated joint can be reduced to an equivalent bare joint by using the concepts of effective microhardness and effective thermal conductivity; and this then enables coated test data to be correlated by means of a correlation [9] developed for bare joints.

It is further concluded that a silver layer can enhance the thermal contact conductance of nominally flat, rough, contacting nickel specimens by as much as an order of magnitude; and that for a given layer thickness, the smoother the bare contacting surface the greater the enhancement will be.

Finally, is should be noted that this research applies only to nominally flat surfaces and is not applicable to nonflat contacting surfaces. In addition, a limited material set was tested, and although we believe the methodology presented is applicable to other materials, this has not been demonstrated.

Acknowledgments

M. M. Yovanovich acknowledges the partial support of the National Science and Engineering Research Council of Canada, under operating grant A7445.

References

1 Fry, E. M., "Measurements of Contact Coefficients of Thermal Conductance," AIAA 65-662, AIAA Thermophysics Specialists Conference, Monterey, CA, Sept. 1965.

2 Fried, E., and Kelley, M. J., "Thermal Conductance of Metallic Contacts in a Vacuum," AIAA-65-661, AIAA Thermophysics Specialists Conference, Monterey, CA, Sept. 1965.

3 Cunnington, G. R., Jr., "Thermal Conductance of Filled Aluminum and Magnesium Joints in Vacuum Environment," ASME Paper No. 64-WA/HT-40, 1964.

4 Molgaard, J., and Smelter, W. W., "The Thermal Contact Resistance at Gold Foil Surfaces," *Int. J. Heat Mass Transfer*, Vol. 13, 1970, pp. 1153-1162.

5 O'Callaghan, P. W., Snaith, B., Probert, S. D., and Al-Astrabadi, F. R., "Prediction of Interfacial Filler Thickness for Minimum Thermal Contact Resistance," *AIAA Journal*, Vol. 21, No. 9, Sept. 1983, pp. 1325-1330.

6 Mal'kov, V. A., and Dobashin, P. A., "The Effect of Soft-Metal Coatings and Linings on Contact Thermal Resistance," *Inzhenerno-Fizicheskii Zhurnal*, Vol. 17, No. 5, Nov. 1969, pp. 871-879.

7 Kharitonov, V. V., Kozhosev, L. S., and Tyurin, Y. A., "Effect of Thermal Conductivity of Surface Layer on Contact Thermal Resistance," *Atomnaya Energiya*, Vol. 36, No. 4, Apr. 1974, pp. 308-310.

8 Yovanovich, M. M., Tien, C. H., and Schneider, G. E., "General Solution of Constriction Resistance Within a Compound Disk," Presented as Paper 79-1178 at the AIAA 17th Aerospace Sciences Meeting, New Orleans, LA, Jan. 1979.

9 Yovanovich, M. M., "Thermal Contact Correlations," in: *AIAA Progress in Astronautics and Aeronautics: Spacecraft Radiative Transfer and Temperature Control*, ed. T. E. Horton, New York, 1982.

10 Chen, W. T., and Engle, P. A., "Impact and Contact Stress Analysis in Multilayer Systems," *Int. J. Solid Structures*, Vol. 8, 1972, pp. 1257-1281.

11 Yovanovich, M. M., Burde, S. S., and Thompson, J. C., "Thermal Constriction Resistance of Arbitrary Planar Contacts With Constant Flux," in: *AIAA Progress in Astronautics and Aeronautics, Thermophysics of Spacecraft and Outer Entry Probes*, ed. A. M. Smith, Vol. 56, New York, 1977, pp. 127-139.

12 Cecco, V. S., and Yovanovich, M. M., "Electrical Measurements of Joint Resistance at Perfect Contact Interfaces: Application to Joint Conductance," AIAA-72-19, AIAA 10th Aerospace Sciences Meeting, San Diego, CA, Jan. 1972.

13 Roess, L. C., "Theory of Spreading Conductance," Appendix to N. D. Weills, and E. A. Ryder, "Thermal Resistance Measurements on Joints Formed Between Stationary Metal Surfaces," presented at Semi-Annual ASME Heat Transfer Division meeting, Milwaukee, WI, 1948.

14 Mikic, B. B., and Rohsenow, W. M., "Thermal Contact Resistance," M.I.T. Heat Transfer Lab Report 4542-42, Sept. 1966.

15 Yovanovich, M. M., "General Expression for Circular Constriction Resistances for Arbitrary Heat Flux Distribution," in: *AIAA Progress in Astronautics and Aeronautics: Radiative Transfer and Thermal Control*, ed. A. M. Smith, Vol. 49, New York, 1976, pp. 301-308.

16 Cooper, M. G., Mikic, B. B., and Yovanovich, M. M., "Thermal Contact Conductance," *Int. J. Heat Mass Transfer*, Vol. 12, 1969, pp. 274-300.

17 Antonetti, V. W., "On the Use of Metallic Coatings to Enhance Thermal Contact Conductance," Ph.D. thesis, University of Waterloo, 1983.

18 Mulhearn, T. O., "The Deformation of Metals by Vickers-Type Pyramidal Indenters," *J. Mech. Phys. Solids*, Vol. 7, 1959, pp. 85-96.

19 Yovanovich M. M., Hegazy, A. H., and DeVaal, J., "Surface Hardness Distribution Effects Upon Contact Gap and Joint Conductances," AIAA-82-0887, Joint AIAA/ASME Heat Transfer, Fluids and Thermophysics Conference, St. Louis, MO, June 1982.

20 Yovanovich, M. M., Hegazy, A., and Antonetti, V. W., "Experimental Verification of Contact Conductance Models Based Upon Distributed Surface Micro-Hardness," AIAA-83-0532, AIAA 21st Aerospace Sciences Meeting, Reno, NV, Jan. 1983.

21 Antonetti, V. W., and Yovanovich, M. M., "Using Metallic Coatings to Enhance Thermal Contact Conductance of Electronic Packages," presented at 1983 ASME Winter Annual Meeting, Heat Transfer in Electronic Equipment Session, Boston, MA, November 1983.

22 Tamai, T., and Tsuchiya, T., "Direct Observation for the Effect Electric Current on Contact Interface," *Proceedings of the Ninth International Conference on Electric Contacts*, Chicago, IL, 1978, pp. 469-474.

A Method for the Solution of Heat Transfer Problems With a Change of Phase

D. Frederick

R. Greif

University of California,
Department of Mechanical Engineering,
Berkeley, CA 94720

A method of broad applicability is presented which can be used to obtain solutions to problems involving a phase change. The solution in one of the phases is specified as a known single-phase solution; an inverse analysis then determines the solution for the other phase. Two problems are studied: The first yields the similarity solution for the planar geometry and the second gives the exact solution to a more general problem. Convergence is shown and error bounds are given. The method can accommodate convection, heat generation, variable properties, nonplanar, and multidimensional systems.

1 Introduction

Transient heat conduction problems with freezing or solidification arise in many important technical applications. Although the equations governing such problems are often easily derived, the solution of these equations has proved to be difficult even for simple problems. These difficulties arise primarily because of the unknown location of the solid–liquid interface that renders the governing equations nonlinear.

In contrast to phase-change problems, single-phase conduction problems can be solved exactly for many geometries and boundary conditions. Useful results would be obtained if the compilation of single-phase solutions [1, 2] could be used to solve phase-change problems. To see how single-phase solutions can be used in this way, recall that the complexity of phase-change problems is primarily a result of the unknown location of the phase change. It is emphasized, however, that both the phase-change problem and the single-phase problem have the same governing equation, the diffusion equation. Thus, a phase-change problem can be solved by solving an equivalent single-phase problem with appropriately specified boundary conditions; that is, the boundary conditions chosen for the single-phase problem must mimic the effects of the phase change that are present in the phase-change problem. Boley's embedding technique [3] makes use of a similar concept. The embedding technique poses the problem directly: i.e., with the interface trajectory unknown and results in coupled integro-differential equations. The method proposed here, however, poses the problem inversely: i.e., the conditions at one boundary are unknown and the interface trajectory is known a priori. This yields simpler analytic results while exploring an area where there are few standard numerical codes available. Inverse phase-change problems arise in control-type applications: e.g., cryopreservation of organs, crystal growth, etc.

The method presented here proceeds by choosing a single-phase problem with a known exact solution $T_s(x, t)$. This solution yields a constant temperature T_F along a trajectory $x_F(t)$; i.e., $T_s(x_F, t) = T_F$. We now utilize this solution to construct a solution to an "equivalent" phase-change problem. Specifically, the phase-change problem would be defined by a known fusion temperature T_F that occurs on the trajectory $x_F(t)$ as given above and a known temperature profile in one of the phases; the single-phase solution $T_s(x, t)$ is assumed to equal the solution for the phase-change problem $T(x, t)$ in the region $x \geq x_F(t)$. This is consistent with the required condition

$$T(x_F(t), t) = T_s(x_F(t), t) = T_F$$

The temperature distribution in the region $0 \leq x \leq x_F(t)$ for the phase-change problem is unknown and is obtained by an inverse conduction analysis. When this solution is obtained, the phase-change problem is solved.

The first problem that is solved illustrates the method and yields Neumann's solution. In the second section, the method is used to solve a more general problem. Convergence criteria and error bounds of this solution are also presented.

2 Analysis

Consider a solid, $0 \leq x \leq H$, that is initially uniform at the temperature T_i. The temperature of the wall, at $x = 0$, is specified and exceeds the fusion temperature T_F. Therefore, melting occurs at an unknown position given by $x = x_F(t)$ (see Fig. 1), with a liquid region $0 \leq x \leq x_F(t)$, and a solid region $x_F(t) \leq x \leq H$. The problem formulation is

$$\frac{\partial T}{\partial t} = \alpha \frac{\partial^2 T}{\partial x^2} \quad \text{for } 0 \leq x \leq x_F(t), \text{ liquid} \tag{1a}$$

$$\frac{\partial T}{\partial t} = \alpha \frac{\partial^2 T}{\partial x^2} \quad \text{for } x_F(t) \leq x \leq H, \text{ solid} \tag{1b}$$

$$T(0,t) = T_w(t) \tag{1c}$$

$$T(H,t) = T_H(t) \tag{1d}$$

$$T(x_F,t) = T_F \tag{1e}$$

$$-k \frac{\partial T}{\partial x}\bigg|_L + k \frac{\partial T}{\partial x}\bigg|_S = \frac{\rho L dx_F}{dt} \quad \text{at } x = x_F(t) \tag{1f}$$

$$T(x,0) = T_i \tag{1g}$$

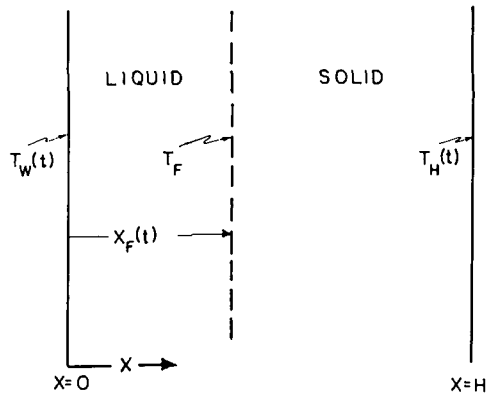

Fig. 1 Phase-change problem

Contributed by the Heat Transfer Division for publication in the JOURNAL OF HEAT TRANSFER. Manuscript received by the Heat Transfer Division October 21, 1983.

We write the solution for the solid region as

$$T(x,t) = T_s(x,t) \qquad x_F(t) \le x \le H \tag{2}$$

Here T_s may be viewed as the known solution to an *appropriate single-phase* problem, one that obeys the same condition at $x = H$; i.e., $T(H, t) = T_H(t)$ and $T(x, 0) = T_i$. The trajectory $x_F(t)$ is determined from $T_s(x_F(t), t) = T_F$. The task is to determine the temperature distribution in the liquid region, $0 \le x \le x_f(t)$.

The solution for the liquid region that will be compatible with a temperature distribution $T_s(x, t)$ in the solid region is obtained from a solution of the problem comprised of equations (1*a*), (1*e*), and (1*f*). This is an inverse conduction problem and the solution is (see Appendix A, equation (A15))

$$T(x,t) = T_s(x,t) + \frac{L}{c}\sum_{n=1}^{\infty} G_n\left(1 - \frac{x}{x_F}\right)^n, \quad 0 \le x \le x_F(t) \tag{3}$$

where the G_n are functions only of $x_F(t)$.

This result is valid for all constant property phase-change problems for the one-dimensional Cartesian geometry. Similar results can be derived for other geometries (see Appendix C).

To evaluate the G_n in equation (3) the trajectory $x_F(t)$ is needed. As stated above, this is obtained from the solution for the solid region at $x = x_F(t)$; i.e., $T_s(x_F,t) = T_F$ yields the trajectory $x_F(t)$. We now illustrate the method.

2.1 Single-Phase Problem: T_{ws} = Const, Semi-Infinite Region. Consider a semi-infinite solid, $x \ge 0$, that is initially uniform at the temperature T_i. The temperature of the wall, at $x = 0$, is instantaneously raised to a constant value T_{ws}, the single-phase wall temperature. The single-phase solution to this problem is given by [1]

$$T_s(x,t) = T_{ws} - (T_{ws} - T_i)\,\mathrm{erf}\eta \tag{4}$$

where

$$\eta = x/2\sqrt{\alpha t} \tag{5}$$

2.2 Application of the Single-Phase Solution to a Phase-Change Problem. The location of the phase-change interface is obtained from

$$T_s(x_F,t) = T_F = T_{ws} - (T_{ws} - T_i)\,\mathrm{erf}\,\lambda \tag{6}$$

where

$$x_F/2\sqrt{\alpha t} = \lambda \tag{7}$$

Since T_F, T_{ws} and T_i are known constants, λ is known and must also be a constant.

The relation above can be rearranged. Equation (6) yields

$$T_{ws} = \frac{T_F - T_i\,\mathrm{erf}\,\lambda}{\mathrm{erfc}\,\lambda} = T_i + \frac{T_F - T_i}{\mathrm{erfc}\,\lambda} \tag{8}$$

which, when substituted into equation (4) yields

$$T(x,t) = T_i + (T_F - T_i)\frac{\mathrm{erfc}\,\eta}{\mathrm{erfc}\,\lambda} \quad \text{for } x \ge x_F(t). \tag{9}$$

The subscript s on $T_s(x,t)$ has been dropped because the relation is also applicable to the phase-change problem, i..e, equation (9) does not contain T_{ws}.

To obtain the solution in the region $0 \le x \le x_F(t)$, equation (3) is used. Substituting the trajectory $x_F(t)$ from equation (7) into equation (3) and summing the series gives (see equation (B4))

$$T(x,t) = T_s(x,t) + \frac{L}{c}\sqrt{\pi}\lambda e^{\lambda^2}\,\mathrm{erf}\,\lambda\left(1 - \frac{\mathrm{erf}\,\eta}{\mathrm{erf}\,\lambda}\right), \quad x \le x_F(t) \tag{10}$$

where T_s is the single-phase solution given by equation (4). At the wall

$$T(0,t) = T_w = T_s(0,t) + \frac{L}{c}\sqrt{\pi}\lambda\, e^{\lambda^2}\,\mathrm{erf}\lambda \tag{11}$$

Recall that $T_s(0,t) = T_{ws}$ is a constant. Thus the solution to the phase-change problem that has been solved is for the constant wall temperature boundary condition, T_w = constant. Equation (10) may be written in a more familiar form by using equation (4) for $T_s(x,t)$ and then using equation (6). The result is

$$T(x,t) = T_w - (T_w - T_F)\frac{\mathrm{erf}\eta}{\mathrm{erf}\lambda}, \quad x \le x_F(t) \tag{12}$$

Now, using equations (9) and (12) and the boundary condition equation (1*f*) yields the following relation for determining λ

$$\frac{L}{c}\sqrt{\pi}\lambda e^{\lambda^2} = \frac{T_w - T_F}{\mathrm{erf}\lambda} + \frac{T_i - T_F}{\mathrm{erfc}\lambda} \tag{13}$$

Equations (9), (12), and (13) constitute the solution to this phase-change problem. The solution to this problem was

Nomenclature

a = constant in equation (C4)
A_n = coefficients in equation (A14)
b = constant in section 2
b = constant in equation (C4)
c = specific heat
c = constant in equation (C4)
C_n = coefficients in equation (A8)
$C_{i,n}$ = coefficients in equation (17)
E_n = coefficients in equation (A11)
F = solution function in equation (15)
G_n = coefficients in equation (3)
H = slab thickness
H_n = series coefficients
k = thermal conductivity
l = length, see section 2
L = latent heat
m = constant in section 4 and equation (45)
P = convection term in equation (C1)
q = heat flux
Q = heat source in equation (C1)
r = spatial coordinate
r_F = solid–liquid interface location
$R_{i,n}$ = ratio defined in equation (17)
$S_{i,n}$ = ratio defined in equation (20)
t = time
T = temperature
T_F = fusion temperature
T_s = single-phase solution
T_{ws} = single-phase wall temperature
x = Cartesian coordinate
x^* = dimensionless Cartesian coordinate, see section 2
x_F = solid–liquid interface location
x_F^* = dimensionless variable, see section 2
y = spatial variable defined by equation (A2)
α = thermal diffusivity
Γ = Gamma function
η = similarity variable in equation (5) or equation (27)
λ = variable in equation (7) or equation (27)
ρ = density
σ = time variable in equation (D3)
τ = dimensionless time, see section 2

Subscripts

F = fusion
i = initial
i = summation index
j = product index
L = liquid
n = summation index
s = single phase
s = solid
w = wall

Table 1 Wall temperature using five terms in the series $\tilde{H}_0$ for $p = 5$

τ	$m=1$ lower bound	$m=1$ upper bound	$m=2$ lower bound	$m=2$ upper bound	$m=4$ lower bound	$m=4$ upper bound	$m=10$ lower bound	$m=10$ upper bound
0.1	0.1052	0.1052	0.0020	0.0020	0.0000	0.0000	0.0000	0.0000
0.2	0.2214	0.2214	0.0162	0.0162	0.0001	0.0001	0.0000	0.0000
0.3	0.3499	0.3499	0.0557	0.0557	0.0009	0.0009	0.0000	0.0000
0.4	0.4918	0.4918	0.1381	0.1381	0.0066	0.0066	0.0000	0.0000
0.5	0.6487	0.6487	0.2903	0.2903	0.0319	0.0319	0.0000	0.0000
0.6	0.8220	0.8221	0.5619	0.5620	0.1202	0.1202	0.0006	0.0006
0.7	1.0136	1.0138	1.0519	1.0524	0.4077	0.4077	0.0115	0.0115
0.8	1.2251	1.2257	1.9742	1.9800	1.4845	1.4869	0.1585	0.1585
0.9	1.4588	1.4598	3.8198	3.8754	7.7113	8.2268	3.6654	3.7276
1.0	1.7167	1.7188	7.7627	8.2233	74.0310		3,791.2500	
1.1	2.0013	2.0050	16.6602	20.3054	1,090.7610		22,688,120.61	
1.2	2.3151	2.3217	37.4412	72.8947	17,299.7977		8.3853×10^{10}	

given by Neumann [1], and the present results are identical to his solution.

2.3 More General Problem: $x_F = bt^m$. We now consider a more general phase-change problem governed by equations (1*a-g*), with an interface trajectory: $x_F = bt^m$ with $T(x,0) = T_F$, $T(H,t) = T_F$. The solution is presented in Appendix D and is given by

$$T(x,t) = T_F + (L/c)F(x,t) \text{ for } x \le x_F(t) \tag{14}$$

with

$$F(x^*,\tau) = \sum_{n=1}^{\infty} (1 - x^*/x^*_F)^n G_n = \sum_{n=0}^{\infty} (-x^*)^n H_n \tag{15}$$

where $x^* = x/l$, $\tau = \alpha t/l^2$, $x_F^* = x_F/l$, $l = [b\alpha^{-m}]^{1/(1-2m)}$
For n even:

$$H_n = (1/n!)\tau^{-n/2} \sum_{i=1}^{\infty} \frac{\tau^{i(2m-1)}}{(2i)!} \prod_{j=0}^{(i-1+n/2)} [2im-j] \tag{16a}$$

for n odd:

$$H_n = (1/n!)\tau^{-n/2} \sum_{i=1}^{\infty} \frac{\tau^{(i-1/2)(2m-1)}}{(2i-1)!} \prod_{j=0}^{(i-3/2+n/2)} [(2i-1)m-j] \tag{16b}$$

Direct substitution into the governing equations (1*a-g*) confirms the above solution. Note that $m = 1/2$ gives Neumann's solution[1] and $m = 1$ gives Stefan's solution [4, 5].

2.4 Convergence: $m > 1/2$. The convergence and error bounds for this solution are now considered for $m > 1/2$. We first determine the convergence of H_n for n even. Define

$$H_n = \sum_{i=1}^{\infty} C_{i,n} \text{ and } R_{i,n} = \frac{C_{i,n}}{C_{i-1,n}} \tag{17}$$

For the series to converge, $R_{i,n} < 1$ as $i \to \infty$ for fixed values of n. $C_{i,n}$ may be written as

$$C_{i,n} = \tau^{i(2m-1)} \frac{\Gamma(2im+1)}{\Gamma(2i+1)\Gamma(2mi-i-[n/2]+1)} \frac{1}{n!} \tau^{-n/2} \tag{18}$$

where Γ is the gamma function. Using $\lim_{p\to\infty} \Gamma(x+p+1) = \Gamma(p+1)p^x$ one obtains for large i

$$R_{i,n} = \frac{(2m)^{2m}\tau^{2m-1}}{4i(2m-1)^{2m-1}} \tag{19}$$

Thus, as $i \to \infty$, $R_{i,n} \to 0$ showing convergence of equation (16*a*). Analysis of H_n, n odd, also yields rapid convergence as $i \to \infty$.

To determine the convergence of the series given in equation (15) the quantity $S_{i,n}$ is defined according to

[1]Note that $\tau^{(2m-1)}|_{m=1/2} = b^2\alpha^{-1}$

Table 2 Wall temperature convergence ratio, $R_{i,0}$ for $m = 1$

τ	$i=2$	$i=3$	$i=4$	$i=5$
0.1	0.0500	0.0333	0.0250	0.0200
0.2	0.1000	0.0667	0.0500	0.0400
0.3	0.1500	0.1000	0.0750	0.0600
0.4	0.2000	0.1333	0.1000	0.0800
0.5	0.2500	0.1667	0.1250	0.1000
0.6	0.3000	0.2000	0.1500	0.1200
0.7	0.3500	0.2333	0.1750	0.1400
0.8	0.4000	0.2667	0.2000	0.1600
0.9	0.4500	0.3000	0.2250	0.1800
1.0	0.5000	0.3333	0.2500	0.2000
1.1	0.5500	0.3667	0.2750	0.2200
1.2	0.6000	0.4000	0.3000	0.2400

Table 3 Wall temperature convergence ratio, $R_{i,0}$ for m = 2

τ	$i=2$	$i=3$	$i=4$	$i=5$
0.1	0.0012	0.0008	0.0006	0.0005
0.2	0.0093	0.0063	0.0047	0.0038
0.3	0.0315	0.0212	0.0160	0.0128
0.4	0.0747	0.0503	0.0378	0.0303
0.5	0.1458	0.0982	0.0739	0.0592
0.6	0.2520	0.1697	0.1276	0.1022
0.7	0.4002	0.2695	0.2027	0.1623
0.8	0.5973	0.4023	0.3025	0.2423
0.9	0.8505	0.5728	0.4308	0.3450
1.0	1.1667	0.7857	0.5909	0.4733
1.1	1.5528	1.0458	0.7865	0.6299
1.2	2.0160	1.3577	1.0211	0.8178

Table 4 Wall temperature convergence ratio, $R_{i,0}$ for m = 4

τ	$i=2$	$i=3$	$i=4$	$i=5$
0.1	0.0000	0.0000	0.0000	0.0000
0.2	0.0000	0.0000	0.0000	0.0000
0.3	0.0005	0.0004	0.0003	0.0002
0.4	0.0041	0.0028	0.0021	0.0017
0.5	0.0195	0.0132	0.0099	0.0079
0.6	0.0700	0.0472	0.0355	0.0285
0.7	0.2059	0.1389	0.1045	0.0837
0.8	0.5243	0.3537	0.2661	0.2132
0.9	1.1957	0.8067	0.6070	0.4862
1.0	2.5000	1.6867	1.2691	1.0166
1.1	4.8718	3.2868	2.4730	1.9810
1.2	8.9580	6.0436	4.5473	3.6426

Table 5 Wall temperature convergence ratio, $R_{i,0}$ for $m = 10$

τ	$i=2$	$i=3$	$i=4$	$i=5$
0.1	0.0000	0.0000	0.0000	0.0000
0.2	0.0000	0.0000	0.0000	0.0000
0.3	0.0000	0.0000	0.0000	0.0000
0.4	0.0000	0.0000	0.0000	0.0000
0.5	0.0000	0.0000	0.0000	0.0000
0.6	0.0004	0.0003	0.0002	0.0002
0.7	0.0074	0.0050	0.0038	0.0030
0.8	0.0937	0.0632	0.0476	0.0381
0.9	0.8781	0.5926	0.4460	0.3572
1.0	6.5000	4.3872	3.3013	2.6446
1.1	39.7534	26.8318	20.1904	16.1741
1.2	207.6620	140.1616	105.4695	84.4895

Table 6 Results for phase-change problem with $x_F^* = \tau^{1/3}$ (H_0, wall temperature factor; H_1, wall heat flux factor; $F(x_F^*/2, \tau)$ midrange temperature factor). Note that $H_0 = -a$, $H_1 = g$ (cf. Chow and Woo [6]).

τ	H_0	H_1	H_2	H_3	H_4	H_5	H_6	H_7	$F(1/2x_F^*,\tau)$
.05	1.040	2.268	−3.906	−4.654	9.160	7.059	−14.765	−8.793	0.527
.10	0.8035	1.4744	−1.4797	−1.5589	1.7210	1.2366	− 1.3805	−0.7728	0.4051
.15	0.6926	1.1388	−0.8414	−0.8126	0.6495	0.4359	− 0.3464	−0.1821	0.3485
.20	0.6239	0.9463	−0.5645	−0.5099	0.3259	0.2067	− 0.1301	−0.0648	0.3136
.30	0.5391	0.7274	−0.3223	−0.2633	0.1235	0.0717	− 0.0328	−0.0150	0.2706
.40	0.4864	0.6029	−0.2168	−0.1644	0.0622	0.0337	− 0.0124	−0.0053	0.2440
.50	0.4493	0.5209	−0.1595	−0.1139	0.0365	0.0187	− 0.0058	−0.0024	0.2253
.60	0.4212	0.4622	−0.1242	−0.0844	0.0237	0.0116	− 0.0031	−0.0012	0.2111
.70	0.3989	0.4176	−0.1005	−0.0654	0.0164	0.0077	− 0.0019	−0.0007	0.1999
.80	0.3805	0.3824	−0.0837	−0.0525	0.0119	0.0054	− 0.0012	−0.0004	0.1907
.90	0.3651	0.3539	−0.0713	−0.0432	0.0090	0.0040	− 0.0008	−0.0003	0.1829
1.00	0.3518	0.3301	−0.0617	−0.0363	0.0070	0.0030	− 0.0006	−0.0002	0.1762
5.00	0.2013	0.1136	−0.0069	−0.0025	0.0002	0.0000	0.0000	0.0000	0.1007
10.00	0.1587	0.0717	−0.0027	−0.0008	0.0000	0.0000	0.0000	0.0000	0.0794
50.00	0.0918	0.0245	−0.0003	−0.0001	0.0000	0.0000	0.0000	0.0000	0.0459
100.00	0.0727	0.0155	−0.0001	0.0000	0.0000	0.0000	0.0000	0.0000	0.0363
200.00	0.0575	0.0097	0.0000	0.0000	0.0000	0.0000	0.0000	0.0000	0.0288

$$S_{i,n} = \frac{C_{i,n}}{C_{i,n-2}} \tag{20}$$

For convergence, $S_{i,n} < 1$ as $n \to \infty$ for fixed values of i. Equation (18) gives

$$S_{i,n} = \frac{\tau^{-1}}{n(n-1)}[2im - i - (n/2) + 1] \tag{21}$$

Thus, $\lim_{n\to\infty} S_{i,n} = 0$ for fixed i. Identical results are obtained for odd values of n.

2.5 Error Bound for Wall Temperature, $m > 1/2$. The error bound for the wall temperature is related directly to the error bound on H_0. From our definitions we have that

$$H_0 = \sum_{i=1}^{\infty} C_{i,0} \tag{22}$$

The estimate for H_0 is given by

$$\tilde{H}_0 = \sum_{i=1}^{p} C_{i,0} \tag{23}$$

We define $R_{p,0} = C_{p,0}/C_{p-1,0}$ and assume that $R_{p,0}$ decreases monotonically as p increases. The error is then given by

$$H_0 - \tilde{H} = \sum_{i=p+1}^{\infty} C_{1,0} \le \sum_{i=p+1}^{\infty} C_{p,0}(R_{p,0})^{i-p} \tag{24}$$

Also note that for $m > 1/2$ all $C_{i,0} \ge 0$. Thus

$$0 \le H_0 - \tilde{H}_0 \le C_{p,0}\frac{R_{p,0}}{1-R_{p,0}} \tag{25}$$

Table 1 gives upper and lower bounds for H_0 for several values of τ and m. Tables 2–5 show that $R_{p,0}$ decreases monotonically as p increases, thus showing the foregoing analysis to be valid over a broad range of values of τ and m.

2.6 Solution for $m = 1/3$. The results for $m = 1/3$ are presented in Table 6. Note that convergence is best for large time. For the case $m = 1/3$, $0 < \tau < 0.8$, Chow and Woo [6] give approximate results for the dimensionless wall temperature and heat flux. Their results correspond to the quantities $H_0(\tau)$ and $H_1(\tau)$ in Table 6. The maximum difference between the results of [6] and the present results is 0.1 percent.

3 Discussion

The method presented in this paper formulates the phase-change problem as an inverse conduction problem. The solution of inverse conduction problems is an active field of research and several solution methods have been developed; e.g., Burggraf [7], Beck et al. [8], and Imber and Kahn [9]. Studies that are concerned with a change of phase; that is, the inverse Stefan problem, have been carried out by Bluman [10], Rubinsky and Shitzer [11], Chow and Woo [6], and Katz and Rubinsky [12].

A more general derivation of the method discussed here is given in Appendix C, and includes spherical and cylindrical geometries, heat generation, and convection. Burggraf [7] and Landram [13, 14] have applied similar methods to include thermally varying properties, numerical implementation, experimental studies, and multidimensional systems.

In section 2, convergence of the solution was shown[2] for a general power law trajectory, $x_F = bt^m$, $m > 1/2$. The convergence of the solution is best for m close to 1/2. One would expect similar interface trajectories—i.e., trajectories that are smoothly varying and monotonically increasing or decreasing (but not necessarily of the form t^m)—to show similar convergence behavior. Thus for such trajectories the present method should work well in obtaining improvements to the quasi-stationary solution to the problem of interest. Other problems may also be solved using the present method; however, convergence of solutions thus obtained has not been shown.

4 Conclusions

A method has been presented which solves phase-change problems. The solution in one of the phases is specified as a known single-phase solution. An inverse analysis then determines a power-series solution for the other phase. The method can accommodate planar, cylindrical, and spherical geometries and convection, heat generation, and differing liquid and solid properties.[3] With more difficulty, the method can include thermal varying properties and multidimensional systems, and can be implemented numerically.

The exact solution to the problem with $x_F = bt^m$ is derived. Convergence is shown and error bounds are given.

Acknowledgments

The authors are indebted to Drs. K. Mahin and C. S. Landram of Lawrence Livermore National Laboratory and to Sandia National Laboratories Livermore for their interest and partial support of this work.

[2]The convergence of the solution is independent of Stefan number. However, the behavior of the solution does depend upon the value of m. For $m > 1/2$, convergence of this solution is most rapid for small time and in the limit $\tau \to 0$ the solution reduces to the quasi-stationary solution [15]. For $m < 1/2$, convergence of the solution is most rapid for large time, and in the limit $\tau \to \infty$ the solution again reduces to the quasi-stationary solution [15].

[3]The recursion equations for these conditions are given in Appendix C.

References

1 Carslaw, H. S., and Jaeger, J. C., *Conduction of Heat in Solids* (2nd ed.), Clarendon Press, London, 1959.

2 Ozisik, M. N., *Heat Conduction*, John Wiley and Sons, New York, 1980.

3 Boley, B. A., "A General Starting Solution for Melting and Solidifying Slabs," *Int. J. Engng. Sci.*, Vol. 6, 1968, pp. 89–111.

4 Stefan, J., *On the Theory of Ice Formation, Especially on Ice Formation in Polar Seas* (Uber die Theorie der Eisbildung, insbesondere uber die eisbildung im Polarmeere), *Sitzungsberichte der Kaiserlichen Akademie Wiss. Wien.*, Math.-naturwiss. KL. 98 (2a), 1890, pp. 965–973.

5 Langford, D., "New Analytic Solutions of the One-Dimensional Heat Equation," *Quarterly of Applied Mathematics*, Vol. 24, 1967, pp. 315–322.

6 Chow, L. C., and Woo, K. C., "An Inverse Stefan Problem," ASME Paper No. 83-HT-19, 1983.

7 Burggraf, O. R., "An Exact Solution of the Inverse Problem in Heat Conduction Theory and Application," ASME JOURNAL OF HEAT TRANSFER, Vol. 86, 1964, pp. 373–382.

8 Beck, J. V., Litkouhi, B., and St. Clair, C. R., Jr., "Efficient Sequential Solution of the Nonlinear Inverse Heat Conduction Problem," *Numerical Heat Transfer*, Vol. 5, 1982, pp. 275–286.

9 Imber, M., and Kahn, J., "Prediction of Transient Thermocouple Distributions With Embedded Thermocouples," *AIAA Journal*, Vol. 10, 1972, pp. 784–789.

10 Bluman, G. W., "Applications of the General Similarity Solution of the Heat Equation to Boundary-Value Problems," *Quarterly of Applied Mathematics*, Jan. 1974, pp. 403–415.

11 Rubinsky, B., and Shitzer, A., "Analytic Solutions to the Heat Equation Involving a Moving Boundary With Applications to the Change of Phase Problem (the Inverse Stefan Problem)," ASME JOURNAL OF HEAT TRANFSER, Vol. 100, 1987, pp. 300–304.

12 Katz, M. A., and Rubinsky, B., "An Inverse Finite Element Technique to Determine the Change of Phase Interface Location in One Dimensional Melting Problems," *Numerical Heat Transfer*, in press.

13 Landram, C. S., "Measurement of Fusion Boundary Energy Transport During Arc Welding," ASME JOURNAL OF HEAT TRANSFER, Vol. 105, 1983, pp. 550–554.

14 Landram, C. S., "Measurement of Fusion Boundary Heat Transfer for Temperature Dependent Properties During Arc Welding," submitted for publication.

15 London, A. L., and Seban, R. A., "Rate of Ice Formation," ASME Transactions, Vol. 65, 1943, pp. 771–778.

APPENDIX A

Exact Solution of Inverse Conduction Problem

Conduction in the Region $0 \le x \le x_F(t)$. The problem considered is that of conduction over the finite interval $0 \le x \le x_F(t)$

$$\frac{\partial T}{\partial t} = \alpha \frac{\partial^2 T}{\partial x^2} \quad 0 \le x \le x_F(t) \tag{A1}$$

subject to $T(x_F,t) = T_F$, $q(x_F,t) = q_{FL}(t)$, with $T(0,t) = T_w(t)$ to be determined. This is an inverse conduction problem.

The phase change interface (or T_F isotherm) is made stationary with the transformation

$$y = x_F - x \tag{A2}$$

so that equation (A1) becomes

$$\left.\frac{\partial T}{\partial t}\right|_x = \left.\frac{\partial T}{\partial t}\right|_y + \left.\frac{\partial T}{\partial y}\right|_t \frac{dx_F}{dt} = \alpha \left.\frac{\partial^2 T}{\partial y^2}\right|_t \tag{A3}$$

Note that

$$\left.\frac{\partial T}{\partial t}\right|_{y=0} = 0; \text{ i.e., } T(0,t) = T_F \tag{A4}$$

$$q(x_F,t) = q_{FL} = -k \frac{\partial T}{\partial y}(0^+,t) \frac{\partial y}{\partial x} = k \frac{\partial T}{\partial y}(0^+,t) \tag{A5}$$

The temperature distribution $T(y,t)$ is obtained by expansion of a Taylor series about $y = 0$ (see Burggraf [7]). Results for the derivatives of the temperature are

$$\frac{\partial T}{\partial y}(0^+,t) = \frac{1}{k} q_{FL}, \frac{\partial^2 T}{\partial y^2}(0^+,t) = 0 + \frac{1}{\alpha k} q_{FL} \frac{dx_F}{dt}$$

$$\frac{\partial^3 T}{\partial y^3}(0^+,t) = \frac{1}{\alpha k} \frac{dq_{FL}}{dt} + \frac{1}{\alpha^2 k} q_{FL} \left(\frac{dx_F}{dt}\right)^2 \ldots \tag{A6}$$

Therefore

$$T(y,t) = T_F + \frac{y}{k} q_{FL} + \frac{y^2}{2!\alpha k} q_{FL} \frac{dx_F}{dt} + \ldots \tag{A7}$$

The expression for the temperature may be written in x,t coordinates as

$$T(x,t) = T_F + \sum_{n=1}^{\infty} \frac{C_n (x_F - x)^n}{n!} \tag{A8}$$

where

$$C_1 = \frac{q_{FL}}{k}, C_2 = \frac{q_{FL}\dot{x}_F}{\alpha k} \text{ and } C_n = \frac{\dot{C}_{n-2}}{\alpha} + \frac{C_{n-1}\dot{x}_F}{\alpha} \text{ for } n \ge 3 \tag{A9}$$

The dots denote differentiation with respect to time t.

Consideration of the Change of Phase. The inclusion of the phase change gives

$$q_{FL} = q_{FS} + \rho L \dot{x}_F \tag{A10}$$

where $q_{FS} = q(x_F^+,t)$ and $q_{FL} = q(x_F^-,t)$ (see equation (A5)). Substituting equation (A10) into (A9) yields

$$T(x,t) = T_F + \sum_{n=1}^{\infty} \frac{(x_F - x)^n}{n!} \left(E_n + \frac{A_n L}{c}\right); x \le x_F(t) \tag{A11}$$

where

$$E_1 = \frac{q_{FS}}{k}, E_2 = \frac{q_{FS}}{\alpha k}\dot{x}_F, E_n = \frac{1}{\alpha}\dot{E}_{n-2} + \frac{E_{n-1}}{\alpha}\dot{x}_F \text{ for } n \ge 3 \tag{A12}$$

$$A_1 = \frac{\dot{x}_F}{\alpha}, A_2 = \left(\frac{\dot{x}_F}{\alpha}\right)^2, A_n = \frac{\dot{A}_{n-2}}{\alpha} + \frac{A_{n-1}}{\alpha}\dot{x}_F \text{ for } n \ge 3 \tag{A13}$$

Note that the solution for no phase change, i.e., $L = 0$, is identical to the solution to the single-phase problem, i.e., $q_{FL} = q_{FS}$ and $E_n = C_n$ and $T(x,t) = T_s(x,t)$. Therefore

$$T(x,t) = T_s(x,t) + \frac{L}{c} \sum_{n=1}^{\infty} \frac{(x_F - x)^n}{n!} A_n, x \le x_F(t) \tag{A14}$$

where $T_s(x,t)$ is the solution to the single-phase problem. It is emphasized that equation (A14) is a general result valid for all wall temperature variations for the one-dimensional Cartesian geometry. Similar results can be derived for other geometries.

Equation (A14) may be written in the form

$$T(x,t) = T_s(x,t) + \frac{L}{c} \sum_{n=1}^{\infty} G_n \left(1 - \frac{x}{x_F}\right)^n, x \le x_F(t) \tag{A15}$$

where

$$G_n = x_F^n A_n / n! \tag{A16}$$

APPENDIX B

Temperature Distribution for the Trajectory, $x_F = 2\lambda\sqrt{\alpha t}$

Using $x_F = 2\lambda\sqrt{\alpha t}$ and equations (A13) and (A16), we obtain

$$G_1 = 2\lambda^2, G_2 = 2\lambda^4, G_3 = -\frac{2}{3}\lambda^4 + \frac{4}{3}\lambda^6, G_4 = -\lambda^6 + \frac{2}{3}\lambda^8$$

$$G_5 = \frac{\lambda^6}{5} - \frac{4\lambda^8}{5} + \frac{4}{15}\lambda^{10}, G_6 = \frac{\lambda^8}{3} - \frac{4\lambda^{10}}{9} + \frac{4}{45}\lambda^{12}, \tag{B1}$$

$$G_7 = -\frac{8}{21} + \frac{2}{7}\lambda^{10} - \frac{4}{21}\lambda^{12} + \frac{8}{315}\lambda^{14}$$

We now define H_n such that

$$\sum_{n=1}^{\infty} G_n\left(1-\frac{\eta}{\lambda}\right)^n = \sum_{n=0}^{\infty}(-1)^n H_n\left(\frac{\eta}{\lambda}\right)^n \tag{B2}$$

and obtain

$$H_0 = \lambda\sqrt{\pi}e^{\lambda^2}\ \text{erf}\,\lambda,\ H_1 = 2\lambda^2 e^{\lambda^2},\ H_2 = 0$$
$$H_3 = -\frac{2}{3}\lambda^4 e^{\lambda^2},\ H_4 = 0 \tag{B3}$$

Equations (A15), (B2), and (B3) yield

$$T(x,t) = T_s(x,t) + \frac{L}{c}\sqrt{\pi}\lambda e^{\lambda^2}\ \text{erf}\,\lambda\left(1-\frac{\text{erf}\,\eta}{\text{erf}\,\lambda}\right),\ x \le x_F(t) \tag{B4}$$

APPENDIX C

Exact Solution of a More General Inverse Conduction Problem

General Considerations. The problem considered is that of conduction over the finite interval $0 \le r \le r_F(t)$. A heat generation term $Q(t)$ and a convection term with parameter $P(t)$ are also included in the analysis. Although P and Q are taken to be uniform here, spatial variations could be accommodated by using a power series in $(r_F - r)$. The problem is governed by

$$\alpha\frac{1}{r^n}\frac{\partial}{\partial r}\left(r^n\frac{\partial T}{\partial r}\right) = \frac{\partial T}{\partial t}\frac{-P}{r^n}\frac{\partial T}{\partial r} - Q \tag{C1}$$

where $n = 0, 1, 2$ for the slab, cylinder and sphere, respectively. The boundary conditions are $T(r_f,t) = T_F$ and $q(r_f,t) = q_{FL}(t)$; this is an inverse problem. The temperature distribution $T(r,t)$ is obtained by expanding in a Taylor series about $r = r_F(t)$

$$T(r,t) = \sum_{n=0}^{\infty}\frac{1}{n!}(r_F - r)^n A_n(t) \tag{C2}$$

The first two coefficients are found from the boundary conditions to be

$$A_0 = T_F,\ A_1 = \frac{1}{k}q_{FL} \tag{C3}$$

The remaining coefficents are found by substituting equation (C2) into equation (C1). A useful relation is

$$r^n = a(r_F - r)^2 + b(r_F - r) + c \tag{C4}$$

where

for a slab, $n = 0, a = 0, b = 0, c = 1$

for a cylinder, $n = 1, a = 0, b = -1, c = r_F$

for a sphere, $n = 2, a = 1, b = -2r_F, c = r_F^2$

The following relations are obtained

$$A_2 = \frac{1}{c\alpha}[c\dot{r}_F A_1 + PA_1 - cQ - b\alpha A_1] \tag{C5a}$$

$$A_3 = \frac{1}{c\alpha}[b\dot{r}_F A_1 + c\dot{r}_F A_2 + c\dot{A}_1 + PA_2 - bQ - 2a\alpha A_1 - 2b\alpha A_2] \tag{C5b}$$

$$A_4 = \frac{2}{c\alpha}\left[a\dot{r}_F A_1 + b\dot{r}_F A_2 + \frac{1}{2}c\dot{r}_F A_3 + b\dot{A}_1 + \frac{1}{2}c\dot{A}_2 + \frac{1}{2}PA_3 - aQ + -3a\alpha A_2 - \frac{3}{2}b\alpha A_3\right] \tag{C5c}$$

for $n > 2$, $A_{n+2} = \frac{1}{c\alpha}[n(n-1)a\dot{r}_F A_{n-1} + nb\dot{r}_F A_n + c\dot{r}_F A_{n+1} + n(n-1)a\dot{A}_{n-2} + nb\dot{A}_{n-1} + c\dot{A}_n + PA_{n+1} - n(n+1)a\alpha A_n - (n+1)b\alpha A_{n+1}]$

Simpler Result for the Spherical Geometry. Simpler results can be obtained for the spherical geometry when $P = 0$. Assume

$$T(r,t) = \sum_{n=0}^{\infty}\frac{1}{n!}\frac{1}{r}(r_F - r)^n A_n(t) \tag{C6}$$

The boundary conditions give

$$A_0 = T_F r_F,\ A_1 = \frac{1}{k}r_F q_{FL} - T_F \tag{C7}$$

Substituting into the differential equation, equation (C1), gives

$$A_2 = \frac{1}{\alpha}[\dot{r}_F A_1 + \dot{A}_0 - Q] \tag{C8a}$$

$$A_{n+2} = \frac{1}{\alpha}[\dot{r}_F A_{n+1} + A_n],\ \text{for}\ n \ge 1 \tag{C8b}$$

Application to the Phase-Change Problem. The inclusion of the phase-change gives (for a liquid region $0 \le r \le r_F(t)$ and a solid region $r \ge r_F(t)$)

$$q_{FL}(t) = -k_s\frac{\partial T_s}{\partial r}\Big|_{r=r_F(t)} + \rho L\dot{r}_F \tag{C9}$$

Thus, knowing $T_s(r,t)$ and $r_F(t)$, equations (C2), (C3), and (C5) can be used to find $T(r,t)$. If there is no convection, i.e., $P = 0$, $T(r,t)$ can be decomposed into the form

$$T(r,t) = \frac{k_s}{k}T_s\left(\sqrt{\frac{\alpha_s}{\alpha}}r,t\right) + \frac{L}{c}F(r,t) \tag{C10a}$$

where

$$F(r,t) = \sum_{n=0}^{\infty}\frac{1}{n!}(r_F - r)^n A_n(t) \tag{C10b}$$

and $A_n(t)$ are given by equations (C5) with $A_0 = 0$ and $A_1 = \dot{r}_F/\alpha$. Two examples will now be considered.

Cylindrical Geometry With $r_F = 2\lambda(\alpha t)^{1/2}$. Substituting $r_F = 2\lambda(\alpha t)^{1/2}$ into equation (C10)

$$A_1 = (\alpha t)^{-1/2}$$
$$A_2 = \left(\lambda^2 + \frac{1}{2}\right)(\alpha t)^{-1} \tag{C11}$$
$$A_3 = \left(\lambda^3 + \frac{1}{2}\lambda + \frac{1}{2\lambda}\right)(\alpha t)^{-3/2}$$
$$A_4 = \left(\lambda^4 + \frac{3}{4} + \frac{3}{4\lambda^2}\right)(\alpha t)^{-2}$$

Define $G_n = 1/n!\ r_F{}^n A_n$ so that equation (C10a) then becomes

$$T(r,t) = T_s(r,t) + \frac{L}{c}\sum_{n=1}^{\infty}G_n\left(1-\frac{r}{r_F}\right)^n \tag{C12}$$

where

$$G_1 = 2\lambda^2$$
$$G_2 = \lambda^2 + 2\lambda^4$$
$$G_3 = \frac{2}{3}\lambda^2 + \frac{2}{3}\lambda^4 + \frac{4}{3}\lambda^6 \tag{C13}$$
$$G_4 = \frac{1}{2}\lambda^2 + \frac{1}{2}\lambda^4 + \frac{2}{3}\lambda^8$$

Note that

$$Ei(-\lambda^2)-Ei(-\eta^2)$$

$$=\sum_{n=0}^{\infty}\frac{1}{n!}(\eta-\lambda)^n\frac{d^n[Ei(-\lambda^2)-Ei(-\eta^2)]}{d\eta^n}\Big|_{\eta=\lambda}$$

$$=\lambda^{-2}e^{-\lambda^2}\left[-\left(1-\frac{\eta}{\lambda}\right)2\lambda^2+\left(1-\frac{\eta}{\lambda}\right)^2(-\lambda^2-2\lambda^4)+\right.$$

$$-\left(1-\frac{\eta}{\lambda}\right)^3\left(\frac{2}{3}\lambda^2+\frac{2}{3}\lambda^4+\frac{4}{3}\lambda^6\right)$$

$$\left.+\left(1-\frac{\eta}{\lambda}\right)^4\left(\frac{-1}{2}\lambda^2-\frac{1}{2}\lambda^4-\frac{2}{3}\lambda^8\right)+\ldots\right.$$

$$=-\lambda^{-2}e^{-\lambda^2}\left[\sum_{n=1}^{\infty}G_n\left(1-\frac{r}{r_F}\right)^n\right] \tag{C14}$$

Thus, equation (C12) becomes

$$T=T_s+\frac{L}{c}\lambda^2e^{\lambda^2}[Ei(-\lambda^2)-Ei(-\eta^2)] \tag{C15}$$

Spherical Geometry With $r_F(t) = 2\lambda(\alpha t)^{1/2}$. Substituting $r_F(t) = 2\lambda(\alpha t)^{1/2}$ into equation (C8) with $A_0 = 0$ and $A_1 = (1/\alpha)r_F\dot{r}_F$ gives

$$\begin{aligned}A_1&=2\lambda^2\\A_2&=2\lambda^3(\alpha t)^{-1/2}\\A_3&=2\lambda^4(\alpha t)^{-1}\\A_4&=(2\lambda^5-\lambda^3)(\alpha t)^{-3/2}\end{aligned} \tag{C16}$$

The liquid temperature is given by

$$T(r,t)=T_s(r,t)+\frac{L}{c}\sum_{n=1}^{\infty}\frac{1}{n!}\frac{(r_F-r)^n}{r}A_n$$

$$=T_s(r,t)+\frac{L}{c}\sum_{n=-1}^{\infty}(-1)^{n+1}\left(\frac{r}{r_F}\right)^nH_n \tag{C17}$$

Solving for the H_n yields

$$\begin{aligned}H_{-1}&=2\lambda^2e^{\lambda^2}\\H_0&=2\lambda^2(1+\lambda\pi^{1/2}e^{\lambda^2}\ \mathrm{erf}\lambda)\\H_1&=2\lambda^4e^{\lambda^2}\\H_2&=0\end{aligned} \tag{C18}$$

Thus, equation (C17) becomes

$$T(r,t)=T_s(r,t)+\frac{L}{c}2\lambda^3e^{\lambda^2}\left[\pi^{1/2}\,\mathrm{erf}\,\lambda-\frac{1}{\lambda}e^{-\lambda^2}+\right.$$

$$\left.-\pi\,\mathrm{erf}\,\eta+\frac{1}{\eta}e^{-\eta^2}\right] \tag{C19}$$

APPENDIX D

Substituting $x_F^* = \tau^m$ into equations (A13) and (A16) gives

$$\begin{aligned}G_1&=m\tau^{2m-1}\\G_2&=\frac{1}{2}m^2\tau^{4m-2}\\G_3&=\frac{1}{6}m^3\tau^{6m-3}+\frac{1}{6}m(m-1)\tau^{4m-2}\\G_4&=\frac{1}{24}m^4\tau^{8m-4}+\frac{1}{8}m^2(m-1)\tau^{6m-3}\\G_5&=\frac{1}{120}m^5\tau^{10m-5}+\frac{1}{20}m^3(m-1)\tau^{8m-4}\\&\quad+\frac{1}{120}m(m-1)(m-2)\tau^{6m-3}\\G_6&=\frac{1}{720}m^6\tau^{12m-6}+\frac{1}{72}m^4(m-1)\tau^{10m-5}\\&\quad+\frac{1}{720}m^2(m-1)(7m-11)\tau^{8m-4}\end{aligned} \tag{D1}$$

Now define

$$\sum_{n=1}^{\infty}G_n\left(1-\frac{x^*}{x_F^*}\right)^n=\sum_{n=0}^{\infty}(-x^*)^nH_n \tag{D2}$$

$$\text{and}\quad \sigma=\tau^{2m-1} \tag{D3}$$

and obtain

$$H_0=m\sigma\left[1+\frac{1}{3!}(4m-1)\sigma+\frac{1}{5!}(6m-1)(6m-2)\sigma^2\right.$$

$$\left.+\frac{1}{7!}(8m-1)(8m-2)(8m-3)\sigma^3+\ldots\right]$$

$$H_1=\tau^{-m}m\sigma\left[1+\frac{1}{2!}(3m-1)\sigma+\frac{1}{4!}(5m-1)(5m-2)\sigma^2+\ldots\right]$$

$$H_2=\frac{1}{2!}\tau^{-2m}m\sigma^2\left[(2m-1)+\frac{1}{3!}(4m-1)(4m-2)\sigma+\ldots\right]$$

$$H_3=\frac{1}{3!}\tau^{-3m}m\sigma^2\left[(m-1)+\frac{1}{2!}(3m-1)(3m-2)\sigma+\ldots\right]$$

$$H_4=\frac{1}{4!}\tau^{-4m}m\sigma^3\left[(2m-1)(2m-2)\right.$$

$$\left.+\frac{1}{3!}(4m-1)(4m-2)(4m-3)\sigma+\ldots\right]$$

$$H_5=\frac{1}{5!}\tau^{-5m}m\sigma^3\left[(m-1)(m-2)\right.$$

$$\left.+\frac{1}{2!}(3m-1)(3m-2)(3m-3)\sigma+\ldots\right]$$

$$H_6=\frac{1}{6!}\tau^{-6m}m\sigma^4[(2m-1)(2m-2)(2m-3)+\ldots] \tag{D4}$$

Equations (16*a*) and (16*b*) may be obtained from these relations.

A. N. Hrymak

G. J. McRae

A. W. Westerberg

Department of Chemical Engineering,
Carnegie-Mellon University,
Pittsburgh, PA 15213

Combined Analysis and Optimization of Extended Heat Transfer Surfaces

This study presents an efficient numerical method to discover the optimal shape for a fin subject to both convective and radiative heat loss. Problem formulation is a finite element approximation to the conduction equation embedded within and solved simultaneously with the shape optimization problem. The approach handles arbitrary equality and inequality constraints. Grid points move to conform to the fin shape during the problem solution, reducing the number of elements required in the solution.

1 Introduction

Extended surfaces are widely used to increase convective and radiative heat transfer to a surrounding medium. One of the most common methods for accomplishing this task is the use of fins. Alternative statements of the single fin optimization problem are: For a given heat dissipation rate find the geometric shape that minimizes the material volume, or determine the maximum heat dissipation for a given amount of material [1]. In either case, if the governing partial differential equation and boundary conditions are nonlinear, the optimization problem is very difficult to solve by variational formulations. The procedure proposed in this paper involves simultaneous numerical solution of the temperature field, using a finite element approximation, and the optimization of values of the parameters defining the fin geometry. As the optimization proceeds, the geometry of the fin changes, and the finite element mesh or grid within the domain of the fin is reinterpolated. The methodology presented is not limited to extended surface heat transfer, but rather it can be applied to a class of problems where the design variables define the geometry of the system and the state of the system can be described by elliptic partial differential equations.

2 Analysis of Heat Transfer From Extended Surfaces

Heat transfer from an extended surface can be described by the governing equation for energy conservation. The fin geometry is presented in Fig. 1.

$$\frac{\partial}{\partial x}\left(k\frac{\partial T}{\partial x}\right)+\frac{\partial}{\partial y}\left(k\frac{\partial T}{\partial y}\right)+Q=0 \quad (x,y)\in\Omega \tag{1}$$

$$k\left(\frac{\partial T}{\partial x}l_x+\frac{\partial T}{\partial y}l_y\right)+q=0 \quad (x,y)\in\Gamma_{BC}\cup\Gamma_{CD} \tag{2}$$

$$k\left(\frac{\partial T}{\partial x}l_x+\frac{\partial T}{\partial y}l_y\right)=0 \quad (x,y)\in\Gamma_{AB} \tag{3}$$

$$T=T_0 \quad (x,y)\in\Gamma_{DA} \tag{4}$$

where $T(\mathbf{x})$ is the temperature distribution inside the fin, Q the internal heat generation rate, k is the thermal conductivity, T_0 is the fin root temperature, l_x and l_y are the direction cosines of the surface, and q is the heat dissipation due to convective and radiative heat transfer along the surface of the fin.

The surface flux for a single fin is given by

$$q = q_c+q_r \tag{5}$$

$$q_c = h_c(T-T_c) \tag{6}$$

$$q_r = h_r(T-T_r) \tag{7}$$

$$h_r = \epsilon\sigma(T^2+T_r^2)(T+T_r) \tag{8}$$

where h_c and h_r are the convective and radiative heat transfer coefficients for temperatures T_c and T_r. Note that the radiative term, h_r, is a function of the temperature of the environment and the temperature of the fin.

3 Review of Previous Work on Optimization of Extended Surfaces

The optimal fin literature deals mainly with the problem of finding the maximum heat dissipation for a given mass of fin. While the bulk of the work deals with single fins, some work has been done with arrays. Most of the previous work in fin optimization employs one-dimensional lumping [1, 2] to allow for the approximation of unidirectional heat flow in thin fins. Usually, the temperature is assumed to be uniform over the base of the fin; however, as shown by Suryanarayana [3], this

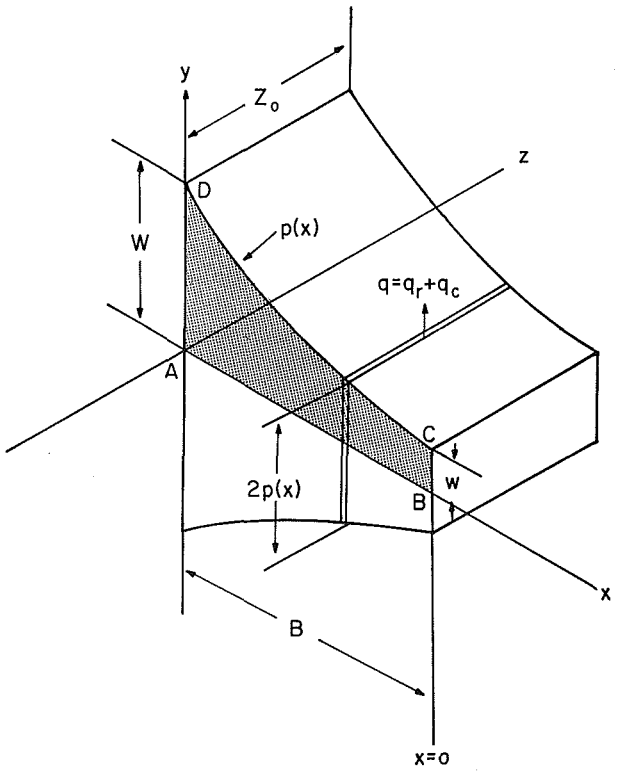

Fig. 1 Schematic representation of the fin and coordinate system

Contributed by the Heat Transfer Division for publication in the JOURNAL OF HEAT TRANSFER. Manuscript received by the Heat Transfer Division June 19, 1984.

may not be true in real fins. There are two-dimensional effects leading to a variation in root temperature which can then affect the value of the heat dissipation calculated. Therefore, the literature assumes the thin fin approximation where the fin has a small width-to-height ratio.

For a conductive fin with convective boundary conditions, Schmidt [4] proposed the first optimal fin solution by assuming that the temperature profile is a linear function of distance from the root of the fin. For a constant convective heat transfer coefficient, the resulting optimal profile is a concave parabola. Using variational methods Duffin [5] proved that Schmidt's assumption was correct. Duffin also considered how the presence of an inequality constraining the length of the fin would change the solution. Wilkins [6] showed that for a minimum mass fin a linear temperature profile was only true for the case of pure convection with constant thermal conductivity and heat transfer coefficients. Analytic solutions are also available for fins having radiation and internal heat generation effects [7–9].

Using a similarity transform Wilkins [10] found a general solution for the minimum mass thin fin problem which could handle combined convection and radiation and temperature dependent emissivity, thermal conductivity, and heat transfer coefficient. Melese and Wilkins [11] found the optimal fin shape for the case of a spatially varying convective heat transfer coefficient and internal heat generation and the optimum dimensions for a variety of prescribed fin shapes (also in [41]). The problem of an optimal fin for boiling heat transfer is especially important because the heat transfer coefficient may vary by a factor of 50 over the length of the fin [12].

Cobble [13] found the optimal profile for a fin subject to simultaneous convection and radiation occurring along the boundary. By assuming that the temperature profile followed a power law and that both the convective heat transfer coefficient and the thermal conductivity were constant, the resulting profile for the optimal fin was a concave function, with a sharp edge. Cobble also suggested that a triangular profile could be abstracted from the optimal shape and that the optimal profile would at least provide a bound. Wilkins [14] showed that the power law approximation is true only if there is pure convection or if there is pure radiation to surroundings at absolute zero. The power law approximation to the temperature profile is, however, a good practical approximation.

In the manufacture of fins there are practical design constraints that must be satisfied. One could select a desired shape and then find the optimal dimensions for that profile. For example, Razelos and Imre [15] require that their annular fin have a trapezoidal profile with only convective heat dissipation. Razelos and Imre dealt with circular fins exclusively but allowed for a variable heat transfer coefficient and thermal conductivity. Another form of constraint requires a minimum material thickness. Barnes [16, 17] used a variational formulation to study the effects of constraints on the maximum and minimum thickness of a convective fin.

Dhar and Arora [18] discuss arrays of fins, where the formulation included the effects of the space between the fins. The formulation also allowed for constraints on the fin root width. Dhar and Arora parametrized the profile of the fin and used a Fibonacci search to find the optimum shape for the fin. The tradeoff between spacing of the fins and the length of the individual fins is shown to be very important for maximizing the heat dissipation from the assembly. Optimization of fin assemblies, combined with the previously mentioned problem of a variable root temperature, suggests that more realistic answers to the minimum mass fin problem will require consideration of two-dimensional effects [19]. For example, when radiation effects are important, heat transfer can take place between the fin surface, the base surface, and adjacent fins [20].

One obvious conclusion, from even a cursory examination of the literature, is that it is very difficult to formulate a general optimization approach that also enables the incorporation of practical design constraints. Profiles determined by variational methods, although satisfying the analysis and optimization problems exactly, present many difficulties. For example, the geometric fin shapes from these methods tend to be difficult to manufacture since the profiles are often very complicated mathematical functions. For classical optimal fin shapes mechanical problems arise due to the fragility of the sharp ends.

A more general approach should have some of the following characteristics:

1 simultaneous convective and radiative heat transfer from the fin surface;

2 variable thermal conductivity (as a function of temperature or position);

3 variable heat transfer coefficient (as a function of position);

4 heat generation within the fin;

5 convection to a varying temperature;

Nomenclature

$\mathbf{A}(T, p, B)$ = $n \times n$ finite element coefficient matrix for discrete approximation
B = fin length (m)
f = finite element forcing function vector
$\mathbf{g}(u)$ = inequality design constraints
h_c = convective heat transfer coefficient (W/m^2 K)
h_r = radiative heat transfer coefficient (W/m^2 K)
$\mathbf{h}(u)$ = equality constraints
H = boundary differential operator
k = thermal conductivity of fin material (W/m K)
L = differential operator
$\mathbf{L}$ = Lagrangian
m = number of design parameters
n = number of computational grid points
N_i = finite element shape functions
$p(x)$ = polynomial describing the fin profile
$\mathbf{p}$ = vector of design parameters $\mathbf{p} = (a_0, a_1, \ldots)$
T_c = temperature for convection (K)
T_0 = temperature at the root of the fin (K)
T_r = temperature for radiation (K)
$T(\mathbf{x})$ = temperature at position $\mathbf{x}$ (K)
T_i = finite element approximation to temperature at node i (K)
q = heat flux at the surface of the fin (W/m^2)
Q = internal heat generation
$\mathbf{u}$ = vector of field values and design variables ($\mathbf{T}$, $\mathbf{p}$, $\mathbf{B}$)
$\mathbf{x}$ = spatial coordinates, (x, y) in 2 dimensions
Z_0 = fin width (m)
ϵ = emissivity of surface
σ = Stefan-Boltzmann constant (W/m^2 K^4)
Γ = boundary of the computational domain
Ω = spatial extent of the computational domain
Φ = objective function

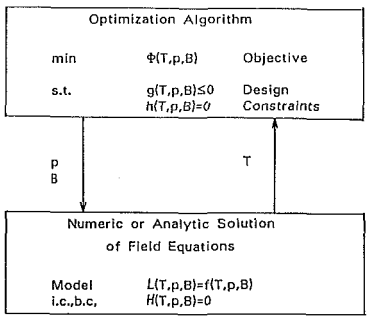

Fig. 2 Methodologies for analysis and optimization

6 radiation to a varying temperature;
7 variable root temperature; and
8 arrays of fins.

In addition there are design constraints that must be considered:

1 control of the fin shape and the basic dimensions;
2 restricted dimensions of the fin base;
3 manufacturing limits for the fin thickness at the tip; and
4 a fin profile that is amenable to automatic machining.

Most of these attributes make the design problem very difficult to solve by classical means.

4 Combined Analysis and Optimization

One way to satisfy all the desirable attributes listed in the previous section is to formulate the fin design problem as a mathematical programming problem of the type

Design Objective

$$\min \Phi(\mathbf{T}, \mathbf{p}, \mathbf{B})$$

s.t.

System Model

Model $L(\mathbf{T}, \mathbf{p}, \mathbf{B}) = f(\mathbf{T}, \mathbf{p}, \mathbf{B})$

Boundary Conditions $H(\mathbf{T}, \mathbf{p}, \mathbf{B}) = 0$

Design Constraints

$$g(\mathbf{T}, \mathbf{p}, \mathbf{B}) \leq 0$$

$$h(\mathbf{T}, \mathbf{p}, \mathbf{B}) = 0 \qquad (9)$$

where the set of variables that will be used are: **T**, the temperature variable, **p**, the design variables that define the shape of the fin, and **B**, the length of the fin. The proposed method depends on solving the heat conduction equation by a numerical approximation method, which results in the solving of a set of nonlinear algebraic equations. The optimization maximizes the objective function, in this case the rate of heat dissipation. Constraints on the geometry (inequality constraints) and the requirement of a given volume for the fin (equality constraint) are also in the mathematical program. In a variational formulation the objective function to maximize the heat transfer is very simple. In reality, the design objective function could be augmented to reflect the tradeoff between better heat transfer and manufacturing certain shapes of fins. In a numerical optimization procedure one can have this more complicated objective function that can reflect the profit of more heat transfer against the cost of having certain parameters for the shape of the fin.

Note that since some of the optimization variables are geometric parameters of the domain, every time the problem is solved the approximation basis is changed completely. In our system we have a governing partial differential equation, boundary conditions and some domain of interest. This information plus some knowledge about the physical properties (parameters) is enough to perform an analysis. Design requirements, expressed through equality or inequality constraints, will usually be needed to complete the problem definition if the goal is optimization of the system performance.

The optimization and analysis procedures can be one master problem, or two procedures passing information between the optimization and the analysis. Both options are shown in Fig. 2.

In practice there are several reasons to couple analysis and optimization and to be able to calculate the values of the design parameters and the values of the state variables that satisfy the governing equations. Optimization criteria and design constraints depend upon the solution of the field variables. Toward a more automated procedure, the works of Cryer [21] and Pironneau [22] handle free boundary problems, which are design problems as the boundary must satisfy a given constraint. Cryer approximated the free boundary as a polynomial expression and solved for the parameters by iterating on a free boundary constraint. Pironneau used optimal control theory. Botkin [23] and Bennett and Botkin [24] present an integrated system for solving the minimum mass problem of structural design. Structural load requirements and allowable stress levels are the design constraints (inequalities), and the design variables are the boundary shape parameters. Further work in the field of structural optimization may be found in [25] and [26]. The COPES/CONMIN system [27–29] is an example of the approach shown in Fig. 2(*a*). In this system the optimization is carried out using a feasible directions algorithm. This method requires a user-supplied subroutine which can analyze a system for a particular set of design parameters.

Simultaneous optimization and analysis procedures are based on the recognition that the analysis equations can be considered to be equality constraints. Chao [30] applied this idea to structural optimization using the Han method, which is an infeasible path approach to optimization. The equations from the finite element approximation are equality constraints in the mathematical program. This approach is represented in Fig. 2(*b*). This formulation handles inequality constraints directly as part of the overall optimization problem.

Rizk [31] also shows an example of a simultaneous approach. While iterating the analysis equations, the objective function is updated, and information is provided to move the values of the design variables. Rizk's method does not easily handle inequalities, however.

5 Numerical Approach to the Heat Transfer Problem

While there are many procedures for solving for the temperature distribution, a finite element approach based on a Galerkin formulation and integration by parts was used in this work to obtain a discrete representation. The resulting set of nonlinear algebraic equations are of the form

$$[A(\mathbf{T}, \mathbf{p}, \mathbf{B})]\{\mathbf{T}\} = \{f\} \qquad (10)$$

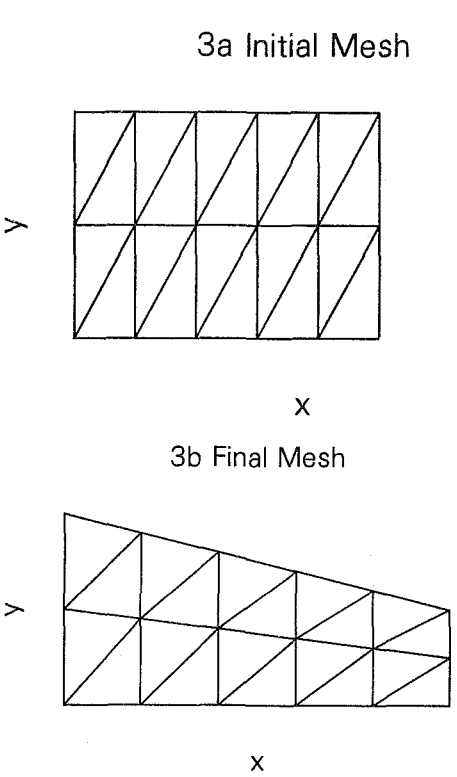

Fig. 3 Evolution of the mesh from a starting approximation to the final optimal form for the fin

$$a_{ij} = \sum \int_{\Omega} k\left(\frac{\partial N_i}{\partial x}\frac{\partial N_j}{\partial x} + \frac{\partial N_i}{\partial y}\frac{\partial N_j}{\partial y}\right) d\Omega + \sum \int_{\Gamma} (h_c + h_r) N_i N_j d\Gamma \tag{11}$$

$$f_i = \sum \int_{\Omega} N_i Q d\Omega + \sum \int_{\Gamma} N_i (h_c T_c + h_r T_r) d\Gamma \tag{12}$$

(note that the algebraic equations are equality constraints in the optimization problem) where $\mathbf{T}$ is the vector of nodal temperatures, and $\mathbf{N}_{i,j}$ are the finite element shape functions. The usual linear finite element approximation for a two-dimensional shape [32–33], based on a typical mesh as shown in Fig. 3, is given by

$$T = \sum N_i(x,y) T_i \tag{13}$$

$$N_i = \frac{1}{2A_i}(\alpha_i + \beta_i x + \gamma_i y) \tag{14}$$

where α_i, β_i, and γ_i are the finite element mesh coefficients.

The following assumptions are made in the formulation:

1 within an element, the thermal conductivity k is a constant;

2 T_c and T_r are constants;

3 the heat generation, Q, is a constant within an element;

4 the emissivity, ϵ, does not change along the length of the fin;

5 in the finite element approximation, the heat transfer coefficient h_c varies linearly along the edge of an element; and

6 the integrals along the boundary use a linear variation in temperature.

The nonlinear radiation integrals were integrated by substituting equations (8), (13), and (14) into equations (11) and (12). The resulting expressions can be integrated by using analytical formulas available for integrating functions in area coordinates [32]. The detailed equations are available in [43].

The finite element equations define a coupled set of nonlinear equations for analysis. If there were fluid flow around the fin, then interaction between the fluid and fin would be reflected in the boundary conditions through h_c and T_c. If there is significant heat flow through the tip of the fin, then the fin tip surface integral could be included in the finite element formulation.

6 Optimization Algorithm

As shown previously the basic mathematical form for many design problems is the general nonlinear programming problem.

$$\begin{aligned} \min_{\mathbf{u}} \quad & \Phi(\mathbf{u}) \\ \text{s.t.} \quad & \mathbf{g}(\mathbf{u}) \le 0 \\ & \mathbf{h}(\mathbf{u}) = 0 \end{aligned} \tag{15}$$

where for the fin design problem the vector of variables, $\mathbf{u}$, would the set $(\mathbf{T}, \mathbf{p}, \mathbf{B})$.

In this work the fin optimization problem will be to maximize the amount of heat dissipated for a given mass of material.

$$\Phi(\mathbf{u}) = \int_{\Gamma} q d\Gamma \tag{16}$$

The parameters defining the boundary of the fin are the design variables, for example for a linear polynomial giving a trapezoidal shape,

$$p(x) = a_0 + a_1 x \tag{17}$$

$$\mathbf{p} = (a_0, a_1) \tag{18}$$

The equality constraints in the nonlinear program are the finite element equations (10) and the equality constraint specifying a given volume of material for the fin. The inequalities are design constraints, such as the length of the fin must be less than some set length (which is a simple bound).

$$\min \quad -\int_{\Gamma} q d\Gamma \tag{19}$$

$$\text{s.t.} \quad [A]\{\mathbf{T}\} - \{f\} = 0 \tag{20}$$

$$2\int_{\Omega} p(x) dx - A_p = 0 \tag{21}$$

$$\mathbf{g}(\mathbf{p}, \mathbf{T}, \mathbf{B}) \le 0 \tag{22}$$

$$\mathbf{h}(\mathbf{p}, \mathbf{T}, \mathbf{B}) = 0 \tag{23}$$

Consider Fig. 2(*a*). For a given set of parameters defining the boundary the finite element equations describe the heat flow, and determine the nodal temperatures. The optimization algorithm searches for the design variables, which are the parameters defining the boundary, to give the maximum heat dissipation. In effect the optimizer, for each trial shape, requests a solution of the finite element equations to determine the heat dissipation.

An alternative approach is shown in Fig. 2(*b*). The finite element equations become nonlinear equality constraints for the general nonlinear mathematical program. In other words the finite element equations describing the heat flow are converged simultaneously as the design variables are driven to their optimal solutions.

The final equations used in the nonlinear program are given by (19–23). The objective function (19) is simply the integral of the heat flux over the surface of the fin. Equation set (20) is given by equations (10–12) and are taken directly from standard finite element texts. The constraint on the profile

given by (21) is simply the sum of the areas of the elements. The only inequalities used presently are bounds on the fin length. Any set of finite element equations that satisfies the governing equation may be used as a set of equality constraints in the optimization.

The technique chosen in this work to solve the nonlinear program is the Han algorithm. The Han method is a relatively complicated approach compared to penalty function methods or feasible path methods. However, it has a number of advantages over other methods: It handles equality and inequality constraints automatically, has superior convergence characteristics, may start from an infeasible point, and may be reformulated to reduce the number of optimization variables by using the equality constraints [34]. The implementation [35] employed in this study used a robust quadratic programming package, QPSOL [36], to solve the quadratic programming subproblems. The method is also available in the Harwell library as VFO2 [42].

Han [27] suggested that the nonlinear optimization could be solved by solving a series of successive quadratic approximation program subproblems

$$\min \quad \nabla\Phi(\mathbf{u})^T\mathbf{d} + \tfrac{1}{2}\mathbf{d}^T\mathbf{B}\mathbf{d} \tag{24}$$

$$\text{s.t.} \quad \mathbf{g} + \nabla\mathbf{g}^T\mathbf{d} \le 0 \tag{25}$$

$$\mathbf{h} + \nabla\mathbf{h}^T\mathbf{d} = 0 \tag{26}$$

where

$$\mathbf{d} = \mathbf{u}^{i+1} - \mathbf{u}^i \tag{27}$$

The matrix $\mathbf{B}$ is an $n \times n$ approximation of the Hessian matrix of Lagrangian function

$$\mathbf{L}(\mathbf{u},\mu,\eta) = \Phi(\mathbf{u}) + \mu^T\mathbf{g}(\mathbf{u}) + \eta^T\mathbf{h}(\mathbf{u}) \tag{28}$$

where μ and η are the Lagrange multipliers for the active inequality constraints and equality constraints, respectively.

Powell's [38] modification of Han's work uses a quasi-Newtonian method to update the Hessian approximation as the optimization proceeds. Further operational details about the method and its implementation are described in [39–40].

The Han method is an infeasible path method. This means that as the optimization proceeds the equality constraints are not necessarily satisfied at every iteration of the algorithm. However, it also means that we may start with an infeasible starting point.

7 Results

Two problems are presented to demonstrate the proposed approach. The first problem is a comparison against a solution obtained using a similarity transform on the governing partial differential equations leading to an ordinary differential equation that was solved numerically. Our formulation was written to solve the problem of maximizing the heat dissipation for a given mass of fin. The alternative is to minimize the mass of material for a given heat dissipation. The physical properties used are presented in Table 1. These values were used for both problems and are based on the parameters in [13]. The calculations were done in FPS units and have been converted to SI units.

Problem 1. We wish to determine the optimum trapezoidal fin with specified minimum thickness, w, with the only mode of heat dissipation being radiation to free space. Further, we specify that the half-fin tip thickness, w, be 1.2698×10^{-3} m.

Wilkins [10] has solved this class of problem and has presented graphs to do this calculation. Wilkins solves the problem of minimizing the profile area of the fin for a given heat dissipation. If we require that 293.1 W be dissipated we can calculate the optimum trapezoidal fin dimensions for a specified fin tip size. We solve the alternate formulation, maximizing the heat dissipation for a given profile area of the fin. Using the optimal area found by Wilkins' method, we calculate the maximum heat dissipation, and the dimensions for the optimal fin. The results are presented in Table 2.

Table 1 Fin Parameters for example problems

h_c	= 5.677 W/m^2 K
ϵ	= 0.95
T_0	= 555 K
k	= 34.61 W/m K
Z_0	= 0.3048 m

Table 2 Optimal fin geometry values for Problem 1

	Wilkins	This work
q[W]	293.1 (specified)	293.0
A_p[m^2]	2.0345×10^{-3}	2.0345×10^{-3} (specified)
B[m]	0.1742	0.1686
a_0	1.2698×10^{-3} (specified)	1.2698×10^{-3} (specified)
a_1	0.05248	0.05651

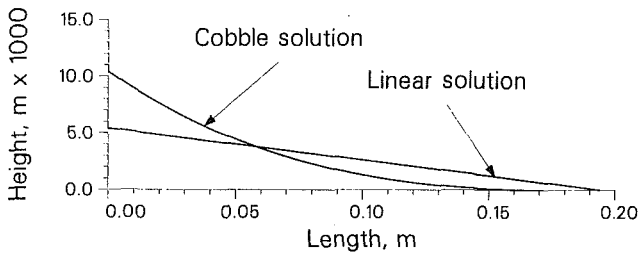

Fig. 4 Cobble's optimal fin solution, and the optimal linear surface fin

Note that our answer for the heat dissipation and for the values of the shape parameters are very close to that calculated when one uses Wilkins' method. We are using a finite element approximation of only 20 triangular elements to calculate the temperature profile within the fin, and are calculating the gradients of the objective function and constraints by finite differencing. The difference in value for the slope of the fin suggests the numerical approximation procedure is more sensitive to the height of the fin than to the slope of the surface. The difference in the fin length determined by Wilkins' methods and by the present optimization scheme is about 3%. Possible sources of numerical error for the fin length discrepancy include: gradients determined by perturbation, piecewise linear temperature profile assumptions, and optimization termination criteria.

From a practical point of view it is also important to note that the starting guess for this solution was purposefully crude. We set $a_0 = 3.48 \times 10^{-4}$, and $a_1 = 0$ (a rectangle), and the initial height was 0.1524 m, with the initial temperature profile approximated by a linear function from 555 K to 333 K. Thus one can start the design from an infeasible starting point, even using the wrong shape. There were the equality constraints for the finite element approximation and two equality constraints specifying the profile area and the fin tip size.

Problem 2. We wish to determine the optimum trapezoidal fin with specified minimum thickness, with heat dissipation from combined convection and radiation. We shall resolve Cobble's [13] problem where $T_c = 289$ K and $T_r = 250$ K. This work was corrected by Wilkins [14] but the corrections to the actual results of the particular problem were slight.

Again the problem solved by Cobble was to minimize the profile area for a given heat dissipation. For a heat dissipation of 293.1 W, Cobble's profile is presented in Fig. 4. The fin has $W = 0.010414$ m, $B = 0.17137$ m, and $A_p = 1.048 \times 10^{-3}$ m^2. The problem was solved using the finite element/Han

approach requiring the same profile area as Cobble's solution, a fin tip of 3.048×10^{-6} m, and a linear profile for the fin leading to a triangular shape.

The resulting fin solution dissipated 269.7 W and the parameters for the trapezoid were: $B = 0.19141$ m, $a_1 = 2.78092 \times 10^{-2}$, $a_0 = 3.048 \times 10^{-6}$. This solution is plotted in Fig. 4.

In both of the sample problems there were inequality constraints, though they were set loosely enough that they did not affect the final solution, i.e., they were not active at the final solution. The use of simple bounds and inequalities is recommended even for problems where the final answer is not on one of these bounds because they can prevent problems during convergence of the optimization. Of course, one could set any inequality bounds or constraints that one needs, since the Han algorithm will be able to activate them as required.

These results show that this procedure could provide a convenient way of finding geometrical values to domains where transport occurs. The finite element approximations also provide values of the temperatures within the fin. The polynomial defining the boundary does not have to be a simple linear expression, but could be a higher-order polynomial. One must recognize, however, that with higher order profile shapes there will be a higher error in calculating the heat dissipation on the boundary due to the linear temperature approximations used. This may be compensated for by increasing the number of nodes within the domain, at the price of higher computational cost.

8 Conclusions

A method has been presented to solve the optimal fin design problem for a prescribed surface polynomial. The method uses a finite element approximation to calculate discrete values for the temperature profile within the fin. Values of the temperatures at the nodal points, the length of the fin, and the polynomial coefficients are calculated for at the same time using a Newton-like method. Design constraints, both equalities and inequalities, can be handled easily.

Acknowledgments

The authors gratefully acknowledge support from the Exxon Foundation. A. Hrymak was also the recipient of an Imperial Oil Graduate Research Fellowship.

References

1 Kern, D. Q., and Kraus, A. D., *Extended Surface Heat Transfer*, McGraw-Hill, New York, 1972.

2 Ozisik, M. N., *Basic Heat Transfer*, McGraw-Hill, New York, 1977.

3 Suryanarayana, N. V., "Two-Dimensional Effects on Heat Transfer Rates From an Array of Straight Fins," ASME JOURNAL OF HEAT TRANSFER, Vol. 97, 1977, pp. 129–132.

4 Schmidt, E., "Die Waermeuebertragung durch Rippen," *Zeitschrift des Vereines Deutscher Ingenieure*, Vol. 70, 1926, pp. 885–889, 947–951.

5 Duffin, R. J., "A Variational Problem Relating to Cooling Fins," *Journal of Mathematics and Mechanics*, Vol. 8, 1959, pp. 47–56.

6 Wilkins, J. E., "Minimum-Mass Thin Fins and Constant Temperature Gradients," *SIAM Journal*, Vol. 10, 1962, pp. 62–73.

7 Liu, C. Y., "On Optimum Rectangular Cooling Fins," *Quarterly Journal of Applied Mathematics*, Vol. 19, 1961, pp. 72–75.

8 Liu, C. Y., "A Variational Problem Relating to Cooling Fins with Heat Generation," *Quarterly Journal of Applied Mathematics*, Vol. 19, 1961, pp. 245–251.

9 Wilkins, J. E., "Minimum-Mass Thin Fins Which Transfer Heat Only by Radiation to Surroundings at Absolute Zero," *SIAM Journal*, Vol. 8, 1960, pp. 630–639.

10 Wilkins, J. E., "Minimum Mass Thin Fins for Space Radiators," *Proceedings of the 1960 Heat Transfer and Fluid Mechanics Institute*, Ed. D. M. Mason, W. C. Reynolds, and W. G. Vincenti, Stanford University Press, Stanford, 1960, pp. 229–243.

11 Melese, G. B., and Wilkins, J. E., "Efficiency of Longitudinal Fins of Arbitrary Shape with Nonuniform Surface Heat Transfer and Internal Heat Generation," *Proceedings of the Third International Heat Transfer Conference*, Vol. 3, American Institute of Chemical Engineers, 1966, pp. 272–280.

12 Haley, K. W., and Westwater, J. W., "Boiling Heat Transfer from Single Fins," *Proceedings of the Third International Heat Transfer Conference*, Vol. 3, American Institute of Chemical Engineers, 1966, pp. 245–253.

13 Cobble, M. H., "Optimum Fin Shape," *Journal of the Franklin Institute*, Vol. 291, 1971, pp. 283–292.

14 Wilkins, J. E., "Optimum Shapes for Fins Rejecting Heat by Convection and Radiation," *Journal of the Franklin Institute*, Vol. 297, 1974, pp. 1–6.

15 Razelos, P., and Imre, K., "The Optimum Dimensions of Circular Fins With Variable Thermal Parameters," ASME JOURNAL OF HEAT TRANSFER, Vol. 102, 1980, pp. 420–425.

16 Barnes, E. R., "A Variational Problem Arising in the Design of Cooling Fins," *Quarterly Journal of Applied Mathematics*, Vol. 34, 1976, pp. 1–17.

17 Barnes, E. R., "Some Max-Min Problems Arising in Optimal Design Studies," in: *Control Theory of Systems Governed by Partial Differential Equations*, Ed. A. K. Aziz et al., Academic Press, 1977, pp. 177–208.

18 Dhar, P. L., and Arora, C. P., "Optimum Design of Finned Surfaces," *Journal of the Franklin Institute*, Vol. 301, 1976, pp. 379–392.

19 Ingham, D. B., Heggs, P. J., Manzoor, M., and Stones, P. R., "Two-Dimensional Analysis of Fin Assembly Heat Transfer: A Comparison of Solution Techniques," in: *Numerical Properties and Methodologies in Heat Transfer: Proceedings of the Second National Symposium*, Ed. T. M. Shih, Hemisphere, New York, 1983.

20 Frost, W., and Eraslan, A. H., "Solution of Heat Transfer in a Fin With Combined Convection and Radiative Interaction Between the Fin and Surrounding Surfaces," *Proceedings of the 1968 Heat Transfer and Fluid Mechanics Institute*, Ed. A. F. Emery and C. A. Depew, Stanford University Press, Stanford, 1968, pp. 206–220.

21 Cryer, C. W., "On the Approximate Solution of Free Boundary Problems Using Finite Differences," *Journal of the Association for Computing Machinery*, Vol. 17, 1970, pp. 397–411.

22 Pironneau, O., *Optimal Shape Design for Elliptic Systems*, Springer-Verlag, New York, 1984.

23 Botkin, M. E., "Shape Optimization of Plate and Shell Structures," *AIAA Journal*, Vol. 20, 1982, pp. 268–273.

24 Bennett, J. A., and Botkin, M. E., "Automated Design for Automotive Structures," ASME *Journal of Mechanical Design*, Vol. 104, 1982, pp. 799–805.

25 Gallagher, R. H., and Zienkiewicz, O. C., *Optimum Structural Design*, Wiley, London, 1973.

26 Kirsch, U., *Optimum Structural Design*, McGraw-Hill, New York, 1981.

27 Vanderplaats, G. N., "CONMIN - A Fortran Package for Constrained Function Minimization," NASA TMX-62282, 1973.

28 Madsen, L., and Vanderplaats, G. N., "COPES-A Control Program for Engineering Synthesis, Users Manual," Naval Post-graduate School Technical Report NPS-69-81-003 VN, Monterey, CA, July, 1981.

29 Hedderich, C. P., Kelleher, M. D., and Vanderplaats, G. N., "Design and Optimization of Air-Cooled Heat Exchangers," ASME JOURNAL OF HEAT TRANSFER, Vol. 104, 1983, pp. 683–690.

30 Chao, N. H., "Application of a Reduced Quadratic Programming Technique to Optimal Structural Design," Ph.D. Thesis, Department of Mechanical Engineering, Carnegie-Mellon University, Pittsburgh, PA, 1981.

30 Rizk, M. H., "The Single-Cycle Scheme: A New Approach to Numerical Optimization," *AIAA Journal*, Vol. 21, 1983, pp. 1640–1647.

32 Zienkiewicz, O. C., *The Finite Element Method*, McGraw-Hill, New York, 1977.

33 Comini, G., Del Guidice, S., Lewis, R. W., and Zienkiewicz, O. C., "Finite Element Solution of Non-Linear Heat Conduction Problems With Special Reference to Phase Change," *International Journal for Numerical Methods in Engineering*, Vol. 8, 1974, pp. 613–624.

34 Locke, M. H., Westerberg, A. W., and Edahl, R. H., "An Improved Successive Programming Optimization Algorithm for Engineering Design Problems," *AIChE Journal*, Vol. 29, 1983, pp. 871–874.

35 Clark, P. A., "Embedded Optimization Problems in Chemical Process Design," Ph.D. Thesis, Department of Chemical Engineering, Carnegie-Mellon University, Pittsburgh, PA, 1983.

36 Gill, P. E., Murray, W., Saunders, M. A., and Wright, M. H., "Documentation for SOL/QPSOL a FORTRAN package for Quadratic Programming," Systems Optimization Laboratory, Department of Operations Research, Stanford University, Stanford, CA 94305.

37 Han, S. P., "A Globally Convergent Method for Nonlinear Programming," *Journal of Optimization Theory and Applications*, Vol. 22, 1977, pp. 297–309.

38 Powell, M. J. D., "A Fast Algorithm for Nonlinearly Constrained Optimization Calculations," *Lecture Notes in Mathematics, Proceedings of the Dundee Conference, 1977*, Vol. 630, Ed. G. A. Watson, Springer-Verlag, Berlin, 1978, pp. 144–157.

39 Fletcher, R., *Practical Methods of Optimization, Volume 2, Constrained Optimization*, Wiley, New York, 1981.

40 Reklaitis, G. V., Ravindran, A., and Ragsdell, K. M., *Engineering Optimization, Methods and Applications*, Wiley, New York, 1983.

41 Razelos, P., and Imre, K., "Minimum Mass Convective Fins With Variable Heat Transfer Coefficient," *Journal of the Franklin Institute*, Vol. 135, No. 4, 1983, pp. 269–282.

42 Harwell Subroutine Library, Computer Science and Systems Division, Atomic Energy Research Establishment, Harwell, Oxfordshire, England, 1984. (contact Mr. S. Marlow, Building 8.9, AERE Harwell, Didcot, Oxon, OX11 ORA, U.K.)

43 Hrymak, A. N., "Adaptive Grid Approaches to the Design and Analysis of Distributed Parameter Systems," Ph.D. Thesis, Department of Chemical Engineering, Carnegie-Mellon University, Pittsburgh, PA, 1984.

Inclination-Induced Direct-Contact Melting in a Circular Tube

E. M. Sparrow
Fellow ASME

T. A. Myrum

Department of Mechanical Engineering,
University of Minnesota,
Minneapolis, MN 55455

Melting of a phase-change medium encapsulated in a circular tube was investigated experimentally at a succession of tube inclinations relative to the vertical. It was found that repeatable and continuous direct contact of the melting solid with the tube wall was established at an inclination of about 15 deg and that further increases in inclination had virtually no effect on the melting results. Direct contact gave rise to substantial enhancements (up to a factor of two) in the amount of melted mass and in the energy transfer, relative to those for natural-convection-dominated melting (e.g., for the vertical tube case). The energy transfer was subdivided into two components, the latent heat supplied to the melting interface and the sensible heat stored in the liquid melt, and a general correlation of the two components was achieved. With regard to the pattern of melting, it was observed that the continuous-contact mode was preceded by a period of partial contact. During that period, the solid was tipped toward the wall while pivoting about its lower edge.

Introduction

In the melting of a solid which is encapsulated in a closed, heated container, the rate of phase change is governed by the ease with which heat can be transported from the wall of the container to the solid–liquid interface. In traditional analytical models of melting, it was assumed that conduction across the liquid melt was the sole means by which heat was carried from the wall to the interface. More recent work, encompassing both experiment and analysis, has demonstrated the key role played by natural convection in the melt layer in the wall-to-interface heat transfer. These studies have documented the marked increase in the melting rate that accompanies the presence of natural convection.

Another mode of melting may be identified in which the melting solid is pressed against the container wall by its own weight, enabling the heat transfer to occur over a very short distance and, therefore, at a high rate. This mode of melting may be termed the direct-contact mode although there is, necessarily, a thin liquid film between the container wall and the melting solid. Such a film exists because of the continuous production of liquid by the melting process. The liquid produced by the melting is continuously squeezed out of the direct-contact zone by the force which presses the solid against the wall.

Both the natural convection and direct-contact heat transfer modes are significantly affected by the orientation of the container in the gravity field. In elaborating this issue, it is appropriate to focus attention on the specific type of container to be investigated here, namely, a cylindrical tube of length–diameter ratio much larger than one. When the tube is vertical, the melting solid is a tapered vertical cylinder, with its diameter decreasing from bottom to top and with its axis coinciding with that of the tube. In this case, there is no direct-contact melting, and natural convection conveys heat from the tube wall to the melting interface.

When the tube is inclined relative to the vertical, a component of the gravity force acts to press the melting solid against the tube wall, provided that the density of the solid exceeds that of the liquid. The pressing force will increase as the inclination increases and, correspondingly, the thickness of the liquid film should decrease, giving rise to higher rates of melting. Thus, a succession of tube orientations which start with the vertical and proceed toward larger inclinations should be characterized by a transition from melting controlled by natural convection to melting controlled by direct contact.

The work to be described here is, seemingly, the first systematic experimental study of the transition between melting controlled by natural convection and by direct contact. The melting rates for the natural convection case serve as a baseline for the identification of the enhancement in melting due to direct contact. The experiments were performed using a copper-walled circular tube filled with a high-purity paraffin (99 percent pure n-eicosane) to yield a length–diameter ratio of approximately 5:1. In a sequence of experiments, melting was first investigated with the tube axis vertical (natural convection case) and then at a succession of nonvertical orientations characterized by the axis inclined at angles of 5, 10, 15, 20, 25 deg to the vertical. At each orientation, data were collected over a range of melting times (up to a time at which about 90–95 percent of the solid was melted). Melting was initiated and maintained by the application of a step-change increase in the tube wall temperature. Two different tube wall temperatures were employed during the course of the work, one yielding a slow rate of melting and the other a rapid rate of melting. All of the experiments were performed with the solid at its phase-change temperature prior to the initiation of melting.

Four types of measurements were made for each data run. One of these yielded the melted mass, from which the energy stored as latent heat was deduced. The second provided the bulk temperature of the liquid melt and, thereby, the energy stored as sensible heat. The measurement of the tube wall temperature distribution at intervals during the data run and of the shape of the unmelted solid yielded information about the mode of the melting and its dependence on inclination.

Prior studies of direct-contact melting have dealt with containment configurations of fixed orientation in the gravity field, namely, the horizontal cylinder [1, 2] and the sphere [3]. Furthermore, in none of these studies was a natural convection baseline case established (by constraining the melting solid and thereby preventing its gravity-related contact with the wall). Therefore, the extent of the enhancement in melting due to direct contact has not heretofore been established. In [4–6], natural-convection-controlled melting in a horizontal cylinder was achieved by constraining the melting solid, but the corresponding direct-contact (i.e., unconstrained) mode was not investigated. Melting in a vertical tube, which, as a matter of course, is controlled by natural convection, was investigated in [7].

Contributed by the Heat Transfer Division for publication in the JOURNAL OF HEAT TRANSFER. Manuscript received by the Heat Transfer Division August 13, 1984.

Experiments

Experimental Apparatus. The main components of the experimental apparatus included a containment tube, a constant-temperature water bath utilized in establishing the thermal state of the solid prior to melting, a second constant-temperature water bath which served to impose a preselected temperature on the wall of the containment tube during melting, and appropriate instrumentation. The essential features of these components will now be described.

The containment tube consisted of three parts: an open-ended, thin-walled copper cylinder and caps used to close the respective ends of the cylinder. The copper cylinder was 39.4 cm in overall length, with an internal diameter of 5.08 cm and a wall thickness of 0.160 cm. When the containment tube was situated in either of the aforementioned constant-temperature water baths, the cap which closed the lower end of the cylinder was in contact with the water, while the upper end cap protruded above the water surface and did not contact the water. Both caps were made of insulating materials to minimize thermal end effects.

The lower end cap fulfilled the dual functions of an insulating barrier and a seal against the intrusion of water into the tube. It consisted of a 3.8-cm-long polystyrene cylinder bonded to a Teflon base that was grooved to house an O-ring which sealed by contact with the inner surface of the copper cylinder. The full length of the polystyrene penetrated the copper cylinder, and only the lower portion of the Teflon base interfaced with the water. A small clearance was allowed between the polystyrene and the tube wall to accommodate an impermeable plastic wrap which covered both the top and the side of the styrene. The wrap provided a smooth, impermeable lower boundary for the paraffin phase-change material (in contrast to the porous, slightly rough surface of the polystyrene).

The upper end cap was a polystyrene cylinder which performed its insulating function by penetrating into the tube by about 5.7 cm. The polystyrene was covered by a self-adhering, impermeable plastic film. An air gap of 5.3 cm was allowed between the lower face of the cap and the upper surface of the solid-phase paraffin in order to accommodate the melting-related increase in the volume of the paraffin (i.e., volume increases due to solid–liquid phase change and subsequent superheating of the liquid). This gap size was sufficient for all of the investigated inclinations. The air displaced from the gap during the melting period by the aforementioned volume increases exited the tube through a small clearance that had been left between the cap and the tube wall.

To facilitate its suspension in either of the constant-temperature water baths, the containment tube was fitted with trunnions at its upper end. The suspension arrangement allowed for the lowermost 33 cm of the copper cylinder to be immersed below the surface of the water in the vertical orientation, while the lowermost 31.5 cm were immersed at the largest investigated inclination (25 deg to the vertical). At all inclinations, the water fully enveloped all portions of the tube containing paraffin.

The wall temperature of the copper cylinder was measured by a total of ten 30-gage, Teflon-coated, chromel-constantan thermocouples. These thermocouples had been calibrated prior to their installation in 0.076-cm-deep grooves machined into the outer surface of the cylinder. Seven of the thermocouples were deployed in-line along the downfacing side of the tube (in the inclined orientation), while the other three thermocouples were deployed along the upfacing side. The emfs of these thermocouples, as well as of those situated in the water baths, were read to 1 μV.

To attain a well-defined thermal state for the solid prior to the onset of melting, the containment tube and its charge of solid paraffin were suspended vertically in an agitated constant-temperature water bath. The bath was a large plexiglass-covered polyethylene tank equipped with a temperature control/water circulation unit. The set point of the temperature controller was adjusted to yield a thermocouple-monitored water-bath temperature just below the melting temperature T^* (= 36.3°C) of the n-eicosane paraffin used in the experiments.

A second constant-temperature water bath served as the thermal environment for the containment tube during the melting experiments. This water bath imposed a step-change temperature increase at the tube wall at the onset of the melting period. The bath consisted of a 50-L stainless steel tank, surrounded on all sides and at the bottom by 10 cm of fiberglass insulation, and housed in a wooden frame equipped with adjustable legs for leveling. The top of the tank was closed by a reinforced plexiglass cover in which apertures had been cut to enable the insertion of the containment tube and two temperature control/water circulation units into the bath. A pair of V-blocks was positioned adjacent to one of the apertures to serve as a seat for the trunnions of the containment tube. Both of the temperature control/circulation units were operated as agitators to yield high water-side heat transfer coefficients (with special care accorded to the portion of the tube where direct-contact melting occurred). One of the units served to control the water temperature, and its set point was monitored by thermocouples immersed in the bath. Two different water-bath temperatures were employed during the course of the experiments, respectively to yield temperature differences ($T_w - T^*$) between the tube wall and the melting point of 4.55 and 28°C (8.2 and 50.4°F).

A fixture seated on the floor of the tank was provided to orient the containment tube at any desired angle of inclination relative to the vertical. The fixture pressed against the Teflon base of the lower end cap. Precise determination of the inclination angle was accomplished with a bubble-level-equipped protractor head held in contact with the precisely machined upper end face of the copper cylinder. Once the desired angle had been set, the fixture was locked in place to preserve the setting. The angle was verified at the completion of each data run.

Experimental Procedure. The preparations for a data run were begun with the containment tube completely free of paraffin (the cleaning operations were performed after the conclusion of the preceding run). A new plastic wrap was applied to the polystyrene portion of the lower end cap, whereafter the cap was inserted into the copper cylinder and locked in place. Then, a fine (0.018 cm diameter) nylon line,

Nomenclature

c = liquid-phase specific heat
E = energy transfer $E_s + E_\lambda$
E_s = sensible energy stored in liquid
E_λ = energy absorbed at latent heat
$E_{\lambda,T}$ = latent energy required to melt total mass
M = melted mass
M_T = total mass of phase-change medium in tube
Ste = liquid-phase Stefan number $c(T_w - T^*)/\lambda$
T_b = bulk temperature of liquid
T_w = tube wall temperature
T^* = melting temperature
t = melting time
λ = latent heat of melting

weighted by a small nut, was carefully lowered into the empty tube until the narrow edge of the nut rested on the bottom. The nut and nylon line served to extract the unmelted solid at the end of the melting run.

At this point, the tube was weighed on a triple-beam balance having a 0.1-g resolution, after which it was filled with liquid paraffin and placed in an ice bath to facilitate solidification. Void formation during the freezing period was prevented by irradiation of the upper surface of the paraffin with a heat lamp set at low intensity. Upon completion of freezing, the upper surface of the frozen paraffin was leveled by contact with a heated disk which locally remelted the solid. The leveling operation also established the precise length of the frozen cylinder of paraffin (22.2 cm).

After the leveling, the tube and its contents were weighed (mass of paraffin $\simeq$ 380 g). The upper end cap was then put in place, and the containment tube was inserted into the equilibration bath for a period of 16–20 hr. During the equilibration period, the temperature of the other bath (i.e., the melting environment bath) was maintained at the temperature level corresponding to the desired value of $(T_w - T^*)$. At the appointed time, the containment tube was transferred from the equilibration bath to the melting environment bath, an operation which required about 10 s. During the melting run, the tube wall and bath temperatures were read at time intervals tailored to the preselected duration of the run.

At the end of the run, the upper end cap was removed and the unmelted solid extracted from the tube by means of the nylon line (in about 5 s). Then the thermocouple used for determining the bulk temperature of the liquid melt, taped to a plastic stirring rod, was inserted into the tube. With well-practiced, vigorous stirring, a steady, uniform temperature could be attained in 30–45 s. The melt was then poured out of the tube into a storage reservoir, after which the tube was disassembled and thoroughly cleaned.

The extracted unmelted solid was weighed and its height and surface contour measured. For the contour measurements, marks were scribed on the surface at intervals of 2.54 cm along the height, and a miter box was employed to section the solid (perpendicular to its axis) at the scribed markings. Subsequently, each cross section of the solid was traced on the page of a notebook.

For each of the two fixed values of $(T_w - T^*)$, six angles of inclination were employed (0, 5, 10, 15, 20, and 25 deg), and a sequence of melting runs of different duration was made for each temperature difference and angle.

Patterns of Melting

The patterns of melting were identified by observation of the shape of the solid–liquid interface (i.e., the contour of the unmelted solid) and from the temperature distribution on the wall of the containment tube. Furthermore, for purposes of corroboration, supplementary melting runs were made during which the upper end cap of the containment tube was removed for brief periods to enable the position of the melting solid to be observed. The melting pattern in an inclined tube was found to be distinctively different from that which occurs in a vertical tube (and also intermittently at small inclinations), as will now be documented.

As noted in the Introduction and illustrated in [7, 8], when the tube is vertical, the unmelted solid is a tapered vertical cylinder whose axis coincides with the axis of the tube and whose diameter decreases from the bottom to the top. The space between the solid and the tube wall is a melt-filled concentric annulus, the width of which increases in the upward direction. The dominant mode of heat transfer between the tube wall and the melting interface is natural convection.

The pattern of inclination-controlled melting is illustrated in Fig. 1. The figure shows longitudinal sectional views of a tube inclined at 25 deg to the vertical. In the figure, the (*a*), (*b*), and (*c*) diagrams respectively correspond to three times during the melting period, with time increasing from left to right. In each diagram, the dotted lines represent the outline of the containment tube, while the unmelted solid is contained within the closed envelope (i.e., within the solid lines). The liquid melt occupies the space between the solid and the tube wall.

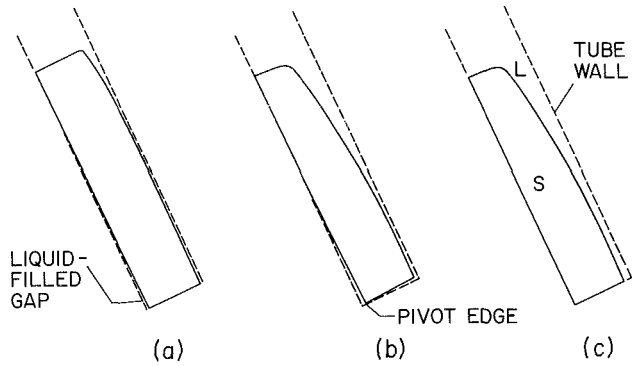

Fig. 1 Patterns of melting in an inclined tube

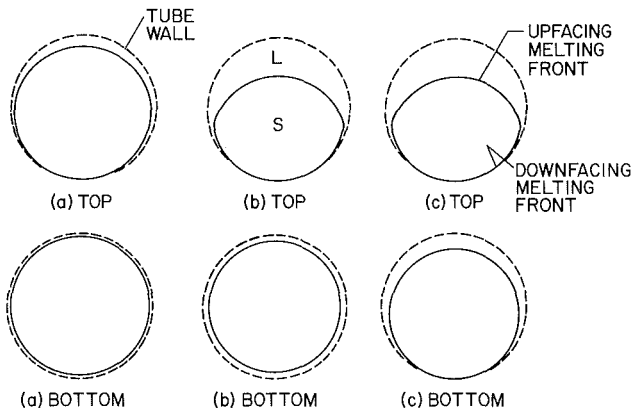

Fig. 2 Top and bottom cross sections corresponding to the melting patterns of Fig. 1

As seen in Fig. 1(*c*), the downfacing inclined portion of the melting solid eventually achieves contact all along its height with the adjacent part of the tube wall. Once this condition is attained, the solid continues to slide into the wall, thereby maintaining the contact. However, as illustrated in Fig. 1(*a*) and 1(*b*), there is only partial contact between the downfacing portion of the solid and the wall at early times, with the contact confined to the upper reaches of the solid. This behavior occurs because the solid does not slide at early times but, instead, tips toward the wall while pivoting about its lowermost edge (i.e., about the pivot point identified in Fig. 1(*b*)). Between the times corresponding to Fig. 1(*a*) and 1(*b*), the direct contact melting at the upper part of the solid brings forth a greater degree of tipping, so that the bottom of the solid heels up. Superheated liquid flows under the thus-raised heel, thereby providing lubrication to facilitate the sliding of the solid. Figures 1(*b*) and 1(*c*) are intended to correspond to times separated only by seconds – immediately prior to and immediately after sliding.

Further perspectives on the melting patterns are conveyed by Fig. 2, which shows cross-sectional views which correspond to the longitudinal sections of Fig. 1. In particular, cross sections cutting through the top and bottom of the solids of Fig. 1 (*a*–*c*) are set forth in Fig. 2. In both Figs. 2(*a*) and 2(*b*), the bottom portion of the melting solid is circular and concentric with the tube, while the top portion

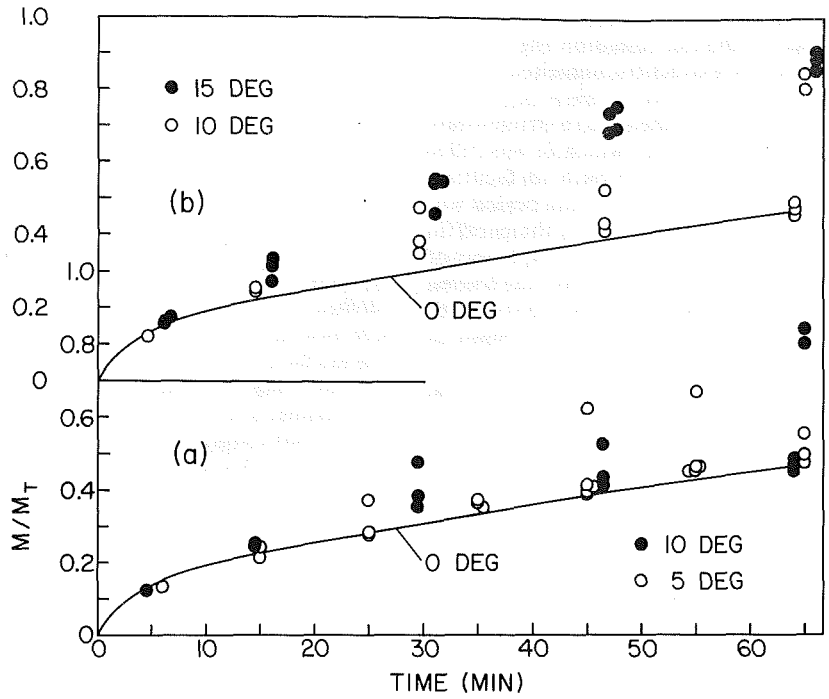

Fig. 3 Timewise variation of the melted mass, 0-, 5-, 10-, and 15-deg inclinations, $(T_w - T^*) = 4.55°C$

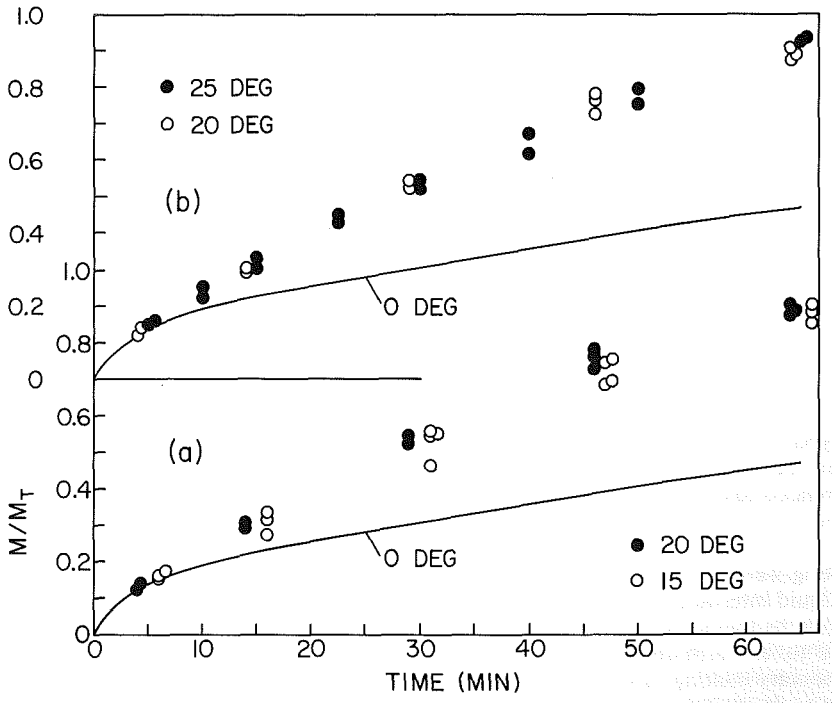

Fig. 4 Timewise variation of the melted mass, 20- and 25-deg inclinations, $(T_w - T^*) = 4.55°C$

lies against the tube wall. Note that the top cross section of the solid of 2(*b*) is beginning to take on a lens-like form. In Fig. 2(*c*), which is separated in time by only a few seconds from Fig. 2(*b*), the bottom cross section has slid against the tube wall while the top cross section remains as it was. From this time onward, the direct contact melting produces lens-like cross-sectional shapes at all axial stations. Diagrams containing more details about the timewise evolution of the shape of the melting solid are available in [8].

At small angles of inclination, 5 and 10 deg, a variety of melting patterns was encountered. In some cases, the melting solid maintained its concentric alignment with the tube axis throughout the entirety of the data run (i.e., no direct contact). In others, a period of concentric alignment was followed by pivoted positioning (upper portion of solid in direct contact with the tube wall) which persisted until the end of the run. In still other cases, the pivoting was followed by sliding of the solid into the tube wall. In view of this variety of melting patterns, the melting rates at low inclinations were not as regular as those for the vertical case or at larger angles of inclination.

The measured tube wall temperatures reflected the aforementioned patterns of melting. Aside from a brief initial transient, the tube wall temperature was virtually independent of time except during the instant when the solid slid into the wall. The wall temperature was spatially uniform in the

direct-contact region and was also spatially uniform in the region of non-contact. the temperatures of the two regions differed by 3-4.5 percent of $(T_w - T^*)$, depending on the operating conditions. Since the majority of the heat transfer occurred through the direct-contact region, $(T_w - T^*)$ was based on the wall temperature T_w of that region.

Melting Rates

The effect of tube inclination on the rate of melting will now be investigated. To this end, the timewise variation of the melted mass at a succession of inclinations will be presented and compared. For the comparisons, the melting characteristics of the vertical orientation will be regarded as a baseline case.

The aforementioned inclination-parameterized comparisons will be made at each of two values of the temperature difference $(T_w - T^*)$, which drives the melting process. The selected values of the temperature difference, 4.55 and 28°C (8.2 and 50.4°F), correspond to liquid-phase Stefan numbers of 0.041 and 0.25. These temperature differences were chosen to provide greatly different melting rates.

Attention is first directed to Figs. 3–4, which display the melting results for the smaller value of $(T_w - T^*)$. Each figure consists of two graphs, which respectively pertain to parametric values of the angle of inclination (vertical tube = 0 deg inclination). The ordinate variable is the ratio M/M_T, where M is the mass melted between the onset of melting (time = 0) and a selected time t, and M_T is the total mass of the phase-change medium in the containment tube. The M/M_T ratio is plotted as a function of the time elapsed since the onset of melting.

Figure 3(*a*) conveys the melting results for inclination angles of 0, 5, and 10 deg. To avoid confusion, the 0-deg case is represented by a curve rather than by the actual data (as can be seen in [8], the 0-deg data exhibited virtually no scatter with respect to the curve).

The 5-deg data (open symbols) appear to exhibit significant scatter. However, the seemingly scattered data actually correspond to the different patterns of melting that were described earlier. In particular, the data which fall on the vertical tube curve correspond to melting in which the solid remains centered in the tube during the entire data run. The data which fall slightly above the curve reflect a period of pivoted positioning of the solid, while the data that are displaced well above the curve correspond to an appreciable time period in which the solid continuously slid into the tube wall. Thus, direct contact enhances melting, but the body force component necessary to guarantee direct contact is not available at the 5-deg inclination.

The data for melting at 10 deg to the vertical are represented by the black symbols in Fig. 3(*a*). It is seen there that whereas the 10-deg data are generally similar in character to the 5-deg data, they depart more frequently from the baseline curve and attain higher values of M/M_T.

Substantially greater regularity (i.e., less apparent scatter) and increased values of M/M_T are in evidence for melting at 15 deg, as seen from the black data symbols in Fig. 3(*b*). For perspective, the graph also shows the 10-deg data as open symbols and the vertical tube data as a solid line. The 15-deg data are characterized by extended periods of continuous direct contact between the solid and the tube wall (i.e., the continuous sliding mode), and this is responsible for both the aforementioned regularity and enhancement.

The melting characteristics for the 20-deg inclination (black symbols) are compared with those for the 15-deg inclination (open symbols) and the vertical tube (solid line) in Fig. 4(*a*). It is relevant to note that although the 20-deg data have attained a high degree of regularity and may be incrementally higher, they are not basically different from the 15-deg data. Thus, the component of gravity needed to cause consistent and continuous sliding of the solid into the wall appears to be available at either angle. In particular, the larger force component available at the 20-deg inclination does not have a material effect on the melting results.

These conclusions are reinforced by the results presented in Fig. 4(*b*). There, the 25-deg data are represented by the black symbols, while the 20-deg and vertical tube data are respectively represented by the open symbols and the solid line. Within the moderate scatter, the 20-deg and 25-deg data are coincident, thereby reflecting a consistent melting pattern that is independent of inclination. This is a pattern dominated by direct contact.

Upon reviewing Figs. 3 and 4, it can be concluded that direct-contact-dominated melting can be regarded as being established at about an inclination of 15 deg. The enhancement in melting due to direct contact, relative to that attainable when natural convection in the liquid phase is the dominant mode of heat transfer, is appreciable. For example, at a time when $M/M_T = 0.3$ for the vertical case, the corresponding M/M_T value for the direct-contact-dominated mode of melting is about 0.52. At a larger time, a comparison of the two modes of melting yields values of 0.45 and 0.85. In view of the appreciable enhancement, there are practical incentives to encourage the direct-contact mode of melting.

Attention is now turned to the melting rate results corresponding to the larger value of the temperature difference $(T_w - T^*)$ which drives the melting, and Figs. 5 and 6 have been prepared for this purpose. These figures are similar in format to Figs. 3 and 4. Note should be taken, however, of the reduction in the duration of the melting period (ie., of the higher melting rate) which accompanies the larger temperature difference.

In general, all of the trends and conclusions which were identified in connection with Figs. 3 and 4 are also applicable to Figs. 5 and 6, but there are important differences in detail. In particular, at the low inclinations, the larger temperature difference increases the probability of the solid sliding into the wall. Thus, at the 5- and 10-deg inclinations, the fraction of the data which fall appreciably above the vertical tube baseline curve is considerably greater in Fig. 5 than in Fig. 3. This behavior can be attributed to the greater superheating of the liquid melt at larger $(T_w - T^*)$ and to the consequent better lubrication afforded by the liquid.

It is also noteworthy that the percentage enhancement in melting due to direct contact is slightly smaller at the higher value of $(T_w - T^*)$ than at the lower value of $(T_w - T^*)$. This is because the natural convection is more efficient for the former than for the latter, thereby leaving less room for improvement.

Energy Transfer

The energy E that is transferred from the tube wall to the phase-change medium during the period between the onset of melting ($t = 0$) and any time t includes two components. One is the energy E_λ which is absorbed as latent heat by the solid-to-liquid phase change (λ = latent heat per unit mass). The other is the sensible energy E_s that is associated with the superheating of the liquid melt above the phase-change temperature T^*.

From the measurement of the mass M melted between times $t = 0$ and $t = t$, the E_λ component follows directly as

$$E_\lambda = \lambda M \tag{1}$$

The sensible energy component E_s was evaluated by making use of the experimental data for the liquid bulk temperature T_b at time t. Each element of the melted mass, when first liquefied, is at the temperature T^*. At the end of the data run (time t), all elements have a common temperature T_b (owing to the mixing process). Therefore,

$$E_s = M\int_{T^*}^{T_b} c\,dT \tag{2}$$

According to Fig. 13 of [9], the liquid-phase specific heat of n-eicosane is a linear function of temperature. The c versus t data were curve-fit and then integrated in accordance with equation (2).

With a view toward comparing the magnitudes of E_λ and E_s, the ratio E_s/E_λ was plotted in [8] as a function of time at a fixed inclination and for a fixed temperature difference $(T_w - T^*)$. For all cases, it is found that aside from scatter, E_s/E_λ was independent of time. This behavior is illustrated in the lower graph of Fig. 7 for three angles of inclination for $(T_w - T^*) = 4.55°C$.

It was also observed that the E_s/E_λ ratio was very nearly equal in magnitude to the liquid-phase Stefan number, where

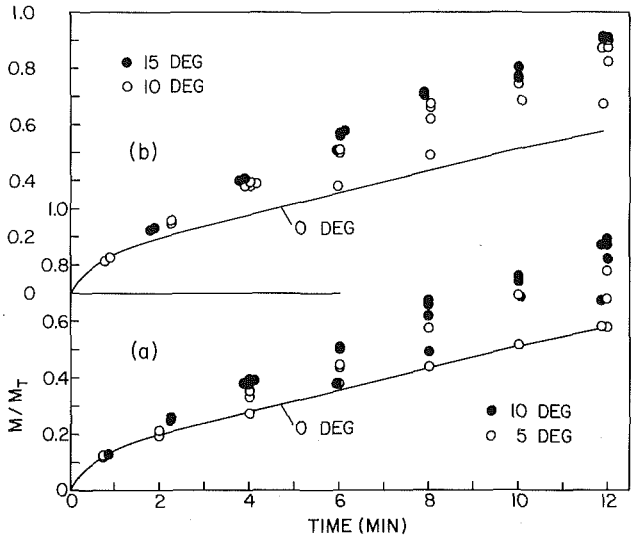

Fig. 5 Timewise variation of the melted mass, 0-, 5-, 10-, and 15-deg inclinations, $(T_w - T^*) = 28°C$

$$\text{Ste} = c(T_w - T^*)/\lambda \tag{3}$$

in which c was evaluated at T^*. Since the ratio $(E_s/E_\lambda)/\text{Ste}$ is virtually independent of time (in common with E_s/E_λ) at a fixed inclination and temperature difference, it was averaged, and the average values are presented in the upper graph of Fig. 7. In the figure, $(E_s/E_\lambda)/\text{Ste}$ is plotted as a function of inclination for parametric values of Ste (which reflect $(T_w - T^*)$). As is seen there, the $(E_s/E_\lambda)/\text{Ste}$ data generally lie in the range between 0.9 and 1.0, with the exception of a single data point. The results are well represented by

$$E_s = 0.95\text{Ste}E_\lambda \tag{4}$$

This equation also applies to the deviant data point, since for that case, moderate errors in E_s can be tolerated because $E_s << E_\lambda$.

A summary of the energy transfer results, which contrasts natural-convection-controlled melting and direct-contact-controlled melting, is presented in Figs. 8 and 9 respectively for Ste = 0.041 and 0.25. In each figure, the results for natural-convection-controlled melting are represented by the vertical tube case (0 deg), while those for direct-contact-controlled melting are represented by the 25-deg case.

Each figure displays two types of energy ratios, namely, $E/E_{\lambda,T}$ and $E_\lambda/E_{\lambda,T}$, where

$$E = E_s + E_\lambda, \quad E_{\lambda,T} = \lambda M_T \tag{5}$$

The quantity $E_{\lambda,T}$ is the latent heat which is required to melt the total contents of the containment tube. It was used as a reference quantity in Figs. 8 and 9 because its value is virtually the same for all the data runs, regardless of $(T_w - T^*)$. The vertical displacement of the $E/E_{\lambda,T}$ data (black symbols) from the $E_\lambda/E_{\lambda,T}$ data (open symbols) is a direct indication of the contribution of the sensible energy E_s.

In Fig. 8, the black and open symbols which correspond to a fixed inclination are only slightly displaced, reflecting the minor contribution of the sensible energy when Ste is very small. The enhancement in the energy transfer E due to direct contact grows during the course of the melting. At t = 15 min, the enhancement is about 45 percent, while at t = 70 min, the enhancement has increased to about a factor of two.

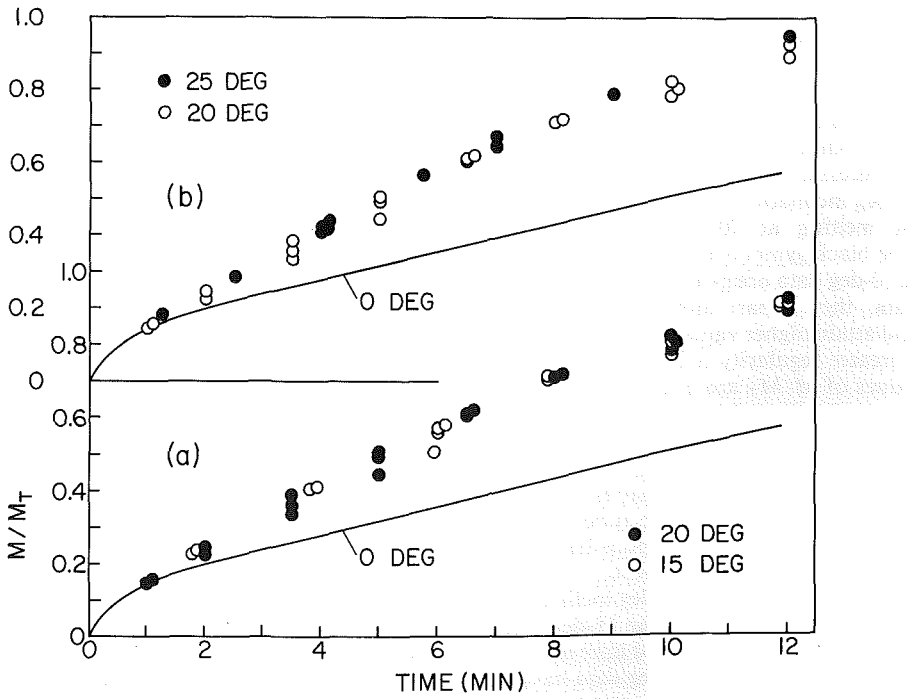

Fig. 6 Timewise variation of the melted mass, 20- and 25-deg inclinations, $(T_w - T^*) = 28°C$

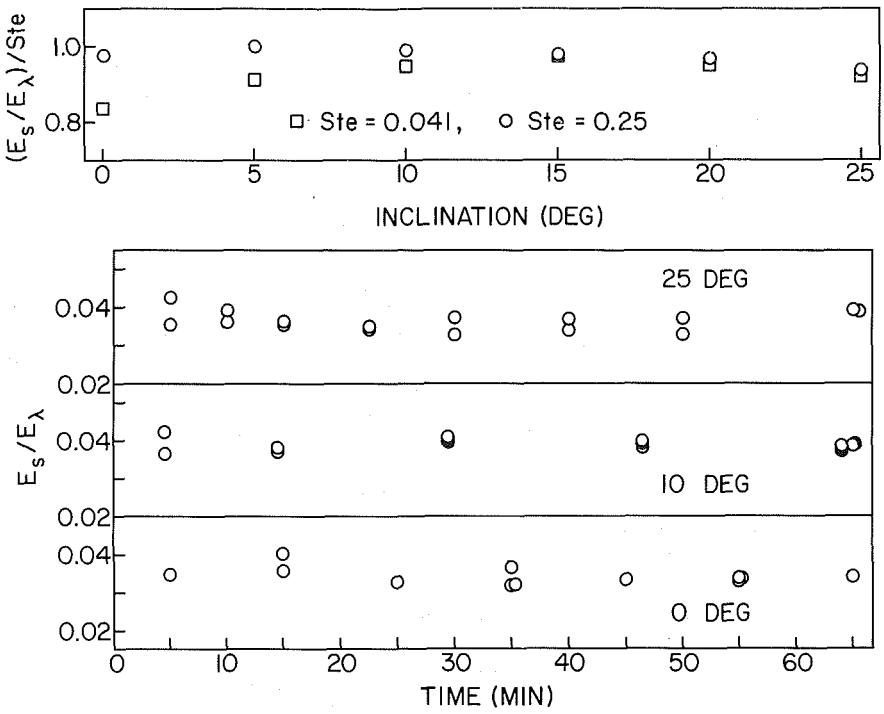

Fig. 7 Relation between the sensible and latent energy components E_s and E_λ

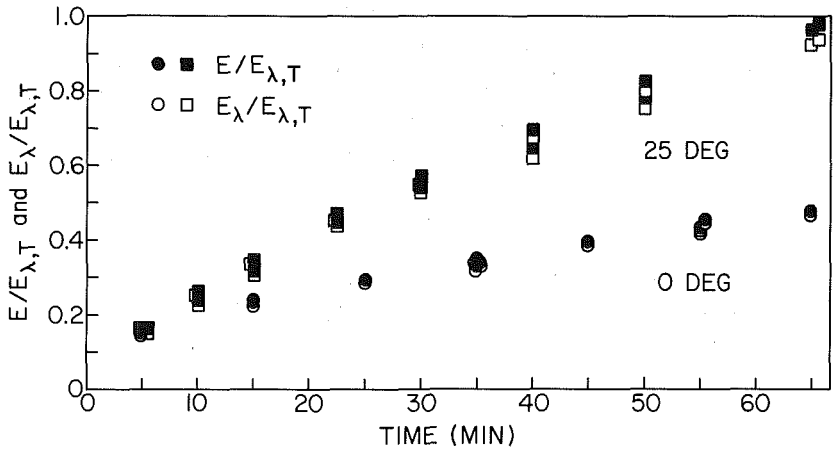

Fig. 8 Energy accounting for Ste = 0.041 ($(T_w - T^*) = 4.55$ °C)

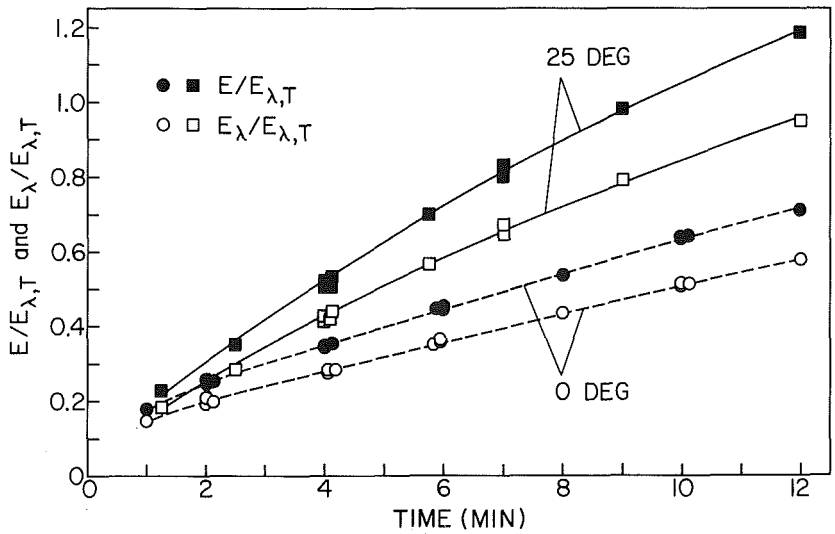

Fig. 9 Energy accounting for Ste = 0.25 ($(T_w - T^*) = 28$°C)

Figure 9 (Ste = 0.25) reflects the increased role of the sensible energy at larger values of Ste. The percentage contribution of E_s to E is virtually the same at the two inclinations, but the absolute contribution is larger at the 25-deg inclination. As before, the enhancement in E due to direct contact increases with time, for example, from 40 percent at t = 2 minutes to 66 percent at t = 12 minutes. These enhancements are somewhat smaller than those encountered in Fig. 11, indicating that direct contact is more beneficial at smaller $(T_w - T^*)$ (i.e., at smaller Ste).

Concluding Remarks

The work reported here is, seemingly, the first systematic experimental study of the effect of tube inclination on the melting of a phase-change medium contained within the tube. When the tube is vertical, the dominant mode of energy transfer between the tube wall and the melting interface is natural convection. On the other hand, when the tube is sufficiently inclined to the vertical, the melting solid is brought into direct contact with the tube wall by the action of gravity, and the direct contact provides the primary path for energy transfer.

It was found that direct-contact-dominated melting was established at an inclination angle of about 15 deg to the vertical and that further increases in inclination had virtually no effect on the melting results. Direct contact gave rise to substantial enhancements in the amount of melted mass and in the energy transfer from the tube wall to the phase-change medium, relative to those for natural-convection-dominated melting (i.e., the vertical tube case). The extent of the enhancement increased during the course of the melting period, with the maximum enhancement encountered during the present experiments being about a factor of two. The percentage extent of the enhancement was greatest at small values of the governing temperature difference.

A careful accounting was made of the energy transferred from the tube to the phase-change medium, both as latent heat E_λ supplied to the melting process and as sensible heat E_s stored in the liquid melt. It was found that the energy components were very well correlated by the relation E_s/E_λ = 0.95Ste, where Ste is the liquid-phase Stefan number.

A variety of melting patterns was identified. When the tube is vertical (and also intermittently at small inclinations), the melting solid is a tapered axisymmetric cylinder whose axis coincides with the axis of the tube. When the tube is inclined and during the initial portion of the melting period, the solid tips toward the tube wall while pivoting about its lowermost edge. As a result, only the upper part of the solid contacts the wall. At later times, the solid slides continuously into the wall, achieving direct contact all along its length. Whereas the aforementioned patterns of melting (i.e., pivoting and sliding) occurred consistently for inclinations of 15 deg and greater, considerable variability existed for the 5- and 10-deg inclinations.

The thermal boundary condition at the lower end of the cylinder was designed to be as close as possible to adiabatic. Had the lower end been heated rather than adiabatic, it may be conjectured that the maximum rate of melting might have been attained at inclination angles smaller than those encountered here. However, the magnitude of the maximum rate of melting would be identical to that measured here. The same is true if a different material had been used as the lower bounding surface of the paraffin specimen.

References

1 Nicholas, D., and Bayazitoglu, Y., "Heat Transfer and Melting Front Within a Horizontal Cylinder," *Journal of Solar Energy Engineering*, Vol. 102, 1980, pp. 229–232.

2 Bareiss, M., and Beer, H., "An Analytical Solution of the Heat Transfer Process During Melting of an Unfixed Solid Phase Change Material Inside a Horizontal Tube," *International Journal of Heat and Mass Transfer*, Vol. 27, 1984, pp. 739–746.

3 Moore, F. E., and Bayazitoglu, Y., "Melting Within a Spherical Enclosure," ASME JOURNAL OF HEAT TRANSFER, Vol. 104, 1982, pp. 19–23.

4 Pannu, J., Joglekar, G., and Rice, P. A., "Natural Convection Heat Transfer to Cylinders of Phase Change Material Used for Thermal Storage," *AIChE Symposium Series*, Vol. 76, No. 198, 1980, pp. 47–55.

5 Katayama, K., Saito, A., Utaka, Y., Saito, A., Matsui, H., Maekawa, H., and Saifullah, A. Z. A., "Heat Transfer Characteristics of the Latent Heat Thermal Energy Storage Capsule," *Solar Energy*, Vol. 27, 1981, pp. 91–97.

6 Ho, C. J., and Viskanta, R., "Heat Transfer During Inward Melting in a Horizontal Tube," *International Journal of Heat and Mass Transfer*, Vol. 27, 1984, pp. 705–716.

7 Sparrow, E. M., and Broadbent, J. A., "Inward Melting in a Vertical Tube Which Allows Free Expansion of the Phase-Change Medium," ASME JOURNAL OF HEAT TRANSFER, Vol. 104, 1982, pp. 309–315.

8 Myrum, T. A., "Effect of Inclination Angle on Melting in a Circular Tube," Thesis, Department of Mechanical Engineering, University of Minnesota, Minneapolis, MN, 1984.

9 Griggs, E. I., and Humphries, W. R., "A Design Handbook for Phase Change Thermal Control and Energy Storage Devices," NASA Technical Paper 1074, 1977.

On the Heat Transfer of a Moving Composite Strip Compressed by Two Rotating Cylinders

W. Y. D. Yuen
Senior Research Officer,
Research and Technology Centre,
John Lysaght (Australia) Limited,
Port Kembla, NSW, 2505, Australia

Two influential parameters in rolling mill analysis are the heat loss to the rolls and the strip temperature distribution. In this paper, the heat transfer process occurring in rolling is modeled by a moving three-layer composite strip, compressed between two rotating cylinders. It is shown that, for the range of parameters representative of strip rolling, the problem can be reduced, to leading order, to one of heat transfer beween slabs with plane parallel boundary contact. The heating effects due to deformation energy generated in the strip, friction energy generated at the strip/cylinder interfaces, and the strip/cylinder bulk temperature difference are considered. Application of the results to rolling analysis is demonstrated.

1 Introduction

The mechanical properties of sheet steel are influenced by the temperature of the steel on exit from the hot strip mill. For products of prime quality, close tolerances are required on this final strip temperature, which depends on the slab (steel plate at the rolling mill entry) temperature as well as the thermal processes occurring during rolling. These include air cooling between the rolling stands, water cooling in the descaling boxes (which remove the oxide layer formed on the strip surface) and heat loss in the rolling stands. Whereas simple heat transfer theory, involving radiation and convection, serves to describe the first two processes, the latter involves frictional and deformation heating, together with heat loss by conduction to the work rolls. Another important factor which should be considered for hot rolling is the buildup of a scale layer (oxide layer) on the strip surface. This scale layer, though normally very thin, is a poor thermal conductor and has been found to cause a significant reduction in heat loss from the strip [1, 2, 3]. Only recently have analytical studies been directed at quantifying this phenomenon.

The strip is reduced in thickness as it passes between the work rolls of a rolling stand. Figure 1 shows a sectional view of the process with a scale layer which remains intact in the contact region. Heat energy is generated in the strip as it is deformed in the roll gap region, and also along the roll/scale layer interfaces due to friction resulting from the differential speeds of the strip and rolls. Hence the heat transfer process near the contact region in a rolling stand is equivalent to that of a moving three-layer composite strip compressed by two rotating cylinders, with energy generated within the strip and at the cylinder/strip interface, and with thermal energy transfer due to the cylinder/strip bulk temperature difference.

Analytical solutions of this problem, disregarding the influence of the scale layer, have been obtained by Cerni [4] and Cerni et al. [5]. Finne et al. [6] derived a set of differential equations, which was solved numerically under the assumption of a constant scale layer thickness. Polukhin et al. [1, 2] obtained an analytical solution using similar model equations which treated the strip and the roll as two semi-infinite slabs. These solutions [1, 2, 6] take the heat capacity of the scale layer to be negligible (an assumption which requires validation). Recently, Pawelski et al. [3] have published results on the strip temperature distribution and heat transfer coefficient with the effects of a scale layer included. Unfortunately this paper [3] is rather obscure and does not give any analytical detail.

In this study, a detailed mathematical model is developed to describe the heat transfer near the contact region in a rolling stand, including the effect of the scale layer and its heat capacity. (The formulation for heating and cooling of the rolls may be found in [7, 8], and from the references quoted therein.) The set of differential equations describing the heat transfer is reduced to a simpler set by introducing the small nondimensional parameters related to the rolling conditions, thus allowing development of a perturbation solution.

2 Problem Definition

Because of the large strip width in relation to its thickness, this study is confined to a two-dimensional analysis of the three-component system: the rolls, the scale layer, and the strip. From symmetry, only the upper half of the system needs to be considered. It is justifiable to assume that the heat transfer in the roll gap is a quasi-steady-state process because variations which occur along the strip, or during processing of a coil, take place on a much longer time scale.

For a coordinate system fixed in space, when the material properties are assumed to be constant in the temperature range under consideration, the heat conduction equation for the three-body system is

$$\mathbf{v}_i \cdot \nabla T_i = \alpha_i \nabla^2 T_i + Q_i/(\rho_i c_i) \tag{1}$$

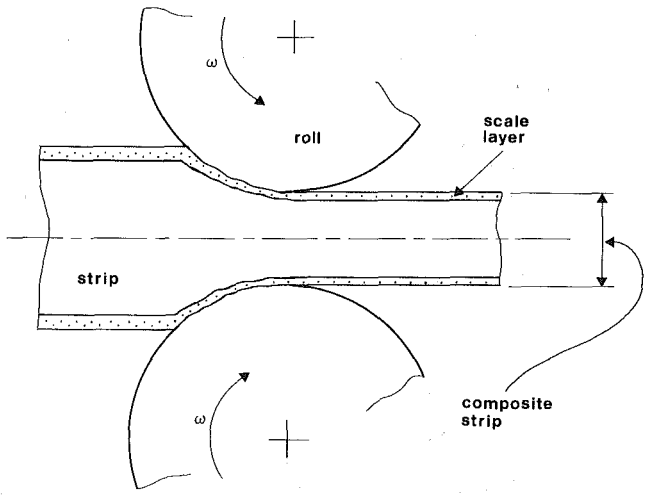

Fig. 1 Roll gap geometry (strip, scale layer, and roll not to scale)

Contributed by the Heat Transfer Division for publication in the JOURNAL OF HEAT TRANSFER. Manuscript received by the Heat Transfer Division August 30, 1982.

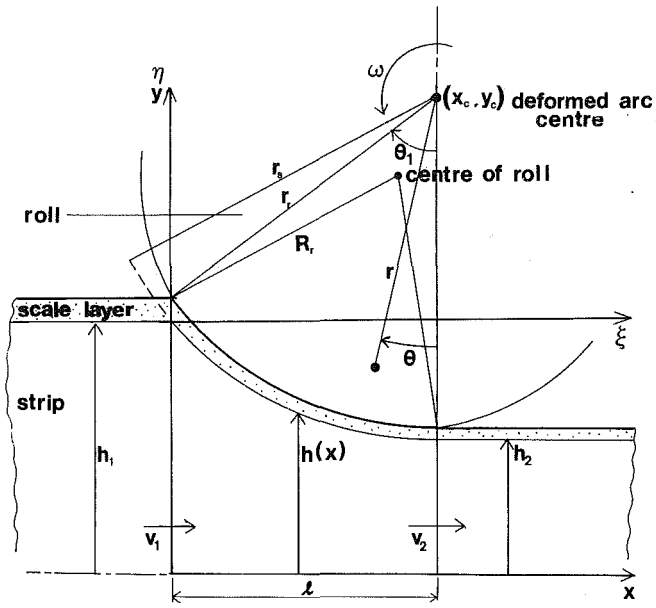

Fig. 2 Roll gap geometry assuming a circular arc of contact (strip, scale layer, and roll not to scale)

where the subscript i can be either r, s, or c, referring to the roll, strip and scale layer respectively. Here c_i is the specific heat; ρ_i the density; α_i the thermal diffusivity; T_i the temperature; $\mathbf{v}_i$ the material velocity; and Q_i the heat sources. It is not the purpose of this paper to develop theoretical expressions for Q_i. Suffice it to say that these may be obtained from any suitable roll gap model (see, for example, [6, 9]).

Since perfect contact is assumed at the interfaces, the boundary conditions to be satisfied at the strip/scale layer and roll/scale layer interfaces are based on the continuity of temperatures and heat fluxes across them, except that the total heat flow into the roll and the scale layer at the roll/scale layer interface equals the frictional energy generated therein due to slipping.

Equation (1) may be written in a two-dimensional Cartesian $(x\text{-}y)$ form for the strip region and in a polar coordinate $(r\text{-}\theta)$ system for the roll and scale layer. For convenience, the origin of the $x\text{-}y$ coordinates is located at the roll gap entry along the strip axis (centerline). The center of the (assumed) circular arc of the deformed roll is taken as the origin of the $r\text{-}\theta$ coordinates as shown in Fig. 2.

A nondimensionalization of the heat conduction equations is now carried out in order to identify their most significant terms.

(*a*) For the strip:

$$\hat{x} = x/(2r_s\Delta h)^{1/2}$$
$$\hat{y} = y/h_1$$
$$\hat{v}_{sx} = v_{sx}/v_1$$
$$\hat{v}_{sy} = \frac{v_{sy}}{v_1(2\Delta h/r_s)^{1/2}}$$
$$\hat{T}_s = T_s/T_{s1}$$

where r_s is the distance from the deformed roll center to the strip/scale layer interface at the roll gap entry; $\Delta h = h_1 - h_2$ the half of the reduction in strip thickness; h_1 and h_2 are half of the strip thicknesses at the roll gap entry and exit respectively; v_1 is the horizontal strip velocity prior to the roll gap entry; T_{s1} a certain reference temperature of the strip; and v_{sx} and v_{sy} are the strip velocity components in the x and y directions respectively.

In the above, $(2r_s\Delta h)^{1/2}$ is approximately the horizontal contact length, l (since $\Delta h/r_s << 1$); $v_1(2\Delta h/r_s)^{1/2}$ is approximately the vertical speed of the strip surface at the roll gap entry point.

(*b*) For the scale layer:

$$\hat{\theta} = \theta/(2\Delta h/r_s)^{1/2}$$
$$\hat{s} = (r - r_r)/s_1$$
$$\hat{v}_{cr} = \frac{v_{cr}}{v_1\Delta s(2r_s\Delta h)^{-1/2}}$$
$$\hat{v}_{c\theta} = v_{c\theta}/v_1$$
$$\hat{T}_c = T_c/T_{c1}$$

Nomenclature

c = specific heat
f_1 = $(\gamma_r - 1)/(\gamma_r + 1)$
f_2 = $(\gamma_s - 1)/(\gamma_s + 1)$
F_c = Fourier number for the scale layer, equation (22)
$\hat{F}_c$ = Fourier number defined in equation (39)
F_r = Fourier number for the roll, equation (23)
F_s = Fourier number for the strip, equation (21)
$\hat{F}_s$ = Fourier number defined in equation (34)
h = half of the strip thickness
k = thermal conductivity
l = contact length
q = rate of heat transfer to a roll
q_f = rate of frictional heat energy generated per unit area at the roll/scale layer interface
Q = rate of heat energy generated per unit volume
Q_s = rate of deformation heat energy generated per unit volume in the strip
r,θ = coordinates defined in Fig. 2
r_r = deformed roll radius, Fig. 2
r_s = radius defined in Fig. 2
R_r = roll radius
s = scale layer thickness
t = time
t_2 = contact time
T = temperature
T_0 = $T_{s1} - T_{r1}$
T' = average temperature
v = horizontal strip velocity
$\mathbf{v}$ = velocity vector
x,y = coordinates defined in Fig. 2
α = thermal diffusivity
β_c = term defined in equation (6)
β_r = term defined in equation (7)
β_s = term defined in equation (5)
γ_r = $(\rho_r k_r c_r)^{1/2}/(\rho_c k_c c_c)^{1/2}$
γ_s = $(\rho_s k_s c_s)^{1/2}/(\rho_c k_c c_c)^{1/2}$
Δh = half of the strip thickness reduction
Δs = scale layer thickness reduction
ϵ_1 = h_1/r_s
ϵ_2 = $\Delta h/h_1$
ϵ_3 = s_1/h_1
ϵ_4 = $\Delta s/s_1$
λ = term defined in equation (19)
ξ,η = coordinates, Fig. 2
ρ = density
ω = angular roll velocity

Subscripts

1 = roll gap entry
2 = roll gap exit
c = scale layer
d = deformation energy
f = friction energy
r = roll (as a first subscript)
r = radial direction (as a second subscript)
s = strip
t = initial strip/roll temperature difference
x = x-direction
y = y-direction
θ = peripheral direction

Symbols

$\hat{}$ = nondimensionalized parameter (see text for detail of nondimensionalization)

where r_r is the deformed roll radius; T_{c1} a certain reference temperature of the scale layer; $\Delta s = s_1 - s_2$ the reduction in scale layer thickness in the radial direction; s_1 and s_2 are the scale layer thicknesses at the roll gap entry and exit respectively (in the radial direction); and v_{cr} and $v_{c\theta}$ are the radial and circumferential velocity components respectively for the scale layer.

Here, $(2\Delta h/r_s)^{1/2}$ is approximately the total angle subtended, θ_1; $v_1 \Delta s (2r_s \Delta h)^{-1/2}$ is approximately the scale layer thickness reduction divided by the contact time. (A general case of nonzero Δs is assumed in the above but, if Δs is zero, $v_{cr} = \hat{v}_{cr} = 0$.)

(*c*) For the roll:

$$\hat{\theta} = \theta/(2\Delta h/r_s)^{1/2}$$
$$\hat{r} = (r_r - r)/h_1$$
$$\hat{v}_{rr} = \frac{v_{rr}}{\omega(r_r - R_r)(2\Delta h/r_s)^{1/2}}$$
$$\hat{v}_{r\theta} = v_{r\theta}/(\omega R_r)$$
$$\hat{T}_r = T_r/T_{r1}$$

where ω is the angular roll speed; R_r the original roll radius; T_{r1} a certain reference temperature of the roll; and v_{rr} and $v_{r\theta}$ are the radial and circumferential velocity components respectively for the roll.

Here, r is nondimensionalized by the entry half strip thickness, h_1; ωR_r is approximately the circumferential speed of the roll surface at the roll gap entry; $\omega(r_r - R_r)(2\Delta h/r_s)^{1/2}$ is approximately the radial speed of the roll surface just prior to the roll gap entry.

Substitution of the nondimensional variables in the conduction equation (1) gives:

$$\hat{v}_{sx}\frac{\partial \hat{T}_s}{\partial \hat{x}} + 2(\Delta h/h_1)\hat{v}_{sy}\frac{\partial \hat{T}_s}{\partial \hat{y}} = \beta_s\left[\frac{1}{2}\left(\frac{h_1/r_s}{\Delta h/h_1}\right)\frac{\partial^2 \hat{T}_s}{\partial \hat{x}^2} + \frac{\partial^2 \hat{T}_s}{\partial \hat{y}^2}\right] + \hat{Q}_s \tag{2}$$

$$(1+\hat{s}s_1/r_r)(\Delta s/s_1)(r_r/r_s)\hat{v}_{cr}\frac{\partial \hat{T}_c}{\partial \hat{s}} + \hat{v}_{c\theta}\frac{\partial \hat{T}_c}{\partial \hat{\theta}} = \beta_c\left[\frac{\partial^2 \hat{T}_c}{\partial \hat{s}^2} + \left(\frac{s_1/r_r}{1+\hat{s}s_1/r_r}\right)\frac{\partial \hat{T}_c}{\partial \hat{s}} + \frac{1}{2}\left(\frac{s_1}{r_r}\right)^2 \frac{r_s/\Delta h}{(1+\hat{s}s_1/r_r)^2}\frac{\partial^2 \hat{T}_c}{\partial \hat{\theta}^2}\right] + \hat{Q}_c \tag{3}$$

$$-2(1-\hat{r}h_1/r_r)[(r_r/R_r)-1]\times(\Delta h/h_1)(r_r/r_s)\hat{v}_{rr}\frac{\partial \hat{T}_r}{\partial \hat{r}} + \hat{v}_{r\theta}\frac{\partial \hat{T}_r}{\partial \hat{\theta}} = \beta_r\left[\frac{\partial^2 \hat{T}_r}{\partial \hat{r}^2} - \left(\frac{h_1/r_r}{1-\hat{r}h_1/r_r}\right)\frac{\partial \hat{T}_r}{\partial \hat{r}} + \frac{1}{2}\left(\frac{h_1}{r_r}\right)^2 \frac{r_s/\Delta h}{(1-\hat{r}h_1/r_r)^2}\frac{\partial^2 \hat{T}_r}{\partial \hat{\theta}^2}\right] + \hat{Q}_r \tag{4}$$

where

$$\beta_s = [(2r_s\Delta h)^{1/2}/v_1]/(h_1^2/\alpha_s) \tag{5}$$
$$\beta_c = [r_r(2\Delta h/r_s)^{1/2}(1+\hat{s}s_1/r_r)/v_1]/(s_1^2/\alpha_c) \tag{6}$$
$$\beta_r = [r_r(2\Delta h/r_s)^{1/2}(1-\hat{r}h_1/r_r)/(\omega R_r)]/(h_1^2/\alpha_r) \tag{7}$$
$$\hat{Q}_s = [Q_s(2r_s\Delta h)^{1/2}/v_1]/(\rho_s c_s T_{s1}) \tag{8}$$
$$\hat{Q}_c = [Q_c r_r(2\Delta h/r_s)^{1/2}(1+\hat{s}s_1/r_r)/v_1]/(\rho_c c_c T_{c1}) \tag{9}$$

and

$$\hat{Q}_r = [Q_r r_r(2\Delta h/r_s)^{1/2}(1-\hat{r}h_1/r_r)/(\omega R_r)]/(\rho_r c_r T_{r_1}) \tag{10}$$

The relevance of the nondimensionalization is now apparent since, in physical terms, β_s, β_c, and β_r are approximately the ratio of contact time to diffusion time for the media, and $\hat{Q}_s$, $\hat{Q}_c$, and $\hat{Q}_r$ are approximately the ratio of heat energy generated in the roll gap to the "stored" energy at the roll gap entry for the media.

In rolling, the entry strip thickness, while normally much larger than the strip thickness reduction, is very much smaller than the deformed roll radius. Moreover, the scale layer, if present, is very thin compared to the strip thickness, and its reduction in thickness will also be very small.

Therefore,

$$\epsilon_1 = h_1/r_s << \epsilon_2 = \Delta h/h_1 << 1$$
$$\epsilon_3 = s_1/h_1 << 1$$

and

$$\epsilon_4 = \Delta s/s_1 << 1$$

From geometry, $r_r/r_s = 1 - s_1/r_s = 1 - \epsilon_1\epsilon_3$. It follows that

$$(s_1/r_r)^2(r_s/\Delta h) = (\epsilon_1/\epsilon_2)[\epsilon_3^2/(1-\epsilon_1\epsilon_3)] << 1$$
$$(h_1/r_r)^2(r_s/\Delta h) = (\epsilon_1/\epsilon_2)(1-\epsilon_1\epsilon_3)^{-2} << 1$$

Thus the dominant terms in equations (2–4) may be identified by writing them in terms of these small parameters. In addition, it is often desirable to express the roll gap variables in terms of the time variable t so that the contact time will then appear explicitly. For the nondimensional variables employed, the relationships are:

$$\hat{v}_{sx} = \frac{(2r_s\Delta h)^{1/2}/v_1}{h_1^2/\alpha_s}\frac{\partial \hat{x}}{\partial \hat{t}}$$

$$\hat{v}_{c\theta} = (r_r/r_s)(1+\hat{s}s_1/r_r)\frac{(2r_s\Delta h)^{1/2}/v_1}{h_1^2/\alpha_s}\frac{\partial \hat{\theta}}{\partial \hat{t}} = \frac{(2r_s\Delta h)^{1/2}/v_1}{h_1^2/\alpha_s}\frac{\partial \hat{\theta}}{\partial \hat{t}} + O(\epsilon_1\epsilon_3)$$

$$\hat{v}_{r\theta} = (r_r/r_s)(1-\hat{r}h_1/r_r)\frac{(2r_s\Delta h)^{1/2}/(\omega R_r)}{h_1^2/\alpha_s}\frac{\partial \hat{\theta}}{\partial \hat{t}} = \frac{(2r_s\Delta h)^{1/2}/(\omega R_r)}{h_1^2/\alpha_s}\frac{\partial \hat{\theta}}{\partial \hat{t}} + O(\epsilon_1, \epsilon_1\epsilon_3)$$

where $\hat{t} = t/(h_1{}^2/\alpha_s)$ is the time parameter, nondimensionalized by the diffusion time across half the strip thickness. Since the effects of temperature gradient and heat transfer are confined mainly to the interface regions, it is more appropriate to transform the $(\hat{x}, \hat{y})$ axes to the $(\hat{\xi}, \hat{\eta})$ axes with the origin set on the strip surface at the roll gap entry (Fig. 2), using the transformations $\hat{\xi} = \hat{x}$ and $\hat{\eta} = \hat{y} - 1$. The relations between $(\hat{r}, \hat{\theta})$ [or $(\hat{s}, \hat{\theta})$] and $(\hat{\xi}, \hat{\eta})$ are

$$\hat{\xi} = \begin{cases} \hat{x}_c - [r_r/(2r_s\Delta h)^{1/2}](1+\hat{s}s_1/r_r)\sin[(2\Delta h/r_s)^{1/2}\hat{\theta}] \\ \quad = \hat{x}_c - \hat{\theta} + O[(\epsilon_1\epsilon_2)^{3/2}, \epsilon_1\epsilon_3] & \text{for the scale layer} \\ \hat{x}_c - [r_r/(2r_s\Delta h)^{1/2}](1-\hat{r}h_1/r_r)\sin[(2\Delta h/r_s)^{1/2}\hat{\theta}] \\ \quad = \hat{x}_c - \hat{\theta} + O(\epsilon_1, \epsilon_1\epsilon_2, \epsilon_1\epsilon_3) & \text{for the roll} \end{cases}$$

$$\hat{\eta} = \begin{cases} \hat{y}_c - 1 - (r_r/h_1)(1+\hat{s}s_1/r_r)\cos[(2\Delta h/r_s)^{1/2}\hat{\theta}] \\ \quad = \epsilon_2(\hat{\theta}^2 - 1) + \epsilon_3(1-\hat{s}) + O(\epsilon_1\epsilon_2, \epsilon_1\epsilon_3) & \text{for the scale layer} \\ \hat{y}_c - 1 - (r_r/h_1)(1-\hat{r}h_1/r_r)\cos[(2\Delta h/r_s)^{1/2}\hat{\theta}] \\ \quad = \hat{r} + O(\epsilon_2, \epsilon_3, \epsilon_1\epsilon_2, \epsilon_1\epsilon_3) & \text{for the roll} \end{cases}$$

It follows that equations (2-4), after the transformation and simplification, become

$$\frac{\partial \hat{T}_s}{\partial \hat{t}} = \frac{\partial^2 \hat{T}_s}{\partial \hat{\eta}^2} + Q_s (h_1^2/\alpha_s)/(\rho_s c_s T_{s1}) + O(\epsilon_2, \epsilon_1/\epsilon_2) \tag{11}$$

$$\frac{\partial \hat{T}_c}{\partial \hat{t}} = (\alpha_c/\alpha_s)\frac{\partial^2 \hat{T}_c}{\partial \hat{\eta}^2} + Q_c (h_1^2/\alpha_s)/(\rho_c c_c T_{c1}) + O(\epsilon_4, \epsilon_1/\epsilon_2, \epsilon_1\epsilon_2, \epsilon_1\epsilon_3, \epsilon_3^2) \tag{12}$$

$$\frac{\partial \hat{T}_r}{\partial \hat{t}} = (\alpha_r/\alpha_s)\frac{\partial^2 \hat{T}_r}{\partial \hat{\eta}^2} + Q_r (h_1^2/\alpha_s)/(\rho_r c_r T_{r1}) + O(\epsilon_1, \epsilon_2, \epsilon_1/\epsilon_2, \epsilon_1\epsilon_2, \epsilon_1\epsilon_3) \tag{13}$$

The boundary conditions in the new coordinate system $(\hat{t}, \hat{\eta})$ are

(a) on the strip axis, $\hat{\eta} = -1$, from symmetry:

$$\frac{\partial \hat{T}_s(\hat{t}, -1)}{\partial \hat{\eta}} = 0 \tag{14}$$

(b) on the strip/scale layer interface, $\hat{\eta} = 0 + O(\epsilon_2, \epsilon_1\epsilon_2)$, for continuity of temperatures and heat fluxes:

$$\hat{T}_s(\hat{t}, 0) = (T_{c1}/T_{s1})\hat{T}_c(\hat{t}, 0) \tag{15}$$

$$\frac{\partial \hat{T}_s(\hat{t}, 0)}{\partial \hat{\eta}} = (k_c/k_s)(T_{c1}/T_{s1})\frac{\partial \hat{T}_c(\hat{t}, 0)}{\partial \hat{\eta}} \tag{16}$$

(c) on the roll/scale layer interface, $\hat{\eta} = \epsilon_3 + O(\epsilon_2, \epsilon_1\epsilon_2, \epsilon_1\epsilon_3)$:

$$\hat{T}_r(\hat{t}, \epsilon_3) = (T_{c1}/T_{r1})\hat{T}_c(\hat{t}, \epsilon_3) \tag{17}$$

$$-\frac{\partial \hat{T}_r(\hat{t}, \epsilon_3)}{\partial \hat{\eta}} = -(k_c/k_r)(T_{c1}/T_{r1})\frac{\partial \hat{T}_c(\hat{t}, \epsilon_3)}{\partial \hat{\eta}} + h_1 q_f/(k_r T_{r1}) \tag{18}$$

where q_f is the rate of friction energy (per unit area) generated at the roll/scale layer interface due to slipping;

(d) on a circular layer in the roll at a sufficient distance from the interfaces such that heat flow across the layer during contact time may be neglected (this assumption is valid since the heating and cooling of the roll confines to a very small region near the roll surface [7, 8]), say, at $\hat{r} = \hat{\lambda}$ where $1 >> \hat{\lambda} >> \epsilon_2\epsilon_3$, i.e., $\hat{\eta} = \hat{\lambda} + O(\epsilon_2, \epsilon_3, \epsilon_1\epsilon_2, \epsilon_1\epsilon_3)$:

$$\frac{\partial \hat{T}_r(\hat{t}, \hat{\lambda})}{\partial \hat{\eta}} = 0 \tag{19}$$

It can be seen that the leading order problem for the heat transfer in the roll gap reduces to equations (11-13) which, with the above set of boundary conditions, describes one-dimensional heat flow between two thick flat slabs separated by a slab of finite thickness. The perturbation formulation, developed here, clarifies the conditions under which this model may be employed and justifies the use of the simplified system introduced as the starting point of the previous analyses [1-6].

3 Solution

In order to obtain an analytic solution, a certain temperature distribution at the roll gap entry must be assumed. Since the strip and roll speeds (or, more precisely, the Peclet numbers, which are defined as $v_{sx}h_1/\alpha_s$ and $\omega R_r^2/\alpha_r$ for the strip and roll respectively) are high, the conduction component is small compared to the advective component, and it is justified to assume a uniform temperature distribution for all three bodies at the roll gap entry, i.e., the strip and scale layer have the same initial temperature, set to equal their reference temperatures, $T_{s1} = T_{c1}$, hence $\hat{T}_s(0, \hat{\eta}) = \hat{T}_c(0, \hat{\eta}) = 1$; and the initial roll temperature is equal to its reference temperature T_{r1} giving $\hat{T}_r(0, \hat{\eta}) = 1$. The initial time, $\hat{t} = 0$, is assumed to be at the roll gap entry.

Since the deformation heat energy generated in the roll and scale layer regions is usually negligible in comparison with that generated in the strip, it is reasonable to set $Q_r = Q_c = 0$.

A first-order solution of equations (11-13) subject to boundary conditions (14-19) can be obtained, using Laplace transforms, with further assumptions that the deformation heat energy Q_s and frictional energy q_f, which may be calculated using a roll gap model (see, for example, [6]), are distributed uniformly throughout the roll gap; and that the transport time is small compared to the diffusion time (i.e., $\hat{t} << 1$) such that the approximation of semi-infinite slabs is valid.

For convenience, and since the problem is linear, the solution is written in component form:

$$\hat{T}_i(\hat{t}, \hat{\eta}) = 1 + \hat{T}_{it}(\hat{t}, \hat{\eta}) + \hat{T}_{id}(\hat{t}, \hat{\eta}) + \hat{T}_{if}(\hat{t}, \hat{\eta}) \tag{20}$$

where $\hat{T}_{it}$, $\hat{T}_{id}$, and $\hat{T}_{if}$ are the temperature changes due to the roll/strip bulk temperature difference, deformation energy, and frictional energy respectively. Although the temperature distribution in the scale layer may also be derived, it is not included here since it has no practical significance.

The solution may best be expressed in terms of Fourier numbers, F_s, F_c, and F_r, which are defined as follows:

$$F_s(\hat{t}, \hat{\eta}) = \alpha_s t/\eta^2 = \hat{t}/\hat{\eta}^2 \tag{21}$$

$$F_c(\hat{t}) = \alpha_c t/s_1^2 = (\alpha_c/\alpha_s)\hat{t}/\epsilon_3^2 \tag{22}$$

$$F_r(\hat{t}, \hat{\eta}) = \alpha_r t/(\eta - s_1)^2 = (\alpha_r/\alpha_s)\hat{t}/(\hat{\eta} - \epsilon_3)^2 \tag{23}$$

where

$$\eta = h_1\hat{\eta}.$$

It should be noted that in the above, the Fourier numbers for the strip and roll, F_s and F_r, are functions of both $\hat{t}$ and $\hat{\eta}$. They give an indication on the extent of heating or cooling of the strip/roll element of interest after the elapsed time. On the other hand, F_c, the Fourier number for the scale layer, is a function only of $\hat{t}$ and is a measure of the elapsed time in comparison with the diffusion time across the scale layer.

It can be shown, after some lengthy mathematical manipulations, that the solutions for the roll and strip temperature distributions are:

$$\hat{T}_{rt}(\hat{t}, \hat{\eta}) = \frac{T_0}{T_{r1}}\frac{1}{\gamma_r + 1}\left\{\sum_{n=0}^{\infty}\left[(f_1 f_2)^n erfc\left(\frac{1}{2}F_r^{-1/2} + nF_c^{-1/2}\right)\right] + f_2\sum_{n=0}^{\infty}\left[(f_1 f_2)^n erfc\left(\frac{1}{2}F_r^{-1/2} + [n+1]F_c^{-1/2}\right)\right]\right\} \tag{24}$$

$$\hat{T}_{rd}(\hat{t}, \hat{\eta}) = 8\hat{t}\frac{h_1^2 Q_s}{k_s T_{r1}}\frac{\gamma_s}{(\gamma_r + 1)(\gamma_s + 1)} \times \sum_{n=0}^{\infty}\left\{(f_1 f_2)^n i^2 erfc\left[\frac{1}{2}F_r^{-1/2} + \frac{1}{2}(2n+1)F_c^{-1/2}\right]\right\} \tag{25}$$

$$\hat{T}_{rf}(\hat{t}, \hat{\eta}) = 2\hat{t}^{1/2}\frac{h_1 q_f}{k_s T_{r1}}\frac{\gamma_s}{\gamma_r + 1}\sum_{n=0}^{\infty}\left\{(f_1 f_2)^n \times \left[ierfc\left(\frac{1}{2}F_r^{-1/2} + nF_c^{-1/2}\right) - f_2 ierfc\left(\frac{1}{2}F_r^{-1/2} + [n+1]F_c^{-1/2}\right)\right]\right\} \tag{26}$$

$$\hat{T}_{st}(\hat{t}, \hat{\eta}) = -2\frac{T_0}{T_{s1}}\frac{\gamma_r}{(\gamma_r + 1)(\gamma_s + 1)} \times \sum_{n=0}^{\infty}\left\{(f_1 f_2)^n erfc\left[\frac{1}{2}F_s^{-1/2} + \frac{1}{2}(2n+1)F_c^{-1/2}\right]\right\} \tag{27}$$

$$\hat{T}_{sd}(\hat{t}, \hat{\eta}) = \hat{t}\frac{h_1^2 Q_s}{k_s T_{s1}}\left\{1\right.$$

$$-\frac{4}{\gamma_s+1}\sum_{n=0}^{\infty}\left[(f_1f_2)^n\left(i^2erfc\left[\frac{1}{2}F_s^{-1/2}+nF_c^{-1/2}\right]\right.\right.$$

$$\left.\left.+f_1i^2erfc\left[\frac{1}{2}F_s^{-1/2}+\{n+1\}F_c^{-1/2}\right]\right)\right]\Bigg\} \tag{28}$$

$$\hat{T}_{sf}(\hat{t},\hat{\eta})=4\hat{t}^{1/2}\frac{h_1q_f}{k_sT_{s1}}\frac{\gamma_s}{(\gamma_r+1)(\gamma_s+1)}\times$$

$$\sum_{n=0}^{\infty}\left\{(f_1f_2)^n ierfc\left[\frac{1}{2}F_s^{-1/2}+\frac{1}{2}(2n+1)F_c^{-1/2}\right]\right\} \tag{29}$$

where

$$\gamma_r=(\rho_rk_rc_r)^{1/2}/(\rho_ck_cc_c)^{1/2}$$

$$\gamma_s=(\rho_sk_sc_s)^{1/2}/(\rho_ck_cc_c)^{1/2}$$

$$f_1=(\gamma_r-1)/(\gamma_r+1)$$

$$f_2=(\gamma_s-1)/(\gamma_s+1)$$

$$T_0=T_{s1}-T_{r1}$$

and k_s is the strip thermal conductivity.

Here, $i^merfc(w)$ is the complementary error function defined as

$$i^merfc(w)=\int_w^{\infty}i^{m-1}erfc(u)\,du \quad m=0,1,2,\ldots$$

where

$$i^0erfc(w)=erfc(w)=1-erf(w)$$

On integration of equations (27-29) with respect to $\hat{\eta}$, the average strip temperature across its section, $\hat{T}_s'(\hat{t})$, may be obtained:

$$\hat{T}_s'(\hat{t})=1+\hat{T}_{st}'(\hat{t})+\hat{T}_{sd}'(\hat{t})+\hat{T}_{sf}'(\hat{t}) \tag{30}$$

where

$$\hat{T}_{st}'(\hat{t})=4\hat{t}^{1/2}\frac{T_0}{T_{s1}}\frac{h_1}{h(t)}\frac{\gamma_r}{(\gamma_r+1)(\gamma_s+1)}\sum_{n=0}^{\infty}\left\{(f_1f_2)^n\times\right.$$

$$\left.\left[ierfc\left(\frac{1}{2}\hat{F}_s^{-1/2}+\frac{1}{2}[2n+1]F_c^{-1/2}\right)-ierfc\left(\frac{1}{2}[2n+1]F_c^{-1/2}\right)\right]\right\} \tag{31}$$

$$\hat{T}_{sd}'(\hat{t})=\hat{t}\frac{h_1^2Q_s}{k_sT_{s1}}\left\{1-\frac{8}{\gamma_s+1}\hat{t}^{1/2}\frac{h_1}{h(t)}\sum_{n=0}^{\infty}\left[(f_1f_2)^n\times\right.\right.$$

$$\left(i^3erfc[nF_c^{-1/2}]-i^3erfc\left[\frac{1}{2}\hat{F}_s^{-1/2}+nF_c^{-1/2}\right]\right.$$

$$+f_1i^3erfc[\{n+1\}F_c^{-1/2}]-f_1i^3erfc\left[\frac{1}{2}\hat{F}_s^{-1/2}\right.$$

$$\left.\left.\left.+\{n+1\}F_c^{-1/2}\right]\right)\right]\Bigg\} \tag{32}$$

and

$$\hat{T}_{sf}'(\hat{t})=8\hat{t}\frac{h_1q_f}{k_sT_{s1}}\frac{h_1}{h(t)}\frac{\gamma_s}{(\gamma_r+1)(\gamma_s+1)}\times$$

$$\sum_{n=0}^{\infty}\left\{(f_1f_2)^n\left[i^2erfc\left(\frac{1}{2}[2n+1]F_c^{-1/2}\right)\right.\right.$$

$$\left.\left.-i^2erfc\left(\frac{1}{2}\hat{F}_s^{-1/2}+\frac{1}{2}[2n+1]F_c^{-1/2}\right)\right]\right\} \tag{33}$$

In the above,

$$\hat{F}_s(\hat{t},h)=F_s[\hat{t},h(t)/h_1]=\alpha_st/h^2(t) \tag{34}$$

Although the average roll temperature may be obtained by a similar approach, the details will not be included here.

The heat flow rate to a roll q_r may be obtained by integrating the heat conduction along the roll/scale layer interface:

$$\hat{q}_r=\frac{q_r}{k_rT_{r1}}\frac{\hat{t}_2}{\hat{l}}=-\int_0^{\hat{t}_2}\frac{\partial\hat{T}_r(\hat{t},\epsilon_3)}{\partial\hat{\eta}}\,d\hat{t}=\hat{q}_{rt}+\hat{q}_{rd}+\hat{q}_{rf} \tag{35}$$

where

$$\hat{q}_{rt}=\frac{1}{2}\frac{T_0}{T_{r1}}\left(\frac{\alpha_s}{\alpha_r}\right)^{1/2}\frac{1}{\gamma_r+1}\left\{\sum_{n=0}^{\infty}\left[(f_1f_2)^nI_1(n\hat{F}_c^{-1/2})\right]\right.$$

$$\left.+f_2\sum_{n=0}^{\infty}\left[(f_1f_2)^nI_1([n+1]\hat{F}_c^{-1/2})\right]\right\} \tag{36}$$

$$\hat{q}_{rd}=4\frac{h_1^2Q_s}{k_rT_{r1}}\frac{\gamma_r}{(\gamma_r+1)(\gamma_s+1)}\times$$

$$\sum_{n=0}^{\infty}\left\{(f_1f_2)^nI_3\left[\frac{1}{2}(2n+1)\hat{F}_c^{-1/2}\right]\right\} \tag{37}$$

and

$$\hat{q}_{rf}=\frac{h_1q_f}{k_rT_{r1}}\frac{\gamma_r}{\gamma_r+1}\times$$

$$\sum_{n=0}^{\infty}\left\{(f_1f_2)^n[I_2(n\hat{F}_c^{-1/2})-f_2I_2([n+1]\hat{F}_c^{-1/2})]\right\} \tag{38}$$

In the above,

$$\hat{F}_c=F_c(1)=(\alpha_c/\alpha_s)/\epsilon_3^2 \tag{39}$$

Here, $l=\hat{l}h_1$ and $t_2=\hat{t}_2(h_1{}^2/\alpha_s)$ are the contact length and contact time respectively. If a detailed roll gap model is not available, these parameters may be approximated by $l=(2r_s\Delta h)^{1/2}$ and $t_2=v_1l$. The integrals I_1, I_2, and I_3, which may be integrated by parts, are defined, with the results of integration given, as follows:

$$I_1(u)=\int_0^{\hat{t}_2}\hat{t}^{-1/2}i^{-1}erfc(u\hat{t}^{-1/2})d\hat{t}$$

$$=2[\hat{t}_2^{1/2}i^{-1}erfc(u\hat{t}_2^{-1/2})-2u\,erfc(u\hat{t}_2^{-1/2})]$$

$$I_2(u)=\int_0^{\hat{t}_2}erfc(u\hat{t}^{-1/2})d\hat{t}$$

$$=(\hat{t}_2+2u^2)erfc(u\hat{t}_2^{-1/2})-u\hat{t}_2^{1/2}i^{-1}erfc(u\hat{t}_2^{-1/2})$$

$$I_3(u)=\int_0^{\hat{t}_2}\hat{t}^{1/2}ierfc(u\hat{t}^{-1/2})d\hat{t}$$

$$=\frac{2}{3}\left\{\hat{t}_2^{3/2}ierfc(u\hat{t}^{-1/2})-\frac{1}{2}u[\hat{t}_2+2u^2erfc(u\hat{t}_2^{-1/2})\right.$$

$$\left.-u\hat{t}_2^{1/2}i^{-1}erfc(u\hat{t}_2^{-1/2})]\right\}$$

where u is a function independent of $\hat{t}$.

When the scale layer is absent, the above solutions can be further simplified, and are found to agree with previous results under the same conditions ([1,2] with the "heat transfer coefficient from the strip to the roll" set to infinity).

4 Numerical Results

Unfortunately, a direct comparison with previous numerical results, and, in particular, with those of [3], has been made difficult by uncertainty of the data values employed therein. (It should be pointed out that the formulation in [3] clearly differs from the present formulation in that the frictional energy is inexplicably taken to be generated at the strip/scale layer interface, and that the strip center-line temperature is assumed to remain unchanged even when deformation energy is generated in the roll gap.) Typical thermal values for hot rolling conditions (Table 1) have been used for all the calculations given in this paper. Terms in the

Table 1 Typical thermal data used in the numerical calculations

Strip		
Conductivity, k_s	(W/m°C)	28
Diffusivity, α_s	(m^2/s)	5.9×10^{-6}
Scale Layer		
Conductivity, k_c	(W/m°C)	2.5
Diffusivity, α_c	(m^2/s)	4.6×10^{-7}
Roll		
Conductivity, k_r	(W/m°C)	31
Diffusivity, α_r	(m^2/s)	5.4×10^{-6}

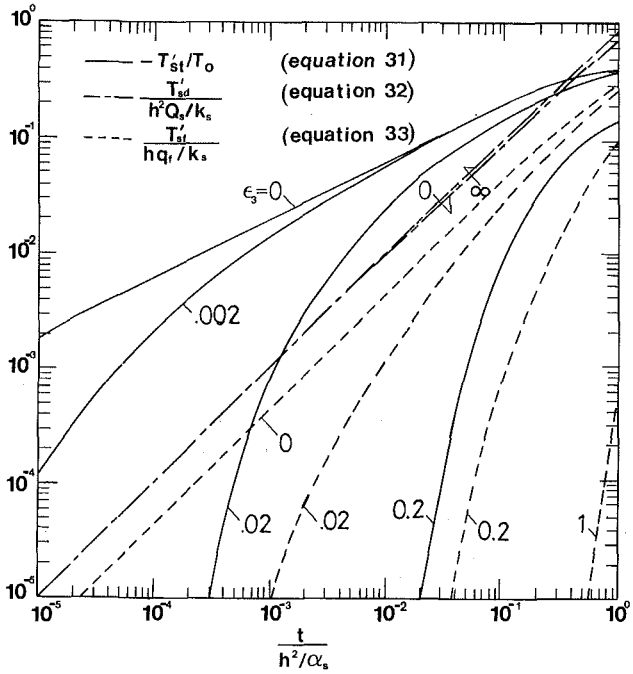

Fig. 3 Variations of the average strip temperature with the scale layer thickness and time

solution were rearranged to eliminate redundant variables so that the most compact form of information may be presented. The figures, which will be described below, are extremely useful for rapid calculation of strip temperature and heat transfer, without the necessity of having to calculate the roll gap parameters accurately. Rational approximation and recurrence relations of the error functions, given in [10], were used in the numerical calculations and it was found that reasonable accuracy could be achieved using only the first few terms of the infinite series solution.

4.1 Average Strip Temperature. The average strip temperature in the roll gap at any instance is shown in Fig. 3, which is a plot of equations (31-33), with the temperature change components, T'_{st}, T'_{sd}, T'_{sf} normalized by T_0, h^2Q_s/k_s, and hq_f/k_s respectively, and time t by the diffusion time, h^2/α_s. The second and third normalizing parameters for the temperature components represent, respectively, an insulated strip temperature change due to the deformation energy generated during the strip diffusion time, and the steady-state temperature difference between the strip center line and strip surface due to heat flux caused by all the frictional energy passing across the half strip. It can be seen from Fig. 3 that the scale layer has a pronounced influence on the bulk temperature difference (T_0) and frictional heating (q_f) effects but is insignificant for the deformation heating (Q_s) effect. In the latter case the normalized average strip temperature is found to approximate a linear relation with the normalized time, signifying that the heat loss to the rolls is insignificant

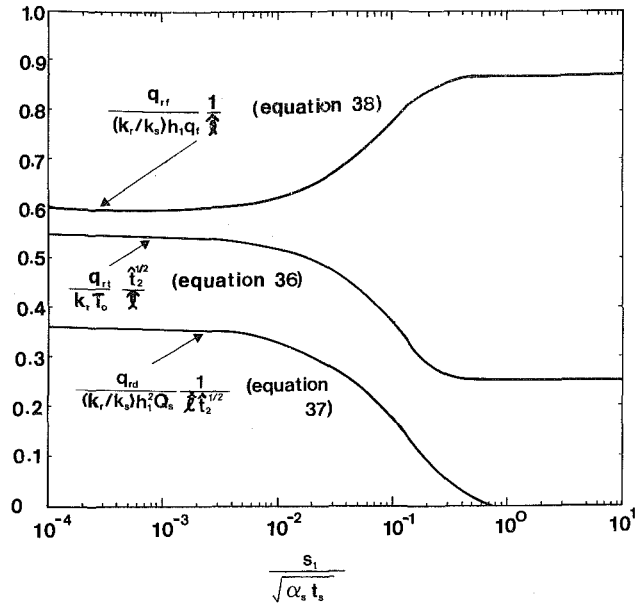

Fig. 4 Variations of heat transfer to the roll with the scale layer thickness and contact time

compared to the energy generated. It should be further noted that the curves shown in Fig. 3 are independent of the actual strip thickness. However, for the theory to be valid, the normalized time should be sufficiently small (certainly less than unity) for the assumption of the "thick slabs" to be justified.

4.2 Heat Transfer to the Rolls. Equations (36-38) may be plotted by rearranging terms such that the heat transfer to the rolls is described in a single diagram. The heat transfer components q_{rt}, q_{rd}, q_{rf} have been normalized by $k_rT_0\hat{l}\hat{t}^{-1/2}$, $(k_r/k_s)h_1{}^2Q_s\hat{l}\hat{t}_2{}^{1/2}$, and $(k_r/k_s)h_1q_f\hat{l}$ respectively, and plotted against $s_1(\alpha_st_2)^{-1/2}$, a parameter dependent on the scale layer thickness and contact time. The three curves shown in Fig. 4 give the normalized heat transfer components to a roll; each curve approaches an upper and a lower limit, and all are dependent on the thermal properties of the strip, scale layer, and the roll. These limits, approached when $s_1(\alpha_st_2)^{-1/2}$ tends to zero and infinity, are equivalent physically to the case of thermal exchanges between two semi-infinite slabs, with the appropriate thermal data adopted. The heat transfer due to T_0 and Q_s is reduced as $s_1(\alpha_st_2)^{-1/2}$ increases due to the insulating effect of the scale layer. Where the scale layer is sufficiently thick (or, more precisely, the diffusion time across the scale layer is large compared to the elapsed time), no deformation energy will reach the roll, whereas the heat transfer due to T_0 will arise solely from the heat capacity stored in the scale layer. Consequently, q_{rt} tends to a finite but nonzero limit while q_{rd} tends to zero. The heat transfer due to q_f is found to increase as $s_1(\alpha_st_2)^{-1/2}$ increases, again due to the insulating effect of the scale layer which, in this case, reduces the frictional energy being transferred to the strip. (The reader is reminded that friction energy is assumed to be generated at the roll/scale layer interface.) Conversion of Pawelski and Bruns' results [3] (only available for q_{rt}), using the thermal data of Table 1, gives excellent agreement for the upper limit of the heat transfer component. However, the fact that their results for the lower limit are approximately 40% lower than those herein may be simply due to the difference in the thermal data values used for the scale layer. It is obvious from Fig. 4 that the heat transfer for all three components has reached its upper and lower limits in regions outside the range $0.003 < s_1(\alpha_st_2)^{-1/2} < 1$.

4.3 Effect of Heat Capacity of the Scale Layer. Most

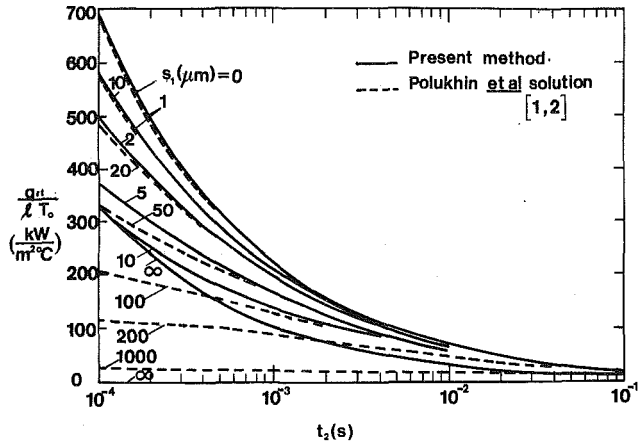

Fig. 5 Comparison of heat transfer to the roll due to an initial strip/roll temperature difference with the Polukhin et al. solution [1,2]

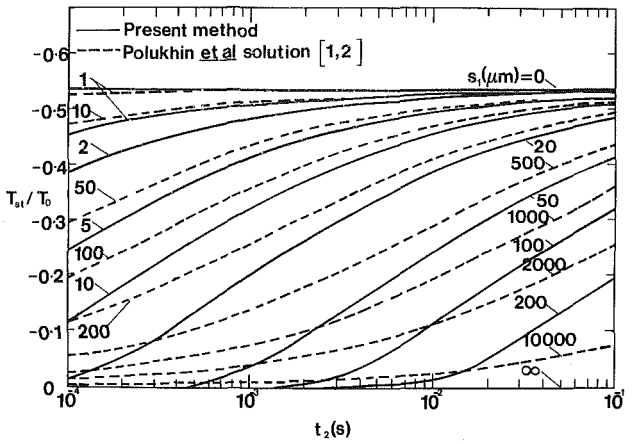

Fig. 7 Comparison of temperature change at the strip/scale layer interface due to an initial strip/roll temperature difference with the Polukhin et al. solution [1,2]

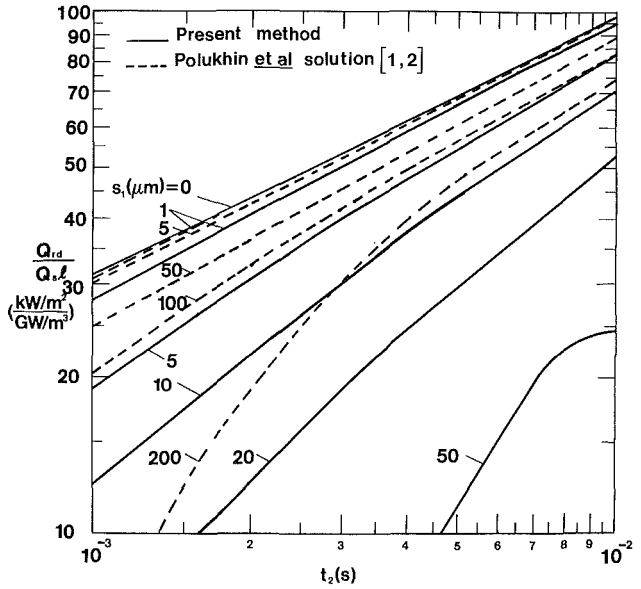

Fig. 6 Comparison of heat transfer to the roll due to deformation energy with the Polukhin et al. solution [1,2]

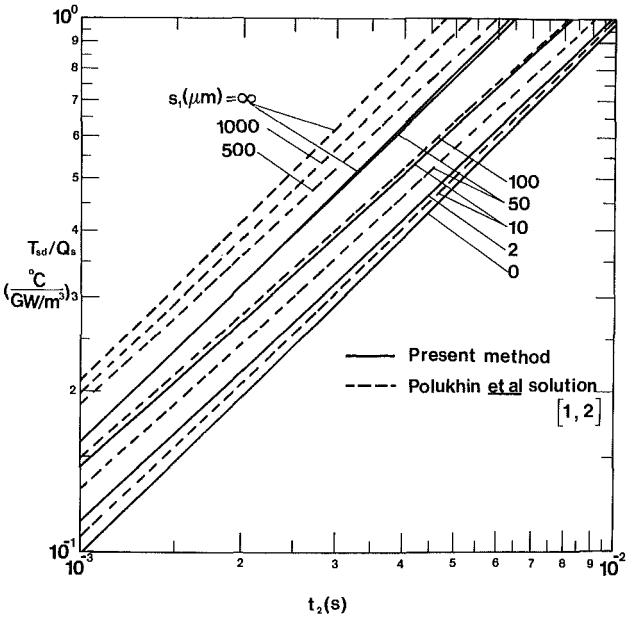

Fig. 8 Comparison of temperature change at the strip/scale layer interface due to deformation energy with the Polukhin et al. solution [1,2]

previous workers have neglected the heat capacity of the scale layer in their calculations because of its negligible thickness. The validity of this approximation can be studied with the current analysis. The present solution is compared, in particular, with that of Polukhin et al. [1, 2], who obtained a solution analytically, on the assumption that the heat transfer coefficient equals (k_c/s_1), i.e., the scale layer has only thermal resistance and no inertia. From their formulae (with the minor typographical errors corrected), the heat transfer to the roll due to T_0 and Q_s, and the strip temperature components at the strip/scale layer interface due to T_0 and Q_s are compared in Figs. 5–8 respectively (expressions for friction energy are not available in [1, 2]). When the scale layer is absent, the two solutions are, of course, identical. However, the results diverge as the scale layer thickness increases, q_{rl} tending to the zero limit in Polukhin's solution but a finite nonzero limit in the present solution due to the heat stored in the scale layer. Similar differences are observed in the other comparisons. These differences appear significant because of the short contact time involved in rolling; the heat capacity in even thin scale layers can thus be quite pronounced. Since under normal rolling conditions the contact time and scale layer are in the range 0.0003 to 0.1 s and 0.005 to 0.5 mm respectively, it is crucial to include the heat capacity of the scale layer in the formulation.

5 Conclusion

An analytical solution for the transfer of heat between the strip and roll, including the effect of an oxide layer on the strip surface, has been obtained. The results are consistent with those of the previous workers when the scale layer is absent. Simple graphs have been generated for the rapid evaluation of the heat transfer and strip average temperature when the heat energy terms, scale layer thickness, and contact time are given. The scale layer has a dominant effect on the heat transfer process. It acts as an insulating layer which can reduce the heat transfer significantly (by up to 50% for typical strip thicknesses and contact times, as evidenced in Fig. 4). It has also been shown that the heat capacity of the scale layer plays an important role in hot rolling thermal analysis and therefore should not be neglected.

The solution presented here, which is applicable to both hot and cold rolling conditions, is valid when the contact time is reasonably small and the roll diameter is large compared to the strip thickness and reduction ratio such that the curvature effect may be neglected. (It has been found that the solution is applicable, for typical rolling conditions, to strip thicknesses

of greater than 1 mm for hot rolling and even less for cold rolling.) The assumed uniform distribution of the frictional and deformation energy is expected to be valid in hot rolling since the overall heat transfer is dominated by the strip/roll bulk temperature difference.

Acknowledgments

The author is indebted to his colleague, Dr. C. H. Ellen, for his comments and interest in this study. Special thanks are also extended to the management of John Lysaght (Australia) Limited for permission to publish this paper.

References

1 Polukhin, P. I., et al., "Thermal Processes in the Deformation Zone During Sheet Rolling, Communication 1," *Steel USSR*, Vol. 4, 1974, pp. 52–54.

2 Polukhin, P. I., et al., "Thermal Process in the Deformation Zone When Rolling Sheet, Communication 2," *Steel USSR*, Vol. 4, 1974, pp. 135–137.

3 Pawelski, O., and Bruns, E., "Heat Transfer and Temperature Fields in Hot Rolling of Sheet with Special Regard to the Influence of Scale," *Stahl Eisen*, Vol. 94, 1976, pp. 864–869.

4 Cerni, S., "The Temperature and Thermal Stresses in the Rolling of Metal Strip," Doctoral Dissertation, Carnegie Institute of Technology, 1961.

5 Cerni, S., Weinstein, A. S., and Zorowski, C. F., "Temperature and Thermal Stresses in the Rolling of Metal Strip," *Iron Steel Engineer Year Book*, 1963, pp. 717–723.

6 Finne, R., Jacob, J. P., and Rissanen, J., "A Mathematical Model of Strip Rolling Mills," *IBM Nordiska Laboratorier*, Sweden, TP 18.094, 1963.

7 Yuen, W. Y. D., "On the Steady-State Temperature Distribution in a Rotating Cylinder Subject to Heating and Cooling Over Its Surface," ASME JOURNAL OF HEAT TRANSFER, Vol. 106, No. 3, Aug. 1984, pp. 578–585.

8 Patula, E. J., "Steady-State Temperature Distributions in a Rotating Roll Subject to Surface Heat Fluxes and Convective Cooling," ASME JOURNAL OF HEAT TRANSFER, Vol. 103, No. 1, Feb. 1981, pp. 36–41.

9 Orowan, E., "The Calculation of Roll Pressure in Hot and Cold Flat Rolling," *Proceedings, Institution of Mechanical Engineers*, Vol. 150, 1943, pp. 140–167.

10 Abramowitz, M., and Stegun, I. A., *Handbook of Mathematical Functions*, National Bureau of Standards, US Department of Commerce, 1972, p. 209.

Analysis of Freeze Coating on a Nonisothermal Moving Plate by a Perturbation Method

F. B. Cheung
Reactor Analysis and Safety Division,
Argonne National Laboratory,
Argonne, IL 60439
Mem. ASME

The behavior of a frozen layer (or "freeze coat") on the surface of a chilled flat plate traveling with a constant velocity through a warm liquid bath is studied analytically. A perturbation technique is employed to solve the equations governing the shape and temperature of the freeze coat, taking full account of the axial variation of the plate temperature and heat convection from the warm liquid to the moving object. Unlike the case of an isothermal plate where the freeze-coat thickness increases monotonically along the axial direction, here the freeze coat is found to grow only within a limited distance from the inlet. Beyond this distance, the freeze coat begins to decay through remelting. The location at which remelting occurs and the maximum freeze-coat thickness are determined displaying the principal effects of three controlling dimensionless parameters. Criteria for selection of the optimum freeze-coating operation conditions are established and discussed.

1 Introduction

When a warm liquid suddenly flows over the surface of a chilled flat plate that is at a temperature below the freezing point of the liquid, a frozen layer may form on the plate. If the plate is kept isothermal as in [1–5] or if it is cooled by a coolant liquid flowing along the other side of the plate as in [6–8], there is a constant renewal of heat sinks at the wall to remove the heat convected from the flowing warm liquid. The frozen layer, once formed, never melts. Rather, it grows continuously in time and eventually approaches a steady-state thickness. If, however, the plate is neither cooled nor kept isothermal [9, 10], freezing of the flow can be achieved only at the expense of the sensible heat of the plate. Solidification proceeds as long as the conductive heat flux into the plate exceeds the convective heat flux from the flowing warm liquid. As the plate temperature rises toward the freezing point of the liquid, convective heat transfer becomes more than what can be conducted away, resulting actually in reduction in the frozen layer thickness through remelting. Since the wall heat capacity is the only heat sink of the system, the conductive heat flux becomes progressively smaller in time. Ultimately, remelting will cause the frozen layer to disappear completely.

In practical application, the above frozen layer growth and decay behavior can be encountered in a continuous metal casting process known as dip-forming [11, 12]. In this process, a cold metal plate or bar is passed continuously through a bath of molten metal. The moving object is at a subcooled temperature below the freezing point of the bath and, as it travels through the bath, freezing of the molten metal occurs over its surface. Remelting of the frozen layer, however, may follow if the immersion time is long. From an economical point of view, it is desired to have the moving object emerge from the bath once the frozen layer thickness reaches its peak value. The optimum time of immersion depends on the initial object temperature, the bath temperature, the speed of the moving object, and the physical properties of the system. A somewhat similar situation arises in the process of fluidized-bed coating [13–15] where a hot object is dipped in a bed of fusible polymeric resin powder through which a current of gas is passed. The object is at a temperature higher than the fusion or softening point of the resin so that a thin film of plastic coating is formed on the surface of the object as it is dipped. In general, the object is made of metal on which the plastic coating is applied to provide a wear-resistant surface and to protect against corrosion.

Recently, Seeniraj and Bose [16] performed an interesting analysis of freeze coating of a molten polymeric substance on a continuous moving metallic object. This solidification process has an important application in chemical industries concerning such as the casting of an insulating coating on metal plates or electricity cables. Its end product is almost the same as that of the fluidized-bed coating process. However, in operation, it is quite similar to the metallic dip-forming process except that the liquid is not a molten metal but a polymeric melt whose Prandtl number is large. In the work of Seeniraj and Bose, the coordinate system is stationary with respect to the liquid bath. By assuming that the moving object remains at a constant uniform temperature during the freeze-coating process and that the liquid is at its freezing temperature, closed-form analytical expressions are obtained for the freeze-coat thickness as a function of the axial distance with the Stefan number as a parameter. The study differs from those of [1–10] in that the thickness of the frozen layer varies spatially rather than with time, which is quite desirable in view of practical application. Unfortunately, the results are valid only for a small immersion distance or, equivalently, a limited immersion time. With the assumption of a constant object temperature, the important feature of frozen layer growth and decay is lost. The assumption that the liquid is saturated (i.e., at its freezing temperature) represents another serious limitation of the work.

In the present study, the constant-object-temperature and the saturated-liquid requirements are relaxed. The process of freeze coating of a superheated polymeric melt on a nonisothermal moving metallic plate is investigated analytically. The problem is again formulated with the coordinate system held stationary with respect to the liquid bath. Convective heat transfer from the warm liquid to the frozen layer on the moving plate is modeled. Also modeled is the axial variation of the plate temperature which is treated as an unknown quantity to be determined in the course of analysis. The governing partial differential equations are transformed in terms of several dimensionless quantities and

Contributed by the Heat Transfer Division for publication in the JOURNAL OF HEAT TRANSFER. Manuscript received by the Heat Transfer Division March 20, 1984.

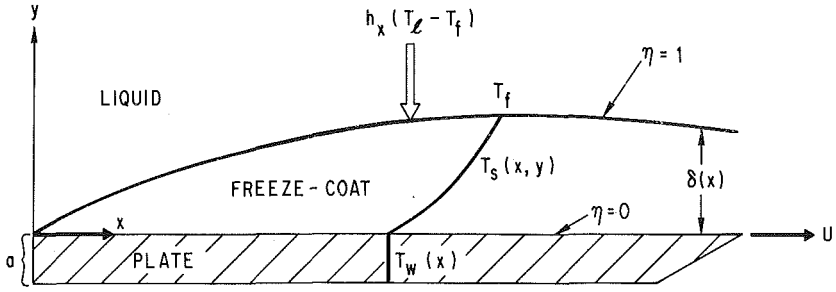

Fig. 1 Schematic of the physical configuration and the freeze coat along the nonisothermal moving plate, indicating nomenclature

the controlling parameters of the system are identified. Meanwhile, the solid–liquid interface is fixed at a constant location in the dimensionless space. The transformed equations are then solved by a perturbation technique [17] which is chosen to facilitate the study of the effects of the nonisothermal boundary condition on the freezing process. In so doing, a system of ordinary differential equations, readily integrated by a standard numerical method, is obtained describing the axial variations of the plate temperature and the shape of the freeze coat. The optimum immersion distance and the maximum freeze-coat thickness are determined for various system conditions.

2 Problem Formulation

The freeze-coating system under consideration is depicted in Fig. 1. A continuous moving plate with a velocity U enters a large body of liquid through a slit or a tight opening in an adiabatic bounding wall at $x = 0$. Before the immersion, the plate is at a uniform temperature T_{w_0} which is below the freezing point T_f of the liquid whereas the liquid is at a uniform temperature T_l above its freezing point. As the plate travels through the body of the liquid, a frozen layer or freeze coat forms on the plate; the coat thickness varies axially in the direction of motion.[1] The freeze-coat thickness $\delta(x)$ is not necessarily a monotonically increasing function of x as in [16]. This is because the plate temperature T_w cannot remain constant but, instead, rises along the x axis. The freeze coat grows at first in the x direction. However, as the local convective heat flux $h_x (T_l - T_f)$ from the liquid to the phase boundary at $\eta = 1$ exceeds the conductive heat flux from the front, the freeze coat starts to decay through remelting. One of our objectives is to determine the axial location at which this occurs. To formulate the problem, the following simplifying assumptions are used:

1 The freeze-coating process is at a steady state. This in turn requires that both the plate velocity U and the far-field liquid temperature T_l remain constant in time.

2 Both the plate and its freeze coat are thin relative to the immersion distance so that heat conduction is negligible in the axial direction.[2]

[1] In actual practice, freeze coats may form on both sides of the plate. The lower freeze coat, however, is identical to the upper one as long as the effect of natural convection is negligible. This is deemed to be the case since forced convection is dominating in the freeze-coating process. Thus only the upper half of the system needs to be considered.

[2] During freeze coating of Hostafoam C on copper, for example, the freeze-coat thickness is typically of the order of 0.05 mm, whereas the immersion distance is about 0.10 m. Thus, the axial dimension is much larger than the vertical dimension.

Nomenclature

a = half-width of the plate
A = convective heat transfer parameter, equation (10c)
c_{p_s} = specific heat of the freeze coat
c_{p_w} = specific heat of the plate
f = an unknown function of η, equation (32)
g = an unknown function of η, equation (41)
h_x = local heat transfer coefficient
k_l = thermal conductivity of the liquid
k_s = thermal conductivity of the freeze coat
Pr = Prandtl number, ν/α_l
R = coat-to-plate thermal ratio, equation (10b)
Re_x = local Reynolds number, Ux/ν
S = Stefan number, equation (10a)
T_f = freezing point of the liquid
T_l = liquid temperature
T_s = temperature of the freeze coat
T_w = plate temperature
T_{w_0} = plate temperature at the inlet
U = plate velocity
x = axial coordinate measured from the inlet along the plate
y = vertical coordinate measured upward from the surface of the plate
α_l = thermal diffusivity of the liquid
α_s = thermal diffusivity of the freeze coat
Δ = dimensionless freeze-coat thickness, equation (5b)
$\Delta_{\max}$ = maximum value of Δ
δ = freeze-coat thickness
η = dimensionless vertical coordinate, equation (5a)
θ_s = dimensionless temperature of the freeze coat, equation (5b)
θ_w = dimensionless plate temperature, equation (5b)
λ = heat of fusion
ν = kinematic viscosity
ξ = dimensionless axial coordinate, equation (5b)
$\xi_{\max}$ = location of ξ at which the value of Δ peaks
ξ_t = location of ξ at which transition to turbulent flow occurs
ρ_s = density of the freeze coat
ρ_w = density of the plate
σ_1 = first-order freeze-coating constant, equation (23)
σ_2 = second-order freeze-coating constant, equation (32)
σ_3 = third-order freeze-coating constant, equation (41)

Subscripts

1 = first-order
2 = second-order
3 = third-order
l = liquid
max = maximum
s = freeze coat
x = local quantity
w = plate

3 The plate temperature varies very slightly in the y direction and may be regarded as a function of x alone. This is probably a good approximation for a thin metallic plate since it is much more conductive than the polymeric substance.[3]

4 The process of freeze coating takes place at a constant temperature T_f. The solidification front is sharp and planar on the scale of the freeze-coat thickness, and thermal equilibrium exists at the phase boundary.

5 All thermophysical properties are constant. In addition, there is no volumetric change upon freezing.

6 For a highly viscous polymeric melt such as Hostafoam C [18], the effect of free convection is negligible.[4]

7 The liquid motion induced by the moving plate is steady and laminar and no transition to turbulent regime occurs. This is normally the case since the polymeric melt is highly viscous [18]. In addition, the freeze coat is thin enough so that there is negligible interaction between the flow and the shape of the solid-liquid phase boundary [19]. Under these circumstances, the convective heat flux from the warm liquid to the solid boundary may be obtained directly from the conventional solution of forced convection over a moving surface without phase change such as those given in [20-22]. Similar arguments have been employed successfully by previous investigators [1-10].

With the above assumptions, the equations governing the temperature of the freeze-coat $T_s\ (x, y)$, the plate temperature $T_w(x)$, and the freeze coat profile $\delta(x)$, can be written as follows:

$$\rho_s c_{p_s} U \frac{\partial T_s}{\partial x} = k_s \frac{\partial^2 T_s}{\partial y^2}, \quad x \geq 0, \quad 0 \leq y \leq \delta(x) \tag{1}$$

$$\rho_w c_{p_w} Ua \frac{dT_w}{dx} = k_s \left(\frac{\partial T_s}{\partial y}\right)_{y=0} \tag{2}$$

$$x=0: \quad \delta = 0, \quad T_w = T_{w_0} \tag{3a}$$

$$y=0: \quad T_s = T_w(x) \tag{3b}$$

$$y=\delta: \quad T_s = T_f \tag{3c}$$

$$\rho_s U \lambda \frac{d\delta}{dx} = k_s \frac{\partial T_s}{\partial y} - h_x (T_l - T_f) \tag{3d}$$

In the above formulation, the inlet plate temperatures T_{w_0}, the liquid temperature T_l, and the plate velocity U are treated as constants. The x axis is measured from the inlet of the plate along the direction of motion whereas the y axis is measured upward from the surface of the plate. Equation (2) is written according to assumption (3). With the plate moving at a constant velocity, the left-hand side of this equation is actually the time rate of change of the enthalpy of the local plate element as we travel with the plate. In view of assumption (7), the local coefficient h_x of convective heat transfer from the liquid to the freeze coat is treated as an input quantity of the problem. For heat transfer in the laminar boundary layer on a moving flat plate, this is given by [22]

$$\frac{h_x x}{k_l} = 0.53 \mathrm{Pr}^{1/2} \mathrm{Re}_x^{1/2}, \quad \mathrm{Pr} >> 1 \tag{4}$$

where $\mathrm{Pr} = \nu/\alpha_l$ is the Prandtl number and $\mathrm{Re}_x = Ux/\nu$ is the local Reynolds number. Note that in the limiting case of an isothermal plate, viz., $T_w = T_{w_0}$, and a saturated liquid, viz., $T_l = T_f$, the present problem reduces to the one studied in [16].

[3] The thermal conductivity of copper, for example, is about 400 W/m°C, whereas that of Hostafoam C is about 0.3 W/m°C. The heat capacity, on the other hand, is about the same for both.

[4] Although the inlet plate temperature, typically about 5°C for freeze coating of Hostafoam C on copper, is much lower than the fusion temperature of Hostafoam C (~167°C), the liquid bath temperature is only several degrees above the fusion temperature in most operations. The Grashof number, which is proportional to $(T_l - T_f)/\mu^2$, is usually below the critical value.

3 The Perturbation Method

Should the plate temperature be maintained constant, the freeze-coat thickness would increase monotonically along the x axis. To determine the axial growth and decay behavior of the freeze coat, therefore, it is essential to understand how the plate deviates from the isothermal condition and how the shape of the freeze coat is being affected. This objective can be achieved by expanding the plate temperature and the freeze-coat thickness in terms of an appropriate perturbation quantity with the basic solution [17] being the one obtained for an isothermal plate. To do this, the following transformation is invoked

$$\xi = Ux/\alpha_s, \quad \eta = y/\delta \tag{5a}$$

$$\Delta = U\delta/\alpha_s, \quad \theta_w = (T_w - T_{w_0})/(T_f - T_{w_0}),$$
$$\theta_s = (T_s - T_{w_0})/(T_f - T_{w_0}) \tag{5b}$$

where $\Delta = \Delta(\xi)$, $\theta_w = \theta_w(\xi)$, and $\theta_s = \theta_s(\xi,\eta)$. In dimensionless space, the solid-liquid phase boundary is fixed at $\eta = 1$. The governing system becomes

$$\frac{\partial^2 \theta_s}{\partial \eta^2} = \Delta^2 \frac{\partial \theta_s}{\partial \xi} - \Delta \dot{\Delta} \eta \frac{\partial \theta_s}{\partial \eta}, \quad \xi \geq 0, \quad 0 \leq \eta \leq 1 \tag{6}$$

$$\dot{\theta}_w = \frac{R}{\Delta} \left(\frac{\partial \theta_s}{\partial \eta}\right)_{\eta=0} \tag{7}$$

$$\dot{\Delta} = \mathrm{S}\left[\frac{1}{\Delta}\left(\frac{\partial \theta_s}{\partial \eta}\right)_{\eta=1} - 0.53 A \xi^{-1/2}\right], \tag{8}$$

$$\theta_s(\xi,0) = \theta_w(\xi), \quad \theta_s(\xi,1) = 1, \quad \theta_w(0) = \Delta(0) = 0, \tag{9}$$

where the dots denote the total derivatives with respect to ξ and S is the Stefan number, R the coat-to-plate thermal ratio, and A the convective heat transfer parameter defined respectively by

$$\mathrm{S} = \frac{c_{p_s}(T_f - T_{w_0})}{\lambda} \tag{10a}$$

$$R = \left(\frac{\rho_s c_{p_s}}{\rho_w c_{p_w}}\right)\left(\frac{Ua}{\alpha_s}\right)^{-1} \tag{10b}$$

$$A = \left(\frac{\alpha_s}{\alpha_l}\right)^{1/2} \left(\frac{k_l}{k_s}\right)\left(\frac{T_l - T_f}{T_f - T_{w_0}}\right) \tag{10c}$$

The value of R is usually much smaller than unity in industrial operations. As indicated by equation (7), the plate is isothermal if R is identically zero.[5] Thus, we may perform a parameter perturbation using R as the perturbation quantity. Expanding Δ, θ_w, and θ_s in terms of R, we have

$$\Delta = \Delta_1 + R\Delta_2 + R^2\Delta_3 + \ldots \tag{11a}$$

$$\theta_w = \theta_{w_1} + R\theta_{w_2} + R^2\theta_{w_3} + \ldots \tag{11b}$$

$$\theta_s = \theta_{s_1} + R\theta_{s_2} + R^2\theta_{s_3} + \ldots \tag{11c}$$

Substituting the above expressions into equations (6-9) and collecting the same-order terms, the following systems of equations governing the first-, second-, and third-order solutions are obtained.

1 First-order system[6]

$$\frac{\partial^2 \theta_{s_1}}{\partial \eta^2} = \Delta_1^2 \frac{\partial \theta_{s_1}}{\partial \xi} - \Delta_1 \dot{\Delta}_1 \eta \frac{\partial \theta_{s_1}}{\partial \eta}, \quad \xi \geq 0, \quad 0 \leq \eta \leq 1 \tag{12}$$

$$\dot{\theta}_{w_1} = 0, \quad \dot{\Delta}_1 = \mathrm{S}\left[\frac{1}{\Delta_1}\left(\frac{\partial \theta_{s_1}}{\partial \eta}\right)_{\eta=1} - 0.53 A \xi^{-1/2}\right] \tag{13}$$

$$\theta_{s_1}(\xi,0) = \theta_{w_1}(\xi), \quad \theta_{s_1}(\xi,1) = 1, \quad \theta_{w_1}(0) = \Delta_1(0) = 0 \tag{14}$$

[5] This corresponds to the case in which the heat capacity of the plate is infinity or the thermal conductivity of the freeze coat is zero.

[6] This system is exact in the limit of $R = 0$, corresponding to the case of an isothermal plate.

2 Second-order system

$$\frac{\partial^2\theta_{s_2}}{\partial\eta^2}=\Delta_1^2\frac{\partial\theta_{s_2}}{\partial\xi}-\Delta_1\dot{\Delta}_1\eta\left[\frac{\partial\theta_{s_2}}{\partial\eta}+\left(\frac{\dot{\Delta}_2}{\dot{\Delta}_1}-\frac{\Delta_2}{\Delta_1}\right)\frac{\partial\theta_{s_1}}{\partial\eta}\right]$$

$$+2\frac{\Delta_2}{\Delta_1}\frac{\partial^2\theta_{s_1}}{\partial\eta^2},\quad \xi\geq 0,\quad 0\leq\eta\leq 1, \tag{15}$$

$$\dot{\theta}_{w_2}=\frac{1}{\Delta_1}\left(\frac{\partial\theta_{s_1}}{\partial\eta}\right)_{\eta=0}, \tag{16}$$

$$\dot{\Delta}_2=\frac{S}{\Delta_1}\left[\left(\frac{\partial\theta_{s_2}}{\partial\eta}\right)_{\eta=1}-\frac{\Delta_2}{\Delta_1}\left(\frac{\partial\theta_{s_1}}{\partial\eta}\right)_{\eta=1}\right], \tag{17}$$

$$\theta_{s_2}(\xi,0)=\theta_{w_2}(\xi),\quad \theta_{s_2}(\xi,1)=\theta_{w_2}(0)=\Delta_2(0)=0. \tag{18}$$

3 Third-order system

$$\frac{\partial^2\theta_{s_3}}{\partial\eta^2}=\Delta_1^2\frac{\partial\theta_{s_3}}{\partial\xi}-\Delta_1\dot{\Delta}_1\eta\left\{\frac{\partial\theta_{s_3}}{\partial\eta}+\left(\frac{\dot{\Delta}_2}{\dot{\Delta}_1}-\frac{\Delta_2}{\Delta_1}\right)\frac{\partial\theta_{s_2}}{\partial\eta}\right.$$

$$\left.+\left[\frac{\dot{\Delta}_3}{\dot{\Delta}_1}-\frac{\dot{\Delta}_2}{\dot{\Delta}_1}\frac{\Delta_2}{\Delta_1}+\left(\frac{\Delta_2}{\Delta_1}\right)^2-\frac{\Delta_3}{\Delta_1}\right]\frac{\partial\theta_{s_1}}{\partial\eta}\right\}$$

$$+2\frac{\Delta_2}{\Delta_1}\frac{\partial^2\theta_{s_2}}{\partial\eta^2}+\left(\frac{3\Delta_2^2-2\Delta_1\Delta_3}{\Delta_1^2}\right)\frac{\partial^2\theta_{s_1}}{\partial\eta^2},$$

$$\xi\geq 0,\quad 0\leq\eta\leq 1 \tag{19}$$

$$\dot{\theta}_{w_3}=\frac{1}{\Delta_1}\left[\left(\frac{\partial\theta_{s_2}}{\partial\eta}\right)_{\eta=0}-\frac{\Delta_2}{\Delta_1}\left(\frac{\partial\theta_{s_1}}{\partial\eta}\right)_{\eta=0}\right] \tag{20}$$

$$\dot{\Delta}_3=\frac{S}{\Delta_1}\left\{\left(\frac{\partial\theta_{s_3}}{\partial\eta}\right)_{\eta=1}-\frac{\Delta_2}{\Delta_1}\left(\frac{\partial\theta_{s_2}}{\partial\eta}\right)_{\eta=1}\right.$$

$$\left.+\left[\left(\frac{\Delta_2}{\Delta_1}\right)^2-\frac{\Delta_3}{\Delta_1}\right]\left(\frac{\partial\theta_{s_1}}{\partial\eta}\right)_{\eta=1}\right\} \tag{21}$$

$$\theta_{s_3}(\xi,0)=\theta_{w_3}(\xi),\quad \theta_{s_3}(\xi,1)=\theta_{w_3}(0)=\Delta_3(0)=0 \tag{22}$$

Higher-order systems may be derived in a similar manner. However, as mentioned above, the value of R is much less than unity in most practical cases. Under such a condition, the solution converges very rapidly as will be demonstrated later. Thus, there is no need to go beyond the third-order solution. This point will be further discussed. The various-order systems will now be solved in sequence.

4 First-Order Solution

Inspection of equations (12–14) indicates that $\theta_{w_1}=0$ for $\xi\geq 0$ and that θ_{s_1} is independent of ξ if we set

$$\Delta_1\dot{\Delta}_1=\text{constant}\quad\text{or}\quad \Delta_1=\sigma_1\xi^{1/2} \tag{23}$$

where σ_1 is a freeze-coating constant. With the above expression, the initial condition is satisfied automatically. The governing system becomes

$$\theta_{s_1}''+\frac{1}{2}\sigma_1^2\eta\theta_{s_1}'=0,\quad 0\leq\eta\leq 1 \tag{24}$$

$$\sigma_1=2S\left[\frac{1}{\sigma_1}\theta_{s_1}'(1)-0.53A\right] \tag{25}$$

$$\theta_{s_1}(0)=0,\quad \theta_{s_1}(1)=1 \tag{26}$$

where the primes denote the total derivatives with respect to η. A closed-form implicit solution to the above equations exists. This is

$$\theta_{s_1}=\frac{erf(\eta\sigma_1/2)}{erf(\sigma_1/2)},\quad 0\leq\eta\leq 1, \tag{27}$$

$$\sigma_1=2S\left[\frac{1}{\sqrt{\pi}}\frac{\exp(-\sigma_1^2/4)}{erf(\sigma_1/2)}-0.53A\right]. \tag{28}$$

Equations (23), (27), and (28) provide an exact description of the freeze coat on an isothermal plate for which $R=0$. Note that σ_1 is a positive quantity for $A\geq 0$ and $S\geq 0$. As $A\to\infty$, σ_1 approaches asymptotically to the value of $(0.53\,A)^{-1}$. In the limit of $A=0$, equation (28) reduces to the one presented in [16].

5 Second-Order Solution

With the first approximation, the function θ_{w_2} governed by equation (16) may be determined. Substituting equations (23) and (27) into equations (15–18), we obtain

$$\frac{\partial^2\theta_{s_2}}{\partial\eta^2}=\sigma_1^2\xi\frac{\partial\theta_{s_2}}{\partial\xi}-\frac{1}{2}\sigma_1^2\eta\left[\frac{\partial\theta_{s_2}}{\partial\eta}+\xi^{1/2}(2\dot{\Delta}_2+\xi^{-1}\Delta_2)\right.$$

$$\left.\frac{\exp(-\eta^2\sigma_1^2/4)}{\sqrt{\pi}erf(\sigma_1/2)}\right],\quad \xi\geq 0,\quad 0\leq\eta\leq 1 \tag{29}$$

$$\dot{\Delta}_2=\frac{S}{\sigma_1}\left[\xi^{-1/2}\left(\frac{\partial\theta_{s_2}}{\partial\eta}\right)_{\eta=1}-\xi^{-1}\Delta_2\frac{\exp(-\sigma_1{}^2/4)}{\sqrt{\pi}erf(\sigma_1/2)}\right] \tag{30}$$

$$\theta_{s_2}(\xi,0)=\theta_{w_2}(\xi)=\frac{2\xi^{1/2}}{\sqrt{\pi}erf(\sigma_1/2)},\ \theta_{s_2}(\xi,1)=\Delta_2(0)=0 \tag{31}$$

Inspection of the above equations indicates that for $\xi\geq 0$ and $0\leq\eta\leq 1$,

$$\Delta_2=\sigma_2\xi\quad\text{and}\quad \theta_{s_2}=\frac{2\xi^{1/2}}{\sqrt{\pi}erf(\sigma_1/2)}f(\eta), \tag{32}$$

where the second-order freeze-coating constant σ_2 and the function f are given by

$$f''=\frac{\sigma_1^2}{2}\left[f-\eta f'-\frac{3}{2}\eta\sigma_2\exp(-\eta^2\sigma_1^2/4)\right], \tag{33}$$

$$\sigma_2=2\left[\frac{\sqrt{\pi}}{S}\sigma_1 erf(\sigma_1/2)+\exp(-\sigma_1^2/4)\right]^{-1}f'(1), \tag{34}$$

$$f(0)=1,\quad f(1)=0. \tag{35}$$

Assuming a value for $f'(1)$, σ_2 may be determined from equation (34). Equation (33) may then be integrated starting from $\eta=1$ as an initial value problem using the Runge–Kutta forward integration scheme. The correct choice of $f'(1)$ is obtained such that the boundary condition at $\eta=0$ is satisfied. Note that σ_2 is always a negative quantity since $\sigma_1>0$ and $f'(1)<0$. Up to the second approximation, we have

$$\Delta\sim\sigma_1\xi^{1/2}+R\sigma_2\xi, \tag{36a}$$

$$\theta_w\sim\frac{2R\xi^{1/2}}{\sqrt{\pi}erf(\sigma_1/2)}, \tag{36b}$$

$$\theta_s\sim\frac{1}{erf(\sigma_1/2)}\left[erf(\eta\sigma_1/2)+\frac{2}{\sqrt{\pi}}R\xi^{1/2}f(\eta)\right]. \tag{36c}$$

For a nonzero, positive value of R, the plate temperature increases according to the square root of ξ. Comparing to the case of an isothermal plate, the relative freeze-coat thickness in the case of a nonisothermal plate is always less than unity, i.e.,

$$\Delta/\Delta_1\sim 1+R(\sigma_2/\sigma_1)\xi^{1/2}<1 \tag{37}$$

The inequality given above is obvious since $\sigma_1>0$ and $\sigma_2<0$.

6 Third-Order Solution

With the second approximation, the function θ_{w_3} governed by equation (20) may be determined. Substituting equations (23), (27), and (32) into equations (19–22), we obtain

$$\frac{\partial^2\theta_{s_3}}{\partial\eta^2}=\sigma_1^2\xi\frac{\partial\theta_{s_3}}{\partial\xi}-\frac{1}{2}\sigma_1^2\eta\frac{\partial\theta_{s_3}}{\partial\eta}$$

$$-\frac{\sigma_1^2\xi}{\sqrt{\pi}erf(\sigma_1/2)}\left[\left(\xi^{-1/2}\dot{\Delta}_3+\frac{1}{2}\xi^{-3/2}\Delta_3\right.\right.$$

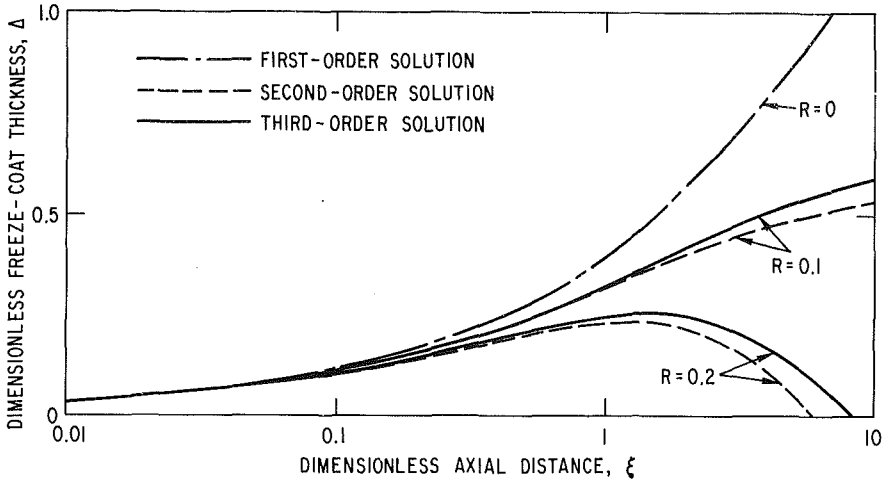

Fig. 2 Axial variation of the dimensionless freeze-coat thickness: comparison of the first-, second-, and third-order solutions ($A = 1$, S = 0.1)

$$-\frac{2\sigma_2^2}{\sigma_1}\Big)\eta\exp(-\eta^2\sigma_1^2/4) + \frac{\sigma_2}{\sigma_1}\eta f' - \frac{4\sigma_2}{\sigma_1^3}f''\Big], \quad \xi \geq 0, \quad 0 \leq \eta \leq 1 \tag{38}$$

$$\dot{\Delta}_3 = \frac{S}{\sigma_1}\left[\xi^{-1/2}\left(\frac{\partial\theta_{s_3}}{\partial\eta}\right)_{\eta=1} - \frac{2\sigma_2\xi^{1/2}f'(1)}{\sqrt{\pi}\sigma_1 erf(\sigma_1/2)} + \xi^{1/2}\left(\frac{\sigma_2^2}{\sigma_1} - \xi^{-3/2}\Delta_3\right)\frac{\exp(-\sigma_1^2/4)}{\sqrt{\pi}erf(\sigma_1/2)}\right] \tag{39}$$

$$\theta_{s_3}(\xi,0) = \theta_{w_3}(\xi) = \frac{2f'(0)-\sigma_2}{\sqrt{\pi}\sigma_1 erf(\sigma_1/2)}\xi, \quad \theta_{s_3}(\xi,1) = \Delta_3(0) = 0 \tag{40}$$

Inspection of the above equations indicates that for $\xi \geq 0$ and $0 \leq \eta \leq 1$,

$$\Delta_3 = \sigma_3\xi^{3/2} \quad \text{and} \quad \theta_{s_3} = \frac{2f'(0)-\sigma_2}{\sqrt{\pi}\sigma_1 erf(\sigma_1/2)}\xi g(\eta) \tag{41}$$

where the third-order freeze-coating constant σ_3 and the function g are given by

$$g'' = \sigma_1^2\Big\{g - \frac{1}{2}\eta g' - [2f'(0)-\sigma_2]^{-1}\Big[\sigma_2\eta f' - \frac{4\sigma_2}{\sigma_1^2}f'' + 2(\sigma_1\sigma_3 - \sigma_2^2)\eta\exp(-\eta^2\sigma_1^2/4)\Big]\Big\}, \tag{42}$$

$$\sigma_3 = \Big[\frac{3}{2}\frac{\sqrt{\pi}}{S}\sigma_1^2 erf(\sigma_1/2) + \sigma_1\exp(-\sigma_1^2/4)\Big]^{-1}\{[2f'(0)-\sigma_2]g'(1) - 2\sigma_2 f'(1) + \sigma_2^2\exp(-\sigma_1^2/4)\} \tag{43}$$

$$g(0) = 1, \quad g(1) = 0 \tag{44}$$

Again, σ_3 may be determined from equation (43) by assuming a value for $g'(1)$. Equation (42) may then be integrated starting from $\eta = 1$ as an initial value problem using the Runge-Kutta forward integration scheme. The correct choice of $g'(1)$ is obtained such that the boundary condition at $\eta = 0$ is satisfied. Note that σ_3 may be either positive or negative in this case. Up to the third approximation, we have

$$\Delta \sim \sigma_1\xi^{1/2} + R\sigma_2\xi + R^2\sigma_3\xi^{3/2} \tag{45a}$$

$$\theta_w \sim \frac{1}{\sqrt{\pi}erf(\sigma_1/2)}\left\{2R\xi^{1/2} + \frac{R^2\xi}{\sigma_1}[2f'(0)-\sigma_2]\right\} \tag{45b}$$

$$\theta_s \sim \frac{1}{erf(\sigma_1/2)}\left\{erf(\eta\sigma_1/2) + \frac{2}{\sqrt{\pi}}R\xi^{1/2}f(\eta) + \frac{R^2\xi}{\sqrt{\pi}\sigma_1}[2f'(0)-\sigma_2]g(\eta)\right\} \tag{45c}$$

From equation (45*a*), the relative freeze-coat thickness can be written as

$$\Delta/\Delta_1 \sim 1 + (\sigma_2/\sigma_1)R\xi^{1/2} + (\sigma_3/\sigma_1)R^2\xi \tag{46}$$

As will be discussed later, the value of Δ/Δ_1 is always less than unity. From equations (45*b*), (45*c*), and (46), it is obvious that the fourth-order solution can be expressed in terms of $R^3\ \xi^{3/2}$. In fact, the present solutions can be obtained by performing a coordinate perturbation with the perturbation quantity being $R\ \xi^{1/2}$. The solutions are convergent as long as the condition $R\ \xi^{1/2} < 1$ is satisfied. For small values of $R\xi^{1/2}$ commonly encountered in practical application,[7] the third approximation differs only slightly from the second, as will be discussed next. Therefore, higher-order solutions are not needed.

7 Results and Discussion

We have identified three independent parameters which control the axial variation of the freeze-coat thickness. These are the convective heat transfer parameter A, the coat-to-plate thermal ratio R, and the Stefan number S. To compare the accuracy of solutions obtained at various levels of approximation and to illustrate the effect of the perturbation quantity R on the solutions, the calculated axial variations of the dimensionless freeze-coat thickness are shown in Fig. 2 for the case of $A = 1$ and S = 0.1. The first-order solution, which is independent of the value of R, can be regarded as the basic solution. It gives the thickness of the freeze coat on an isothermal plate as a monotonically increasing function of ξ. The basic solution is exact in the limit of $R = 0$. At $R = 0.1$, the isothermal condition is no longer valid. Based on the third-order solution, the first-order solution is found to significantly overestimate the freeze-coat thickness, especially at large ξ. The second-order solution, on the other hand, slightly underestimates the freeze-coat thickness. The same behavior is observed at $R = 0.2$, with the differences among the various-order solutions being more remarkable. In this case, however, both the second- and third-order solutions

[7] Normally, R is very small. The present solutions are valid even at relatively large values of ξ and therefore, they are not small-ξ solutions.

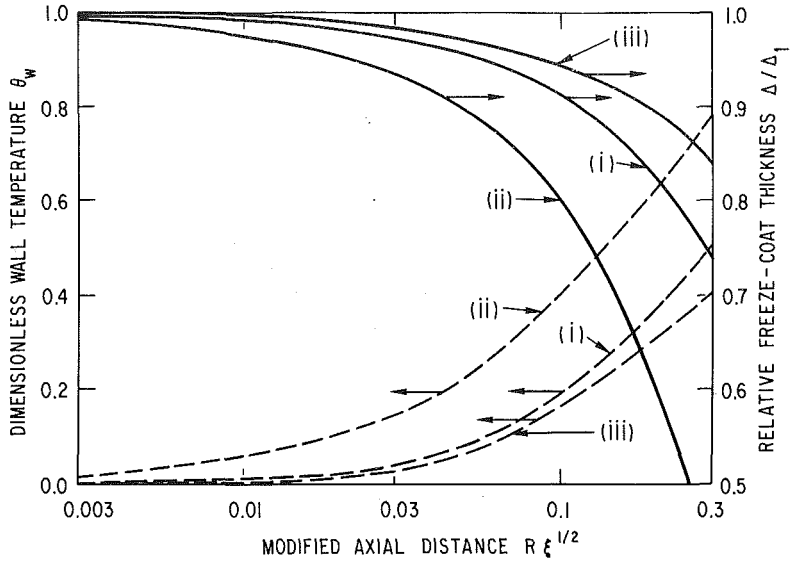

Fig. 3 Variation of the dimensionless wall temperature and the relative freeze-coat thickness along the modified axial distance: (*i*) A = 1, S = 1; (*ii*) A = 1, S = 0.1; (*iii*) A = 0.1, S = 1

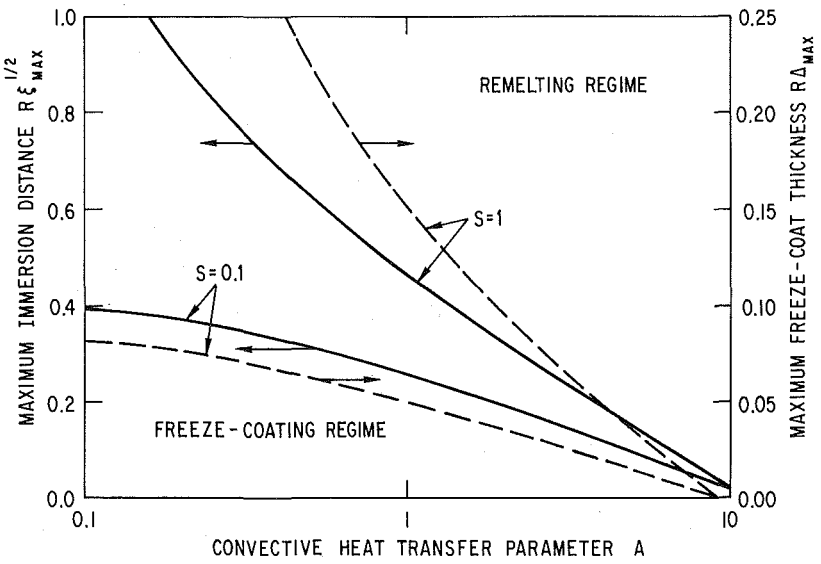

Fig. 4 Remelting criteria for the freeze-coating system – selection of the optimum operation conditions

predict a maximum for the freeze-coat thickness in the vicinity of $\xi_{max} = 1.8$ beyond which the freeze coat begins to decay through remelting.[8] The positions of the curves for various levels of approximation indicate that the present perturbation method is able to yield rapidly converging solutions. This is true as long as $R\,\xi^{1/2} < 1$. It should be noted that the first-, second-, and third-order solutions all approach the same curve as $\xi < 0.1$.

Variations of the dimensionless wall temperature and the relative freeze-coat thickness along the modified axial distance, $R\,\xi^{1/2}$, given by the third-order solutions, equations (45*b*) and (46), respectively, are presented in Fig. 3 for three different cases: (*i*) $A = 1$, S = 1; (*ii*) $A = 1$, S = 0.1; (*iii*) A = 0.1, S = 1. As shown in the figure, the assumption of an isothermal plate, viz., $\theta_w = 0$, is a reasonable approximation if $R\,\xi^{1/2} < 0.01$. At larger values of $R\,\xi^{1/2}$, the isothermal conditions fail to apply. In all cases, the plate temperature rises monotonically along the axial distance toward the liquid freezing point at which $\theta_w = 1$. Beyond this temperature, the freeze coat ceases to exist. The extent of deviation from the isothermal condition is measured by the relative freeze coat thickness, Δ/Δ_1, which is always less than unity. This indicates that the assumption of an isothermal plate always overestimates the thickness of the freeze coat. At $R\,\xi^{1/2}$ = 0.3, for example, the relative error ranges from 15 to 56 percent in the three cases presented in the figure. As the value of S decreases, both the plate temperature and the relative error increase, indicating a larger deviation from the isothermal condition. The reverse is true as the value of A decreases, although the solution is less sensitive to the change in the value of A. The above results are quite expected. A smaller value of A corresponds to a lower rate of convective heating and thus a smaller deviation from the isothermal condition. On the contrary, the shielding effect of the freeze coat, measured by the Stefan number, becomes less effective as the value of S decreases, resulting in a larger deviation

[8] This growth and decay behavior exists in all cases of $R > 0$. It does not show up in Fig. 2 for the case of $R = 0.1$ simply because ξ_{max} is larger than 10 in this case.

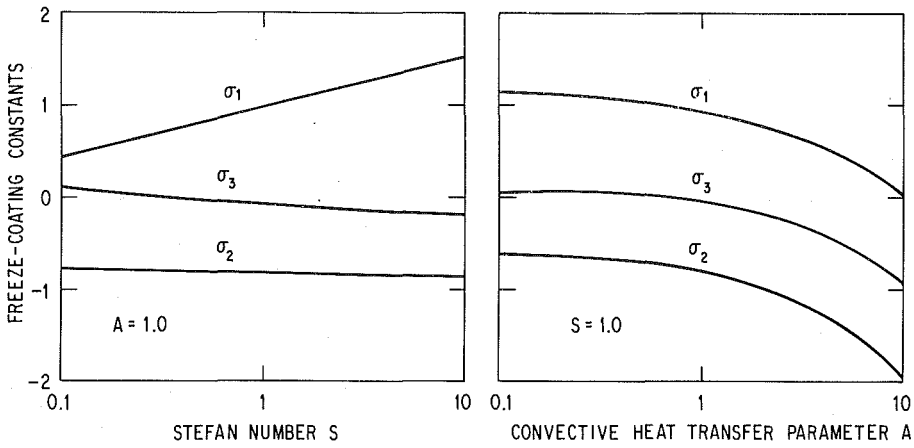

Fig. 5 Effects of the Stefan number and the convective heat transfer parameter on the various freeze-coating constants

from the isothermal condition. Note that the actual physical location beyond which the isothermal condition becomes a poor approximation depends very strongly on the value of R since $\xi \sim 0.01\, R^{-2}$.

We have demonstrated that for a nonisothermal plate, the freeze-coat thickness exhibits a maximum Δ_{max} at the axial location ξ_{max}. In actual operation, it is desired to have the plate emerge from the liquid before remelting takes place. To determine the value of Δ_{max} and ξ_{max}, equation (45*a*) is differentiated with respect to ξ and Δ is set equal to zero in the resultant equation. This gives an implicit expression for ξ_{max} as

$$\sigma_1 + 2\sigma_2 R \xi_{max}^{1/2} + 3\sigma_3 R^2 \xi_{max} = 0 \tag{47}$$

with which Δ_{max} may be obtained from equation (45*a*). Criteria may thus be established to predict the operation conditions for which remelting would occur in the freeze-coating system. Results are presented in Fig. 4 which show Δ_{max} and ξ_{max} as functions of R, A, and S. Again, ξ_{max} is a strong function of R. It varies according to $\xi_{max} \sim R^{-2}$. The effect of convective heat transfer is to suppress the axial growth of the freeze coat. As can be seen from the figure, both Δ_{max} and ξ_{max} decrease as A increases. On the contrary, an increase in S results in larger ξ_{max} and Δ_{max}. Obviously the freeze coat would grow much faster for materials with smaller latent heats of fusion. In Fig. 4, the solid curves separate the freeze-coating regime from the remelting regime. To be economical, the operation conditions should be chosen such that they would fall in the freeze-coating regime but close to the solid curves.

The effects of A and S on the various freeze-coating constants are shown in Fig. 5. In the present perturbation analysis, the freeze-coating constants are independent of R. Once the values of σ_1, σ_2, and σ_3 are known, the shape of the freeze coat is completely determined by equation (45*a*). For a given value of A, σ_1 increases very sharply with S as has been observed in [1-5, 16]. On the other hand, the higher-order constants σ_2 and σ_3, which exist only in the case of a nonisothermal plate, are much less sensitive to the change in S. For a given value of S, an increase in A leads to decreases in all values of the freeze-coating constants. Thus the axial growth of the freeze coat is severely retarded by the convective heat transfer from the warm liquid. For $A > 10$, the freeze coat may be completely remelted in a very short distance from the inlet. Note that σ_1 is always a positive quantity[9] whereas σ_2 is always a negative quantity. Meanwhile, σ_3 can be either positive or negative. However, its absolute value is relatively small, at least for $A < 3$. This clearly indicates that the freeze coat is thinner in the case of a nonisothermal plate. Since the value of A is seldom larger than unity in industrial operations, the second approximation may be accurate enough for practical purpose and certainly, there is no need to go beyond the third approximation.

[9] The value of σ_1 approaches asymptotically to $(0.53\ A)^{-1}$ at very large values of A (not shown in the figure).

8 Final Remarks

We have assumed the flow to be laminar in modeling the local convective heat transfer from the liquid to the moving plate. The value of ξ_{max} has been so determined to indicate the location at which the freeze coat begins to decay through remelting. This approach is sound as long as there is no transition to turbulent flow in the region $0 \le \xi \le \xi_{max}$. If transition occurs at $\xi_t < \xi_{max}$, then the remelting criteria given by Fig. 4 are no longer valid. At the transition point ξ_t, there is a substantial increase in the heat transfer coefficient [23, 24]. This may cause a marked decrease in the freeze-coat thickness which induces the onset of remelting. In actual practice, therefore, it is desired to have the plate emerge from the liquid at a distance shorter than ξ_t. Note that the value of ξ_t is related to the critical Reynolds number by

$$\xi_t = \left(\frac{\alpha_l}{\alpha_s}\right) \mathrm{Pr}\, \mathrm{Re}_c \tag{48}$$

Under certain conditions in which the flow-freezing interaction [19] is strong, the value of Re_c can be much lower than the one without phase change. The work of Hirata et al. [24] on forced convection flow over an ice layer formed on a constant-temperature plate, for example, has shown that the Reynolds number at which transition begins on the ice surface is an order of magnitude lower than those for a flat plate with no ice. Therefore, one must be cautious in determining the value of ξ_t and thus the actual location of Δ_{max}. It is felt that the present method may be modified to analyze the more realistic case in which the moving object is a cylindrical rod.

Acknowledgments

The author wishes to thank Jackie Bracken and Marsha Mehaffey for typing the manuscript. This work was performed under the auspices of the U.S. Department of Energy.

References

1 Libby, P. A., and Chen, S., "The Growth of a Deposited Layer on a Cold Surface," *Int. J. Heat Mass Transfer*, Vol. 8, 1965, pp. 395-402.

2 Lapadula, C., and Mueller, W. K., "Heat Conduction With Solidification and a Convective Boundary Condition at the Freezing Front," *Int. J. Heat Mass Transfer*, Vol. 9, 1966, pp. 702-705.

3 Beaubouef, R. T ., and Chapman, A. J., "Freezing of Liquids in Forced Flow," *Int. J. Heat Mass Transfer*, Vol. 10, 1967, pp. 1581–1588.

4 Savino, J. M., and Siegel, R., "An Analytical Solution for Solidification of a Moving Warm Liquid Onto an Isothermal Cold Wall," *Int. J. Heat Mass Transfer*, Vol. 12, 1969, pp. 803–809.

5 Elmas, M., "On the Solidification of a Warm Liquid Over a Cold Wall," *Int. J. Heat Mass Transfer*, Vol. 13, 1970, pp. 1060–1062.

6 Siegel, R., and Savino, J. M., "An Analysis of the Transient Solidification of a Flowing Warm Liquid on a Convectively Cooled Wall," *Proc. Third Int. Heat Transfer Conf.*, Vol. 4, 1966, pp. 414–451.

7 Siegel, R., and Savino, J. M., "Transient Solidification of a Flowing Liquid on a Cold Plate Including Heat Capacities of Frozen Layer and Plate," NASA TN D-4353, 1968.

8 Stephan, K., "Influence of Heat Transfer on Melting and Solidification in Forced Flow," *Int. J. Heat Mass Transfer*, Vol. 12, 1969, pp. 199–214.

9 Epstein, M., "The Growth and Decay of a Frozen Layer in Forced Flow," *Int. J. Heat Mass Transfer*, Vol. 19, 1976, pp. 1281–1288.

10 El-Genk, M. S., and Cronenberg, A. W., "Stefan-like Problems in Finite Geometry," *AIChE Symp. Ser.*, No. 189, Vol. 75, 1979, pp. 69–80.

11 Carrekar, R. P., Jr., "Dip-Forming—A Continuous Casting Process," *J. Metals*, Vol. 15, 1963, pp. 774–780.

12 Horvay, G., "The Dip-Forming Process," ASME JOURNAL OF HEAT TRANSFER, Vol. 87, 1965, pp. 1–16.

13 Gutfinger, C., and Chen, W. H., "Heat Transfer With a Moving Boundary—Application to Fluidized-Bed Coating," *Int. J. Heat Mass Transfer*, Vol. 12, 1969, pp. 1097–1108.

14 Gutfinger, C., and Chen, W. H., "An Approximate Theory of Fluidized Bed Coating," *Chem. Engng. Prog. Symp. Ser.*, Vol. 101, 1970, pp. 91–97.

15 Bourne, D. E., and Dixon, H., "The Cooling of Fibres in the Formation Process," *Int. J. Heat Mass Transfer*, Vol. 14, 1971, pp. 1323–1332.

16 Seeniraj, R. V., and Bose, T. K., "Freeze-Coating on a Continuous Moving Sheet and on an Axially Moving Cylinder," *Warme- und Stoffubertragung*, Vol. 15, 1981, pp. 239–243.

17 Van Dyke, M., *Perturbation Methods in Fluid Mechanics*, The Parabolic Press, Stanford, CA, 1975.

18 Stammers, E., and Beek, W. J., "The Melting of a Polymer on a Hot Surface," *Polymer Engr. Sci.*, Vol. 9, 1969, pp. 49–57.

19 Cheung, F. B., and Epstein, M., "Solidification and Melting in Fluid Flow," *Adv. Transport Processes*, Vol. 3, Wiley, New York, 1984, pp. 35–118.

20 Sakiadis, B. C., "Boundary-Layer Behavior on Continuous Solid Surfaces: II. The Boundary Layer on a Continuous Flat Surface," *AIChE Journal*, Vol. 7, 1961, pp. 221–225.

21 Tsou, F. K., Sparrow, E. M., and Goldstein, R. J., "Flow and Heat Transfer in the Boundary Layer on a Continuous Moving Surface," *Int. J. Heat Mass Transfer*, Vol. 10, 1967, pp. 219–235.

22 Erickson, L. E., Cha, L. C., and Fan, L. T., "The Cooling of a Moving Continuous Flat Sheet," *AIChE Chem. Engr. Prog. Symp. Ser.*, Heat Transfer—Los Angeles, Vol. 62, 1966, pp. 157–165.

23 Schlichting, H., *Boundary Layer Theory*, 6th ed., McGraw-Hill, New York, 1968.

24 Hirata, T., Gilpin, R. R., and Cheng, K. C., "The Steady State Ice Layer Profile on a Constant Temperature Plate in a Forced Convection Flow. II. The Transition and Turbulent Regimes," *Int. J. Heat Mass Transfer*, Vol. 22, 1979, pp. 1435–1443.

Application of a Viscous-Inviscid Interaction Procedure to Predict Separated Flows With Heat Transfer

E. J. Hall[1]
Research Assistant.
Assoc. Mem. ASME

R. H. Pletcher
Professor.
Mem. ASME

Department of Mechanical Engineering,
Iowa State University,
Ames, IA 50011

A viscous-inviscid interaction procedure is described for predicting heat transfer in separated flows. The separating flow in a rearward-facing step/asymmetric channel expansion is considered. For viscous regions, the boundary layer momentum and continuity equations are solved inversely in a coupled manner by a finite-difference numerical scheme. The streamwise convective term is altered to permit marching the solution through regions of reversed flow. The inviscid flow is computed by numerically solving the Laplace equation for streamfunction in the region bounded by the displacement surfaces used in the inverse boundary layer solution. The viscous and inviscid solutions are repeated iteratively until the edge velocities obtained from both solutions are in agreement. Predictions using this method compare favorably with experimental data and other predictions.

Introduction

The accurate prediction of heat transfer rates is essential in the design of any thermal system. Due to continuing demands on engineers to develop smaller, more efficient heat exchangers, forced flow separation has been utilized as a mechanism to enhance convective heat transfer. Since the exact characteristics of recirculating flows are not known analytically, designers must resort to the use of experimental and/or numerical data in developing models for predicting heat transfer rates.

This paper deals primarily with the separated flow which occurs as the result of an abrupt channel expansion formed by a rearward-facing step in a two-dimensional channel. This configuration is depicted in Fig. 1. The rearward-facing step is found in many important engineering devices such as heat exchangers, combustors, and nuclear reactor cooling channels. The symmetric expansion formed by identical steps on both walls of a two-dimensional channel and the axisymmetric pipe expansion also occur frequently in engineering applications.

Numerous experimental studies have been reported for the rearward-facing step geometry. The majority of these have dealt with hydrodynamic aspects of the flow. The status of research in turbulent step flows was described in the recent review by Eaton and Johnston [1]. Heat transfer in separated flows has been recently reviewed by Aung [2]. Most of the heat transfer studies for the rearward-facing step/sudden expansion geometry have dealt with turbulent flows. The experimental studies for turbulent flow by Aung and Goldstein [3], Seban [4], and Filleti and Kays [5] indicate a 20–100 percent increase in heat transfer due to the separated region. This overall increase compared to an identical attached flow is mainly due to a sharp increase in heat transfer near the point where the streamline dividing the mainstream from the separated region meets the wall. This point is commonly referred to as the reattachment point. The only experimental study providing quantitative heat transfer data for incompressible laminar flow over a rearward-facing step was reported by Aung [6]. Aung found that the overall heat transfer in the separated region was only 50–60 percent of the value for an identical attached flow without a step.

Recent studies involving numerical predictions for heat transfer in sudden expansions using the Reynolds averaged Navier–Stokes equations include those by Chieng and Launder [7], Zemanick and Dougall [8], Johnson and Launder [9], Kang and Suzuki [10], and Watkins, Gooray, and Aung [11].

In this paper, a viscous-inviscid interaction procedure is described to predict heat transfer in the separating flow over a rearward-facing step/asymmetric sudden expansion channel. The interaction procedure couples viscous effects assumed confined to relatively thin regions near solid boundaries with an inviscid freestream using the displacement thickness concept. It is anticipated that the interaction solution procedure may prove to be both simpler and more efficient than current Navier–Stokes procedures for the same flow. Since the primary purpose of this study is to present and evaluate the solution method, the comparisons have been limited to laminar flows, thus avoiding the additional uncertainties introduced by turbulence modeling.

The calculation procedure follows the method presented by Kwon [12] for the prediction of isothermal incompressible flow over a rearward-facing step. Kwon employed the FLARE [13] approximation which neglects the streamwise convective derivative in regions of reversed flow. The present

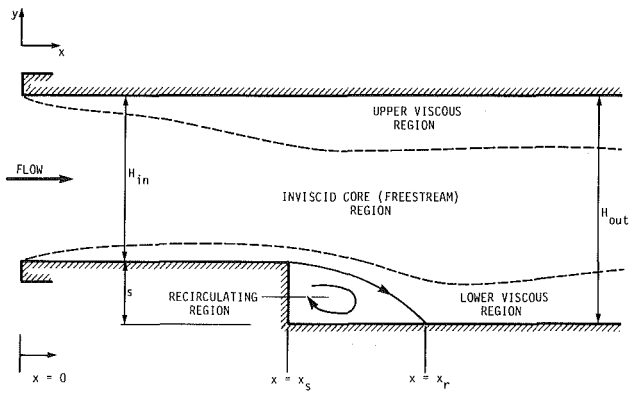

Fig. 1 Two-dimensional rearward-facing step/asymmetric expansion flow geometry

[1]Present address: Allison Gas Turbine Division, General Motors Corporation, Indianapolis, Indiana.

Contributed by the Heat Transfer Division for publication in the JOURNAL OF HEAT TRANSFER. Manuscript recevied by the Heat Transfer Division December 15, 1983. Paper No. 83-WA/HT-7.

study represents one of the first detailed evaluations of this approximation for the energy equation. Computations are presented which utilize the energy equation with and without the FLARE approximation. The procedure is capable of treating variable properties although the properties were assumed to be constant for some of the results to be presented where temperature variations were small.

Analysis

General. The overall calculation scheme involves matching viscous and inviscid solutions. The analysis for the viscous regions will be discussed first following by a discussion of the analysis for the inviscid flow. Finally, the method used for matching the two solutions interactively will be presented.

Viscous Flow. Recently, several investigators [12, 14, 15] have demonstrated the applicability of the boundary-layer equations for separated flows when proper treatment of the freestream is included. To overcome the singularity of the equations at separation, an inverse solution scheme is utilized whereby the displacement thickness is specified as the outer boundary condition, and the pressure gradient is obtained as part of the solution. The streamwise convective terms are assumed negligibly small in separated regions and are dropped from the equations, thus permitting the solution to be marched in the mainstream direction. This idea follows a suggestion first made by Flügge-Lotz and Rehyner [13] and is referred to as the FLARE approximation. In this present study, the FLARE approximation was always used for the momentum equation. The energy equation has been solved with and without the FLARE approximation in a manner to be described below.

Kwon [12] suggests that for separated flows, the boundary-layer continuity and momentum equations be solved simultaneously to avoid unrealistic oscillations in the wall shear stress, and thus it becomes advantageous to introduce the streamfunction for compressible flow as

$$\rho u = \frac{\partial \psi}{\partial y} \tag{1}$$

$$\rho v = -\frac{\partial \psi}{\partial x} \tag{2}$$

Making use of the FLARE approximation, the governing equations for a two-dimensional variable property steady laminar viscous flow become

Continuity

$$\rho u = \frac{\partial \psi}{\partial y} \tag{3}$$

Momentum

$$c\rho u \frac{\partial u}{\partial x} - \frac{\partial \psi}{\partial x}\frac{\partial u}{\partial y} = -\frac{dp}{dx} + \frac{\partial}{\partial y}\left[\mu \frac{\partial u}{\partial y}\right] \tag{4}$$

Energy

$$c\rho u \frac{\partial H}{\partial x} - \frac{\partial \psi}{\partial x}\frac{\partial H}{\partial y} = \frac{\partial}{\partial y}\left[\frac{\mu}{\mathrm{Pr}}\frac{\partial H}{\partial y} + \mu\left(1 - \frac{1}{\mathrm{Pr}}\right)u\frac{\partial u}{\partial y}\right] \tag{5}$$

where $c = 1.0$ for $u > 0$, and $c = 0.0$ for $u \le 0$, and the energy equation (5) employs total enthalpy as the dependent variable defined in accordance with the boundary layer assumptions using $H = c_p T + u^2/2$.

The appropriate boundary conditions for equations (3–5) become

No slip along walls

$$u(x,0) = \psi(x,0) = 0 \tag{6}$$

Specified wall temperature or heat flux

$$H(x,0) = c_p T_w(w) \tag{7}$$

or

$$\left(-\frac{\mu}{\mathrm{Pr}}\frac{\partial H}{\partial y}\right)_w = \dot{q}_w(x) \tag{8}$$

Outer boundary condition for an inverse solution

$$\delta^*(x) = \int_0^\infty \left(1 - \frac{\rho u}{\rho_e u_e}\right) dy = \text{known} \tag{9}$$

Constant enthalpy freestream

$$\text{as } y \to \infty,\ H(x,y) = H_\infty \tag{10}$$

For fully developed flows, no inviscid core can be identified, thus the viscous solution procedure is applied to the entire channel width. When this is done, the boundary condition of equation (9) is replaced by a global mass flow constraint enforced by requiring that the viscous flow streamfunction be a specified value at the outer boundary. For such cases the entire solution is obtained from a single marching sweep of the viscous flow calculation procedure.

The majority of the calculations were performed using equations (3–5) for viscous regions. However, as a check on the importance of streamwise diffusion and convection in

Nomenclature

c = constant in FLARE approximation
c_p = specific heat
c_f = skin-friction coefficient
H = total enthalpy = $c_pT + u^2/2$
$\hat{H}$ = dimensionless total enthalpy = H/H_{ref}
H_{in} = channel inlet height
H_{out} = channel outlet height
h = heat transfer coefficient
k = thermal conductivity
L_e = length of the effective inviscid flow channel
$\hat{L}_e$ = dimensionless inviscid flow channel length = $L_e/(\nu_{\text{ref}}/u_{\text{ref}})$
M = dimensionless viscosity coefficient = μ/μ_{ref}
N = dimensionless viscous dissipation coefficient = $(\mu/\mu_{\text{ref}})(1 - 1/\mathrm{Pr})$
Nu = Nusselt number = hH_{in}/k
p = pressure
Pr = Prandtl number = $c_p\mu/k$
$\dot{q}$ = heat flux
Q = dimensionless conductive coefficient = $\mu/\mu_{\text{ref}}\mathrm{Pr}$
Re = Reynolds number
Re_s = Reynolds number based on step height
s = step height
T = temperature
u = x component of velocity
U = dimensionless x component of velocity = u/u_{ref}
v = y component of velocity
x = coordinate parallel to surface
X = dimensionless x coordinate = $u_{\text{ref}}x/\nu_{\text{ref}}$
ΔX^+ = $X^{i+1} - X^i$
ΔX^- = $X^i - X^{i-1}$
y = coordinate normal to surface
Y = dimensionless y coordinate = $u_{\text{ref}}y/\nu_{\text{ref}}$
ΔY^+ = $Y_{j+1} - Y_j$
ΔY = $Y_j - Y_{j-1}$
ΔY_{tot} = $\Delta Y^+ + \Delta Y^-$
δ^* = displacement thickness
$\hat{\delta}^*$ = dimensionless displacement thickness = $\delta^* u_{\text{ref}}/\nu_{\text{ref}}$
δ_L^* = lower displacement surface for inviscid flow
δ_U^* = upper displacement surface for inviscid flow
δ_{UL}^* = $\delta_U^* - \delta_L^*$
δ_T = thermal boundary layer

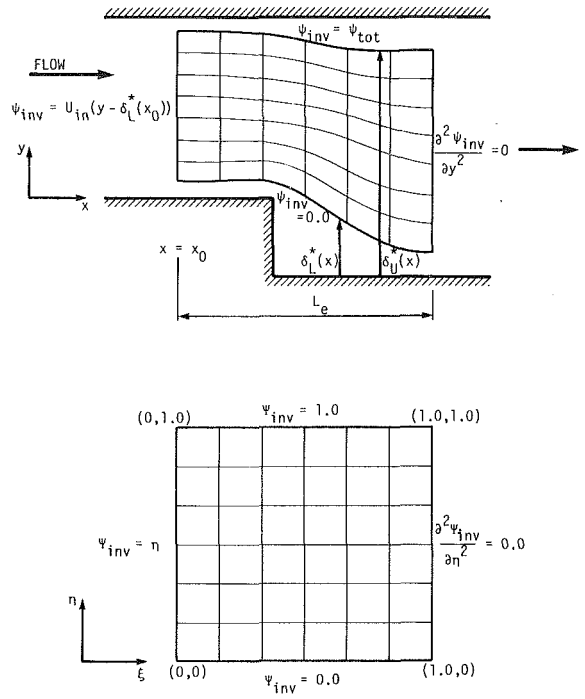

Fig. 2 Effective flow channel for inviscid analysis and transformed coordinate system

regions of reversed flow, a few calculations were performed with a form of the energy equation which retains terms representing these effects:

Energy equation (elliptic form)

$$\rho u c_p \frac{\partial T}{\partial x} + \rho v c_p \frac{\partial T}{\partial y} = \frac{\partial}{\partial x}\left[k \frac{\partial T}{\partial x}\right] + \frac{\partial}{\partial y}\left[k \frac{\partial T}{\partial y}\right] \qquad (11)$$

Equation (11) will be referred to as the elliptic form of the energy equation in subsequent discussions. Properties were assumed to be constant when equation (11) was employed. Viscous dissipation is neglected in equation (11) as it can be easily demonstrated that dissipation is negligible in the flows considered here.

Equation (11) was solved downstream of the step after obtaining velocity results from the viscous-inviscid interaction procedure using equations (3, 4). The temperature results obtained from equation (5) were used as an inlet boundary condition at the step, along with a specified wall and freestream temperature. An outflow boundary condition

$$\frac{\partial^2 T}{\partial x^2} = 0 \qquad (12)$$

was used at a point far enough downstream to avoid unrealistically influencing the solution in the separated region. Thus, a direct comparison of the results from equations (5) and (11) was possible.

Finite-Difference Form of the Equations. Utilizing the dimensionless variables defined in the nomenclature, equations (3-5) are expressed in finite-difference form for a variable grid [see equations (20-22) in the Appendix].

Application of an iterative updating scheme based on Newton linearization [12] for the nonlinear terms involving products of U^{i+1} and ψ^{i+1} in equation (21) allows the algebraic equations for the unknowns in equations (20) and (21) to be written as

$$\begin{bmatrix} B_j & 0 \\ b_j & 1 \end{bmatrix} \begin{Bmatrix} U_{j-1}^{i+1} \\ \Psi_{j-1}^{i+1} \end{Bmatrix} + \begin{bmatrix} D_j & E_j \\ d_j & -1 \end{bmatrix} \begin{Bmatrix} U_j^{i+1} \\ \Psi_j^{i+1} \end{Bmatrix} + \begin{bmatrix} A_j & 0 \\ 0 & 0 \end{bmatrix} \begin{Bmatrix} U_{j+1}^{i+1} \\ \Psi_{j+1}^{i+1} \end{Bmatrix} = \begin{Bmatrix} H_j \chi + C_j \\ 0 \end{Bmatrix} \qquad (13)$$

where all nonlinear terms not affected by the Newton linearization are linearized by using values from a previous iteration or marching step. The coefficients A_j, B_j, C_j, D_j, E_j, H_j, b_j, and d_j in equation (13) are defined in the Appendix.

The block tridiagonal matrix of equations obtained at each marching step by writing equation (13) for each grid point may be solved by the modified Thomas algorithm [16] to obtain an updated velocity field. Knowledge of the velocities from the solution of equation (13) yields a tridiagonal, linear set of equations for the unknowns in equation (22) which can be efficiently solved by elimination. This solution process at each step is repeated until changes between successive iterations are small.

The elliptic form of the energy equation [equation (11)] was differenced using the quadratic upstream interpolation convective modeling scheme suggested by Leonard [17] to reduce the effects of artificial (numerical) diffusion [see equations (23) and (24) in the Appendix].

Nomenclature (cont.)

thickness $= \int_0^\infty [(T - T_\infty)/(T_w - T_\infty)]dy$
η = transverse transformed coordinate
θ = dimensionless temperature $= (T - T_\infty)/(T_w - T_\infty)$
μ = viscosity
ν = kinematic viscosity $= \mu/\rho$
ξ = streamwise transformed coordinate
ρ = density
$\hat{\rho}$ = dimensionless density $= \rho/\rho_{ref}$
χ = dimensionless pressure gradient $= (\nu_{ref}/\rho_{ref} u_{ref}^3)\, dp/dx$
ψ = streamfunction (viscous flow)
ψ_{inv} = streamfunction (inviscid flow)
Ψ = dimensionless streamfunction (viscous flow) $= \psi/\mu_{ref}$
Ψ_{inv} = dimensionless streamfunction (inviscid flow) $= \psi_{inv}/\psi_{tot}$
ω = relaxation factor

Superscripts

i = mesh index corresponding to x or ξ
n = iteration
$\hat{}$ = denotes dimensionless quantity
$\tilde{}$ = denotes value from previous iteration level

Subscripts

BL = boundary layer result
e = edge value
H_{in} = based on channel inlet height
in = inlet
inv = inviscid result
j = mesh index corresponding to y or η
L = lower wall
0 = starting value
out = outlet
ref = reference value
s = occurring at the step
tot = total
w = wall value
x = based on x distance
δ^* = based on displacement thickness
∞ = freestream value

Equations (23) and (24) were solved iteratively using successive overrelaxation by lines. The lagging procedure suggested by Han et al. [18] was used to enhance stability and accelerate convergence.

Inviscid Flow. The inviscid freestream is confined to an effective flow channel defined by the displacement surfaces of the viscous flow regions ($\delta_U^*(x)$, $\delta_L^*(x)$) (see Fig. 2). For the purposes of this study, the inviscid flow was assumed to be incompressible. Essentially, this indicates that thermal effects are confined to the viscous flow regions normally requiring that the fluid Prandtl number be greater than or equal to 1.0. However, the flows under consideration are all developed with an initial unheated starting length, so the thermal boundary layer development lags the momentum boundary layer development and Prandtl numbers slightly less than 1.0 can be tolerated with little or no error.

If the freestream is also assumed to be irrotational, the governing inviscid equation is simply Laplace's equation for streamfunction

$$\frac{\partial^2 \psi_{\text{inv}}}{\partial x^2} + \frac{\partial^2 \psi_{\text{inv}}}{\partial y^2} = 0 \tag{14}$$

where

$$u = \frac{\partial \psi_{\text{inv}}}{\partial y}, \qquad v = -\frac{\partial \psi_{\text{inv}}}{\partial x} \tag{15}$$

subject to the boundary conditions of a specified inlet velocity, no flow across the displacement surfaces, and an unrestrictive exit condition. The mathematical specifications of these boundary conditions are shown in Fig. 2.

Since the flow domain is irregular with respect to the Cartesian coordinate system in which equations (14) and (15) are written, it becomes advantageous to define a new set of independent variables

$$\xi = \frac{x - x_0}{L_e}, \qquad \eta = \frac{y - \delta_L^*(x)}{\delta_U^*(x) - \delta_L^*(x)} \tag{16}$$

and transform equation (14) to

$$\frac{\partial^2 \psi_{\text{inv}}}{\partial \xi^2} - \frac{2}{\delta_{UL}^*}\left(\frac{d\delta_L^*}{d\xi} + \eta \frac{d\delta_{UL}^*}{d\xi}\right)\frac{\partial^2 \psi_{\text{inv}}}{\partial \xi \partial \eta} + \frac{1}{\delta_{UL}^{*2}}\left\{L_e^2 + \left(\frac{d\delta_L^*}{d\xi} + \eta \frac{d\delta_{UL}^*}{d\xi}\right)^2\right\}\frac{\partial^2 \psi_{\text{inv}}}{\partial \eta^2} + \left\{\frac{2}{\delta_{UL}^{*2}}\frac{d\delta_{UL}^*}{d\xi}\left(\frac{d\delta_L^*}{d\xi} + \eta \frac{d\delta_{UL}^*}{d\xi}\right) - \frac{1}{\delta_{UL}^*}\left(\frac{d^2\delta_L^*}{d\xi^2} + \eta \frac{d^2\delta_{UL}^*}{d\xi^2}\right)\right\}\frac{\partial \psi_{\text{inv}}}{\partial \eta} = 0 \tag{17}$$

The physical aspects of this transformation are shown in Fig. 2, as well as the transformed boundary conditions.

After employing central differences to represent terms in equation (17), the resulting linear system of equations was solved by an alternating direction implicit (ADI) scheme [12].

Viscous-Inviscid Interaction. The interaction procedure is initiated by prescribing a guessed distribution of displacement thickness along each solid wall in the interaction region. Successful solution of the flow in the viscous and inviscid flow regions using a common specified displacement thickness results in a set of edge velocities from each solution, [$U_{e_{BL}}(X)$, $U_{e_{\text{inv}}}(X)$], which may be used to update the displacement thickness distribution in a manner which will provide a better solution. An updated displacement thickness may be found by following a concept [14] which locally maintains a constant volume flow rate in the boundary layer

$$\delta^{*n+1} = \omega \delta^{*n} \frac{U_{e_{BL}}}{U_{e_{\text{inv}}}} + (1 - \omega)\delta^{*n} \tag{18}$$

where ω is an overrelaxation factor ($0 < \omega < 2.0$) used to accelerate convergence.

The entire viscous and inviscid solutions are repeated iteratively until the edge velocities obtained from both solutions are in agreement. Convergence is obtained when

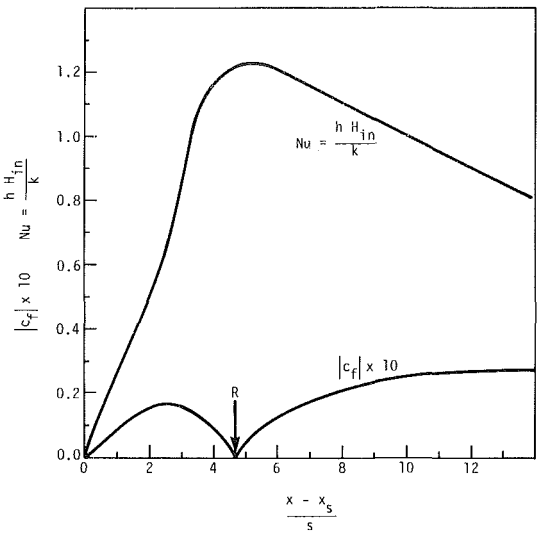

Fig. 3 Heat transfer and skin friction downstream of the step for the fully developed flow in an asymmetric expansion channel

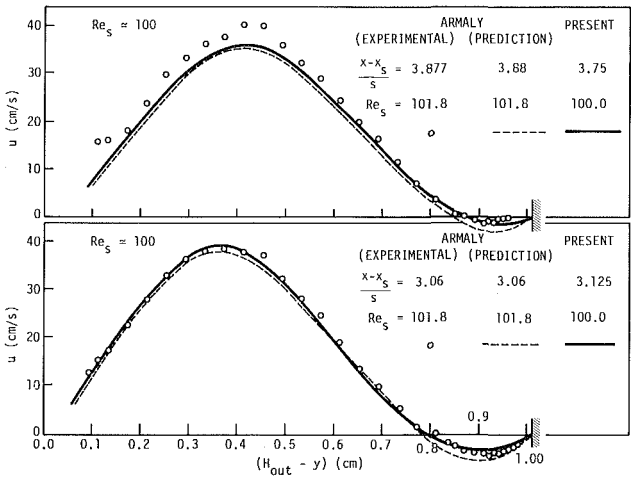

Fig. 4 Velocity profiles downstream of the step for the fully developed flow in an asymmetric expansion channel

$$\frac{|U_{e_{BL}}(X) - U_{e_{\text{inv}}}(X)|}{U_{e_{BL}}(X)} < \epsilon \tag{19}$$

Results

The main emphasis in the present study was on flows in which viscous-inviscid interaction was important. However, the evaluation of the once-through calculation procedure for fully developed flows is also of interest. For this reason, the fully developed asymmetric expansion flow studied experimentally by Armaly et al. [19] was computed with the objective of comparing the predicted and measured values of Nusselt numbers. The flow was computed under constant property assumptions for isothermal wall conditions, Re_s = 100 and an area expansion ratio of 1.94. The channel inlet height was 0.52 cm. The heat transfer predictions are shown in Fig. 3. Unfortunately, the heat transfer measurements in [19] were obtained from a point heat source in an otherwise unheated wall; therefore a direct comparison with the present two-dimensional prediction was not possible. The results of Fig. 3 will be useful to future investigators who may report computational or experimental results for this configuration. The computed skin-friction coefficient (based on the average channel velocity) is also shown in Fig. 3 to demonstrate that the Reynolds-Colburn analogy relating friction and heat

transfer is not valid for separated flows. This point was also made by Armaly et al. [19]. The predicted reattachment point (x/s = 4.8) is indicated on the figure and is in fairly good agreement with the measured value of x/s = 5.00. The predicted Nusselt number is seen to reach a maximum very close to the reattachment point. A comparison with velocity profiles in the separated region measured for the same flow, but reported in [20], is shown in Fig. 4. Predictions reported in [20] obtained from a numerical solution of the full Navier–Stokes equations are also shown in the figure. The present one-pass procedure based on the boundary-layer equations is seen to match the measurements at least as closely as the Navier–Stokes solutions.

Kwon's results [12] indicate that viscous-inviscid calculation procedures can provide acceptable results for flow parameters and this conclusion is confirmed by the present study. A comparison of predicted and measured reattachment lengths can be found in [12, 21].

The only subsonic laminar step flow experimental data with heat transfer results available for comparison were reported by Aung [6]. Aung's flow data specify a velocity and a displacement thickness at the step. When using the present interaction solution procedure, it is desirable to fix conditions upstream of the step so that the step may influence the flow upstream through the inviscid stream. Therefore, it was not possible to exactly match Aung's flow conditions at the step. Instead, conditions were fixed upstream of the step to match the specified channel mass flow rate. This gave rise to small differences between the predicted and measured displacement thicknesses at the step and the following comparisons should be considered with this in mind.

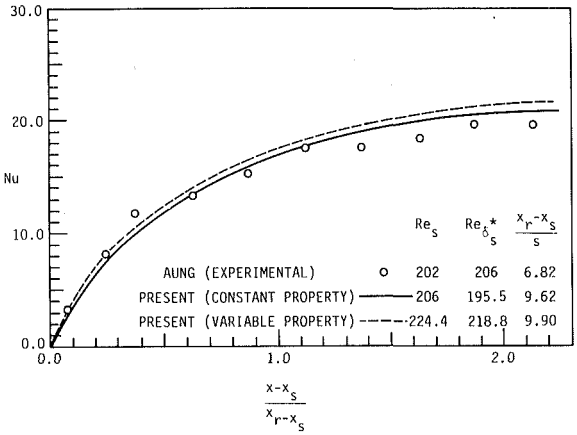

Fig. 5 Nusselt number downstream of the step for the separating flow in an asymmetric expansion channel (s = 0.38 cm)

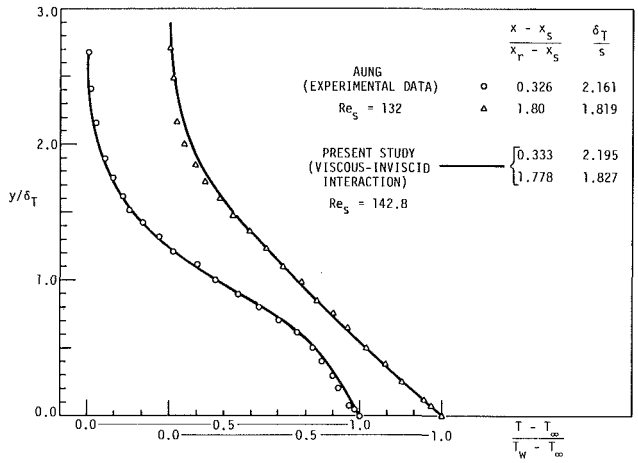

Fig. 6 Temperature profiles downstream of the step for the separating flow in an asymmetric expansion channels (s = 0.38 cm)

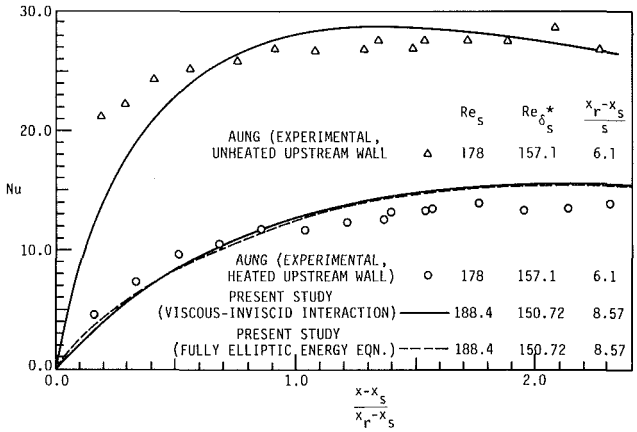

Fig. 7 Nusselt number downstream of the step for the separating flow in an asymmetric expansion channel (s = 0.64 cm)

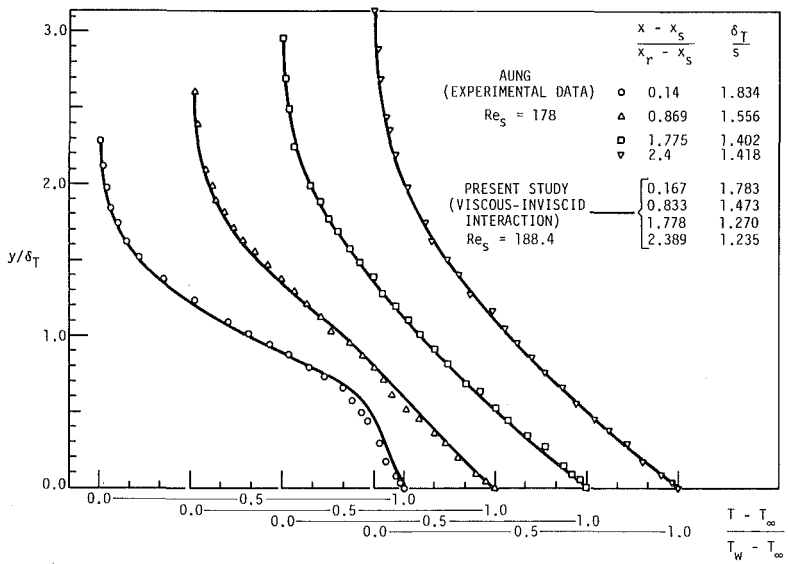

Fig. 8 Temperature profiles downstream of the step for the separating flow in an asymmetric expansion channel (s = 0.64 cm)

Three step heights (0.38 cm, 0.64 cm, 1.27 cm) were investigated for heat transfer in a channel with an asymmetric sudden expansion and an inlet duct height H_{in} = 20 cm. The experimental wall and stream temperature conditions were matched in the calculations resulting in a typical temperature difference of about 21°C. Figures 5 and 6 compare Nusselt number and temperature profiles for the smallest of the step heights investigated. Both variable property and constant property solutions are presented based on a distance scale which was normalized by the reattachment length. This normalization helps to compensate for the inability to exactly match the experimental flow conditions. Differences in the results due to variable properties were found to be small, and in fact, the reattachment length was nearly identical to the value obtained from a similar constant property solution. Figures 7 and 8 display similar comparisons for a slightly larger step height (s = 0.64 cm), including results obtained when the wall upstream of the step is unheated. Figures 9 and 10 compare data for the largest of the step heights investigated (s = 1.27 cm). The apparent discrepancy in the results in the separated region for this case (s = 1.27 cm) remains unexplained, although a recent laminar computation by Chiu [22] using a partially parabolic Navier–Stokes procedure tended to substantiate the present interaction results.

The boundary-layer form of the energy equation has not often been used for separated flows. Consequently, it is of some interest to assess the validity of this approach which includes the neglect of the streamwise convection term when the flow is reversed (FLARE approximation). To this end, a more complete (fully elliptic) energy equation [equation (11)] was used to solve for the temperature distribution in several step flow cases. The procedure used was to first solve the problem using the boundary-layer form of the governing equations under constant property assumptions. This flow field was then used to obtain the numerical solution to the more complete energy equation for the region downstream of the step. The fully elliptic results are included in Figs. 9 and 11. Although equation (11) includes both axial conduction and streamwise convection in separated regions (both of which were neglected in the boundary-layer energy equation), the results were in good agreement with those obtained from the boundary-layer form of the energy equation.

For the viscous-inviscid interaction calculations made for comparison with the data of Aung [6], the interaction zone extended 3 channel inlet heights upstream and downstream of the step for the two larger step heights and 1-1/2 channel inlet heights upstream and downstream of the step for the smallest step height. Typically 30-100 grid points were used across the viscous flow and approximately 200 streamwise steps were used to span the interaction zone. A 50 × 60 grid was normally used for the inviscid region. Further refinement of the grids from these values showed no significant change in the solution. Normally 8-12 global iterations were necessary for convergence of the viscous-inviscid interaction procedure to $\epsilon = 0.5 \times 10^{-3}$ [see equation (24)], requiring approximately three minutes of CPU time on the NAS-AS/6 computer. A direct comparison of the efficiency of the interaction method with current Navier–Stokes solution schemes was not possible since the interaction procedure is dependent on an arbitrary initial specification of the displacement thickness. However, even rough initial estimates for the displacement thickness resulted in solutions with computer times competitive with other solution methods, especially when the large number of grid points used (typically in excess of 15,000) in the present calculations are taken into account.

Conclusions

A viscous-inviscid interaction scheme was developed which provided stable, accurate predictions of heat transfer in separated flow. Clearly, the lack of available laminar experimental data prohibits extensive comparison, but the method appears to be capable of predicting results for both developing and fully developed flows. For fully developed flows, the calculation proceeds in a once-through manner requiring very small computation times. Although the method was developed to include the effects of variable properties, no significant differences occurred from the use of constant properties for the temperature range tested. It was noted that the Reynolds number based on displacement thickness at the step appeared to be a critical parameter, with small changes inducing significant differences in the results.

The results obtained from solving the fully elliptic energy equation were found to be in good agreement with those obtained from the boundary-layer form of the energy equation indicating that the errors introduced by use of the FLARE approximation and the neglect of axial conduction terms are small for separated flows of the type considered in the present paper.

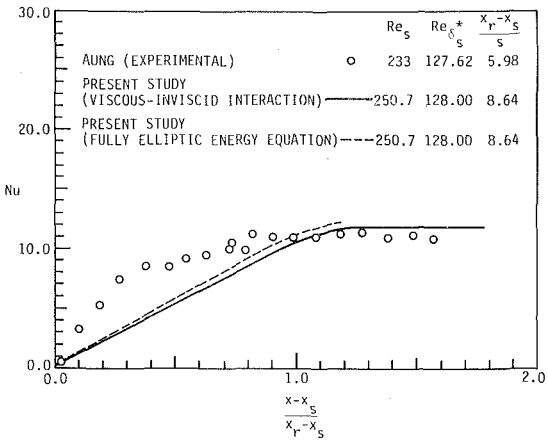

Fig. 9 Nusselt number downstream of the step for the separating flow in an asymmetric expansion channel (s = 1.27 cm)

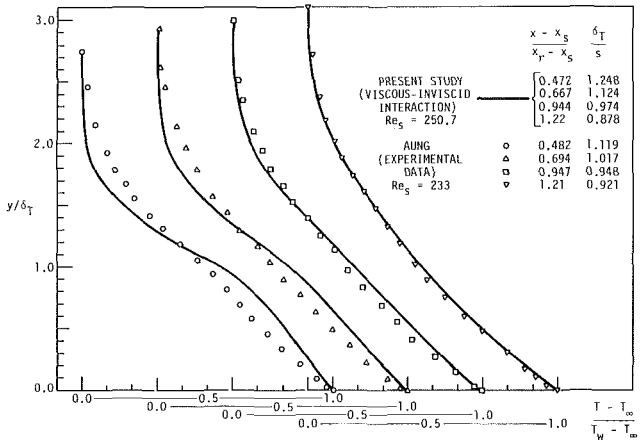

Fig. 10 Temperature profiles downstream of the step for the separating flow in an asymmetric expansion channel (s = 1.27 cm)

Acknowledgments

This material is based upon work supported by the National Science Foundation under Grants CEE-781290 and MEA-8211713. Partial support from the National Aeronautics and Space Administration under Grant NGT-016-002-801 is also gratefully acknowledged. The authors wish to thank Dr. O. K. Kwon for his interest and help during the early stages of this work.

References

1 Eaton, J., and Johnston, J. P., "A Review of Research on Subsonic Turbulent Flow Reattachment," *AIAA Journal*, Vol. 19, No. 9, 1981, pp. 1093–1100.

2 Aung, W., "Separated Forced Convection," *Proceedings of the 1983 ASME-JSME Thermal Engineering Conference*, Vol. II, 1983, pp. 499-511.

3 Aung, W., and Goldstein, R. J., "Heat Transfer in Turbulent Separated Flow Downstream of a Rearward-Facing Step," *Israel Journal of Technology*, Vol. 10, Nos. 1-2, 1972, pp. 35-41.

4 Seban, R. A., Emery, A., and Levy, A., "Heat Transfer to Separated and Reattached Subsonic Turbulent Flows Obtained Downstream of a Surface Step," *Journal of the Aerospace Sciences*, 1959, pp. 809-814.

5 Filleti, E. G., and Kays, W. M., "Heat Transfer in Separated, Reattached, and Redevelopment Regions Behind a Double Step at Entrance to a Flat Duct," *Journal of Heat Transfer*, Vol. 89, 1967, pp. 163-167.

6 Aung, W., "Heat Transfer in the Separated Region Beyond a Rearward-Facing Step," Ph.D. thesis, University of Minnesota, 1969.

7 Chieng, C. C., and Launder, B. E., "On the Calculation of Turbulent Heat Transport Downstream From an Abrupt Pipe Expansion," *Momentum and Heat Transfer Processes in Recirculating Flows*, ASME-HTD-13, 1980, pp. 9-19.

8 Zemanick, P. P., and Dougall, R. S., "Local Heat Transfer Downstream of Abrupt Circular Channel Expansion," ASME JOURNAL OF HEAT TRANSFER, Vol. 92, 1970, pp. 53-61.

9 Johnson, and Launder, B. E., "Discussion on the Calculation of Turbulent Heat Transport Downstream From an Abrupt Pipe Expansion," *Numerical Heat Transfer*, Vol. 5, No. 4, 1982, pp. 493-496.

10 Kang, Y., and Suzuki, K., "Numerical Study of Wall Heat Transfer in the Recirculating Flow Region of a Confined Jet," *Heat Transfer—Japanese Research*, Vol. 11, No. 1, 1982, p. 44.

11 Watkins, A. M., Gooray, C. B., and Aung, W., "Numerical Calculations of Turbulent Recirculating Heat Transfer Beyond Two-Dimensional Back Steps and Sudden Pipe Expansions," Office of Naval Research, Work Unit No. NR-097-444, 1982.

12 Kwon, O. K., and Pletcher, R. H., "Prediction of the Incompressible Flow Over a Rearward-Facing Step," Engineering Research Institute, Iowa State University, Technical Report HTL-26, CFD-3, ISU-ERI-Ames-82019, 1981.

13 Reyhner, T. A., and Flügge-Lotz, "The Interaction of a Shock Wave With a Laminar Boundary Layer," *International Journal of Non-linear Mechanics*, Vol. 3, No. 2, 1968, pp. 173-199.

14 Kwon, O. K., and Pletcher, R. H., "Prediction of Incompressible Separated Boundary Layers Including Viscous-Inviscid Interaction," *Journal of Fluids Engineering*, Vol. 101, 1979, pp. 466-472.

15 Pletcher, R. H., Kwon, O. K., and Chilukuri, R., "Prediction of Separating Turbulent Boundary Layers Including Regions of Reversed Flow," Engineering Research Institute, Iowa State University, Technical Report HTL-22, ISU-ERI-Ames-80112, 1980.

16 Blottner, F. G., "Investigation of Some Finite-Difference Techniques for Solving the Boundary Layer Equations," *Computer Methods in Applied Mechanics and Engineering*, Vol. 6, 1975, pp. 1-30.

17 Leonard, B. P., "A Stable and Accurate Convective Modeling Procedure Based on Quadratic Upstream Interpolation," *Computer Methods in Applied Mechanics and Engineering*, Vol. 19, 1979, pp. 59-98.

18 Han, T., Humphrey, J. A. C., and Launder, B. E., "A Comparison of Hybrid and Quadratic Upstream Differencing in High Reynolds Number Elliptic Flows," University of California, FM-31-1. 1981.

19 Armaly, B. F., Durst, F., and Kottke, V., "Momentum, Heat, and Mass Transfer in Backward-Facing Step Flows," Third Symposium on Turbulent Shear Flows, University of California, Davis, Sept. 1981.

20 Armaly, B. F., Durst, F., Pereira, J. C. F., and Schönung, B., "Experimental and Theoretical Investigation of Backward-Facing Step Flow," *Journal of Fluid Mechanics*, Vol. 127, 1983, pp. 473-496.

21 Hall, E., "Application of Viscous-Inviscid Interaction to Separated Flows With Heat Transfer Including Rearward Facing Step Flows," M.S. thesis, Iowa State University, 1983.

22 Chiu, I.-T., "Prediction of Laminar Flows Over a Rearward-Facing Step Using the Partially Parabolized Navier-Stokes Equations," M.S. thesis, Iowa State University, 1984.

APPENDIX

Equations (3-5) are expressed in finite-difference form as

$$\frac{(\hat{\rho}_j^{i+1}U_j^{i+1}+\hat{\rho}_{j-1}^{i+1}U_{j-1}^{i+1})}{2}=\frac{\Psi_j^{i+1}-\Psi_{j-1}^{i+1}}{\Delta Y^-} \tag{20}$$

$$c\hat{\rho}_j^{i+1}U_j^{i+1}\frac{(U_j^{i+1}-U_j^i)}{\Delta X^+}-\frac{(\Psi_j^{i+1}-\Psi_j^i)}{\Delta X^+}\left[\frac{\Delta Y^-}{\Delta Y_{\text{tot}}}\frac{(U_{j+1}^{i+1}-U_j^{i+1})}{\Delta Y^+}+\frac{\Delta Y^+}{\Delta Y_{\text{tot}}}\frac{(U_j^{i+1}-U_{j-1}^{i+1})}{\Delta Y^-}\right]=-\chi+\left[M_{j+1/2}^{i+1}\frac{(U_{j+1}^{i+1}-U_j^{i+1})}{\Delta Y^+}-M_{j-1/2}^{i+1}\frac{(U_j^{i+1}-U_{j-1}^{i+1})}{\Delta Y^-}\right]\Big/(\Delta Y_{\text{tot}}/2) \tag{21}$$

$$c\hat{\rho}_j^{i+1}U_j^{i+1}\frac{(\hat{H}_j^{i+1}-\hat{H}_j^i)}{\Delta X^+}-\frac{(\Psi_j^{i+1}-\Psi_j^i)}{\Delta X^+}\left[\frac{\Delta Y^-}{\Delta Y_{\text{tot}}}\frac{(\hat{H}_{j+1}^{i+1}-\hat{H}_j^{i+1})}{\Delta Y^+}+\frac{\Delta Y^+}{\Delta Y_{\text{tot}}}\frac{(\hat{H}_j^{i+1}-\hat{H}_{j-1}^{i+1})}{\Delta Y^-}\right]=\left\{\left[Q_{j+1/2}^{i+1}\frac{\hat{H}_{j+1}^{i+1}-\hat{H}_j^{i+1})}{\Delta Y^+}-Q_{j-1/2}^{i+1}\frac{(\hat{H}_j^{i+1}-\hat{H}_{j-1}^{i+1})}{\Delta Y^-}\right]+\frac{u_{\text{ref}}^2}{H_{\text{ref}}}\left[N_{j+1/2}^{i+1}\frac{(U_{j+1}^{i+1}+U_j^{i+1})}{2}\frac{(U_{j+1}^{i+1}-U_j^{i+1})}{\Delta Y^+}-N_{j-1/2}\frac{(U_j^{i+1}+U_{j-1}^{i+1})}{2}\frac{(U_j^{i+1}-U_{j-1}^{i+1})}{\Delta Y^-}\right]\right\}\Big/(\Delta Y_{\text{tot}}/2) \tag{22}$$

where the $j+1/2$, $j-1/2$ subscript indicates values averaged between grid points.

The finite-difference form of equation (11) for constant grid spacing becomes:

for $u_{i,j}\geq 0$

$$\frac{U_{i,j}}{\Delta X}\left[\frac{\theta_j^{i-2}}{8}-\frac{7}{8}\theta_j^{i-1}+\frac{3}{8}\theta_j^i+\frac{3}{8}\theta_j^{i+1}\right]+V_j^i\frac{(\theta_{j+1}^i-\theta_{j-1}^i)}{2\Delta Y}=\frac{1}{\hat{Pr}}\left[\frac{(\theta_j^{i+1}-2\theta_j^i+\theta_j^{i-1})}{\Delta X^2}+\frac{(\theta_{j+1}^i-2\theta_j^i+\theta_{j-1}^i)}{\Delta Y^2}\right] \tag{23}$$

and for $u_{i,j}<0$

$$\frac{U_j}{\Delta X}\left[-\frac{\theta_j^{i+2}}{8}+\frac{7}{8}\theta_j^{i+1}-\frac{3}{8}\theta_j^i-\frac{3}{8}\theta_j^{i-1}\right]+V_j^i\frac{(\theta_{j+1}^i-\theta_{j-1}^i)}{2\Delta Y}=\frac{1}{\hat{Pr}}\left[\frac{(\theta_j^{i+1}-2\theta_j^i+\theta_j^{i-1})}{\Delta X^2}+\frac{(\theta_{j+1}^i-2\theta_j^i+\theta_{j-1}^i)}{\Delta Y^2}\right] \tag{24}$$

where velocities are assumed known.

The coefficients appearing in equation (13) are defined as:

$$A_j=-\left(\frac{\Delta Y^-}{\Delta Y^+}\frac{(\tilde{\Psi}_j^{i+1}-\Psi_j^i)}{\Delta X^+}+\frac{2M_{j+1/2}^{i+1}}{\Delta Y^+}\right)\Big/\Delta Y_{\text{tot}} \tag{25}$$

$$B_j=\left(\frac{\Delta Y^+}{\Delta Y^-}\frac{(\tilde{\Psi}_j^{i+1}-\Psi_j^i)}{\Delta X^+}-\frac{2M_{j-1/2}^{i+1}}{\Delta Y^-}\right)\Big/\Delta Y_{\text{tot}} \tag{26}$$

$$C_j=\frac{c\hat{\rho}_j^{i+1}(\tilde{U}_j^{i+1})^2}{\Delta X^+}-\frac{\tilde{\Psi}_j^{i+1}\tilde{U}_j^{i+1}}{\Delta X^+\Delta Y_{\text{tot}}}\left(\frac{\Delta Y^-}{\Delta Y^+}-\frac{\Delta Y^+}{\Delta Y^-}\right) \tag{27}$$

$$D_j=c\hat{\rho}_j^{i+1}\frac{(2\tilde{U}_j^{i+1}-U_j^i)}{\Delta X^+}+\left(\frac{\Delta Y^-}{\Delta Y^+}-\frac{\Delta Y^+}{\Delta Y^-}\right)\frac{(\tilde{\Psi}_j^{i+1}-\Psi_j^i)}{\Delta X^+\Delta Y_{\text{tot}}}+2\left(\frac{M_{j+1/2}^{i+1}}{\Delta Y^+}+\frac{M_{j-1/2}^{i+1}}{\Delta Y^-}\right)\Big/\Delta Y_{\text{tot}} \tag{28}$$

$$E_j=\left(-\frac{\Delta Y^-}{\Delta Y^+}\tilde{U}_{j+1}^{i+1}+\left(\frac{\Delta Y^-}{\Delta Y^+}-\frac{\Delta Y^+}{\Delta Y^-}\right)\tilde{U}_j^{i+1}+\frac{\Delta Y^+}{\Delta Y^-}\tilde{U}_{j-1}^{i+1}\right)\Big/(\Delta X^+\Delta Y_{\text{tot}}) \tag{29}$$

$$H_j=1.0 \tag{30}$$

$$b_j=\frac{\hat{\rho}_{j-1}^{i+1}\Delta Y^-}{2} \tag{31}$$

$$d_j=\frac{\hat{\rho}_j^{i+1}\Delta Y^-}{2} \tag{32}$$

A Numerical Study of Laminar and Turbulent Heat Transfer in a Periodically Corrugated Wall Channel

R. S. Amano
Associate Professor.
Department of Mechanical Engineering,
University of Wisconsin—Milwaukee,
Milwaukee, WI 53201
Mem. ASME

A numerical study is reported on hydrodynamic and heat transfer characteristics in a periodically corrugated wall channel for both laminar and turbulent flows. For turbulent flows the k–ϵ turbulence model with a refined near-wall model is adopted for the computation of the flow field for step ratios H/W ranging from two to four. The Reynolds number considered in this study varies from 10 to 25,000. The solution method of the governing transport equations is based on the modified hybrid scheme. As a result of extensive computations, the complex flow patterns in the perpendicularly corrugated wall channel are clarified and the mechanisms of heat transfer are explained relating to the flow phenomena of separation, deflection, recirculation, and reattachment. Finally it was observed that the effect of the step ratio on the local Nusselt number is minor. Moreover, it was found that both skin friction and heat transfer patterns change drastically from laminar to turbulent flows.

Introduction

For compact heat exchangers using plate-fin geometries, one way of augmenting heat transfer is the use of a corrugated surface for the plate [1]. While research on heat exchangers is very popular, studies of heat exchangers with corrugated wall channels have not been reported in number. Goldstein and Sparrow [2, 3] investigated the mass and heat transfer in corrugated wall channels for a range of Reynolds numbers from 150 to 8550. They measured the local mass transfer rates in a corrugated wall channel by using the naphthalene sublimation technique. Faas and McEligot [4] made computations on heat transfer rates and friction factors of laminar flows in perpendicularly corrugated wall channels. More recently, Izumi et al. [5] measured experimentally the local heat transfer rates along the wall of a channel which has two right-angled bends. Numerical studies were reported by Amano [6] on the same channel configurations as those considered by Izumi et al. [5] for laminar flows. This study was further extended to turbulent flows by employing the standard k–ϵ model with a special near-wall treatment [7]. The comparison of the numerical results with the data obtained by Izumi et al. [5] showed quite reasonable agreement. Izumi et al. extended their measurement of heat transfer rates and friction factors to corrugated wall channels which have many periodic bends [8]. The range of the Reynolds number considered by Izumi et al. [8] spans from 500 to 25,000.

Although studies of the flow in corrugated wall channels are scarce, similar but simpler flow configurations have been considered by many researchers in the subsonic range [9–11]. For instance, the flow in a channel which has steps or sharp bends is often seen in many actual engineering situations, such as diffusers, airfoils with separation bubbles, combustors, etc. An analysis of such flows is still not easy since the flow is accompanied by flow separation, reattachment, and recirculation.

Tani et al. [9] studied a turbulent flow over a backward-facing step and reported that the skin friction due to a reversal flow is not negligible. Bradshaw and Wong [10] reported that the turbulent Reynolds stresses usually become much larger near the reattachment than those in a simple plane mixing layer. Eaton and Johnston [11] reviewed the reattaching flow extensively and pointed out several important factors that might cause high heat transfer augmentation in the reattachment region.

Besides experimental studies numerous theoretical studies have been reported on the turbulent flow over steps. Chieng and Launder [12] developed a new near-wall model for the generation and dissipation rates of the k equation and applied it to the flow in a pipe with a sudden expansion. This work was continued by Johnson and Launder [13] by including a functional relation of diffusion effect in the dimensionless viscous sublayer thickness. This near-wall model improved the prediction of heat transfer rates in the whole region including recirculating, reattaching, and redeveloping regions.

A near-wall model which evaluates the main generation and destruction terms of the ϵ equation was developed by Amano [14] and was applied to the calculation of heat transfer rates along the walls of the pipes with sudden expansions. It was shown that the prediction of the reattachment length was improved by 10–20 percent by incorporating this near-wall model for the ϵ equation. More recently the approach of [14] was extended by Amano [15] by dividing a near-wall region into three distinct parts: viscous sublayer, buffer layer, and fully turbulent layer. Then the corresponding near-wall models were obtained for both the k and ϵ equations. It was shown that this three-layer model was superior to the two-layer model of Amano [14], particularly for high Reynolds number flows.

Another similar study by Gooray, Watkins, and Aung [16] employed solutions of the $k \sim \epsilon$ model involving a two-pass procedure with corrections made to the turbulence model for low Reynolds numbers and streamline curvature. After establishing the reattachment point on the first pass, the turbulence model based on the algebraic stress model was applied to define the coefficients, and then this model was used on the second pass to obtain final results. A review of separated flows in general was made by Aung [17].

The present paper deals with a channel which has a cyclically corrugated wall at a 90 deg angle, whereas a relatively simple geometric configuration was considered in references [6, 7], such as an infinitely long channel which has only two bends at 90 deg angles. In computational processes

Contributed by the Heat Transfer Division for publication in the JOURNAL OF HEAT TRANSFER. Manuscript received by the Heat Transfer Division January 19, 1984. Paper No. 84-HT-73.

an unforeseen numerical instability arose when a periodic boundary condition was applied. To overcome this problem 2½ cycles of the corrugated wall channel was considered as a computational domain instead of one cycle. Moreover, a two-pass procedure was employed for an application of the periodic condition. The details of these methods are described in the section on Numerical Procedure. For a laminar flow computation, the method used in [6] is employed, and for a turbulent flow computation, the standard k-ϵ model is adopted with the use of the three-layer, near-wall treatment of Amano [15].

Mathematical and Numerical Models

Numerical Solution Procedure. The governing differential equations for the present problem are continuity, momentum, and energy equations along with the standard k-ϵ model for turbulent flow computations. These equations have been explained in the previous work: the laminar flow case in [6] and the turbulent flow case in [7]. Therefore, these will not be repeated here.

The numerical differencing method of the aforementioned transport equations is based on the modified hybrid scheme of Amano [15] in which the combined mode of convection and diffusion is derived by expanding the analytical one-dimensional solution of Spalding [8] up to the fourth-order term. The finite-volume form was derived by integrating the governing equations over the numerical cell. For instance, the discretization equation for the ϕ equation can be put in the following form:

$$A_{ij}\phi_{ij} = A_{i+1,j}\phi_{i+1,j} + A_{i-1,j}\phi_{i-1,j} + A_{i,j+1}\phi_{i,j+1} + A_{i,j-1}\phi_{i,j-1} + B \tag{1}$$

where

$$A_{i+1,j} = \frac{\mu_{\text{eff}}}{\delta x} f(\text{Re}_{i+1,j}) + \max\{-(\rho U)_{i+1,j}, 0\}, \text{ etc} \tag{2}$$

and

$$B = S_\phi \delta(\text{Vol})$$

$$f(\text{Re}_{ij}) = \max\left\{0, 1 - \frac{1}{2}|\text{Re}_{ij}| + \frac{1}{12}|\text{Re}_{ij}|^2 - \frac{1}{720}|\text{Re}_{ij}|^4\right\} \tag{3}$$

$$\text{Re}_{ij} = \rho U_{ij} \delta x / \mu_{\text{eff}}$$

S_ϕ = source term

Equation (1), which has an elliptic form, is computed by using a line-by-line iterative method. The solution procedure and the cell structures for the momentum equations are those of Gosman et al. [19] with the pressure treatment of Patankar and Spalding [20].

The boundary conditions used for the present numerical method are described in the following two subsections.

Wall Boundary Conditions and the Near-Wall Model of the k-ϵ. At the wall boundaries *ABCDE* and *FGHIJ*, the velocities and turbulence quantities must be specified functionally according to the drag law (for laminar flows) or the law of the wall (for turbulent flows). For example, the tangential velocity can be expressed in terms of wall shear stress as a functional expression of the boundary condition coupled with the no-slip condition as

$$F = \tau \delta A \tag{4}$$

where δA = wall area of the cell.

The expression of (4) is incorporated through the source term S_ϕ while the coefficient A in equation (2) representing the wall side is set equal to zero, thus suppressing the diffusive and convective actions toward the wall. The velocity component normal to the wall is zero. The computational procedure for laminar flows is relatively straightforward and is mostly based on that of Amano [6]. The treatment for the turbulence quantities, on the other hand, is more complex and thus will be explained here.

Since the turbulence model employed in this computation is

Nomenclature

a, b = constants used in the near-wall model
A_{ij} = coefficient (used in equation (1))
C_1, C_2, C_μ = coefficients in turbulence model
f = Fanning's average friction factor
H = step height (defined in Fig. 1)
k = turbulence kinetic energy
Nu = Nusselt number based on $2W$
$\overline{\text{Nu}}$ = average Nusselt number based on $2W$
$\text{Nu}_{\max}$ = maximum Nusselt number based on $2W$
P = pressure
P_k = generation rate of turbulent kinetic energy, k
$\dot{q}_w$ = wall heat flux
Re = Reynolds number based on $2W$
Re_{ij} = cell Reynolds number
Re_v = viscous sublayer Reynolds number = $\rho k^{1/2} y_v / \mu$
S = heat transfer area
T = temperature
T_b = bulk temperature
T_w = wall temperature
U = mean velocity in x direction
U^* = friction velocity = $\sqrt{\tau_w/\rho}$
U_{av} = average mean velocity
V = mean velocity in y direction
W = channel width (defined in Fig. 1)
x = coordinate (defined in Fig. 1)
y = coordinate (defined in Fig. 1)
y^+ = dimensionless distance from the wall = yU^*/ν
Γ = thermal conductivity
δA = area of numerical cell
ϵ = energy dissipation rate
κ = von Karman's constant
μ = dynamic viscosity
μ_{eff} = effective viscosity = $\mu + \mu_t$
μ_t = turbulent viscosity
ν = kinematic viscosity
ρ = density
τ = turbulent shear stress

Subscripts

B = values at the outer edge of buffer layer
BL = values in the buffer layer
FTL = values in the fully turbulent layer
i, j = numerical discrete points
n = values at the boundary of P and N cells
N = values at node point N
P = values at node point P
v = values at the edge of viscous sublayer
w = wall values

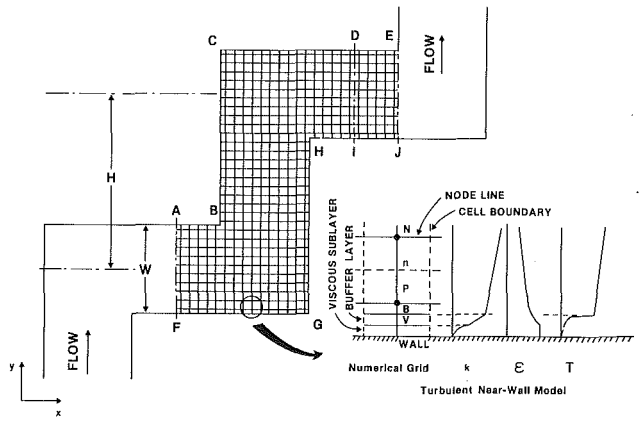

Fig. 1 Physical geometry and numerical grid

the high Reynolds number form, it is necessary to introduce the "wall-function" approach into the normal procedure for turbulence computation for the wall adjacent numerical cells.

The near-wall model adopted for the evaluations of the k and ϵ equations in the wall-vicinity region is based on the three-layer model of the author's previous work [15]. In this procedure, the wall adjacent control volume is divided into three distinct regions: a viscous sublayer ($0 < y^+ < 5$), a buffer layer ($5 < y^+ < 30$), and a fully turbulent layer ($30 < y^+ < 400$). Then the mean values of generation and destruction terms of the k and ϵ-equations were obtained by integrating these terms throughout the near-wall numerical control volume (shown in Fig. 1) after local variations of the turbulence quantities were incorporated. In this way the effect from the wall is taken into account in the numerical cells next to the wall. Here it is assumed that the first node point P lies in the fully turbulent layer. However, the cases when P lies in the buffer layer or in the viscous sublayer can also be computed automatically in the program. The rest of the cells other than wall adjacent ones are handled in a normal manner.

The results are quite similar to those obtained in [15] except for the incorporation of both primary and secondary strains attributed to the flows along the x and y directions. Therefore, only the final forms are listed below. The notations used in the following equations are given in Fig. 1.

k Equation. Mean generation rate, $\bar{P}_k$:

$$\bar{P}_k = \frac{1}{y_n}\left[\int_{y_v}^{y_B} \tau_B \left(\frac{y}{y_B}\right)^3 \left(\frac{\partial U}{\partial y}+\frac{\partial V}{\partial x}\right)_{BL} dy + \int_{y_B}^{y_n} \left\{\tau_w + (\tau_n - \tau_w)\frac{y}{y_n}\right\}\left(\frac{\partial U}{\partial y}+\frac{\partial V}{\partial x}\right)_{FTL} dy\right] \quad (5)$$

Mean dissipation rate, $\bar{\epsilon}$:

$$\bar{\epsilon} = \frac{2k_v^{3/2}}{y_n \mathrm{Re}_v} + \frac{1}{y_n \kappa C_\mu^{-1/4}}\left\{\frac{2}{3}k_B^{3/2}\left[\left(\frac{k_n}{k_B}\right)^{3/2} - \left(\frac{y_v}{y_B}\right)^{3/2}\right] + 2ak_B^{1/2}\left[\left(\frac{k_n}{k_B}\right)^{1/2} - 1\right] + a^2\lambda\right\} \quad (6)$$

ϵ *Equation.* Mean generation rate, $\overline{C_1 P_k \epsilon/k}$:

$$\overline{C_1 P_k \epsilon/k} = \frac{C_1}{y_n}\int_{y_v}^{y_B} \frac{\epsilon}{k}\tau\left(\frac{\partial U}{\partial y}+\frac{\partial V}{\partial x}\right)_{BL} dy + \int_{y_B}^{y_n} \frac{\epsilon}{k}\tau\left(\frac{\partial U}{\partial y}+\frac{\partial V}{\partial x}\right)_{FTL} dy \quad (7)$$

Mean destruction rate, $\overline{C_2 \epsilon^2/k}$:

$$\overline{C_2 \epsilon^2/k} = C_2\left[\frac{12}{y_n y_v}\left(\frac{k_v}{\mathrm{Re}_v}\right)^2 + \left(\frac{k_B}{\kappa C_\mu^{-1/4}}\right)^2 \frac{1}{y_B y_n}\left(1-\frac{y_v}{y_B}\right) + \frac{1-y_B/y_n}{\kappa^2 C_\mu^{-1/2}}\left(\frac{a^2}{y_B y_n} + \frac{2ab}{y_n - y_B}\ln\frac{y_n}{y_B} + b^2\right)\right] \quad (8)$$

where

$$\lambda = \begin{cases} \dfrac{1}{a^{1/2}}\ln\left[\dfrac{(k_n^{1/2}-a^{1/2})(k_B^{1/2}+a^{1/2})}{(k_B^{1/2}-a^{1/2})(k_n^{1/2}+a^{1/2})}\right] & (a>0) \\ \dfrac{2}{(-a)^{1/2}}\left[\tan^{-1}\left(\dfrac{k_n}{-a}\right)^{1/2} - \tan^{-1}\left(\dfrac{k_B}{-a}\right)^{1/2}\right] & (a<0) \end{cases} \quad (9)$$

and where

$$a = k_P - \frac{k_P - k_N}{y_P - y_N}y_P, \qquad b = \frac{k_N - k_B}{y_N - y_B} \quad (10)$$

Computations of Nusselt Numbers and Friction Factors. The average friction factor is computed as

$$f = -\frac{W}{\rho U_{\mathrm{av}}^2}\frac{\Delta P}{L} \quad (11)$$

where L is the distance between corresponding planes and ΔP is the average pressure drop between these planes.

For the computation of the heat transfer coefficient, a condition of constant heat flux is used at the wall boundary. Then the local Nusselt number is obtained by the following equation

$$\mathrm{Nu} = \frac{(\dot{q}_w/\Gamma)2W}{|T_w - T_b|} \quad (12)$$

and the bulk temperature T_b is obtained as

$$T_b = \int T|U|dy / \int |U|dy \quad (13)$$

where the integrals are to be carried over the cross-sectional area of the channel. The absolute value of the velocity is taken so that the regions with reverse flow are also properly represented. Accordingly, the averaged Nusselt number is defined as

$$\overline{\mathrm{Nu}} = \frac{2W}{S\Gamma}\int h dS \quad (14)$$

Inflow/Outflow Boundary Conditions. As is shown in Fig. 1, the channel shape changes periodically. Thus we can take just one cycle as a computational domain. However, 2½ cycles are taken in the present computations (*A-B-C-D-E-J-I-H-G-F-A*) because a numerical divergence occurs. With a one-cycle domain it was difficult to apply a periodic boundary condition at the inlet and outlet sections; the solution always diverged at the moment when the conditions at the outlet were used as the inlet conditions. It is noteworthy to compare the present method with that of Faas and McEligot [4], since much of the procedure used here is quite similar to theirs. When developing the computational model this author did not realize that this work was available. Faas and McEligot had the same problem with periodic boundary conditions and, thus, they extended the solution domain from one cycle to two cycles. After a sufficient iteration with prescribed inlet/outlet conditions, they subsequently copied the field data at the midsection of the two-cycle domain to both the inlet and outlet conditions until the periodicity was satisfied.

In the present model 2½ cycles of the domain is used because the two-cycle domain is still not stable enough to attain a converged solution for turbulent flow computations.

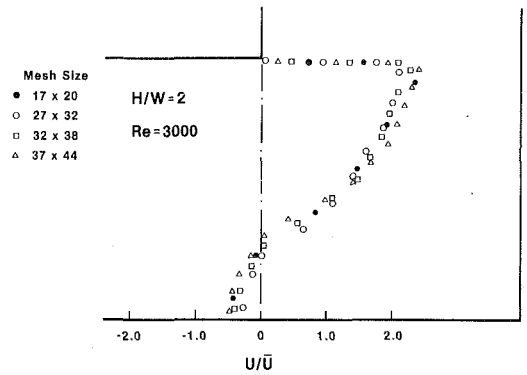

Fig. 2 Streamwise velocity profiles in the channel for different mesh sizes

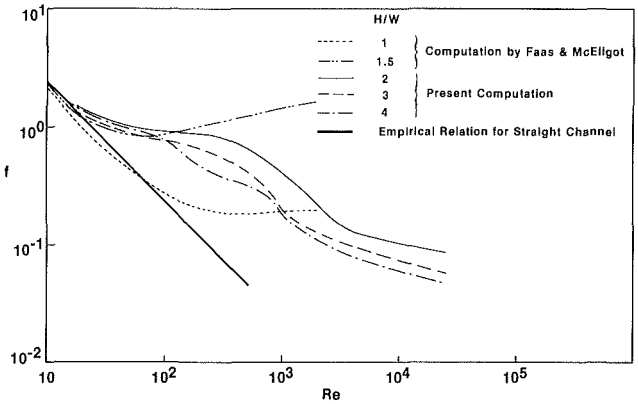

Fig. 3 Average friction factor as a function of Reynolds number

Note that the flow regime of Faas and McEligot is laminar. At the initial stage of the iteration, prescribed values are given at the inlet (*AF*) whereas a continuing outflow boundary condition is applied at the outlet (*EJ*); i.e., derivatives of the properties with respect to the streamwise direction are zero at *EJ*. The iterative procedure is repeated until the mass residual source term decreases and becomes sufficiently small (for example less than 3 percent of the total mass). Then the periodic boundary condition is initiated by replacing the field data at the inlet (*AF*) with the computed solutions at the pertinent position (*DI*) in each iteration step. Periodicity is checked by comparing the computed data between the outlet (*EJ*) and the same position at the corner *B*. The computation was terminated when the periodicity was satisfied, which was normally attained when the mass residual source became less than 1 percent of the total mass.

Computing Details. Exploratory test runs were made for several different meshes for the case of the step ratio $H/W = 2$ and for a turbulent flow with Re = 3000. The velocity profiles for these meshes at the first corner *B* are plotted in Fig. 2. The maximum changes in velocity between the most coarse mesh (17 × 20) and the finest mesh (37 × 44) are within 5 percent. Thus, we chose the medium-size mesh 27 × 32 for the geometry $H/W = 2$ to maintain relatively moderate computer costs while obtaining sufficiently accurate results. The meshes for other geometries were determined to maintain equal size of meshes over the solution domain; namely, they are 42 × 42 and 57 × 52 for step ratios $H/W = 3$ and 4, respectively.

Typically, the first convergence criterion was attained after 150 iterations followed by 100 more iterations in the second pass to converge for $H/W = 3$ with a total CPU time of approximately 7 min on UNIVAC 1100.

Results and Discussion

Average Friction Factors. The computed average friction factors are plotted as a function of the Reynolds number and are shown in Fig. 3. The trend of the slope is slightly different in the laminar and turbulent regions. Initially f falls off from about 2.4 at Re = 10 as Re increases, and then f becomes nearly constant in the range between Re = 50 and 200. For Re greater than 300, f again drops rapidly until it reaches Re = 1000–3000 depending on the channel step ratio. Finally, in the turbulent regime the curve of f changes to a slow decreasing one. It is also noted that the change in the level is larger from $H/W = 2$ to 3 than from $H/W = 3$ to 4.

In Fig. 3 the friction factors for $H/W = 1$ and 1.5 computed by Faas and McEligot are also shown. Their trend is similar to the present results mainly in the range of Re less than 300. Just for reference the friction factor for a straight channel with infinite width is also compared with the computations. In the limiting state at Re ≃ 10 all of the computed results approach the $f = 24/\text{Re}$ relation. This agreement gives a certain level of confidence in the calculations for heat transfer.

Flow Field. In Fig. 4, the streamwise velocity profiles are shown in the channels of $H/W = 2$, 3, and 4 for Reynolds numbers of Re = 100, 1000, and 25,000. In every channel, the flow separates at the corner *B* and reattaches on the wall *BC*, thus creating a recirculating flow along the wall *BC*. This feature is represented by a peak velocity at the corner *B* and the negative velocity on the *BC* wall just downstream from the corner *B* in the figure. The separated flow at the corner *B* will also cause a flow deflection toward the opposite side of the channel wall. As a result the velocity reaches its peak at the position closer to the corner *H*. This process repeats at every corner.

In this figure we also notice a strong dependence of Reynolds numbers on the velocity profiles. The maximum velocities for turbulent flows occur at locations much closer to the walls than those for laminar flows. This flow deflection becomes larger as the Reynolds number is increased.

Local Heat Transfer. Local Nusselt numbers were computed along the channel walls to investigate the local heat transfer characteristics affected by the channel shape.

In Figs. 5–7 the computed local Nusselt number distributions are shown for $H/W = 2$–4 and for Re = 100–8000. The Nusselt numbers are plotted on the *BC* and *CE* walls only because the distributions on the other walls are similar due to periodicity. In each case we can see similar trends in the distribution of local Nusselt numbers.

In Fig. 5 the local Nusselt numbers along the channel wall of $H/W = 2$ are compared for different Reynolds numbers. For Re = 100, the Nusselt number decreases sharply from the corner *B* due to the flow separation and it remains at a nearly constant value up to the concave corner *C* where the Nusselt number becomes minimum due to a reversed corner flow. The Nusselt number, then, increases to its peak value at about a half channel width to the right of the corner *C* because of the flow impingement from upstream. The position of the edge of the cornering flow is indicated by a triangle in the figure. The distribution also shows another peak in Nusselt number at about one and a half channel widths downstream from the corner *C* attributed to the flow deflection promoted by the separated flow at the corner *H*. For Re = 500 the pattern of the Nusselt number distribution is the same as that for Re = 100 except that the variation in the levels of the Nusselt number becomes somewhat smoother.

The Nusselt number distribution along the *BC* wall changes from $H/W = 2$ to 3 for laminar flows; while the distributions for $H/W = 2$ are relatively monotonic, these are rather zigzag

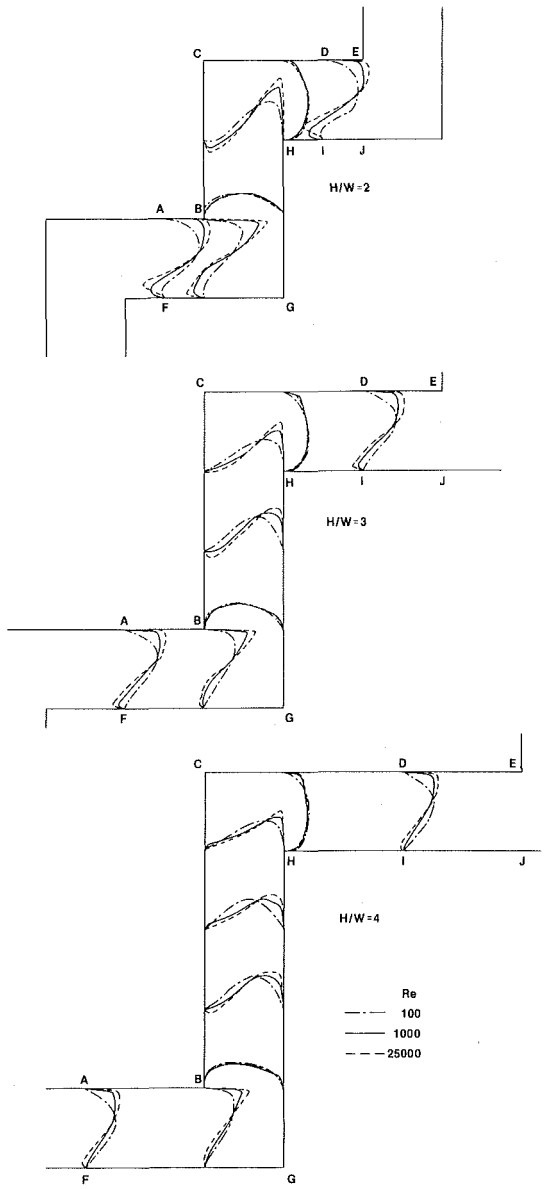

Fig. 4 Streamwise velocity profiles for different step ratios and Reynolds numbers

for $H/W = 3$ and 4. As indicated in Figs. 6 and 7 by the triangles, the flow reattachment occurs near corner B, and the flow reversal is causing a small peak in the Nusselt number. The cornering flows near the concave corner C also induce small peaks at about 1/3 W upstream from C. The edges of the corner flow regions are marked by the triangle symbols. It is noted that the reversal flow region spans the whole BC wall for Re = 500; thus, the Nusselt number distributions become smooth. Although the reattachment of the flow appears downstream of the corner B for $H/W = 4$, if the flow is turbulent, this does not cause any abrupt change in the Nusselt number distributions.

Generally, the Nusselt number distributions are smooth for turbulent flows throughout the whole region. The maximum Nusselt numbers always occur at about 1 W downstream from the corner C due to the deflected flow on the GH wall producing high turbulence kinetic energy augmentation when separated at the convex corner H. This will result in a high rate of heat transfer on the CE wall. It is also evident in these figures that the peak Nusselt number on the CE wall becomes larger as the Reynolds number increases.

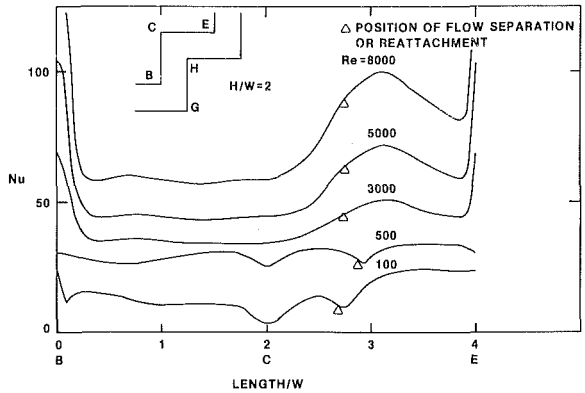

Fig. 5 Local Nusselt number distribution along the channel of $H/W = 2$

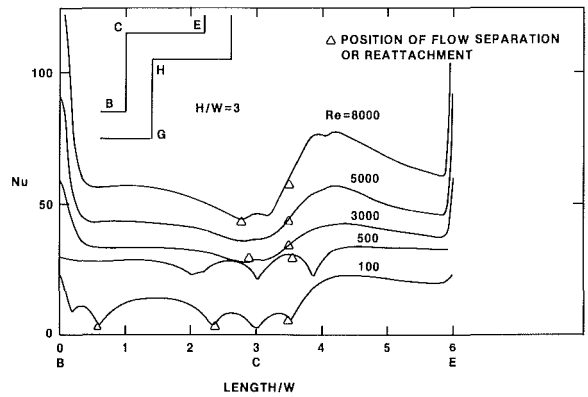

Fig. 6 Local Nusselt number distribution along the channel of $H/W = 3$

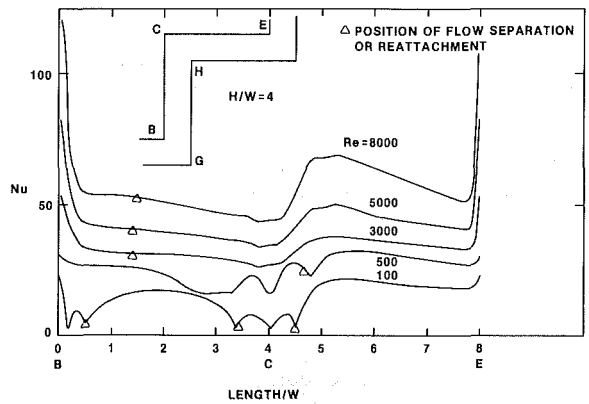

Fig. 7 Local Nusselt number distribution along the channel of $H/W = 4$

Average Heat Transfer. Figure 8 displays the average Nusselt number as a function of the Reynolds number. Here the computed results are compared with the experimental data obtained by Izumi et al. [8]. Except at the transition region, the dependency of the computed average Nusselt number on the Reynolds number agrees well with the experimental data although the levels of the Nusselt number do not coincide. The discrepancies between the computed and measured data with regard to their levels are as high as 100 percent. The causes of these discrepancies may be interpreted in several ways. First, there is some difference in the assumed conditions in the computation and the experimental situations. This is despite an attempt to maintain uniform conditions because the choice of the fluid properties causes some deviation from the experimental condition. Secondly, the three dimensionality in the experiment causes some deviation from the

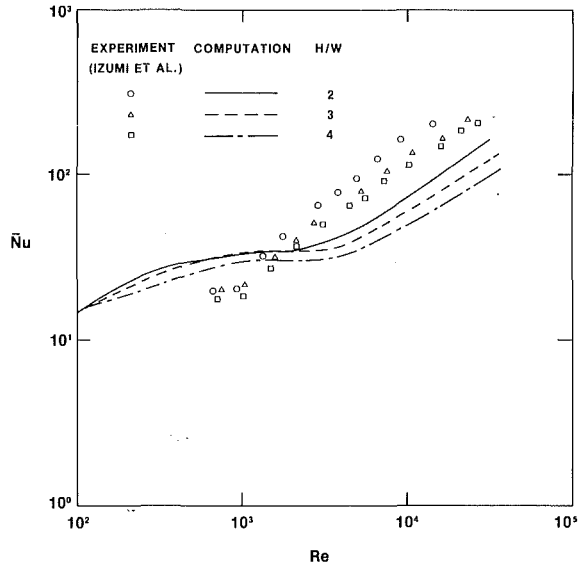

Fig. 8 Average Nusselt number as a function of Reynolds number

two-dimensional assumption in the computation; the aspect ratio is 12 in the experiment. The third reason may be due to the turbulence model employed in the present computations. Although significant improvement has been made for the evaluation of wall values by using the near-wall model, the turbulence model used for the computation is the k–ϵ model which is based on the Boussinesq viscosity concept. This model has many limitations in the prediction of complex turbulent flows since it assumes an isotropic turbulence. With regard to the modeling aspect, the authors are investigating by including the second-order closure model of turbulence for such complex turbulent flow predictions. However, it could be stressed that the trend obtained by the present model is at least in accordance with the measured data although the levels are not.

It is observed that in the turbulent flow regime the Nusselt numbers are more sensitive to the Reynolds number than in the laminar regime. This feature is similar to the computed results of the flow in a channel with two right-angled bends [7]. The average Nusselt number for turbulent flows is found numerically to be expressed by the following formula

$$\overline{\mathrm{Nu}} = 0.307 \mathrm{Re}^{0.642} (H/W)^{-0.592} \tag{12}$$

Conclusions

A numerical study was performed for the flow in perpendicularly corrugated wall channels. The main conclusions to emerge from this study may be summarized as follows:

1 The effect of the step ratio on the local Nusselt number is generally minor for H/W larger than or equal to 3.

2 The flow and heat transfer patterns change drastically from laminar to turbulent flows.

3 The average Nusselt number was suggested to be

$$\overline{\mathrm{Nu}} = 0.307\ \mathrm{Re}^{0.642}\ (H/W)^{-0.592}$$

for the range H/W = 2–4. This relation differs from the case in the channel with two right-angled bends in which the dependency of step ratios H/W was minor.

4 The average friction factor changes slightly more from H/W = 2 to 3 than from H/W = 3 to 4. This fact indicates that the geometric influence on the flow could be significant in this range of step ratios.

Acknowledgments

This research was supported under a research grant from the Graduate School, University of Wisconsin – Milwaukee. Thanks are due to Mr. A. Mamdoh who assisted in the computation and reduction of results. Thanks are also due to Dr. D. M. McEligot who provided us with many useful suggestions.

References

1 Kays, W. M., and London, A. L., *Compact Heat Exchangers*, McGraw-Hill, New York, 1964.

2 Goldstein, L., and Sparrow, E. M., "Experiments on the Transfer Characteristics of a Corrugated Fin and Tube Heat Exchanger Configuration," ASME JOURNAL OF HEAT TRANSFER, Vol. 98, No. 2, 1976, pp. 26–34.

3 Goldstein, L., and Sparrow, E. M., "Heat/Mass Transfer Characteristics for Flow in a Corrugated Wall Channel," ASME JOURNAL OF HEAT TRANSFER, Vol. 99, 1977, pp. 187–195.

4 Faas, S. E., and McEligot, D. M., "Convective Heat Transfer for Ship Propulsion," Report No. 1248-7, Office of Naval Research, Aerospace and Mechanical Engineering Department, University of Arizona, Jan. 1980.

5 Izumi, R., Oyakawa, K., Kaga, S., and Yamashita, H., "Fluid Flow and Heat Transfer in Corrugated Wall Channels," *JSME Journal*, Vol. 47, No. 416, 1981, pp. 657–665.

6 Amano, R. S., "Laminar Heat Transfer in a Channel With Two Right-Angled Bends," ASME JOURNAL OF HEAT TRANSFER, Vol. 106, No. 3, 1984, pp. 591–596.

7 Amano, R. S., "Turbulent Heat Transfer in a Channel With Two Right-Angled Bends," AIAA Paper No. 84-04094, AIAA Aerospace Sciences Meeting, Reno, Jan. 1984.

8 Izumi, R., Yamashita, H., Kaga, S., and Miyajima, N., "Fluid Flow and Heat Transfer in Corrugated Wall Channels—Experimental Study for Many Bends," *Proceedings of the 19th JSME Symposium on Heat Transfer*, Paper No. A101, 1982.

9 Tani, I., Iuchi, M., and Komoda, H., "Experimental Investigation of Flow Separation Associated With a Step or Groove," Aeronautical Research Institute, University of Tokyo, Rept. 364, 1961.

10 Bradshaw, P., and Wong, F. Y. F., "The Reattachment and Relaxation of a Turbulent Shear Layer," *Journal of Fluid Mechanics*, Vol. 52, Part 1, 1972, pp. 113–135.

11 Eaton, J. K., and Johnston, J. P., "A Review of Research on Subsonic Turbulent Flow Reattachment," *AIAA Journal*, Vol. 19, No. 9, Sept. 1981.

12 Chieng, C. C., and Launer, B. E., "On the Calculation of Turbulent Heat Transport Downstream From an Abrupt Pipe Extension," *Numerical Heat Transfer*, Vol. 3, 1980, pp. 189–207.

13 Johnson, R. W., and Launder, B. E., "Discussion of the Calculation of Turbulent Heat Transport Downstream From an Abrupt Pipe Expansion," *Numerical Heat Transfer*, Vol. 5, 1982, pp. 493–496.

14 Amano, R. S., "A Study of Turbulent Flow Downstream of an Abrupt Pipe Expansion," *AIAA Journal*, Vol. 21, No. 10, Oct. 1983, pp. 1400–1405.

15 Amano, R. S., "Development of Turbulent Near-Wall Model and Its Application to Separated and Reattached Flows," *Numerical Heat Transfer*, Vol. 7, No. 1, 1984, pp. 59–75.

16 Gooray, A. M., Watkins, C. B., and Aung, W., "A Two-Pass Procedure for the Calculation of Heat Transfer in Recirculating Turbulent Flow," *Numerical Heat Transfer*, Vol. 6, No. 4, 1983, pp. 423–440.

17 Aung, W., "Separated Forced Convection," *Proceedings of the ASME/JSME Thermal Engineering Joint Conference*, Vol. 2, 1983, pp. 499–515.

18 Spalding, D. B., "A Novel Finite-Difference Formulation for Differential Expressions Involving Both First and Second Derivatives," *International Journal of Numerical Methods in Engineering*, Vol. 4, 1972, pp. 551–559.

19 Gosman, A. D., Pun, W. M., Runchal, A. K., Spalding, D. B., and Wolfshtein, M., *Heat and Mass Transfer in Recirculating Flows*, Academic Press, 1969.

20 Patankar, S. V., and Spalding, D. B., "A Calculation Procedure for Heat, Mass and Momentum Transfer in Three-Dimensional Parabolic Flows," *International Journal of Heat and Mass Transfer*, Vol. 15, 1972, pp. 1787–1806.

R. S. Kane
Chairman,
Mechanical Engineering Department,
Manhattan College,
Riverdale, NY 10471
Mem. ASME

R. Pfeffer
Chairman,
Chemical Engineering Department,
City College of New York,
New York, NY 10031

Heat Transfer in Gas-Solids Drag-Reducing Flow

Heat transfer coefficients of air–glass, argon–glass, and argon–aluminum suspensions were measured in horizontal and vertical tubes. The glass, 21.6 and 36.0-μ-dia particles, was suspended at gas Reynolds numbers between 11,000 and 21,000 and loading ratios between 0 and 2.5. The presence of particles generally reduced the heat transfer coefficient. The circulation of aluminum powder in. the 0.870-in.-dia closed loop system produced tenacious deposits on protuberances into the stream. In the vertical test section, the Nusselt number reduction was attributed to viscous sublayer thickening; in the horizontal test section to particle deposition.

Introduction

Drag reduction in liquid–polymer solutions has been widely reported [1, 2, 3]. Drag reduction in gas–solid suspensions has not been investigated as thoroughly although it has been reported by several investigators. A literature review is provided in [4]. A more recent mention of the phenomena is in [5]. Because of the analogy between turbulent momentum and heat transfer, it would be expected that Nusselt number reduction during heat transfer in turbulent flow should occur simultaneously with friction factor or drag reduction. A number of workers with gas–solid suspensions have reported Nusselt number reduction [6–13, 17–19].

Although experimental restrictions may have dictated the results, Nusselt number reduction has generally been limited to small particle sizes, small pipe diameters, low loading ratios, and low turbulent Reynolds numbers. Only two of the previous investigators have measured both drag and Nusselt number reduction in the same test apparatus. However, neither varied particle diameter, particle type, or test section orientation. In this study, three different particle diameters, two different particle types, and two different test section orientations were considered for conditions known to produce drag reduction. The particles were two grades of glass beads, averaging 21.6 μ and 36.0 μ diameter by weight, and one grade of aluminum powder averaging 30.0 μ diameter by weight. The glass beads were, according to the supplier and microphotographs, as spherically shaped as possible; the aluminum powder was not as uniform and was characterized in terms of an equivalent sphere according to standard sizing measurements. The test sections were vertical and horizontal 22.1 mm inside diameter tubes. The suspensions were circulated at gas (air or argon) Reynolds numbers between 11,000 and 21,000 and at loading ratios between 0 and 2.5.

Experimental Apparatus and Procedures

The suspension was circulated through a closed loop system, originally designed for pressure drop and flow measurements but modified for heat transfer measurements. The closed loop system as modified for heat transfer is shown in Fig. 1.

The gas flow rate was measured with a sharp-edged orifice even with particles in suspension. Earlier studies [4, 14] had shown that the calibration of an orifice was unaffected by dilute volumetric concentrations of solids suspended in the gas. The solid flow rate was determined with the aid of a cantilevered target meter equipped with strain gauges.

Solids were added to the loop before a set of data runs by pouring a given weight of sifted particles into the solid inlet port located near the circulator intake. The port was sealed and the circulator was started to disperse the particles through the loop. A warmup period of not less than 1 hr with the circulator running preceded each set of heat transfer runs with a given amount of particles in the loop. The cooling water temperature and maximum wall temperature in the vertical test section had to stabilize before reliable data could be taken. Because of the limitations on the allowable tape temperature, the voltage regulator setting was adjusted so that the maximum wall temperature in the vertical test section did not exceed 215°C. For argon gas measurements, the system was purged of air by forcing the denser argon into the lower loop and venting the lighter air from the upper loop.

Clean Gas Test Results

Prior to suspension tests, heat transfer measurements were used to calculate the Nusselt numbers for the two gases, air and argon. The direction and instrumentation of the heat transfer was different for the vertical and horizontal test sections. The vertical test section was a heated section; the horizontal test section was a cooled section. It was necessary to have two different directions of heat flow in order to provide a proper heat sink for the system and to protect equipment downstream. Two different techniques were therefore used to calculate the gas side heat transfer coefficient and Nusselt number.

The flow was provided by a centrifugal circulator which was capable of pumping gas and solids simultaneously. Miniature chromel-alumel thermocouples were located at either end of the test section and positioned to measure centerline bulk temperature. Two diametrically opposed chromel-alumel thermocouple junctions were spaced evenly along the test section to measure outside wall temperatures.

The heat input in the vertical test section was supplied by an electrical resistance tape wrapped around the tube. The tape was controlled by a 0 to 120 V range voltage regulator and supplied a maximum of 384 W. Several inches of fiberglass and asbestos wool insulation were wrapped around the tape to minimize heat conduction to the atmosphere. A final layer of aluminum foil was added to minimize radiative heat losses.

In the vertical test section, the heat input was calculated from:

$$Q = W_g C_{pg} (T_{OUT} - T_{IN}) \tag{1}$$

The heat input was equated to:

$$Q = UA (\bar{T}_W - \bar{T}_B) \tag{2}$$

where $\bar{T}_W$ was an average wall temperature weighted in accordance with the linear spacing of the 12 thermocouples along the heated section with UA given by:

Contributed by the Heat Transfer Division for publication in the JOURNAL OF HEAT TRANSFER. Manuscript received by the Heat Transfer Division February 21, 1984.

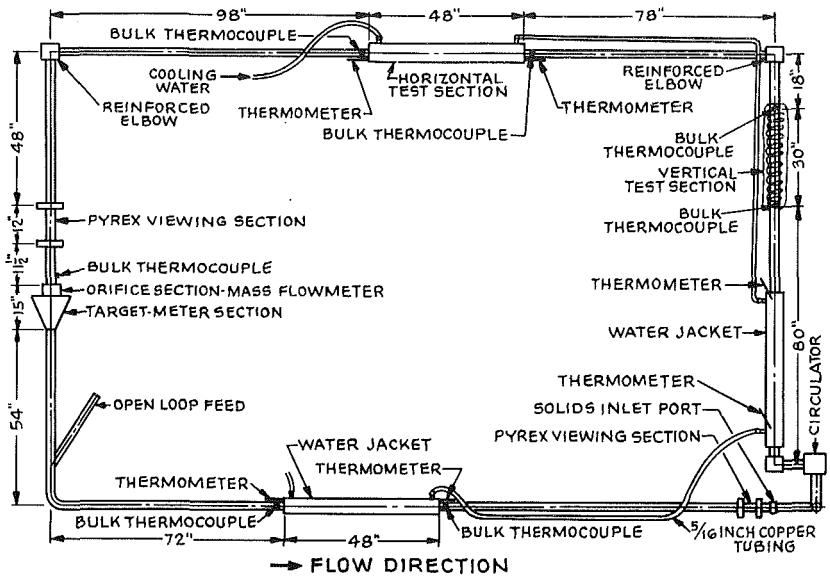

Fig. 1 Closed loop modified for heat transfer

$$UA = \frac{1}{\frac{t_{ss}}{k_{ss}\bar{A}} + \frac{1}{h_i A_i}} \tag{3}$$

With the heat input and all the temperatures as known quantities, the gas side heat transfer coefficient was calculated directly.

In the horizontal test section, a counterflow heat exchanger equation was used to evaluate UA. The gas side heat loss was calculated from:

$$Q = W_g C_{pg} (T_{IN} - T_{OUT}) \tag{4}$$

The heat loss was equated to:

$Q = UA\text{LMTD}$ where

$$\text{LMTD} = \frac{(T_{OUT} - T_{WOUT}) - (T_{IN} - T_{WIN})}{\ln\left(\frac{T_{OUT} - T_{WOUT}}{T_{IN} - T_{WIN}}\right)} \tag{5}$$

and

$$UA = \frac{1}{\frac{t_{ss}}{k_{ss}\bar{A}} + \frac{1}{h_o A_o} + \frac{1}{h_i A_i}}$$

In operation, the water temperature remained almost constant from the inlet to the outlet of the cooling jacket. The logarithmic temperature difference was almost exclusively dependent on variations in the gas side coefficient. The resistance of the stainless steel tube wall was negligible in both test sections.

Nomenclature

A = heat transfer surface area in equations (2), (3), and (5), m^2

A_i = inside heat transfer surface area, m^2

A_o = outside heat transfer surface area, m^2

$\bar{A}$ = average heat transfer surface area for conduction, m^2

C_{pg} = specific heat capacity of gas, $Jkg^{-1}K^{-1}$

C_{pp} = specific heat capacity of a particle, $Jkg^{-1}K^{-1}$

C_{ps} = specific heat capacity of suspension, $Jkg^{-1}K^{-1}$

D = pipe inside diameter, m

h_i = inside heat transfer coefficient, $Wm^{-2}K^{-1}$

h_o = outside heat transfer coefficient, $Wm^{-2}K^{-1}$

k_g = gas thermal conductivity, $Wm^{-1}K^{-1}$

k_{ss} = stainless steel thermal conductivity, $Wm^{-1}K^{-1}$

LMTD = logarithmic mean temperature difference, °C

Nu_g = $h_i D k_g^{-1}$, Nusselt number in clean gas flow

Nu_s = $h_i D k_g^{-1}$, Nusselt number in suspension flow

Pr = $C_{pg}\mu k_g^{-1}$, Prandtl number of gas

Q = heat transferred, W

Re_g = $UD\nu^{-1}$, Reynolds number based upon gas properties

t_{ss} = thickness of stainless steel tube wall, m

T_g = gas temperature, °C

T_{IN} = inlet suspension temperature, °C

T_{OUT} = outlet suspension temperature, °C

T_{WIN} = inlet water temperature, °C

T_{WOUT} = outlet water temperature, °C

$\bar{T}_B$ = average of inlet and outlet suspension temperatures, °C

$\bar{T}_W$ = weighted average of wall temperatures in vertical test section, °C

U = bulk average gas velocity in definition of Reynolds number, ms^{-1}

U = overall heat transfer coefficient, $Wm^{-2}K^{-1}$

W_g = mass flow rate of gas only, kgs^{-1} or $kghr^{-1}$

W_p = mass flow rate of particles only, kgs^{-1} or $kghr^{-1}$

W_s = mass flow rate of suspension, kgs^{-1} or $kghr^{-1}$

δ = ratio of specific heat of particle to specific heat of gas

η = $W_p W_g^{-1}$, loading ratio

μ = gas viscosity, $kgm^{-1}s^{-1}$

ν = gas kinematic viscosity, m^2s^{-1}

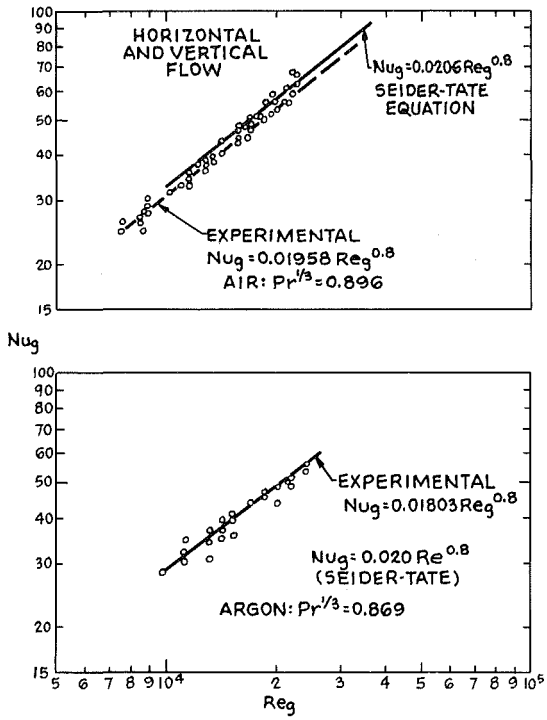

Fig. 2 Clean gas Nusselt number versus Reynolds number

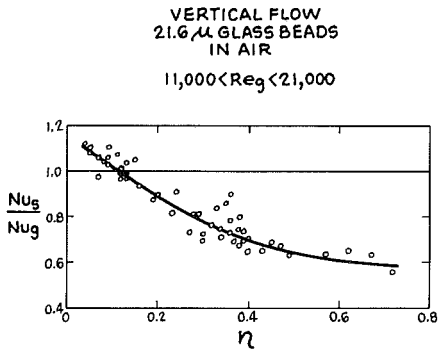

Fig. 3 Vertical Nusselt number ratio versus loading ratio: 21.6 μ glass beads

The Nusselt number was evaluated at the average bulk gas temperature. The results for air and argon are shown in Fig. 2 where Nusselt number is plotted versus Reynolds number. The measured Nusselt numbers were about 10 percent lower than the Nusselt numbers calculated from the Sieder–Tate equation which correlates experimental data within wide 30 percent limits [15]. Prandtl number dependence was not an important factor because the 1/3 power of the Prandtl number for air and argon is essentially constant for the experimental range of temperatures. The clean gas values were the same in both the vertical and horizontal test sections and the lower horizontal cooling section as well. Clean gas Nusselt numbers were measured before and after suspension tests and were found to be unchanged.

Suspension Test Results and Discussion

The suspension heat transfer measurements were used to calculate Nusselt numbers for the two gases carrying suspended glass beads or aluminum powder. The circulation of suspensions required revision of the clean gas formulae for heat input in the vertical test section and heat loss in the horizontal test section. The mass flow rate now included the contribution of the suspended solids:

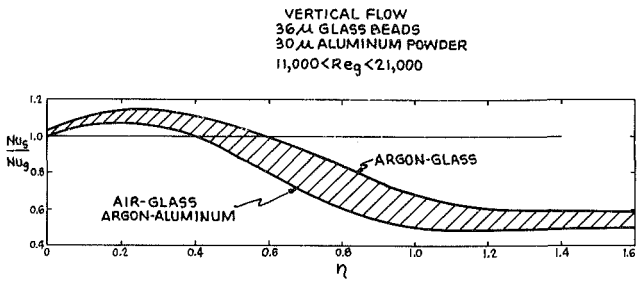

Fig. 4 Vertical Nusselt number ratio versus loading ratio: 36.0 μ glass beads and 30.0 μ aluminum powder

$$W_s = W_g(1+\eta) \tag{6}$$

The specific heat of the suspension was calculated from a weighted average of the separate gas and solid specific heats

$$C_{ps} = C_{pg}\frac{1+\delta\eta}{1+\eta}$$

where

$$\delta = \frac{C_{pp}}{C_{pg}} \tag{7}$$

The final calculations and correlations of Nusselt numbers were based on the gas properties (density, thermal conductivity, specific heat, and viscosity) in order to provide a direct comparison with the clean gas results. For the loading ratios of this study, the assumption that the effective thermal conductivity of the suspension was the same as the gas thermal conductivity introduced negligible error [16]. The response time lag for conduction in the small particles and dilute suspensions considered in the study was much smaller than the thermal relaxation time for heat transfer to the gas, simplifying treatment of the particles in the data reduction.

The results of the vertical test section heat transfer measurements are shown in Fig. 3 for suspensions of the 21.6 μ glass beads in the air and in Fig. 4 for suspensions of the 36.0 μ glass beads in air and argon and suspensions of 30.0 μ aluminum powder in argon. The graphs were plotted as the ratio of the suspension Nusselt number to the clean gas Nusselt number versus loading ratio at corresponding gas Reynolds numbers. Nusselt number reduction was indicated by values of the Nusselt number ratio below unity. Figure 4 shows the envelope of the actual data. The upper limit generally represented the argon–glass results. The lower limit generally represented the air–glass and argon–aluminum results.

The glass–air suspension measurements indicated that the 21.6 and 36.0 μ glass beads were much more effective in reducing Nusselt numbers than in reducing friction factors [4]. Reductions of up to 44 and 52 percent were achieved in the vertical test section for the 21.6 and 36.0 μ glass beads, respectively. Like friction factor results, there was a minimum loading ratio for the onset of Nusselt number reduction. Also like friction factor results, the onset of Nusselt number reduction was further delayed (with loading ratio) as the particle size increased. Neither of the two glass bead suspensions showed any Reynolds number effect on the onset of Nusselt number reduction or the amount of Nusselt number reduction.

The suspensions of 21.6 μ glass beads showed a monotonic decrease in Nusselt number ratio after the onset of Nusselt number reduction. Before the onset of Nusselt number reduction at a loading ratio of 0.12, a moderate increase in Nusselt number was noted. The increase was attributed to an initial widely dispersed deposit on the test section wall. The deposit was sufficient to disturb the viscous sublayer, producing additional turbulence and heat transfer.

The suspensions of 36.0 μ glass beads in air showed a

tendency toward a flat minimum at a loading ratio of 1.2. Before the onset of Nusselt number reduction at a loading ratio of 0.4, a slight increase in Nusselt number was noted. The increase was also attributed to a widely dispersed deposit on the vertical test section wall. That the increase was smaller for the 36.0 μ glass beads than for the 21.6 μ glass beads was consistent with the relative ability of the two bead sizes to plate out. For both bead sizes, the deposit, rather than accumulating further, was probably worn away by heavier loadings and did not affect the vertical test section results past the onset of Nusselt number reduction.

The heat transfer measurements for suspensions of aluminum powder in argon indicated that particle thermal properties had no effect on Nusselt number reduction in the vertical test section. The 30.0 μ aluminum powder gave similar results to the 36.0 μ glass beads. The similarity in behavior of the two different particles in the vertical test section suggested that the Nusselt number reduction was a coincidental result of the drag reduction mechanism, that is, a thickening of the viscous sublayer. The thickening of the sublayer is apparently sufficient to overcome any tendencies toward net improvements in heat transfer because of direct contact (without the formation of an insulating deposit) between particles and the wall.

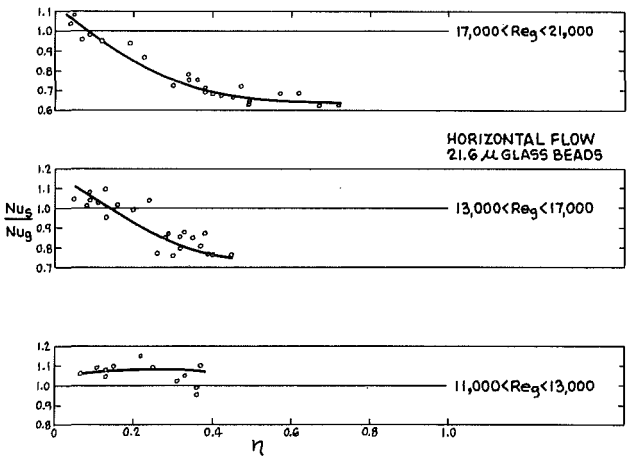

Fig. 5 Horizontal Nusselt number ratio versus loading ratio: 21.6 μ glass beads

The results of the horizontal test section heat transfer measurements are shown in Fig. 5 for suspensions of the 21.6 μ glass beads in air and in Fig. 6 for suspensions of the 36.0 μ glass beads in air and argon and for suspensions of 30.0 μ aluminum powder in argon. Significant Nusselt number reduction, up to 38 and 44 percent for the 21.6 and 36.0 μ glass beads in air, respectively, was also achieved for the horizontal test section. However, the horizontal test section Nusselt number results were not as consistent with previous friction factor results as those in the vertical test section [4]. (In the vertical test section Nusselt number reduction occurred under the same conditions as the previously observed drag reduction. In the horizontal test section, Nusselt number reduction occurred even for those cases where drag increases and not drag reduction were previously observed.) Gravity sedimentation and thermophoresis causing deposition on the cool wall of the horizontal heat transfer test section apparently complicated the results.

The 21.6 μ glass beads (like the previous friction factor results) showed very similar results in both horizontal and vertical test sections with the exception of a detectable Reynolds number effect in the horizontal test section. The amount of Nusselt number reduction progressively decreased with decreasing Reynolds number. The onset of Nusselt number reduction was progressively delayed, from loading ratios of 0.07 to 0.16, with decreasing Reynolds numbers until the lowest Reynolds numbers, about 12,000, were reached. At Reynolds numbers of about 12,000, Nusselt number reduction was not generally noted. The observed loss of entrainment at these Reynolds numbers could presumably explain the anomalous results as the presence of large quantities of solids in direct contact with the tube wall would drastically change the heat transfer mechanism. With the exception of the low Reynolds number results, the trends of the heat transfer measurements for the 21.6 μ glass beads were reasonably consistent with the trends of the previous pressure drop measurements. However, it could not be concluded that the controlling mechanism in the horizontal test section was the same for both cases. Thickening of the sublayer was probably more important for the pressure drop measurements, and particle deposition was probably more important for the heat transfer measurements.

The results for suspensions of 36.0 μ glass beads in air were less predictable and systematic than the results for the 21.6 μ glass beads. Whereas friction factor increases were previously

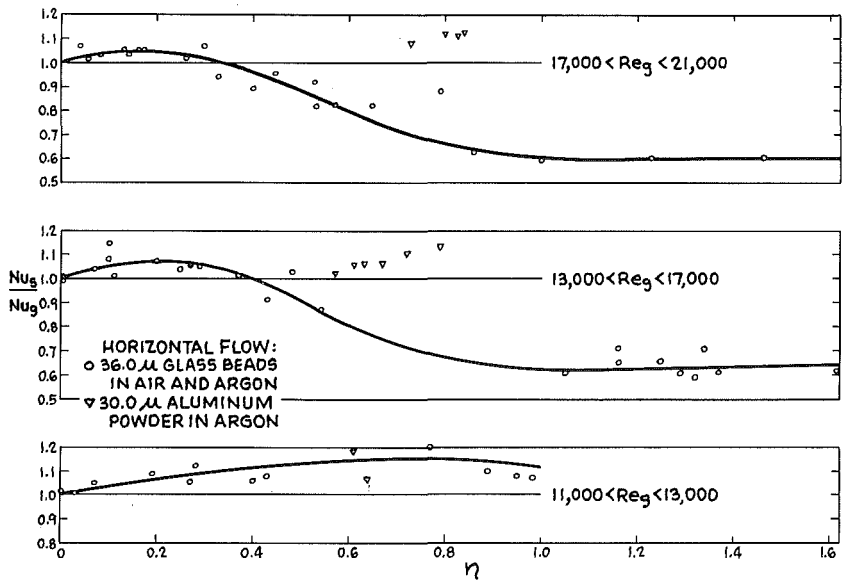

Fig. 6 Horizontal Nusselt number ratio versus loading ratio: 36.0 μ glass beads and 30.0 μ aluminum powder

noted at all test conditions for the 36.0 μ glass beads [4], Nusselt number increases were found only for loading ratios less than 0.4 for Reynolds numbers of about 12,000. In general, substantial Nusselt number decreases were observed. The friction factor and heat transfer results for the 36.0 μ glass beads tended to confirm the conjecture that particle deposition was more important for the Nusselt number reduction in the horizontal test section than any uniform sublayer changes. The onset and amount of Nusselt number reduction did not follow the consistent pattern observed with tests of 21.6 μ glass bead suspensions. It was apparent that the Reynolds analogy which predicts corresponding effects on heat transfer and momentum transfer was not valid for the horizontal flow. The particles did not just distort the structure of the turbulence as they did in vertical flow, but actually became an active part of the heat transfer mechanism.

The data obtained with suspensions of 36.0 μ glass beads in argon were in agreement with the air suspension data. However, the aluminum-argon suspension data always indicated Nusselt number increases regardless of loading ratio or Reynolds number. These results were probably caused by deposition of the powder on the cool wall of the horizontal test section. The unusual nature of the aluminum deposits (rock-hard buildups on metallic obstructions) probably disturbed the flow pattern and produced additional turbulence. (It is noted that the aluminum deposits were so tenacious that they defied usual cleaning methods; some equipment had to be replaced after this work.) Reductions in local heat transfer rates directly at the deposit locations were probably quite small because of the high thermal conductivity of the aluminum. Therefore, it was likely that the additional turbulence, aiding heat transfer, more than offset the local fouling factors, hindering heat transfer.

Conclusions

The presence of particles generally reduced the heat transfer coefficients below those of the clean gas at corresponding gas flow rates. Reductions of up to 44 and 52 percent were achieved in the vertical test section for the 21.6 and 36.0 μ glass beads, respectively. Reductions of up to 38 and 44 percent were also achieved in the horizontal test section for the 21.6 and 36.0 μ glass beads, respectively. The exceptions to the general occurrence of Nusselt number reduction appeared either at low loading ratios or at low Reynolds numbers. The Nusselt number increases were always less than 20 percent and were usually less than 10 percent. With the exception of cases where deposition complicated the results, the suspension Nusselt numbers were independent of the carrying gas (air or argon) and were independent of particle properties (other than diameter).

The Nusselt number reduction in the vertical test section was considered as a coincident result of the drag reduction that had been observed earlier using the same experimental apparatus. The thickening of the viscous sublayer, the cause of the drag reduction, was also believed to be the primary cause of the Nusselt number reduction. Visual observations of nonuniform particle concentration and of deposition in the horizontal test section indicated that the particles here took a more active role in the heat transfer mechanism. Therefore the Nusselt number reduction in the horizontal test section could not be attributed solely to the distortion of the fluid structure by the presence of particles. Thickening of the sublayer was probably more important in the vertical test section, and particle deposition was probably more important in the horizontal test section.

References

1 Sylvester, N. D. (ed.), "Drag Reduction in Polymer Solutions," AIChE Symposium Series, Vol. 69, No. 130, 1973.

2 Savins, J. G., and Virk, P. S. (eds.), "Drag Reduction," AIChE Symposium Series, Vol. 67, No. 111, 1971.

3 Hough, G. R. (ed.), "Viscous Flow Drag Reduction," AIAA Series, Vol. 72, 1981.

4 Kane, R. S., "Drag Reduction in Dilute Flowing Gas-Solids Suspensions," Ph.D. thesis, City University of New York, 1973.

5 Bryant, H. S., Silverman, R. W., and Zenz, F. A., "How Dust in Gas Affects Cyclone Pressure Drop," *Hydrocarbon Processing*, June 1983, pp. 87-90.

6 Farbar, L., and Morley, M. J., "Heat Transfer to Flowing Gas-Solids Mixtures in a Circular Tube," *Ind. Eng. Chem.*, Vol. 49, 1957, pp. 1143-1150.

7 Tien, C. L., and Quan, V., "Local Heat Transfer Characteristics of Air-Glass and Air-Lead Mixtures in Turbulent Pipe Flow," ASME Paper No. 62-HT-15, 1962.

8 Abel, W. T., Bluman, D. E., and O'Leary, J. P.,"Gas-Solids Suspensions as Heat-Carrying Mediums," ASME Paper No. 63-WA-210, 1963.

9 Depew, C. A., and Farbar, L., "Heat Transfer to Pneumatically Conveyed Glass Particles of Fixed Size," ASME JOURNAL OF HEAT TRANSFER, Vol. 85, 1963, pp. 164-172.

10 Farbar, L., and Depew, C. A., "Heat Transfer Effects to Gas-Solids Mixtures Using Solid Spherical Particles of Uniform Size," *Ind. Eng. Chem. Fundamentals*, Vol. 2, 1963, pp. 130-135.

11 Jepson, G., Poll, A., and Smith, W., "Heat Transfer From Gas to Wall in a Gas-Solids Transport Line," *Trans. Instn. Chem. Engrs.*, Vol. 41, 1963, pp. 207-211.

12 Garrett, T., "Heat Transfer Characteristics of Dilute Phase Solids-Air Suspensions in Turbulent Pipe Flow," Ph.D. thesis, Dept. of Engg., Cambridge University, England, 1964.

13 Szekely, J., and Carr, R., "Heat Transfer in a Cyclone," *Chem. Eng. Sci.*, Vol. 21, 1966, pp. 1119-1132.

14 Pfeffer, R., and Rossetti, S. J., "Experimental Determination of Pressure Drop and Flow Characteristics of Dilute Gas-Solid Suspensions," NASA CR-1894, 1971.

15 Kreith, F., *Principles of Heat Transfer*, 3rd ed., IEP-Dun Donnelly, 1976, p. 431.

16 Pfeffer, R., Rossetti, S., and Lieblein, S., "Analysis and Correlation of Heat Transfer Coefficient and Friction Factor Data for Dilute Gas-Solid Suspensions," NASA TN D-3603, 1966.

17 Sukomel, A. S., Tsvetkov, F. F., and Kerimov, R. V., "A Study of Local Heat Transfer Coefficients, From a Tube Wall to a Turbulent Flow of Gas Bearing Suspended Solid Particles," *Teploenergetika*, Vol. 14, 1967, pp. 77-80; *App. Mech. Rev.*, Vol. 21, 1968, p. 6834.

18 Boothroyd, R. G., and Haque, H., "Fully Developed Heat Transfer to Gaseous Suspension of Particles Flowing Turbulently in Ducts of Different Size," *J. Mech. Eng. Sci.*, Vol. 12, 1970, pp. 191-200.

19 Depew, C. A., and Cramer, E. R., "Heat Transfer to Horizontal Gas-Solid Suspension Flows," ASME JOURNAL OF HEAT TRANSFER, Vol. 92, 1970, pp. 77-82.

S. Neti

A. S. Warnock

E. K. Levy

Lehigh University,
Bethlehem, PA

K. S. Kannan
Universiti Teknologi Malaysia,
Kuala Lumpur, Malaysia

Computation of Laminar Heat Transfer in Rotating Rectangular Ducts

Cooling passages are often used in the rotor windings of large electrical generators, where the flow channel rotates about an axis parallel to but displaced from its axis of symmetry. In such a rotating passage, Coriolis accelerations and density gradients caused by the heated wall lead to the development of secondary flows which can have strong effects on heat transfer and pressure drop characteristics. Finite difference solutions were obtained for laminar flow of air in a rotating rectangular duct with aspect ratio 2/1, where the duct wall is subjected to a uniform heat flux. The solutions show the effect of rotation on the development of the flow patterns and velocity and temperature variations. Results for Nusselt number and friction factor are presented in both the inlet and fully developed regions over a range of Grashof and Reynolds numbers.

Introduction

As the size and energy density in large, high-performance electrical generators increased, it became standard design practice to provide cooling passages in the stator and rotor windings. By circulating coolant through channels in the windings, it was possible to increase the electrical and magnetic loadings without exceeding the temperature limitation of the electrical insulation. A major portion of a typical rotor cooling circuit involves flow channels which are parallel to the rotor axis. Coolant is transferred to and from the windings through radial ducting systems containing distribution and collection plenum chambers.

In the case of a duct rotating about an axis, parallel to but displaced from the axis of symmetry, the density gradients caused by the heated wall interact with the centrifugal acceleration to cause a secondary flow. The cooler and more dense fluid in the core flows radially outward while the warmer fluid near the walls flows inward toward the axis of rotation. In addition, Coriolis accelerations induced by the transverse velocity components lead to further adjustments in the flow patterns.

This study is concerned with laminar flow in ducts of rectangular cross section, a geometry which is of commercial importance in the power generation industry. There are a number of investigations cited in the literature which are relevant to the parallel rotating duct, but most of these deal with flows in circular pipes. Theoretical solutions for the fully developed circular tube case were obtained by Morris [1] using a series expansion technique, Mori and Nakayama [2] using an integral method, and Woods and Morris [3] with a numerical finite difference approach.

An extensive review of heat transfer in rotating channels has been presented by Morris [4]. The review includes results reported for fully developed laminar heat transfer through a rotating circular tube by Morris [5–7], Davies and Morris [8], Woods and Morris [9], and Woods [10]. Data for air, water, and glycerol are contained in [5–10], but caution should be used in applying these results to the fully developed laminar case since the test sections were relatively short. In addition, a significant amount of the data with air were obtained in the Reynolds number range from 1900 to 2500 where transition phenomena may be important.

The only theoretical solutions on flow development in a circular tube rotating about a parallel axis are by Skiadaressis and Spalding [11]. Experimental data for the laminar entrance region are reported by Woods [10] and Sakamoto and Fukui [12] for air.

Although no results have been published on the rotating rectangular duct, Dias [13] and Morris and Dias [14] studied the case of a rotating square duct with laminar flow. Theoretical results for the fully developed flow are given in [14] with a limited amount of data using air as the working fluid.

In the present paper, finite difference solutions are presented for laminar flow of air in a rectangular duct with an aspect ratio of 2/1, where the wall heat flux is uniform in both the axial and circumferential directions. The results show the effect of rotation on the flow development, and solutions for Nusselt number and friction factor are presented in both the inlet and fully developed regions over a wide range of Grashof and Reynolds numbers.

Governing Equations and Calculation Procedures

Figure 1 shows the duct geometry of interest in this investigation. All the calculations are for the aspect ratio b/a =

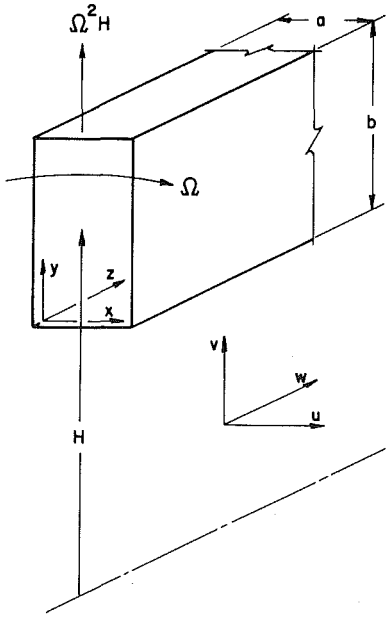

Fig. 1 Coordinate system

Contributed by the Heat Transfer Division for publication in the JOURNAL OF HEAT TRANSFER. Manuscript received by the Heat Transfer Division April 20, 1983. Paper No. 83-HT-6.

2/1, where the larger side of the rectangle is aligned in the radial direction.

The equations that need to be solved for the convective heat transfer in a rotating duct are the three momentum equations, the continuity equation, the energy equation, and the equation of state for the fluid. Since no recirculation is expected in the primary flow direction (z direction), the downstream influence on the flow can be neglected. The momentum and energy equations were reduced to a form that does not include the axial diffusion terms [15–17] and were written as:

$$\rho\left(u\frac{\partial w}{\partial x}+v\frac{\partial w}{\partial y}+w\frac{\partial w}{\partial z}\right)= -\frac{\partial p}{\partial z}+\frac{\partial}{\partial x}\left(\mu\frac{\partial w}{\partial x}\right)+\frac{\partial}{\partial y}\left(\mu\frac{\partial w}{\partial y}\right) \quad (1)$$

$$\rho\left(u\frac{\partial u}{\partial x}+v\frac{\partial u}{\partial y}+w\frac{\partial u}{\partial z}\right)=-\frac{\partial p}{\partial x}+\frac{\partial}{\partial x}\left(\mu\frac{\partial u}{\partial x}\right)+\frac{\partial}{\partial y}\left(\mu\frac{\partial u}{\partial y}\right)-2\rho\Omega v \quad (2)$$

$$\rho\left(u\frac{\partial v}{\partial x}+v\frac{\partial v}{\partial y}+w\frac{\partial v}{\partial z}\right)=-\frac{\partial p}{\partial y}+\frac{\partial}{\partial x}\left(\mu\frac{\partial v}{\partial x}\right)+\frac{\partial}{\partial y}\left(\mu\frac{\partial v}{\partial y}\right)+2\rho\Omega u+\rho\Omega^2 H \quad (3)$$

$$\rho C_p\left(u\frac{\partial T}{\partial x}+v\frac{\partial T}{\partial y}+w\frac{\partial T}{\partial z}\right)=\frac{\partial}{\partial x}\left(k\frac{\partial T}{\partial x}\right)+\frac{\partial}{\partial y}\left(k\frac{\partial T}{\partial y}\right) \quad (4)$$

In the real flow, the net buoyancy force combines rotational and normal gravitational effects and is thus dependent on the angular orientation of the system. This analysis accounts only for the centrifugal acceleration and ignores normal gravity (see equation (3)); and the results are expected to be valid only in the situation where the rotational acceleration is at least an order of magnitude greater than the normal gravitational acceleration g. In addition, it is assumed that $H >> b$.

The last term in equation (3) can be expressed as

$$\Omega^2 H[\rho-\rho_b]+\rho_b\Omega^2 H \quad (5)$$

For a gas $\rho = \rho(P,T)$, and in general

$$\Delta\rho=\left(\frac{\partial\rho}{\partial T}\right)_P\Delta T+\left(\frac{\partial\rho}{\partial P}\right)_T\Delta P+\left(\frac{\partial^2\rho}{\partial P\partial T}\right)\Delta T\Delta P+\tfrac{1}{2}\left(\frac{\partial^2\rho}{\partial T^2}\right)\Delta T^2+\tfrac{1}{2}\left(\frac{\partial^2\rho}{\partial P^2}\right)\Delta P^2+\ldots$$

Defining

$$\beta\equiv-\frac{1}{\rho}\left(\frac{\partial\rho}{\partial T}\right)_P$$

and letting $\Delta p \sim \Omega^2 H D_H \Delta\rho$, for a perfect gas this yields

$$\Delta\rho=\frac{-\rho\beta\Delta T+\rho\dfrac{\Delta T^2}{T^2}}{1-\dfrac{\Omega^2 H D_H}{RT}+\dfrac{\Delta T\Omega^2 H}{RT^2}}$$

where $\Delta\rho$, ΔP and ΔT are spanwise variations. For the problem of interest $\Delta T/T << 1$; $\Omega^2 H D_H/RT << 1$ and the expression for $\Delta\rho$ reduces to

$$\Delta\rho=-\rho\beta\Delta T \quad (6)$$

Equation (5) thus becomes

$$-\beta\rho\Omega^2 H[T-T_b]+\rho_b\Omega^2 H \quad (7)$$

where

T_b = local bulk temperature,
ρ_b = local density based on local bulk temperature, and
$\beta = 1/T_b$

In a practical rotating duct situation with high wall heat fluxes, the bulk temperature, density, and other properties can vary quite significantly in the axial direction, leading to large axial variations in Re and Gr. To account for this, the fluid properties were assumed to be constant in the transverse direction and allowed to vary with bulk temperature in the Z direction. The local value of bulk temperature T_b is obtained from the uniform wall heat flux condition

$$q_w(2a+2b)=\rho_b(ab)W_b C_p\frac{dT_b}{dZ} \quad (8)$$

There was one exception to the assumption of constant properties in the transverse direction. This is in equations (3) and (7) where density was allowed to vary in the transverse plane, giving rise to the buoyancy term.

Nomenclature

a, b = lengths of sides of rectangular duct (see Fig. 1)
c_p = specific heat
D_H = hydraulic diameter $= \dfrac{4ab}{2(a+b)}$
f = friction factor $= \dfrac{\bar{\tau}_w}{\dfrac{\rho_b w_b^2}{2}}$
f_0 = fully developed friction factor from variable property solution in stationary duct with no body forces
Gr = Grashof number $= \dfrac{\Omega^2 H\beta q_w D_H^4}{k\nu^2}$
h = heat transfer coefficient $= \dfrac{q_w}{(T_{w,\text{avg}}-T_b)}$
h^+ = local heat transfer coefficient $= \dfrac{q_w}{(T_{w,\text{local}}-T_b)}$
H = radial distance from axis of rotation to duct
k = fluid thermal conductivity
l = linear distance around duct perimeter
$\dot{m}$ = mass flow rate
n = distance normal to wall
Nu = Nusselt number based on $T_{w,\text{avg}}$ $= \dfrac{hD_H}{k}$
Nu_0 = fully developed Nusselt number from variable property solution in stationary duct with no body forces
p = pressure
p_0 = pressure at inlet
$p(z)$ = pressure at point (z)
P = dimensionless pressure $= \dfrac{p}{\rho w_b^2}$
$\bar{P}$ = spaced-averaged pressure over cross-sectional plane
Pr = Prandtl number

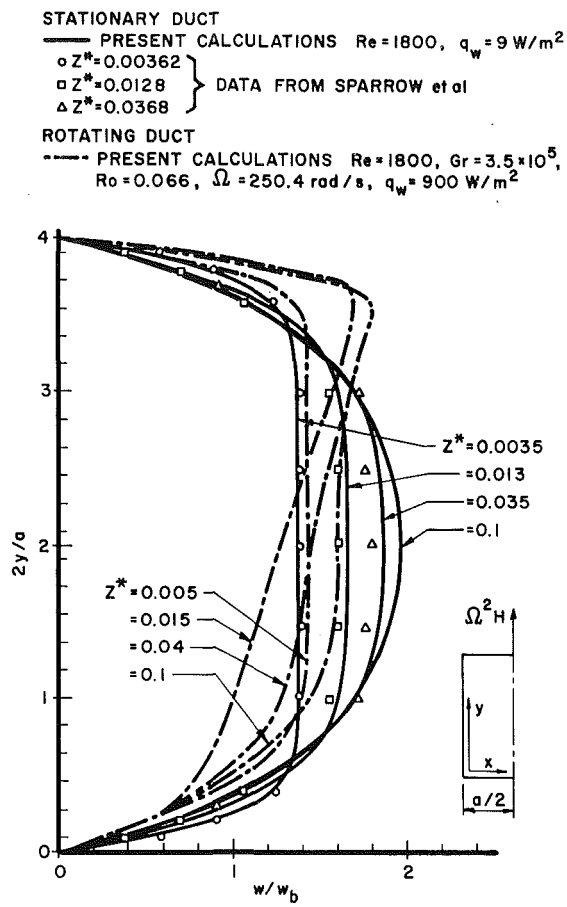

Fig. 2 Development of axial velocity profiles at $x = a/2$; stationary duct without body force and rotating duct

Following Patankar and Spalding [16] the axial (z direction) and lateral momentum equations were uncoupled and the shear stresses acting on the lateral plane were neglected. The pressures in the axial and lateral momentum equations are uncoupled and computed separately. In the axial momentum equation, the quantity $\hat{p}$ is considered to be a space-averaged pressure over the cross-sectional plane and, as will be seen later, $\partial\bar{p}/\partial z$ is assumed known before the other two pressure gradients $\partial p/\partial x$ and $\partial p/\partial y$ are calculated. This practice is implicit in traditional calculations of two-dimensional boundary layers as well. In that case, the lateral momentum equation is not solved, so the approximation is not obvious.

Substituting equation (7) into equation (3) and using all the assumptions described above leads to the final version of the equations solved in this study. In nondimensional form they are:

$$U\frac{\partial W}{\partial X}+V\frac{\partial W}{\partial Y}+W\frac{\partial W}{\partial Z}=-\frac{\partial \bar{P}}{\partial Z}+\frac{1}{\mathrm{Re}}\left[\frac{\partial^2 W}{\partial X^2}+\frac{\partial^2 W}{\partial Y^2}\right] \tag{9}$$

$$U\frac{\partial U}{\partial X}+V\frac{\partial U}{\partial Y}+W\frac{\partial U}{\partial Z}=-\frac{\partial P}{\partial X}+\frac{1}{\mathrm{Re}}\left[\frac{\partial^2 U}{\partial X^2}+\frac{\partial^2 U}{\partial Y^2}\right]-2\mathrm{Ro}V \tag{10}$$

$$U\frac{\partial V}{\partial X}+V\frac{\partial V}{\partial Y}+W\frac{\partial V}{\partial Z}=-\frac{\partial P}{\partial Y}+\frac{1}{\mathrm{Re}}\left[\frac{\partial^2 V}{\partial X^2}+\frac{\partial^2 V}{\partial Y^2}\right]+2\mathrm{Ro}U+\left(\frac{H}{D_H}\right)\mathrm{Ro}^2-\frac{\mathrm{Gr}}{\mathrm{Re}^2}\theta \tag{11}$$

$$\left(\frac{\partial U}{\partial X}+\frac{\partial V}{\partial Y}\right)+\frac{\partial(\rho_b W)}{\rho_b \partial Z}=0 \tag{12}$$

$$U\frac{\partial \theta}{\partial X}+V\frac{\partial \theta}{\partial Y}+W\frac{\partial \theta}{\partial Z}+\frac{4W}{\mathrm{RePr}}=\frac{1}{\mathrm{RePr}}\left[\frac{\partial^2 \theta}{\partial X^2}+\frac{\partial^2 \theta}{\partial Y^2}\right] \tag{13}$$

The initial conditions at $Z = 0$ are:

$$\theta=0, W=1, U=0, \text{ and } V=0$$

The wall boundary conditions are given as

$$W=U=V=0$$

$$\frac{\partial \theta}{\partial n}=-\frac{1}{D_H}$$

The calculation procedure solves a three-dimensional problem using a marching technique to calculate the

Nomenclature (cont.)

q_w = wall heat flux
Re = Reynolds number $= \dfrac{w_b D_H}{\nu}$
Re(0) = Reynolds number at duct inlet
Ro = rotation number $= \dfrac{\Omega D_H}{w_b}$
R = gas constant
T = temperature
T_b = bulk fluid temperature
T_w = wall temperature
$T_{w,\mathrm{avg}}$ = average wall temperature $= \dfrac{1}{2(a+b)}\int T_w dl$
$T_{w,\mathrm{local}}$ = local wall temperature
u, v, w = velocity components (see Fig. 1)
U, V, W = dimensionless velocity components; $U=\dfrac{u}{w_b}, V=\dfrac{v}{w_b}, W=\dfrac{w}{w_b}$
w_b = average axial velocity
x, y, z = Cartesian coordinates (see Fig. 1)
X, Y, Z = dimensionless coordinates; $X=\dfrac{x}{D_H}, Y=\dfrac{y}{D_H}, Z=\dfrac{z}{D_H}$
Z^* = dimensionless axial distance $\equiv \dfrac{z}{D_H \mathrm{Re}(0)}$
β = coefficient of thermal expansion
θ = dimensionless temperature $= \dfrac{(T-T_b)k}{q_w D_H}$
μ = absolute viscosity
ν = kinematic viscosity
ρ = density
ρ_b = bulk density
τ_w = wall shear stress
$\bar{\tau}_w$ = average wall shear stress $= \dfrac{1}{2(a+b)}\int \tau_w dl$
Ω = angular velocity

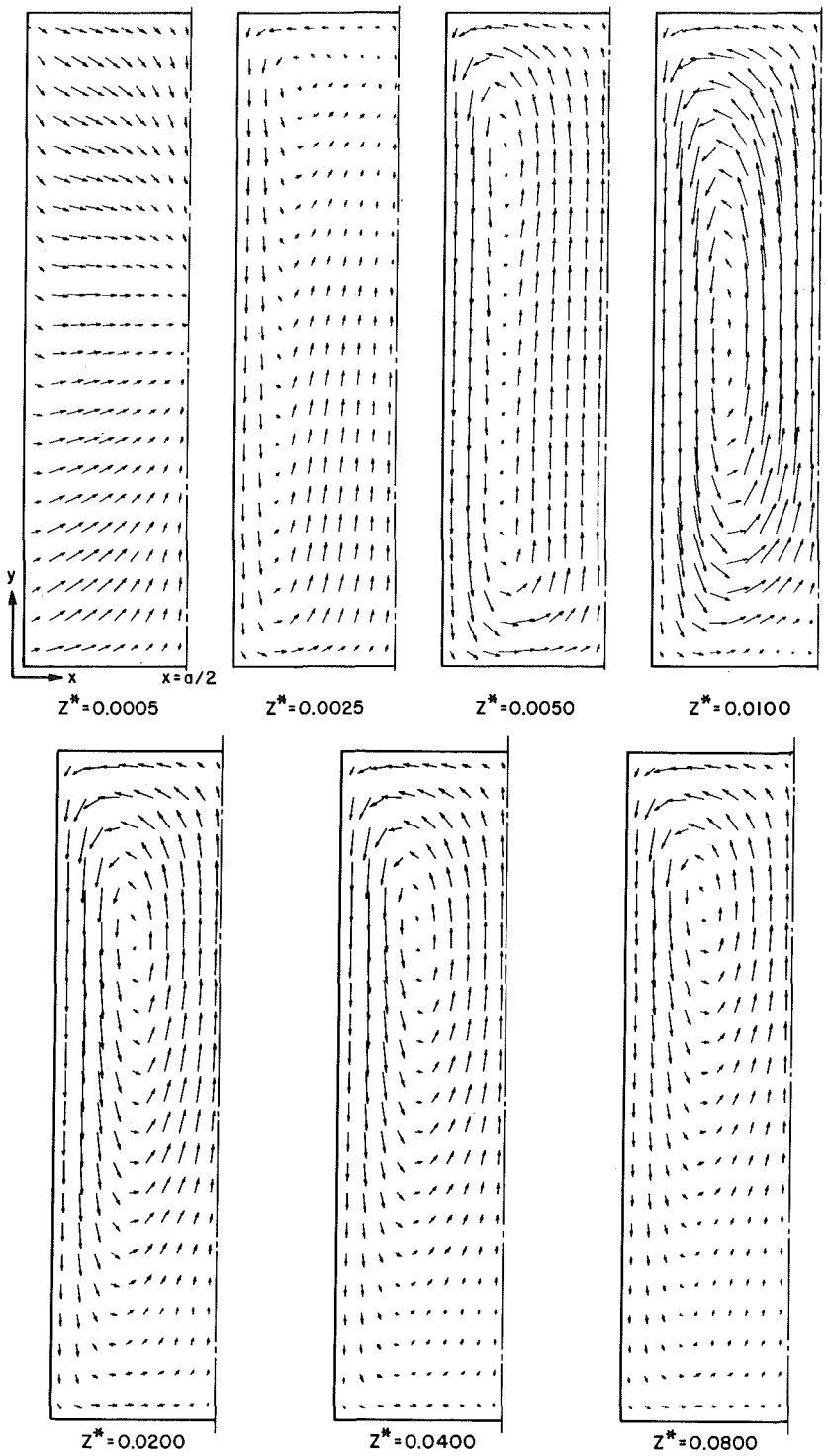

Fig. 3 Development of transverse flow patterns: Re = 1800, Ro = 0.066, Gr = 3.5 x 10^5, Pr = 0.7

sequential development of the flow along its primary direction. The method is described in detail by Patankar and Spalding [16] and Neti and Eichhorn [17] and some of the important features are described below.

The deletion of the stresses in the lateral plane and the uncoupling of the longitudinal ($\bar{P}$) and lateral (P) pressures allow two-dimensional computer storage and marching integration. The solution procedure uses a staggered uniform grid [18]. Some of the assumptions made in deriving the difference equation for a dependent variable ϕ with a transport property Γ are: (*i*) In the z-direction ϕ is assumed to vary in a stepwise manner, with the downstream ϕ values prevailing over the interval of integration. This makes the difference scheme fully implicit. (*ii*) In the x–y plane, the value of ϕ is assumed to remain uniform and equal to its value at the center of the downstream face of the control volume. (*iii*) A combination of central and upwind differencing is used in the computations.

The choice of central or upwind differencing is based on the local value of the Peclet number. This procedure has been shown to be an effective technique for solving viscous flow problems [16, 19]. While the authors know of no other results for a rectangular duct with which to compare these results, Neti and Eichhorn [20] used upwind differencing to compute

the laminar flow in a square duct. A comparison of their results with those of Carlson and Hornbeck [21], who used central differences for the convective terms, showed very good agreement for both lateral and axial velocities.

The computational procedure consists of estimating axial pressure drop and calculating the corresponding downstream axial velocity field using the upstream parameters. The newly calculated axial velocity field, which may not satisfy continuity, is then corrected using the overall mass flow balance and corrected values of axial pressure drop. This iteration is continued until the correct axial velocities and pressure drop are determined. The equations for the cross plane velocities (u and v) and the corresponding pressure field are then solved with a similar guess and correction procedure using the known axial velocity distributions. The energy equation is then solved to complete the solution for one step.

For this class of problems, it is possible to define the heat transfer coefficient and friction factor in various ways. The parameters are used as follows in this study:

- At any axial position, the heat transfer coefficient h is based on the peripheral average of the wall temperatures at that z location. Hence

$$h \equiv \frac{q_w}{T_{w,\text{avg}} - T_b} \quad \text{and} \quad \text{Nu} \equiv \frac{hD_H}{k}$$

- At any axial position, the friction factor f is based on the peripheral average of the wall shear stresses at that z location, leading to

$$f \equiv \frac{\bar{\tau}_w}{\frac{1}{2}\rho_b w_b^2}$$

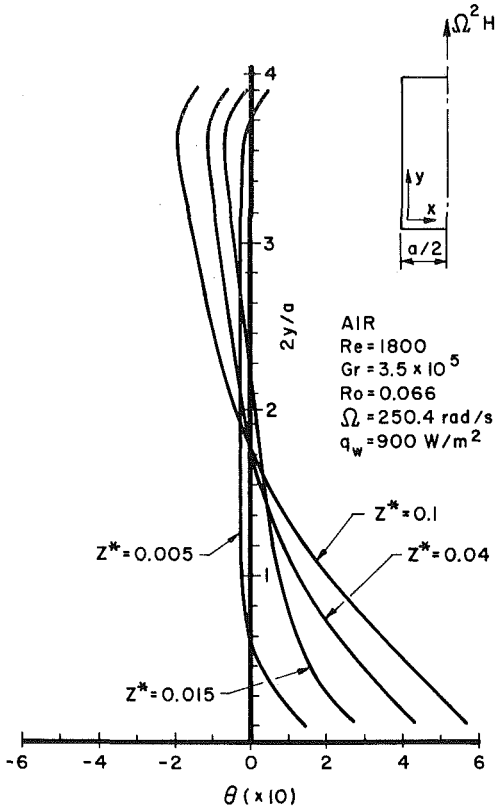

Fig. 4 Development of temperature profiles along duct centerline

Verification of Computations and Numerical Results

As with others, the computational procedure used is subject to computational instabilities and numerical truncation and roundoff errors; and a series of computer runs was carried out for the stationary duct case using different grid spacings and axial step sizes to determine the effects of spacing on accuracy and stability. One group of calculations, carried out for mesh sizes in the 2 × 1 rectangular duct from 16 × 16 to 32 × 32, showed that increases in mesh fineness beyond 24 × 24 caused less than a 2.5 percent change in dimensionless pressure drop. Calculations on the effect of axial step size showed that reductions in dimensionless step size from $\Delta Z^* = 0.0005$ to 0.000125 caused changes in dimensionless pressure drop of less than 1 percent. These calculations were all done for the first part of the inlet region and all the comparisons indicated above were made at the axial position $Z^* = 0.003$. Similar calculations with the same program for 1/4 of a square duct using 11 × 11 and 15 × 15 grids showed less than a 1 percent difference in fully developed friction factor and Nusselt number between the two cases. As a result of these trial runs, the 24 × 24 mesh and axial step size of $Z^* = 0.00025$ were used for all subsequent calculations presented in this paper for the 2 × 1 duct.

Preliminary calculations were performed for air for the case of the stationary duct without buoyancy or Coriolis terms in the equations and with small heat flux q_w. In this case the solution of the momentum equations is independent of the energy equation and the computed velocities and pressures can be compared directly to isothermal flow measurements obtained by Sparrow et al. [22]. The results for dimensionless pressure drop, centerline velocity, and the axial velocity profiles are in good agreement with the experimental data; and a comparison is given for the axial velocity profiles in Fig. 2. However, agreement on axial velocity and pressure variations does not necessarily guarantee agreement on the secondary flows. Since there are no experimental or analytical results that can be used to compare the u and v velocity components, it is not possible to directly validate that part of the solution. However, as already noted, one of the authors has obtained results for laminar developing flow in a square duct [20] using this technique and was able to show excellent agreement in his secondary flows with those obtained by other investigators.

Theoretical results for fully developed friction factors in rectangular ducts are summarized in Shah and London [23] for the 2 × 1 configuration. These show that $f\text{Re} = 15.545$, which is in close agreement with the value of 15.4 obtained from the present calculations. For the stationary duct, the results of the present calculations for Nusselt number versus Z^* converge to a value of Nu = 3.1 at large values of Z^*. Using solution techniques for the fully developed case, Shah [24] and Iqbal et al. [25] reported fully developed values of Nu = 3.02.

Results for air with a high heat flux ($q_w = 900\ W/m^2$) were also obtained and these indicate a significant influence of axial property variation on the solutions. Later in this paper, values for fully developed friction factor (f_0) and Nusselt number (Nu_0) in a stationary duct are used as reference values against which to measure rotational effects. Values from the variable property solutions are used for the purpose of these comparisons.

The effects of rotation on the development of the flow in the rectangular duct are shown in Fig. 3 for the left half of the duct for Re = 1800, Gr = 3.5 × 10^5, and Ro = 0.067. The arrows represent the velocity vectors in the transverse plane. At the inlet to the duct, the flow develops as a classical boundary layer, where all the transverse velocities are directed toward the center of the duct. As the fluid reaches a non-dimensional axial distance $Z^* = 0.005$ the effects of the body forces start to dominate, resulting in a reorganization of the transverse flow patterns. Further downstream, the flow exhibits a typical mixed convection behavior with the fluid "rising" along the hot wall against the body force. The axial

development of the axial velocity and temperature profiles are shown in Figs. 2 and 4.

The flow cells shown in Fig. 3 indicate the presence of a severe asymmetry in the direction of the buoyancy term. The effect of this on the temperature distribution is shown in Fig. 5 where the fully developed wall temperature is indicated as a function of position around the perimeter. Strong circumferential variations in the local Nusselt number Nu^+ based on the local wall temperature, and shear stress also occur.

The analysis allows for axial variations of temperature and pressure; thus the Reynolds number, Grashof number, and rotation number also vary along the axis. Figure 6 shows the axial variations in these quantities for the case illustrated in Figs. 3–5.

Similar calculations were performed for Reynolds numbers varying from 250 to 2000 and Grashof numbers from zero up to 10^7. The rotation number Ro varied as shown in Table 1 during the course of these runs.

A summary of the effects of Grashof number on Nu and friction factor in the inlet region is given in Figs. 7 and 8. The abrupt changes in the slopes of the curves in the range of $Z^* = 0.0025$ to 0.010 is due to reorientation of the transverse flow patterns as described earlier. This effect becomes negligible at low values of Gr number, but is quite severe in the higher Gr range. At the very highest values of Gr for which computations were made, there was evidence of the development of additional rotational cells in the transverse plane (see Fig. 9).

The results for Nu and friction factor for the fully developed case are given in Figs. 10 and 11 as plots of Nu/Nu_0 and $f\mathrm{Re}/(f\mathrm{Re})_0$ versus Gr. These show a very good correlation for different values of Re and a limited range of Ro. Also shown on these plots are results from the numerical solutions of Morris and Woods for a circular duct [4] and Morris and Dias for a square duct [14] rotating about a parallel axis.

Finally shown in Fig. 12 is a comparison between the numerical results for heat transfer with some recent data obtained from experiments with air in a rotating heated rectangular duct with a 2/1 aspect ratio [26]. The figure shows the measured values of Nusselt number as a function of Grashof number in the inlet region at $Z^* = 0.029$. Additional data for both Nusselt number and nondimensional pressure drop were obtained at other locations in the entrance region, and a full description of these along with a thorough comparison with the finite difference results will be given in a future paper.

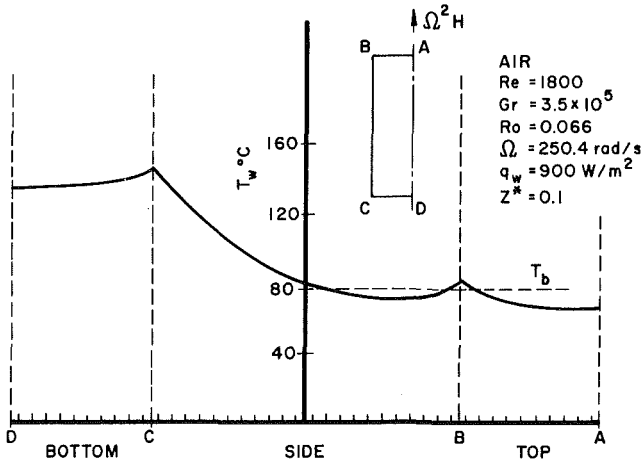

Fig. 5 Circumferential variation of wall temperature at $Z^* = 0.1$

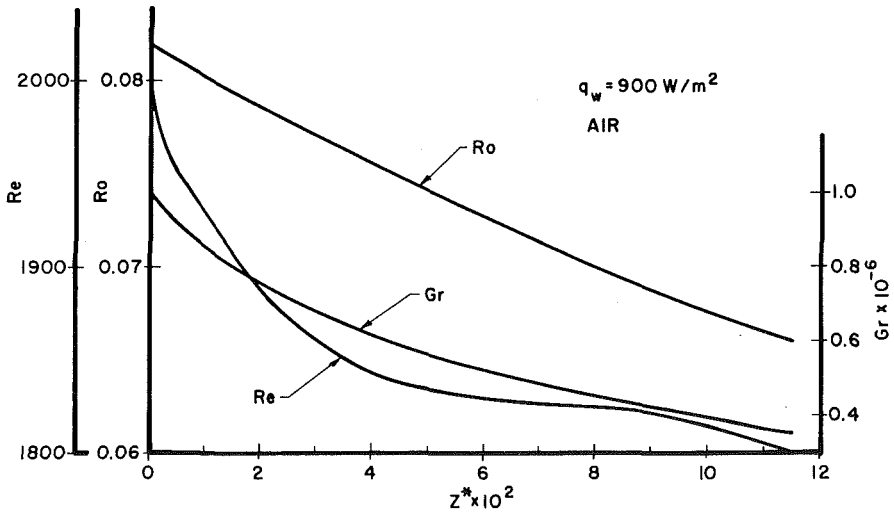

Fig. 6 Axial variation of Re, Gr, Ro

Summary

- At the very beginning of the entrance region in the duct, the transverse velocities are all directed toward the center of the duct. Within a short axial distance the flow reorganizes and a recirculating flow pattern develops.

Table 1 Tabulation of Gr, Re, and Ro at $Z^* = 0$ and $Z^* = 0.12$; $q_w = 900$ W/m²

Run	Gr(0)	Gr(0.12)	Re(0)	Re(0.12)	Ro(0)	Ro(0.12)
A	0	0	2000	1800	0	0
B	6.3×10^4	2.1×10^4	500	450	0.082	0.066
C	1.6×10^5	5.4×10^4	250	225	0.26	0.21
D	6.4×10^5	2.25×10^5	500	450	0.26	0.21
E	1.6×10^6	5.5×10^5	1000	900	0.21	0.17
F	2.5×10^6	8.8×10^5	2000	1800	0.13	0.1
G	1×10^7	3.3×10^6	2000	1800	0.26	0.21

• The flow slowly approaches a fully developed condition, reaching asymptotic values of Nu, fRe, and velocity profile shape at values of Z^* in excess of 0.12. The fully developed solutions for Nu and fRe are independent of Reynolds number and are relatively insensitive to Ro. These results are in good qualitative agreement with fully developed solutions for gases in square ducts and circular tubes. The results of the analysis for heat transfer in the entrance region are in very

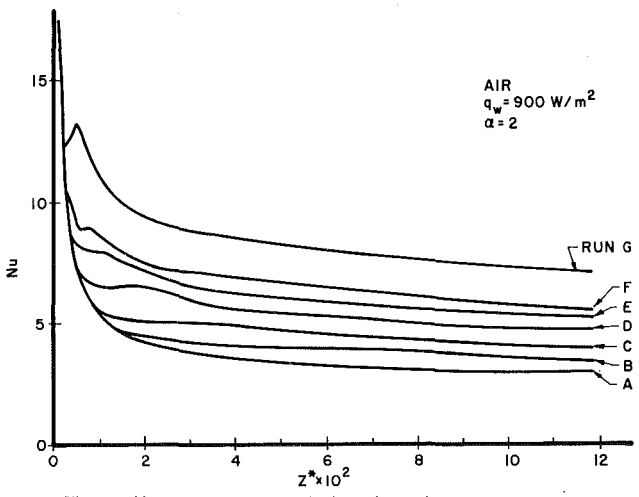

Fig. 7 Nusselt number variation along duct for different Gr

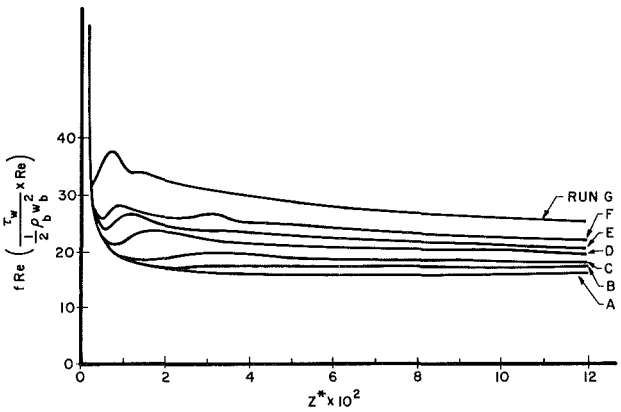

Fig. 8 Friction factor variation along duct for different Gr

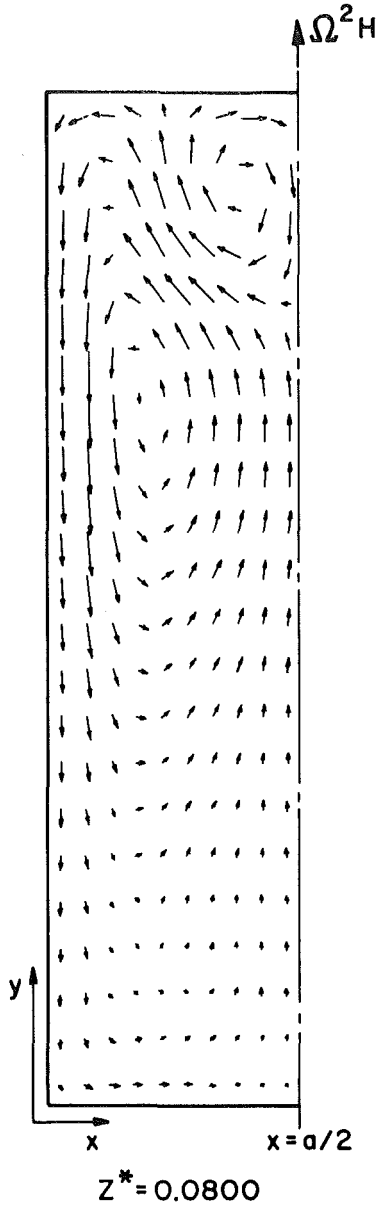

Fig. 9 Flow pattern at $Z^* = 0.08$ for Gr = 1.15 × 10^6 (run *F*)

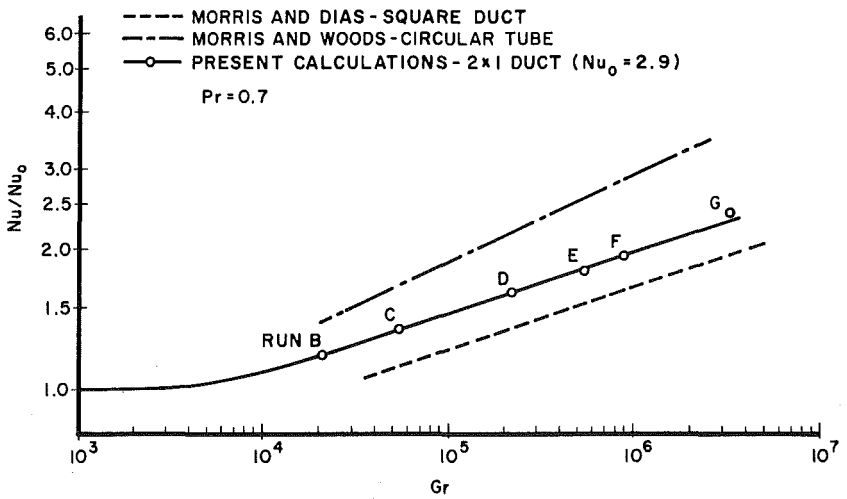

Fig. 10 Effect of Gr on Nu for fully developed flow

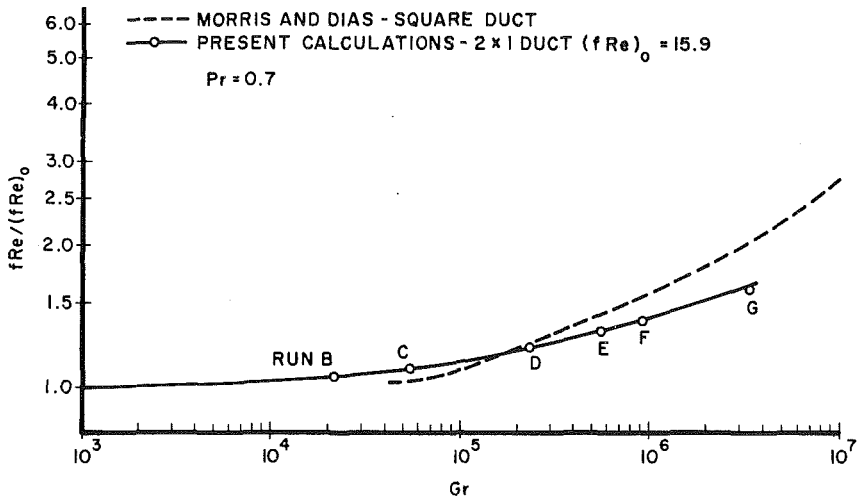

Fig. 11 Effect of Gr on friction factor for fully developed flow

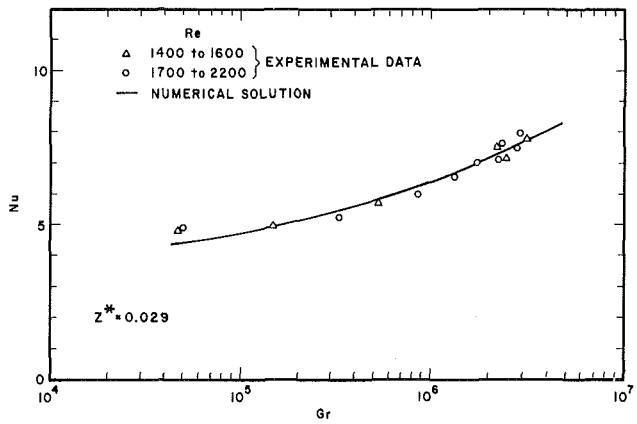

Fig. 12 Variation of Nu with Gr in inlet region: comparison of theory with experiment

close quantitative agreement with recent experimental data obtained with air in a rectangular duct.

- The effects of rotation on Nusselt number and friction factor can be quite large. For a fully developed flow at Grashof number of 5×10^6, the Nusselt number is 2.3 times the low Grashof number value and the friction factor is 1.8 times the value for low Gr. Rotation has an influence on Nusselt number and friction factor for values of Gr in excess of 5×10^3.
- As a consequence of the transverse circulation patterns developed in the flow there are significant circumferential temperature variations around the duct. These lead to large variations in heat transfer coefficient for the uniform wall heat flux case. The standard definition of a local heat transfer coefficient h^+ is not very useful here, due to situations where the local wall temperature is less than the local bulk temperature, leading to negative local heat transfer coefficients.

Acknowledgments

This study was supported by the National Science Foundation under Grant MEA 7923751.

References

1 Morris, W. D., "Laminar Convection in a Heated Vertical Tube Rotating About a Parallel Axis," *Journal Fluid Mechanics*, Vol. 21, Part 3, 1965, p. 453.

2 Mori, Y., and Nakayama, W., "Forced Convective Heat Transfer in a Straight Pipe Rotating About a Parallel Axis (Laminar Region)," *Int. J. Heat Mass Trans.*, Vol. 10, 1967, p. 1179.

3 Woods, J. L., and Morris, W. D., "An Investigation of Laminar Flow in the Rotor Windings of Directly-Cooled Electricial Machines," *J. Mech. Eng. Sci.*, Vol. 16, 1974, p. 408.

4 Morris, W., *Heat Transfer and Fluid Flow in Rotating Coolant Channels*, Research Studies Press, 1981.

5 Morris, W. D., "Heat Transfer Characteristics of a Rotating Thermosyphon," Ph.D. thesis, University of Wales, Swansea, 1964.

6 Morris, W. D., "Thermal Laminar Convection in a Uniformly Heated Rectangular Duct," Thermo and Fluid Mech. Convention. I. Mech. E., Bristol, Paper No. 4, 1968.

7 Morris, W. D., "Some Observations on the Heat Transfer Characteristics of a Rotating Mixed Convection Thermosyphon," Min. Tech. ARC CP No. 1115, 1970.

8 Davies, T. H., and Morris, W. D., "Heat Transfer Characteristics of a Closed Loop Rotating Thermosyphon," *Proc. Third Int. Heat Transfer Conf.*, AIChE, Chicago, Vol. 2, 1966, p. 172.

9 Woods, J. L., and Morris, W. D., "An Investigation of Laminar Flow in the Rotor Windings of Directly Cooled Electric Machines," *J. Mech. Eng. Sci.*, Vol. 16, 1974, p. 408.

10 Woods, J. L., "Heat Transfer and Flow Resistance in a Rotating Duct System," D. Phil. thesis, University of Sussex, Falmer, England, 1975.

11 Skiadaressis, D., and Spalding, D. B., "Laminar Heat Transfer in a Pipe Rotating About a Parallel Axis," Imperial Coll. Science and Tech. Mech. Eng. Report No. HTS/76/23, 1976.

12 Sakamoto, M., and Fukui, S., "Convective Heat Transfer of a Rotating Tube Revolving About an Axis Parallel to Itself," Elec. and Nuclear Eng. Lab., Tokyo Shibaura Elec. Co. Ltd., Kawasaki, Japan, 1971.

13 Dias, F. M., "Heat Transfer and Resistance to Flow in Rotating Square Tubes," D. Phil. thesis, University of Sussex, Falmar, England, 1978.

14 Morris, W. D., and Dias, F. M., "Laminar Heat Transfer in Square-Sectioned Ducts Which Rotate in the Parallel-Mode," *Power Ind. Res.*, Vol. 1, 1981.

15 Patankar, S., *Numerical Heat Transfer and Fluid Flow*, McGraw-Hill, 1980.

16 Patankar, S., and Spalding, G., "A Calculation Procedure for Heat, Mass and Momentum Transfer in Three Dimensional Parabolic Flows," *Int. J. Heat Mass Transfer*, Vol. 15, 1972, p. 1787.

17 Neti, S., and Eichhorn, R., "Computations of Developing Turbulent Flow in a Square Duct," in: *Turbulent Boundary Layers*, ed. H. Weber, ASME, New York, 1979.

18 Harlow, F., and Amsden, A., "Numerical Calculation of Almost Incompressible Flow," *Journal of Computational Physics*, Vol. 3, 1968, p. 1.

19 Spalding, D. B., "A Novel Finite Difference Formulation for Differential Expressions Involving Both First and Second Derivatives," *Int. J. Numerical Methods in Eng.*, Vol. 4, 1972, pp. 551–559.

20 Neti, S., and Eichhorn, R., "Combined Hydrodynamic and Thermal Development in a Square Duct," *Numerical Heat Transfer*, Vol. 6, No. 4, 1983, pp. 497–510.

21 Carlson, G. A., and Hornbeck, R. W., "A Numerical Solution for Laminar Entrance Flow in a Square Duct," *Transactions ASME*, Vol. 95, 1973, pp. 25–30.

22 Sparrow, E., Hixon, C., and Shavit, G., "Experiments on Laminar Flow Development in Rectangular Ducts," *ASME J. Basic Engineering*, March 1967, p. 116.

23 Shah, R., and London, A., *Laminar Flow Forced Convection in Ducts*, Supplement 1: Advances in Heat Transfer, Academic Press, 1978.

24 Shah, R., "Laminar Flow Friction and Forced Convection Heat Transfer in Ducts of Arbitrary Geometry," *Int. J. Heat Mass Transfer*, Vol. 18, 1975, p. 849.

25 Iqbal, M., Khatry, A., and Aggarwala, B., "On the Second Fundamental Problem of Combined Free and Forced Convection Through Vertical Noncircular Ducts," *Appl. Sci. Res.*, Vol. 26, 1972, p. 183.

26 Bayat, F., "Heat Transfer and Pressure Drop in a Rotating Rectangular Duct," MS thesis, Lehigh University, Department of Mechanical Engineering and Mechanics, Sept. 1984.

Natural Convection Heat Transfer for a Concentric Tube Thermosiphon

J. L. Steimke
E. I. du Pont de Nemours & Co.,
Savannah River Laboratory,
Aiken, SC 29806

Natural convection heat transfer for a single-phase thermosiphon formed by two concentric tubes and a central rod filled with water is studied theoretically and experimentally. The two annuli between the tubes and the rod are joined at the top and bottom and form a flow loop. The middle tube is heated while the outer tube is cooled. In this one-dimensional model equations for continuity, momentum, and energy for steady laminar flow are written and solved numerically. There is reasonably good agreement between the analytically and experimentally determined temperatures and convective velocities in the thermosiphon.

Introduction

There are a number of engineering applications for thermosiphons. Examples listed by Japikse [1] include the cooling of turbine blades, electrical machine rotors, transformers, nuclear reactors, and internal combustion engines. Two other applications are for solar water heaters [2] and the Trombé method for solar house heating [3]. Concentric tube thermosiphons have been proposed for the extraction of geothermal energy and investigated experimentally by Seki et al. [4]. Chato [5], Keller [6], Welander [7], Creveling et al. [8], Greif et al. [9], Zvirin et al. [10], and Kaizerman et al. [11] have analyzed different types of closed loop thermosiphons.

This study is concerned with a closed loop thermosiphon where the channels are the annuli between three concentric cylindrical surfaces. The Savannah River Plant (SRP) near Aiken, SC has nuclear reactors filled with tubular assemblies containing uranium. Under certain conditions after reactor shutdown the residual decay heat in the assemblies is removed by natural convection only. The assemblies act as thermosiphons. This study allowed a determination of the amount of heat that could be removed from the assemblies without exceeding the maximum temperature limit.

The concentric tube thermosiphon is more complicated than the usual closed loop thermosiphon because the annuli are coupled by conduction through the middle tube as well as convection around the loop and because recirculation cells form in the outer annulus. The method of analysis described here is directly applicable to single-phase geothermal concentric tube thermosiphons and also to Trombé solar heating which is mathematically similar. The method was applied to the two-tube concentric thermosiphon of Seki et al. [4]. The calculated heat transfer rates agree well with the Seki experimental data.

Description of Thermosiphon

The concentric thermosiphon is shown in Fig. 1. It consists of an inner rod, a heater tube, and a casing. The tubes and the rod have longitudinal ribs which separate them and form annular passages. The casing is longer than the heater tube and there are spaces inside the casing above and below the heater tube that join the annuli. During operation of the thermosiphon, water in the inner annulus is heated and rises. Water in the outer annulus descends as it loses heat to the relatively cool casing and the basin water surrounding it. Heat loss to the basin is by natural convection.

Contributed by the Heat Transfer Division for publication in the JOURNAL OF HEAT TRANSFER. Manuscript received by the Heat Transfer Division March 10, 1983.

Experimental Apparatus

A dimensionally exact replica of one type of SRP reactor assembly was built for testing. The casing, heater, and inner rod were made from aluminum, stainless steel, and glass-filled polyester, respectively. Stainless steel was chosen for the heater because it has a relatively high electrical resistivity and it has a thermal conductivity similar to that of uranium. The heater was electrically insulated from the casing by ribs made of glass-filled polyester. Up to 24 kW of power for the heaters was supplied by two large rectifiers. Copper cables passing through holes in the casing were connected to the ends of the heater. The holes were sealed with Teflon® gaskets to prevent water flow in or out of the thermosiphon. The entire assembly was placed in a tank of water. The top portion of the casing was above the surface of the water.

Instrumentation of Thermosiphon

The thermosiphon was instrumented with electrical conductivity probes for fluid velocity measurements and thermocouples. The test assembly held five thermocouples, one at each end of both annuli and one embedded in the heater two inches from the top. In addition, there were three thermocouples in the tank water surrounding the thermosiphon: at the top, bottom, and midheight.

The thermosiphon also held four electrical conductivity probes, one at each end of the two annuli. The conductivity probes consisted of double wires whose bare tips were separated by 6 mm. The probes were used to measure the length of time required for a pulse of salt tracer to be carried the length of the thermosiphon. The salt tracer solution was

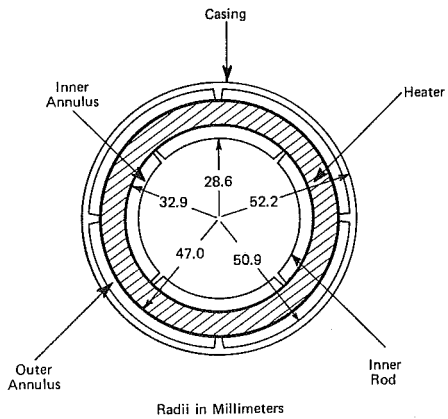

Fig. 1 Cross-sectional view of thermosiphon

made neutrally buoyant with the addition of ethanol. The accuracy of the method was estimated by comparing experimental and theoretical ratios of the velocities in the inner and outer annuli for a series of tests. The discrepancies ranged up to 26 percent. The estimated uncertainty in measurements was taken to be 26 percent.

Derivation of Equations Describing Thermosiphon

Equations are written for conservation of mass, momentum, and energy. The equation for conservation of mass is

$$\pi(r_2^2 - r_1^2)V_A = \pi(r_4^2 - r_3^2)V_B = Q$$

The momentum equation is derived first starting with an equation used by Zvirin et al. [10]

$$\frac{\partial p}{\partial s} + \rho g \mathbf{e}_z \cdot \mathbf{e}_s + F_F = 0 \tag{1}$$

In this one-dimensional analysis the coordinate s follows the flow loop in the direction of the convective flow. Some manipulation is necessary to put equation (1) in a useful form. Integrating the equation around the loop eliminates the pressure term. Substituting coefficients of frictional losses for the frictional term gives

$$g\rho dz + (R_{FA} + R_{FB})Q = 0 \tag{2}$$

where coefficients R_{FA} and R_{FB} are defined as the frictional loss in the corresponding annulus divided by Q. The coefficients do not include entrance and exit losses because those losses are negligible at the low velocities encountered in this study. The experimentally measured Reynolds number never exceeded 800. The frictional loss for a simple laminar flow in the annulus is given by Bird et al. [12]. For the inner annulus the coefficient is

$$R_{FA} = \frac{8\mu L/\pi r_2^4}{1 - r_1^4/r_2^4 - \dfrac{(1 - r_1^2/r_2^2)^2}{\ln r_2/r_1}} \tag{3}$$

The radii of the tubes and the rod are labeled in Fig. 2.

While the flow in the outer annulus is laminar, the pattern

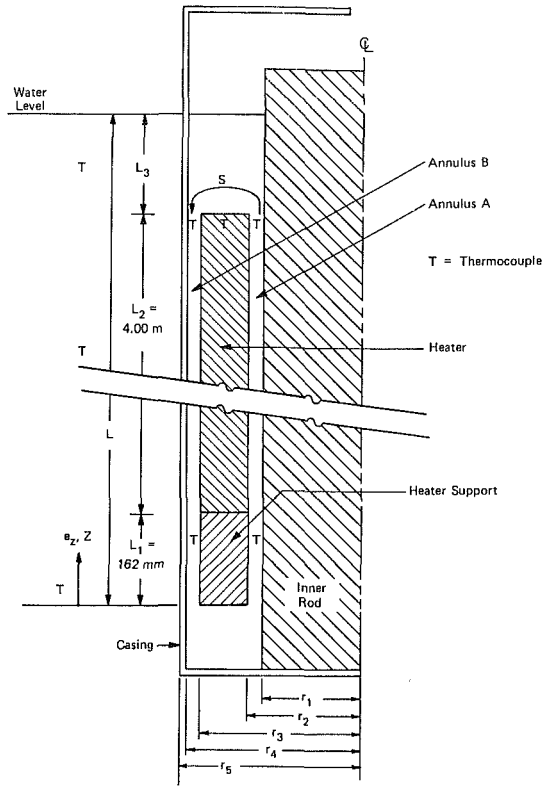

Fig. 2 Side view of thermosiphon

is much more complicated because of the relatively large temperature gradient across that annulus not found in the inner annulus. The flow pattern affected both the frictional loss and heat transfer in the outer annulus. Elder [13] showed experimentally that under some conditions a number of convection cells form when a temperature gradient is impressed on a tall, thin cavity filled with liquid. The convection cells, which are stacked one upon another, enhance heat transfer across the cavity. Randall et al. [14] found that

Nomenclature

A = annulus cross-sectional area
C = specific heat
$\mathbf{e}_s, \mathbf{e}_z$ = unit vectors in s and z directions
F_F = frictional force per unit volume
g = acceleration of gravity
G = volumetric heat generation rate
Gr = Grashof number, $\dfrac{L^3\rho^2 g\beta\Delta T}{\mu^2}$
Gr_B = Grashof number, $\dfrac{\rho^2 g\beta\Delta T(r_4 - r_3)^3}{\mu^2}$
h = heat transfer coefficient, $q/\Delta T$
k = thermal conductivity
L = submerged length of thermosiphon
L_1, L_2, L_3 = lengths of sections of thermosiphon
Nu = hL/k
Nu_B = $h(r_4 - r_3)/k$
Nu_x = $\dfrac{q_0 X}{\Delta T k}$
Pr = Prandtl number, $\mu C/k$
Q = volumetric flowrate
q = heat flux
r = radius
Ra_x = $\dfrac{g\beta\Delta T x^4 C\rho^2}{\mu L k}$
R_{FA}, R_{FB} = coefficients of frictional loss
s = spatial coordinate following flow
T = temperature
U = overall heat transfer coefficient
V = velocity
x = $\dfrac{r_o^2 - r_i^2}{r_o}$
z = vertical dimension
β = coefficient of thermal expansion
μ = viscosity
ρ = density

Subscripts

1,2,3,4,5 = refer to concentric surfaces
A, B = refer to annuli
i, o = inner, outer
w = tank water
0 = reference

convection cells formed at Rayleigh numbers above 10^4 for high aspect ratio geometries, such as the present annuli. Convection cells presumably occurred in the present outer annulus because the Rayleigh number ranged from 10^4 to 2×10^5. There was additional evidence for the presence of convection cells. When salt tracer was injected in the top of the outer annulus it dispersed markedly, which would not be expected for simple laminar flow. Because the mechanisms for convection of heat and momentum are nearly the same for the multiple convection cells, a Reynolds-type analogy is used to calculate the coefficient of frictional resistance for the relatively slow bulk flow down the outer annulus. The Nusselt number for annulus B is defined as the ratio of the heat transfer coefficient in the presence of convection cells to the heat transfer coefficient for conduction only. In the absence of cells $\mathrm{Nu}_B = 1$. The frictional loss in annulus B is approximately equal to the frictional loss in the absence of cells multiplied by Nu_B.

Therefore

$$R_{FB} = \frac{\mathrm{Nu}_B 8\mu L/\pi {r_4}^4}{1 - {r_3}^4/{r_4}^4 - \dfrac{(1 - {r_3}^2/{r_4}^2)^2}{\ln r_4/r_3}} \tag{4}$$

Randall et al. [14] measured heat transfer coefficients for natural convection between vertical parallel plates at different temperatures. The correlation is

$$\mathrm{Nu}_B = 0.0965(\mathrm{Gr}_B \mathrm{Pr})^{0.29} \tag{5}$$

Having evaluated the coefficients of frictional resistance it remains to expand density in the form

$$\rho(T) = \rho_0 - (T - T_0)\rho_0 \beta \tag{6}$$

where ρ_0 is the density at reference temperature T_0. The reference temperature is the average temperature in the annulus under consideration. Substituting (6) into (2) gives

$$g\rho_0(1 + T_0\beta)\,dz - g\rho_0 \beta T dz + (R_{FA} + R_{FB})Q = 0$$

The left-hand integral is zero giving the final form of the momentum equation, the first of the equations to be solved simultaneously:

$$g\rho_0 \beta T dz = (R_{FA} + R_{FB})Q \tag{7}$$

The rest of the equations are now derived. The heat fluxes are written in terms of heat transfer coefficients

$$q_2 = h_2(T_A - T_2) \tag{8}$$

$$q_3 = h_3(T_3 - T_B) \tag{9}$$

$$q_4 = U(T_B - T_W) \tag{10}$$

The individual heat transfer coefficients are evaluated as follows. Lundberg et al. [15] calculated that the Nusselt number for heat transfer to a long annulus in laminar flow is 5.38. The heat transfer coefficient for the inner annulus is

$$h_2 = \frac{5.38k}{2(r_2 - r_1)} \tag{11}$$

The possibility that local buoyancy forces affected heat transfer in the inner annulus was investigated. Equation (65) in [16] was evaluated and indicated that buoyancy forces had a negligible effect.

The Nusselt number for heat transfer across the outer annulus is given by equation (5). The heat transfer coefficient is

$$h_B = \frac{\mathrm{Nu}_B k}{r_4 - r_3} \tag{12}$$

It is assumed that half of the resistance to heat transfer across the outer annulus is the film resistance from a wall to the bulk fluid. Therefore the film coefficient is twice the annular coefficient

$$h_4 = \frac{2\mathrm{Nu}_B k}{r_4 - r_3} \tag{13}$$

Also h_3 equals h_4.

The overall heat transfer coefficient, U, is composed of film coefficients inside and outside the casing. The thermal resistance of the casing is negligible.

$$U = \frac{1}{\dfrac{1}{h_4} + \dfrac{1}{h_5}} \tag{14}$$

Coefficient h_5 is for natural convection from a vertical cylinder [17]

$$h_5 = \frac{\mathrm{Nu}k}{L} \tag{15}$$

where

$$\mathrm{Nu} = 0.13(\mathrm{Gr}\,\mathrm{Pr})^{1/3} \tag{16}$$

Substituting equations (13) and (15) in (14) gives the overall heat transfer coefficient

$$U = \frac{1}{\dfrac{r_4 - r_3}{2\mathrm{Nu}_B k} + \dfrac{L}{\mathrm{Nu}k}} \tag{17}$$

A conservation of energy equation is written for a differential length of heater tube. If axial conduction is neglected the specific heater power, G, is related to the surface heat fluxes by

$$r_3 q_3 - r_2 q_2 = \frac{({r_3}^2 - {r_2}^2)G}{2} \tag{18}$$

A second conservation equation equates the heat generated by the heater to the total heat loss from the casing

$$2\pi r_4 \int_0^L q_4 dz = \pi({r_3}^2 - {r_2}^2)GL_2 \tag{19}$$

Heat losses to air above the water surface were ignored as negligible. The energy equations for annuli A and B are

$$\rho_0 CQ \frac{dT}{dz} = -q_2 2\pi r_2 \tag{20}$$

$$\rho_0 CQ \frac{dT}{dz} = 2\pi(q_4 r_4 - q_3 r_3) \tag{21}$$

The equation for the unheated lower section of annulus B is

$$\rho_0 CQ \frac{dT}{dz} = 2\pi q_4 r_4 \tag{22}$$

The temperatures at the inner and outer surfaces of the heater tube are related by the differential equation for radial conduction in a cylinder (axial conduction was neglected)

$$\frac{-Gr}{k} = \frac{d}{dr}\left(r\frac{dT}{dr}\right) \tag{23}$$

Integrating equation (23) twice gives

$$T(r) = T(r_2) - \frac{G}{4k}(r^2 - {r_2}^2) + \left(\frac{G{r_2}^2}{2k} + r_2 \frac{dT(r_2)}{dr}\right)\ln\frac{r}{r_2} \tag{24}$$

The radial heat fluxes at the surfaces are

$$q_2 = -k\left.\frac{dT}{dr}\right|_{r_2} \qquad q_3 = -k\left.\frac{dT}{dr}\right|_{r_3} \tag{25}$$

Solving equation (18) for G and substituting the resulting equation and equation (25) into equation (24) and evaluating at $r = r_3$ yields the relation between radii, temperatures, and heat fluxes at the inside and outside surfaces of the cylinder.

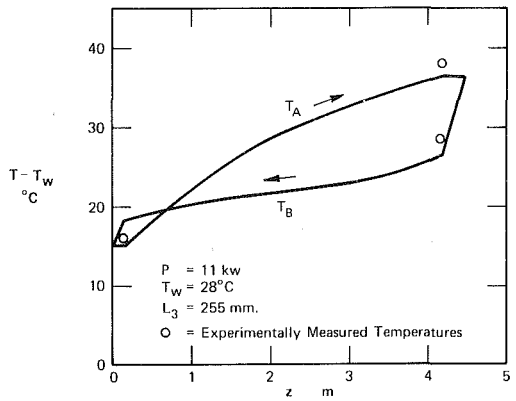

Fig. 3 Water temperature as function of position

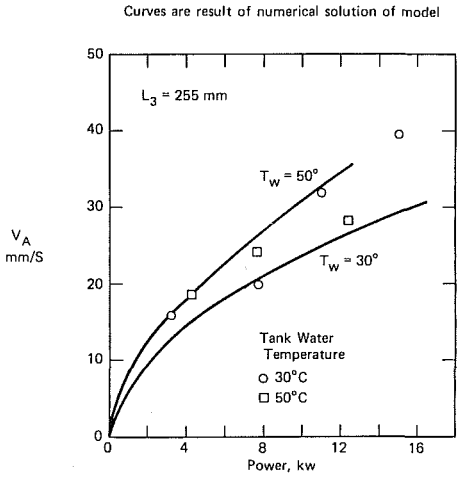

Fig. 4 Inner annulus water velocity

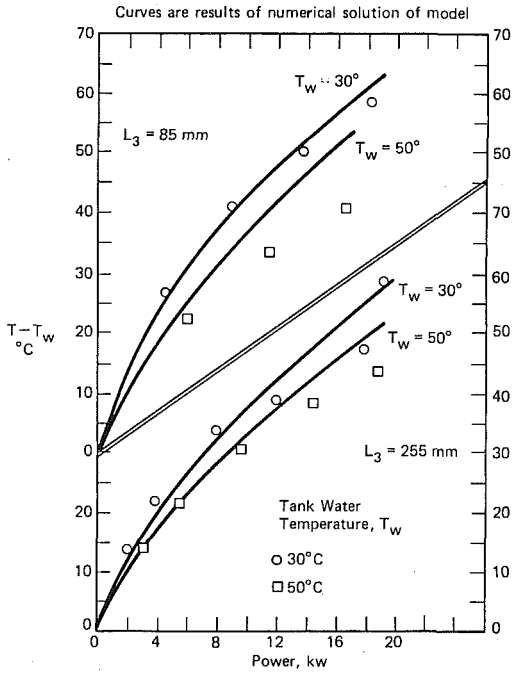

Fig. 5 Metal temperature at top of heater

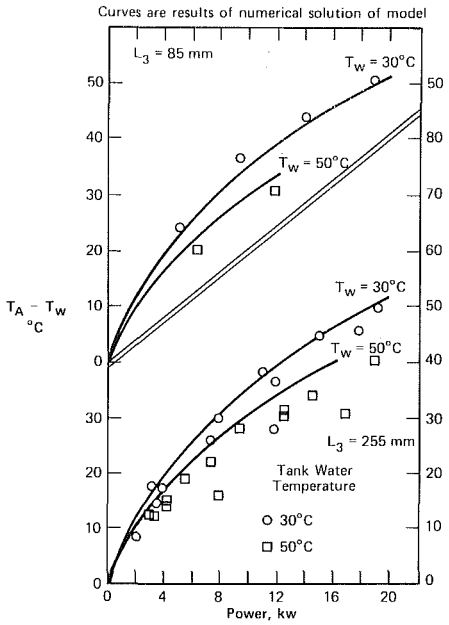

Fig. 6 Water temperature at top of inner annulus (*A*)

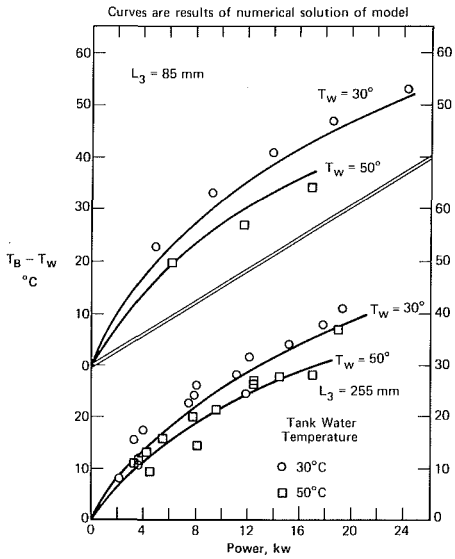

Fig. 7 Water temperature at top of outer annulus (*B*)

$$T_3 = T_2 + q_2\left[\frac{r_2}{2k} - \frac{{r_2}^3}{k({r_3}^2 - {r_2}^2)}\ln\frac{r_3}{r_2} - \frac{r_2}{k}\ln\frac{r_3}{r_2}\right] + q_3\left[-\frac{r_3}{2k} + \frac{{r_2}^2 r_3}{k({r_3}^2 - {r_2}^2)}\ln\frac{r_3}{r_2}\right] \quad (26)$$

Finite Difference Solution of Equations

Eleven equally spaced node points were positioned in each of the two annuli, on both surfaces of the heater tube, and on the inner surface of the casing. Also, there were nodes on the casing above and below the heater. The 22 nodes on the surfaces of the heater and the 22 annular nodes all had an associated temperature. All 35 surface nodes had an associated heat flux. Adding Q as a variable gave a total of 80 variables.

Equations (7) and (19) were rewritten in a form that performed numerical integration with the trapezoidal rule. For example, equation (19) became

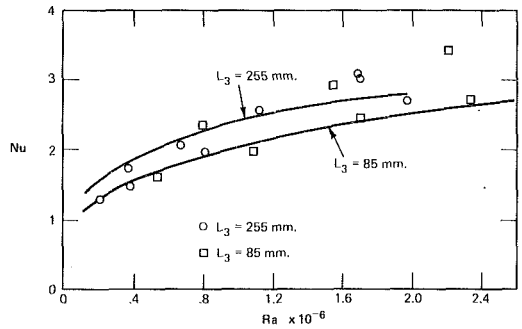

Fig. 8 Overall Nusselt number

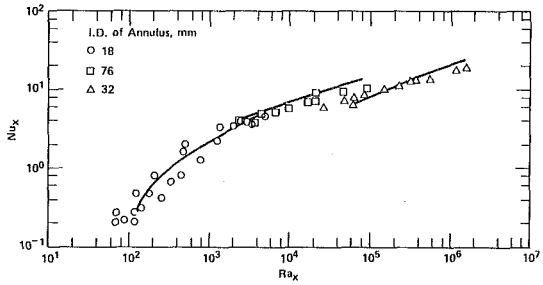

Fig. 9 Comparison of model results with Seki data

$$q_4(L_1/2)L_1 + 0.5q_4(L_1)L_2/10 + \sum_{i=1}^{9} q_4(iL_2/10 + L_1)L_2/10$$
$$+ 0.5q_4(L_1 + L_2)L_2/10 + q_4(L_1 + L_2 + L_3/2)L_3$$
$$= \frac{(r_3^2 - r_2^2)GL_2}{2r_4}$$

The first term is the loss from the unheated section at the bottom. The second, third, and fourth terms are the losses from the heated section. The fifth term is the loss from the unheated section at the top. Equations (8), (9), (10), (18), (20), (21), (22), and (26) were rewritten in finite difference form. For example, equation (8) became

$$q_2(i\Delta z) = h_2[T_A(i\Delta z) - T_2(i\Delta z)]$$
$$i = 1,11$$

There was a total of eighty equations in eighty unknowns. In order to use matrix inversion the nonlinear terms in the equations were first linearized. For example, a term containing volumetric flowrate multiplied by temperature was linearized around a reference temperature (the average temperature of the water in the annulus) T_0 and volumetric flow Q_0. The following Taylor series expansion was made

$$QT \simeq Q_0 T_0 + T_0(Q - Q_0) + Q_0(T - T_0)$$

An iterative method was used to solve the equations. Initial estimates were made for reference temperatures and the reference flow. The viscosities and coefficients of thermal expansion at reference temperatures were substituted into the equations. The linearized equations were then solved by matrix inversion. The calculated temperatures and flow were used as the new reference values. The process converged in less than ten iterations and provided a virtually exact solution to the original nonlinear equations. The fluid velocities in the annuli were then calculated

$$V_A = \frac{Q}{A_A}$$

$$V_B = \frac{Q}{A_B}$$

Results and Discussion

Figure 3 traces the temperature of the water circulating through the thermosiphon and compares experimental data with calculations. The sharp temperature decreases at the top and bottom occurred because these sections of the thermosiphon were not heated and lost heat relatively rapidly to the tank water. Temperatures and velocities calculated by the model are compared with experimental data in Figs. 4–7 for two different values of water level L_3 and for tank water temperatures of 30°C and 50°C. Figure 4 shows the convective velocity in the inner annulus. Figure 5 shows the metal temperature near the top of the heater. The metal temperature was calculated as the average of the temperatures of the nodes at height (L_1 + L_2) and radii 2 and 3. Figures 6 and 7 show the water temperatures at the inner and outer annuli referenced to the tank water temperature. The Nusselt number for the overall heat transfer process is plotted in Fig. 8. Agreement between calculated and measured temperatures, velocities, and Nusselt numbers is reasonably good. The discrepancies between measured and calculated quantities are most likely due to approximations involved in the model.

There are five significant approximations:

1 Equation (4) for R_{FB} is an approximation

2 Randall's correlation, equation (5), has an estimated uncertainty of 16 percent

3 The film heat transfer coefficients for the inner and outer halves of annulus B are assumed equal

4 The heat transfer coefficient in the open region above the heaters is assumed equal to the heat transfer coefficient in the outer half of annulus B

5 The heater support is more complicated than the simple cylindrical piece shown in Fig. 2

The choice of the number of nodes seems to have made little difference. Increasing the number of nodes made almost no difference in the results. Similar models were applied to all types of reactor assemblies at SRP to determine how much heat could be removed by natural convection. In some situations these calculated maximum heat removal rates were the limiting and controlling factors in reactor operation. For example, the assembly shown in Figs. 1 and 2 can dissipate a maximum of 24 kW in 30°C tank water without boiling.

Application of Model to Experimental Data of Seki et al.

Seki et al. [4] experimented with a concentric two-tube thermosiphon. Heat applied to the outer tube caused an upflow in the annulus between the tubes. At the top of the thermosiphon the working fluid entered a tank, was cooled to 10°C and then allowed to return via the inner tube. They experimented with tubes of different dimensions and measured temperatures and heat fluxes. The working fluids were water and fluorocarbon R-11. The data were reported in terms of the Nusselt number, Nu_x, and a modified Rayleigh number, Ra_x. Nu_x and Ra_x were based on the temperature difference between the heated outer tube and the returning cooled fluid.

The analytical technique described in this paper was applied to the two-tube thermosiphon for water and seven different tube sizes. The primary differences between this and the previous analysis were that flow in the inner tube was modeled as a pipe flow, not an annular flow and that water at the top of the thermosiphon was cooled to a fixed temperature and then returned. The calculated results were expressed as Nu_x and Ra_x. The experimental data and the calculated results agreed well. Data for three typical tube sizes are plotted for comparison in Fig. 9.

References

1 Japikse, D., "Advances in Thermosyphon Technology," in: *Advances in Heat Transfer*, edited by T. F. Irvine and J. P. Hartnett, Vol. 9, 1973, pp. 1-111.

2 Kreider, J. F., and Kreith, F., *Solar Energy Handbook*, 1981.

3 Pratt, R. C., and Karaki, S., "Natural Convection Between Vertical Plates With External Frictional Losses—Application to Trombé Walls," *Proc. of Natl. Passive Solar Conf.*, San Jose, CA, 1979, pp. 61-68.

4 Seki, N., Fukusako, S., and Koguchi, K., "Single-Phase Heat Transfer Characteristics of Concentric-Tube Thermosiphon," *Wärme- und Stoffübertragung*, Vol. 14, 1980, pp. 189-199.

5 Chato, J. C., "Natural Convection Flows in Parallel-Channel Systems," ASME JOURNAL OF HEAT TRANSFER, Vol. 85, 1963, pp. 339-345.

6 Keller, J. B., "Periodic Oscillations in a Model of Thermal Convection," *J. Fluid Mechanics*, Vol. 26, 1966, pp. 599-606.

7 Welander, P., "On the Oscillatory Instability of a Differentially Heated Fluid Loop," *J. Fluid Mechanics*, Vol. 29, 1967, pp. 17-30.

8 Creveling, H. F., de Paz, J. F., Baladi, J. Y., and Schoenhals, R. J., "Stability Characteristics of a Single Phase Free Convection Loop," *J. Fluid Mechanics*, Vol. 67, 1975, pp. 65-84.

9 Greif, R., Zvirin, Y., and Mertol, A., "The Transient and Stability Behavior of a Natural Convection Loop," ASME JOURNAL OF HEAT TRANSFER, Vol. 101, 1979, pp. 684-688.

10 Zvirin, Y., Jeuck, P. R., Sullivan, C. W., and Duffey, R. B., "Experimental and Analytical Investigation of a Natural Convection System With Parallel Loops," ASME JOURNAL OF HEAT TRANSFER, Vol. 103, 1981, pp. 645-652.

11 Kaizerman, S., Wacholder, E., and Elias, E., "Stability and Transient Behavior of Vertical Toroidal Thermosiphon," ASME Paper No. 81-WA/HT-11, 1981.

12 Bird, R. B., Stewart, W. E., and Lightfoot, E. N., *Transport Phenomena*, 1966.

13 Elder, J. W., "Laminar Free Convection in Vertical Slot," *J. Fluid Mechanics*, Vol. 23, 1965, pp. 77-98.

14 Randall, K. R., Mitchell, J. W., and El-Wakil, M. M., "Natural Convection Heat Transfer Characteristics of Flat Plate Enclosures," ASME JOURNAL OF HEAT TRANSFER, Vol. 101, 1979, pp. 120-125.

15 Lundberg, R. E., McCuen, P. A., and Reynolds, W. C., "Heat Transfer in Annular Passages," *Int. J. Heat Mass Transfer*, Vol. 6, 1963, pp. 495-529.

16 Porter, J. E., "Heat Transfer at Low Reynolds Number," *Trans. Instn. Chem. Engrs.*, Vol. 49, 1971, pp. 1-29.

17 McAdams, W. H., *Heat Transmission*, 1954.

Thermal Stability of a Vertical Fluid Layer With Volumetric Energy Source

A. H. Shaaban
Assoc. Mem. ASME

M. N. Özişik
Mem. ASME

Mechanical and Aerospace Engineering Department,
North Carolina State University,
Raleigh, N.C. 27650

The effects of nonuniform volumetric energy sources on the thermal stability of natural convection in a vertical fluid layer are investigated using the linear theory of stability. The neutral states of stability are obtained for four values of Prandtl number, ranging from 0.71 to 100, and for different values of β in the range $0.1 \leq \beta \leq 10$. The critical parameters and the energetics of the critical disturbances are determined for each case. For all values of Prandtl number and β studied here, the critical instabilities set in as traveling waves, moving in the direction of gravity. In the low range of Prandtl number, 0.71 to 5, the critical curves approach the same asymptotic value for $\beta \geq 10$. The critical disturbances are found to be buoyancy driven for all Prandtl numbers and β considered here, except for the low range of Prandtl number, for which they become shear driven disturbances as β increases.

1 Introduction

In the presence of a nonuniform temperature distribution within a vertical fluid layer in the gravity field, under certain conditions, a laminar convective motion sets in with the fluid moving in the direction of buoyancy forces, and heat is transferred mainly by conduction. The velocity profile of this laminar motion may vary from an even-symmetric flow to an odd-symmetric one, depending on the energy source causing the temperature nonuniformity. Such a source can be internal energy generation or simply heating one side of the vertical layer and cooling the other.

The thermal instability of a vertical fluid layer having an odd cubic symmetric flow field, caused by keeping the two vertical sides at different but uniform temperatures, has been the subject of numerous investigations since its first investigation by Gershuni [1] about three decades ago. The works of Rudakov [2, 3], Vest and Arpaci [4], Gill and Kirkham [5], Korpela et al. [6] and many others, have established the well-known trend of the thermal stability of the conduction regime. Their results show that for $Pr < 12.7$, the transient regime sets in as horizontal stationary cells with Grashof number nearly independent of Prandtl number, while for $Pr \geq 12.7$, the instabilities set in as two traveling waves moving in opposite directions.

The problem of the stability of a horizontal fluid layer with internal energy generation, has also received much attention. Sparrow et al. [7] have studied the effect of general boundary conditions and nonlinear temperature profile; Catton and Suo-Antilla [8] have reported numerical results for heat transfer in a layer with uniform heat generation; and Yücel and Bayazitoglu [9] studied the nonuniform heat generation effect with convective boundary conditions on the thermal stability of a horizontal layer.

In the present investigation, the thermal stability of a vertical layer of fluid containing nonuniform volumetric energy sources is studied. The energy generation within the fluid layer can be due to radioactive decay, chemical reaction, or absorption of incident radiation. The energy source function is assumed to have an exponential form, and the effect of various types of source distribution, within the medium, on the onset of stability is investigated.

2 Analysis

The schematic diagram of the physical model considered in this study is shown in Fig. 1. It consists of Newtonian fluid contained between two long, vertical, parallel plates maintained at the same uniform temperature T_W. The fluid is heated by a nonuniform volumetric energy source. The Boussinesq approximation is invoked, i.e., the fluid properties are assumed to be constant except for the density which appears in the body force term of the momentum equation. The governing equations of motion and energy for the fluid layer are given in the vector notation as

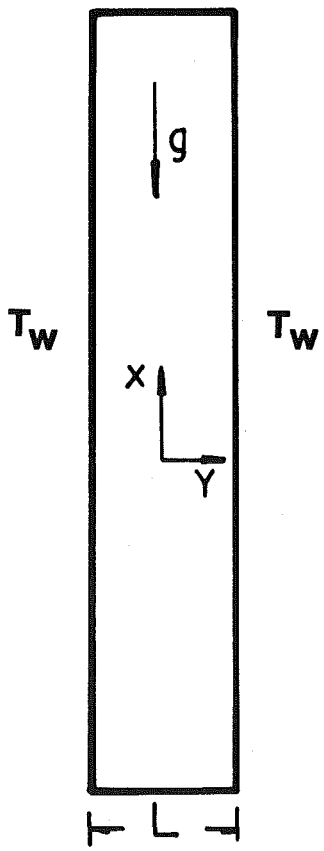

Fig. 1 Geometry and coordinates

Contributed by the Heat Transfer Division for publication in the JOURNAL OF HEAT TRANSFER. Manuscript received by the Heat Transfer Division October 7, 1983.

Continuity

$$\nabla \cdot \hat{V} = 0 \tag{1}$$

Momentum

$$\frac{\partial \hat{V}}{\partial t} + \hat{V} \cdot \nabla \hat{V} = -\frac{1}{\rho_o} \nabla P - \frac{\rho}{\rho_o} g \hat{e}_x + \nu \nabla^2 \hat{V} \tag{2}$$

Energy

$$\frac{\partial T}{\partial t} + \hat{V} \cdot \nabla T = \alpha \nabla^2 T + \frac{\dot{Q}}{\rho c_p} \tag{3}$$

where $\nabla = \hat{e}_x \, \partial/\partial X + \hat{e}_y \, \partial/\partial Y + \hat{e}_z \, \partial/\partial Z$, $\hat{V} = \hat{e}_x \, u + \hat{e}_y \, v + \hat{e}_z \, w$ and the equation of state is defined by assuming a linear density-temperature relation in the form

$$\frac{\rho}{\rho_o} = 1 - \gamma (T - T_w) \tag{4}$$

The volumetric rate of energy generation in the fluid $q(y)$ is assumed in the form of exponential function

$$\dot{q}(y) = \frac{\dot{Q}(y)}{q_o} = e^{-\beta(1/2 - y)} \tag{5}$$

Clearly, such a representation covers a wide range of distributions, from a uniform energy source for $\beta = 0$, to an impulse source function as $\beta \to \infty$.

In the case of energy generation resulting from the absorption of solar radiation, the volumetric rate of energy generation in the fluid is an exponential one in the form [9]

$$\dot{q}(y) = \frac{\dot{Q}(y) L}{I_o} = \beta e^{-\beta(1/2 - y)} \tag{6}$$

If the energy generation is sufficiently small, a steady-state convective motion (base flow) exists, the flow inside the vertical gap is parallel and in the direction of the buoyancy forces.

2.1 Base Flow Analysis. The equations governing the initial steady motion of a fluid in the vertical gap are given in the dimensionless form as

$$\frac{d^2 \bar{U}}{dy^2} = \Lambda - \bar{\theta} \tag{7}$$

$$\frac{d^2 \bar{\theta}}{dy^2} = -\dot{q} \tag{8}$$

subject to the boundary conditions

$$\bar{U} = \bar{\theta} = 0 \quad \text{at} \quad y = \pm 1/2 \tag{9}$$

The gross mass balance for the closed system is taken as

$$\int_{-1/2}^{1/2} \bar{U} dy = 0 \tag{10}$$

and used to evaluate the constant Λ in equation (7). The solution of the above system of equations yields the steady-state temperature and velocity profiles for the input energy source $\dot{q}$. If the energy source is given by equation (5), the base temperature and velocity distributions are given as

$$\bar{\theta} = b_0 + b_1 y + b_2 e^{\beta y} \tag{11}$$

$$\bar{U} = c_0 + c_1 y + c_2 y^2 + c_3 y^3 + c_4 e^{\beta y} \tag{12}$$

where

Nomenclature

a = wave number in the x-direction, nondimensional
D = operator, $\frac{d}{dy}$
$\hat{e}_i$ = unit vector in i-direction
g = acceleration of gravity
I_o = intensity of the incident radiation transmitted into the fluid
Gr = Grashof number, $\gamma g q_o L^5 / k \nu^2$
Gr^r = radiative Grashof number, $\gamma g I_o L^4 / k \nu^2$
GrR_1^* = energy contribution due to shear forces, GrR_1/R_3
k = thermal conductivity
L = width of the gap
P = pressure
Pr = Prandtl number, ν/α
$\dot{q}$ = rate of energy generation, nondimensional, $\frac{\dot{Q}}{q_o}$ or $\frac{\dot{Q}L}{I_o}$
q_o = energy generation strength
$\dot{Q}$ = rate of energy generation
R_2^* = energy contribution due to buoyancy forces, R_2/R_3
S = wavespeed in x-direction, nondimensional
t = time
$T, \bar{T}, T_w, T_o$ = temperature, base flow temperature, wall temperature, reference temperature
u', v', w' = dimensionless perturbed velocity components $(u, v, w)/u_o$
u_o = reference velocity, $\gamma g q_o L^4 / k\nu$ or $\gamma g I_o L^3 / k\nu$
$\bar{U}$ = dimensionless base flow velocity, $\bar{u}/u_o$
X, Y, Z = Cartesian coordinates with Z normal to the plane of the paper
x, y, z = $(X, Y, Z)/L$

Greek Letters

α = thermal diffusivity
β = coefficient in equation (5) or fluid layer optical thickness in equation (6)
γ = thermal expansion coefficient
$\bar{\theta}$ = dimensionless base flow temperature, $(\bar{T} - T_w)/(q_o L^2/k)$ or $(\bar{T} - T_w)/(I_o L/k)$
θ' = dimensionless perturbed temperature, $T'/(q_o L^2/k)$ or $T'/(I_o L/k)$
Λ = $(T_o - T_w)/(q_o L^2/k)$ or $(T_o - T_w)/(I_o L/k)$
ν = kinematic viscosity
ρ = density
τ = dimensionless time, $\nu t/L^2$

Subscript

c = critical state

Superscripts

$-$ = base flow quantity
$*$ = perturbed quantity
r = radiative quantity

$$
\left.
\begin{aligned}
b_0 &= (1+e^{-\beta})/2\beta^2 \\
b_1 &= (1-e^{-\beta})/\beta^2 \\
b_2 &= -e^{-\frac{\beta}{2}}/\beta^2 \\
c_0 &= \frac{1}{4\beta^4}\left\{\left(1-\frac{6}{\beta}\right)+e^{-\beta}\left(1+\frac{6}{\beta}\right)\right\} \\
c_1 &= (1-e^{-\beta})\left(1-\frac{1}{24\beta^2}\right)/\beta^2 \\
c_2 &= -\frac{3}{\beta^4}\left[\left(1-\frac{2}{\beta}\right)+e^{-\beta}\left(1+\frac{2}{\beta}\right)\right] \\
c_3 &= -(1-e^{-\beta})/6\beta^2 \\
c_4 &= e^{-\frac{\beta}{2}}/\beta^4
\end{aligned}
\right\} \tag{13}
$$

In the case of energy generation resulting from the absorption of the solar energy, the source term is given by equation (6). For such a case, the solution of the system of equations (7-10) also yields the same forms of $\bar{\theta}$ and $\bar{U}$ as given by equations (11-12), respectively, except the coefficients in equations (13) are multiplied by the optical thickness β.

2.2 The Stability Analysis. To study the condition under which the laminar natural flow solution, given in section 2.1, is stable against small disturbances, we follow the standard procedure of the linear stability theory. Consider the total quantities slightly perturbed as

$$F(\tau,x,y,z)=\bar{F}(y)+F'(\tau,x,y,z) \tag{14}$$

where $\bar{F}=\bar{U}, \bar{\theta}$, etc. denote the base flow quantities and $F'=u', v', w', \theta'$, etc., the dimensionless perturbed quantities. The linearized equations governing the initial decay or growth of the disturbances are obtained with the conventional approach by introducing equation (14) into the system of equations (1-4), subtracting the base flow equations (7) and (8), and neglecting the perturbation terms of the second and higher orders. By Squire's theorem [10], two-dimensional system of disturbances in x-y plane is considered, the dependence of the perturbation quantities on x, y, and τ is taken as a superposition of the Fourier modes of the form

$$F'(\tau,x,y)=F^*(y)\exp(iax+\sigma\tau) \tag{15}$$

where $F=p, u, v, w$, or θ, and "a" is the wave number in the x-direction and the complex wave frequency σ is given by

$$\sigma=\sigma_r+i\sigma_i \tag{16}$$

and the wave speed is defined as

$$S=-\sigma_i/a\mathrm{Gr} \tag{17}$$

The solution (15) is introduced into the linearized equations and the variables p^*, u^*, w^*, are eliminated among the resulting expressions and the stream function ψ^* replaced v^* through the relation $v^* = -ia\psi^*$. The following perturbation equations are obtained.

$$\sigma(D^2-a^2)\Psi^*=[(D^2-a^2)^2 - ia\mathrm{Gr}\{\bar{U}(D^2-a^2)-D^2U\}]\Psi^*+D\theta^* \tag{18}$$

$$\sigma\theta^*=ia\mathrm{Gr}D\bar{\theta}\Psi^*+[\mathrm{Pr}^{-1}(D^2-a^2)-ia\mathrm{Gr}\bar{U}]\theta^* \tag{19}$$

with the boundary conditions

$$\theta^*=\Psi^*=D\Psi^*=0 \text{ at } y=\pm 1/2 \tag{20}$$

Clearly, the parameters which control the stability include the Grashof number Gr, Prandtl number Pr, wave number a, and β. For certain combinations of these parameters, the real part of σ becomes zero, and the neutral state of stability occurs.

2.3 Disturbances Energy Balance. To study the driving forces and mechanisms of disturbances at the critical points, we applied a power integral method used by Stuart [11] to study the nonlinear mechanics of hydrodynamic stability and later adapted by Bergholz [12], to calculate the relative magnitudes of the energy sources and sinks of the disturbances.

In this method, equation (18) is multiplied by $\hat{\psi}$, the complex conjugate of ψ^*, integrated over the region $-\frac{1}{2} \le y \le \frac{1}{2}$, the physical significance of this procedure is examined by considering only the real part of the resulting expression, given by (see Appendix, and Gill and Davey [13]; p. 779)

$$\sigma_r E=\mathrm{Gr}R_1+R_2+R_3 \tag{21}$$

The meaning of each of the terms in this expression is as follows:

$\sigma_r E$ is time rate of growth of the disturbance kinetic energy E.

$\mathrm{Gr}R_1$ represents the rate of transfer of kinetic energy fron the mean flow to the disturbance due to Reynolds stress (shear forces).

R_2 represents the rate of transfer of kinetic energy to the disturbance due to buoyancy forces.

R_3 represents the rate of viscous dissipation of energy of the disturbance and is always negative.

In calculating the relative magnitudes of the energy terms, equation (21) was normalized by setting the rate of viscous dissipation term R_3 equal to -1, thereafter,

$$\mathrm{Gr}R_1^*+R_2^*-1=0 \tag{22}$$

since $\sigma_r = 0$ at the critical points. Here R_1^* and R_2^* are the relative magnitudes of R_1 and R_2 in relation to R_3, respectively.

2.4 Method of Solution. The eigenvalue problem defined by equations (18-20) can be solved by the Galerkin method as now described. Following Chandrasekhar and Reid [14], the solutions for $\psi^*(y)$ and $\theta^*(y)$ that satisfy the boundary conditions (20) are taken in the form

$$\psi^*(y)=\sum_{m=1}^{N} a_m C_m(y)+b_m S_m(y) \tag{23}$$

$$\theta^*(y)=\sum_{m=1}^{N} d_m \sin[2m\pi y]+e_m\cos[(2m-1)\pi y] \tag{24}$$

where the even functions $C_m(y)$ and the odd functions $S_m(y)$ are those discussed by Harris and Reid [15], and the coefficients a_m, b_m, d_m, and e_m are in general complex. Equations (23) and (24) are introduced into equations (18) and (19). The expression resulting from equation (18) is multiplied first by $C_n(y)$ and then by $S_n(y)$, and for each case integrated over the region. Similarly, the expression resulting from equation (19) is multiplied first by $\sin(2n\pi y)$ and then by $\cos[(2n-1)\pi y]$, and for each case integrated over the region. This procedure leads to an eigenvalue problem for the determination of Gr, and the resulting equations are written in the matrix form as

$$\sigma AX=BX \tag{25}$$

In this equation $X=[a_m, b_m, d_m, e_m]^T$ is the coefficient vector; A and B are $4N \times 4N$ matrices, and A real and symmetric, and B complex, arising from the orthogonalization, and N is the number of terms considered in approximating the eigenfunctions given by equations (23) and (24). The elements of A and B are given in the Appendix. The matrix equation (25) was solved by using International Mathematical and Statistical Libraries, IMSL [16], and the neutral stability curves were constructed for each given value of Pr and β. Each point on such curves was obtained by applying a secant method of iteration to Gr with "a" fixed,

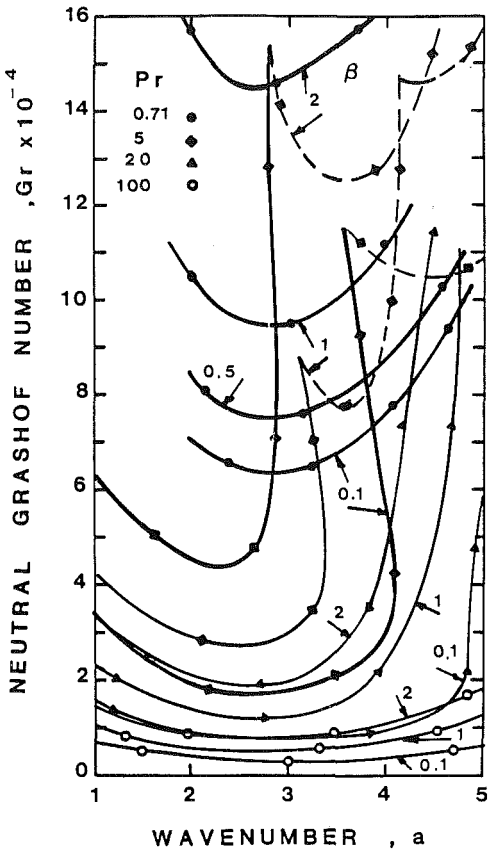

Fig. 2 Neutral stability curves for various values of Prandtl number and the coefficient β as defined by equation (5)

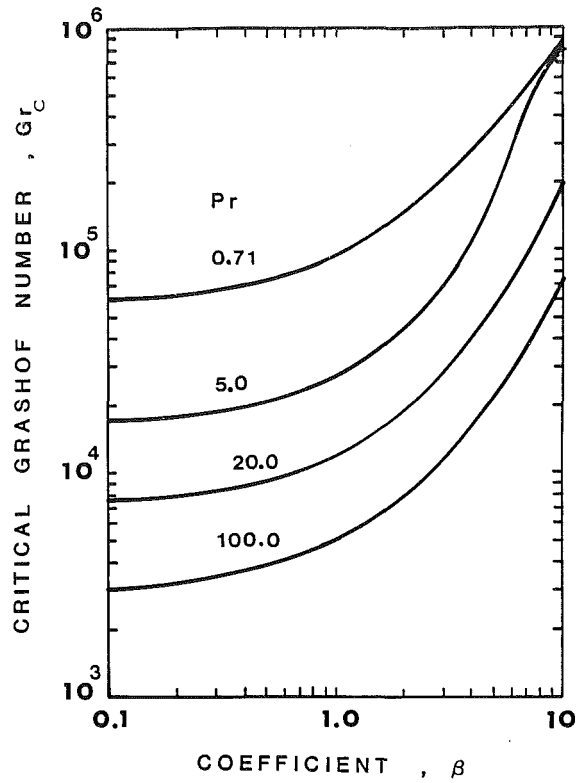

Fig. 3 Critical Grashof number as a function of β as defined by equation (5) for various values of Prandtl number

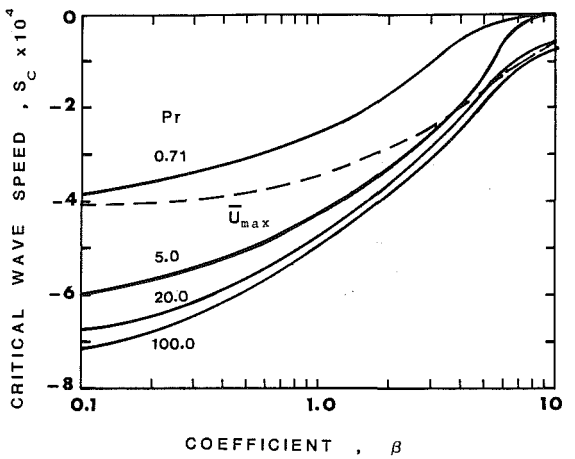

Fig. 4 Critical wavespeed as a function of β as defined by equation (5) for various values of Prandtl number

by satisfying the requirement that the real part of the highest eigenvalue of the matrix equation (25) equals zero within a specified error of $\pm$ 0.25 for the Grashof number. In solving equation (25), functions (23) and (24) were approximated by four to ten terms, and a convergence criterion less than 0.5 percent is satisfied in the determination of the actual neutral Grashof number.

3 Results and Discussion

The effect of the Prandtl number and the coefficient β upon the neutral stability, critical Grashof number, wave number, and wavespeed were investigated for four different values of Prandtl number, 0.71, 5, 20, and 100, and for $0.1 \leq \beta \leq 10$. Here we consider the exponential energy source defined in the form given by equation (5); the special case $\beta = 0$, which represents a uniform energy source, was discussed in [17, 18].

Figure 2 shows the portion of the neutral curves that control the critical stability, for all four values of Prandtl numbers and for $0.1 \leq \beta \leq 2$. For $Pr \geq 5$, it is found that the neutral stability curves have more than one unstable mode in the case of $Pr = 5$, the unstable modes for each value of β are also shown. The effect of β is strongest for $Pr = 0.71$, but β does not seem to change the flat shape around the critical point for $Pr = 100$.

Figure 3 shows the effect of β on the critical Grashof number Gr_c for four values of Prandtl number. Increasing β reduces the strength of the source term, which in turn stabilizes the flow for all values of Prandtl number. It is interesting to note that the critical stability curve for $Pr = 5$ approaches that of $Pr = 0.71$ as β increases. The reason for this is that the base flow velocity profile tends to change from the even distribution to the odd profile as β increases; and with the odd symmetric velocity, as reported by Korpela et al. [6], the critical Grashof number becomes independent of Prandtl number for $Pr < 12.7$. The effect of increasing Prandtl number on the critical states is to destabilize the flow for all β up to 10.

The effect of β on the critical wavespeed S_c is shown in Fig. 4 for the four values of Prandtl number. For all values of β and Pr the instability sets in as traveling waves moving in the direction of gravity. The curves for $Pr = 0.71$ and 5 near $\beta = 10$ approach zero asymptotically suggesting that the instabilities set in as stationary cells for $\beta > 10$. For $Pr = 0.71$, the wavespeed is always less than the maximum base flow velocity $\bar{U}_{max}$ in the gravity direction, while for $Pr > 20$, S_c is greater than $\bar{U}_{max}$. However, for $Pr = 5$, first S_c is greater than $\bar{U}_{max}$, and after a crossover at $\beta = 3.6$, it becomes less than $\bar{U}_{max}$. Similar behavior occurs for $Pr = 20$, with crossover at $\beta = 5.3$.

In Table 1, selected cases of the critical Grashof number,

Table 1 Critical parameters and energy source/sink terms

β	0.1	0.25	0.5	0.75	1.0	2.0	5.0	10.0
	Pr = 0.71							
Gr_c	61720	66435	74914	86519	94375	145037	343396	892198
a_c	2.85	2.85	2.84	2.77	2.78	2.65	3.4	3.215
$S_c \times 10^3$	-0.381	-0.354	-0.314	-0.281	-0.255	-0.170	-0.029	-0.0057
$Gr_c R_1^*$	0.274687	0.276452	0.281685	0.291584	0.298968	0.367023	0.731153	0.838971
R_2^*	0.725313	0.723548	0.718315	0.708416	0.701032	0.632977	0.268847	0.161029
	Pr = 5.0							
Gr_c	17474	18846	21390	24271	2749	44124	164038	817838
a_c	2.7	2.7	2.65	2.60	2.52	2.26	1.56	3.125
$S_c \times 10^3$	-0.600	-0.558	-0.504	-0.458	-0.423	-0.311	-0.142	-0.0047
$Gr_c R_1^*$	0.010535	0.010348	0.00915	0.009334	0.009066	0.010997	0.040046	0.619961
R_2^*	0.989465	0.989652	0.990085	0.990666	0.990934	0.989003	0.959954	0.380039
	Pr = 20.0							
Gr_c	7754	8364	9492	10756	12147	18888	54756	205168
a_c	2.79	2.785	2.75	2.69	2.64	2.49	2.26	2.0
$S_c \times 10^3$	-0.673	-0.628	-0.567	-0.518	-0.476	-0.349	-0.16	-0.061
$Gr_c R_1^*$	-0.001356	-0.001512	-0.001927	-0.002402	-0.002932	-0.004964	-0.007457	-0.008878
R_2^*	1.001356	1.001512	1.001927	1.002402	1.002982	1.004964	1.007457	1.008878
	Pr = 100.0							
Gr_c	3266	3524	4001	4529	5105	7830	21803	75795
a_c	2.855	2.835	2.8	2.73	2.7	2.6	2.52	2.46
$S_c \times 10^3$	-0.703	-0.658	-0.595	-0.546	-0.500	-0.367	-0.168	-0.0644
$Gr_c R_1^*$	-0.000472	-0.000499	-0.000614	-0.000713	-0.000881	-0.001385	-0.002483	-0.004640
R_2^*	1.000472	1.000499	1.000614	1.000713	1.000881	1.001385	1.002483	1.004640

wave number, and wavespeed are listed. The effect of β on the critical wave number a_c can be examined from this table. Increasing β decreases a_c for all Prandtl numbers studied. For low range Prandtl number (0.71 and 5), a_c will first decrease and then start to increase with increasing the value of the coefficient β. The transition occurs in the range $2 > \beta > 5$ for Pr = 0.71 and in the range $5 > \beta > 7.5$ for Pr = 5. This behavior, for Pr = 5, is illustrated in Fig. 5 for the cases β = 5 and 7.5. The solid curve is for the low wave number unstable mode while the dashed line is for high wave number unstable mode. As β increases from 5 to 7.5, the relative position of the two minima is switched in such a manner that the low wave number unstable mode controls the stability for β = 5 and the high wave number mode controls it for β = 7.5.

Figures 6 and 7 are prepared for the case of source term as specified by equation (6), which is encountered in radiation attenuation within the medium.

Figure 6 shows the effects of the optical thickness of the fluid layer β on the critical Grashof number Gr_c^r for the four values of Prandtl number. The critical Grashof number decreases with the increase of β until it reaches its minimum and then increases. This effect is observed for all Prandtl numbers studied. To explain this behavior, we study the effect of the optical thickness β on the volumetric rate of energy generation shown in Fig. 3. Increasing β until unity increases the energy generation level, which results in destabilizing the flow, continuing the increase of β beyond unity reduces the strength of energy generation which causes the flow to stabilize. For Pr $\leq$ 5, the curves show that Gr_c^r is approaching an asymptotic value for $\beta > 10$.

The effects of optical thickness on the critical wavespeed S_c^r are shown in Fig. 7. Increasing β increases S_c^r in the gravity direction to a maximum value and then decreases it. For Pr = 0.71, S_c^r is always less than $\bar{U}_{max}$, the maximum base flow velocity in the gravity direction; and it is much smaller than $\bar{U}_{max}$ in the range $\beta > 2$. For Pr = 5, S_c^r equals $\bar{U}_{max}$ at β = 3.6; greater than $\bar{U}_{max}$ for $\beta < 3.6$; and it is less than $\bar{U}_{max}$ for $\beta > 3.6$. The same behavior is observed for Pr = 20, but the cross point is at β = 5.3. For Pr = 100, the critical wavespeed is higher than $\bar{U}_{max}$ for the range of β studied.

The computation of the kinetic energy balance was conducted to provide enough information to explain the behavior of the critical states of stability. The relative energy source/sink terms due to the work of the shear forces GrR_1^* and that due to the act of the buoyancy forces R_2^* were calculated by using equations (A3, A4, and A5). Table 1 lists the values of GrR_1^* and R_2^* at the critical points as a function of β and Prandtl number. The examination of these results shows that for Pr = 0.71, at first, the disturbances derive their energy from the buoyancy forces since R_2^* is dominant. As β increases, the contribution of the shear forces GrR_1^* increases and becomes dominant for $\beta > 5$. The same behavior is observed for Pr = 5, but the contribution of the shear forces becomes dominant at a value of β higher than that of Pr = 0.71. The domination change from buoyancy to shear forces as β increases can be seen from Fig. 5, for Pr = 5. In this figure, the solid lines represent the unstable mode where R_2^* is dominating GrR_1^* and the dashed line represents the unstable mode where GrR_1^* is dominant at its critical point. Nachtsheim [19], in his study of the flux-plate problem, has also found the double minima neutral stability curve for Pr = 0.733. He observed that the low wave number minimum

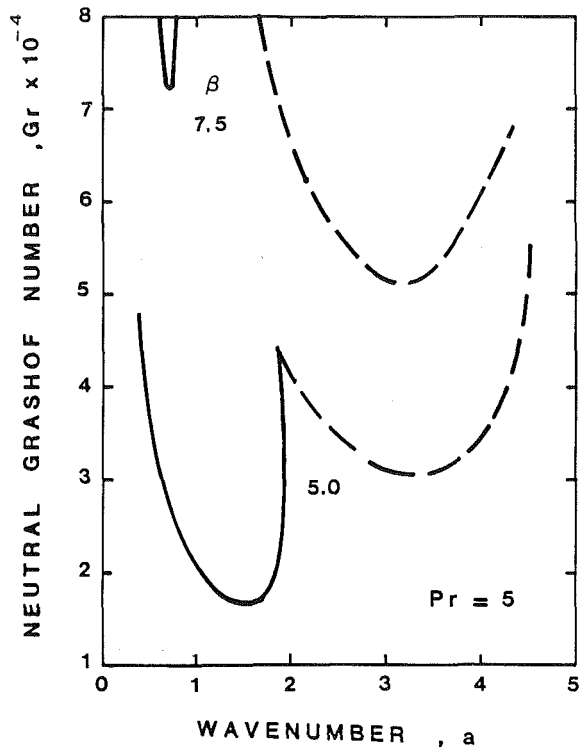

Fig. 5 The neutral stability curves for Pr = 5, in the range of β where the critical unstable mode switches from low to high wave number mode

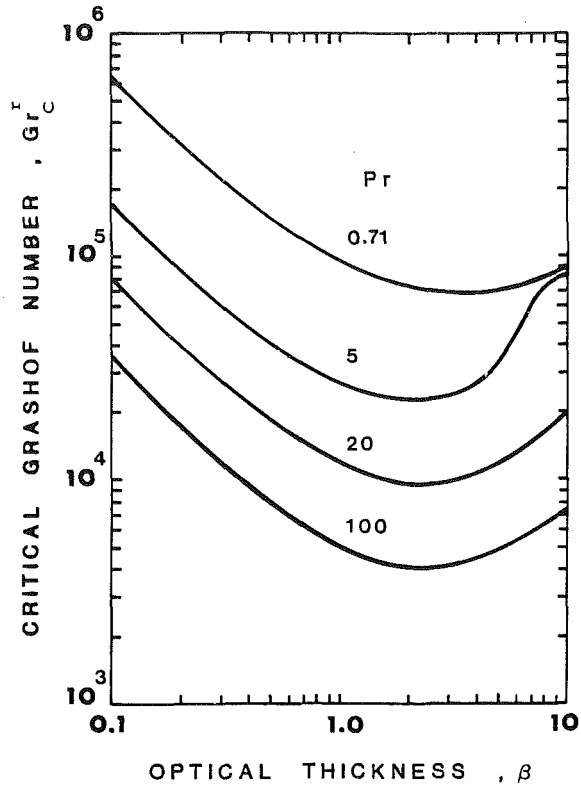

Fig. 6 Critical radiative Grashof number, as a function of the optical thickness, for various values of Prandtl number

would disappear if the buoyancy effects were ignored. Accordingly, increasing β will diminish the effect of thermal disturbances for Pr $\leq$ 5.

For Pr $\geq$ 20 the critical disturbances are entirely buoyancy driven, since GrR_1^* is always negative, energy sink, for any value of β. Increasing β will increase the magnitude of the energy sink of the shear forces GrR_1^*.

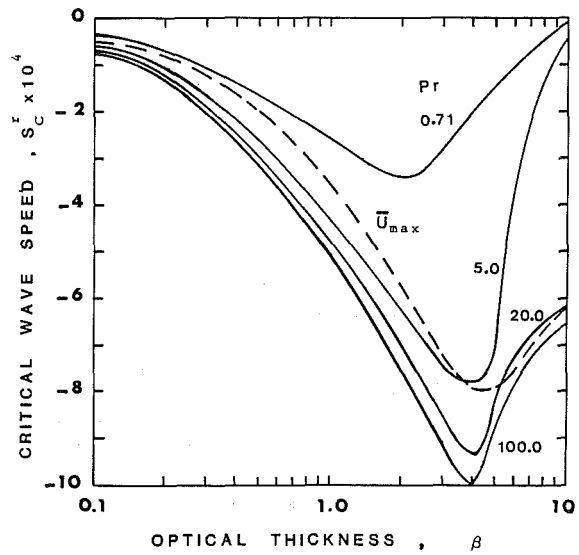

Fig. 7 Critical radiative wavespeed, as a function of the optical thickness β, for various values of Prandtl number

Acknowledgment

This work was supported in part through the National Science Foundation Grant #MEA-8 110 705.

References

1 Gershuni, G. Z., "Stability of Plane Convection Motion of a Liquid," *Zh. Tech. Fiz.*, Vol. 23, 1953, pp. 1838–1844.

2 Rudakov, R. N., "On Small Perturbations of Convective Motion Between Vertical Parallel Walls," *P.M.M.*, Vol. 30, No. 2, 1967a, pp. 439–445.

3 Rudakov, R. N., "Spectrum of Perturbations of Stability of Convective Motion Between Vertical Planes," *P.M.M.*, Vol. 31, No. 2, 1967b, pp. 349–355.

4 Vest, C. M., and Arpaci, V. S., "Stability of Natural Convection in a Vertical Slot," *J. Fluid Mech.*, Vol. 36, 1969, pp. 1–15.

5 Gill, A. E., and Kirkham, C. C., "A Note on the Stability of Convection in a Vertical Slot," *J. Fluid Mech.*, Vol. 42, 1970, pp. 125–127.

6 Korpela, S. A., Gözüm, D., and Baxi, C. B., "On the Stability of the Conduction Regime in a Vertical Slot," *International Journal of Heat and Mass Transfer*, Vol. 16, 1970, pp. 1683–1690.

7 Sparrow, E. M., Goldstein, R. J., and Jonsson, V. K., "Thermal Instability in a Horizontal Layer: Effect of Boundary Conditions and Non-Linear Temperature Profile." *J. Fluid Mech.*, Vol. 18, 1964, pp. 513–528.

8 Catton, I., and Suo-Antilla, A. J., "Heat Transfer from a Volumetrically Heat Horizontal Layer," *Proc. of the 5th Int. Heat Transfer Conf.*, Vol. III, 1974, pp. 69–73.

9 Yücel, A., and Bayazitoglu, Y., "On Set of Convection in Fluid Layers with Nonuniform Volumetric Energy Sources," ASME JOURNAL OF HEAT TRANSFER, Vol. 101, 1979, pp. 666–671.

10 Squire, H. B., "On the Stability of Three-Dimensional Disturbances of Viscous Fluid Flow Between Parallel Walls," *Proc. Roy. Soc.*, Vol. A142, 1969, pp. 621–835.

11 Stuart, J. T., "On the Non-Linear Mechanics of Hydrodynamic Stability," *J. Fluid Mech.*, Vol. 4, 1958, pp. 1–21.

12 Bergholz, R. F., "Instability of Steady Neutral Convection in a Vertical Fluid Layer," *J. Fluid Mech.*, Vol. 84, 1978, pp. 743–768.

13 Gill, A. E., and Davey, A., "Instabilities of a Buoyancy-Driven System," *J. Fluid Mech.*, Vol. 35, 1969, pp. 775–798.

14 Chandrasekhar, S., and Reid, W. H., "On the Expansion of Functions which Satisfy Four Boundary Conditions," *Proc. U.S. Nat. Acad. Sci.*, Vol. 43, No. 5, May 1957.

15 Harris, D. L., and Reid, W. H., "On Orthogonal Functions which Satisfy Four Boundary Conditions," *Astrophysical J. Suppl.*, Series 33, 1958, pp. 429–458.

16 *IMSL Library*, Edition 7, Houston, Texas, 1979.

17 Gershuni, G. Z., Zhukhovitskii, E. M., and Yakimov, A. A., "On Stability of Plane-Parallel Convective Motion Due to Internal Heat Source," *International Journal of Heat and Mass Transfer*, Vol. 17, 1974, pp. 717–726.

18 Shaaban, A. H., and Özişik, M. N., "Thermal Stability of a Vertical Fluid Layer with Uniform Energy Source," National Heat Transfer Conference, Aug. 5–8, 1984, Symposium Vol. G00248.

19 Nachtsheim, P. R., "Stability of Free-Convection Boundary-Layer Flows," NASA Tech. Note D-2089, 1963.

APPENDIX

The Inner Product Matrices and the Power Integral Terms

The matrices A and B of the matrix equation (25) are written in the form

$$A=\begin{bmatrix} C & 0 & 0 & 0 \\ 0 & D & 0 & 0 \\ 0 & 0 & E & 0 \\ 0 & 0 & 0 & F \end{bmatrix} \tag{A1}$$

$$B=\begin{bmatrix} GR & 0 & KR & LR \\ 0 & QR & SR & TR \\ 0 & 0 & WR & 0 \\ 0 & 0 & 0 & ZR \end{bmatrix} + ia\mathrm{Gr}\begin{bmatrix} GI & HI & 0 & 0 \\ PI & QI & 0 & 0 \\ 0 & VI & WI & XI \\ MI & 0 & YI & ZI \end{bmatrix} \tag{A2}$$

where the elements of the submatrices are given by the inner products

$$C_{m,n}=<\mathfrak{L}C_m,C_n>,\ D=<\mathfrak{L}S_m,S_n>,\ E=<\sin 2m\pi y,\sin 2n\pi y>$$

$$F_{m,n}=<\cos[(2m-1)\pi y],\cos[(2n-1)\pi y]>$$

$$GR_{m,n}=<\mathfrak{L}^2C_m,C_n>,\ GI=-<\mathfrak{L}_*C_m,C_n>$$

$$HI_{m,n}=-<\mathfrak{L}_*S_m,S_n>$$

$$KR_{m,n}=<D[\sin(2m\pi y)],C_m>,$$

$$LR=<D[\cos((2m-1)\pi y)],C_n>$$

$$PI_{m,n}=-<\mathfrak{L}_*C_m,S_n>$$

$$QR_{m,n}=<\mathfrak{L}^2S_m,S_n>,\ QI=-<\mathfrak{L}_*S_m,S_n>$$

$$SR_{m,n}=<D[\sin 2m\pi y],S_n>$$

$$TR_{m,n}=<D[\cos((2m-1)\pi y)],S_n>$$

$$VI_{m,n}=<D\bar{\theta}S_m,\sin(2n\pi y)>$$

$$WR_{m,n}=\mathrm{Pr}^{-1}<\mathfrak{L}\sin(2m\pi y),\sin(2n\pi y)>$$

$$WI_{m,n}=-<\bar{U}\sin(2m\pi y),\sin(2n\pi y)>$$

$$XI_{m,n}=-<\bar{U}\cos((2m-1)\pi y),\sin(2n\pi y)>$$

$$MI_{m,n}=<D\bar{\theta}\cos((2m-1)\pi y),\cos((2n-1)\pi y)>$$

$$YI_{m,n}=-<\bar{U}\sin(2m\pi y),\cos((2n-1)\pi y)>$$

$$ZR_{m,n}=\mathrm{Pr}^{-1}<\mathfrak{L}\cos((2m-1)\pi y),\cos((2n-1)\pi y)>$$

$$ZI_{m,n}=-<\bar{U}\cos((2m-1)\pi y),\cos((2n-1)\pi y)>$$

The power integral terms R_1, R_2, and R_3, which occur in equation (21), are given by

$$R_1=\Re\tfrac{1}{2}ia[\hat{a}_n\hat{b}_n]\begin{bmatrix} GI & HI \\ PI & QI \end{bmatrix}\begin{bmatrix} a_m \\ b_m \end{bmatrix} \tag{A3}$$

$$R_2=\Re\tfrac{1}{2}[\hat{a}_n\hat{b}_n]\begin{bmatrix} KR & LR \\ SR & TR \end{bmatrix}\begin{bmatrix} d_m \\ e_m \end{bmatrix} \tag{A4}$$

$$R_3=\Re\tfrac{1}{2}[\hat{a}_n\hat{b}_n]\begin{vmatrix} GR & 0 \\ 0 & QR \end{vmatrix}\begin{vmatrix} a_m \\ b_m \end{vmatrix} \tag{A5}$$

where $\Re$ stands for real part of the expression, $\mathfrak{L}=(D^2-a^2)$, $\mathfrak{L}_*=[\bar{U}(D^2-a^2)-D^2\bar{U}]$, and $\hat{a}_n$, $\hat{b}_n$ are the complex conjugate of a_n and b_n.

The eigenfunctions $C_m(y)$ and $S_m(y)$ that are used in the expansion of the disturbance stream function $\Psi(y)$ are solutions of the fourth-order eigenvalue problem

$$\frac{d^4\Psi}{dy^4}-\lambda^4\Psi=0 \quad -\tfrac{1}{2}\le y\le\tfrac{1}{2} \tag{A6}$$

$$\Psi=\frac{d\Psi}{dy}=0 \quad \text{at} \quad y=\pm\tfrac{1}{2} \tag{A7}$$

The solutions Ψ_m form a complete orthogonal set of functions. They fall into two noncombining groups; the even, $C_m(y)$, and the odd, $S_m(y)$, solutions in the form

$$C_m(y)=\frac{\cosh(\alpha_m y)}{\cosh(\alpha_m/2)}-\frac{\cos(\alpha_m y)}{\cos(\alpha_m/2)} \tag{A8}$$

$$S_m(y)=\frac{\sinh(\beta_m y)}{\sinh(\beta_m/2)}-\frac{\sin(\beta_m y)}{\sin(\beta_m/2)} \tag{A9}$$

where the eigenvalues α_m and β_m are the positive roots of the transcendental equations

$$\tanh(\alpha/2)+\tan(\alpha/2)=0 \tag{A10}$$

$$\tanh(\beta/2)-\tan(\beta/2)=0 \tag{A11}$$

Free Convective Heat Transfer in a Liquid-Filled Vertical Annulus

V. Prasad
Department of Mechanical Engineering,
Columbia University,
New York, NY 10027
Mem. ASME

F. A. Kulacki
Department of Mechanical and
Aerospace Engineering
University of Delaware,
Newark, DE 19716
Mem. ASME

An experimental study of convective heat transfer in liquid-filled vertical annulus of radius ratio $\kappa = 5.338$ has been conducted for the height-to-gap width ratio A = 0.5, 1, and 1.5. By using water, heptane, and ethylene glycol as the test fluids, a Rayleigh number range of $8 \times 10^6 < Ra < 3 \times 10^{10}$, and a Prandtl number range of $4 < Pr < 196$ have been covered. Curvature effects on the temperature field are significant and result in a lower effective sink temperature for the boundary layer on the isothermally heated inner wall. The Nusselt number Nu thus increases with radius ratio κ. However, the slope of ln (Nu) versus ln (κ) curve is not a constant, and decreases with an increase in κ. The effect of Prandtl number is weak. In the laminar flow regime, the Nusselt number is weakly dependent on the aspect ratio when Nu and Ra are considered in terms of the annulus height L. The start of laminar flow regime is delayed with an increase in radius ratio. For A = 0.5, $\kappa = 5.338$, the critical Grashof number is $Gr_L = 7 \times 10^4$, which decreases with an increase in A. Turbulence is initiated when the local Grashof number $Gr_x \simeq 4 \times 10^9$.

Introduction

In spite of the importance of convective heat transfer in vertical annular enclosures in many practical applications, very few basic studies have so far been conducted for this system. The first study of the problem was by Beckmann [1], who conducted some experiments with a couple of vertical coaxial tubes, and tentatively suggested using the same heat transfer rates as for horizontal annuli. However, Jakob [2] did not agree to it, and recommended using the data for plane vertical layers employing a mean area (at radius r_m). Gershuni [3] attempted to solve the problem analytically by decoupling the momentum and energy by assuming that the velocity terms do not interact with the energy equation. This approach was unsatisfactory.

Sheriff [4] conducted experiments with CO_2-filled vertical annuli of radius ratios $\kappa = 1.03$, 1.11, and 1.23 for the height-to-gap width ratio $A = 38$, 76, and 228. The inner cylinder in his experiments was heated by applying a uniform heat flux. The heat transfer correlation he obtained did not show any radius ratio dependence owing to the small range of radius ratio he considered. He also concluded that the transition from a laminar to a turbulent boundary layer takes place somewhere between $Gr_x = 10^8$ and 10^9.

Utilizing a double boundary layer model, Nagendra et al. [5] developed an approximate analysis for the isothermally heated vertical annuli. Based on their analytical and experimental results, they presented three correlations for different categories of annuli. Their analysis suffers from a large discrepancy in the energy balance due to the logarithmic nature of conduction temperature profile.

The first extensive study of free convection in isothermally heated vertical annuli was reported by de Vahl Davis and Thomas [6], which was further extended by Thomas and de Vahl Davis [7]. They used the finite difference numerical technique to solve the governing equations for a wide range of parameters, $Ra \leq 2 \times 10^5$, $0.5 < Pr < 10^4$, $1 \leq A \leq 33$, and $1 \leq \kappa \leq 10$, though the majority of the results were obtained for Pr = 1 and $1 \leq \kappa \leq 4$. Their results indicate that the temperature and velocity fields, and consequently the heat transfer rates, are not only functions of Ra and A, but depend strongly on the radius ratio. The dependence on Prandtl number, other than that included in Ra, is very weak. Analyzing the temperature and flow fields, they presented the criteria for various flow regimes: conduction, asymptotic, and boundary layer [7] in terms of Ra and A. The delimitation of regimes was reported to be independent of the radius ratio. The heat transfer correlations obtained by them are [7]

Conduction regime

$$\mathrm{Nu} = 0.595\mathrm{Ra}^{0.101}\mathrm{Pr}^{0.024}A^{-0.052}\kappa^{0.505} \quad (1)$$

Asymptotic regime

$$\mathrm{Nu} = 0.202\mathrm{Ra}^{0.294}\mathrm{Pr}^{0.097}A^{-0.246}\kappa^{0.423} \quad (2)$$

Boundary layer regime

$$\mathrm{Nu} = 0.286\mathrm{Ra}^{0.258}\mathrm{Pr}^{0.006}A^{-0.238}\kappa^{0.442} \quad (3)$$

They have also reported multicellular flow behavior depending on Ra and A.

Another attempt to solve the problem by using a finite-difference method was made by Schwab and Dewitt [8]. The heat transfer results obtained by them are quite limited (only 24 combinations of Ra, Pr, and A with $\kappa = 2$). In general, the heat transfer coefficients reported by them are 30 to 50 percent higher than those predicted by the correlations of Thomas and de Vahl Davis [7]. Lee, Korpela, and Horne [9] also report limited heat transfer results for Pr = 0.71 in a study primarily aimed at flow structure. Their numerical results indicate multicellular flow behavior in vertical annuli.

Some other recent reports on vertical annuli are from Keyhani, Kulacki, and Christensen [10], Bhushan et al. [11], and Keyhani [12]. All of these studies are experimental for the case when constant heat flux is applied on the inner wall. Keyhani et al. [10] conducted experiments with air and helium as test fluids for $\kappa = 4.33$ and $A = 27.6$ for a wide range of Rayleigh number and report that in the conduction regime, the heat transfer rate for constant flux boundary condition is 10 percent higher than that for the isothermal case [10]. This difference further increases as Ra increases, and for $Ra = 2 \times 10^5$, it is 44 percent [7, 10]. Bhushan et al. [11] extended this work for two other combinations of aspect and radius ratios, $A = 52.82$, $\kappa = 2.77$, and $A = 38.38$, $\kappa = 8.28$, and presented heat transfer correlations for various regimes. Their correlation for boundary layer regime is

$$\mathrm{Nu} = 0.281\mathrm{Ra}^{0.322}A^{-0.407}\kappa^{0.455} \quad (4)$$

From this review of the literature, it is clear that the curvature effects on heat transfer in vertical annuli are not well

Contributed by the Heat Transfer Division for publication in the JOURNAL OF HEAT TRANSFER. Manuscript received by the Heat Transfer Division March 1, 1984.

understood. Most of the studies available are for high aspect ratios, except for the work of Thomas and de Vahl Davis [6, 7] who have considered A as low as unity. Nothing has been reported for $A < 1$. To our knowledge, no experimental study has been conducted so far for a closed annulus with an isothermally heated inner wall. The experimental work of Sheriff [4], Keyhani et al. [10], Bhushan et al. [11], and Keyhani [12] are all for constant heat flux on the inner wall and, except for Bhushan et al. [11], they do not establish a radius ratio dependence for the annulus problem. The only heat transfer correlations which include curvature effects are from Thomas and de Vahl Davis [7] and Bhushan et al. [11]. They have reported a fixed slope for ln (Nu) versus ln (κ) curve (equations (1-3, 10)) for fixed values of Ra, Pr, and A. This is not accurate as will be shown later.

To improve the understanding of convective heat transfer in vertical annuli, an experimental study has been conducted for an isothermally heated vertical annulus of radius ratio $\kappa = 5.338$ for the aspect ratios in the vicinity of 1, $A = 0.5$, 1, and 1.5. Water, heptane, and ethylene glycol have been used as the test fluids to cover a Rayleigh number range of $8 \times 10^6 < \text{Ra} < 3 \times 10^{10}$ and a Prandtl number range of $4 < \text{Pr} < 196$. To study the temperature fields, temperatures have been recorded at several locations in the medium. The overall heat transfer rates have been obtained and the effects of radius ratio and aspect ratio have been analyzed. The effect of radius ratio on the flow regimes and the initiation of turbulence have also been examined.

Experimental Apparatus and Procedure

The vertical annulus for experimental apparatus was constructed out of two brass cylinders, one 57.1 mm o.d. and 3 mm thick, and the other 304.8 mm i.d. and 5.1 mm thick. This resulted in a radius ratio of 5.3338 for the present experiments. The inner cylinder was made out of a wood rod, a glass-epoxy cylinder, and the brass cylinder. To obtain a constant temperature inner surface, eight thermofoil heaters (six 31.8 mm wide and two 6.4 mm wide) were wrapped and cemented around the glass-epoxy cylinder which was then inserted into the brass cylinder. A wood rod was then shrink fitted into the glass-epoxy cylinder for rigidity. To monitor the temperature at various locations on the inner cylinder surface, 15 thermocouples were embedded in the wall by making slots of 2.5 mm depth in the brass cylinder. The slots were then covered with copper cement and sanded for a smooth inner surface. Two thermocouples were provided for each heater except for the first one. The exact locations of heaters and thermocouples are given in [13].

The outer cylinder was maintained at a constant temperature by circulating water through a 12.7 mm o.d. copper tube wrapped and soldered around it. The circulating water was supplied by a constant temperature circulator with a control accuracy of $\pm 0.1°C$. Five thermocouples were embedded in the outer cylinder wall (close to inner surface) to monitor temperatures on the outer surface of the annulus. For the base plate and top cover, a 37.5-mm-thick phenolite laminated plastic sheet ($k_s = 0.293$ W/mK) was used. The inner and outer cylinders were attached to the base plate by making slots into it. For convenience, the base plate also served as a table top. All the thermocouple wires and heater leads were taken out from the bottom side of this plate. The top cover was free to move up and down and could be held at any height by providing O-rings on the side wall. This facilitated conducting experiments for three different aspect ratios $A = 0.5$, 1, and 1.5.

The power was supplied to each heater through an independent circuit which contained a variac and arrangements for measuring the current and voltage. These variacs were connected in parallel to a voltage regulator through another heavy duty variac to have a better control of power. All the thermocouples were connected to a datalogger, which was able to read temperatures to $\pm 0.1°C$. Temperatures were also recorded on inner and outer surfaces of the top plate to estimate the conduction losses and inside the medium to examine the temperature field. A detailed account of the experimental arrangements is presented in [13, 14].

To conduct the experiment, the annular gap was filled up to the required height with the test fluid, water, heptane, or ethylene glycol. The top plate was always kept horizontal and parallel to the bottom plate. The height of the annulus could be measured to an accuracy of 0.5 mm. The holes provided in the top plate allowed the extra fluid to come out. Mostly, the experiment was conducted while increasing the power. This made sure that the annulus was always filled with liquid.

The power was supplied to the heaters in parallel to the medium and to the top and bottom plates. The upper and lower heaters acted as guard against the axial conduction loss. Every one or two hours the temperature distribution on the inner surface was checked to make sure that the isothermal condition was achieved. Depending upon the requirements, powers in the various heaters were changed to obtain an isothermal inner surface to a reasonable accuracy, generally less than 5 percent of ΔT. The steady-state conditions were

Nomenclature

A = aspect ratio, L/D
C = isobaric specific heat of fluid, J/kg-K
D = gap width of annular layer, $(r_o - r_i)$, m
g = acceleration due to gravity, m/s^2
Gr = Grashof number based on gap width, $g\beta D^3 \Delta T/\nu^2$
h = average heat transfer coefficient on inner wall, $q/(2\pi r_i L \Delta T)$, W/m^{2}K
k = fluid thermal conductivity, W/m-K
k_s = thermal conductivity of conducting wall, W/m-K
L = height of annulus, m
Nu = Nusselt number based on gap width, hD/k
Pr = Prandtl number, ν/α
q = net power (power input-conduction losses), W
R = dimensionless distance on r axis, $(r - r_i)/(r_o - r_i)$
Ra = Rayleigh number based on gap width, $g\beta D^3 \Delta T/\nu\alpha$
T = temperature, K
T_f = mean temperature, $(T_i + T_o)/2$, K
T_i = temperature on inner wall, K (average temperature for the constant flux case)
ΔT = temperature difference across annular layer, $(T_i - T_o)$, K
r,x = axisymmetric coordinates, m
X = dimensionless distance on x axis, x/L
α = thermal diffusivity of fluid, $k/\rho C$, m^2/s
β = isobaric coefficient of thermal expansion, K^{-1}
θ = dimensionless temperature, $(T - T_o)/\Delta T$
ν = kinematic viscosity of fluid, m^2/s
κ = radius ratio, r_o/r_i
ρ = density of fluid, kg/m^3

Subscripts

i = inner
L = based on annulus height, L
m = mean value
o = outer
x = local value

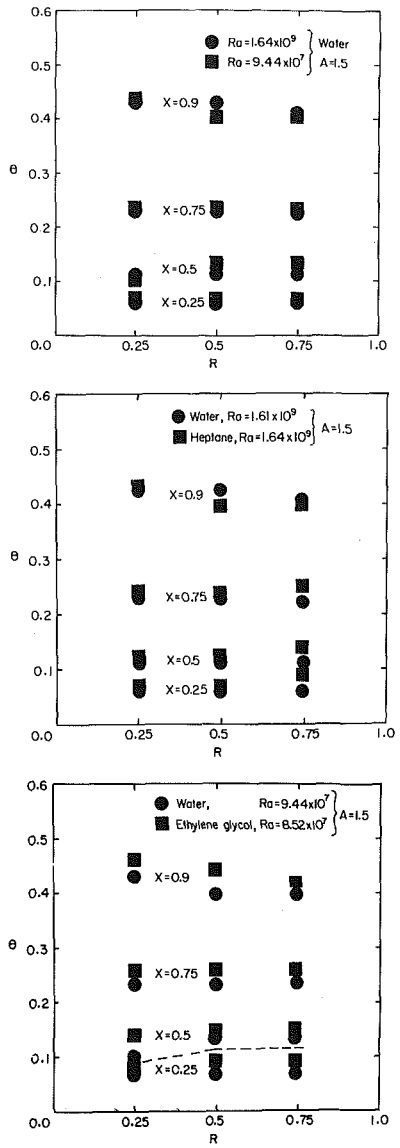

Fig. 1 Recorded temperatures at $R = 0.25, 0.5$, and 0.75 for $A = 1.5$ for various fluids: (*a*) water, (*b*) water and heptane, and (*c*) water and ethylene glycol

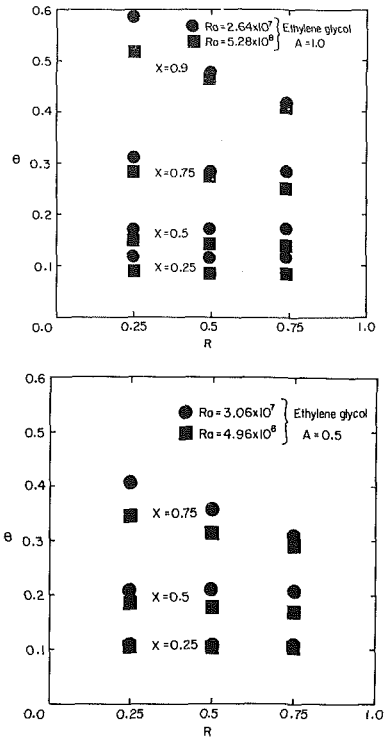

Fig. 2 Recorded temperatures for ethylene glycol as test fluid for (*a*) $A = 1$, and (*b*) $A = 0.5$

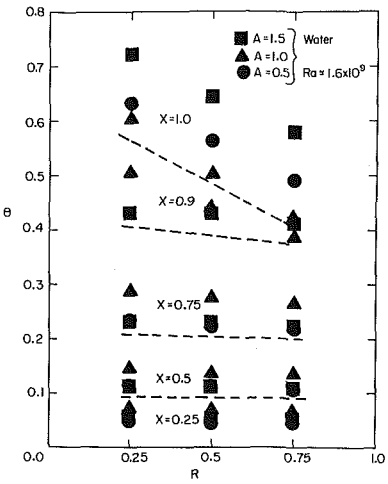

Fig. 3 Effect of aspect ratio on temperature distributions for water experiments

achieved before taking the readings. The uncertainty in power measurements was up to 1 percent.

The maximum temperature variation on the inner surface was 5.41 percent of the temperature difference ΔT for water experiments, $A = 1$. On the outer wall, the variation was as high as 6.18 percent for heptane experiments with $A = 1.5$. In most of the cases, the variation was less than 2 percent. Due to low velocities in the corners, the temperatures were mostly higher in lower and upper regions on the inner surface, particularly for high Rayleigh numbers.

Temperature corrections were applied to the thermocouple readings for the distance away from the inner and outer surfaces. To estimate the conduction loss through the top plate, temperatures were recorded at five radial locations on the inner and outer surfaces. The maximum loss through the top plate was up to 7 percent. This loss was highest at the lowest Rayleigh number and decreased as the Rayleigh number was increased. The loss through the bottom plate was neglected owing to its small percentage [13]. The temperature at the bottom surface was very close to T_o except for a very small distance from the inner surface. The losses from the exposed surfaces of inner cylinder were also estimated.

Temperatures within the medium were measured at three radial locations with copper-constantan grounded thermocouple probes with an inconel sheath of 3.2 mm diameter. These probes were positioned to within ± 0.5 mm through holes in the top plate.

Heat transfer coefficient at the inner wall was calculated by dividing net power with the mean temperature difference and area. To evaluate Grashof, Rayleigh, and Nusselt numbers, all the properties were evaluated at the mean fluid temperature T_f. A detailed account of experimental apparatus, associated instrumentation, and procedure is presented in [13, 14].

Results and Discussion

Temperature Distributions. To study the heat transfer behavior, temperatures were recorded at $R = 0.25$, 0.5, and 0.75 at various heights. Some of these temperature profiles

are presented in Figs. 1–3. These temperature distributions, when compared with the temperature profiles reported for the vertical cavity, reveal that the temperature field is strongly influenced by the curvature effects. The dimensionless temperature θ at $R = 0.5$, $X = 0.5$ varies between 0.23 and 0.11 in these figures, whereas that for the vertical cavity ($\kappa = 1$) is 0.5. For the present experiments, θ ($R = 0.5$) is 0.5 only when $X > 0.75$.

An increase in radius ratio beyond unity, thus, results in a thick cold layer in the bottom region, where the vertical temperature gradient, $\partial\theta/\partial X$, increases very slowly with X. On the other hand, in a region very close to the top wall, the enhancement in $\partial\theta/\partial X$ is quite rapid. Qualitatively, this is in agreement with the temperature field established by de Vahl Davis and Thomas [6], Schwab and DeWitt [8], and Lee et al. [9] through numerical computation.

Another interesting aspect of the curvature effect is the reduction in effective sink temperature for the boundary layer on the inner (hot) wall. For a large portion of the annulus, the temperatures at even $R = 0.25$ are much lower than the temperatures at $R = 0.5$ in the case of a planar cavity [15, 16]. As for example, for $A = 1.5$, this temperature θ ($R = 0.25$) is lower than 0.3 at least for $X \leq 0.75$ (Fig. 1). This reduction in sink temperature for $\kappa > 1$ results in higher rates of heat transfer for annuli. A large drop in temperature within a small distance from the inner wall is consistent with the logarithmic nature of the conduction temperature profile.

In Fig. 1(*a*) the recorded temperatures are presented for water for $A = 1.5$. A change in Rayleigh number from 9.44×10^7 to 1.64×10^9 does not seem to influence the temperature distribution much, provided the test fluid is the same. The radial temperature gradient, $\partial\theta/\partial R$, for $0.25 \leq R \leq 0.75$ is very small at least up to $X = 0.75$, which indicates that the radial heat transfer through the core is negligible.

Another phenomenon which can be observed in Fig. 1(*a*) is the inverse temperature gradient near the inner wall. The temperature at (0.5, 0.5) is higher than that at (0.25, 0.5) for $\text{Ra} = 9.44 \times 10^7$. This is in agreement with the *S*-shaped temperature profiles reported by de Vahl Davis and Thomas [6]. However, at $\text{Ra} = 1.64 \times 10^9$, no such inverse temperature gradient is observed at any location for water and heptane experiments (Figs. 1(*a*) and 1(*b*)). But for glycol, the temperatures at $R = 0.5$ are greater than that at $R = 0.25$ for $X \leq 0.5$ (Fig. 1(*c*)). A comparison between water and glycol temperature indicates that this behavior, i.e., the inversion of temperature gradient, is more pronounced for higher Grashof number. The disappearance of this behavior at higher Ra (or Gr) in these figures may be due to the fact that the location for inversion of $\partial\theta/\partial R$ moves closer to the inner wall as the Rayleigh number increases as observed by McGregor and Emery [15] and Yin et al. [16] for the vertical cavity.

In Fig. 1(*b*) the temperature for heptane indicates an inverse temperature gradient near the cold wall at $\text{Ra} = 1.64 \times 10^9$, though water temperatures do not show such behavior. Moreover, this inversion of $\partial\theta/\partial R$ near the cold wall is not present for heptane experiments at $\text{Ra} = 2.25 \times 10^{10}$ ($A = 1.5$). It would be interesting to know when the inverse temperature gradients appear, how they move toward the inner and outer walls, and what effects they have on the heat transfer rates. The present data are not sufficient to have conclusive answers to these questions.

From Figs. 1(*b*) and 1(*c*), it may further be observed that the Prandtl number of the medium also affects the temperature field. In Fig. 1(*b*) the temperatures for heptane ($\text{Pr} = 6.37$) are very close to those for water ($\text{Pr} = 4.76$) for a fixed Ra. A larger variation in temperature is observed when the Prandtl number changes significantly. The temperature for glycol ($\text{Pr} = 168.6$) is higher than that for water ($\text{Pr} = 6.4$) at all locations (Fig. 1(*c*)). Based on Grashof number, the

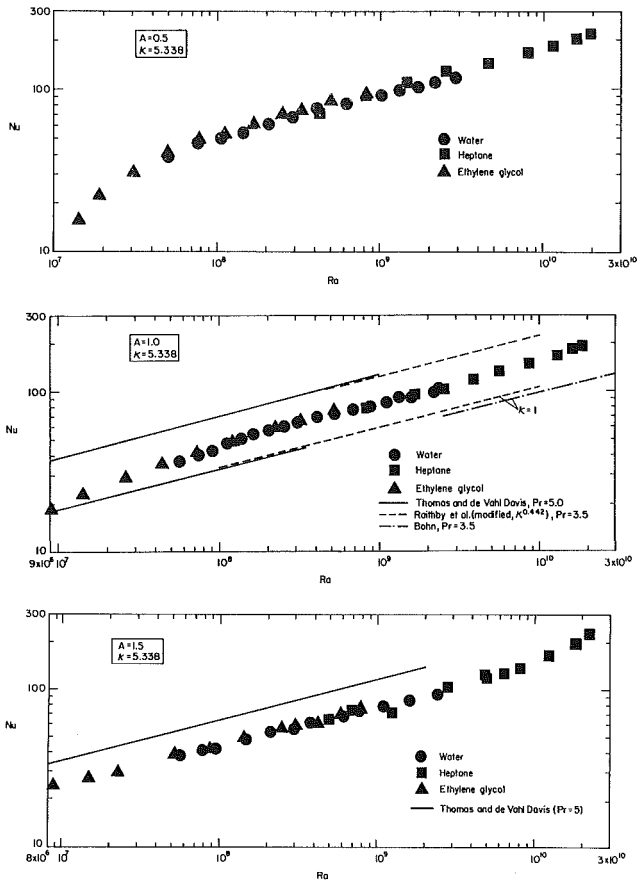

Fig. 4 Heat transfer rates for a vertical annulus of radius ratio κ = 5.338: (*a*) $A = 0.5$, (*b*) $A = 1.0$, and (*c*) $A = 1.5$

recorded temperatures (Figs. 1(*a*) to 1(*c*)) clearly indicate that the temperature in the core decreases for at least $X \leq 0.9$. It may be noted that in the case of a vertical cavity, the isotherms for $X < 0.5$ move downward whereas those for $X > 0.5$ move upward as Gr increases [16].

Recorded temperatures for $A = 1$ and 0.5 for glycol as test medium are presented in Fig. 2. As the aspect ratio decreases, the influence of Rayleigh number on the temperature at any location is seen to increase. A larger variation in temperature is observed for $A = 0.5$ compared to $A = 1$ for a comparable increase in Ra. Furthermore, the temperature at any dimensionless location increases in a major portion of the annulus, $X < 0.9$, as the aspect ratio is decreased. This is also evident from Fig. 3, in which the temperatures for water experiments are presented for $A = 0.5$, 1, and 1.5 ($\text{Ra} \simeq 1.6 \times 10^9$). In the case of a vertical cavity, the temperature decreases in the lower region, $X < 0.5$ and increases in the upper region, $X > 0.5$, with an increase in A [16]. However, in the presence of curvature effects, this behavior is changed.

Flow Regimes. Heat transfer coefficients in terms of the average Nusselt number on inner wall are presented in Figs. 4(*a–c*) for $A = 0.5$, 1, and 1.5, respectively. The values of Ra and Nu in these figures are based on the annular gap width D. Most of the experimental data presented in these figures are for laminar flow regime. In Fig. 4(*a*), glycol data exhibit a sharp change in heat transfer rates between $10^7 < \text{Ra} < 10^8$, indicating that the laminar flow regime possibly starts at a Rayleigh number close to 10^8, for $A = 0.5$ and $\kappa = 5.338$. This can further be confirmed by verifying the temperature distributions. The temperature profiles for $A = 0.5$, presented in Fig. 2(*b*), show that the temperature gradient in the core is not negligible for $X > 0.5$, a condition necessary for the laminar regime [7]. The gradient $\partial\theta/\partial R$ at $X = 0.75$

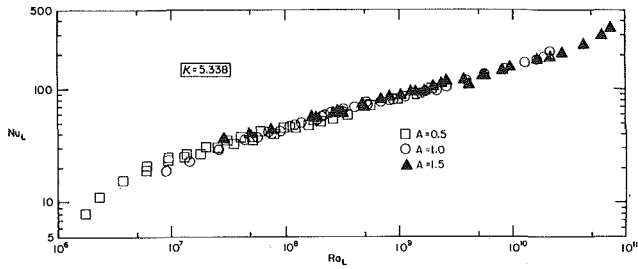

Fig. 5 Effects of aspect ratio on heat transfer rates (Nusselt and Rayleigh numbers in terms of cavity height)

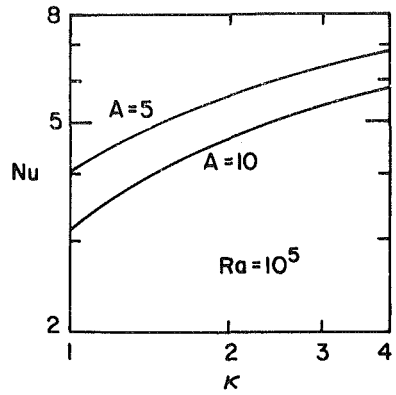

Fig. 6 Effect of radius ratio on heat transfer rates; results of de Vahl Davis and Thomas [6] reproduced

decreases as the Rayleigh number increases, but is not negligible even at Ra = 4.96×10^8, for glycol. For water experiments, this gradient is very small at Ra = 2.07×10^8. This implies that the proper parameter for expressing the flow regime criteria may be the Grashof number, not Ra.

For $A = 1$, a very moderate change in slope for ln (Nu) versus ln (Ra) curve is noticed for Ra > 7×10^7 (Fig. 4(*b*)), whereas for $A = 1.5$ no such change in heat transfer behavior is present (Fig. 4(*c*)). It is thus obvious that the flow is laminar even at Ra = 10^7 when $A = 1.5$. This agrees with the general observation that the laminar regime is delayed as the aspect ratio is reduced below a value lying between 1 and 2.

Since the characterization of flow regimes in terms of the Rayleigh or Grashof number based on the enclosure height is more suitable, the Nusselt numbers and Rayleigh numbers based on the annulus height are presented in Fig. 5, for all three aspect ratios. The change in flow regime from asymptotic to laminar can again be observed in this figure. It now seems reasonable to conclude that at least for $\kappa = 5.338$ and $A = 0.5$, the laminar flow regime starts at $Ra_L = 10^7$, which corresponds to $Gr_L = 7 \times 10^4$. (The advantage or disadvantage of choosing height L instead of the gap width as a characteristic length are the same as experienced in the case of a planar cavity. It is well established that the vertical cavity is a specific case of the annulus, for which $\kappa = 1$ [6, 7, 9].)

For a rectangular cavity of height-to-width ratio of 0.5, Bejan and Tien [17] have reported that the laminar regime starts at $Ra_L = 10^5$. If this value of a "critical" Ra_L is accepted, then the reason for the present value of $Ra_{L,\,critical}$ being higher can only be contributed to the presence of curvature effects. This increase in critical Rayleigh number with an increase in the radius ratio does not support the observation of Thomas and de Vahl Davis [7] that $Ra_{L,\,critical}$ is nearly independent of radius ratio. It may be noted that their criteria for delimiting flow regimes are independent of κ.

In Fig. 4(*b*), a change in heat transfer behavior can again be noticed for Ra > 10^{10}, which is much stronger in case of $A = 1.5$ (Fig. 4(*c*)). A similar change in slope is also demonstrated by the ln (Nu_L) versus ln (Ra_L) curve (Fig. 5) for $Ra_L > 10^{10}$. The reason for this behavior can only be attributed to transition from laminar to turbulent flow. Since in our experimental apparatus, the thermocouples on the inner surface were embedded in the brass wall, fluctuations in the recorded temperatures were damped. To characterize the transition from laminar to turbulent flow, several thermocouples were therefore attached to the inner surface, and experiments were repeated with heptane as the test fluid, for $A = 1$ and 1.5.

For $A = 1.5$, no fluctuation in temperature was recorded at any location for $Ra_L \leq 1.7 \times 10^{10}$. At $Ra_L = 2.76 \times 10^{10}$, the fluctuation was recorded at $X = 0.95$, indicating that the turbulent behavior was initiated at $Ra_x \simeq 2.37 \times 10^{10}$. This Rayleigh number corresponds to $Gr_x = 3.94 \times 10^9$. For an annulus heated by a uniform heat flux on the inner surface ($A = 27.6$, $\kappa = 4.33$), Keyhani [12] has reported that the turbulence is initiated at $10^9 < Gr_x < 3 \times 10^9$. For a water-filled vertical cavity, the data of Cowan et al. [18] conclude this range to be $2.3 \times 10^9 < Gr_x < 5.4 \times 10^9$ [12]. The present value of Gr_x is in excellent agreement with them even *though the values of A and κ are quite different in these three* experiments. Generally, the overall manner in which A, κ, and the thermal boundary condition on the inner wall affect the initiation of turbulence cannot be conclusively answered by the present and previously published data.

Effects of Prandtl Number. When presented in terms of Rayleigh number, the temperature field is affected by a change in Prandtl number, as discussed earlier, though its influence on the heat transfer rate is not significant (Figs. 4(*a–c*)). For $A = 1.5$, the Nusselt numbers for glycol are up to 5 percent higher compared to that for water. This difference increases up to 8 percent for $A = 0.5$, whereas for $A = 1$, no significant variation can be noticed. This weak effect of Prandtl number on the heat transfer supports the results of Thomas and de Vahl Davis [7] who have obtained an exponent of 0.006 for Pr. This is also in agreement with the experimental results of Dropkin and Somerscales [19], and McGregor and Emery [15] for a liquid-filled vertical cavity, and the analytical work of Grabel [20].

Curvature Effects. Increase in the radius ratio enhances the heat transfer coefficient by modifying the temperature field such that the effective sink temperature for the inner boundary layer continually decreases. For an aspect ratio of 1, the present Nusselt numbers are 34 to 74 percent higher than that reported by Raithby et al. [21] and Bohn [22] for the vertical cavity (Fig. 4(*b*)). But the present values are considerably lower than that predicted by equation (3), the correlation obtained by Thomas and de Vahl Davis [7] for the vertical annuli. The difference is as large as 50 percent based on the present values of Nusselt number. A similar variation is obtained if the correlation of Raithby et al. [21] is used after modifying it with the radius ratio dependence reported by Thomas and de Vahl Davis [7], i.e., $\kappa^{0.442}$. The present results for $A = 1.5$ are in similar disagreement with the predicted value (Fig. 4(*c*)). The difference in this case is about 40 percent.

As can be seen in Fig. 4(*b*), the predictions by the correlations of Thomas and de Vahl Davis [7] are in excellent agreement with those by Raithby et al. [21] for a square cavity. This indicates that the correlation of Thomas and de Vahl Davis can be extended to a higher range of Rayleigh number than their computational range (Ra up to 2×10^5) provided the flow is in the laminar regime. It is thus concluded that the large variation in the present experimental values and the predictions by equation (3) for $\kappa = 5.338$ is mainly a result of the overestimation of heat transfer rates in the case of annuli. That is, the exponent of κ is higher. Thomas and de Vahl Davis [7] have reported a fixed value of the exponent for κ for the entire range of radius ratio, i.e., κ

Table 1 Values of C, m, and n for equation (6)

Data correlated*	Aspect ratio A	C	m	n	Standard deviation, %	Rayleigh number range
W,H	0.5	0.302	0.276	0	3.42	$7.6\times10^7 < Ra < 2\times10^{10}$
W,H,G		0.374	0.267	0	4.55	
W,H,G		0.275	0.278	0.028	3.02	
W,H	1	0.305	0.271	0	3.49	$5\times10^7 < Ra < 2\times10^{10}$
W,H,G		0.324	0.269	0	3.77	
W,H,G		0.287	0.273	0.017	3.35	
W,H	1.5	0.373	0.257	0	3.87	$5\times10^7 < Ra < 10^{10}$
W,H,G		0.440	0.250	0	3.69	
W,H,G		0.360	0.257	0.015	3.23	

*W – water, H – heptane, and G – ethylene glycol

≥ 1. It may be noted that their conclusion is based on the computation for $1 \leq \kappa \leq 10$, though the majority of their results are for $1 \leq \kappa \leq 4$.

To clearly understand the dependence of Nusselt number on the radius ratio, the results of de Vahl Davis and Thomas [6] are reproduced in Fig. 6, where the Nusselt number is plotted against the radius ratio. This plot is directly based on Fig. 9 in [6]. As is evident, the slope of the ln (Nu) versus ln (κ) curve decreases very fast as the radius ratio is increased. The curve for $A = 10$ changes slope from about 0.7 at $\kappa = 1$ to about 0.3 at $\kappa = 4$. A similar behavior is indicated by the curve for $A = 5$. A fixed exponent of 0.442 (equations (3)), hence, considerably underestimates the heat transfer rates for $1 < \kappa < 2$ and overestimates them for $\kappa > 3$. This overestimation of Nusselt number for $\kappa > 3$ increases as the radius ratio increases. This is why the predicted values are significantly higher than the present experimental values for $\kappa = 5.338$ (Figs. 4(b) and 4(c)), and are considerably lower than the Nusselt number reported by Schwab and Dewitt for $\kappa = 2$ [8]. A similar argument is applicable to the correlations of Bhushan et al. [11].

Effects of Aspect Ratio. In the laminar flow regime, the Nusselt numbers for $A = 1.5$ are all lower than those for $A = 1$, which, in turn, are all smaller than those for $A = 0.5$ (Figs. 4(a–c)). The difference between the heat transfer coefficients for $A = 0.5$ and 1 or $A = 1$ and 1.5 is up to 15 percent. This results in a difference as large as 30 percent between the Nusselt numbers for $A = 0.5$ and 1.5 for a fixed Ra. This indicates that for the present range of Rayleigh number, which covers almost the entire laminar regime for these aspect ratios, the Nusselt numbers for $A = 0.5$ are maximum.

In the numerical work of Inaba et al. for a vertical cavity [23], the aspect ratio at which the Nusselt number is maximum decreases from $A = 1.7$ at $Ra = 10^4$ to $A = 1.5$ at $Ra = 10^5$. Bejan [24] has predicted that the highest value of Nusselt number will occur at $A = 0.4$ for $Ra = 10^6$, at $A = 0.25$ for $Ra = 10^7$, and at $A = 0.18$ for $Ra = 10^8$. Though this behavior is fully acceptable for the vertical cavities and annuli, one caution is necessary. That is, whenever we compare the values of Nu for a fixed Ra, it must be ascertained that the flow is laminar in each case. The present results for $A = 0.5$ and 1 (Fig. 4(a) and 4(b)) show that the Nusselt numbers for $A = 1$ are greater than those for $A = 0.5$, at least up to $Ra = 2.5 \times 10^7$.

When the Nusselt and Rayleigh numbers are presented in terms of cavity height (Fig. 5), the effect of aspect ratio is observed to be very weak. In the laminar regime, $10^7 < Ra_L < 10^{10}$, Nu_L for $A = 0.5$, 1, and 1.5 are all within ±8 percent for any given Ra_L. This weak dependence on aspect ratio is consistent with what has been observed for the vertical cavity, provided the flow is laminar. The correlation of Thomas and de Vahl Davis (equation (3)) for the vertical annuli reduces to

$$Nu_L = 0.286 Ra_L^{0.258} Pr^{0.006} A^{-0.012} \kappa^{0.442} \quad (5)$$

and agrees with the present behavior.

The present results for $A = 1.5$, 1, and 0.5 further suggest that the heat transfer coefficient is a weak function of aspect ratio, irrespective of the aspect ratio range, provided the variation in A does not change the laminar flow regime. It may be noted that several studies conclude this behavior only for tall cavities, $A > 2$, and the work of Thomas and de Vahl Davis [7] for vertical annuli supports this for $A \geq 1$.

Heat Transfer Correlations. For the laminar flow regime, the present experimental data for heat transfer coefficients may be correlated as

$$Nu = C Ra^m Pr^n, \quad \kappa = 5.338 \quad (6)$$

the values of C, m, and n have been obtained for each aspect ratio and are presented in Table 1. For obtaining the correlations, three different cases have been considered:

1 Prandtl number effect neglected ($n = 0$) and only water and heptane data correlated

2 Prandtl number effect neglected and data for all the test fluids correlated

3 Data for all the fluids correlated with Prandtl number effect taken into account ($n \neq 0$)

For the third case, when Prandtl number effect is considered, the exponent for Pr is observed to increase as the aspect ratio is reduced: from 0.015 for $A = 1.5$ to 0.028 for $A = 0.5$. This exponent for $A = 1.5$ is very close to what has been reported by McGregor and Emery [15] for tall cavity ($n = 0.012$), whereas that for $A = 0.5$ supports the value obtained by Inaba et al. ($n = 0.024$) for shallow cavity, $A < 1$ [23], through numerical computation.

For the height-to-gap width ratio of 1.5, the exponent for Ra ($m = 0.257$) is in excellent agreement with that reported by Thomas and de Vahl Davis (equation (3)) [7]. This value is also close to 0.25, an exponent obtained by several investigators for a vertical cavity, $A > 1$ [2, 15, 21, 23 and others]. In fact, the present value of m reduces to 0.25 once all the data for $A = 1.5$ are correlated with $n = 0$ (Table 1).

The exponent for Ra is observed to increase if the aspect ratio is decreased. For $A = 1$, the present value is 0.273 whereas the values reported by Raithby et al. [21], Inaba et al. [23], and Bohn [22] are all 0.25. On the other hand, the values for m obtained by Newell and Schmidt [25] and Han [26] are 0.397 and 0.313, respectively. The numerical work of Said and Trupp [27] indicates that the exponent of Ra continuously increases as the aspect ratio is decreased from 1.2 to 0.5. Further consideration of the value of m reported by Tseng [28] for $A = 0.5$ ($m = 0.329$) leads us to conclude that the exponent of Rayleigh number depends on the aspect ratio, particularly when the enclosure is not tall, $A < 2$. The lower the aspect ratio, the higher is this exponent.

It may be noted that the values of m for water and heptane data (case 1, $n = 0$) are very close to that for water, heptane, and glycol data with Prandtl number effect taken into account (case 3, $n \neq 0$).

Finally, the present experimental data for $A = 0.5$, 1.0, and

1.5 can also be correlated in terms of Nusselt and Rayleigh numbers based on annulus height L as

$$\mathrm{Nu}_L = 0.272\mathrm{Ra}_L^{0.274}\mathrm{Pr}^{0.020} \quad (7)$$

for $10^7 < \mathrm{Ra}_L < 2 \times 10^{10}$. The standard deviation for this correlation is 4.06 percent. If the Prandtl number effect is neglected, a modified correlation is obtained as

$$\mathrm{Nu}_L = 0.322\mathrm{Ra}_L^{0.269}, \quad 10^7 < \mathrm{Ra}_L < 2 \times 10^{10} \quad (8)$$

with a standard deviation of 4.83 percent.

Conclusion

Experimental results are reported for an isothermally heated vertical annulus of radius ratio 5.338, for $A = 0.5$, 1, and 1.5. Using water, heptane, and glycol as test fluids, a Rayleigh number range of $8 \times 10^6 < \mathrm{Ra} < 3 \times 10^{10}$ and a Prandtl number range of $4 < \mathrm{Pr} < 196$ are covered. The temperature field and the heat transfer rates obtained in this study lead to the following conclusions:

1 The temperature field is significantly influenced by an increase in radius ratio. The effective sink temperature for the boundary layer on the inner wall decreases as the radius ratio is increased. This results in an enhancement of heat transfer rate.

2 The slope of the ln (Nu) versus ln (κ) curve is not constant and is observed to decrease with an increase in κ. The maximum value of this slope exists at $\kappa = 1$. This puts a restriction over the correlations based on a fixed exponent of κ [7, 11].

3 The aspect ratio at which the Nusselt number is maximum depends on the Rayleigh number and the radius ratio. The higher the Rayleigh number and/or the radius ratio, the lower is the aspect ratio for maximum Nusselt number.

4 In the laminar flow regime, the average heat transfer coefficient is a very weak function of the aspect ratio irrespective of its range or the curvature effects.

5 The effect of Prandtl number is very weak for $\mathrm{Pr} > 4$.

6 The start of laminar flow regime is delayed as the radius ratio is increased, and for $A = 0.5$, $\kappa = 5.338$, this takes place at $\mathrm{Gr}_L = 7 \times 10^4$. An increase in A up to 1.5 results in an early start of this regime.

9 The turbulence is initiated when the local Grashof number at the inner wall is $\mathrm{Gr}_x \simeq 4 \times 10^9$.

Finally, the heat transfer rates are correlated separately for each aspect ratio, and are presented in equation (6) and Table 1.

Acknowledgments

The authors express their appreciation to Keith Stone for his assistance in conducting the experiments.

References

1 Beckmann, W., *Forschung a. d. Geb. d. Ingenieurwes*, Vol. 2, 1931 (see [2]).

2 Jacob, M., *Heat Transfer*, Vol. 1, Wiley, New York, 1949, pp. 539–542.

3 Gershuni, G., *Dokl. Akad. Nauk. SSSR*, Vol. 86, No. 4, 1952, pp. 687–694.

4 Sheriff, N., "Experimental Investigation of Natural Convection in Single and Multiple Vertical Annuli With High Pressure Carbon Dioxide," *Proceedings 3rd Int. Heat Transfer Conf.*, Vol. 2, Chicago, 1966, pp. 132–138.

5 Nagendra, H. R., Tirunarayanan, M. A., and Ramachandran, A., "Free Convection Heat Transfer in Vertical Annuli," *Chemical Engineering Science*, Vol. 5, 1970, pp. 605–610.

6 de Vahl Davis, G., and Thomas, R. W., "Natural Convection Between Concentric Vertical Cylinders," *High Speed Computing in Fluid Dynamics, Physics of Fluids, Supplement II*, 1969, pp. 198–207.

7 Thomas, R. W., and de Vahl Davis, G., "Natural Convection in Annular and Rectangular Cavities—A Numerical Study," *Proceedings 4th International Heat Transfer Conference*, Paris, Vol. 4, Paper NC 2.4, Elsevier, Amsterdam, 1970.

8 Schwab, T. H., and DeWitt, K. J., "Numerical Investigation of Free Convection between Two Vertical Coaxial Cylinders," *AIChE Journal*, Vol. 16, 1970, pp. 1005–1010.

9 Lee, Y., Korpela, S. A., and Horne, R. N., "Structure of Multicellular Natural Convection in a Tall Vertical Annulus," *Proceedings 7th Int. Heat Transfer Conf.*, Vol. 2, Munich, Paper NC 17, 1982.

10 Keyhani, M., Kulacki, F. A., and Christensen, R. N., "Free Convection in a Vertical Annulus With Constant Heat Flux on the Inner Wall," ASME JOURNAL OF HEAT TRANSFER, Vol. 105, 1983, pp. 454–459.

11 Bhushan, R., Keyhani, M., Christensen, R. N., and Kulacki, F. A., "Correlation Equations for Free Convection in a Vertical Annulus With Constant Heat Flux on the Inner Wall," ASME JOURNAL OF HEAT TRANSFER, Vol. 105, 1983, pp. 910–912.

12 Keyhani, M., *Free Convection in a Vertical Annulus and Rod Bundle*, Ph.D. dissertation, The Ohio State University, 1983.

13 Prasad, V., and Kulacki, F. A., "Natural Convection in Porous Media Bounded by Short Concentric Vertical Cylinders," ASME JOURNAL OF HEAT TRANSFER, Vol. 107, No. 1, Feb. 1985, pp. 147–154.

14 Prasad, V., Kulacki, F. A., and Keyhani, M., "Natural Convection in Porous Media," *Journal of Fluid Mechanics*, Vol. 150, 1985, pp. 89–119.

15 McGregor, R. K., and Emery, A. F., "Free Convection Through Vertical Plane Layers—Moderate and High Prandtl Number Fluids," ASME JOURNAL OF HEAT TRANSFER, Vol. 91, 1969, pp. 391–403.

16 Yin, S. H., Wung, T. Y., and Chen, K., "Natural Convection in Air Layer Enclosed Within Rectangular Cavities," *International Journal of Heat and Mass Transfer*, Vol. 21, 1978, pp. 307–315.

17 Bejan, A., and Tien, C. L., "Laminar Natural Convection Heat Transfer in a Horizontal Cavity with Different End Temperatures," ASME JOURNAL OF HEAT TRANSFER, Vol. 100, 1978, pp. 641–647.

18 Cowan, G. H., Lovegrove, P. C., and Quarini, G. L., "Turbulent Natural Convection Heat Transfer in Vertical Single Water-Filled Cavities," *Proceedings 7th International Heat Transfer Conference*, Munich, 1982, pp. 195–203.

19 Dropkin, D., and Somerscales, E., "Heat Transfer by Natural Convection in Liquids Confined by Two Parallel Plates Which Are Inclined at Various Angles With Respect to the Horizontal," ASME JOURNAL OF HEAT TRANSFER, Vol. 87, 1965, pp. 77–84.

20 Grabel, W. P., "The Influence of Prandtl Number on Free Convection in a Rectangular Cavity," *International Journal of Heat and Mass Transfer*, Vol. 24, 1981, pp. 125–131.

21 Raithby, G. D., Hollands, K. G. T., and Unny, T. E., "Analysis of Heat Transfer by Natural Convection Across Vertical Fluid Layers," ASME JOURNAL OF HEAT TRANSFER, Vol. 99, 1977, pp. 287–293.

22 Bohn, M. S., "Experimental Study of Three-Dimensional Convection at High Rayleigh Number," Solar Energy Research Institute, Report No. SERI/TR-252-1912, 1983.

23 Inaba, H., Seki, N., Fukusako, S., and Kanayama, "Natural Convection Heat Transfer in a Shallow Rectangular Cavity with Different End Temperatures," *Numerical Heat Transfer*, Vol. 4, 1981, pp. 459–468.

24 Bejan, A., "A Synthesis of Analytical Results for Natural Convection Heat Transfer Across Rectangular Enclosures," *International Journal of Heat and Mass Transfer*, Vol. 23, 1980, pp. 723–726.

25 Newell, M. E., and Schmidt, E. W., "Heat Transfer by Laminar Natural Convection Within Rectangular Enclosures," ASME JOURNAL OF HEAT TRANSFER, Vol. 92, 1970, pp. 159–167.

26 Han, J. T., "A Computational Method to Solve Nonlinear Elliptic Equations for Natural Convection in Enclosures," *Numerical Heat Transfer*, Vol. 2, 1979, pp. 165–175.

27 Said, M. N. A., and Trupp, A. C., "Laminar Free Convection in Vertical Air-Filled Cavities With Mixed Boundary Conditions," ASME Paper No. 79-HT-110, 1979.

28 Tseng, Wen-Fa, "Numerical Experiments on Free Convection in a Tilted Rectangular Enclosure of Aspect Ratio 0.5," M.S. thesis, Clarkson College, 1979.

M. A. Hessami
Department of Mechanical Engineering,
The University of Calgary,
Calgary, Alberta, Canada
Assoc. Mem. ASME

A. Pollard
Department of Mechanical Engineering,
Queen's University,
Kingston, Ontario, Canada
Mem. ASME

R. D. Rowe
Department of Mechanical Engineering,
The University of Calgary,
Calgary, Alberta, Canada

D. W. Ruth
Geotech Engineering,
Calgary, Alberta, Canada

A Study of Free Convective Heat Transfer in a Horizontal Annulus With a Large Radii Ratio

Steady laminar natural convective heat transfer in a horizontal annulus with a large radii ratio (R) *of 11.4 (and inner-cylinder diameter* D_i *of 1.27 cm) has been investigated. Experimental data for air, glycerin, and mercury in the ranges of* $0.023 \leq Pr \leq 10{,}000$ *and* $0.03 \leq Gr_{D_i} \leq 3 \times 10^6$ *are reported. The influence of the variation of fluid properties as compared to the usual assumption of constant fluid properties has been explored numerically for air and glycerin. The heat transfer computations for air do not change with variation of fluid properties, whereas for glycerin significant differences in the local heat transfer distributions and flow patterns are observed. The experimental data have been correlated with some other data from the literature for smaller values of* R, *and it has been shown that the heat transfer from the inner cylinder should be almost the same as that in an infinite medium when* $R \geq 10$.

Introduction

Natural convective heat transfer in annuli with large radii ratio (R) has not received much attention in the literature, and no experimental study for this type of heat transfer for low Pr fluids has been carried out. In this study, an experimental and numerical investigation has been undertaken of free convective heat transfer in air, glycerin, and mercury for a large radii ratio of $R = 11.4$. These fluids were chosen so that a wide range of Pr could be covered. Glycerin was specifically selected because its properties rapidly change with temperature, and thus it provided an appropriate medium for numerical investigations of the effects of variation of fluid properties on heat transfer. In the experimental part of the investigation, heat transfer data for these fluids were collected and the experimental natural convective heat transfer coefficient has been calculated. The data obtained covered the ranges $0.03 \leq Gr_{D_i} \leq 3 \times 10^6$ and $0.023 \leq Pr \leq 10{,}000$ at $R = 11.4$.

There are a large number of publications in the literature on natural convective heat transfer in horizontal annuli. Some recent publications since 1980 are listed in [1-7]. A thorough review of the literature was completed recently by Hessami [8], and will therefore not be repeated here. However, it should be noted that this literature survey [8] indicated that the present study is unique in the following ways: (*i*) The largest value of R employed previously in a laboratory experiment was 8.1 as compared to 11.4 in the present work; (*ii*) no experimental data for mercury have been reported before; and (*iii*) the effect of the variations of the fluid properties on heat transfer in this geometry is numerically investigated here for the first time.

The problem of natural convective heat transfer in horizontal annuli is mathematically described by the continuity, momentum, and energy equations in cylindrical form. In order to simplify these equations, many authors have used various approximations and methods of dimensional analysis. The general consensus as a result of all the different dimensional analyses is that Nu is a function of R, Pr, and Gr; a review of these analyses has been made by Hessami and Rowe [9]. The results of their dimensional analysis, which used the method reported by Hellums and Churchill [10], confirmed the above consensus. In addition, as a result of this type of dimensional analysis, Gr and R appear only in the dimensionless boundary conditions whereas Pr is a parameter in the dimensionless energy equation. To our knowledge, this feature has never been found for other geometries or nondimensionalization schemes.

Some investigators have used the gap width L for the length scale in the Grashof number (and the average Nusselt number) while other investigators have used the inner cylinder diameter D_i. Either length could be used for Gr (and Nu) in the results of the dimensional analysis of Hessami and Rowe [9]. In this paper, Gr_{D_i} and Nu_{D_i} are used so that our results for an annulus with a large radii ratio can be compared with those for cylinders in infinite media.

Experimental Investigation

Experimental Design and Procedure. The major part of the apparatus used in the experimental investigation was the inner cylinder which generated the heat for the inducement of the natural convective flow (see Fig. 1). The inner cylinder was heated by passing direct current through a 0.041-cm-dia nichrome wire which was wound over a threaded glass rod, 0.64 cm in diameter and 27.94 cm long; the nichrome wire was wound over the central 17.78 cm of the glass rod at the rate of 20 turns per in. Two copper electrical leads were soldered to the nichrome wire, 2.223 cm apart, at the center of the glass rod. The voltage drop over the so-called test section of the inner cylinder was measured across these leads, which in turn provided the heat flow rate from the inner cylinder to the convection medium. The current was measured by determining the voltage across a standard resistor in series in the circuit. Only the central portion of the inner cylinder was used for the measurement of the heat dissipation so that the influence of the end losses was minimized.

After insulating the heater, i.e., the glass rod and the nichrome wire, as shown in Fig. 1, the outer casing (ID = 0.914 cm, OD = 1.27 cm and 17.78 cm long), which had been machined from a low-carbon steel rod, was placed around the heater. Steel was used for the casing of the inner cylinder because it does not react with mercury as well as being a good thermal conductor. Rectangular grooves were cut over and along the surface of the casing to accommodate twelve thermocouples which were placed on the outer surface of the inner cylinder, as indicated in Fig. 1. Four thermocouples

Contributed by the Heat Transfer Division and presented at the 21st National Heat Transfer Conference, Seattle, Washington, July 24-27, 1983. Manuscript received by the Heat Transfer Division March 7, 1984.

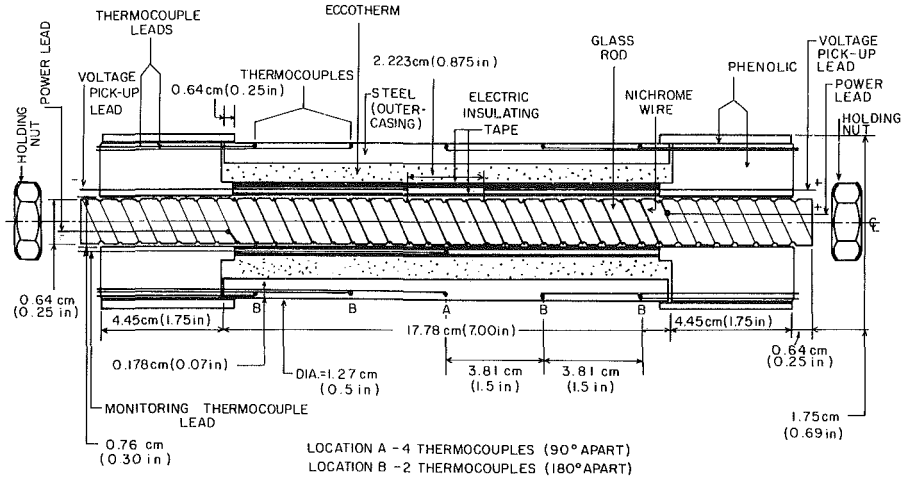

Fig. 1 Schematic diagram of inner cylinder (heater)

were placed 90 deg apart, in the vertical and horizontal planes, at the middle of the inner cylinder, and the remaining eight thermocouples were placed axially along the top and bottom of the inner cylinder. The thermocouples were of the alumel-chromel (K) type – nickel aluminum versus nickel chromium – 0.076 cm in diameter covered with a layer of teflon 0.076 cm thick. The thermocouples were placed inside the grooves, covered with plastic steel, which has properties similar to those of steel, and then thoroughly polished.

The ends of the inner cylinder were made of phenolic resin (an insulating material) tubes (ID = 0.76 cm and OD = 1.75 cm) in order to minimize the axial end losses. The phenolic resin tubes were put in place and pressed against the steel outer casing by screwing two nuts, one at each end of the threaded glass rod. When the inner cylinder was placed inside the heat transfer chamber, the phenolic ends of the inner cylinder contacted the plexiglas (lucite) side walls of the chamber. Plexiglas was used for the side walls of the chamber because it is transparent and has a low thermal conductivity. If an axial temperature gradient along the inner cylinder was observed by the thermocouples, guard heaters were placed over the phenolic ends to minimize end losses; this was found necessary for the air experiments only. The maximum conduction loss through the ends has been calculated to be less than 1 percent of the convective heat transfer [8].

The outer cylinder was formed by the inner surface of a cooling jacket made of steel; the coolant (in this case water), which was kept at a fixed temperature by a constant temperature bath, circulated around the outer cylinder to provide an isothermal surface. A thermocouple was placed at both inlet and outlet of the cooling jacket; the increase in the temperature of the coolant was always insignificant. No thermocouples were placed on the surface of the outer cylinder, because this apparatus was designed for the study of free convective heat transfer from the inner cylinder to a large volume of fluid.

The experimental runs took, on average, 4, 8, and 15 hr for air, glycerin, and mercury, respectively, to reach steady state, which was verified by studying the temperatures that were recorded every 30 min. When steady state had been achieved, the voltage drop across the test section and the standard resistor and the temperatures were recorded. The maximum heat loss by radiation as a percentage of the total heat convected, which was accounted for in the determination of $\overline{\text{Nu}}$,

Nomenclature

c_1, c_2, c_3 = constants
C_p = specific heat at constant pressure
D = diameter of the cylinder
g = acceleration due to gravity
Gr = Grashof number = $\rho^2 g\beta l^3 \Delta T/\mu^2$
h = coefficient of heat transfer
k = thermal conductivity
k_1, k_2, k_3 = constants
L = gap width = $(D_o - D_i)/2$
l = characteristic length = D_i or L
m_1, m_2 = constants
Nu = Nusselt number = hl/k
Pr = Prandtl number = $C_p\mu/k$
r = radial coordinate
R = radii ratio = D_o/D_i
Ra = Rayleigh number = PrGr
T = temperature
u = angular velocity, positive clockwise
v = radial velocity, positive radially outward
V = resultant speed = $(u^2 + v^2)^{1/2}$
W = percent water content of glycerin
β = volumetric coefficient of thermal expansion
Γ_{false} = numerical diffusivity
Δ = change of
θ = angular coordinate
μ = dynamic viscosity
ν = kinematic viscosity = μ/ρ
ρ = density
σ = standard deviation
ψ = stream function

Subscripts

D_i = based on inner diameter
D_o = based on outer diameter
f = evaluated at mean film temperature, $T_f = (T_o + T_i)/2$
i = inner cylinder
L = based on gap width
max = maximum
o = outer cylinder

Superscripts

$\overline{\quad}$ = average value
$*$ = dimensionless

Abbreviations

2D = two dimensional
3D = three dimensional
CFP = constant fluid properties
CPU = central processing unit
EXP = experimental
ID = inside diameter
NUM = numerical
OD = outside diameter
VFP = variable fluid properties

Table 1 Ranges of the experimental data

Parameters	Fluids					
	Air		Glycerin		Mercury	
	min	max	min	max	min	max
ΔT(°C)	13.8	135.4	2.0	69.9	1.6	10.1
$\overline{\mathrm{Nu}}_{D_i}$	3.34	4.77	1.99	8.76	1.93	2.59
Pr	0.69	0.71	867	9744	0.023	0.025
Gr_{D_i}	3.3×10^3	1.5×10^4	0.025	114.6	4.5×10^5	3.0×10^6
Ra_{D_i}	2.4×10^3	1.0×10^4	2.4×10^2	9.9×10^4	1.1×10^4	7.0×10^4
Ra_L	3.4×10^5	1.4×10^6	3.4×10^4	1.4×10^7	1.5×10^6	9.8×10^6

It should be noted that while Table 1 provides the maximum and minimum values of Pr and Gr_{D_i} for each fluid, they do not necessarily correspond to each other, e.g., high Gr_{D_i} generally goes with low Pr (please see Table 5).

Table 2 Axial and angular temperature variation

Fluid	Max. variation, δT(K)		Overall ΔT(K)	$100\,\delta T/\Delta T$	
	Axial	Angular		Axial	Angular
Air (Run #50)	0.4	1.4	135.4	0.3	1.0
Glycerin (Run #94)	1.3	6.0	69.9	1.9	8.6
Mercury (Run #123)	0.2	4.2	10.1	2.0	41.6

was calculated to be 8.7 percent for air and 1.2 percent for glycerin. The surface of the inner cylinder was highly polished, which may explain why the radiation loss for air is lower than that reported by some previous investigators (e.g., [25]).

An investigation of the experimental errors reveals that the uncertainty in the measurement of temperature, which could only be achieved to the nearest tenth of a degree, dominates all other measurement errors. It can be shown that the error in the determination of $\overline{\mathrm{Nu}}_{D_i}$ could be as large as $14/\Delta T$ percent, where ΔT is the temperature difference across the annular gap [8].

Experimental Results. The length of the heated inner cylinder is 17.78 cm; this length was determined by the amount of mercury which we could afford to purchase, and also should be long enough so that the flow is truly 2D in the central region of the annulus. Primitive flow visualization in air and glycerin has indicated that the flow pattern is 2D and laminar.

The ranges of the experimental data are listed in Table 1, and the maximum axial and angular temperature variations are provided in Table 2. It should be noted that the maximum angular temperature variation for mercury is very large (41.6 percent), and thus the intended constant temperature boundary condition on the inner cylinder was very poorly satisfied for mercury.

The properties of the fluids which are used in the calculation of the experimental results were determined at the fluid mean film temperature T_f defined by the following equation

$$T_f = 0.5(T_i + T_o) \tag{1}$$

As discussed in the introduction, for fixed R, $\overline{\mathrm{Nu}}$ is a function of Gr and Pr. A least-squares analysis was performed on each of the three sets of experimental data and an equation of the form

$$\overline{\mathrm{Nu}}_{D_i} = k_1 \mathrm{Pr}^{k_2} \mathrm{Gr}_{D_i}{}^{k_3} \tag{2}$$

was found for each fluid. The values of the constants with the standard deviation σ (calculated with reference to the experimental $\overline{\mathrm{Nu}}_{D_i}$) are given in Table 3. It is evident from this table that these equations represent the experimental data with good accuracy.

In an attempt to find a single correlation equation which represents all of these experimental data, the functional form

Table 3 Constants in equation (2) for various fluids

Fluid	k_1	k_2	k_3	σ(%)	
Air	0.158	−4.18	0.197	1.43	(2*a*)
Glycerin	0.167	0.387	0.282	0.85	(2*b*)
Mercury	0.0101	−1.006	0.117	1.21	(2*c*)

Table 4 Constants in equation (3) for different data sets; m_2 = 0.952 is the value reported by Hyman, Bonilla, and Ehrlich [13]

Data Set		m_1	m_2	σ(%)
(*A*)	Present air, glycerin, and mercury experimental data	0.514	1.356	11.1
		0.504	0.952	14.5
(*B*)	Present air and glycerin experimental data	0.509	0.250	3.0
		0.519	0.952	6.5
(*C*)	Selected air, glycerin, and mercury experimental data	0.515	1.111	15.4
		0.510	0.952	16.8
(*D*)	Selected air and glycerin experimental data	0.504	0.207	2.4
		0.525	0.952	8.2

represented by equation (2) was found to produce an unsatisfactory result. A correlation equation (given by equation (3)) which has been widely used in the literature for both horizontal annuli and horizontal cylinders in infinite media has also been investigated [11–14].

$$\overline{\mathrm{Nu}}_{D_i} = m_1 \left(\frac{\mathrm{Pr}^2}{\mathrm{Pr} + m_2} \mathrm{Gr}_{D_i} \right)^{1/4} \tag{3}$$

where m_1 and m_2 are constants. The values of m_1 and m_2 which best describe all of the experimental data are given in Table 4(*A*). Table 4 also includes the case where m_2 was set equal to the value reported by Hyman, Bonilla, and Ehrlich [13] for natural convection from horizontal cylinders in infinite media, and the best value of m_1 was calculated. The study of Hyman, Bonilla, and Ehrlich [13] is the only experimental investigation reported in the literature for free convection from horizontal cylinders in infinite media of low Pr (mercury and other liquid metals); in addition, they also investigated the entire Pr range reported in this paper. The values of m_1 and m_2 which were reported in [13] are 0.53 and 0.952, respectively. Table 4(*B*) provides values of m_1 and m_2 for all of the air and glycerin experimental data; as evident from the table, a significant reduction in the standard deviation is observed by excluding the mercury data from the analysis. The constants m_1 and m_2 in Tables 4(*A*) and 4(*B*) are

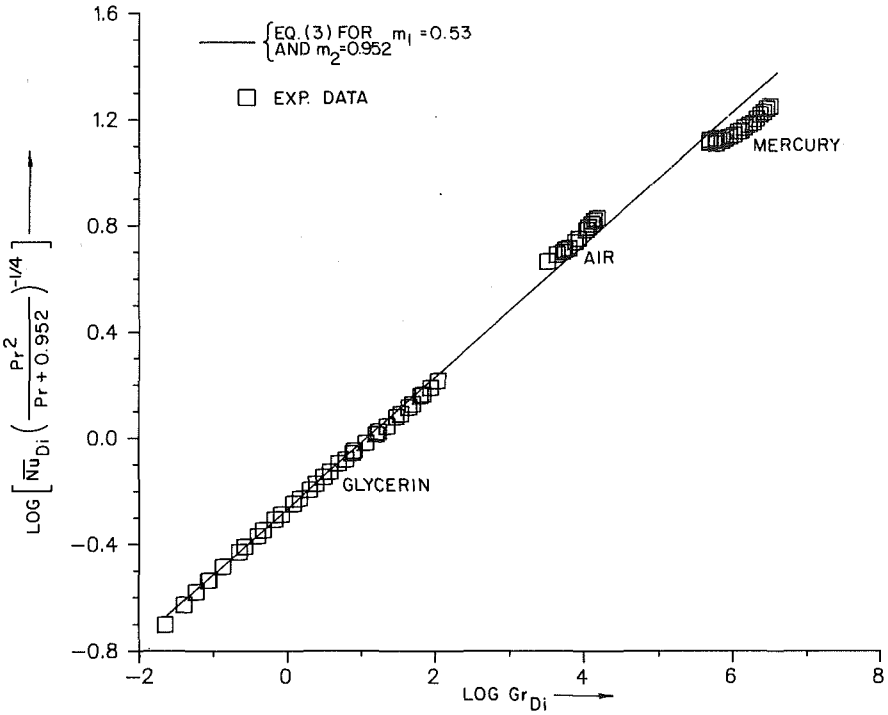

Fig. 2 Experimental data and equation (3)

based on unequal numbers of data for each of the three fluids: 14 air, 36 glycerin, and 30 mercury data points. In order to eliminate this bias in the analysis, a data set (Table 5) with equal numbers of arbitrarily selected data for each of the three fluids has been analyzed and these results are provided in Tables 4(*C*) and 4(*D*); also, the experimental data for mercury with $\Delta T < 3°C$ were eliminated because of the relatively larger experimental error associated with these data.

The values of m_1 provided in Table 4 for fixed values of m_2, i.e., $m_2 = 0.952$, are only slightly lower than that reported in [13], i.e., $m_1 = 0.53$, for horizontal cylinders in infinite media. This result suggests that the geometry used for the generation of the experimental data in this study, i.e., $R = 11.4$, is almost large enough to be used to investigate the heat transfer from a horizontal cylinder in an effectively infinite medium. In order to demonstrate this result graphically, all of the experimental data and equation (3) with $m_1 = 0.53$ and $m_2 = 0.952$ are plotted in Fig. 2.

Table 5 Selected experimental data ($R = 11.4$, $D_i = 1.27$ cm)

T_f(K)	ΔT(K)	Pr	Gr_{D_i}	$EXP\overline{Nu}_{D_i}$
Air data				
311.4	19.2	0.704	4.43×10^3	3.535
323.7	44.3	0.701	8.55×10^3	4.093
339.7	75.0	0.698	11.65×10^3	4.511
342.0	97.2	0.697	14.65×10^3	4.768
359.5	112.8	0.694	13.59×10^3	4.681
Glycerin data				
298.2	9.9	6836.7	0.224	3.405
305.9	25.4	3729.6	2.132	4.951
314.5	42.8	2033.8	12.358	6.430
320.7	55.2	1363.2	36.004	7.435
327.1	66.7	940.1	92.806	8.499
Mercury data				
294.7	3.1	0.0245	0.897×10^6	2.070
296.0	5.0	0.0243	1.427×10^6	2.205
299.0	7.0	0.0240	2.060×10^6	2.362
301.6	8.5	0.0234	2.504×10^6	2.476
304.7	9.9	0.0229	2.997×10^6	2.585

Numerical Study

The computer program which was used in the numerical investigation was based on the continuity, momentum, and energy equations with variable fluid properties. The partial differential equations were transformed to finite-difference equations by using a central-differencing scheme, except for the convection term which was discretized by using a hybrid-differencing technique developed by Spalding [15]. For the variable property computations, each property value was updated at each grid point at each iteration; for the constant property computations each property was evaluted at the fluid mean film temperature. The differential equations, the boundary conditions and the solution procedure for two-dimensional steady laminar flows using this program are described elsewhere [16, 17]. Hessami, Pollard, and Rowe [17] reported numerical computations for air and glycerin for the same geometry as that used by Kuehn and Goldstein [18], i.e., for $R = 2.6$. The accuracy of the computer program was checked against the experimental air and water data of [18] and the agreement was very good [17].

The properties of air were formulated to vary with temperature in accordance with the equations reported by Hessami, Pollard, and Rowe [17]. However, the glycerin equations given in [17] are only valid for a small range of temperature; the following equations are accurate fits to the experimental property data for glycerin for the range $0°C \le T \le 240°C$

$$\rho = 1266.44 - 0.2623T - 0.00369T^2 + 4.81\times10^{-6}T^3 - 9.79\times10^{-9}T^4 \quad (4)$$

$$C_p = 2269.04 + 3.493T + 0.0327T^2 - 1.98\times10^{-4}T^3 + 4.05\times10^{-7}T^4 \quad (5)$$

$$k = 0.2737 + 2.49\times10^{-4}T - 1.56\times10^{-6}T^2 + 5.93\times10^{-9}T^3 \quad (6)$$

$$\mu = \exp\left(4.303 - \frac{6.03\times10^3}{T+273} + \frac{2.01\times10^6}{(T+273)^2} - 0.0965W\right) \quad (7)$$

where W in equation (7) is the water content of glycerin in percent; SI units are used in equations (4–7). These equations

are based on the property data reported by Vargaftik [19], and the functional form of equation (7) has been deduced from Miner and Dalton [20].

In order to economize the computer costs, a numerical solution was obtained for only two experimental points each for air and glycerin; these points were chosen such that they effectively cover the entire range of experimental ΔT for that fluid. An attempt was also made to compute solutions for mercury for the present geometry with $R = 11.4$. However, converged solutions could not be obtained for either the constant or variable property case despite the application of a variety of techniques which are believed to help achieve convergence [8]. Indeed, a solution could not even be obtained for an annulus with 1/4 of the radii ratio, i.e., $R = 2.84$. We were able to obtain solutions for $R = 2.6$, and thus we could compare our local Nu distributions with those published by Kuehn and Goldstein [1]; these results will be reported in a subsequent paper.

The numerical solutions for air (Run #60, $\Delta T = 20.3°C$ and Run #50, $\Delta T = 135.4°C$) were obtained using both constant and variable fluid property formulations. It is found that no significant difference between the numerical solutions using the two aforementioned formulations exists. The isotherms, streamlines, Nu, T, u, and v profiles are available in Hessami [8], and for reasons of conciseness are not reported here.

The average heat transfer results for Runs #50 and 60 are given in Table 6. The grid distribution required for both runs to achieve grid independent solutions was 30×170, and the converged solution was obtained for Run #60 after 590 and for Run #50 after 900 iterations. The numerical solutions were obtained by running the computer program on a Honeywell Multics System; the CPU (central processing unit) times are also listed in Table 6; these times are quite long because 2D solutions have been obtained from a program designed for general 3D problems and the Multics System is designed for

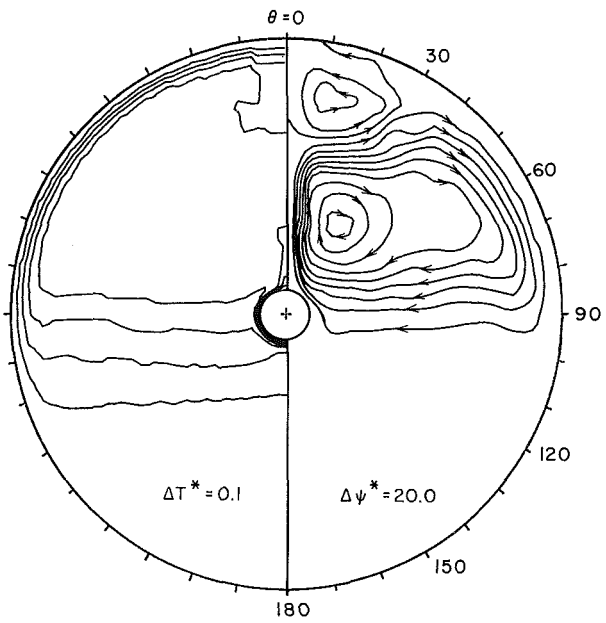

Fig. 3(*a*) Numerical isotherms and streamlines for glycerin for ΔT = 64.3°C, using VFP formulations

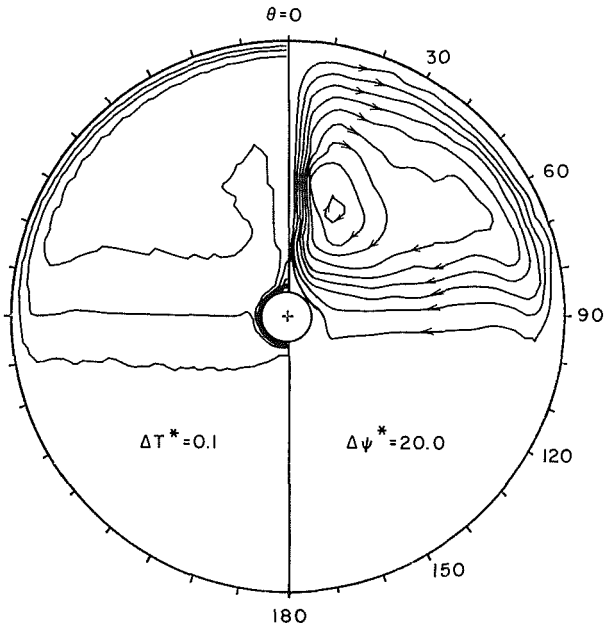

Fig. 3(*b*) Numerical isotherms and streamlines for glycerin for ΔT = 64.3°C, using CFP formulations

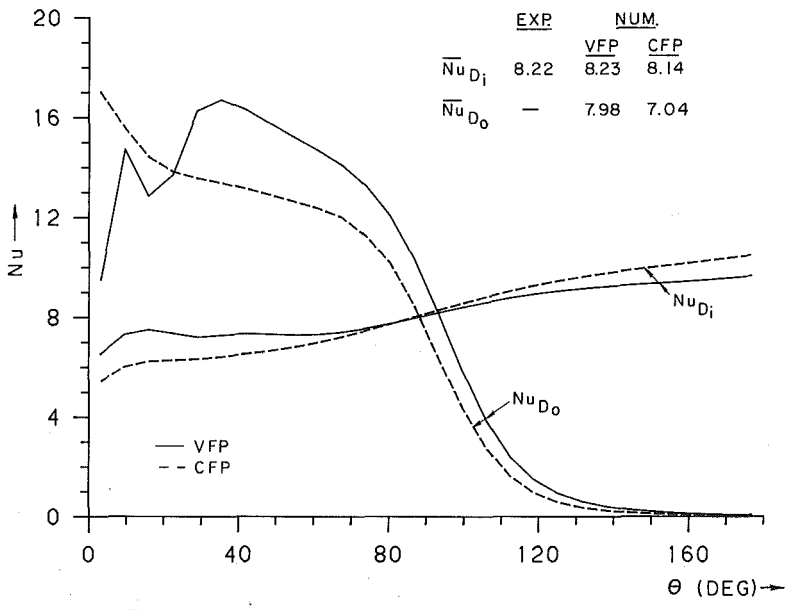

Fig. 3(*c*) Numerical Nu profiles for glycerin for ΔT = 64.3°C

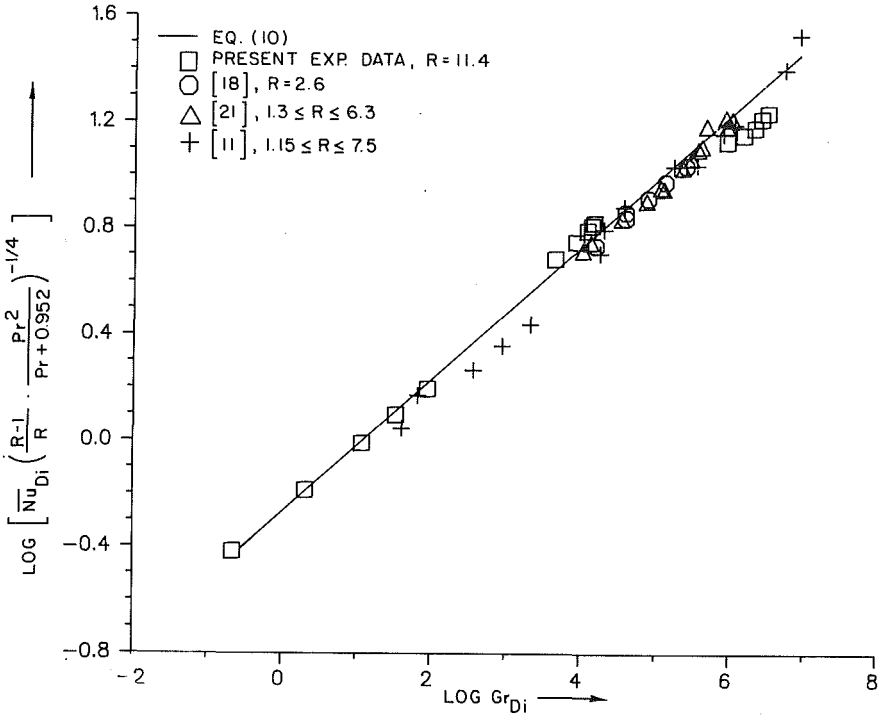

Fig. 4 Data for various R and Pr and equation (10)

Table 6 Experimental and numerical heat transfer results

Run #	EXP $\overline{Nu}_{D_i}$		NUM $\overline{Nu}_{D_i}$	NUM $\overline{Nu}_{D_o}$	$(\Gamma_{false})_{max}$ (m^2/s)	ν (m^2/s)	CPU time (hr) (m^2/s)
60	3.63		3.65	3.11	2.1×10^{-5}	1.6×10^{-5}	24
50	4.77		4.80	4.08	5.9×10^{-5}	2.3×10^{-5}	37
65	3.79	VFP	3.80	3.20	1.1×10^{-7}	5.6×10^{-4}	22
		CFP	3.81	3.10	1.2×10^{-7}	5.6×10^{-4}	14
93	8.22	VFP	8.23	7.98	1.4×10^{-6}	9.6×10^{-5}	45
		CFP	8.14	7.04	8.0×10^{-7}	9.6×10^{-5}	32

interactive use rather than number crunching. It should be noted that the computed $\overline{Nu}_{D_o}$ values are smaller than the $\overline{Nu}_{D_i}$ values; these two Nusselt numbers should be equal for a perfect energy balance. Although this inequality casts some doubt on the accuracy of these computations, similar differences have been reported for other free convection situations (see, for example, de Vahl Davis [26]). It is believed that the $\overline{Nu}_{D_i}$ values are more accurate than the $\overline{Nu}_{D_o}$ values because the grid spacing in the radial direction is much finer near the inside diameter.

The glycerin numerical solutions (Run #65, $\Delta T = 13.3°C$ and Run #93, $\Delta T = 64.3°C$), unlike those for air, are affected by assuming constant fluid properties (CFP), and significant discrepancies were observed between the CFP and VFP (variable fluid properties) cases, especially at high ΔT. The flow fields and Nu profiles for Run #93 ($\Delta T = 64.3°C$) are shown in Fig. 3; due to the symmetry of the flow about the vertical axis, the solution for only half of the annular gap is reported. The grid density required to achieve grid independence and the number of iterations to obtain convergence for Runs #65 and 93 were 40 × 100 and 400, and 30 × 150 and 800, respectively.

The numerical $\overline{Nu}_{D_i}$ for air and glycerin show very favorable agreement with the experimental values, and exhibit no significant difference between the CFP and VFP cases (Table 6). The Nu, T, u, and v profiles under these two formulations differ significantly for glycerin (see for example, Fig. 3*c*) while negligible variation was observed for air [8]. Thus, assuming constant fluid properties for air (which can be extended to all gases because of their similar property variations) does not affect the heat transfer results.

The numerical solution for glycerin with $\Delta T = 13.3°C$ showed some difference between the CFP and VFP results, but the difference was not significant enough to alter the flow pattern substantially. However, in the numerical results for glycerin with $\Delta T = 64.3°C$ (Fig. 3), a major change of the flow pattern is evident due to the appearance of a counter-rotating secondary cell (Figs. 3*a* and 3*b*). The cell covers an area near the outer cylinder between $\theta \cong 0$ deg and $\theta \cong 30$ deg. The relatively lower speed of the secondary cell, as evident in Fig. 3(*a*), retards the heat transfer process and thus results in a lower Nu field (Fig. 3*c*).

The convergence criteria reported in [17] were also used in the present study. The maximum false (or numerical) diffusivity for each numerical run was calculated from [17, 22]

$$(\Gamma_{false})_{max} = 0.707 V \frac{(r\Delta\theta)\Delta r}{r\Delta\theta + \Delta r} \tag{8}$$

As shown in Table 6, the maximum false diffusivities for air are only of the same order of magnitude as the real diffusivity (or kinematic viscosity) ν. A similar situation occurred for the air computations reported in [17] and therefore the present air results should not possess significant numerical errors. It is believed that the maximum false diffusivity criterion of de Vahl Davis and Mallinson [22] can be relaxed in this situation because the flow is normally closely aligned with the grid lines throughout the flow field, and where the speed has the largest value, in the plume above the inner cylinder, the velocity is almost tangent to the grid lines. The false diffusivity for glycerin is very much smaller than the real diffusivity, and therefore the numerical errors should be insignificant.

Table 7 Constants for equation (9) for the combined experimental data

	c_1	c_2	c_3	σ (%)
(*a*)	0.451	0.139	0.493	11.0
(*b*)	0.463	0.148	0.952	11.1
(*c*)	0.53	0.249	0.952	13.1
(*d*)	0.53	0.25	0.952	13.1

Influence of Radii Ratio

In order to account for the effect of R on $\overline{\mathrm{Nu}}_{D_i}$ experimental data for various values of R and Pr have been taken from the literature. Experimental data from three publications are included in the present analysis for the following reasons.

1 The data of Liu, Mueller, and Landis [11] cover a wide range of R and Pr, i.e., $1.15 \leq R \leq 7.5$ and $0.7 \leq \mathrm{Pr} \leq 3600$. Their air data have not been included because large discrepancies (30–60 percent) were found between these data and the correlation equation.

2 The experimental data reported by Grigull and Hauf [21] covered the range of $1.3 \leq R \leq 6.3$ for $\mathrm{Pr} = 0.71$.

3 The accuracy of the experimental data of Kuehn and Goldstein [18] has been confirmed by numerical investigators [4, 17].

The data from the above three publications have been combined with the selected data set from our experiments (listed in Table 5) for the analyses in this section.

Correlation equations of the type given by equation (3) can be multiplied by a function of R such that in the limiting cases as $R \to 1$ and $R \to \infty$, $\overline{\mathrm{Nu}}_{D_i}$ approaches the situations of zero natural convection heat transfer and natural convection heat transfer from horizontal cylinders in infinite media, respectively. An equation which satisfies these conditions is

$$\overline{\mathrm{Nu}}_{D_i} = c_1 \left(\frac{R-1}{R}\right)^{c_2} \left(\frac{\mathrm{Pr}^2}{\mathrm{Pr}+c_3}\mathrm{Gr}_{D_i}\right)^{1/4} \tag{9}$$

where c_1, c_2, and c_3 are constants. The best values of these constants for the combined set of experimental data covering the ranges $1.15 \leq R \leq 11.4$ and $0.023 \leq \mathrm{Pr} \leq 10{,}000$ are provided in Table 7. In case (*a*), all of the constants were allowed to vary to find the best fit; in case (*b*), the constant c_3 was fixed at the value reported by Hyman, Bonilla, and Ehrlich [13]; in case (*c*), both c_1 and c_3 are set equal to those of [13]. Because the value of c_2 (=0.249) calculated in case (*c*) is so close to 1/4, c_2 was also fixed at 0.25 for case (*d*). In order to show an example of the scatter of the combined set of experimental data, they are plotted in Fig. 4 together with equation (9) for case (*d*) when $c_1 = 0.53$, $c_2 = 0.25$, and $c_3 = 0.952$.

$$\overline{\mathrm{Nu}}_{D_i} = 0.53\left(\frac{R-1}{R} \cdot \frac{\mathrm{Pr}^2}{\mathrm{Pr}+0.952} \cdot \mathrm{Gr}_{D_i}\right)^{1/4} \tag{10}$$

The largest deviations from the straight line representing equation (10) in Fig. 4 are shown by our mercury data and the data of [11]. According to equation (10), when $R = 11.4$, $\overline{\mathrm{Nu}}_{D_i}$ has reached 97.7 percent of its value for an infinite medium.

A similar analysis for determining the limiting values of R has been undertaken by Kuehn and Goldstein [27]; for example, when $\mathrm{Pr} = 100$, they found that the annuli heat transfer coefficient is within 95 percent of that for an infinite medium if $R > 360$ at $\mathrm{Ra}_{D_i} = 10^7$ and $R > 700$ at $\mathrm{Ra}_{D_i} = 0.1$. The results of the present study indicate that the limiting value for R does not need to be nearly as large as suggested by Kuehn and Goldstein.

The aforementioned combined set of experimental data have also been compared with some other correlation equations in the literature [1, 11, 12, 14, 18, 21, and 23]. None of these equations showed reasonable agreement with all of the data, while partial conformity has been revealed [8]. All of the equations included in the analysis showed very large discrepancy with the present mercury data. This is believed to be due to the lack of experimental data for low Pr fluids in the literature. Finally, it should be added that the equations developed in this study may fail to accurately predict $\overline{\mathrm{Nu}}_{D_i}$ in different ranges of Pr and Gr_{D_i} than those tested here, e.g., low Pr and low Gr_{D_i}.

Conclusions

Experiments are reported for steady laminar free convection with air, glycerin, and mercury in a wide horizontal annulus ($R = 11.4$). The experimental data are unique because there are no experimental data in the literature for $R > 8.1$. In addition, no experimental data exist for mercury except for the mixed convection experiments of Huetz and Petit [24] and the free convection in infinite media investigations of Hyman, Bonilla, and Ehrlich [13].

The numerical results exhibited the general flow patterns expected for natural convection in horizontal annuli, i.e., the fluid near the higher temperature inner cylinder rises due to its lower density and impinges upon the outer cylinder via a narrow vertical plume; it then moves downward along the outer surface before joining rising fluid in the lower annular gap. The numerical results for glycerin show significant variation in the local heat transfer distribution and the flow pattern when the different formulations of constant and variable fluid properties were employed, while no such discrepancy was observed for air. The average Nusselt number has been found to be almost independent of the variation of fluid properties, and excellent agreement between the experimental and numerical results for the average Nusselt number has been achieved. The local Nusselt number and the flow field were not measured in these experiments; much more work would be required to provide a detailed local comparison between experimental and numerical results. Care was taken to ensure that the numerical computations satisfied grid independence as well as established convergence criteria.

Correlations have been developed to represent the present experimental data (equation (3)) and the combination of these data with some other data taken from the literature for smaller values of R (equations (9) and (10)). These correlations suggest that the geometry used in this study ($R = 11.4$) is large enough to be used to determine $\overline{\mathrm{Nu}}_{D_i}$ for a horizontal cylinder in an effectively infinite medium. For example, according to equation (10), when $R = 10$, Nu_{D_i} has reached 97.4 percent of its value for an infinite medium.

References

1 Kuehn, T. H., and Goldstein, R. J., "A Parametric Study of Prandtl Number and Diameter Ratio Effects on Natural Convection Heat Transfer in Horizontal Cylindrical Annuli," ASME JOURNAL OF HEAT TRANSFER, Vol. 102, Nov. 1980, pp. 768-770.

2 Jeschke, M. C., and Farshchi, M., "Boundary Layer Regime for Laminar Free Convection Between Horizontal Circular Cylinders," ASME JOURNAL OF HEAT TRANSFER, Vol. 102, May 1980, pp. 288-235.

3 Yao, L. S., "Analysis of Heat Transfer in Slightly Eccentric Annuli," ASME JOURNAL OF HEAT TRANSFER, Vol. 102, May 1980, pp. 279-284.

4 Projahn, U., Reiger, H., and Beer, H., "Numerical Analysis of Laminar Natural Convection Between Concentric and Eccentric Cylinders," *Numerical Heat Transfer*, Vol. 4, 1981, pp. 131-146.

5 Boyd, R. D., "Unified Theory for Correlating Steady Laminar Natural Convection Heat Transfer Data from Horizontal Annuli," *Int. J. of Heat Mass Transfer*, Vol. 24, No. 9, 1981, pp. 1545-1548.

6 Farouk, B., and Guceri, S. I., "Laminar and Turbulent Natural Convection in the Annulus Between Horizontal Concentric Cylinders," ASME JOURNAL OF HEAT TRANSFER, Vol. 104, Nov. 1982, pp. 631-636.

7 Cho, C. H., Chang, K. S., and Park, K. H., "Numerical Simulation of Natural Convection in Concentric and Eccentric Horizontal Cylindrical Annuli," ASME JOURNAL OF HEAT TRANSFER, Vol. 104, Nov. 1982, pp. 624-630.

8 Hessami, M. A., "Natural Convection Heat Transfer in a Wide Horizontal Annulus," Ph.D. thesis, Department of Mechanical Engineering, University of Calgary, Alberta, May 1983.

9 Hessami, M. A., and Rowe, R. D., "Dimensional Analysis of the Governing Differential Equations for Natural Convection Heat Transfer in a Horizontal Annulus," Department of Mechanical Engineering, Report #263, University of Calgary, Alberta, Jan. 1983.

10 Hellums, J. D., and Churchill, S. W., "Dimensional Analysis and Natural Circulation," *Chemical Engineering Progress Symposium Series on Heat Transfer*, Vol. 57, No. 32, 1961, pp. 75–80.

11 Liu, Chen-Yan, Mueller, W. K., and Landis, F., "Natural Convection Heat Transfer in Long Horizontal Cylinders," *Int. Developments in Heat Transfer, Proc. of Heat Transfer Conf.*, Colorado, 1969, pp. 976–984.

12 Raithby, G. D., and Hollands, K. G. T., "A General Method of Obtaining Approximate Solutions to Laminar and Turbulent Free Convection Problems," *Advances in Heat Transfer*, Vol. 11, 1975, pp. 265–315.

13 Hyman, S. C., Bonilla, C. F., and Ehrlich, S. W., "Natural Convection Transfer Processes: I. Heat Transfer to Liquid Metals and Nonmetals at Horizontal Cylinders," *Chemical Engineering Progress Symposium*, No. 5, Vol. 49, 1953, pp. 21–31.

14 Churchill, S. W., and Chu, H. H. S., "Correlating Equations for Laminar and Turbulent Free Convection From a Horizontal Cylinder," *Int. J. of Heat Mass Transfer*, Vol. 18, 1975, pp. 1049–1053.

15 Spalding, D. B., "A Novel Finite Difference Formulation for Differential Expressions Involving Both First and Second Derivations," *Int. J. Num. Methods Eng.*, Vol. 4, 1972, pp. 551–559.

16 Hessami, M. A., and Pollard, A., "Numerical Calculations of Free Convective Heat Transfer Between Horizontal Concentric Isothermal Cylinders," Department of Mechanical Engineering, Report #213, University of Calgary, Alberta, Dec. 1981.

17 Hessami, M. A., Pollard, A., and Rowe, R. D., "Numerical Calculations of Natural Convection Heat Transfer Between Horizontal Concentric Isothermal Cylinders—Effects of Variation of Fluid Properties," ASME JOURNAL OF HEAT TRANSFER, Vol. 106, Aug. 1984, pp. 668–671.

18 Kuehn, T. H., and Goldstein, R. J., "An Experimental and Theoretical Study of Natural Convection in the Annulus Between Horizontal Concentric Cylinders," *J. of Fluid Mechanics*, Vol. 74, Part 4, 1976, pp. 695–719.

19 Vargaftik, N. B., *Tables on the Thermophysical Properties of Liquids and Gases*, Wiley, New York, 1975.

20 Miner, C. S., and Dalton, N. N., *Glycerol*, Reinhold, New York, 1953.

21 Grigull, V., and Hauf, W., "Natural Convection in Horizontal Cylindrical Annuli," *Proc. of 3rd Int. Heat Transfer Conf.*, Vol. 2, 1966, pp. 154–158 and 182–195.

22 de Vahl Davis, G., and Mallinson, G. D., "False Diffusion in Numerical Fluid Mechanics," School of Mech. and Ind. Eng., Report #1972/FMT/1, University of New South Wales, 1972.

23 Itoh, M., Fujita, T., Nishiwaki, N., and Hirata, M., "A New Method of Correlating Heat Transfer Coefficient for Natural Convection in Horizontal Cylindrical Annuli," *Int. J. of Heat Mass Transfer*, Vol. 13, 1970, pp. 1362–1368.

24 Huetz, J., and Petit, J. P., "Natural and Mixed Convection in Concentric Annular Spaces—Experimental and Theoretical Results for Liquid Metals," *5th Int. Heat Transfer Conf.*, Tokyo, Vol. 3, 1974, pp. 169–172.

25 Keyhani, M., Kulacki, F. A., and Christensen, R. N., "Free Convection in a Vertical Annulus with Constant Heat Flux on the Inner Wall," ASME JOURNAL OF HEAT TRANSFER, Vol. 105, Aug. 1983, pp. 454–459.

26 de Vahl Davis, G., "Natural Convection of Air in a Square Cavity: A Bench Mark Numerical Solution," *International Journal for Numerical Methods in Fluids*, Vol. 3, 1983, pp. 249–264.

27 Kuehn, T. H., and Goldstein, R. J., "Correlating Equations for Natural Convection Heat Transfer Between Horizontal Circular Cylinders," *Int. J. Heat Mass Transfer*, Vol. 19, 1976, pp. 1127–1134.

Experimental Investigation of Free Convection in a Vertical Rod Bundle—A General Correlation for Nusselt Numbers

M. Keyhani
Department of Mechanical and Aerospace Engineering, The University of Tennessee, Knoxville, TN 37996-2210
Mem. ASME

F. A. Kulacki
Department of Mechanical and Aerospace Engineering, University of Delaware, Newark, DE 19716
Mem. ASME

R. N. Christensen
Department of Mechanical Engineering, The Ohio State University, Columbus, OH 43210

Free convection in two vertical, enclosed rod bundles has been experimentally investigated for a wide range of Rayleigh numbers. A uniform power dissipation per unit length is supplied to each rod, and the enclosing outer cylinder is maintained at constant temperature. Nusselt numbers for each rod, as well as an overall value for each bundle, have been obtained as a function of Rayleigh number. Comparison of the results for air and water as the working fluid indicate that, for a fixed Rayleigh number, an increase in the Prandtl number produces a reduction in the Nusselt number. This is contrary to what has been reported for vertical cavities and is attributed to curvature effects. Furthermore, the data reveal the interesting fact that it is quite possible for the individual rods in the bundle to exchange energy with the working fluid via different but coexisting regimes at a given power dissipation. Also, as the Rayleigh number is increased, the rods each tend to assume nearly the same heat transfer coefficient. Finally, a correlation for the overall convective Nusselt number is developed in terms of Rayleigh number and geometric parameters.

Introduction

Heat transfer measurements are presented for free convection in enclosed vertical rod bundles. Two rod bundles have been studied in the present work: a 3 × 3 array with $P/d = 3.08$, $L/d = 138$, and $L/D = 10.62$, and a 5 × 5 array with $P/d = 2.25$, $L/d = 92.42$, and $L/D = 5.79$. A uniform power dissipation per unit length in each rod is maintained, while the enclosing outer cylinder is held at constant temperature. The results include individual rod temperature distributions, heat transfer coefficients, and correlations for Nusselt numbers, all as a function of Rayleigh number and geometric parameters.

The plans for storage or disposal of spent fuel rod bundles from nuclear power reactors, encapsulated in air or helium-filled canisters, have led to a number of studies in this area. Previous studies on natural convection in rod bundles were concerned with temporary storage at the reactor site where the rod bundles are not enclosed [1]. In the case of an air or helium-filled canister containing the spent fuel rod bundle, the heat transfer problem becomes quite involved and difficult. The three modes of heat transfer, conduction, convection, and radiation, are superimposed. Moreover, the power dissipated by the rod bundle decays with time and is not uniform along the length of each rod.

Radiative heat transfer within an enclosed rod bundle has been studied by a number of investigators [2, 3, 4]. Also, some center rod temperature measurements of an actual spent fuel rod bundle, 15 × 15 rods with $P/d = 1.33$, enclosed in an air or helium-filled canister are available [5]. These temperature measurements are in good agreement with the predictions by a computer code, HYDRA-I, developed by McCann [6]. His code is programmed to treat transient three-dimensional coupled conduction, convection, and radiation in an enclosed rod bundle. The code provides a finite-difference solution in Cartesian coordinates to the continuity, momentum, and energy equations. In his study, the equation of motion is based on a generalization of flow through porous media, where the term for viscous forces is retained. The results obtained through the HYDRA-I code are temperature profiles of the rods in the array for different test fluids and boundary conditions on the canister surface. No parametric dependence of the heat transfer coefficient on the outer cylinder surface to flow parameter, Ra_D, or geometric factors is reported. Furthermore, the HYDRA-I code does not provide any information with respect to the relative contribution of convective heat transfer to the total energy transferred.

The main objective of the present study is to provide basic heat transfer data, convection Nusselt number as a function of Rayleigh number, in rod bundles where (*a*) coupled radiation, conduction, and convection heat transfer processes are present and (*b*) the pitch-to-diameter ratio, P/d, and the outer cylinder diameter are large enough so that porous media assumptions used in [6] are no longer valid.

Experimental Apparatus and Procedure

3 × 3 Rod Bundle. An existing outer cylinder with the associated controls and instrumentation [7] is used in the present study. The rod bundle that is placed in this canister consists of the top plate, nine heater rods, and the guide. The guide is 0.32-cm-thick Phenolite and is attached at the bottom of the rod bundle so that the desired pitch distance is maintained.

The top plate is carbon steel and is threaded for fastening with the cylinder, which is threaded internally. Nine holes of 0.64 cm diameter are drilled and tapped to accept the fittings at the top ends of the heater rods. These holes are on a square grid of 3.92 cm × 3.92 cm, which fits inside a circle of 8.26 diameter. The pitch distance between the holes is 1.95 cm.

Three 0.64-cm-dia holes on 3.22-cm centers are drilled and tapped in the top plate. Two Conax thermocouple connectors are fitted in these holes. The third hole is fitted by a Quick-Connect for the purpose of pressurizing or evacuating the system.

A square groove of 0.64 cm × 0.64 cm is cut into the lower surface of the top plate. The groove connects one of the holes

Contributed by the Heat Transfer Division for publication in the JOURNAL OF HEAT TRANSFER. Manuscript received by the Heat Transfer Division February 1, 1984. Paper No. 84-HT-72.

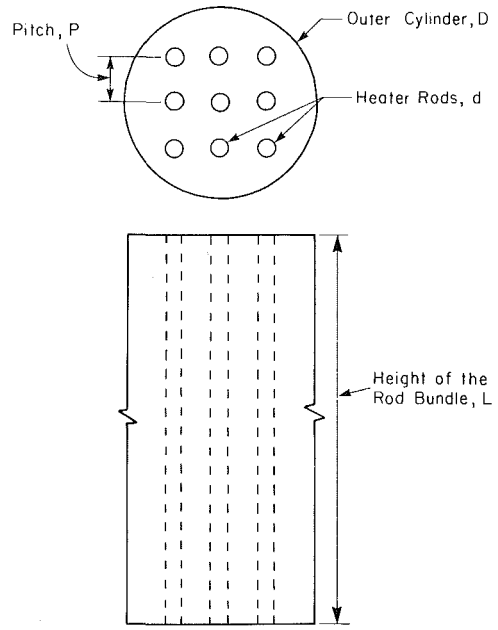

Fig. 1 Schematic of the enclosure and the assigned nomenclature for the length scales

for a Conax thermocouple connector to the hole for the center heater rod. This groove is used to channel the thermocouples close to the center rod. Then the thermocouples are lowered into the cylinder parallel to the heater rod. The thermocouples are affixed to the surface of the rod with plastic steel. The other rods in the bundle are instrumented in a similar manner.

The rod bundle comprises nine 0.635 cm dia × 91.44 cm cartridge heaters. The length includes a 1.27-cm-long threaded fitting at the top of the heater element. Each heater has an effective heated length of 87.6 cm and is designed to provide uniform electrical power dissipation per unit length. It comprises a nickel-chromium wire wound around a magnesium oxide core with a 0.05-cm Incoloy sheath.

The outer cylinder is of carbon steel and is 8.25 cm i.d. × 9.53 cm o.d. × 92.17 cm. To maintain it at constant temperature, 30.48 m of 0.9-cm-dia soft copper tubing is used to provide a cooling coil around the outer surface. This coil is wound in a counter flow manner to give a uniform surface temperature. A gap of 0.64 cm is provided between consecutive turns of the coil for emplacement of thermocouples along the surface. Figure 1 presents a schematic of the enclosure and the assigned nomenclature for the length scales.

5 × 5 Rod Bundle. The design of the apparatus for the 5 × 5 array is comprised of four major components: top plate, cylinder, and heated elements. In general, these components are configured similarly to those in the apparatus for the 3 × 3 array.

The top plate is a 2.54-cm-thick piece of brass with a 33.97-cm diameter. Twenty-five holes 1.91 cm in diameter are drilled and tapped in this plate for mounting the heating elements. These holes are located on a 21.44 cm × 21.44 cm square, which fits inside a circle of 30.31 cm diameter. The pitch distance between the holes is 4.29 cm. For introducing either air or another gas into the cylinder, a 0.63-cm-dia threaded hole on 13.28 cm center is drilled into the top plate. Four holes of 1.91-cm diameter on 12.86-cm centers are drilled and tapped in the top plate to accommodate four Conax thermocouple connectors.

The brass cylinder is 30.48 cm i.d. × 31.43 cm o.d. and 185.42 cm long. Two collars of 31.43 cm i.d. × 33.97 cm o.d. with a thickness of 1.27 cm are silver soldered to the top

Nomenclature

A_d = area of heater rod, m^2
A_D = area of outer cylinder, m^2
AR = height-to-diameter ratio of the cylinder or rod
C_p = specific heat at constant pressure, J/kg-K
d = diameter of a heater rod, m
d_i = diameter of equivalent inner cylinder, Nd, m
D = diameter of outer cylinder, m
g = gravitational constant, m/s^2
Gr = Grashof number, $g\beta l^3 \Delta T/\nu^2$
h_D = convective heat transfer coefficient on the inner cylinder, W/m^2
h_{di} = overall convective heat transfer coefficient on outer cylinder, $Q_c/A_D\Delta T$, W/m^2-K
h = convective heat transfer coefficient on the ith rod, $W_c/A_d(T_{MRi} - T_{MC})$, W/m^2-K
H = aspect ratio, L/l
k = thermal conductivity, W/m-K
K = radius ratio, r_o/r_i
l = annular gap, $r_o - r_i$, m
L = height of the cylinder or rod, m
N = number of rows in the square rod array
Nu = convective Nusselt number, hl/k
Nu_D = overall convective Nusselt number, $h_D D/k$
Nu_{di} = convective Nusselt number on ith rod, $h_{di}d/k$
P = center-to-center distance between the rods in a row, m
Pr = Prandtl number
q = convective heat flux based on the inner cylinder area, W/m^2
Q = total power input, W
r = radius, m
Ra = Rayleigh number, GrPr
Ra* = modified Rayleigh number, $\left(\frac{gB}{\alpha\nu}\right)\left(\frac{gl}{k}\right)l^3$
Ra_D = Rayleigh number based on diameter of outer cylinder, $(g\beta/\alpha\nu)D^3\Delta T$
Ra_{di} = Rayleigh number based on diameter of heater rod for rod i $(g\beta/\alpha\nu)(T_{MRi} - T_{MC})d^3$
T = temperature, K
ΔT = characteristic temperature difference, $T_{MR} - T_{MC}$, °C, for rod bundles T_{MR} is evaluated on the center rod
W = power per rod, W
W_c = energy transferred by convection for a given heater rod, W
y = coordinate measuring distance along rod from bottom, m
α = thermal diffusivity, $k/\rho C_p$, m^2s
β = isobaric coefficient of thermal expansion, K^{-1}
ϵ = emissivity
ν = kinematic viscosity, m^2/s
ρ = density, kg/m^3
σ = Stefan-Boltzmann constant, 5.669×10^{-8}, W/m^2-K^4

Subscripts

c = convection
d = based on rod
D = based on outer cylinder
i = inner
MC = mean value on outer cylinder
MR = mean value on rod
o = outer
R = rod

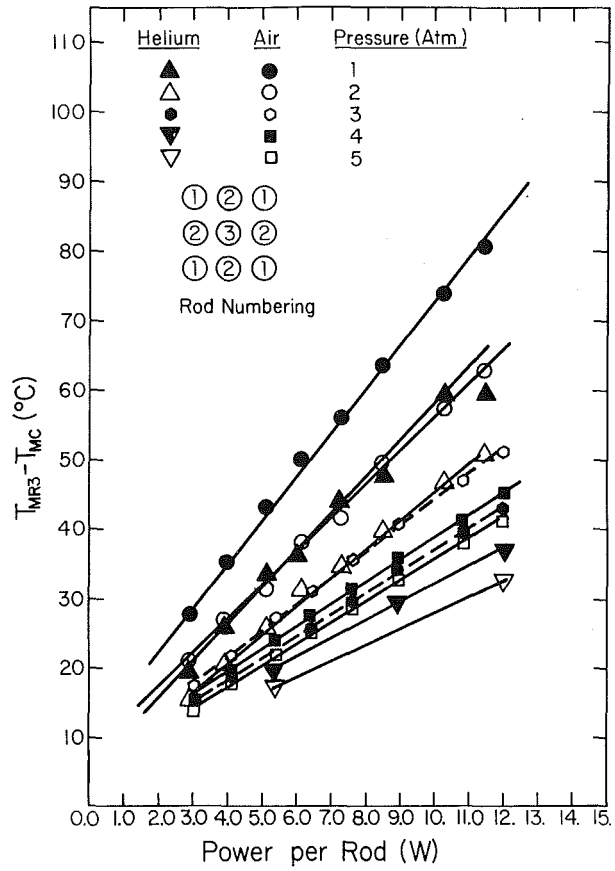

Fig. 2 Average temperature difference on center rod $T_{MR3} - T_{MC}$ as a function of total power per rod

and bottom ends of the cylinder. Sixteen equally spaced holes of 0.95-cm diameter on 16.75-cm centers are drilled through the end plates and collars. These holes facilitate the bolting of the end plates to the cylinder. Also, two separate soft copper cooling coils of 0.95-cm diameter are soft soldered to the top and bottom half of the cylinder. This coil will be used for circulating water to maintain the cylinder wall at constant temperature. Forty-eight holes of 0.13-cm diameter are drilled along the length of the cylinder. These holes are located along four lines, twelve holes per line, that divide the cylinder into four equal parts. Surface temperature thermocouples are placed in these holes.

The rod bundle comprises twenty-five 1.91-cm-dia cartridge heaters with an effective heated length of 176.5 cm. The basic design of the heater elements is similar to those used in the 3 × 3 rod bundle. A 30-cm-dia × 1.27-cm-thick Phenolite guide with twenty-five holes of 1.91-cm diameter on a square grid the same as the top plate is attached to the bottom of the rods to maintain the square array. Thermocouples are attached to the rods in this array in a manner similar to that for the 3 × 3 rod bundle.

Measurements of rod temperatures are made to within 0.1°C to 0.2°C using a variety of recording data loggers and voltmeters. Power to the heated rods is supplied through a filtered voltage regulator and transformers. Power to each rod in the bundle is held to within 1 percent of the set value under normal conditions for free convection. The radiation correction for each rod, however, requires that power input be adjusted to produce a predetermined mean rod temperature. This was done manually after the system had been allowed to reach steady state under a vacuum. Normally, a data run for a rod bundle required from several days to three weeks owing to the time required to reach steady state and the trial-and-error procedure needed to obtain the radiative correction. A more detailed description of the experimental apparatus, instrumentation and procedure are given in [8, 9].

Results and Discussions

3 × 3 Rod Bundle

Air and Helium. Heat transfer data obtained from these experiments include total and convective Nusselt number for each rod as well as an overall value for the bundle for a wide range of Rayleigh number. The characteristic length used in the definition of overall Nusselt and Rayleigh numbers is the diameter of the outer cylinder. The temperature difference is taken as the difference between the average value of the center rod and that of the outer cylinder. The heat transfer coefficient is based on the area of the outer cylinder. In terms of overall Rayleigh number, heat transfer data cover the range of $1.95 \times 10^4 \leq \mathrm{Ra}_D \leq 4.5 \times 10^7$. This range covers the conduction to boundary layer flow regimes. The numbering of rods in the bundle is given in Fig. 2.

Seventy runs with air and helium at various pressures and power inputs to the rods were conducted. The characteristic temperature difference for the rod bundle, $T_{MR3} - T_{MC}$, is plotted as a function of power input to the rods in Fig. 2. For a given test gas and power input, an increase in the pressure corresponds to an increase in the Grashof number; consequently, a lower temperature difference is observed. Furthermore, for a given test gas and pressure, the dependence of the temperature difference on the variation in the power input is qualitatively indicative of the flow regime encountered. It should be noted that these temperature differences are a result of superimposed processes of conduction, convection, and radiation heat transfer. The following comparison of two data points is a good example of the interdependent effects of these processes. With air at a pressure of 5 atm, a temperature difference $T_{MR3} - T_{MC}$ of 22.42°C is obtained for a power input of 4.99 W/rod. In comparison, under a vacuum (a pressure of 9.2×10^{-5} atm), a temperature difference of 86.37°C is observed for the same power input. These data points correspond, respectively, to a convection-dominated heat transfer process to one in which radiation is the primary means of energy transfer.

Owing to the symmetry of the rod bundle, temperature measurements on only three rods in the square array are needed. In order to minimize the disturbance of the flow field, temperatures on Rods 1 and 2 are measured only at three locations (y/L = 0.25, 0.50, 0.75), whereas the temperature distribution on the center rod is measured on seven locations, starting at y/L = 0.125 with 0.125 intervals. For about 5 W/rod, temperature profiles on the rods with air, helium, water, and a vacuum are graphically presented in Fig. 3.

In the conduction regime, with helium as the convective medium, temperature distributions on the rods are nearly uniform. As the Rayleigh number is increased to 1.77×10^6, with air as the test gas, temperature profiles show a steady increase from the leading edge to the top of the heaters. This is particularly evident from the data on the center rod, for which temperatures are measured at seven locations.

With air and helium as the convective media, at the same axial location, the center rod, Rod 3, has the highest temperature compared to those for Rods 2 and 1. This difference between the temperatures on the rods is more pronounced in the conduction regime. Although the presence of radiation heat transfer results in a variation in the temperatures of rods, it is not the only factor. Consider the enclosure filled with fluid such that thermal radiation is not present. In the conduction regime, and with the same power input to each rod, one would expect the lowest mean temperature on the rod closest to the outer cylinder, and the highest on the center rod. Thereafter, as the Grashof number is increased, upward flows

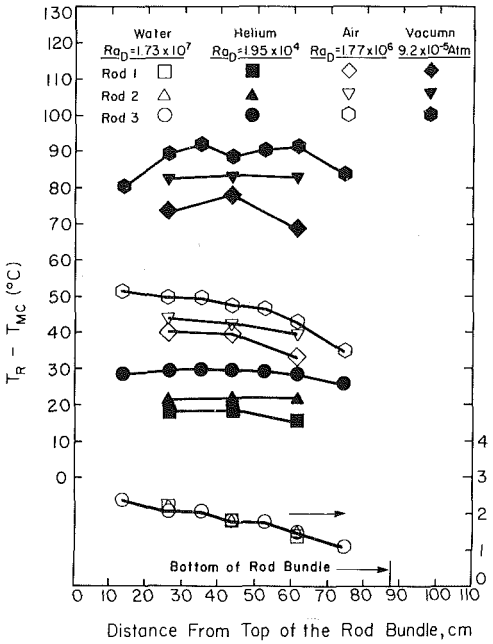

Fig. 3 Local temperature difference on Rods 1, 2, and 3 for various Rayleigh numbers

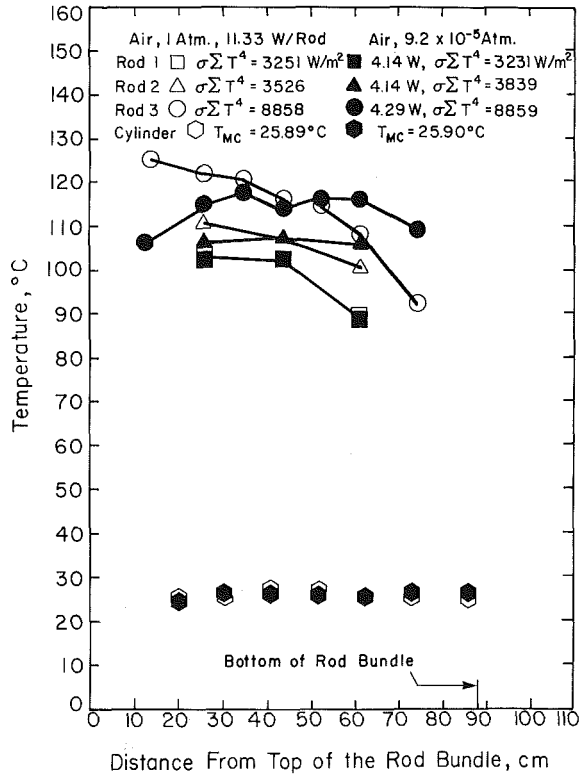

Fig. 4 Temperature distributions in the 3 × 3 rod bundle under vacuum conditions

are initiated around the individual rods. Each rod will have a distinct temperature profile which depends on its position in the bundle. Quantitatively, air and helium temperature data support this explanation.

This explanation, however, is not supported by the water data, as can be seen from Fig. 3; the temperature profiles on Rods 1, 2, and 3 are nearly the same. One possible reason is that, in the boundary layer regime in a vertical enclosure, the Nusselt number (with the height of the enclosure as the length scale) shows a weak or nonexistent dependence on the height-to-gap width ratio [10–13]. Extending this observation to the present case, one can state that, in the boundary layer regime, the distance of a given rod in the bundle to the outer cylinder has no effect on the heat transfer coefficient for that rod. It should also be mentioned that for same Rayleigh number range, flow regimes for water ($Pr > 1$) and air ($Pr < 1$) do not necessarily correspond.

Temperature distributions on Rods 1, 2, and 3 for a power input of 5.0 W/rod at a pressure of 9.2×10^{-5} atm are also given in Fig. 3. At this pressure, radiation is the predominant mode of heat transfer, but conduction effects are not totally eliminated. As discussed earlier, both of these modes of heat transfer have a strong effect on the extent of temperature variations from one rod to another. This is due to exposure and distance of various rods to the outer cylinder (see Fig. 1).

In order to obtain convective heat transfer coefficients the following procedure is followed. For a given gas and power input per rod, mean temperatures on Rods 1, 2, and 3 are obtained. The cavity is then evacuated, and the outer cylinder temperature is maintained the same as when the gas is present. The power inputs to Rods 1, 2, and 3 are simultaneously adjusted until the mean temperatures on these rods are the same as those obtained with the convection present. These power inputs are considered to be the radiation contribution augmenting the heat transfer process when the gas is present. At the vacuum condition, the Rayleigh number Ra_D is about 0.02, which is well below the value obtained for conduction regime ($Ra_D = 1.3 \times 10^4$). Nevertheless, at this low Rayleigh number, some energy is still transferred by conduction. This conduction effect is estimated [8] and is included in the uncertainty in the Nusselt number.

Temperature distributions obtained from a typical experiment under a vacuum are plotted in Fig. 4. Superimposed on these temperatures are the profiles observed with convective heat transfer present. Under vacuum conditions, the average temperatures on the individual rods and the outer cylinder are reproduced to within 0.9 percent of the values observed with the convective effects present. Although the temperature profiles on the rods under vacuum conditions are different from those observed with convection present, the calculated values of the parameter $\Sigma\sigma T^4$ (emissive power) for the individual rods are nearly the same for the two conditions. Therefore, it is felt that the radiation heat transfer contributions are adequately accounted for.

The radiation heat transfer contributions for Rods 1, 2, and 3 vary with the test gas and the Rayleigh number. In the conduction regime, with helium as the convective medium, the radiation contributions as percentages of the power input per rod, for Rods 1, 2, and 3 are approximately 15, 16, and 26 percent, respectively. At $Ra_D = 5.81 \times 10^5$, the corresponding values are 11.4, 11.9, and 14.1 percent. With air at 1 atm, $Ra_D = 1.77 \times 10^6$, the radiation contributions for Rods 1, 2, and 3 are about 37, 37, and 42 percent of the total Nusselt numbers, respectively, whereas at 5 atm, $Ra_D = 4.47 \times 10^7$, the corresponding values are reduced to about 16, 16, and 18 percent.

Convective Nusselt numbers Nu_d for Rods 1, 2, and 3 are graphically presented as a function of Rayleigh number Ra_d in Fig. 5. The characteristic length used in the definition of Ra_d and Nu_d is the rod diameter. The temperature difference is taken as the difference between the average values on the given rod and that of the outer cylinder. The heat transfer coefficient is defined based on the rod area. All the thermophysical properties are evaluated at the mean value of temperatures of the given rod and that of the outer cylinder.

The individual rods in the bundle, under a given condition of uniform power input per rod, can exchange energy with the working fluid via different but coexisting flow regimes. At $Ra_d = 44.8$ the Nusselt number for Rod 1 is 10 percent higher than its asymptotic conduction value and can be classified as

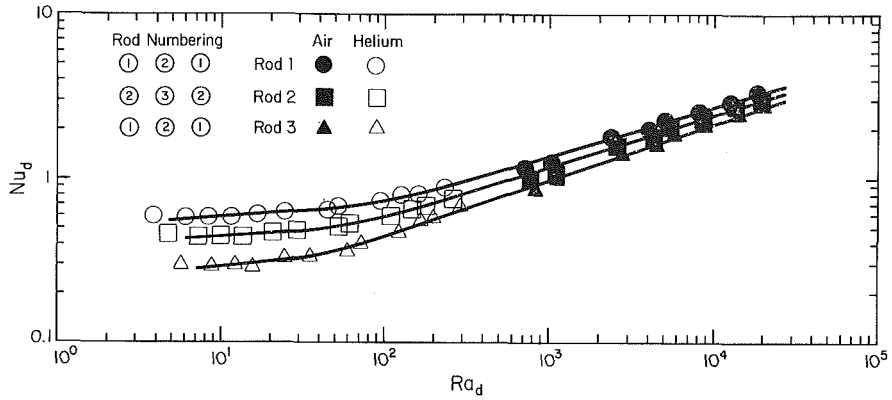

Fig. 5 Average convective Nusselt numbers for the individual rods in the 3 × 3 rod bundle

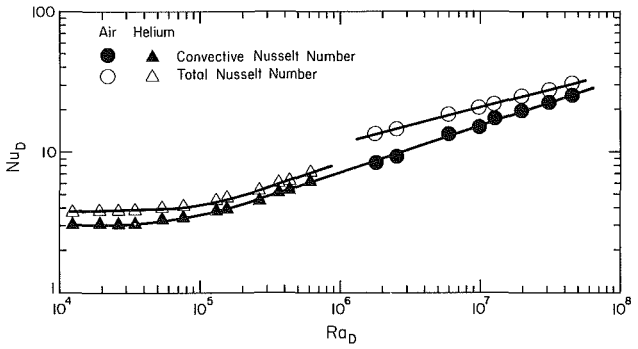

Fig. 6 Overall convective Nusselt numbers for the 3 × 3 rod bundle

being in the conduction flow regime (see flow regime classification given in [13]). Under the same conditions, Rod 3 is at $Ra_d = 59.7$ and the Nusselt number is 26 percent higher than its asymptotic conduction value. Hence, under a given condition, Rod 1 is in conduction flow regime while Rod 3 is in transition flow regime.

The fact that the conduction flow regime ends at a lower Rayleigh number for Rod 3 than for Rods 1 and 2 should not be unexpected. In a vertical cavity or annulus, the Rayleigh number at which conduction regime ends is proportional to the aspect ratio, where the aspect ratio is defined as the ratio of the height of the layer to distance between cold and hot surfaces [10, 13]. In the 3 × 3 rod bundle, the height of the heated surface is the same for Rods 1, 2, and 3, but the characteristic distance between the hot and cold surfaces is a maximum for the center rod, and a minimum for Rod 1. Therefore, if a characteristic aspect ratio is to be defined for the rods in the bundle, highest and lowest characteristic aspect ratios would be assigned to Rods 1 and 3, respectively.

As can be seen from Fig. 5, Rod 1 has the highest convective Nusselt number, which is a direct consequence of proximity to the outer cylinder. The center rod, farthest from the outer cylinder, has the lowest heat transfer coefficient. The difference between the convective Nusselt numbers of the three rods is more pronounced in the conduction regime. However, it seems that with increase in Ra_d the Nusselt numbers for the three rods are converging.

The experimental data are correlated for the conduction and boundary layer regimes. The convective Nusselt numbers as a function of Rayleigh number for the individual rods in the array are as follows:

Rod 1

$$Nu_{d1} = 0.472Ra_{d1}^{0.086},\ 6 \le Ra_{d1} \le 1.3 \times 10^2 \quad (1)$$

$$Nu_{d1} = 0.159Ra_{d1}^{0.307},\ 1.3 \times 10^2 \le Ra_{d1} \le 1.84 \times 10^4 \quad (2)$$

Rod 2

$$Nu_{d2} = 0.347Ra_{d2}^{0.097},\ 7 \le Ra_{d2} \le 90 \quad (3)$$

$$Nu_{d2} = 0.126Ra_{d2}^{0.321},\ 90 \le Ra_{d2} \le 1.93 \times 10^4 \quad (4)$$

Rod 3

$$Nu_{d3} = 0.218Ra_{d3}^{0.124},\ 8 \le Ra_{d3} \le 50 \quad (5)$$

$$Nu_{d3} = 0.093Ra_{d3}^{0.341},\ 50 \le Ra_{d3} \le 2.04 \times 10^4. \quad (6)$$

The above correlations describe over 90 percent of the experimental data to within 5 percent, and the maximum deviation does not exceed 8.5 percent.

Overall convection and total Nusselt numbers as a function of Rayleigh number are graphically presented in Fig. 6. With air or helium, as the Rayleigh number is increased the radiation heat transfer contribution decreases. For air, radiation heat transfer accounts for 17–38 percent of the total power input, whereas with helium the radiative heat transfer is reduced to 13–19 percent of the total Nusselt number. The correlations for the convective Nusselt number as a function of Rayleigh number in conduction and boundary layer flow regimes are

$$Nu_D = 1.27Ra_D^{0.087},\ 1.95 \times 10^4 \le Ra_D \le 1.2 \times 10^5, \quad (7)$$

$$Nu_D = 0.072Ra_D^{0.332},\ 1.2 \times 10^5 \le Ra_D \le 4.5 \times 10^7. \quad (8)$$

The above correlations describe the experimental convective Nusselt numbers with a maximum deviation of 6 percent.

The experimental errors due to uncertainty in the measured quantities and thermophysical properties are about 5 and 6 percent for the Nusselt and Rayleigh numbers, respectively. However, the convective heat loss from the top plate, the axial conduction loss along the rods, which are partially accounted for in the radiation corrections, and the conduction heat transfer present in the vacuum experiments add to the uncertainty in the convective Nusselt number. A detailed analysis of the effects discussed above [8] indicates that 90 percent of the overall Nusselt numbers are underestimated by about 3.2 percent or less, with the maximum deviation not exceeding 7.1 percent for all the data points. Considering the complex geometry of the problem, however, it is felt that the reported uncertainties are satisfactory.

Water. The objective of these experiments is to provide baseline values for the convective Nusselt number. The air and helium results, with the appropriate Prandtl number effect taken into account, should be in agreement with those obtained with water. Otherwise, one can conclude that the radiation heat transfer effects are not adequately accounted for. A total of ten experimental runs with the power input to the heater rods varying from 2.38 to 35.8 W/rod were conducted. The Grashof number range covered is $1 \times 10^6 \le Gr_D \le 3.2 \times 10^7$. In some of the experiments, the Grashof number is increased by increasing the cylinder temperature

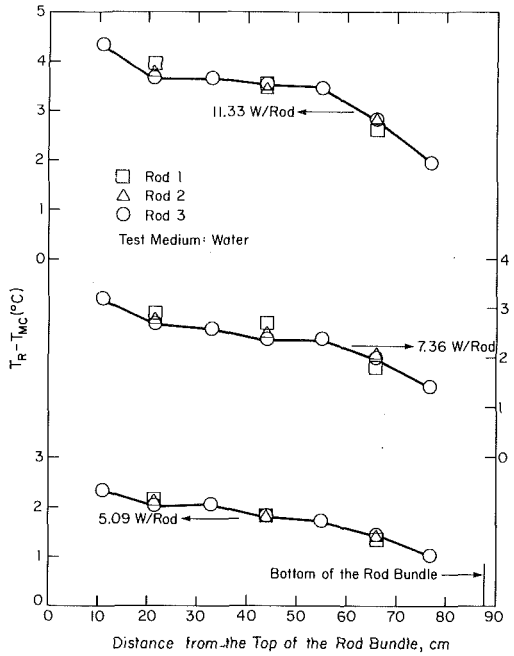

Fig. 7 Local temperature difference on Rods 1, 2, and 3 for various power inputs per rod (for water)

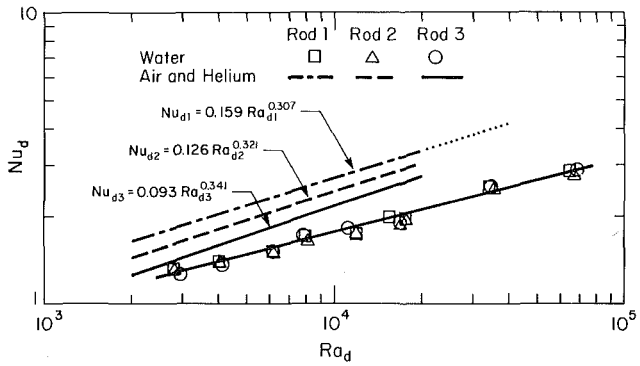

Fig. 8 Average Nusselt numbers for the individual rods in the 3 × 3 rod bundle (water results)

rather than the power input, i.e., raising the mean fluid temperature and as a result the value of the product of properties included in the Grashof number.

Temperature profiles on Rods 1, 2, and 3 for three experimental runs are given in Fig. 7. As mentioned earlier, the temperature profiles on the rods are nearly the same. One possible explanation for this behavior was offered, and will not be discussed further. The point which merits attention, however, is a discussion of the angular dependence of the temperature. The thermocouples on Rod 3 are facing Rod 1. As can be seen from Fig. 7, the measured temperatures, for a given axial location, regardless of their angular and radial positions, are nearly the same. This observation can be very helpful in analytical modeling of the problem. With the above observation in mind, one can state that, with air or helium as the test gas, at a given location the temperature of any rod in the bundle would exhibit a small variation along its periphery. Clearly, the extent of this variation is dependent on the degree of the exposure of the given rod to hot and cold surfaces.

Nusselt numbers for the individual rods in the array Nu_d are plotted as a function of Rayleigh number Ra_d in Fig. 8. The correlations obtained for the convective Nusselt number for Rods 1, 2, and 3 with the air and helium experiments are also graphically presented in this figure. The water results indicate that for a given Ra_d, the heat transfer coefficient is the same for the three rods. In comparison, as discussed

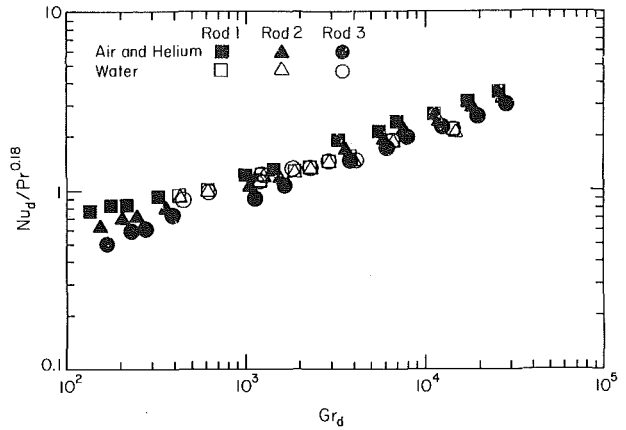

Fig. 9 Normalized Nusselt numbers for the individual rods in the 3 × 3 rod bundle $Nu_d/Pr^{0.18}$ as a function of Gr_d

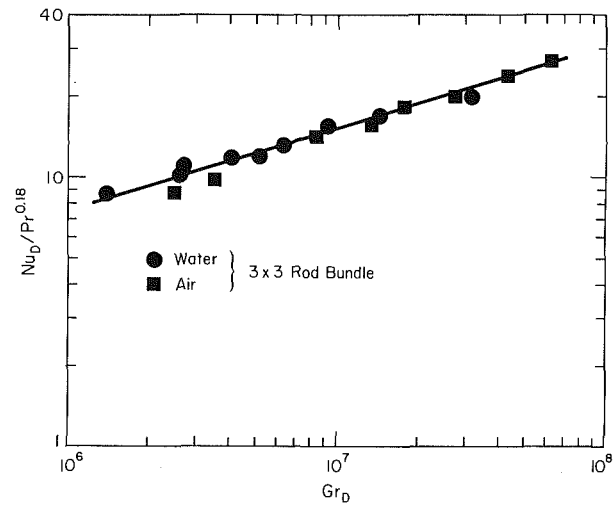

Fig. 10 Normalized overall Nusselt numbers for air and water as a function of Gr_D

earlier, there is a distinct difference in the convective Nusselt numbers of Rods 1, 2, and 3 when air or helium is the convective medium. As can be seen from the figure, the air and helium results, for a given Ra_d, yield a higher Nusselt number compared to that obtained from water experiments. This is contrary to the expected Prandtl number effect as reported for vertical cavities [11, 14] and annular enclosures [13]. However, a recent analytical and experimental study by Kubair and Simha [12] on free convection in annular enclosures reports a similar behavior to that found here. Their analytical results indicate that a correlation of Nusselt number as a function of Grashof and Prandtl numbers leads to a 0.18 exponent for the latter. Prandtl number range in their study was $0.01 \leq Pr \leq 5.0$. The results of their experiments with mercury and water confirmed their analytical findings. Moreover, this Prandtl number effect is confirmed through favorable agreement of the air and helium results reported in [7] with the water data obtained with the same annulus [8].

In order to find a reason for the possible difference between the Prandtl number effect in a vertical cavity as opposed to an annulus, one should concentrate on the studies on free convection about a vertical cylinder. However, none of the existing studies on this subject give an explicit Prandtl number effect on heat transfer. Nevertheless, the information given by Sparrow and Gregg [15], qualitatively, can be of help. Their analysis indicates that, for a fixed local Grashof number, a decrease in the Prandtl number results in a higher value for the ratio of the local heat transfer coefficient of the cylinder to that of a flat plate. Therefore, implicitly one can conclude that enhancement of the heat transfer coefficient due to

curvature effects becomes more pronounced as the Prandtl number is reduced. It should be mentioned that only two Prandtl numbers, 0.72 and 1.0, were considered by Sparrow and Gregg.

Assuming the same Prandtl number effect holds for the present case, the normalized Nusselt numbers $Nu_d/Pr^{0.18}$ for the individual rods and those for the rod bundle as a whole $Nu_D/Pr^{0.18}$, obtained with air, helium, and water are presented as a function of their respective Grashof number in Figs. 9 and 10, respectively. The water data for the individual rods, as can be seen from Fig. 9, are bracketed with those obtained with air and helium for Rods 1, 2, and 3. Considering the fact that air and helium results are different for each rod, and the water data are nearly the same for Rods 1, 2, and 3, it seems that a Prandtl number effect of $Pr^{0.18}$ is also adequate for the present case. Moreover, normalized overall convective Nusselt numbers obtained from air and helium experiments are in good agreement with those for water (see Fig. 10). Therefore, it is felt that air and helium data are properly corrected for the radiation effects.

The experimental water Nusselt numbers Nu_d for the individual rods in the array can be correlated in terms of Rayleigh number Ra_d with a maximum deviation of 6 percent. However, a single correlation can describe all the data obtained for the three rods to within 8 percent. Therefore, it is felt that a single correlation as

$$Nu_d = 0.162 Ra_d^{0.257}, \quad 2.8 \times 10^3 \le Ra_d \le 6.8 \times 10^4, \qquad (9)$$

is adequate.

The overall water Nusselt numbers for the rod bundle can be correlated in terms of Rayleigh number as

$$Nu_D = 0.151 Ra_D^{0.274}, \quad 6.5 \times 10^6 \le Ra_D \le 1.4 \times 10^8. \qquad (10)$$

Equation (10) describes the experimental data with a maximum deviation of 7 percent. The total uncertainties in the calculation of the Nusselt and Rayleigh numbers for the water experiments are estimated to be about 7 and 8 percent, respectively.

Flow Visualization. For these experiments, the 3 × 3 rod bundle assembly is placed inside a transparent acrylic cylinder of 7.46 cm i.d. The height-to-diameter ratio is 11.81. The aspect ratio AR of the outer cylinder in the heat transfer experiments was 10.61. The somewhat larger AR value for the acrylic cylinder is not expected to affect the flow field significantly. Ethylene glycol with suspended aluminum particles (5 to 50 μ) is used as the working medium. Illumination of the particles is done with a high-intensity lamp shining through a narrow slit so as to produce a plane of light.

Prior to flow visualization experiments, the bundle and the outer cylinder are calibrated with thermocouples in place. The thermocouples were then removed and a few grams of aluminum powder were poured into the cylinder. The system was allowed to reach steady state prior to illumination with the light source.

Results reported here are for $Ra_D = 2.92 \times 10^7$, $Ra_d = 1.83 \times 10^4$, and $Pr = 46.4$. (It should be noted that the rod Rayleigh number Ra_d is the same for Rods 1, 2, and 3 because the temperature field is nearly same for these rods.) The flow fields in the bottom, above midheight, and the top of bundle are given in Fig. 11. These photographs were taken with an exposure time of 20 to 60 s. The scale to the right in each

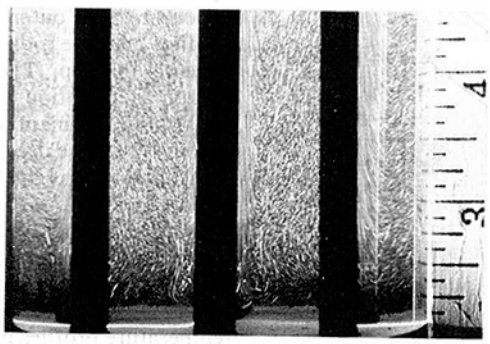

Fig. 11(a)

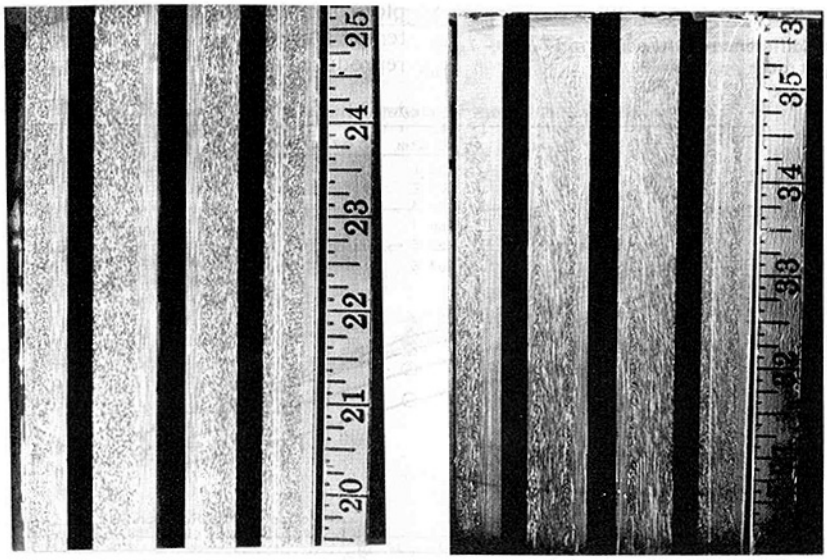

Fig. 11(b) Fig. 11(c)

Fig. 11 Flow field in the 3 × 3 rod bundle for $Ra_d = 1.83 \times 10^4$ and Pr = 46.4: (a) $0 \le y/L \le 0.07$, (b) $0.51 \le y/L \le 0.67$, (c) $0.81 \le y/L \le 1.0$

photograph is in inches, with the bottom of the bundle at 2 in. and the top at 36 in. One should keep in mind that these photographs were taken at an angle slightly off perpendicular to the plane of the light so one can see beyond the front row of rods facing the camera.

The major results of the flow visualization are that there is no interaction between the upward flow around adjacent rods. Except for the end regions, less than 5 cm from the ends, the upward flow around the rods has a uniform thickness. An unexpected finding is that there is a low-speed downward flow between the rods. This may be a result of the rather large P/d of this particular bundle (P/d = 3.08). This downward flow between the rods, in conjunction with the upward flow around the center rod and the cross flow at the end regions, results in vortex rings around the center rod in the end regions. In Fig. 11(*c*), one can see the traces of downward flow. Flow next to the outer cylinder can only be seen on the right-hand side of the graph next to the scale.

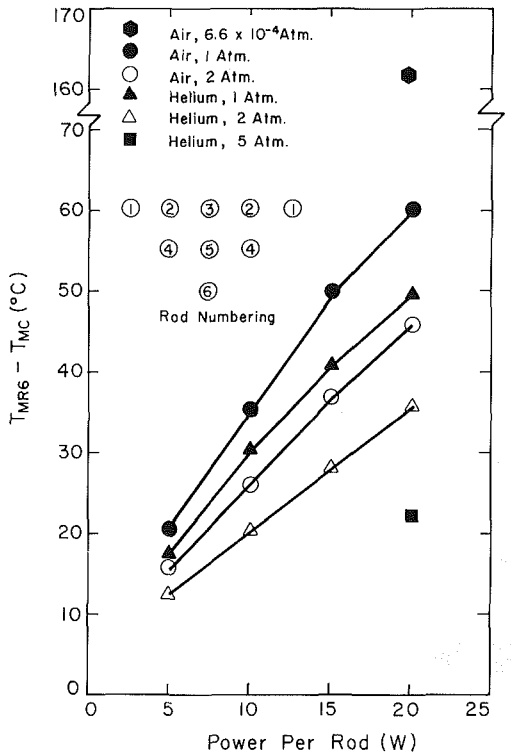

Fig. 12 Average temperature difference on the center rod $T_{MR6} - T_{MC}$ as a function of total power per rod

5 × 5 Rod Bundle. Total and convective heat transfer coefficients for each rod in the array as well as an overall value for the bundle are obtained for a wide range of Rayleigh number. Although Rayleigh number Ra_D was varied from 2.6×10^5 to 1.06×10^9, the conduction flow regime was not encountered. With helium at atmospheric pressure as the convective medium, the heat transfer results of the 3 × 3 rod bundle experiments were indicative of conduction flow regime. However, in the present case, the results obtained with helium at atmospheric pressure are indicative of the boundary layer flow regime.

The characteristic temperature difference for the rod bundle $T_{MR6} - T_{MC}$ as a function of power input to the rods for air and helium at various pressures is plotted in Fig. 12. The rod numbering is also given in that figure. The numbering of the rods is done in such a way that the rod closest to the outer cylinder, i.e., the rod on the corner of the square array, is numbered 1, and the center rod is number 6. A qualitative discussion of the temperature in this figure is similar to that given for Fig. 2.

Typical temperature profiles on Rods 1 to 6 obtained with air at 2 atm, $Ra_D = 3.83 \times 10^8$, are plotted in Fig. 13. There are several points about these temperature profiles which should be noted. The interior rods, i.e., Rods 4, 5, and 6, have nearly the same profile. Furthermore, Rods 2 and 3 also share the same temperature profile. Rod 1, closest to the outer cylinder and with most exposure to it, experiences the lowest temperature in the bundle. For this experimental run, the mean temperatures on Rods 1 to 6 are, respectively, 63.92°C, 67.4°C, 66.94°C, 69.78°C, 70.0°C, and 70.17°C. As the mean temperatures indicate, Rods 4, 5, and 6 are surrounded by high-temperature surfaces. Also, these rods have little exposure to the outer cylinder. Furthermore, the temperature profiles on these rods show a steady increase from the leading edge to the top. Therefore, it can be concluded that the combined radiation and conduction heat transfer processes are not the dominant mode of heat transfer from these rods.

The procedure used for the correction of the radiation heat transfer effects is the same as that followed in the 3 × 3 rod bundle experiments. Temperature distributions on Rods 1 and 6 obtained from a typical experiment in vacuum condition, at a pressure of 6.6×10^{-4} atm with Ra_D = 22.5, are plotted in Fig. 14. Superimposed on these profiles are the temperatures observed with the convective heat transfer present. The temperature profiles on Rods 2, 3, 4, and 5 are very close and similar to those given for Rods 1 and 6, hence they are not plotted in Fig. 14. Under vacuum conditions, the average temperatures on the individual rods and the outer cylinder are reproduced to within 1.2 percent of the values observed with

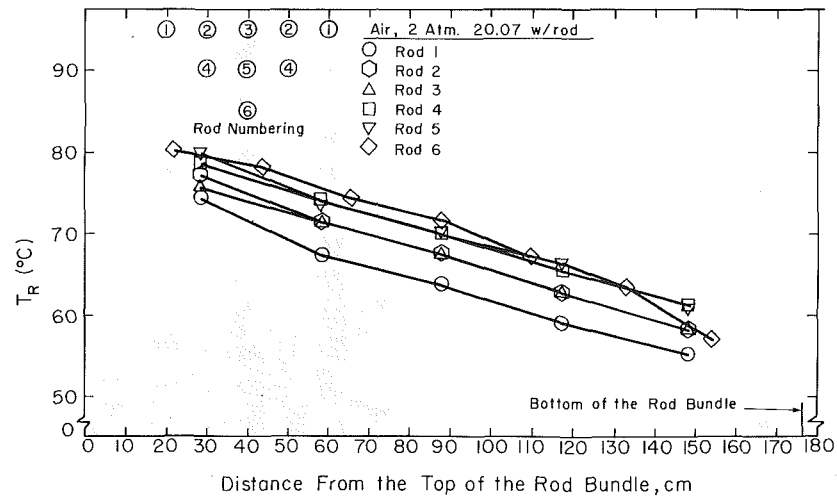

Fig. 13 Temperature profiles on Rods 1-6 at $Ra_D = 3.83 \times 10^8$

the convective effects present. However, based on absolute temperature, the difference is negligible.

The maximum radiative heat transfer contributions for Rods 1 to 6 obtained with air at atmospheric pressure at $Ra_D = 5.16 \times 10^7$, are 57, 30, 30, 25, 21, and 21 percent of the power input per rod, respectively. As the Rayleigh number is increased to 1.06×10^9 the corresponding values are reduced to, respectively, 26.5, 13.9, 13.9, 11.8, 9.8, and 9.8 percent of the power input per rod. The minimum values of the radiation heat transfer contributions for Rods 1 to 6 observed with helium at $Ra_D = 2.02 \times 10^7$ are 16.5, 8.7, 8.7, 7.5, 6.2, and 6.2 percent of the power input per rod, respectively. As can be seen from these percentages, the rods with least and most exposure to the outer cylinder, i.e., Rods 6 and 1, for a given power input per rod and test gas, have the lowest and highest heat transfer due to radiation, respectively.

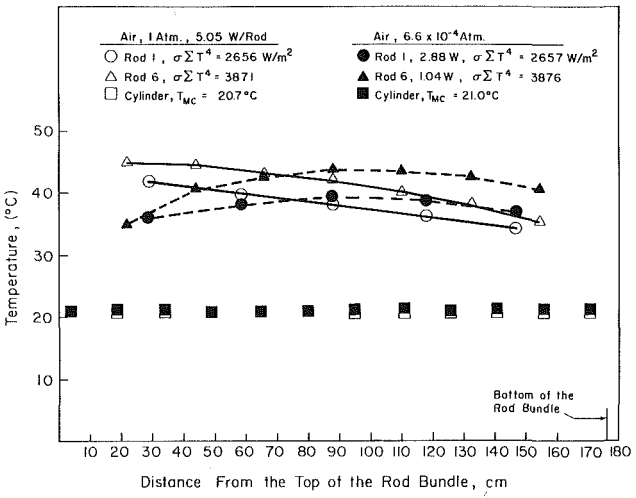

Fig. 14 Temperature profiles on Rods 1 and 6 under vacuum conditions

The convective Nusselt numbers Nu_d for Rods 1 to 6 are graphically presented as a function of Rayleigh number Ra_d in Fig. 15. As can be seen from the figure, Rods 2, 3, 4, 5, and 6, for a given Ra_d, have nearly the same heat transfer coefficient. Also, eight data points for Rod 1, out of a total of thirteen points, are within 15 percent of the values obtained for other rods. The primary reason for the scatter in the data obtained for Rod 1 is that the radial conduction heat transfer effect, present in the vacuum experiments, is most pronounced for this rod. This is due to the fact that Rod 1 is closest to the outer cylinder. Consequently, the convective heat transfer coefficients obtained for this rod are overcorrected for radiation effect. This is especially evident from the data obtained with air at pressures of 1 and 2 atm (see Fig. 15, $Ra_d = 10{,}000$ to $60{,}000$).

The convective Nusselt number for Rods 1 to 6, except five data points for Rod 1, can all be represented as a function of Ra_d through a single correlation with a maximum deviation of 12 percent. However, it is preferred to provide correlations for each rod in the array with much lower deviations from the experimental values. These correlations are as follows

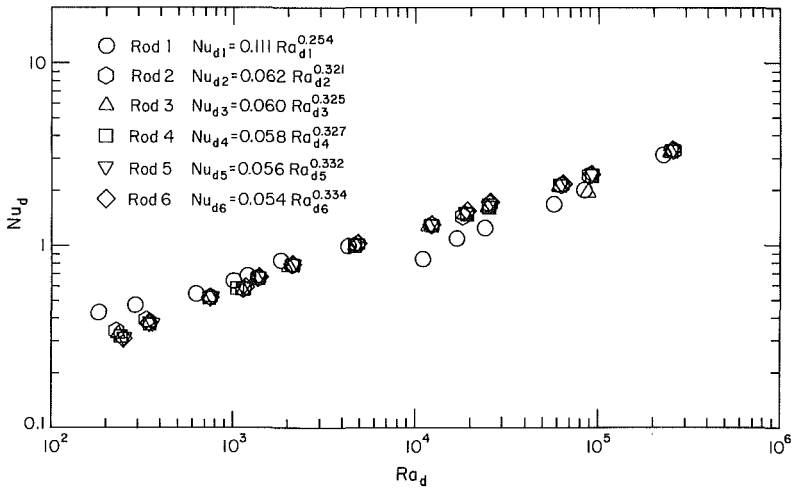

Fig. 15 Convective Nusselt numbers for the individual rods in the 5 × 5 rod bundle

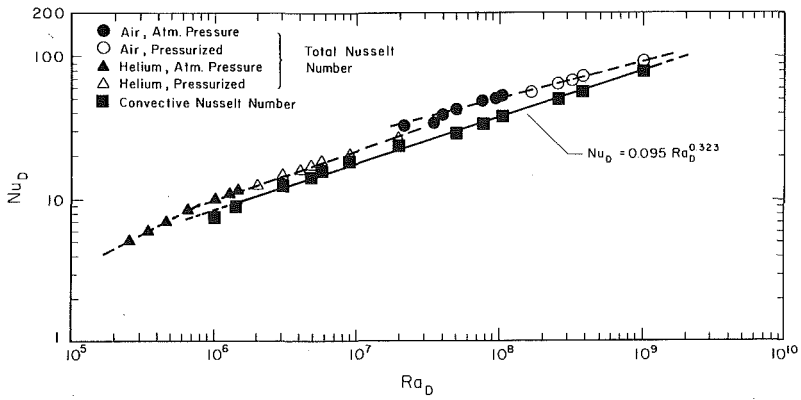

Fig. 16 Overall convective Nusselt number for the 5 × 5 rod bundle as a function of Ra_D

Table 1 Geometric parameters of the three experimental facilities

$N \times N$	d (cm)	P/d	L (cm)	D (cm)	L/D
1×1*	1.91	1	87.63	8.255	10.62
3×3	0.635	3.08	87.63	8.255	10.62
5×5	1.91	2.25	176.53	30.48	5.79

*Annulus experiments [7]

Rod 1

$$\mathrm{Nu}_{d1} = 0.111\mathrm{Ra}_{d1}^{0.254},\ 1.8 \times 10^2 \le \mathrm{Ra}_{d1} \le 2.3 \times 10^5 \quad (11)$$

Rod 2

$$\mathrm{Nu}_{d2} = 0.062\mathrm{Ra}_{d2}^{0.321},\ 2.2 \times 10^2 \le \mathrm{Ra}_{d2} \le 2.5 \times 10^5 \quad (12)$$

Rod 3

$$\mathrm{Nu}_{d3} = 0.06\mathrm{Ra}_{d3}^{0.325},\ 2.3 \times 10^2 \le \mathrm{Ra}_{d3} \le 2.5 \times 10^5 \quad (13)$$

Rod 4

$$\mathrm{Nu}_{d4} = 0.058\mathrm{Ra}_{d4}^{0.327},\ 2.4 \times 10^2 \le \mathrm{Ra}_{d4} \le 2.6 \times 10^5 \quad (14)$$

Rod 5

$$\mathrm{Nu}_{d5} = 0.056\mathrm{Ra}_{d5}^{0.332},\ 2.5 \times 10^2 \le \mathrm{Ra}_{d5} \le 2.6 \times 10^5 \quad (15)$$

Rod 6

$$\mathrm{Nu}_{d6} = 0.054\mathrm{Ra}_{d6}^{0.334},\ 2.5 \times 10^2 \le \mathrm{Ra}_{d6} \le 2.6 \times 10^5. \quad (16)$$

The above correlations, except equation (11), describe the experimental data with a maximum deviation of 6 percent. The correlation given for Rod 1, obtained through correlating all the data points for that rod, deviates from the experimental data as much as 40 percent. As mentioned before, the four data points obtained with air at 1 and 2 atm are overcorrected for the radiative heat transfer effect for this rod. If one neglects these four points the rest of the data can be correlated, with a maximum deviation of 7 percent, as

$$\mathrm{Nu}_{d1} = 0.1\mathrm{Ra}_{d1}^{0.272}. \quad (17)$$

Although the errors in some of the convective Nusselt numbers obtained for Rod 1 are very high, the effect on the overall convective Nusselt numbers Nu_D is rather small. This is due to the fact that there are only four rods out of a total of twenty-five rods numbered 1.

Overall convective and total Nusselt numbers as a function of Rayleigh number are graphically presented in Fig. 16. For air, radiation heat transfer accounts for 15–32 percent of the total power input, whereas with helium the radiation contribution is reduced to 12–23 percent. The correlation for the convective Nusselt number as a function of Rayleigh number is

$$\mathrm{Nu}_D = 0.095\mathrm{Ra}_D^{0.323},\ 1.48 \times 10^6 \le \mathrm{Ra}_D \le 1.06 \times 10^9. \quad (18)$$

Equation (18) describes the experimental data with a maximum deviation of 6 percent.

The experimental errors due to uncertainty in the measured quantities and thermophysical properties are about 5 and 8 percent for the Nusselt and Rayleigh numbers, respectively. As we discussed for the 3×3 rod bundle, the losses and the radial conduction effect in the vacuum experiments add to the uncertainty in the Nusselt number. An analysis of these effects [8] indicates that over 90 percent of the overall Nusselt numbers are underestimated by about 3.6 percent or less, with the maximum deviation not exceeding 7.4 percent for all data points. Considering the complicated geometry of the problem, the total uncertainty of about 8 to 12 percent in the overall convective Nusselt numbers is not unreasonable.

Generalized Correlation

In this section the results for an annulus [7], the 3×3 rod bundle, and the 5×5 rod bundle are brought together and analyzed. The objective is to establish an "equivalent" annulus model which can describe overall convective heat transfer from a rod bundle to its enclosing cylinder while the effects of the appropriate geometric parameters are taken into account. The geometric parameters of the three experiments are given in Table 1.

It is reasonable to state that, as far as the interior surface of a canister enclosing a rod bundle is concerned, it is receiving energy by convection, owing to a characteristic temperature difference, from the descending hot fluid. The average convective heat transfer coefficient encountered due to this heat transfer can be assumed to result from the presence of a fictitious cylinder concentric with the canister. Such an equivalent annulus should satisfy two conditions. First, the point of departure from the conduction regime should comply with the criteria set for an annulus. Second, the dependence of the effective, or overall Nusselt number on the Rayleigh number should, within the limits of experimental uncertainties, agree with those of an annulus. However, the magnitude of the Nusselt numbers for such an equivalent annulus cannot be expected to be the same as those obtained from generalized correlations for free convection in an annulus. Therefore, the pitch-to-diameter ratio and the number of rows in the bundle are expected to enter any generalized correlation for thermal convection.

Thus, in order to successfully represent thermal convection in a rod bundle with an equivalent annulus model the following tasks should be accomplished:

1 To establish the radius ratio and aspect ratio effects on heat transfer in an annulus. Furthermore, provide criteria for the extent of conduction regime as a function of the geometric parameters of H and K.

2 To identify an equivalent inner cylinder for rod bundles in such a way that the criteria for the extent of conduction regime in an annulus are satisfied.

3 To identify the effects of pitch-to-diameter ratio P/d and N, the number of rows in the square rod array, through normalizing the results for the annulus and those of rod bundles, defined based on the equivalent annulus, with respect to the H and K effects.

The annulus results of Keyhani, Kulacki, and Christensen [7] for $K = 4.33$ and $H = 27.6$, with the power law dependence of aspect and radius ratios as reported by Thomas and de Vahl Davis [13] for the conduction and boundary layer regimes are,

$$\mathrm{Nu} = 0.797\mathrm{Ra}^{0.077}H^{-0.052}K^{0.505}, \quad (19)$$

and

$$\mathrm{Nu} = 0.188\mathrm{Ra}^{0.322}H^{-0.238}K^{0.442}, \quad (20)$$

for $\mathrm{Ra} \le 2.3 \times 10^6$ and $\mathrm{Pr} = 0.71$.

It should be noted that the numerically predicted effects of radius and aspect ratios [13] have been verified through favorable agreement with the experimental results of Sheriff [16] in [7].

As for the extent of the conduction regime, Thomas and de Vahl Davis [13] have suggested the following for critical Rayleigh number:

$$\mathrm{Ra} \le 400H. \quad (21)$$

It may be noted that equation (21) does not include the radius ratio K as a parameter which influences the extent of the conduction regime. They have indicated, however, that the

Table 2 Experimental Rayleigh numbers indicating the extent of conduction regime for an annulus

	H	K	Ra_{exp}	Equation (21)	Equation (22)	$\frac{Ra_{exp}}{\text{Equation (21)}}$	$\frac{Ra_{exp}}{\text{Equation (22)}}$
Keyhani et al. [7]	2.76	4.33	6.6×10^6	1.10×10^4	6.52×10^3	1.67	0.99
Bhushan	38.38	8.28	8.79×10^3	1.54×10^4	9.85×10^3	1.74	1.12
et al. [17]	52.82	2.77	1.89×10^4	2.11×10^4	9.55×10^3	1.74	0.51
Choi and Korpela [18]	38.89	1.46	5.32×10^3	1.55×10^4	6.44×10^3	2.96	1.23

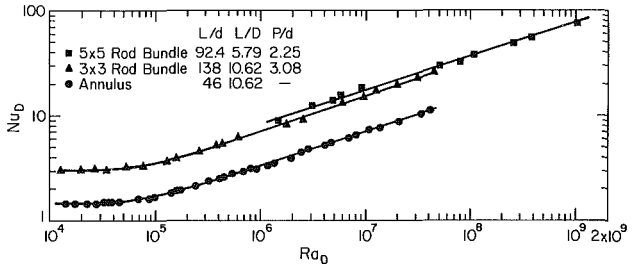

Fig. 17 Comparison of the overall convective Nusselt numbers Nu_d for the 3 × 3 and 5 × 5 rod bundles with the annulus results [7]

radius ratio has a weak effect. On the other hand, equations (19) and (20) indicate that the conduction regime is delimited by

$$Ra \leq 363 K^{0.25} H^{0.76}. \tag{22}$$

The values of the critical Rayleigh numbers for the end of the conduction regime, as predicted by equations (21) and (22), are compared with the available experimental data for annular enclosures in Table 2. The criterion given by Thomas and de Vahl Davis [13] yields a good agreement with only one piece of experimental data. The relation suggested by the present work, however, provides good agreement with three experimental values. It is felt, therefore, that equation (22) yields an acceptable value for the extent of the conduction regime.

For the annulus case, the aspect ratio and radius ratio effects and the criteria for the extent of conduction regime are experimentally established. In order to present the 3 × 3 and 5 × 5 data based on an equivalent annulus, as discussed earlier, two conditions should be met. First, the criteria for the conduction regime should be satisfied. Second, the dependence of the overall Nusselt number on the Rayleigh numbers should, within the limits of experimental uncertainties, agree with that of an annulus. The correlations obtained for the 3 × 3 and 5 × 5 rod bundles yield exponents for the Rayleigh number which are very close to that obtained for the annulus. Therefore, the second condition is adequately satisfied. As for the first condition, the conduction regime was only observed with the 3 × 3 rod bundle.

The annulus data, $K = 4.33$, $H = 27.6$, represented in terms of Ra_D and Nu_D are graphically presented along with those of 3 × 3 and 5 × 5 rod bundles in Fig. 17. As can be seen from the figure, the dependence of Nusselt number on Rayleigh number is nearly the same for the three geometries. It is only the magnitudes of the Nusselt numbers which are different. Further examination of Fig. 17 reveals that the extent of conduction regime in terms of Ra_D is nearly the same for the annulus and the 3 × 3 rod bundle. It should be mentioned here that the same outer cylinder was used for both annulus and the 3 × 3 rod bundle experiments.

Heat transfer correlations for the 3 × 3 rod bundle, equations (7) and (8), indicate that the conduction regime in that geometry is delimited by $Ra_D \leq 1.22 \times 10^5$. Furthermore, equation (22) in terms of Ra_D relates the value of the critical Rayleigh number to the geometric parameters by

$$Ra_D = 363 \left[\frac{D}{d_i}\right]^{0.25} \left[\frac{2L}{D-d_i}\right]^{0.76} \left[\frac{2D}{D-d_i}\right]^{3}, \tag{23}$$

where d_i, D, and L are diameters of the equivalent inner cylinder, diameter of the outer cylinder, and height of the cylinder or rod, respectively. With the values of Ra_D, D, and L known, one can readily solve for the diameter of the equivalent inner cylinder. It is found that a choice of inner cylinder with a diameter equal to that of a circle fitted inside the square formed by the rods as if they were close packed, i.e., $d_i = Nd$, would result in an equivalent annulus which satisfies the criteria for conduction regime, equation (23), to within 5.7 percent of the experimental value. Based on this fictitious inner cylinder, the equivalent annulus for the 3 × 3 rod bundle would have the geometric parameters of $H = 27.6$ and $K = 4.33$. Fortuitously, this equivalent annulus for the 3 × 3 rod bundle has the same aspect and radius ratios as the annulus case. The equivalent annulus for the 5 × 5 rod bundle, with $d_i = Nd$, would have the geometric parameters of $H = 16.85$ and $K = 3.2$.

With the equivalent annulus for the rod bundles selected, the experimental Nusselt and Rayleigh numbers can be calculated for such geometry. The overall convective Nusselt numbers are calculated based on the surface area of the equivalent inner cylinder. The characteristic length used in the definition of Rayleigh and Nusselt numbers would be $l = (D - Nd)/2$. In order to empirically obtain the effects of pitch-to-diameter ratio P/d and N, the number of rows in the square rod array, the experimental Nusselt numbers for the three cases can be normalized as $Nu/H^{-0.238} K^{0.442}$, where the aspect and radius ratio effects used here are the same as those reported by Thomas and de Vahl Davis for the boundary layer regime. Any difference between the three sets of normalized Nusselt numbers as a function of Rayleigh number can then be attributed to the P/d and N effects. Based on this analysis, the effects of P/d and N are empirically found as $(P/d)^{0.045N+0.541}$.

As should be expected, the effects of P/d and N are interdependent. For example, consider a close-packed 15 × 15 rod bundle, i.e., $P/d = 1$ and $N = 15$. The number of rods in this case does not have any effect on convective heat transfer other than that already included in the definition of the equivalent inner cylinder. Heat is conducted from the interior rods to the outside rods. Thereafter, the energy is transferred to the outer cylinder through combined processes of radiative and convective heat transfer. Therefore, the fact that P/d has an exponent which includes N has a physical basis. Furthermore, the constant 0.541 in the exponent of the P/d term can also be explained. Since the equivalent inner cylinder is taken as if the rod bundle were close packed, the curvature effects of the rods are not fully accounted for yet. Each curvature enhances heat transfer, and the term $(P/d)^{0.541}$ accounts for the additional curvature effect which is not incorporated into the radius ratio term.

The overall convective Nusselt numbers obtained from the 3 × 3 rod bundle experiment are calculated for the equivalent annulus of $H = 27.6$ and $K = 4.33$ and normalized as $Nu/(P/d)^{0.045N+0.541}$. These values are compared to the annulus results ($K = 4.33$, $H = 27.6$) in Fig. 18. As can be seen from the figure, the agreement between the two results is very good. It may be noted that the 3 × 3 rod bundle results defined in terms of the equivalent annulus indicate that the conduction regime ends at $Ra = 6.8 \times 10^3$, where the an-

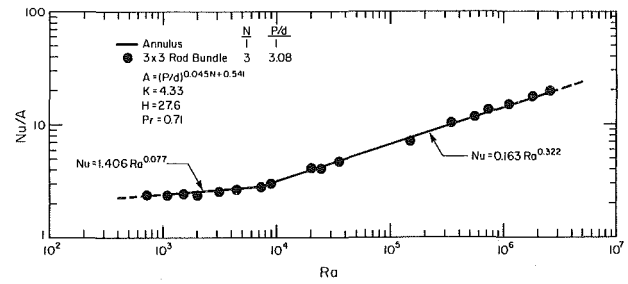

Fig. 18 Comparison of the overall convective Nusselt numbers for the 3 × 3 rod bundle, defined for the equivalent annulus, with the annulus results [7]

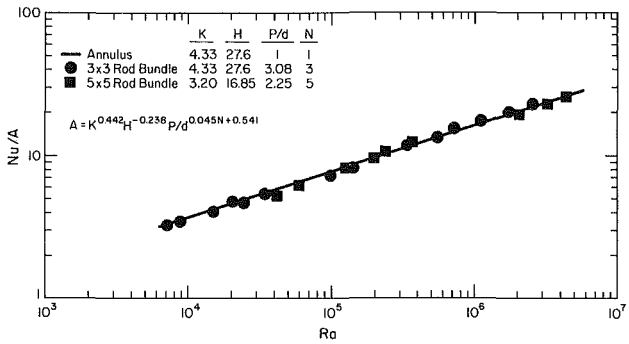

Fig. 19 The annulus [7], 3 × 3, and 5 × 5 rod bundle Nusselt numbers normalized with respect to *K*, *H*, *P/d*, and *N* effects

nulus results yield a value of $\mathrm{Ra} = 6.6 \times 10^3$. Therefore, it is felt that the appropriate equivalent inner cylinder is selected.

The annulus results and the overall convective Nusselt numbers for the 3 × 3 and 5 × 5 rod bundles defined for their respective equivalent annulus are normalized, i.e., dividing the Nusselt number for each geometry with its respective $K^{0.442}\ H^{-0.238}\ (P/d)^{0.045N+0.541}$, and graphically presented in Fig. 19 as a function of Rayleigh number. Considering the complexity of the geometries studied here, the agreement between the three sets of results is very good.

The effects of aspect ratio H, radius ratio K, pitch-to-diameter ratio P/d, and N, the number of rows in the square rod array, as selected here, lead to an adequate description of the experimental results for the annulus, 3 × 3 and 5 × 5 rod bundles. In the boundary layer regime, with the geometric effects taken as selected above, the experimental results for the three geometries can be correlated as

$$\mathrm{Nu} = 0.188K^{0.442}H^{-0.238}(P/d)^{0.045N+0.541}\mathrm{Ra}^{0.322}. \quad (24)$$

The above correlation describes over 90 percent of the data for the annulus, the 3 × 3 rod bundle, and the 5 × 5 rod bundle to within 7 percent. In the conduction regime, a correlation of the form

$$\mathrm{Nu} = 0.797K^{0.505}H^{-0.052}(P/d)^{0.045N+0.541}\mathrm{Ra}^{0.077} \quad (25)$$

describes over 90 percent of the data for the annulus and the 3 × 3 rod bundle to within 6 percent. For the 5 × 5 rod bundle, the experimental apparatus did not permit data in the conduction regime. Based on the equivalent annulus Rayleigh number, the lowest value covered is $\mathrm{Ra} = 5 \times 10^4$. Using the criteria given for the conduction regime, equation (22), conduction regime should be observed in the 5 × 5 rod bundle for $\mathrm{Ra} \leq 4.15 \times 10^3$. It may be noted that equations (24) and (25) can readily be represented in terms of a modified Rayleigh number based on the convective heat flux rather than temperature difference, i.e., $\mathrm{Ra}^* = \mathrm{RaNu}$.

Conclusions

A comparison of air and water results obtained with the 3 × 3, $P/d = 3.08$, rod bundle essentially confirms the Prandtl number effect found in [8] and [12] for an annulus. Therefore, it is felt that the radiation correction, as applied to the rod bundle results, is accurate. With air or helium as the convective media, different heat transfer coefficients for each rod in the array are found. The difference is most pronounced in the conduction regime and decreases with increase in Ra_d. Furthermore, the end of conduction regime data show that it is quite possible for the individual rods in the array, at a given condition, to exchange energy with the working fluid via different but coexisting flow regimes.

The water results which are obtained at high Rayleigh numbers, but overlapping the later part of air data, yield nearly the same heat transfer coefficient for the rods in the bundle. This observation may prove helpful in approximate analysis of rod bundle problems for high Rayleigh number flow. It may be noted that the 5 × 5, $P/d = 2.25$, rod bundle experiments with air and helium also resulted in nearly the same heat transfer coefficients for the individual rods in the array.

An equivalent annulus model for enclosed rod bundles is proposed. Based on this model, the boundary layer data obtained with air and helium from an annulus in [7], the 3 × 3 rod bundle, and the 5 × 5 rod bundle are correlated by a single equation in terms of Ra, H, K, P/d, and N. Furthermore, the conduction regime data for the annulus and the 3 × 3 rod bundle are also represented by a correlation in terms of the above parameters. In addition, the conduction regime data obtained with the 3 × 3 rod bundle, defined based on the equivalent annulus model, complies with the conduction regime criteria for an annulus (equation (22)).

It is found that, for a fixed H and K as defined for the rod bundles, an increase in the pitch-to-diameter ratio P/d, and/or N, the number of rows in the square rod array, results in an increase in the overall convective heat transfer coefficient. Moreover, for a fixed outer cylinder, an increase in P/d and/or N enhances the convective heat transfer from the rod bundle to the outer cylinder.

Acknowledgments

We gratefully acknowledge the support of this work by the Office of Nuclear Waste Isolation under Contract E512-03900 to The Ohio State University Research Foundation and the Department of Mechanical and Aerospace Engineering at the University of Delaware.

References

1 Davis, L. P., and Perona, J. L., "Development of Free Convection Axial Flow Through a Tube Bundle," *International Journal of Heat and Mass Transfer*, Vol. 16, 1973, pp. 1425–1438.

2 Cox, R. L., *Radiative Heat Transfer in Arrays of Parallel Cylinders*, Ph.D. dissertation, University of Tennessee, 1976.

3 Reilly, J. T., Chan, C. K., Edwards, D. K., and Kastenberg, W. E., "The Effects of Thermal Radiation on the Temperature Distribution in Fuel Rod Arrays," *Nuclear Engineering and Design*, Vol. 48, 1978, pp. 340–351.

4 Watson, J. S., "Heat Transfer From Spent Reactor Fuels During Shipping: A Proposed Method for Predicting Temperature Distribution in Fuel Bundles and Comparison With Experimental Data," Oak Ridge National Laboratory, ORNL-3439, May 1963.

5 Driesen, G. E., Moran, D. F., Sherba, P. S., and Steffan, R. J., "Heat Transfer Associated with Dry Storage of Spent LWR Fuel," *Heat Transfer in Nuclear Waste Disposal*, ed. F. A. Kulacki and R. Lyczkowski, HTD Vol. 11, American Society of Mechanical Engineers, 1980, pp. 9–18.

6 McCann, R., "Thermal Hydraulic Analysis of a Spent Fuel Assembly Contained Within a Canister," *Heat Transfer in Nuclear Waste Disposal*, ed. F. A. Kulacki and R. Lyczkowski, HTD Vol. 11, American Society of Mechanical Engineers, 1980.

7 Keyhani, M., Kulacki, F. A., and Christensen, R. N., "Free Convection in a Vertical Annulus With Constant Heat Flux on the Inner Wall," ASME JOURNAL OF HEAT TRANSFER, Vol. 105, 1983, pp. 454–459.

8 Keyhani, M., *Free Convection in a Vertical Annulus and Rod Bundle*, Ph.D. dissertation, Department of Mechanical Engineering, The Ohio State University, 1983.

9 Keyhani, M., Kulacki, F. A., and Christensen, R. N., "Heat Transfer

Within Spent Fuel Canisters: An Experimental Laboratory Study — Final Report," Office of Nuclear Waste Isolation, Battelle Memorial Institute, Columbus, in press.

10 Korpela, S. A., Lee, Y., and Drummond, J. E., "Heat Transfer Through a Double Pane Window," ASME JOURNAL OF HEAT TRANSFER, Vol. 104, 1982, pp. 539–544.

11 MacGregor, R. K., and Emery, A. F., "Free Convection Through Vertical Plane Layers—Moderate and High Prandtl Number Fluids," ASME JOURNAL OF HEAT TRANSFER, Vol. 91, 1969, pp. 391–403.

12 Kubair, V. G., and Simha, C. R. V., "Free Convection Heat Transfer to Mercury in Vertical Annuli," *Int. J. Heat Mass Transfer*, Vol. 25, 1982, pp. 339–407.

13 Thomas, R. W., and de Vahl Davis, G., "Natural Convection in Annular and Rectangular Cavities. A Numerical Study," *Proceedings Fourth International Heat Transfer Conference*, Paris, Vol. 4, Paper NC.2.4, Elsevier, Amsterdam, 1970.

14 Graebel, W. P., "The Influence of Prandtl Number on Free Convection in a Rectangular Cavity," *Int. J. Heat Mass Transfer*, Vol. 24, 1981, pp. 125–131.

15 Sparrow, E. M., and Gregg, J. L., "The Laminar Free Convection Heat Transfer From the Outer Surface of a Vertical Cylinder," *Transactions ASME*, Vol. 78, 1956, pp. 1823–1828.

16 Sheriff, N., "Experimental Investigations of Natural Convection in Single and Multiple Vertical Annuli With High Pressure Carbon Dioxide," *Proceedings Third International Heat Transfer Conference*, Chicago, Vol. 2, 1966, pp. 132–138.

17 Bhushan, R., Keyhani, M., Christensen, R. N., and Kulacki, F. A., "Correlations for Convective Heat Transfer in Vertical Annular Gas Layers with Constant Heat Flux on the Inner Wall," ASME JOURNAL OF HEAT TRANSFER, Vol. 105, 1983, pp. 910–912.

18 Choi, I. G., and Korpela, S. A., "Stability of the Conduction Regime of Natural Convection in a Tall Vertical Annulus," *Journal of Fluid Mechanics*, Vol. 99, 1980, pp. 725–741.

M. J. Chamberlain
Building Engineering Group.

K. G. T. Hollands
Thermal Engineering Group.
Mem. ASME

G. D. Raithby
Thermal Engineering Group.
Mem. ASME

University of Waterloo,
Waterloo, Ontario, Canada

Experiments and Theory on Natural Convection Heat Transfer From Bodies of Complex Shape

Measurements of the heat transfer by natural convection from isothermal bodies to air are reported and compared to the predictions of the method proposed by Raithby and Hollands [7, 8]. The bodies tested were the cube in various orientations and a body consisting of two touching spheres (a bisphere). The experimental Rayleigh number range extended from 10 to 10^7. The experimental method incorporated measuring the heat transfer by the transient method and varying the Rayleigh number by varying the pressure. The predictions agreed with the measurements to within an average error of about 3 percent. The results are correlated by single equations, which can be extended to fluids other than air.

Introduction

Many workers have measured the rate of natural convective heat transfer from isothermal bodies immersed in an extensive fluid. But with few exceptions (e.g., Bovy and Woelk [1], King [2], Astrauskas [3]) these workers have restricted themselves to bodies of simple two-dimensional shape, such as plates or cylinders, or to bodies of simple axisymmetric shape, such as spheres and spheroids; very few measurements have been reported for bodies of more complex shape, such as cubes and tetrahedrons. This paucity of data has prevented analytical methods for predicting the heat transfer from being tested on bodies of complex shape.

Several analytical methods have, however, been tested on bodies of simple shape. The early methods, which used the laminar boundary layer equations at their starting point, proved unsatisfactory. They predicted the heat transfer accurately only over a very narrow intermediate range in Rayleigh number (Ra). They failed at low Ra because the boundary layer assumption is invalid (the boundary layers are too thick) and at high Ra because the laminar assumption is invalid (turbulence exists over part of the body). For example, Saville and Churchill's 1967 laminar boundary layer solution for a horizontal cylinder [4] predicted the measured heat transfer within 10 percent only for the narrow Rayleigh number range from 10^6 to 10^7. Recent solutions incorporating thick boundary layer effects have followed one of two lines, one exact, the other approximate. In 1979–1980 Kuehn and Goldstein [5] and Fujii, Fujii, and Matsunaga [6] each computed solutions to the two-dimensional laminar equations for horizontal cylinders, and their results showed close agreement with measured data over a wide Ra range extending from Ra = 1 to Ra = 5×10^6; for Ra > 10^6 turbulence caused the theory to underpredict the heat transfer. This approach has helped to place laminar external natural convection on a firm foundation, but because, for accurate results, it is limited to two-dimensional laminar flows and because it requires extensive computational effort and skill, it is unlikely to be practical for the heat transfer practitioner to implement directly, at least not for some time. In 1975–1978 Raithby and Hollands [7, 8] presented a simpler, approximate method which is based on the idea of the conduction layer and which extended the early work of Langmuir [9]. This general method (called here, for brevity, the R–H method) accounts for thick boundary layer effects and turbulence and has been validated over a large range in Ra for several bodies of simple shape [7, 10, 11].

Contributed by the Heat Transfer Division for publication in the JOURNAL OF HEAT TRANSFER. Manuscript received by the Heat Transfer Division April 5, 1984.

But since the R–H method is approximate, confidence in its accuracy and reliability must be established by comparing its predictions with data for as wide a range of Rayleigh number and body shapes as possible. In addition to new measurements for spheres, the present paper reports measurements over a broad range of Ra of the heat transfer from a cube (in three different orientations) and a bisphere (two touching spheres). The bisphere and the cube in one of its orientations are particularly difficult problems for the methods, and were specifically designed to test its limits of applicability. Comparisons are made between the measurements and the predictions of the R–H method for each case. In addition, correlation equations for calculating the heat transfer are provided. In all experiments air was the ambient fluid.

Experiment

Measurement Procedure. Heat transfer measurements were made for the body shapes and orientations shown in Fig. 1. The body dimensions are recorded in Table 1. The measurements for each case were taken when the body was suspended in the central portion of a pressure vessel 960 mm in diameter and 750 mm long. The Rayleigh number was varied over a range from 10 to 10^7 by repeating the measurements at different pressure levels [12, 10] between 1 and 700 kPa, and by varying the temperature difference ΔT between the body and its ambient air from 10 to 20 K. The vessel was sufficiently large relative to the body that, for the Ra range studied, the boundary layers on the body did not interfere significantly with those on the vessel walls. The vessel was well sealed so that no significant pressure drift occurred over the time (up to several hours) required for the heat transfer measurement. Furthermore, the vessel wall was isothermal to within 0.1 K, its temperature drift over the heat transfer measurement period was less than 0.1 K, and its effective emissivity for radiation from the body was very close to unity. The air temperature T_a in the central region of the vessel, except in the immediate vicinity of the body and in its wake, was measured to be uniform to within 0.2 K and very close to the temperature of the vessel wall T_v.

Each body was machined from Aluminum Alloy 6061-T6 to a 0.1 mm tolerance, and then polished to a high sheen with emery cloths and commercial polish. The high conductivity of the material guaranteed that the body temperature would be very nearly uniform, and the low emissivity of the polished surface minimized that radiative heat loss from the body.

Each body was suspended in the vessel on 0.08-mm nylon

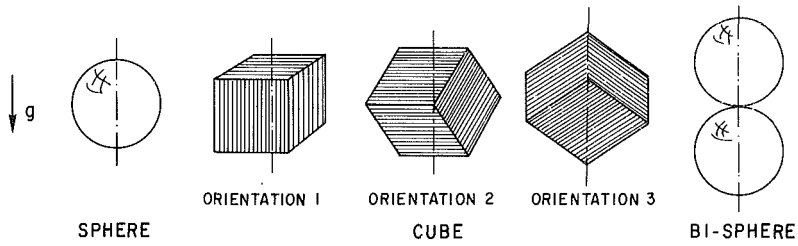

Fig. 1 Shapes and orientations of bodies tested

Table 1 Dimensions of bodies tested

Body	Quantity chosen for characteristic dimension, X	Value of X, m
Large sphere	Diameter	0.0600
Small sphere	Diameter	0.0400
Cube	Length of side	0.0432
Bisphere	Diameter of each sphere	0.0432

lines glued into small holes drilled in the body. The body temperature T_b was measured using a copper-constant thermocouple cemented into another hole with its junction 15 ± 6 mm from the body surface. The bisphere had two such junctions, one in each sphere. A 1000-Ω resistance heater, cemented into a hole 8 mm in diameter and 30 mm deep, provided the means of heating the body. To minimize heat losses from the bodies the diameter of the thermocouple leads and the copper heater leads were kept as small as practical (0.075 mm). In order to ensure that the bodies remained as nearly isothermal as possible, a high conductivity cement was used, made from 80 percent fine aluminum particles and 20 percent epoxy resin by weight. Further details are provided elsewhere [13].

The total heat transfer rate from a body Q_T was calculated from the transient cooling equation using the total heat capacity of the body (MC_p) and the measured cooling rate. The mass M was measured, and the effective C_p calculated from mass-weighted values for the aluminum, the heater, the cement, and the thermocouple. The mass of the aluminum bodies in all cases exceeded 99 percent of the total mass so that precise values of C_p for the other materials were not required.

For a given body, orientation, and pressure level, the body temperature was first raised to about 300 K (35 K above ambient) by passing current through the heater. With the current then shut off, the temperature was allowed to fall to about 325 K before the start of the test period. At regular time intervals Δt during the test period a microprocessor automatically logged the time and output from thermocouples which later permitted the ambient and body temperatures to be found. The test period was terminated when the body temperature fell to within about 5 K of the ambient temperature. Depending on the pressure level, the length of the test period varied from 30 min to 15 hr. The Δt interval between readings was chosen such that the number of readings N over the test period was about 50.

Nomenclature

A = surface area of body, m^2
C_l^*, C_t^* = defined by equations (10) and (11)
D = diameter of sphere, m
F_{b-v} = radiant form factor from body to vessel
g = gravitational acceleration, m/s^2
k = thermal conductivity of fluid, W/m K
L = length of side of cube, m
m = exponents in Churchill-Usagi mixing of laminar and turbulent solutions (equation (9))
(MC_p) = heat capacity of body, J/K
N = number of readings over one test period
Nu = Nusselt number = $QX/A\Delta Tk$, with k evaluated at the mean film temperature
Nu_c = conduction Nusselt number; Nusselt number when Ra→0
Nu_l = R-H method solution for Nu when step (*iii*) replaced by $\Delta_x = \Delta_{lx}$
Nu_t = R-H method solution for Nu when step (*iii*) replaced by $\Delta_x = \Delta_{tx}$
Nu_{lx}^T = thin-layer solution for local Nusselt number for laminar flow
Nu_{tx}^T = thin-layer solution for local Nusselt number for turbulent flow
Pr = Prandtl number = ν/α
q_x = local heat flux from body at location x, W/m^2
Q = rate of heat transfer from body to fluid (air), W
Q_T = total rate at which body is losing heat, including both convective and radiative rates, W
Q_R = rate at which body loses heat by radiation, W
R = radius of sphere, m
R_x = local radius of curvature of body, m
Ra = Rayleigh number = $g\beta\Delta TX^3/\nu\alpha$, with β evaluated at T_a and other properties at mean film temperature
t = time since start of test period, s
T_a = fluid temperature far from the body, K
T_b = body temperature, K
T_m = average value of T_a over one test period, K
T_v = mean temperature of pressure vessel walls, K
$\Delta T = T_b - T_a$, K
x = coordinate along the surface from the lowest point to a local point on the body, m
X = characteristic dimension of body, see Table 1, m
α = thermal diffusivity of fluid, m^2/s
β = volumetric coefficient of thermal expansion of fluid, K^{-1}
δ = thickness of uniform layer offering same thermal resistance as actual conduction layer, m
Δ_{lx} = local laminar conduction layer thickness, defined as X/Nu_{lx}^T, m
Δ_m = harmonic mean value of Δ_x, defined by equation (4), m
Δ_{tx} = local turbulent conduction layer thickness defined as X/Nu_{tx}^T, m
Δ_x = local conduction layer thickness, m
ϵ = emissivity of body surface

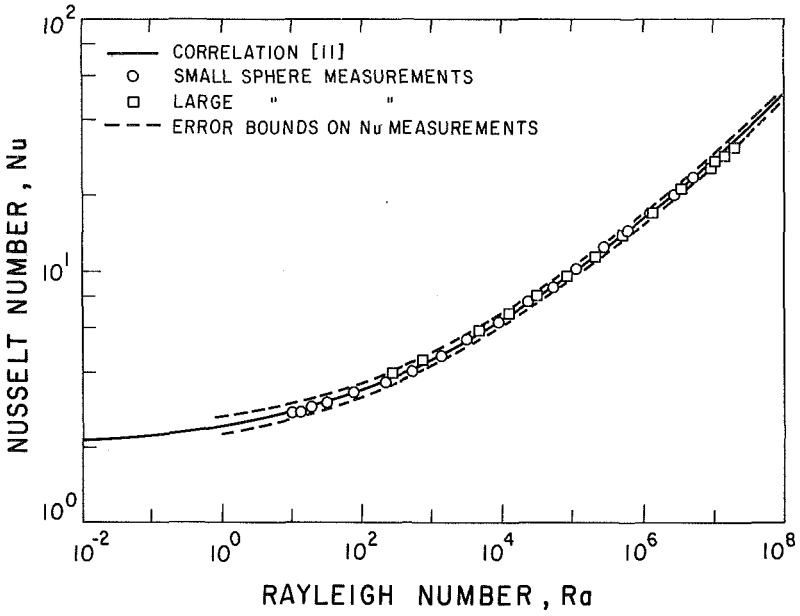

Fig. 2 Results for sphere

These data were post-processed to find the average air temperature T_m over the test period. A least-squares fit to the data, plotted as $P(t) = \ln(T_b - T_m)$ versus t, yielded the coefficients A_i in the cubic $P(t) = \Sigma_{i=0}^{3} A_i t^i$. The total heat flow at any time t in the test period is therefore given by

$$Q_T = (M\,C_p)\,\frac{dT_b}{dt} = (M\,C_p)\,\frac{dP}{dt}\exp(P) \tag{1}$$

The cubic fit is most accurate [14] at the three times $t_1 = N\Delta t/2$, $t_2 = t_1 + 0.7N\Delta t$, and $t_3 = t_1 - 0.7N\Delta t$. The three values of Q_T derived from each transient test were obtained by evaluating equation (1) at these times.

The net heat transfer by natural convection Q was calculated by subtracting from Q_T the radiative heat loss to the vessel wall Q_R where

$$Q_R = A\sigma(T_b^4 - T_v^4)/(\epsilon^{-1} + F_{b-v}^{-1} - 1) \tag{2}$$

Based on measurements [13] using a Gier-Dunkle DB-100 Reflectometer (without the filter) the hemispherical emissivity of the body surface ϵ was estimated to be 0.05 ± 0.01. The value of Q_R represented from 40 percent (at low Ra) to 2 percent (at high Ra) of the measured Q_T.

Conduction away from the body along the thermocouple and heater leads, as well as the suspension lines, was shown by analysis to be negligible (<0.5 percent of Q_T), and was neglected in the calculation of Q. Separate experiments were performed which confirmed this conclusion [13].

The Nusselt (Nu) and Rayleigh numbers that existed at the times of each Q_T determination were calculated from the corresponding Q value, the coincident $\Delta T = T_b - T_a$, the representative dimension X of the body, and the fluid properties. The fluid properties were calculated at the arithmetic mean of T_b and T_a, except for β, which was evaluated at T_a. Property equations were evaluated from least-square fits to the tabulated data by Hilsenrath et al. [15].

After the measurements just described were completed at the lowest pressure level, the vessel pressure was increased and the measurement steps retraced. This procedure was repeated at about 20 pressure levels (which therefore yielded 60 data points) until the maximum admissible vessel pressure was reached. The pressure increments were chosen such that the Ra values obtained were roughly equally spaced on a logarithmic scale.

Error Analysis. As part of the error analysis, the isothermality of the bodies was checked. Because of the thermal constriction between its two parts, a comparison of the upper and lower-sphere temperatures of the bisphere gave the worst-case check for isothermality. Within three minutes of switching the electrical heater off, the upper and lower spheres were the same within 0.15 K, a difference resulting in an error in the Nusselt number of less than 1 percent.

A detailed error analysis [13] took into account all calibrated and instrumental uncertainties. The dominant source of error in the Rayleigh number was the (40 Pa) uncertainty in the pressure transducer. Assuming worst-case conditions, the maximum error dRa in the Rayleigh number was found to be given by $d\mathrm{Ra}/\mathrm{Ra} = 0.25/\mathrm{Ra}^{1/2} + 0.02$; this represents a possible error of 10 percent at Ra = 10, decreasing to 5 percent at Ra = 10^2 and to 2 percent at Ra = 10^7. The dominant source of error in the Nusselt number was the uncertainty in the body surface emissivity measurement. The maximum error dNu in the Nusselt number was found to be given by $d\mathrm{Nu}/\mathrm{Nu} = 0.14/\mathrm{Nu} + 0.02$; this represents a possible error of 9 percent at Nu = 2, decreasing to 7 percent at Nu = 3 and to 2.5 percent at Nu = 20.

Results. The Nu-Ra results for the large and small spheres are plotted in Fig. 2, with the above error bounds shown on the plots. There is very little scatter, and the results for the two spheres are in excellent agreement. The solid curve plots a correlation equation developed previously by Raithby et al. [10] which, for air, simplifies to

$$\mathrm{Nu} = [(2 + 0.452\,\mathrm{Ra}^{1/4})^6 + (0.099\,\mathrm{Ra}^{1/3})^6]^{1/6} \tag{3}$$

There is excellent agreement between the measurements and this equation; the maximum difference is less than 2 percent for both the large and small spheres. The low degree of scatter and the close agreement between the two spheres and with equation (3) lend confidence to the experimental procedure.

The results for the complex bodies are given in Fig. 3. The solid curves in Fig. 3 are the results of an analysis, which is now described.

Analysis

Predictions of the R-H Method. Raithby and Hollands [7, 8, 16] have suggested a method for closely estimating the natural convection heat transfer from bodies. When the flow is three dimensional, the body is isothermal, and the fluid temperature far away is uniform, this R-H method reduces to the following algorithm:

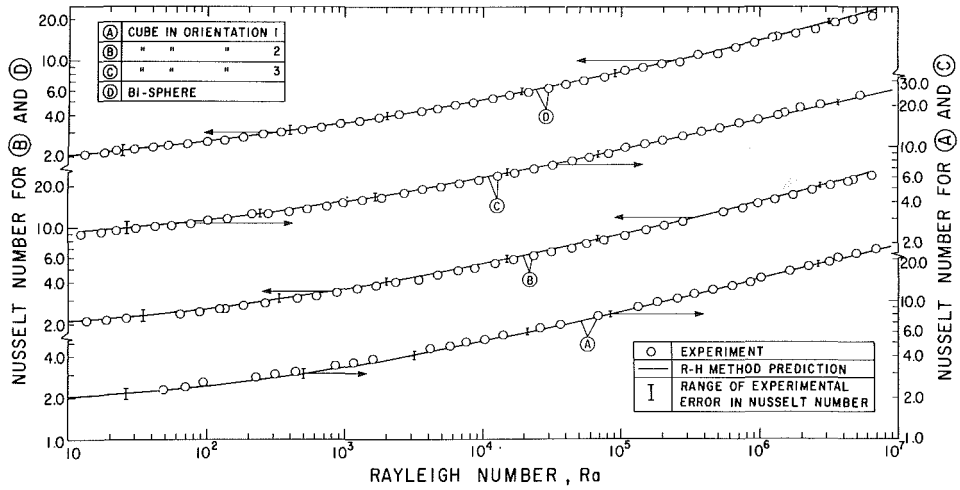

Fig. 3 Results for cubes and bisphere

(*i*) Calculate the Nu_{lx}^T, the laminar boundary layer (or thin layer) solution for the local Nusselt number, as estimated by a specified equation [8] containing a line integral extending along the surface of the body from the body's lowest point up to the local point x; calculate the corresponding local laminar conduction layer thickness Δ_{lx}, given by $\Delta_{lx} = X/Nu_{lx}^T$.

(*ii*) Calculate the Nu_{tx}^T, the turbulent boundary layer "solution" for the local Nusselt number at the same location x, as estimated by another specified algebraic equation (not containing a line integral); calculate the corresponding local turbulent conduction thickness Δ_{tx}, given by $\Delta_{tx} = X/Nu_{tx}^T$.

(*iii*) At every x location determine the actual local conduction layer thickness Δ_x as follows: If $\Delta_{lx} < 4/3\ \Delta_{tx}$, $\Delta_x = \Delta_{lx}$; otherwise $\Delta_x = \Delta_{tx}$.

(*iv*) Surround the body by a stationary fluid layer of local thickness Δ_x. Assign T_a to the outer surface of this layer and T_b to the inner (body) surface. Calculate the heat flow that the fluid would conduct through this layer. The heat flow Q so conducted is the desired heat transfer and the Nusselt number is $QX/(k(T_b - T_a)A)$.

Even though steps (*ii–iii*) have reduced the natural convection problem to the simpler conduction problem, the complete solution may still require considerable effort because of difficulties encountered at step (*iv*). A further simplification is therefore desirable.

Approximate Conduction Evaluation (Step iv). Two simplified approaches to step (*iv*) are outlined here. The first approach notes that substantial simplification and probably small error result if one can replace the layer of nonuniform thickness Δ_x by an equivalent one of uniform thickness δ. Clearly the best choice for δ is some average of Δ_x. By setting δ equal to the harmonic mean Δ_m of Δ_x given by

$$\frac{1}{\Delta_m} = \frac{1}{A}\int_A \frac{dA}{\Delta_x} \tag{4}$$

one ensures that in the thin layer limit where $\Delta_x \ll X$ (i.e. at large Ra), the uniform thickness layer conducts heat at the same rate as the nonuniform layer. Once δ has been so determined, one may be able to readily solve the simpler conduction problem or to find its solution in the conduction literature.

The second approach to simplifying step (*iv*) starts by noting that if the body were a sphere with a locally uniform layer of thickness Δ_x, the local heat flux q_x will be given by

$$q_x = k(T_b - T_a)\left(\frac{1}{R} + \frac{1}{\Delta_x}\right) \tag{5}$$

where R is the sphere radius. As an approximation, equation (5) may be extended to other three-dimensional bodies by everywhere replacing R by the body's local radius of curvature R_x. Integrating the resulting equation over the body surface to obtain the total heat transfer and expressing the results in terms of the Nusselt number gives

$$Nu = Nu_c + X/\Delta_m \tag{6}$$

where

$$Nu_c = \frac{X}{A}\int_A \frac{dA}{R_x} \tag{7}$$

Since the latter integral is independent of Ra, it can be evaluated once and for all. We note, however, that when Ra $\to 0$, $\Delta_m \to \infty$ and Nu $\to Nu_c$. Hence for equation (6) to be exact Nu_c would have to represent the Nusselt number in the conduction limit (wherein the body is immersed in an extensive stationary medium), and values of Nu_c obtained by solving the limiting conduction problem will therefore be more exact than those obtained by carrying out the integration indicated in equation (7). Values of Nu_c for many bodies exist in the conduction literature. If Nu_c is not available in the literature, it must be obtained by some numerical, analytical, or analog scheme.

With step (*iv*) simplified by one of the above approaches, the R-H method was used to predict Nusselt numbers for the bodies tested. Implementing the algorithms to calculate Nu_{lx}^T and Nu_{tx}^T, step (*i*) presented no special problems; see Chamberlain [13] for details. The line integrals required for Nu_{lx}^T were usually evaluated numerically; although analytical integration was possible in each case, the numerical integration was more straightforward and more compatible with quick evaluation of Δ_m in step (*iv*). Since step (*i*) found that both Δ_{lx} and Δ_{tx} are infinite on the lower horizontal face of the cube in orientation 1, step (*iii*) predicted an infinite layer thickness Δ_x on that face. Step (*iii*) also indicated that turbulent heat transfer ($\Delta_{tx} < 3/4\ \Delta_{lx}$) existed over the top face of the cube in orientation 1 and over some part of the top surface of the bisphere for the whole experimental range in Ra, and that laminar heat transfer ($\Delta_{lx} < 4/3\ \Delta_{tx}$) existed everywhere on the cube in orientation 3, also for all Ra tested.

We adopted the first approach to step (*iv*) for the cube, using the equation given by Schneider [17] to calculate the conduction.[1] With $X = L$, the length of one side, this procedure gave the following equation, which was used for calculating the Nusselt number

[1] Schneider restricted his equation to $\delta < 5L$ (or, with $\delta = \Delta_m$, to $\Delta_m < 5L$), but in fact the equation appears to be restricted to $\delta < 2L$. In any event, Δ_m was less than $2L$ in each instance of the present analysis.

Table 2 Parameters in correlation equation fit to results of R-H method

Body	Orientation	C_l^*	C_t^*	m	Maximum error of fit, %	Average error of fit, %
Cube	1	0.343	0.092	2.45	5.	3.
Cube	2	0.444	0.106(5)	5.25	3.	0.7
Cube	3	0.449	0.106(4)	16.	0.5	0.1
Bisphere	—	0.378	0.104	4.8	2.	1.

$$\mathrm{Nu} = 1.08 + L/\Delta_m + 0.2\,\Delta_m/L \tag{8}$$

We adopted the second approach for the bisphere, calculating the Nusselt number from equation (6) with $\mathrm{Nu}_c = 1.386$ [17] and X equal to the diameter of the spheres.

The resulting predictions are compared with the experimental data in Fig. 3. Generally speaking, the agreement is excellent for both the bisphere and the cube. The average deviation of the theoretical from the measured Nusselt number is close to 3 percent and the maximum deviation is 7 percent. Except for the high Ra range for the bisphere and the cube in orientation 3, the agreement is everywhere within the experimental error.

The error bounds shown for Nu are, however, the maximum expected, and the consistency of the data for the sphere indicate that these bounds overestimate the actual errors. Thus it is highly unlikely that experimental error is the only reason for the observed deviation; the simplifications in step (*iv*) and approximations inherent in the R-H method itself must account for some of it.

Correlation of the Data. The predictions of the R-H method can usually be well correlated by a single equation by a curve-fitting strategy which may be summarized as follows [16]. Let Nu_l be the Nusselt number function of Ra produced by the R-H method on changing step (*iii*) to read $\Delta_x = \Delta_{lx}$ everywhere on the body, and let Nu_t be the Nusselt number function of Ra produced by the method on changing step (*iii*) to read $\Delta_x = \Delta_{tx}$ everywhere on the body. Then a Churchill-Usagi [19] mixing of these two solutions, given by

$$\mathrm{Nu} = (\mathrm{Nu}_l^m + \mathrm{Nu}_t^m)^{1/m} \tag{9}$$

will, through appropriate choice of the constant m, give the desired correlation equation. One can show that the Δ_m which arises on determining Nu_l can always be expressed in the form

$$\Delta_m = X/(C_l^* \mathrm{Ra}^{1/4}), \tag{10}$$

and that the Δ_m which arises on determining Nu_t can always be expressed

$$\Delta_m = X/(C_t^* \mathrm{Ra}^{1/3}), \tag{11}$$

where C_l^* and C_t^* are constants, independent of Ra, which can be evaluated once and for all by a single integration over the surface of the body. Thus when equations such as (6) or (8) are used for calculating Nu_l, the resulting Nu_l equation will show terms in $C_l^* \mathrm{Ra}^{1/4}$, and similarly the resulting Nu_t equation will show terms in $C_t^* \mathrm{Ra}^{1/3}$. Terms in the latter equation other than the term X/Δ_m are normally very small when Nu_t is high enough to play a significant role in equation (9); consequently it is permissible to take the Nu_t in equation (9) to be given only by that term, as follows

$$\mathrm{Nu}_t = X/\Delta = C_t^* \mathrm{Ra}^{1/3} \tag{12}$$

Applying this strategy to the cube and the bisphere has given the following results. For the cube we obtained

$$\mathrm{Nu} = \{[[1.08 + C_l^* \mathrm{Ra}^{1/4} + 0.2/(C_l^* \mathrm{Ra}^{1/4})]^m + [C_t^* \mathrm{Ra}^{1/3}]^m\}^{1/m} \tag{13}$$

where the appropriate values of C_l^*, C_t^*, and m are given in Table 2. Values of m, chosen to give the best fit to the predictions of the R-H method, are given in Table 2, as are the maximum and rms average deviations applying to each fit. For the bisphere we obtained

$$\mathrm{Nu} = [(1.38 + C_l^* \mathrm{Ra}^{1/4})^m + (C_t^* \mathrm{Ra}^{1/3})^m]^{1/m} \tag{14}$$

with the appropriate values of C_l^*, C_t^*, and m and the deviations being given again in Table 2. Equations (13) and (14), with the values of the parameters given in Table 2, fit the experimental data with an average deviation of 3 percent or less.

Extension to Other Pr. The results for cubes and bispheres can be extended to other Prandtl numbers Pr, and to a wider range of Rayleigh number, using the R-H theory. The quantity C_l^* is proportional to $(1 + 0.67\ \mathrm{Pr}^{-9/16})^{-4/9}$, so the values given in Table 2 can be corrected to Prandtl numbers other than those for air by multiplying them by the factor f given by

$$f = 1.3[1 + 0.67\ \mathrm{Pr}^{-9/16}]^{-4/9} \tag{15}$$

The correction to C_t^* is not so straightforward, since the correction factor depends on the relative distribution of the two types of turbulence on the body [7, 16], which in turn depends on the Rayleigh number. But provided $\mathrm{Ra} < 10^7$, C_t^* plays only a modest role in equations (13, 14) for Nu, and provided $0.7 < \mathrm{Pr} < 100$, C_t^* is only weakly affected by changes in Pr. Hence little error will result from using the values of C_t^* given in Table 2 for fluids other than air.

Extension to Low Ra. Referring now to extensions in the Rayleigh number, it is first noted that equation (14) for the bisphere should, according to the method, be accurate for the full range in Ra from zero to infinity. Equation (13) for the cube, however, will fail at very low Ra because the conduction formula given by Schneider becomes invalid. For $\mathrm{Ra} < 10$, the formula for Nu_l resulting from the second approach to step (*iv*) is preferable, since it has the correct limit at $\mathrm{Ra} \to 0$. Moreover, for $\mathrm{Ra} < 10$, $\mathrm{Nu}_t \approx 0$, so $\mathrm{Nu} = \mathrm{Nu}_l$. Thus for cubes with $\mathrm{Ra} < 10$ the following equation for Nu is recommended:

$$\mathrm{Nu} = 1.383 + C_l^* \mathrm{Ra}^{1/4} \tag{19}$$

Discussion

Which of the two approaches to step (*iv*) gives the most accurate results is a question for conjecture. Some guidelines, however, can be deduced from the arguments which went into their development. Since the second approach assumed a curvature similar to a sphere, it may be expected to work best on surfaces with smoothly varying curvature, such as spheroids. Thus Raithby et al. [10] found the second approach works well for prolate and oblate spheroids. Except at the point of contact between its two spheres, the bisphere has constant curvatures, so the second approach should also work well for the bisphere, a presumption confirmed by Fig. 3. For prismatic bodies with flat surfaces and sharp corners, on the other hand, the curvature varies discontinuously, from zero on the flats to infinity on the corners, and the second approach may therefore be deduced to be less accurate. When applied to a cube, for example (Nu_c for a cube is equal to 1.383 [20]), the second approach was found to be slightly inferior to the first approach, giving results when deviated from the data by up to 11 percent in the Nusselt number.

The first approach, which assumed a uniform layer thickness, should start to fail when the actual layer thickness becomes highly nonuniform. As has been noted, for the cube in orientation 1, the lower face has $\Delta_x = \infty$ and the upper face has a turbulent boundary layer whose thickness is very much greater at low Ra than the relatively uniform thickness of the laminar layers on the sides. This nonuniformity of the layers in orientation 1 probably explains the larger discrepancies between the analysis and measurement that were observed for this orientation (Table 2).

Conclusions

1 Varying the pressure and measuring the heat transfer by the transient method provides a reliable, easily programmable, wide-Rayleigh-number method for determining Nu–Ra relations for bodies immersed in gases.

2 The Raithby–Hollands method has predicted the heat transfer from cubes and bispheres with an average accuracy of about 3 percent.

3 The heat transfer from cubes and bispheres immersed in air for Ra ranging from 10 to 10^7 can be closely estimated by equations (13) and (14). With the modifications noted in the paper, their use can be extended to other fluids and other Rayleigh numbers.

Acknowledgments

This work was supported through a Natural Sciences and Engineering Research Council of Canada (NSERC) Scholarship (to M. J. Chamberlain) and an NSERC Operating Grant. This support, the laboratory assistance of R. Kaptein and M. Van Reenan, the advice of M. M. Yovanovich, and the assistance of V. Hassani in making the fits, are all gratefully acknowledged.

References

1 Bovy, A. J., and Woelk, G., "Untersuchungen zur frier Konvektion an ebenen Waenden," *Waerme- und Stoffuebertragung*, Vol. 4, 1971, pp. 105–112.

2 King, W. J., "The Basic Laws and Data of Heat Transmission," *Mech. Engineering*, Vol. 54, 1932, pp. 347–353.

3 Astrauskas, P., "Natural Convection Mass Transfer to Particles," M.A.Sc. thesis, Department of Chemical Engineering, McGill University, Montreal, 1980.

4 Saville, D. A., and Churchill, S. W., "Laminar Free Convection in Boundary Layers Near Horizontal Cylinders and Vertical Axisymmetric Bodies," *J. Fluid Mechanics*, Vol. 29, 1967, pp. 391–399.

5 Kuehn, T. H., and Goldstein, R. J., "Numerical Solution to the Navier–Stokes Equations for Laminar Natural Convection About a Horizontal Isothermal Circular Cylinder," *Int. J. Heat Mass Transfer*, Vol. 23, 1980, pp. 971–979.

6 Fujii, T., Fujii, M., and Matsunaga, T., "A Numerical Analysis of Laminar Free Convection Around an Isothermal Horizontal Circular Cylinder," *Numerical Heat Transfer*, Vol. 2, 1979, pp. 329–344.

7 Raithby, G. D., and Hollands, K. G. T., "A General Method of Obtaining Approximate Solutions to Laminar and Turbulent Free Convection Problems," in: *Advances in Heat Transfer*, Vol. 11, eds. T. F. Irvine and J. P. Hartnett, Academic Press, 1975, pp. 266–315.

8 Raithby, G. D., and Hollands, K. G. T., "Analysis of Heat Transfer by Natural Convection (or Film Condensation) for Three-Dimensional Flows," *Proc. 6th Int. Heat Transfer Conf.*, Toronto, Vol. 2, 1978, pp. 187–192.

9 Langmuir, I., "Convection and Conduction of Heat in Gases," *Physical Review*, Vol. 34, 1912, pp. 401–422.

10 Raithby, G. D., Pollard, A., Hollands, K. G. T., and Yovanovich, M. M., "Free Convection Heat Transfer from Spheroids," ASME JOURNAL OF HEAT TRANSFER, Vol. 98, 1976, pp. 452–458.

11 Raithby, G. D., and Hollands, K. G. T., "Laminar and Turbulent Free Convection From Elliptic Cylinders, With a Vertical Plate and Horizontal Circular Cylinder as Special Cases," ASME JOURNAL OF HEAT TRANSFER, Vol. 98, 1976.

12 Saunders, O. A., "The Effect of Pressure on Natural Convection in Air," *Royal Society, Series A*, Vol. 157, 1936, pp. 278–291.

13 Chamberlain, M. J., "Free Convection Heat Transfer From a Sphere, Cube and Vertically Aligned Bi-Sphere," M.A.Sc. thesis, University of Waterloo, 1983.

14 Guest, P. G., *Numerical Methods of Curve Fitting*, Cambridge Press, 1961, pp. 263–268.

15 Hisenrath, J., et al., *Tables of Thermal Properties of Gases*, National Bureau of Standards, Circular 564 (1955).

16 Raithby, G. D., and Hollands, K. G. T., *Handbook of Heat Transfer*, Chapter 6, Fundamentals, McGraw-Hill, New York, in press.

17 Schneider, P. J., "Conduction," in: *Handbook of Heat Transfer*, eds. W. M. Rohsenow and J. P. Hartnett, McGraw-Hill, New York, 1973, pp. 3–124.

18 Morrison, F. A., Jr., and Reed, L. D., "Low Knudson Number Heat Transfer from Two Spheres in Contact," ASME JOURNAL OF HEAT TRANSFER, Vol. 96, 1974, pp. 478–482.

19 Churchill, S. W., and Usagi, R., "A General Expression for the Correlation of Rates of Transfer and Other Phenomena," *AIChE Journal*, Vol. 18, 1972, pp. 1121–1128.

20 Greenspan, D., "Resolution of Classical Capacity Problems by Means of a Digital Computer," *Canadian Journal of Physics*, Vol. 44, 1966, pp. 2605–2614.

An Analytical Mixing Model for Buoyant Jet Injected Into Pipe Flow

J. H. Kim
Electric Power Research Institute,
Palo Alto, CA 94303
Mem. ASME

An analytical model based on jet trajectory, jet diffusion layer, and flow establishment which predicts mixing of a cold jet injected at an angle into a hot crossflow in a horizontal pipe is presented. The impetus of the present study is to provide a method for calculating fluid temperature when a cold jet is injected into a pipe carrying a hot fluid, without recourse to a sophisticated multidimensional computer program. Such a method is urgently needed to resolve the so-called pressurized thermal shock issue in nuclear industry. The model prediction is compared with representative cases of existing test data, and is shown to predict the temperature distribution reasonably well.

Introduction

The problem of a buoyant jet injected into a confined crossflow has many important industrial applications, such as in nuclear reactor safety analysis, mixing of two fluids in chemical process units, jet impingement cooling of gas turbine blades, fuel injection in combustion chambers, discharge of the effluent pollutant into a stream, and cooling water discharge systems for thermal power plants, to name a few.

As an example, it is common in chemical process units to mix two fluids at a junction such as a tee in a pipe with subsequent transport to other locations, a method often referred to as pipe-flow mixing or in-line mixing.

To cite another example, one of the urgent needs in the analysis of the so-called pressurized thermal shock issue [1, 2] in nuclear industry is a simple method for predicting the mixing of cold water introduced from the high-pressure safety injection line with hot loop flow circulating in the cold leg pipe and downcomer of a pressurized water reactor. The thermal-hydraulic conditions in the downcomer are strongly affected by mixing in the cold leg pipe [5] and therefore the fluid temperature distribution in the downcomer is largely determined by that of the cold leg, as evidenced by test data [3, 4].

When a cold fluid is injected from the top of a pipe carrying a hot fluid, the density difference and the downward momentum of the jet pull down the jet while the momentum of the hot flow forces the jet to bend in the horizontal direction. A large amount of the hot ambient water is entrained into the jet during this process. Once the jet impinges on the bottom of pipe, it forms a stably stratified layer and mixing is much abated with suppression of turbulence.

Simple methods to predict mixing of a buoyant jet injected into a pipe flow have begun to draw attention, and only recently [24, 27, 29]. Currently, sophisticated multidimensional computer codes have been the main tool available for analyzing such mixing problems [6–9]. Mixing of nonbuoyant jet in a pipe was analyzed by several authors with the main aim to study optimum mixing [10, 11, 30–32]. In contrast to buoyant jet mixing in a pipe, similar problems in an unbounded medium have been richly investigated experimentally, analytically, and numerically [12–21].

The purpose of this paper is to present a simple analytical model to predict thermal mixing of a round cold jet injected into a warmer flow in a pipe. The results predicted by the analytical model are compared with available experimental data.

Contributed by the Heat Transfer Division for publication in the JOURNAL OF HEAT TRANSFER. Manuscript received by the Heat Transfer Division July 3, 1984. Paper No. 83-WA/HT-42.

Modeling of Jets and Plumes

We consider the situation depicted in Fig. 1. The jet is deflected by the pipe flow but eventually hits the bottom of the pipe because of gravity as well as downward momentum. The jet, after impinging on the bottom, divides into two streams, one going upstream and the other flowing downstream. The portion that travels upstream forms a countercurrent flow with the oncoming flow and eventually becomes entrained into the oncoming flow, part of which reenters the jet. The other portion of the jet that flows downstream forms a stably stratified layer without significant mixing. Previous studies [3, 4, 6, 7] show that approximately 80–90 percent of mixing occurs in the region between the origin and the jet impingement point. Therefore, this "near" region deserves a more detailed analysis than the downstream "far" region where a much simpler mixing model may do adequately. The present model embodies three significant lineaments: the jet trajectory relations, the growth of jet diffusion layer, and the flow establishment length.

The following major assumptions are made: The flow is assumed to be steady. The jet centerline trajectories in the near region are assumed to follow asymptotically those of a buoyant jet in an unbounded crossflow. The temperature profiles and flow development within the jet are assumed to be similar to those of a vertical round buoyant jet. Finally, the temperature profiles downstream of the jet impingement point are assumed to be invariant with the downstream distance.

With the above assumptions, the jet trajectories can be determined by modifying the work of Wright [13, 14], whereas the growth of the jet diffusion layer, the normalized temperature distribution, and the flow establishment length within the jet can be determined by following the work of Lee and Jirka [12].

The present modeling approach was adopted because of lack of turbulence and entrainment data for the system and conditions modeled, and difficulty in solving three-dimensional flow and energy equations numerically for such flow conditions.

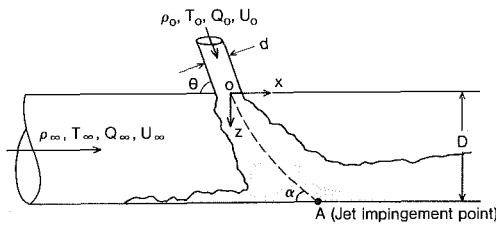

Fig. 1 A cold jet injected into a hot stream in a horizontal pipe

We first develop mixing regions from jet theory, then establish temperature distribution.

(a) Jet Trajectory Model. Following the work of Wright [13, 14], the jet trajectories are determined in various flow regimes identified as momentum-dominated near field (mdnf), momentum-dominated far field (mdff), buoyancy-dominated near field (bdnf), and buoyancy-dominated far field (bdff), depending on the jet initial momentum and buoyancy length scales. Wright [13, 14] derived his trajectory relations based on dimensional analysis using the jet mass flux, the jet momentum flux, the jet buoyancy flux, the crossflow velocity, and the vertical distance. He then introduced momentum and buoyancy length scales and was able to express the jet trajectories in terms of these quantities.

In the present study, the jet trajectories developed by Wright should be modified to account for the jet injection angle θ and to make the trajectories smooth and continuous across various flow regime boundaries.

Let us first introduce the buoyancy length scale:

$$l_b = B_0/U_\infty^3 = \frac{\pi}{4} d^2 g(\Delta\rho_0/\rho_\infty)U_0/U_\infty^3 \tag{1}$$

where $\Delta\rho_0 = \rho_0 - \rho_\infty$.

The momentum length scale in the vertical direction is defined by

$$l_m = M_0^{1/2}/U_\infty = \left(\frac{\pi}{4} d^2 U_0^2 \sin\theta\right)^{1/2}/U_\infty \tag{2}$$

There are essentially two trajectory sequences [14]: mdnf→mdff→bdff when $l_m > l_b$, and mdnf→bdnf→bdff when $l_m < l_b$. These two cases are developed in the following.

Case 1: $l_m > l_b$

In this case, the trajectory sequence is mdnf→mdff→bdff.

(*i*) For $z < l_m$, the jet is in the momentum-dominated near field (mdnf), and the jet asymptotic trajectory [13] is $z \sim 1.8\, l_m(x/l_m)^{1/2}$. Therefore, let us assume

$$z = 1.8 l_m[(x+x_1)/l_m]^{1/2} + b_1 \tag{3}$$

The constants x_1 and b_1 are determined by the conditions that $z=0$ and $dz/dx = \tan\theta$ at $x=0$. These constants are given in the Appendix.

For $\theta = \pi/2$, the above expression reduces to Wright's original expression. At the regime boundary, i.e., at $z = l_m$,

$$x = x_m = (l_m - b_1)^2/(3.24 l_m) - x_1 \tag{4}$$

(*ii*) For $l_m \le z < z_t$, the jet is in the momentum-dominated far field (mdff). Here, $z = z_t$ corresponds to a location where $x = x_t = 3.3\, l_m(l_m/l_b)^{1/2}$ on the jet centerline. The point (x_t, z_t) is the transition point from mdff to bdff. In the mdff, the asymptotic trajectory as described by Wright [13] is $z \sim 1.6\, l_m(x/l_m)^{1/3}$. We assume a trajectory of the form

$$z = 1.6 l_m[(x+x_2)/l_m]^{1/3} + b_2 \tag{5}$$

where x_2 and b_2 are constants. These constants are determined by requiring that the two trajectories given by equations (3) and (5) join smoothly at $x = x_m$ (i.e., at $z = l_m$). That is, z and dz/dx should be continuous at (x_m, l_m). x_2 and b_2 thus determined are listed in the Appendix.

At the transition point $x = x_t$, one obtains

$$z = z_t = 1.6 l_m^{2/3}(x_t + x_2)^{1/3} + b_2 \tag{6}$$

(*iii*) For $z \ge z_t$, the jet is in the buoyancy-dominated far field (bdff). The asymptotic jet centerline trajectory in this region [13] is given by $z \sim 0.85\, (l_m/l_b)^{1/6}\, l_b\, (x/l_b)^{2/3}$. So, we assume

$$z = 0.85(l_m/l_b)^{1/6} l_b[(x+x_3)/l_b]^{2/3} + b_3 \tag{7}$$

The constants x_3 and b_3 are determined by requiring that z and dz/dx match at $x = x_t$ (i.e., $z = z_t$) between the two trajectories given by equations (5) and (7). These are given in the Appendix.

Case 2: $l_m \le l_b$

In this case, the jet trajectory follows the sequence mdnf→bdnf→bdff.

(*i*) For $z < l_m$, the jet is in the momentum-dominated near field and the jet centerline trajectory is given by equation (3).

(*ii*) For $l_m \le z < l_b$, the jet is in the buoyancy-dominated near field (bdnf). In this region, the jet centerline has the

Nomenclature

b = thickness of jet diffusion layer
b' = width of potential core of jet
B_0 = buoyancy flux of jet at the origin
d = jet injector diameter
D = pipe diameter
F_0 = Froude number of jet = $U_\infty/(\Delta\rho_0/\rho_a g d)^{1/2}$
g = gravitational acceleration
l_b = buoyancy length scale
l_m = momentum length scale
M_e = momentum flux of jet at flow establishment, i.e., at $S = S_e$
M_0 = momentum flux of jet at the origin
Q_e = flow rate entrained in the jet in the near region (see Fig. 3)
Q_I = flow rate going downstream after jet hits the bottom of pipe (see Fig. 3)
Q_{II} = flow rate of the ambient fluid (see Fig. 3)
Q_{III} = flow rate going upstream after jet hits the bottom of pipe (see Fig. 3)
Q_0 = jet flow rate at the origin
Q_∞ = pipe flow rate at upstream infinity
r = radial distance from jet centerline
s = distance along jet centerline
s_e = flow establishment length along jet centerline
T = temperature
T_a = temperature of ambient fluid
T_c = temperature at jet centerline axis
T_I = average temperature of jet after the jet impinges on the bottom of pipe
T_0 = temperature of jet at the origin
T_∞ = temperature of pipe flow at upstream infinity
U_∞ = pipe flow velocity at upstream infinity
x = coordinate in horizontal direction
x_b = value of x corresponding to $z = l_b$
x_m = value of x corresponding to $z = l_m$
x_t = value of x at which momentum-dominated far field transits to buoyancy-dominated far field for the case $l_m > l_b$
z = coordinate in vertical downward direction
z_t = value of z at which momentum-dominated far field transits to buoyancy-dominated far field for the case $l_m > l_b$, i.e., value of z corresponding to $x = x_t$
α = jet impingement angle
ϵ = rate of spread of jet diffusion layer
η = parameter characterizing jet flow split after jet impinges on the bottom of pipe
θ = jet injector angle
λ = parameter related to turbulent Schmidt number
ρ_a = density of ambient fluid
ρ_0 = density of jet at the origin
ρ_∞ = density of loop flow at upstream infinity

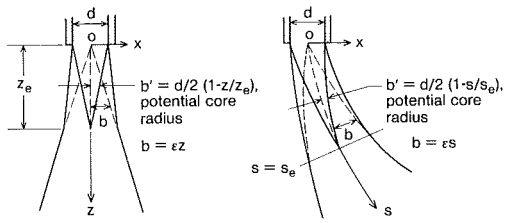

Fig. 2 Development of a cold jet discharging into a hot ambient fluid

asymptotic trajectory [13] given by $z \sim 1.85\, l_b\, (x/l_b)^{3/4}$. Let us assume

$$z = 1.85 l_b [(x+x_4)/l_b]^{3/4} + b_4 \tag{8}$$

The constants x_4 and b_4 are determined by matching z and dz/dx at $x = x_m$ (i.e., $z = l_m$) between the two trajectories given by equations (3) and (8). They are given in the Appendix.

At the regime boundary, i.e., at $z = l_b$, we obtain

$$x = x_b = (1.85)^{-4/3} l_b^{-1/3} (l_b - b_4)^{4/3} - x_4 \tag{9}$$

(*iii*) For $z \geq l_b$, the jet is in the buoyancy-dominated far field (bdff). The jet centerline trajectory has a form similar to equation (7) with different constants. That is,

$$z = 0.85 (l_m/l_b)^{1/6} l_b [(x+x_5)/l_b]^{2/3} + b_5 \tag{10}$$

The conditions that z and dz/dx match at $x = x_b$ (i.e., at $z = l_b$) between the two trajectory relations given by equations (8) and (10) determine the constants x_5 and b_5, and are given in the Appendix.

(*b*) Temperature Profile and Development of Jet. A good assumption for normalized temperature profile within a turbulent buoyant jet is a Gaussian profile [12, 17, 22]. In the present model, we adopt the normalized temperature profiles (equivalent to normalized density profiles) assumed by Lee and Jirka [12] in their analysis of a round turbulent buoyant jet discharging vertically into an otherwise quiescent body of fluid. In their model, the jet spreading angle is assumed to be constant so that the jet diffusion layer spreads linearly with increasing distance along the centerline. Figure 2(*a*) illustrates the schematic structure of a vertical round jet. This consists of a region where flow and temperature are still developing ($z \leq z_e$), in which the turbulent shear layer has not penetrated to the jet axis, and a region of fully developed flow ($z > z_e$), in which the normalized temperature profiles are similar at all levels. Let us adopt the same approach to the present problem and assume that the jet is merely deflected by the crossflow with its profiles and characteristics maintained. This situation is illustrated in Fig. 2(*b*).

With these assumptions, the normalized temperature profile in the region of developing flow (for $s \leq s_e$) is

$$\Delta T/\Delta T_0 = (T_a - T)/(T_a - T_0) = 1 \text{ for } r \leq b' \tag{11}$$

$$\Delta T/\Delta T_0 = (T_a - T)/(T_a - T_0) = e^{-(r-b')^2/\lambda^2 b^2} \text{ for } r > b' \tag{12}$$

where b' is the potential core radius given by $b' = d/2\,(1 - s/s_e)$, $b = \epsilon s$ is the thickness of the jet diffusion layer, T_a is the ambient temperature, and λ is a parameter related to the turbulent Schmidt number Sc by $\mathrm{Sc} = 1/\lambda^2$. According to Forstal and Gaylord [23], experimental values of Sc lie in the range $0.75 < \mathrm{Sc} < 0.85$ so that $1.08 < \lambda < 1.16$. Lee and Jirka [12] recommend $\lambda = 1.14$, which will be used in the present analysis. In the region of established flow, $s > s_e$, the normalized temperature profile is assumed to be

$$\begin{aligned} \Delta T/\Delta T_0 &= (T_a - T)/(T_a - T_0) \\ &= (T_a - T_c)/(T_a - T_0) e^{-r^2/\lambda^2 b^2} \end{aligned} \tag{13}$$

where T_c denotes jet centerline temperature. In general, it is expected that $\Delta T/\Delta T_0$ will depend on x/d, z/d, d/D, Q_∞/Q_0, l_m/l_b, and θ. These temperature profiles are expected to be valid over a wide range of conditions. However, the *velocity* profile of a buoyant jet in a confined flow is not expected to resemble those in an unbounded medium. For instance, the velocity profile may be reasonably approximated by a Gaussian profile up to a certian distance from the origin, but as the jet approaches the bottom of pipe, the centerline velocity will start to decrease until it vanishes at the impingement point. Thus, the velocity profile will no longer retain a Gaussian form as the jet approaches the bottom of pipe. Nevertheless, the *temperature* profile is expected to maintain a Gaussian form even in the region close to the bottom of pipe. Indeed, experimental data obtained in a turbulent buoyant jet discharged vertically into a water of finite depth substantiate the Gaussian temperature profile as a good approximation all the way up to a short distance (~one jet diameter) from the free surface [17].

As the ambient fluid is entrained into the jet, the jet will spread and diffuse. The jet spreading rate ϵ is assumed to be constant. For unbounded jet in a quiescent ambient fluid, the value of ϵ recommended by Lee and Jirka [12] is 0.109. However, it is obvious from the dye experiments [3] that this value will severely underpredict the spread of the diffusion layer for jets injected into a pipe flow. From the color photographs of these dye tests, the value of ϵ appears to be 0.2 ~ 0.3. This increased spreading rate is probably due to the presence of the crossflow as well as the wall effect, both of which tend to enhance mixing. A nominal value of $\epsilon = 0.25$ has been used in the present analysis.

(*c*) Determination of Flow Establishment Length s_e and Jet Centerline Temperature T_c. The flow establishment length along the jet axis is determined the same way as in the case of a vertical round buoyant jet [12]. The length s_e is calculated from

$$1 + \frac{4}{F_0^2}\left[\frac{s_e/d}{12} + \frac{\sqrt{\pi}\lambda\epsilon}{12}(s_e/d)^2 + \frac{\lambda^2\epsilon^2}{3}(s_e/d)^3\right] = \frac{(1+\lambda^2)^2}{8\lambda^4\epsilon^2}\frac{1}{(s_e/d)^2} \tag{14}$$

where $F_0 = U_\infty/(\Delta\rho_0/\rho_a g d)^{1/2}$ is the Froude number of the buoyant jet and $\Delta\rho_0 = \rho_0 - \rho_a$. The normalized temperature on the jet axis in the region of established flow ($s > s_e$) can be determined from

$$\begin{aligned} \Delta T_c/\Delta T_0 &= (T_a - T_c)/(T_a - T_0) \\ &= \frac{1+\lambda^2}{4\lambda^2\epsilon^2}(s/d)^{-1}\left\{\left(\frac{M_e}{2\epsilon^2 M_0}\right)^{3/2} + \frac{3(1+\lambda^2)}{8\epsilon^2 F_0^2}[(s/d)^2 - (s_e/d)^2]\right\}^{-1/3} \end{aligned} \tag{15}$$

$$\frac{M_e}{M_o} = 1 + \frac{4}{F_0^2}\left[\frac{s_e/d}{12} + \frac{\sqrt{\pi}\lambda\epsilon}{12}(s_e/d)^2 + \frac{\lambda^2\epsilon^2}{3}(s_e/d)^3\right] \tag{16}$$

The above expression for the jet centerline temperature is used in conjunction with equation (13).

(*d*) Calculation of the Ambient Temperature T_a. The ambient temperature T_a surrounding the buoyant jet is not the same as the pipe flow temperature far upstream. This is due to the fact that the jet divides into upstream and downstream after impacting the bottom of the pipe, with the layer traveling upstream eventually entrained into the oncoming pipe flow, and thus lowering the ambient temperature (Fig. 3). It should be noted here that there is no restriction on the flow direction of Q_{II} and countercurrent flow between Q_I and Q_{II} is allowable.

Assuming density and specific heat are constant, one can write the one-dimensional conservation equations for mass and energy for the control volume bounded by AA' and BB'

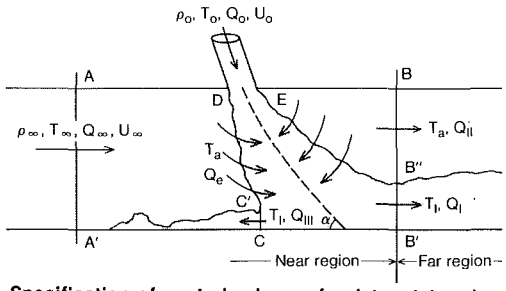

Fig. 3 Specification of control volumes for determining the ambient temperature T_a

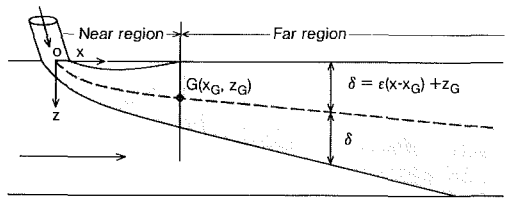

Fig. 4 Near region and far region description when the jet touches the top of pipe

$$Q_I + Q_{II} = Q_0 + Q_\infty \tag{17}$$

$$Q_I T_I + Q_{II} T_a = Q_0 T_0 + Q_\infty T_\infty \tag{18}$$

Likewise, let us write the conservation equations for the control volume enclosing the jet boundaries $DC'CB'B''E$ to obtain

$$Q_I + Q_{III} = Q_0 + Q_e \tag{19}$$

$$(Q_I + Q_{III}) T_I = Q_0 T_0 + Q_e T_a \tag{20}$$

The ambient temperature around the jet is assumed to be uniform. This assumption is reasonable because the jet does not block the pipe and the pipe flow can go around the jet [24].

The flow split Q_I and Q_{III} for the upstream traveling layer and the downstream flowing layer is approximated by a two-dimensional idealized jet flow. Then, one obtains [25]

$$Q_{III} = (1 - \cos\alpha)/(1 + \cos\alpha) Q_I \equiv \eta Q_I \tag{21}$$

where α is the jet impingement angle which can be determined from the jet trajectory relations. This simple jet split model turns out to be a satisfactory one as has been shown in a transient cooldown analysis for stagnant loop flow [27].

Finally, the relation between T_I and T_a can be obtained by calculating the average value of T across the jet at the jet impingement point using either equation (13) or equations (11) and (12) depending on whether or not the jet has been fully developed. This yields a linear relation

$$T_I = a_1 T_a + a_2 \tag{22}$$

where a_1 and a_2 are constants obtained from the integrations.

Equations (17–22) completely determine Q_I, Q_{II}, Q_{III}, Q_e, T_I, and T_a. In particular, the ambient temperature is found

$$T_a = \frac{(1+\eta) Q_\infty T_\infty + \eta Q_0 T_0}{(1+\eta) Q_\infty + \eta Q_0} \tag{23}$$

***(e)* Temperatures at Far Downstream.** The temperature distribution in the near region can be determined completely from the foregoing equations. After the jet hits the bottom of pipe, the temperature profile in the plane normal to the jet centerline at the jet impingement point will be assumed to hold for the vertical distribution of temperature in the far region downstream of the impingement point. This assumption is justified by experimental evidence that the cold layer flowing on the bottom forms a stably stratified layer which does not promote further mixing. It is known from linear stability analysis [26] that the minimum critical Reynolds number on the neutral stability curve increases with density difference, and above a certain Richardson number (which is the inverse square of the Froude number F_0) the flow becomes stable for all Reynolds numbers. Turbulence is thus suppressed and mixing is abated. Suppression of turbulent mixing in a stably stratified flow is further evidenced by test results [3, 4]. Those tests showed most of mixing took place in the near region, while little mixing occurred farther downstream in the pipe where the flow became stably stratified.

Specifically, Tests Nos. 46 and 55 of [3] provide a good example. Those two tests are almost identical except for the location of the jet injector, which for Test No. 55 is located much farther upstream (by 0.63 m) than that for Test No. 46. Yet, the temperature distributions for the two cases near the downstream end of pipe are very similar, thus confirming that little mixing takes place in the pipe downstream of jet impingement points. Therefore, the present analysis assumes the temperature distribution downstream of the jet impingement point to be the same as that at the impingement point.

If the momentum of the loop flow is substantially larger than that of the jet and the buoyancy flux is small, the jet may be deflected severely and the jet upper boundary may hit the top of pipe before the jet impinges on the bottom of pipe. In such a situation, the section downstream of the location where the jet touched the ceiling will be treated as a far region. This situation is illustrated in Fig. 4. In this case, the jet is so unstably stratified that mixing is tremendously enhanced, and the temperature of the fluid farther downstream is expected to be close to the mixed mean temperature. Indeed, this was the case in Test No. 48 of [3], as will be discussed later. When the jet boundary touches the top of pipe, the jet upper boundary will be assumed always to coincide with the top of pipe, and the jet diffusion layer will be assumed to increase linearly as before (see Fig. 4). After the jet centerline finally touches the bottom of pipe, the temperature profile from then on is assumed to be invariant.

Table 1 Test Conditions Used in the Present Study

	Creare Test Number (Ref. 3)				
	42	48	51	55	63
d/D	0.356	0.356	0.356	0.356	0.0486
θ	60°	60°	60°	60°	90°
Q_∞/Q_0	9.35	46.73	1.87	4.67	8.06
l_m/l_b	0.627	17.06	0.029	0.163	0.332

Results and Discussion

The present model was used to obtain temperature distribution for a number of representative cases of mixing tests [3] and the results are compared with the data.

The scale of the test facility is approximately 1/5 that of a typical pressurized water reactor (PWR) and consists of a horizontal pipe of 0.1427 m (5.62 in.) diameter and a vertical downcomer. There are two types of injector: one having 0.0508 m (2 in.) diameter with 60 deg angle of injection and the other having 0.006934 m (0.273 in.) diameter with 90 deg injection angle. The downstream end of the horizontal pipe is attached to a planar downcomer section simulating a 90 deg sector of a PWR downcomer. Table 1 summarizes geometric and hydrodynamic conditions of the Creare tests selected for the present study.

During the test, a hot flow was circulated through the loop while the cold coolant jet was injected into the hot loop flow from the top of pipe. The tests typically lasted approximately 200 s, at which time steady states were nearly achieved. Comparison between the model prediction and the test data is presented in Figs. 5–9 for five representative cases. These comparisons were made at a location approximately 0.15 m (~6 in.) upstream from the downcomer and at another

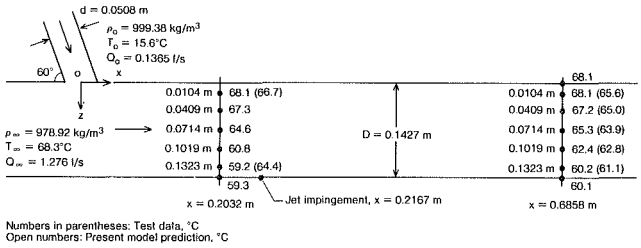

Fig. 5 Comparison of present model prediction with Creare mixing Test No. 42 [3], mixed mean temperature = 63.2°C

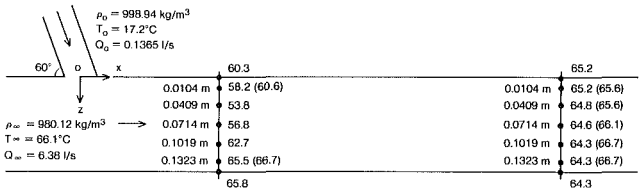

Fig. 6 Comparison of present model prediction with Creare mixing Test No. 48 [3]; mixed mean temperature = 65°C; jet touched the top of pipe at x = 0.01 m; dimensions and thermocouple locations same as in Fig. 5

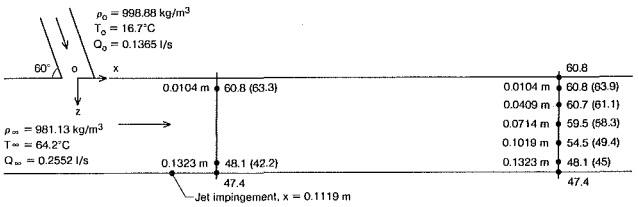

Fig. 7 Comparison of present model prediction with Creare mixing Test No. 51 [3]; mixed mean temperature = 47.8°C; dimensions and thermocouple locations same as in Fig. 5

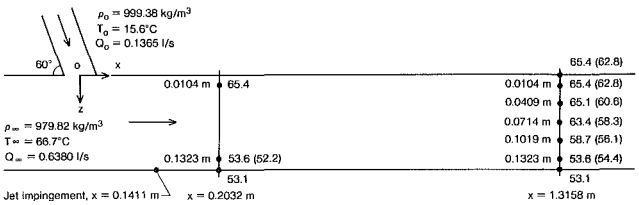

Fig. 8 Comparison of present model prediction with Creare mixing Test No. 55 [3]; mixed mean temperature = 57.2°C; the injector is located much farther upstream than the previous three cases; other dimensions are the same as in Fig. 5

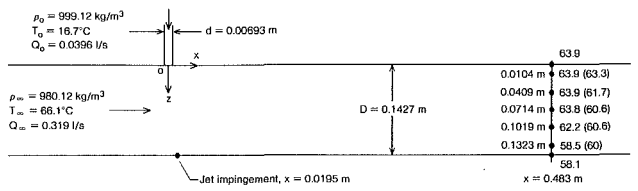

Fig. 9 Comparison of present model prediction with Creare mixing Test No. 63 [3]; mixed mean temperature = 61.1°C; small 90 deg injector

location farther upstream from it. In the test facility, the horizontal cold leg pipe has a 30 deg bend before it joins the downcomer. In the present model, this bend is not taken into account. However, the effect of this bend on mixing was found to be minute [28].

Figure 5 shows a comparison between data and the present model prediction for Test No. 42 of [3]. The trend of the temperature distribution in the far region is correctly captured, although the model predicts less mixing than the test data. The predicted temperature in the near region also shows a higher thermal stratification (hereinafter expressed in terms of the maximum temperature difference in the vertical direction) than the test data. However, the overall agreement

Table 2 $(T_{predicted} - T_{measured})/(T_a - T_0)$ at downstream thermocouples

TC Location From Top (m)	Creare Test Number (Ref. 3) 42	48	51	55	63
0.0104	4.75%	-0.82%	-7.03%	5.22%	1.27%
0.0409	4.18%	-1.52%	-0.91%	9.04%	4.66%
0.0714	2.66%	-3.07%	2.72%	10.24%	6.78%
0.1019	0.76%	-4.91%	11.56%	5.22%	3.39%
0.1323	-1.71%	-4.91%	7.03%	-1.61%	-3.18%
RMS Value	3.18%	3.48%	6.94%	6.98%	4.26%

is satisfactory. The trajectory calculation indicated that the jet would undergo mdnf→bdnf→bdff before it hits the bottom of pipe.

Figure 6 shows a comparison for Test No. 48 of [3]. In this test, the pipe flow rate was so much higher than the jet injection flow rate (a ratio of 46.6) that the jet was deflected very strongly and the jet upper boundary almost immediately touched the top of the pipe. Calculation based on the present model also correctly predicted this phenomenon. Since the jet was severely deflected, it experienced an unstable, reverse stratification which eventually enhanced mixing. The temperature at the downstream end of the pipe thus became almost uniform. Both the test and the prediction show an almost uniform, well-mixed temperature in the far region. The reverse thermal stratification (i.e., cold fluid above hot fluid) is shown in the temperature distribution immediately downstream of the jet injector. The trajectory calculation showed that the jet would undergo the momentum-dominated near field before the jet upper boundary touches the top of pipe. Uncertainty of ±0.6°C (±1°F) in the temperature measurement is displayed at the downstream location where the test data show a higher temperature (66.7°C) than the pipe flow temperature (66.1°C).

Figure 7 presents a comparison for Test No. 51 of [3]. This is a case of a relatively low pipe flow to jet injection flow ratio (ratio of 1.9). In direct contrast to the previous case, the cold jet was brought down to the bottom quickly and a stably stratified fluid layer was formed on the bottom which resulted in little mixing as it traveled downstream. The thermal stratification expressed in terms of the maximum temperature difference is quite severe. All these features were correctly captured by the present model, although the model predicted less stratification than the test data for this case. The trajectory calculation indicated that the jet would undergo mdnf all the way to the bottom of the pipe.

In Fig. 8, the results of the model prediction and the data for Test No. 55 of [3] are compared. The injector for this test was located much farther upstream than in the three cases discussed above, in order to demonstrate that modeling of far region mixing is not of primary importance. The comparison shows that the predicted temperature distribution at the jet impingement location, which was translated to the downstream end without further mixing, still agrees reasonably well with the test data obtained at the downstream end of the pipe. This implies that little mixing has occurred in the pipe section downstream of the jet impingement point because the jet formed a stably stratified layer of fluid after it impinged on the pipe bottom. The trajectory calculation showed that the jet would undergo mdnf and bdnf before impinging on the bottom of pipe.

Figure 9 compares the results for Test No. 63 of [3]. In this test, the injector had 90 deg angle and the size of the injector was very small. The jet Froude number is very high ($F_0 = 28.5$ versus approximately 0.7 for other cases investigated in the present study) and it is expected that the jet trajectory should be more vertical. The jet trajectory and the impingement point calculated by the present model predicted this behavior correctly, in agreement with the color photograph of the test reported in [3]. The predicted temperature distribution shows good agreement with the test data. The trajectory calculation

indicated that the jet would be in momentum-dominated near field all the way down to the bottom of pipe.

Table 2 presents (predicted T − measured T)/($T_a - T_0$) at downstream thermocouple locations as a measure of accuracy of the present model. An overall RMS error of 5.24 percent was calculated.

Summary and Conclusions

A simple analytical mixing model based on jet trajectory, diffusion, and flow establishment was proposed in this paper. The model predicts mixing of a cold coolant jet injected into the top of a pipe carrying a hot flow, a situation similar to that in a pressurized water reactor during an overcooling transient which is a precursor to a hypothetical thermal shock event. The model applies to steady-state flow. The model is easy and straightforward to use and is general enough to cover a wide range of conditions: arbitrary angle of injection, pipe and injector sizes, range of loop flow to injection flow ratio, and arbitrary temperature difference between the loop flow and the cold jet.

The predictions by the present model show reasonable agreement with the representative test data selected for comparison. Many salient features are correctly captured by the model, such as temperature distribution, mixing enhancement with reverse stratification, and mixing abatement with stable stratification.

Several points of discussion are in order. First, the parameter ϵ characterizing the jet diffusion layer growth was assumed to be a constant (0.25) for all cases. It is expected that ϵ will depend on other parameters. Secondly, the flow split at the jet impingement on the bottom of pipe is based on a simple two-dimensional idealized jet model, and therefore a degree of uncertainty is expected. Finally, the pipe wall effect on the mixing is not known, especially the effect on the jet trajectory. However, these effects are of second order and need not be considered in many practical engineering problems involving buoyant jet mixing.

References

1 "Reactor Safety and the Research Budget," *Science*, Vol. 214, Nov. 13, 1981, pp. 766-768.

2 Chexal, B., Marston, T., and Sun, B. K.-H., "Tackling the Pressurized Thermal Shock Issue," *Nuclear Engineering International*, Vol. 27, No. 327, May 1982, pp. 38-42.

3 Rothe, P. H., and Ackerson, M. F., "Fluid and Thermal Mixing in a Model Cold Leg and Downcomer with Loop Flow," EPRI NP-2312, Apr. 1982.

4 Rothe, P. H., and Fanning, M. W., "Evaluation of Thermal Mixing Data From a Model Cold Leg and Downcomer," EPRI NP-2773, Dec. 1982.

5 Kim, J. H., Sun, K. H., and Lin, C.-L., "Phenomenological Understanding of Thermal Hydraulic Aspects of the Pressurized Thermal Shock," *ANS Transactions*, Vol. 41, June 1982, pp. 260-261.

6 Lin, C.-L., Kim, J. H., and Sun, B. K.-H., "Numerical Simulation of Thermal and Fluid Mixing in the Cold Leg and Downcomer of a Model Geometry During a PWR Primary Side Overcooling," *Thermal-Hydraulics of Nuclear Reactors*, Vol. II, Proceedings of the Second International Topical Meeting on Nuclear Reactor Thermal Hydraulics, ANS Publication, Jan. 1983, pp. 988-996.

7 Kim, J. H., and Lin, C.-L., "Analysis of Transient Thermal Mixing in the Downcomer of a Model PWR Geometry During High Pressure Injection," *ANS Transactions*, Vol. 43, Nov. 1982, pp. 447-448.

8 Hassan, Y. A., "COMMIX Predictions of a Thermal Mixing Test," *ANS Transactions*, Vol. 41, June 1982, pp. 387-390.

9 Lyczkowski, R. W., et al., "Three-Dimensional Analysis of Thermal and Fluid Mixing in Cold Leg and Downcomer of PWR Geometries," EPRI NP-3321, Dec. 1983.

10 Fitzgerald, S. D., and Holley, E. R., "Jet Injections for Optimum Mixing in Pipe Flow," WRC Research Report No. 144, University of Illinois Water Resources Center, Urbana, Illinois, Dec. 1979.

11 Forney, L. J., and Lee, H. C., "Optimum Dimensions for Pipeline Mixing at a T-junction," *AIChE Journal*, Vol. 28, No. 6, Nov. 1982, pp. 980-987.

12 Lee, J. H. W., and Jirka, G. H., "Vertical Round Buoyant Jet in Shallow Water," *Journal of the Hydraulics Division*, HY12, ASCE, Dec. 1981, pp. 1651-1675.

13 Wright, S. J., "Mean Behavior of Buoyant Jets in a Crossflow," *Journal of the Hydraulics Division*, HY5, ASCE, May 1977, pp. 499-513.

14 Wright, S. J., "Effects of Ambient Crossflows and Density Stratification on the Characteristic Behavior of Round Turbulent Buoyant Jets," Report No. KH-R-36, W. M. Keck Laboratory of Hydraulics and Water Resources, California Institute of Technology, Pasadena, CA, 1977.

15 Chu, V. H., and Goldberg, M. B., "Buoyant Forced-Plumes in Cross Flow," *Journal of the Hydraulics Division*, HY 9, ASCE, Sept. 1974, pp. 1203-1214.

16 Chen, C. J., and Chen, C. H., "On Prediction and Unified Correlation for Decay of Vertical Buoyant Jets," ASME JOURNAL OF HEAT TRANSFER, Vol. 101, Aug. 1979, pp. 532-537.

17 Pryputniewicz, R. J., and Bowley, W. W., "An Experimental Study of Vertical Buoyant Jets Discharged Into Water of Finite Depth," ASME JOURNAL OF HEAT TRANSFER, Vol. 97, No. 2, May 1975, pp. 274-281.

18 Hwang, S. S., and Pletcher, R. H., "Prediction of Buoyant Turbulent Jets and Plumes in a Cross Flow," *Proceedings of the 6th International Heat Transfer Conference*, Toronto, Canada, Aug. 1978.

19 Hirst, E., "Buoyant Jets Discharged to Quiescent Stratified Ambients," *Journal of Geophysical Research*, Vol. 76, No. 30, Oct. 1971, pp. 7375-7384.

20 Chen, C.-J., and Rodi, W., "On Decay of Vertical Buoyant Jets in Uniform Environment," *Proceedings of the 6th International Heat Transfer Conference*, Toronto, Canada, Aug. 1978.

21 Campbell, J. F., and Schetz, J. A., "Analysis of the Injection of a Heated Turbulent Jet Into a Cross Flow," NASA TR R-413, Dec. 1973.

22 Jiji, L. M., and Moghadam, S. M., "Theoretical and Experimental Investigation of Three-Dimensional Buoyant Turbulent Jets," *Proceedings of the 7th International Heat Transfer Conference*, Vol. 2, Munich, West Germany, Sept. 1982.

23 Forstal, W., and Gaylord, E. W., "Momentum and Mass Transfer in a Submerged Water Jet," *Journal of Applied Mechanics*, Vol. 22, No. 2, June 1955, pp. 161-164.

24 Sun, K.-H., and Oh, S., "A Correlation for Entrainment of Water in a Reactor Cold Leg by Coolant Injection Under Stagnant Loop Flow," ASME Paper No. 83-WA/HT-39, presented at the 1983 ASME Winter Annual Meeting, Boston, Nov. 13-18, 1983.

25 Batchelor, G. K., *An Introduction to Fluid Dynamics*, Cambridge University Press, 1967.

26 Gage, K. S., and Reid, W. H., "The Stability of Thermally Stratified Plane Poiseuille Flow," *Journal of Fluid Mechanics*, Vol. 33, Part 1, 1968, pp. 21-32.

27 Oh, S., Sursock, J.-P., and Sun, B. K.-H., "A Mixing Model for Transient Cooldown in a Reactor Cold Leg and Downcomer Under Stagnant Loop Flow," ASME Paper No. 83-HT-13, presented at the 21st ASME/AIChE National Heat Transfer Conference, Seattle, July 1983.

28 McGriff, R. W., et al., "Analysis of Fluid Mixing in the Cold Leg and Downcomer of a 3-Loop CE Plant During an MSLB Transient," NSAC-65, Electric Power Research Institute, Mar. 1984.

29 Theofanous, T. G., et al., "Decay of Buoyancy Driven Stratified Layers With Applications to Pressurized Thermal Shock (PTS)," NUREG/CR-3700, 1984.

30 Forney, L. J., "Jet Injection for Optimum Pipeline Mixing," *Encyclopedia of Fluid Mechanics*, Vol. II, Chapter 32, Gulf Publishing Co., 1985.

31 Maruyama, T., Suzuki, S., and Mizushina, T., "Pipeline Mixing Between Two Fluid Streams Meeting at a T-Junction," *International Chemical Engineering*, Vol. 21, No. 2, Apr. 1981, pp. 205-212.

32 Maruyama, T., Mizushina, T., and Watanabe, F., "Turbulent Mixing of Two Fluid Streams at an Oblique Branch," *International Chemical Engineering*, Vol. 22, No. 2, Apr. 1982, pp. 287-294.

APPENDIX

The constants appearing in the jet trajectory equations (3-10) are given here.

$$x_1 = 0.81\, l_m/\tan^2\theta$$

$$b_1 = -1.62\, l_m/\tan\theta$$

$$x_2 = (1.6/2.7)^{3/2} l_m{}^{1/4}(x_m + x_1)^{3/4} - x_m$$

$$b_2 = 1.8\, l_m{}^{1/2}(x_m + x_1)^{1/2} + b_1 - 1.6\, l_m{}^{2/3}(x_m + x_2)^{1/3}$$

$$x_3 = (1.7/1.6)^3 (l_b/l_m)^{1/2}(x_t + x_2)^2/l_m - x_t$$

$$b_3 = 1.6\, l_m{}^{2/3}(x_t + x_2)^{1/3} + b_2 - 0.85\,(l_m/l_b)^{1/6} l_b{}^{1/3}(x_t + x_3)^{2/3}$$

$$x_4 = (5.55/3.6)^4 (l_b/l_m{}^2)(x_m + x_1)^2 - x_m$$

$$b_4 = 1.8\, l_m{}^{1/2}(x_m + x_1)^{1/2} + b_1 - 1.85\, b_1{}^{1/4}(x_m + x_4)^{3/4}$$

$$x_5 = (6.8/16.65)^3 (l_m/l_b)^{1/2} l_b{}^{1/4}(x_b + x_4)^{3/4} - x_b$$

$$b_5 = 1.85\, l_b{}^{1/4}(x_b + x_4)^{3/4} + b_4 - 0.85\,(l_m/l_b)^{1/6} l_b{}^{1/3}(x_b + x_5)^{2/3}$$

Measurements and Predictions of Laminar Mixed Convection Flow Adjacent to a Vertical Surface

N. Ramachandran
Assoc. Mem. ASME

B. F. Armaly
Mem. ASME

T. S. Chen
Mem. ASME

Department of Mechanical and Aerospace Engineering,
University of Missouri—Rolla,
Rolla, MO 65401

Measurements and predictions of laminar mixed forced and free convection air flow adjacent to an isothermally heated vertical flat surface are reported. Local Nusselt numbers and the velocity and temperature distributions are presented for both the buoyancy assisting and opposing flow cases over the entire mixed convection regime, from the pure forced convection limit (buoyancy parameter $\xi = Gr_x/Re_x^2 = 0$) to the pure free convection limit ($\xi = \infty$). The measurements are in very good agreement with predictions and deviate from the pure forced and free convection regimes for buoyancy assisting flow in the region of $0.01 \le \xi \le 10$ and for opposing flow in the region of $0.01 < \xi < 0.2$. The local Nusselt number increases for buoyancy assisting flow and decreases for opposing flow with increasing value of the buoyancy parameter. The mixed convection Nusselt numbers are larger than the corresponding pure forced and pure free convection limits for buoyancy assisting flow and are smaller than these limits for opposing flow. For buoyancy assisting flow, the velocity overshoot and wall shear stress increase, whereas the temperature decreases but the temperature gradient at the wall increases as the buoyancy parameter increases. The reverse trend is observed for the opposing flow. Flow reversal near the wall was detected for the buoyancy opposing flow case at a buoyancy parameter of about $\xi = 0.20$.

Introduction

Thermal buoyancy forces play a significant role in forced convection heat transfer when the flow velocity is relatively small and the temperature difference between the surface and the free stream is relatively large. The buoyancy force modifies the flow and the temperature fields and hence the heat transfer rate from the surface.The thermal buoyancy force may be either assisting or opposing the forced flow, depending on the forced flow direction and the surface temperature relative to the free-stream temperature. Mixed convection occurs in many heat transfer devices, such as the cooling system of a nuclear power plant, large heat exchangers, and cooling of electronic equipment. Figure 1 shows a schematic of the two flow cases in which $T_w > T_\infty$ that are considered in this study.

Numerical predictions of mixed convection in laminar boundary layer flow have been reported for vertical, horizontal, and inclined flat plates [1-20]. In these studies, various solution methods, such as a perturbation series, local similarity method, local nonsimilarity method, and finite difference techniques, have been used. On the other hand, few measurements have been reported for this flow geometry [7-10]. Kliegel [7] was the first to report on the measurements of mixed convection flow along an isothermal vertical surface. He employed an interferometric method to measure the local heat transfer, but temperature and velocity distributions were not measured. Gryzagoridis [9] extended the investigation of Kliegel for buoyancy assisting air flow to higher values of the buoyancy parameter, $0 < \xi < 400$, and presented measured local velocity and temperature distributions. He employed hot-wire anemometry to measure the velocity and temperature distributions, but his measured velocities deviated significantly from the numerical predictions [4, 5] at large values of the buoyancy parameter. For example, at a buoyancy parameter of $\xi = 2.0$, the measured velocity deviated by more than 70 percent from the numerical prediction. The significant deviations between measured and predicted velocities at large buoyancy parameters have not been resolved so far.

Measurements of buoyancy opposing mixed convection air flow adjacent to a vertical isothermal surface were reported by Kliegel [7] and more recently by Hishida et al. [10]. Heat transfer data reported by Kliegel deviated significantly from numerical predictions [20] even at small values of the buoyancy parameter. For a buoyancy parameter of $\xi = 0.011$ the measured heat transfer rate deviated by about 35 percent from the numerical prediction. In the latter investigation,

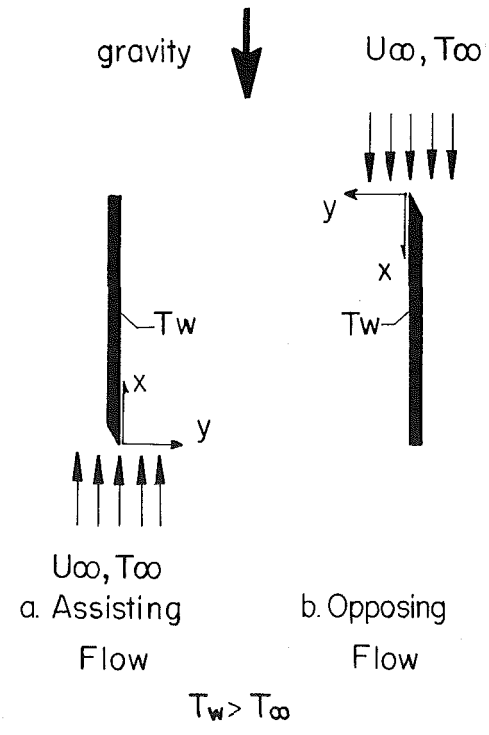

Fig. 1 Schematic of flow geometry

Contributed by the Heat Transfer Division for publication in the JOURNAL OF HEAT TRANSFER. Manuscript received by the Heat Transfer Division March 28, 1984. Paper No. 84-HT-63.

laser-doppler velocimetry was used to measure the velocity distributions, but the temperature distributions in the boundary layer were not measured. The local heat transfer was deduced from measured electric energy input to the surface by correcting for the radiation and conduction losses. Measured results agree favorably with numerical predictions at very small values of the buoyancy parameter, but deviate significantly for larger values of the buoyancy parameter. This deviation could be due to the fact that the heated plate was quite small (16×10 cm) and the air tunnel had a sudden expansion, thus possibly causing the main flow to become turbulent.

The above survey on measurements of laminar mixed convection boundary layer flow adjacent to an isothermal vertical surface clearly demonstrates that simultaneous measurements of velocity and temperature distributions are still needed for both the assisting and the opposing flow cases. This need has motivated the present study.

Experimental Apparatus and Procedure

The experimental investigation was performed in a low-turbulence, open circuit wind tunnel which could be rotated and fixed at any desired inclination angle. The tunnel has a smooth converging nozzle with a contraction ratio of 9:1, a straight test section and a smooth diverging diffuser. Plastic honeycomb material (10.00 cm thick) and several wire screens were used in the front section of the tunnel and along the nozzle length and diffuser to straighten the flow and to reduce the turbulence level in the test section. The free-stream turbulence intensity was measured to be less than 1 percent. The tunnel was constructed from 0.64-cm-thick plexiglass material with adequate frames and supports to provide a rigid structure. Variable speed fans were used at the diffuser end to provide air velocities of 0.3 to 3 m/s through the test section. A schematic of the tunnel is shown in Fig. 2. The test section of the tunnel was instrumented with a hot-wire anemometer system for velocity and temperature measurements. Small channels were machined in the upper side of the test section (instrumented side) to permit passage and movement of the hot-wire probe and its support to any desired location within the test section via a traverse mechanism. During measurements at a selected location, these channels were sealed to provide a smooth upper surface in the test section. The normal motion of the probe (relative to the plane of the heated surface) was controlled by a stepper motor and by a sweep drive unit capable of moving the probe to within 0.02 mm of a desired location. The movement of the probe along the other two directions (along the plate length and across its width) was manually controlled by a lead screw to an accuracy level of 1 mm. This traversing capability was utilized to scan through the boundary layer and throughout the flow domain over the heated surface.

The heated plate consists of four layers which are held together by screws and instrumented to provide an isothermal heated test surface. The upper layer (test surface) is an aluminum plate (30×104 cm and 1.58 cm thick) instrumented with 13 copper-constantan thermocouples. Each thermocouple is inserted into a small hole on the back of the plate and its measuring junction is about 0.3 cm below the testing surface. The middle two layers consist of six heater pads which are backed by a 0.64-cm-thick insulation tiles. The power input to each of the six heating pads is controlled by individual rheostats to maintain a uniform temperature over the entire length of the heated test surface. An aluminum plate, 0.64 cm thick, serves as the bottom layer and as a backing and support to keep the four-layer structure together. The plate assembly is placed in the test section of the wind tunnel and is fastened by screws to the side walls through the backing plate. The rotating tunnel could be placed vertically in either the buoyancy assisting or buoyancy opposing flow condition. Flow visualization, by smoke, indicated the presence of a laminar boundary layer flow adjacent to the vertical plate. The two dimensionality of the flow/thermal field was also verified by measurements. The heated plate could be maintained at a uniform and constant temperature to within 0.1°C by controlling the voltage across the individual heaters. It took approximately 4 hr to reach a steady-state operating condition, and measurements were performed at the center of the test section width.

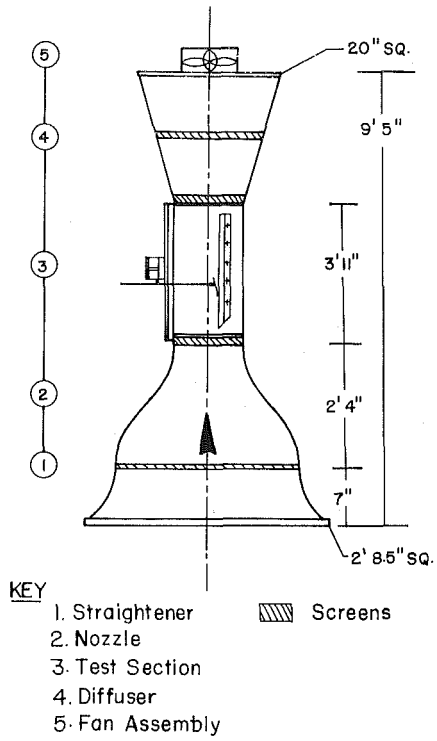

Fig. 2 Schematic of the vertical air tunnel

Nomenclature

C_f = local friction factor
F = reduced stream function, equation (6)
g = gravitational acceleration
Gr_x = $g\beta(T_w - T_\infty)x^3/\nu^2$, local Grashof number
k = thermal conductivity
Nu_x = $q_w x/(T_w - T_\infty)k$, local Nusselt number
Pr = Prandtl number
Re_x = $u_\infty x/\nu$, Reynolds number
T = fluid temperature
T_w = wall temperature
T_∞ = free-stream temperature
u = axial velocity component
u_∞ = free-stream velocity
x = axial coordinate
y = transverse coordinate
α = thermal diffusivity
β = coefficient of thermal expansion
η = pseudo-similarity variable, equation (5)
θ = $(T - T_\infty)/(T_w - T_\infty)$, dimensionless temperature, equation (6)
μ = dynamic viscosity
ν = kinematic viscosity
ξ = $\mathrm{Gr}_x/\mathrm{Re}_x^2$, buoyancy parameter
τ_w = wall shear stress
ψ = stream function, equation (6)

Superscripts

$'$ = denotes partial derivative with respect to η

Velocity and temperature measurements were made by a single DISA boundary-layer probe using the appropriate control bridge (constant resistance and constant current) in the hot-wire anemometer (DISA 55M system). Data acquisition and reduction were performed on a PDP 11/23 computer. The probe was calibrated for the range of velocities and temperatures encountered in the experiment. These calibrations were checked periodically and were repeated if any deviations were detected. The method proposed by Freymuth [21] to interpret hot-wire anemometer output in a thermally stratified flow was used in this study to analyze the output of the hot-wire anemometer during velocity measurements. Additional details regarding this method can be found in [22]. Velocity and temperature profiles were measured for several free-stream velocities and plate temperatures. They were done for both buoyancy assisting and opposing flows and covered wide ranges of the buoyancy parameter.

The uncertainty associated with temperature measurements was determined to be 0.1°C and with velocity measurements was 8 percent for low velocity (0 ~ 0.5 m/sec) and 2 percent for higher velocities.

Numerical Analysis

The problem of laminar mixed convection flow over a heated, isothermal, semi-infinite vertical flat plate has been studied by many investigators [3-11]. The governing conservation equations are given by

$$\frac{\partial u}{\partial x} + \frac{\partial v}{\partial y} = 0 \tag{1}$$

$$u\frac{\partial u}{\partial x} + v\frac{\partial u}{\partial y} = \pm g\beta(T - T_\infty) + \nu\frac{\partial^2 u}{\partial y^2} \tag{2}$$

$$u\frac{\partial T}{\partial x} + v\frac{\partial T}{\partial y} = \alpha\frac{\partial^2 T}{\partial y^2} \tag{3}$$

The boundary conditions for equations (1-3) are

$$u = v = 0;\ T = T_W \text{ at } y = 0$$
$$u \to u_\infty;\ T \to T_\infty \text{ as } y \to \infty \tag{4}$$

The first term on the right-hand side of equation (2) represents the influence of buoyancy, with the plus and minus signs pertaining to thermal buoyancy force assisting and opposing situations, respectively, when $T_w > T_\infty$.

To facilitate the solution of the above set of equations over the regime of mixed forced and free convection, these equations are transformed from the (x, y) coordinates to the $(\xi(x), \eta(x, y))$ coordinates by introducing

$$\xi = \mathrm{Gr}_x/\mathrm{Re}_x^2;\ \eta = y(u_\infty/\nu x)^{1/2} \tag{5}$$

In addition, a reduced stream function $F(\xi,\eta)$ and a dimensionless temperature $\theta(\xi,\eta)$ are defined, respectively, as

$$F(\xi,\eta) = \psi(x,y)/(\nu u_\infty x)^{1/2}$$
$$\theta(\xi,\eta) = (T - T_\infty)/(T_w - T_\infty) \tag{6}$$

where $\psi(x,y)$ is the stream function that satisfies the continuity equation (1). The transformed system of equations is

$$F''' + \frac{1}{2}FF'' \pm \xi\theta = \xi\left(F'\frac{\partial F'}{\partial \xi} - F''\frac{\partial F}{\partial \xi}\right) \tag{7}$$

$$\frac{1}{\mathrm{Pr}}\theta'' + \frac{1}{2}F\theta' = \xi\left(F'\frac{\partial \theta}{\partial \xi} - \theta'\frac{\partial F}{\partial \xi}\right) \tag{8}$$

$$F'(\xi,0) = F(\xi,0) = 0;\ \theta(\xi,0) = 1$$
$$F'(\xi,\infty) = 1;\ \theta(\xi,\infty) = 0 \tag{9}$$

In the foregoing equations, the primes denote partial differentiation with respect to η.

The primary physical quantities of interest are the local

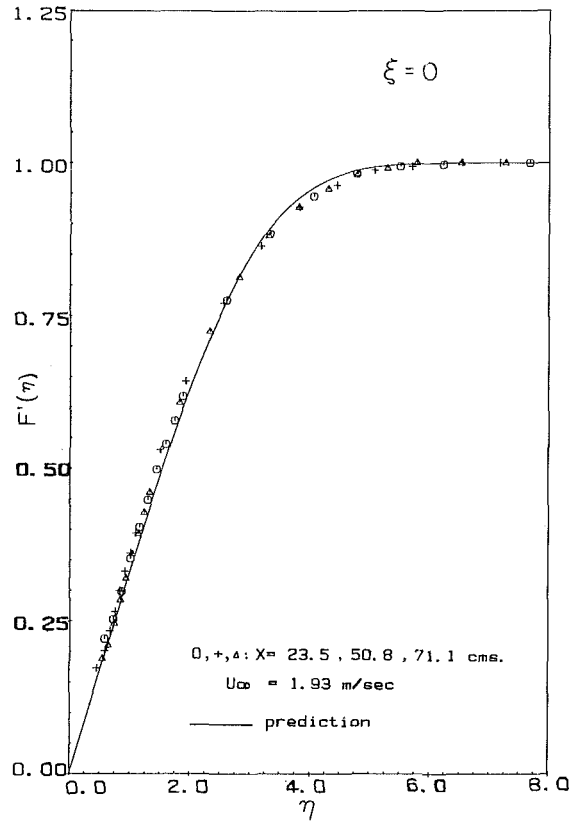

Fig. 3 Velocity distribution, forced convection limit

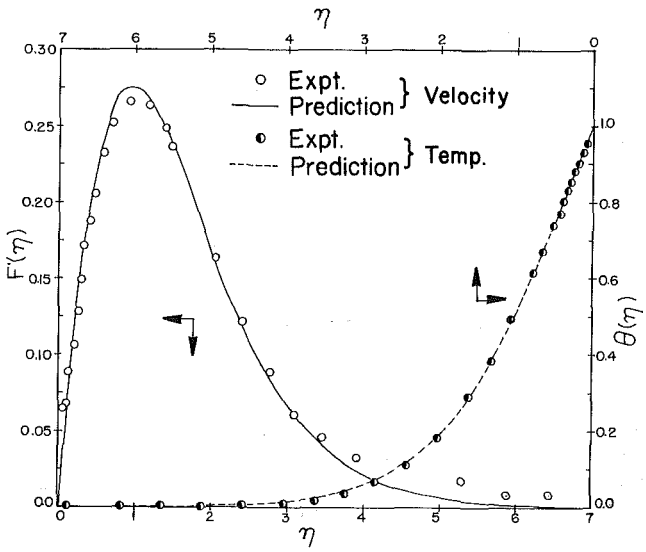

Fig. 4 Velocity and temperature distributions, free convection limit

Nusselt number Nu_x, the local friction factor C_f, the velocity distribution $u/u_\infty = F'(\xi,\eta)$, and the temperature distribution $\theta(\xi,\eta)$. The first two quantities can be expressed, respectively, by

$$\mathrm{Nu}_x\mathrm{Re}_x^{-1/2} = -\theta'(\xi,0);\ C_f\mathrm{Re}_x^{1/2} = 2F''(\xi,0) \tag{10}$$

Local similarity and local nonsimilarity solution techniques have been employed in earlier investigations [4, 23] of the same problem. In the present investigation the governing equations were solved by a finite difference solution scheme which is a modified version of that developed by Keller and Cebeci [24, 25]. The use of this solution scheme, which has been successfully employed in [19], provided a more accurate solution for a wider range of buoyancy parameters.

For low buoyancy parameters the three solution methods

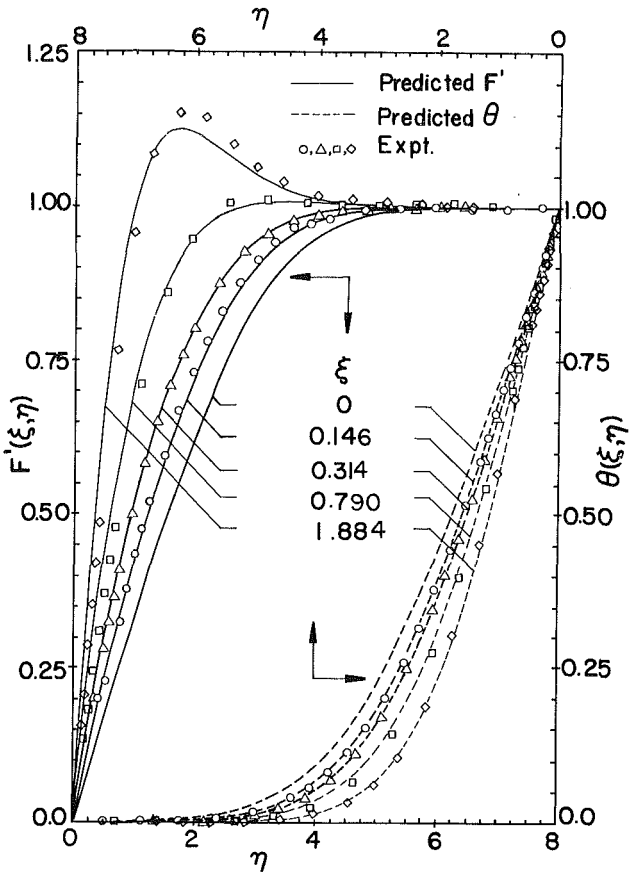

Fig. 5 Velocity and temperature distributions for buoyancy assisting case

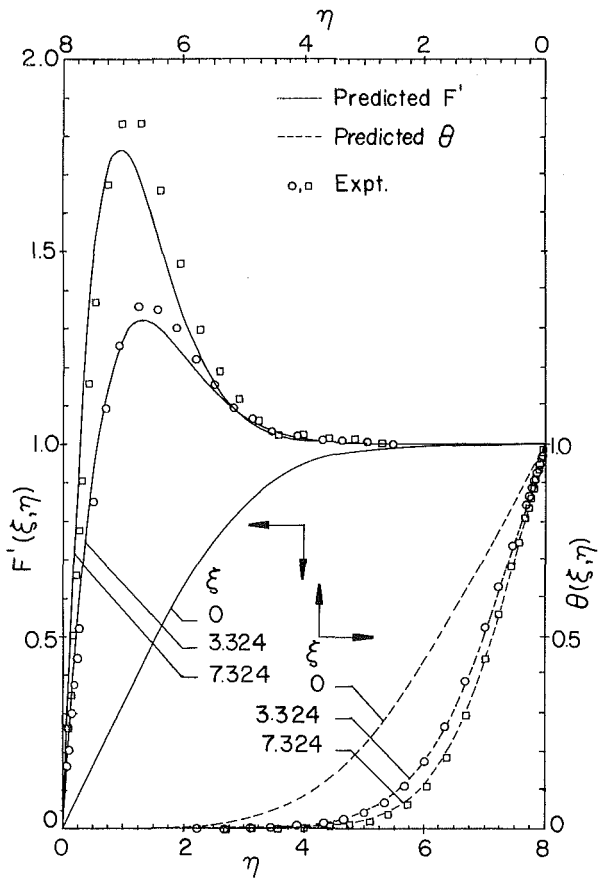

Fig. 6 Velocity and temperature distributions for buoyancy assisting case

provide identical results, but as the buoyancy parameter increases deviations occur. For example, at a buoyancy parameter of unity, $\xi = 1$, $F''(\xi,0)$ deviates from the local similarity value by 12.6 percent when using a local non-similarity method and by 15.7 percent when using a finite difference method. Under the same conditions, $\theta'(\xi,0)$ deviates only by 2.2 percent and by 1.7 percent, respectively. Numerical solutions were carried out for the same values of the buoyancy parameter ξ as those obtained during the experiment, thus eliminating the need of any interpolations. The Prandtl number used in the computations was 0.70.

Results and Discussion

To test the operation of the wind tunnel and its instrumentation, the pure forced and the pure free convection cases were measured. The measured and the predicted values are compared for pure forced convection, $\xi = 0$, in Fig. 3. Similarly, the measured and predicted [26] values for the pure free convection case, $\xi = \infty$, are compared in Fig. 4. It is evident from these two figures that the measurements are in very good agreement with predictions, thus validating the performance of the wind tunnel and its instrumentation.

The velocity and temperature distributions for the buoyancy assisting case were measured for buoyancy parameter ξ in the range of $0 < \xi < 16$. The highest value of the buoyancy parameter was limited by the maximum, safely attainable plate temperature of 95°C and the lowest velocity of 0.3 m/s. For this case of buoyancy assisting flow, the air tunnel was placed in the vertical direction, with air suction from the top and the leading edge of the plate facing down. Representative velocity and temperature profiles for the assisting flow case are shown in Figs. 5–7. In all these figures, the solid and the dashed lines represent, respectively, the predicted velocity and temperature distributions from the numerical solution of equations (7–9) for the indicated value

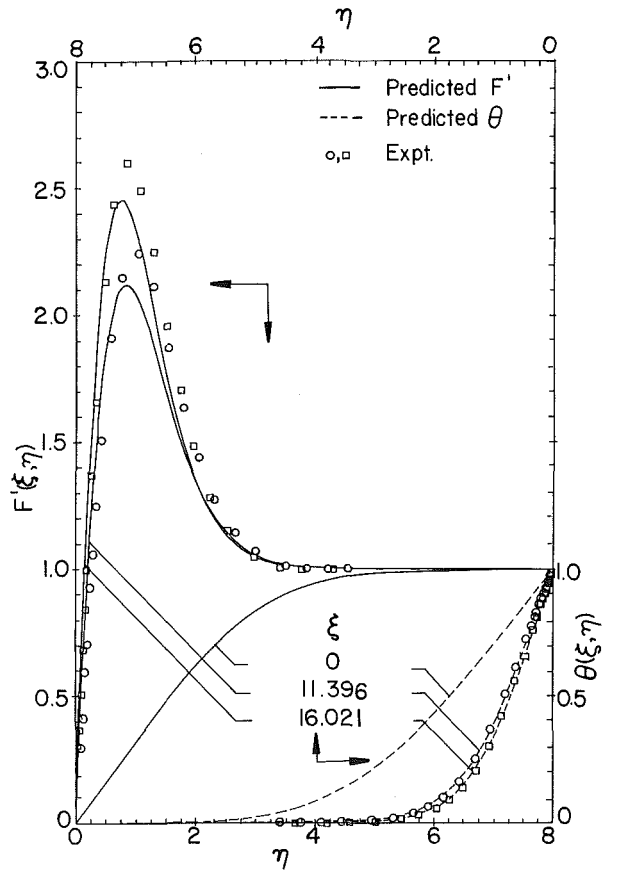

Fig. 7 Velocity and temperature distributions for buoyancy assisting case

of the buoyancy parameter. The predicted velocity and temperature distributions for pure forced convection ($\xi = 0$) are presented in each figure for comparison. Measured velocity and temperature data were reduced and transformed into the ξ, η coordinate system for comparison with the predicted values. Fluid properties were evaluated at the film temperature $T_f = (T_W + T_\infty)/2$. These figures demonstrate that measured velocity and temperature distributions are in very good agreement with the predictions. The agreement between the measured and the predicted temperature distributions is better than that for the velocity distributions. The velocity field is seen to be more sensitive to changes in the value of the buoyancy parameter than the temperature field and this sensitivity increases as the buoyancy parameter increases. It can be seen from these figures that as the buoyancy parameter increases, both the velocity and temperature boundary layer thicknesses decrease and the velocity and temperature gradients at the wall increase, causing an increase in both the local wall shear stress and the local surface heat transfer rate. It is also evident that the measured velocity distributions show a slightly higher overshoot than the predictions. For example, at a buoyancy parameter of $\xi = 16.021$ the experimental results deviate by 6.12 percent from the predicted values.

The vertical air tunnel which was used to study the buoyancy assisting mixed convection flow was rotated 180 deg in order to examine the buoyancy opposing flow case. For this case the suction fan was at the bottom of the tunnel and the leading edge of the plate was pointing upward toward the inlet section of the tunnel. Measurements in this case were limited to a buoyancy parameter range of $0 \le \xi \le 0.2$, because flow reversal occurs when $\xi > 0.2$. The hot-wire anemometer is not sensitive to the flow direction and thus could not be used to measure the flow reversal in such a region. In fact, the governing equations for this case also failed to yield converged numerical solutions for values of buoyancy parameter larger than $\xi = 0.18$, because the model cannot be used in regions where flow reversal occurs. Flow visualization by smoke injections confirmed the existence of a reversed flow region at a buoyancy parameter of 0.20. Measured velocity and temperature distributions for the opposing flow case are presented in Fig. 8. In that figure the solid and the dashed lines represent, respectively, the velocity and temperature distribution predicted by the numerical solution of equations (7-9) for the indicated value of the buoyancy parameter. Measured velocities and temperatures are seen to be in reasonable agreement with the predicted values (within 10 percent), but this agreement is not as good as the one reported for the buoyancy assisting flow case. As the buoyancy parameter increases, the velocity and temperature gradients at the wall decrease, causing a decrease in both the local wall shear stress and the local surface heat transfer rate. The measured results for a buoyancy parameter of 0.208 are presented in Fig. 8 and they clearly demonstrate the existence of a separated region near the wall. Predicted results are not presented for this value because a converged solution could not be obtained beyond a value of $\xi = 0.18$. The data reported by Kliegel [7] indicate flow separation at about $\xi = 0.2$ which agrees with the present findings. Hishida et al. [10] observed a similar behavior in their experimental study of this geometry, but they concluded that a laminar boundary layer existed up to a buoyancy parameter value of $\xi = 0.25$, which seems to be higher than the present findings. At this time it is not clear to the authors how Hishida et al. [10] were able to predict the reversed flow via the normal parabolic governing equations.

The measured temperature distribution was used to determine the temperature gradient at the wall which was in turn utilized to determine the local Nusselt number. The uncertainty associated with determining the temperature gradient at the wall and consequently the Nusselt number was

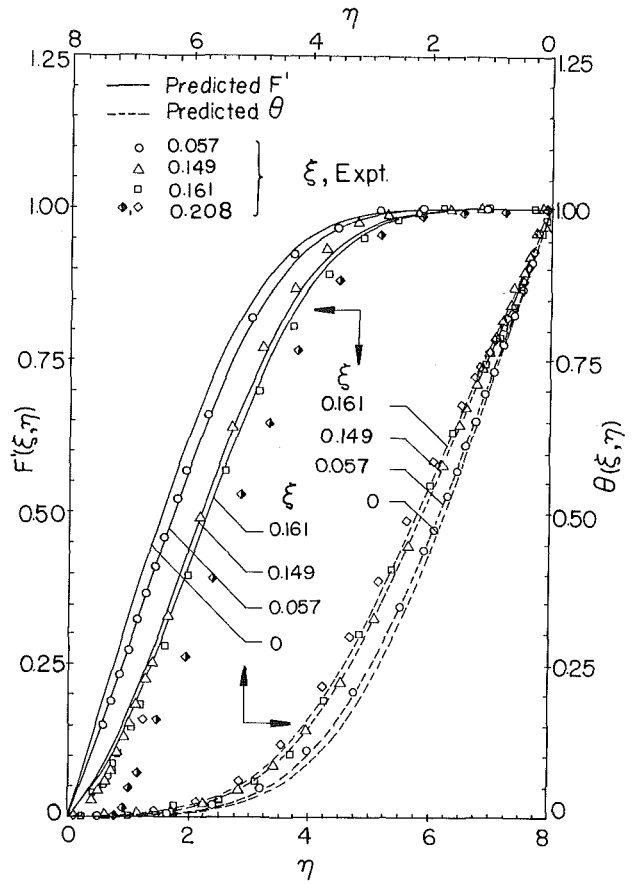

Fig. 8 Velocity and temperature distributions for buoyancy opposing case

determined to be less than 5 percent. The variation of the deduced Nusselt number as a function of the buoyancy parameter is presented in Fig. 9. A sample of data reported by Kliegel [7] is also presented for comparison. As can be seen from the figure, the agreement between the experimental and the predicted local Nusselt numbers is very good for both the present study and that of Kliegel [7]. For buoyancy assisting flow, the mixed forced and free convection results asymptotically approach the pure forced ($\xi = 0$) and the pure free ($\xi = \infty$) convection limits, and the mixed convection Nusselt numbers are higher than the equivalent pure forced or pure free convection flow. An increase in the buoyancy parameter results in a higher velocity overshoot, a steeper temperature gradient at the wall and hence a higher Nusselt number. As pointed out in [4, 9], the regime of mixed convection is represented by the buoyancy parameter range of $0.10 \le \xi \le 3.0$ when based on a 5 percent departure from pure forced and pure free convection results. However, the actual deviations from the pure convection results occur in the region of $0.01 \le \xi \le 10$, as can be seen from Fig. 9. The local Nusselt numbers can be 25 percent higher than the corresponding pure forced or pure free convection values in this region of buoyancy assisting flow. The local Nusselt number variation with the buoyancy parameter for the buoyancy opposing flow case is also shown in Fig. 9, along with the numerically predicted values. Good agreement (better than 10 percent) is seen between the experimental and the predicted values. The reported results by Kliegel [7] for these conditions deviate significantly, 35 percent, from the predicted values. As the buoyancy parameter increases, the heat transfer decreases gradually and then rapidly in the vicinity of $\xi = 0.20$, when flow reversal starts to occur. In that region the mixed convection Nusselt number deviates by more than 40 percent from the pure forced convection value. For the buoyancy opposing flow case, the mixed convection Nusselt numbers

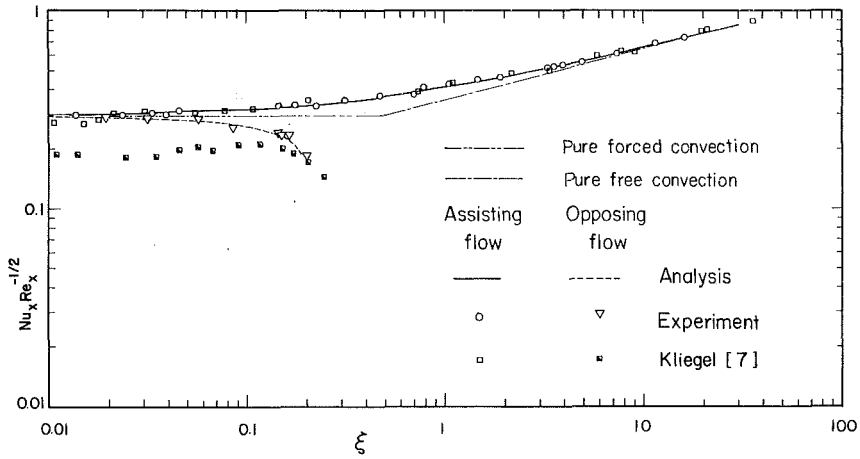

Fig. 9 Measured and predicted mixed convection regime

are lower than the corresponding pure forced convective values.

Conclusions

In the present study, representative velocity and temperature distributions were measured and local Nusselt numbers obtained for laminar mixed convection flow of air adjacent to a heated, isothermal vertical plate for both the buoyancy assisting and the buoyancy opposing flow cases. Measurements were also conducted for pure forced convection and pure free convection from this geometry, and these measurements represent the two limiting cases of the mixed convection regime. A comparison between the measured and the predicted temperature and velocity profiles reveals a very good agreement between the two, with a maximum velocity deviation of less than 6.2 percent. The local Nusselt number has been found to increase with increasing buoyancy parameter for the buoyancy assisting flow and to decrease for the buoyancy opposing flow. The mixed convection Nusselt numbers are always higher for buoyancy assisting flow (with deviations of 25 percent) and are lower for buoyancy opposing flow (with deviations of 40 percent) than the corresponding values for pure forced or pure free convection. The velocity distributions for the buoyancy assisting flow exhibit a significant overshoot above the free-stream value. In addition, the velocity field has been found to be more sensitive to the buoyancy effect than the temperature field. The mixed convection domain, defined as the region where the Nusselt numbers resulting from mixed convection calculations deviate by more than 5 percent from either the pure forced or the pure free convection values, is given by $0.1 \leq \xi \leq 3.0$ for the assisting flow case. A very good agreement between the measured and the predicted results has been obtained for both the assisting and opposing flow cases.

Acknowledgments

This study was supported in part by grants from the National Science Foundation (NSF MEA 83-00785 and NSF MEA 81-11673).

References

1 Sparrow, E. M., and Gregg, J. L., "Buoyancy Effects in Forced-Convection Flow and Heat Transfer," ASME *Journal of Applied Mechanics*, Vol. 81, 1959, pp. 133-134.

2 Szewczyk, A. A., "Combined Forced and Free Convection Laminar Flow," ASME JOURNAL OF HEAT TRANSFER, Vol. 86, 1964, pp. 501-507.

3 Merkin, J. H., "The Effect of Buoyancy Forces on the Boundary-Layer Flow Over a Semi-Infinite Vertical Flat Plate in a Uniform Free Stream," *Journal of Fluid Mechanics*, Vol. 35, 1969, pp. 439-450.

4 Lloyd, J. R., and Sparrow, E. M., "Combined Forced and Free Convection Flow on Vertical Surfaces," *International Journal of Heat and Mass Transfer*, Vol. 13, 1970, pp. 434-438.

5 Oosthuizen, P. H., and Hart, R., "A Numerical Study of Laminar Combined Convective Flow Over Flat Plates," ASME JOURNAL OF HEAT TRANSFER, Vol. 95, 1973, pp. 60-63.

6 Wilks, G., "Combined Forced and Free Convection Flow on Vertical Surfaces," *International Journal of Heat and Mass Transfer*, Vol. 16, 1973, pp. 1958-1964.

7 Kliegel, J. R., "Laminar Free and Forced Convection Heat Transfer from a Vertical Flat Plate," Ph.D. Thesis, University of California, Berkeley, 1959.

9 Babezha, A. V., Gimbutis, G. I., and Shvenchyanas, P. P., "Heat Transfer at a Vertical Flat Surface with the Combined Effect of Forced and Free Convection in the Same Direction," *Institute of Chemical Engineering*, Vol. 21, No. 1, 1981, pp. 135-138.

9 Gryzagoridis, J., "Combined Free and Forced Convection from an Isothermal Vertical Plate," *International Journal of Heat and Mass Transfer*, Vol. 18, 1975, pp. 911-916.

10 Hishida, K., Yoshida, A., and Maeda, M., "Buoyancy Effects on Boundary Layer Flow and Forced Convective Heat Transfer Over a Vertical Isothermally Heated Plate," Presented at the ASME-JSME Thermal Engineering Joint Conference, Honolulu, Hawaii, March 20-24, 1983, Vol. 3, pp. 163-168.

11 Sparrow, E. M., and Minkowycz, W. J., "Buoyancy Effects on Horizontal Boundary-Layer Flow and Heat Transfer," *International Journal of Heat and Mass Transfer*, Vol. 5, 1962, pp. 505-511.

12 Mori, Y., "Buoyancy Effects in Forced Laminar Convection Flow Over a Horizontal Flat Plate," ASME JOURNAL OF HEAT TRANSFER, Vol. 83, 1961, pp. 479-482.

13 Hauptmann, E. G., "Laminar Boundary-Layer Flows With Small Buoyancy Effects," *International Journal of Heat and Mass Transfer*, Vol. 8, 1965, pp. 289-295.

14 Redekopp, L. G., and Charwat, A. F., "Role of Buoyancy and the Boussinesq Approximation in Horizontal Boundary Layers," *Journal of Hydronautics*, Vol. 6, 1972, pp. 34-39.

15 Leal, L. G., "Combined Forced and Free Convection Heat Transfer from a Horizontal Flat Plate," *Journal of Applied Mechanics and Physics (ZAMP)*, Vol. 24, 1973, pp. 20-42.

16 Hieber, C. A., " Mixed Convection Above a Heated Horizontal Surface," *International Journal of Heat and Mass Transfer*, Vol. 16, 1973, pp. 769-785.

17 Robertson, G. E., Seinfeld, J. H., and Leal, G. E., "Combined Forced and Free Convection Flow Past a Horizontal Flat Plate," *AIChE Journal*, Vol. 19, 1973, pp. 998-1008.

18 Chen, T. S., Sparrow, E. M., and Mucoglu, A., "Mixed Convection in Boundary Layer Flows on a Horizontal Plate," ASME JOURNAL OF HEAT TRANSFER, Vol. 99, 1977, pp. 66-71.

19 Mucoglu, A., and Chen, T. S., " Mixed Convection on Inclined Surfaces," ASME JOURNAL OF HEAT TRANSFER, Vol. 101, 1979, pp. 422-426.

20 Moutsoglou, A., Tzuoo, S. K. L., and Chen, T. S., "Mixed Convection in Boundary Layer Flows Over Inclined Surfaces," *AIAA 15th Thermophysics Conference*, Snowmass, Colorado, July 14-16, 1980, Paper No. AIAA-80-1525.

21 Freymuth, P., "Hot-Wire Anemometer Thermal Calibration Errors," *Instruments and Control Systems*, Oct. 1970, pp. 82-83.

22 Ramachandran, N., "Measurements and Predictions of Laminar Mixed Convection from Flat Surfaces," M. S. Thesis, University of Missouri, Rolla, 1983.

23 Chen, T. S., and Mucoglu, A., "Buoyancy Effects on Forced Convection Along a Vertical Cylinder," ASME JOURNAL OF HEAT TRANSFER, Vol. 97, 1975, pp. 198-203.

24 Keller, H. B., and Cebeci, T., "Accurate Numerical Methods for Boundary Layer Flows. I: Two-Dimensional Laminar Flows," *Proceedings of 2nd International Conference on Numerical Methods in Fluid Dynamics*, Springer-Verlag, Berlin, 1971.

25 Keller, H. B., and Cebeci, T., "Accurate Numerical Methods for Boundary Layer Flows. II: Two-Dimensional Turbulent Flows," *AIAA Journal*, Vol. 10, 1972, pp. 1193-1199.

26 Ostrach, S., "An Analysis of Laminar Natural Convection Flow and Heat Transfer About a Flat Plate Parallel to the Direction of the Generating Body Forces," NACA TN 2635, 1952.

An Experimental Investigation of Heat Transfer in Variable Porosity Media

K. Vafai
The Ohio State University,
Columbus, OH
Mem. ASME

R. L. Alkire
Owens-Corning Fiberglas,
Granville, OH

C. L. Tien
University of California,
Berkeley, CA
Fellow ASME

This paper presents an experimental investigation on the effects of a solid impermeable boundary and variable porosity on forced convection in porous media. Emphasis is placed on the channeling effects on heat transfer in packed beds. The local volume-averaging technique is used to establish the governing equations and a numerical scheme is developed which incorporates the boundary and variable porosity effects on heat transfer. The experimental results for the heat flux at the boundary are presented as a function of the pertinent variables in a packed bed. The Nusselt number is found to increase almost linearly with an increase in the Reynolds number based on the pore diameter. The experimental results are found to be in good agreement with the theoretical results which account for the variable porosity effects. A comparison between the numerical and the experimental results demonstrates the importance of boundary and variable porosity effects on heat transfer in variable porosity media.

1 Introduction

Heat transfer in porous media has been the subject of numerous investigations due to increasing interest in chemical catalytic reactors, building thermal insulation, heat exchangers, petroleum reservoirs, geothermal operations, packed-sphere beds, and many others. This increased use of porous media has made it essential to have a better understanding of the associated transport processes. Most of the existing studies such as Burns and Tien [1] deal primarily with the mathematical simplification based on Darcy's law which neglects the effects of a solid boundary, inertial forces, and variable porosity on flow through porous media. In many applications, for example, packed-bed catalytic reactors, the porous medium is bounded, the fluid velocity is high, and the porosity is variable; therefore, it is important to investigate these boundary, inertia, and variable porosity effects. The boundary and inertia effects on convective flow and heat transfer were analyzed by Vafai and Tien [2] for constant porosity media and expressed in terms of several governing parameters. These effects were further investigated by an experiment [3] for transient mass transfer through constant porosity media. In some applications, such as fixed-bed catalytic reactors, packed bed heat exchangers, drying, chemical reaction engineering and metal processing, the constant porosity assumption does not hold because of the influence of an impermeable boundary. Therefore, there is a need to focus on the variable porosity effects on forced convection in the vicinity of an impermeable boundary. The region close to an external boundary is of particular importance since for most applications the quantities of interest, such as the heat flux at the boundary, are closely involved in that region.

The variable porosity close to an impermeable boundary leads to a number of important effects such as flow maldistribution and channeling. Channeling, which refers to the occurrence of a maximum velocity in a region close to an external boundary, has been reported by a number of investigators such as Schwartz and Smith [4], and Schertz and Bischoff [5]. Their velocity measurements in packed beds show a maximum close to the boundary. Furthermore, the measurements of Benenati and Brosilow [6] show a distinct porosity variation in packed beds. Their results show a high porosity region close to the external boundary. The porosity as a function of the distance from the boundary can be obtained from these measurements. Chandrasekhara and Vortmeyer [7] used these measurements to solve numerically for the velocity profile in isothermal packed beds.

Most of the heat transfer investigations in packed beds such as Denloye and Botterill [8], and Schlunder [9] are presented in terms of correlations based on Colburn-Chilton j-factors. These correlations express the heat transfer from bulk of the packed bed; the effects of boundary and variable porosity on the heat transfer are seldom, if ever, discussed.

This paper starts with general governing equations presented in [2] and applies them to a common case of variable porosity media, namely packed beds. The effects of variable porosity and higher velocities on forced convection in a region close to an external boundary will be investigated experimentally. The experimental setup, which is described in detail later on, will be used to measure the total heat flux at the boundary for forced convective flow through variable porosity media. This is then compared with the total heat flux obtained from the numerical solution of the theoretical model.

The end result of the experimentation and the numerical results is to show the effects of an external boundary and variable porosity on heat transfer for flow through a variable porosity media. The experimental results are shown to be in good agreement with the theoretical results which account for the variable porosity effects.

2 Governing Equations

To illustrate the important effects of variable porosity and the momentum boundary layer on heat transfer close to an impermeable boundary, an analysis is made for an incompressible, two-dimensional flow through a variable porosity medium confined by an external boundary, as shown in Fig. 1. The developments for momentum and the energy equations are quite different. In developing the momentum equation only the fluid phase is involved, while for the energy equation both the solid as well as the fluid phases have to be considered. The developments of these equations are discussed in detail in Vafai and Tien [2] and Whitaker [10]. The two-dimensional boundary layer equations for forced convection through variable porosity media were derived to be [11]

Contributed by the Heat Transfer Division for publication in the JOURNAL OF HEAT TRANSFER. Manuscript received by the Heat Transfer Division March 26, 1984.

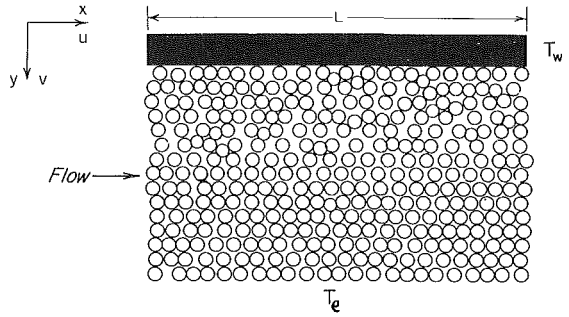

Fig. 1 Flow through a variable porosity medium confined by an external boundary

$$\frac{\mu_f}{\delta}\frac{d^2<u>}{dy^2} - \frac{\mu_f}{K}<u> - \rho_f F\sqrt{\delta}\gamma<u>^2 - \frac{d<P>^f}{dx} = 0 \quad (1)$$

$$<u>\frac{\partial<T>}{\partial x} = \frac{\alpha_e}{\delta}\frac{\partial^2<T>}{\partial y^2} \quad (2)$$

where

$$\gamma = \sqrt{\frac{\delta}{K}} \quad <P>^f = \frac{1}{V_f}\int_{V_f} P\,dV \quad \alpha_e = \frac{k_e}{\rho_f c_f} \quad (3)$$

μ_f is the fluid viscosity, δ the porosity, $\mathbf{V}$ the velocity vector, K the permeability, ρ_f the fluid density, c_f the fluid heat capacity, F an empirical function which depends primarily on the microstructure of the porous medium, T the temperature, $<P>^f$ the intrinsic phase average of the pressure, as described in Whitaker [10], and k_e the effective thermal conductivity of the saturated porous medium. The concept of k_e has been widely used and studied [12]. In the above equations the $\mu_f<u>/K$ term is the viscous force caused by the micropore structure and the symbol $<\phi>$ refers to the local volume average of a quantity associated with the fluid and is defined as in Whitaker [10]:

$$<\phi> = \frac{1}{V}\int_{V_f}\phi\,dV \quad (4)$$

Furthermore it has been shown in [2] that the boundary layer growth is significant only over a length of the order of $(K/\nu_f)u_c$. This shows that the entrance length, for almost all practical cases and certainly for packed beads, is very small and negligible.

The functional dependence of the porosity on the distance from the boundary can be found from the experimental results of Benenati and Brosilow [6]. These results can be represented very well by an exponential function of the following form:

$$\delta = \delta_e[1 + b\exp(-c\,y/d_p)] \quad (5)$$

This result neglects the small oscillations of the porosity which are considered to be secondary. The emphasis here is on the decay of the porosity from the external surface which has the primary effect. The empirical constants b and c are dependent on the ratio of the bed to particle diameter. The particle diameters used in the experimental study were 5 and 8 mm. These correspond to experimental bed to particle diameter ratios of 10 and 6.25 respectively. From the results of Benenati and Brosilow [6] the porosity variation as a function of y/d_p is found to be almost identical for these bed to particle diameter ratios. The constants chosen to represent the porosity variation were $b = 1$; $c = 2$ for the 5 mm beads and $b = 0.9$ for the 8 mm beads. These are similar to the constants used by Chandrasekhara and Vortmeyer [7].

3 Experimental Apparatus and Procedures

The apparatus employed to study the variable porosity effects on convective heat transfer through porous media is depicted schematically in Fig. 2. The setup is designed to provide accurate flow and heat flux measurements. The purpose of the experiment is to obtain the total heat flux at the boundary for forced convective flow through the test section filled with a porous medium. This is then compared with the total heat flux obtained from the numerical solution of a theoretical model.

The experimental apparatus is constructed of acrylic plastic which is 1.27 cm thick. The test section has approximate dimensions of 30 × 20 × 5 cm (length, width, height respectively). The porous medium is located inside the test section. The upper portion of the test section is removable so that the porous medium can be easily placed in the test section. The test section is filled with uniform size beads. The beads were poured randomly inside the section using a beaker until the test section was filled. The beads used in this experiment were 5 and 8 mm and made of different compositions. This type of packed-sphere bed arrangement is used extensively in industrial applications such as chemical reactors, heat exchangers, fluid filters, and many others. Two stainless steel screens are placed on either side of the test section to hold the beads in place. Two pressure taps are located on the bottom of the test section in order to measure the pressure drop across the porous media. An inclined

Nomenclature

c_f = fluid's heat capacity (Ws/kg K)
d_p = particle diameter (m)
K = permeability of the porous medium (m^2)
K_e = free-stream permeability (m^2)
k_e = effective thermal conductivity (W/m K)
L = horizontal extent of the external boundary (m)
Nu = Nusselt number defined in equation (18)
$\overline{\text{Nu}}$ = average Nusselt number defined in equation (19)
Pr_e = effective Prandtl number, ν_f/α_e
Re_p = Reynolds number based on pore diameter, $u_c d_p/\nu_f$
T = temperature (K)
T_e = free-stream temperature (K)
T_w = external boundary temperature (K)
u = x-component velocity (m/s)
u_c = convective velocity, $-(K_e/\mu_f)\frac{d<P>^f}{dx}$ (m/s)
x = spatial coordinate, horizontal (m)
y = spatial coordinate, vertical (m)
α_e = effective thermal diffusivity, $k_e/\rho_f c_f$ (m^2/s)
γ = porous media shape parameter, $\sqrt{\delta/K}$ (m^{-1})
γ_e = free-stream shape parameter, $\sqrt{\delta_e/K_e}$ (m^{-1})
δ = porosity of the porous medium
δ_e = free-stream porosity
η = dimensionless vertical length scale, $y\gamma_e/\xi^{1/2}$
θ = dimensionless temperature, $(T-T_w)/(T_e-T_w)$
μ_f = fluid's dynamic viscosity (kg/ms)
ν_f = fluid's kinematic viscosity (m^2/s)
ξ = dimensionless horizontal length scale, x/l
ρ_f = fluid's density (kg/m^3)

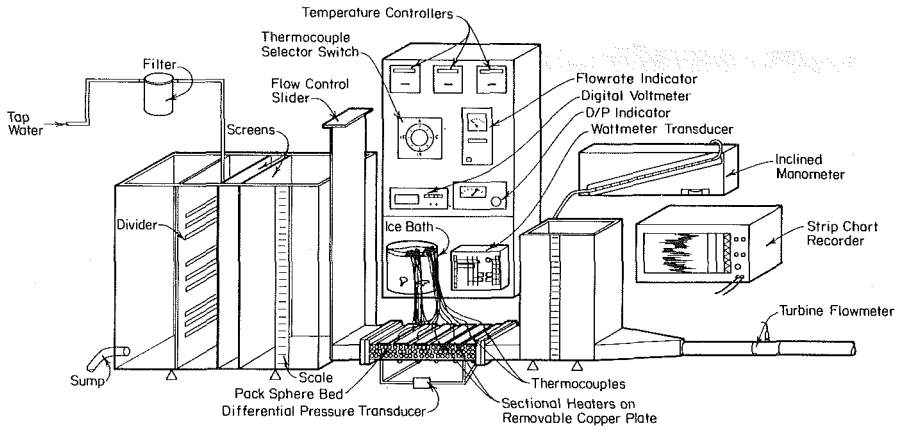

Fig. 2 Schematic diagram of the experimental apparatus

manometer and a differential pressure transducer are connected by a "T" at each of these taps. The inclined manometer was designed and set up to give increased accuracy when reading very small differential pressures of up to 1200 N/m^2 with an accuracy of + 0.5 percent of the full scale. The differential pressure transducer could measure a differential pressure of 6900 N/m^2 with + 1 percent full-scale accuracy.

The upper part of the test section is heated with sectional heaters. The upper boundary is used in place of the lower boundary in order to eliminate natural convection. The top of the test section is constructed of a copper plate 1.6 cm thick to achieve both uniform temperature and strength. Six Chromolox strip heaters are clamped down the length of the copper plate in three sets of two, each 1.6 cm apart. The heaters are made from a rust-resisting iron sheath material. Each heater provides 200 watts. Before clamping to the plate, a thin layer of a high thermally conductive silicone paste was applied to the bottom of each heater. Three Chromolox digital temperature controllers with automatic reset and rate, type J thermocouple input, and 1 A triac output are used to maintain a uniform temperature across the plate. Three single-pole mercury displacement relays, with a-c resistive load ratings of 120 V and 35 A each, are used in series with the temperature controllers for loads that exceed the capacity of the controllers. The temperature is monitored and recorded over the entire area of the copper plate by the placement of 11 thermocouples. The bare wires of each thermocouple were threaded through a 1.9-cm ceramic sleeve, made of aluminum oxide, a nonelectrically conductive material. Then the iron and constantan wires were twisted together at the bottom of the sleeve and spot welded to form a small bead. The sleeves were then mounted into small wells which had been drilled into the top of the copper plate. Two layers of special ceramic adhesive were then cured between the sleeve and the plate. Eight of the 11 thermocouples are wired into a thermocouple selector switch which is connected to a voltmeter after passing through an ice bath. The other three thermocouples are used with the temperature controllers to maintain a uniform temperature across the plate. The surface temperature of the upper plate was found to be very uniform (within $\pm$ 0.3°C) for all of the experimental runs. Six other iron-constantan thermocouples were installed at the interface between the glass beads and the bottom plate. These thermocouples were used for measuring the effective thermal conductivity of the water-saturated packed-bed system. This effective thermal conductivity was found independently through a series of one-dimensional conduction heat transfer experiments. This is further explained in Section 5. In order to measure the heat flux supplied by the temperature controllers to the copper plate, a three-phase wattmeter transducer was wired into the control system. The output of the wattmeter transducer is wired to a strip chart recorder to record the total heat input over a given time into the plate. The top of the test section was insulated with Durablanket to withstand the high temperature from the strip heaters. A 2.5-cm-thick piece of carborundum insulation along with a 5-cm-thick piece of Owens-Corning Fiberglas insulation was used to minimize the heat losses from the test section. Using a one-dimensional conduction-convection model the magnitude of the heat losses was estimated to be around 2 percent of the total heat input.

Upstream of the test section is a reservoir 76 × 51 × 76 cm (length, width, height respectively) capable of achieving a range of accurately designated fluid levels. This is done through a connection via a divider to an auxiliary tank connected to a sump. Two mesh screens installed in the reservoir help reduce any disturbances in the fluid before it enters into the test section. An accurate flow control slider disconnects the reservoir from the test section. The slider allows the attainment of steady-state operating conditions upstream of the test section before any fluid runs through it. This kind of design, coupled with the selection of a large reservoir capacity, permits steady flow conditions to be reached within a very short time. This can be checked from the pressure indicator and fluid levels in the upstream and downstream reservoirs. The downstream reservoir is used for maintaining a constant pressure difference at every height along the test section. Flow measurements were made with an Invalco turbine flowmeter, which is linear in the range 0.2 – 2.9 m^3/hr. The flowmeter was factory calibrated. The factory calibration was checked and found consistent against the laboratory measurements. Furthermore, the volume flow rate found from the analysis was comparable to the experimentally measured flow rate.

The experiments were performed carefully, with particular emphasis on cleaning the copper plate and the upstream and downstream reservoirs after each run. In addition, the test section was thoroughly cleaned and the fluid filter was changed periodically. Consideration was given to observe the presence of any bubbles, in the test section, during the experimental runs. This was done by removing the insulation covers at one point in some of the experiments and looking all around and below the test section. No bubbles were observed at any time.

The average heat flux to the copper plate was obtained in two ways: measurement of the average increase in bulk temperature across the test section, and by a direct measurement of the heat flux supplied to the controllers through the electrical heaters on the plate. The average increase in bulk temperature may be found by measuring the bulk temperatures at the entrance and exit of the test section. Since the values of the mass flowrate and the specific heat of the fluid are known quantities, the heat flux may then be calculated. This way of obtaining the heat flux was of course very crude and no attempt was made to make this an accurate

measurement. This measurement was used just as a crude check on the heat flux measurement by the wattmeter transducer. The heat flux measurement by the average increase in bulk temperature was found to be within approximately 15 percent of the wattmeter transducer measurements. The heat flowrate measurement by the wattmeter transducer is used to compute the average experimental Nusselt number as:

$$\overline{\mathrm{Nu}} = \frac{Q_{\exp}}{k_e W(T_w - T_e)} \tag{6}$$

Here, $Q_{\exp}$ is the total measured heat rate supplied to the test section, W is the width of the test section, and T_e is the free-stream temperature.

4 Computational Procedure

To analyze the convection in packed beds some constitutive equations have to be supplied for the geometric function F and the permeability K in the momentum equation. However, the energy equation needs no modification. These constitutive equations are obtained from the experimental results of Ergun [13]. After some algebraic manipulations to obtain the constitutive relations and using a coordinate transformation to achieve a fast and accurate numerical scheme, the governing equations (1) and (2) are transformed to [11]

$$\frac{1}{\xi}\frac{\partial^2 <\tilde{u}>}{\partial \eta^2} - H_1^2(\xi,\eta)<\tilde{u}> - Q(\xi,\eta)<\tilde{u}>^2 + H^2(\xi,\eta) = 0 \tag{7}$$

$$u\xi\frac{\partial <\theta>}{\partial \xi} - \frac{1}{2}u\eta\frac{\partial <\theta>}{\partial \eta} = S(\xi,\eta)\frac{\partial^2 <\theta>}{\partial \eta^2} \tag{8}$$

where

$$<\tilde{u}> = \frac{<u>}{u_c} \qquad \theta = \frac{T - T_w}{T_e - T_w} \tag{9}$$

$$\eta = y\gamma_e/\xi^{1/2} \qquad \xi = \frac{x}{L} \tag{10}$$

$$\gamma_e = \frac{\sqrt{150}(1-\delta_e)}{\delta_e d_p} \qquad u_c = \frac{-K_e}{\mu_f}\frac{d<p>^f}{dx} \tag{11}$$

$$Q(\xi,\eta) = \frac{1.75[1-\delta(\xi,\eta)]\delta_e{}^2}{150(1-\delta_e)^2\delta(\xi,\eta)}\mathrm{Re}_p,\ \mathrm{Re}_p = \frac{u_c d_p}{\nu_f},\ \mathrm{Pr}_e = \frac{\nu_f}{\alpha_e} \tag{12}$$

$$H_1 = \frac{\gamma(\xi,\eta)}{\gamma_e},\ H(\xi,\eta) = \frac{\delta(\xi,\eta)}{\delta_e},$$

$$S(\xi,\eta) = \frac{L\,d_p}{K_e H(\xi,\eta)\mathrm{Re}_p\mathrm{Pr}_e} \tag{13}$$

$$K = \frac{\delta^3 d_p{}^2}{150(1-\delta)^2} \qquad F = \frac{1.75}{\sqrt{150}\delta^{3/2}} \tag{14}$$

Here Re_p is the Reynolds number based on particle diameter, and K_e and δ_e are the free-stream permeability and porosity. Equation (14) presents the constitutive relations which are obtained from the experimental results of Ergun [13] and used in equations (7) and (8). The function F is described in detail in [2]. The corresponding boundary conditions for equations (7) and (8) are

$$\eta = 0 \quad <\tilde{u}> = 0 \quad <\theta> = 0 \tag{15}$$

$$\eta \to \infty \quad <\tilde{u}> = \{-1 + \sqrt{1+4\psi_e}\}/2\psi_e \quad <\theta> = 1 \tag{16}$$

where

$$\psi_e = (1.75\delta_e \mathrm{Re}_p)/150(1-\delta_e) \tag{17}$$

The above boundary conditions are based on the independence of the upper and lower walls of the test section. To check this the problem was solved numerically accounting for both walls. The numerical results made it clear that the influence of the lower wall on the upper boundary was negligible. The wall heat flux is used to investigate the effects of variable porosity on convection in a region close to an external boundary. The Nusselt number, which characterizes the wall heat flux, is expressed as

$$\mathrm{Nu} = -\left.\frac{\partial <T>}{\partial y}\right|_{y=0} \Big/ \frac{(T_w - T_e)}{L} = \frac{\gamma_e L}{\xi^{1/2}}\left.\frac{\partial \theta}{\partial \eta}\right|_{\eta=0} \tag{18}$$

and the average Nusselt number, as defined in equation (6), is found to be

$$\overline{\mathrm{Nu}} = \frac{-\int_0^L \left.\frac{\partial <T>}{\partial y}\right|_{y=0} dx}{(T_w - T_e)} \tag{19}$$

5 Discussion of Results and Conclusions

From equations (7-18), it can be seen that the average Nusselt number can be presented in the following functional form:

$$\overline{\mathrm{Nu}} = \overline{\mathrm{Nu}}(\mathrm{Re}_p, \delta_e, \mathrm{Pr}_e, K_e, \chi, \Gamma) \tag{20}$$

where

$$\chi = \frac{L\,d_p}{K_e} \qquad \Gamma = \frac{L}{d_p} \tag{21}$$

For a given fluid, a given packing structure, and a specified type of particle the average Nusselt number will be a function of the Reynolds number based on pore diameter, Re_p, and the free-stream porosity, δ_e; therefore

$$\overline{\mathrm{Nu}} = \overline{\mathrm{Nu}}(\mathrm{Re}_p, \delta_e) \tag{22}$$

This can be seen from equations (20) and (21) and noting that K_e is a function of d_p and δ_e. The experimental data and the numerical results are obtained in the functional form presented in equation (22). The fluid used in both the experimental and numerical results was water. Two types of glass beads were used to simulate the packed bed. These were uniform 5 and 8-mm glass beads of different but known compositions. The experimental results for these two types of glass bead were compared against the numerical results. The comparison was done in the form presented in equation (22). For each type of glass bead the numerical results were obtained for two different cases. These were:

Case I: Accounting for the variable porosity, the presence of a solid boundary and the inertial forces.

Case II: Using the modified Darcy's Law which neglects the presence of a solid boundary and variable porosity, but accounts for the inertial forces.

In this work the effective thermal conductivity of the fluid-saturated porous media is assumed to be a constant across the bed. However, due to the porosity variations, it is expected that the thermal conductivity will vary across the packed bed. The effective thermal conductivity of the packed bed was measured by the experimental setup, but independent of the main experiment, by performing a number of one-dimensional conduction heat transfer experiments. This was done by closing off both sides of the test section and saturating it with water. The top and the side of the test section were insulated as before but the outer side of the bottom plate was exposed to an external air flow parallel to the bottom plate. The air flow was generated by a fan. The effective thermal conductivity was found by measuring the heat flow rate and the very uniform temperatures at the in-

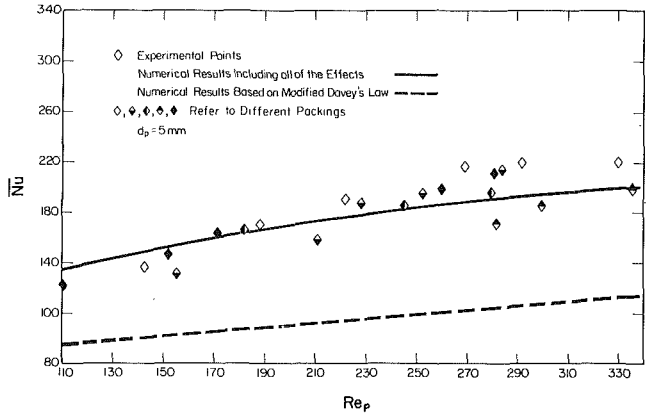

Fig. 3 The variation of the average Nusselt number with the Reynolds number (for d_p = 5 mm) for three different cases: I) experimental results, II) numerical results accounting for all of the effects, III) numerical results based on modified Darcy's law

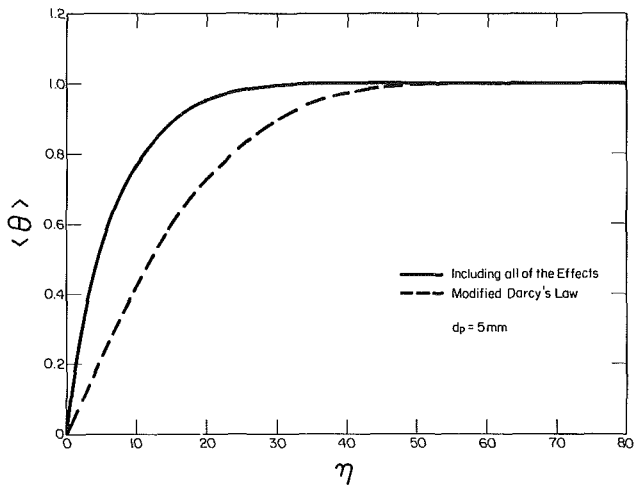

Fig. 4 Comparison of the theoretical temperature distribution with the temperature distribution based on modified Darcy's law for Re_p = 228 and d_p = 5 mm

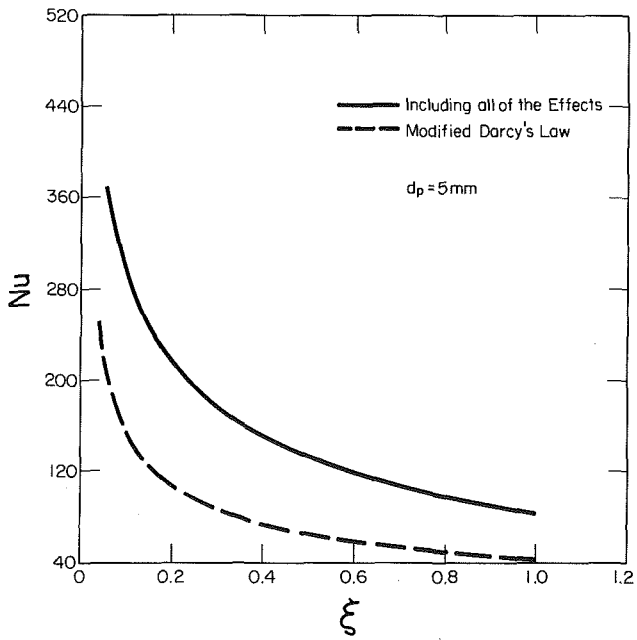

Fig. 5 Nusselt number variations corresponding to the two cases shown in Fig. 4

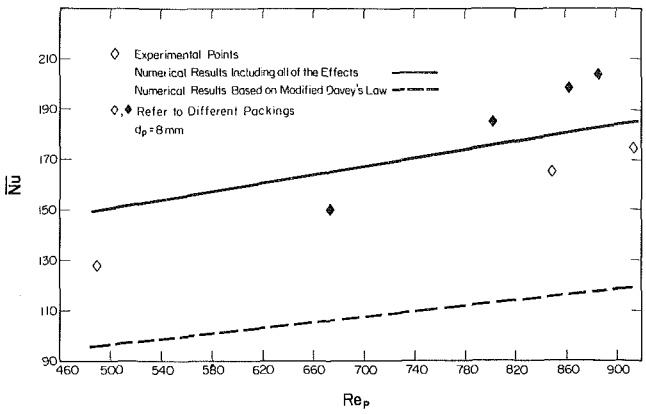

Fig. 6 Variation of the average Nusselt number with the Reynolds number (for d_p = 8 mm) for three different cases: I) experimental results, II) numerical results accounting for all of the effects, III) numerical results based on modified Darcy's law

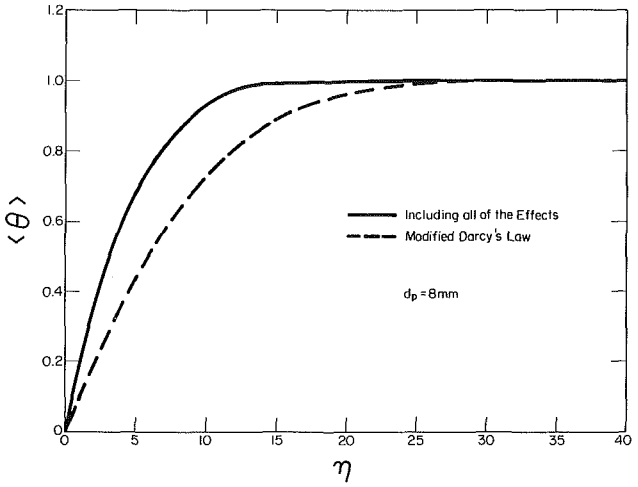

Fig. 7 Comparison of the theoretical temperature distribution with the temperature distribution based on modified Darcy's law for Re_p = 802 and d_p = 8 mm

terfaces between the glass beads and the top and bottom plates. The measured effective thermal conductivities were found to be quite close for the two types of beads which were used (the beads had different compositions). The effective thermal conductivity was found to be about 3.15 W/m^2 K with an accuracy of ± 5 percent. The effective thermal conductivity was determined for one set of packing in each case (5-mm and 8-mm beads). This measured thermal conductivity was used in the numerical calculations for all the different packings.

The numerical scheme was based on finite difference versions of equations (7) and (8) supplied with the boundary conditions given in equations (15) and (16). All of the coefficients in equations (7) and (8) are functions of the ξ and η coordinates. This is because Q, H, and S are functions of the porosity and the permeability which are in turn functions of ξ and η. The upstream condition for the energy equation is taken as uniform temperature at T_e at $x = 0$. The finite difference scheme was based on using upwind differencing in the ξ direction and an implicit routine in the η direction, along with the linearization of the momentum equation. The resulting set of algebraic equations were solved by tridiagonalizing the solution matrix. The linearization scheme used for equation (7) was checked by increasing the number of iterations used for convergence. The numerical scheme resulted in a very efficient and stable system. The accuracy of the finite-difference solution was tested by increasing the

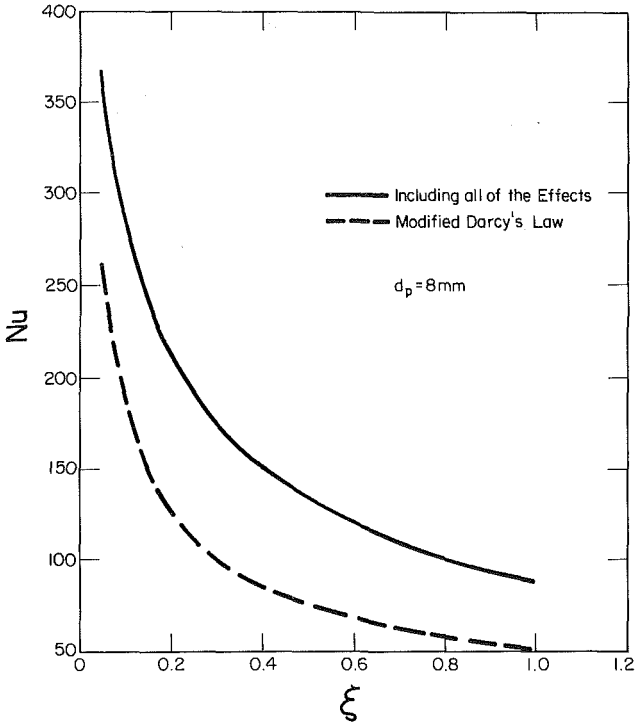

Fig. 8 Nusselt number variations corresponding to the two cases shown in Fig. 7

number of grid points, and investigating some limiting cases, such as the constant porosity case.

In obtaining the numerical results the following input parameters were used: the driving pressure force, the particle diameter d_p, the porosity variation from the experimental results of Benenati and Brosilow [6], and the thermophysical properties of the fluid and the solid matrix.

Presented in Fig. 3 are the experimental and numerical results for the average Nusselt number. These results are presented for the uniform 5-mm glass beads. Two different numerical Nusselt numbers are presented in Fig. 3. These are the theoretical Nusselt number which accounts for all of the effects and the Nusselt number based on modified Darcy's law. It can be seen from Fig. 3 that there is a good agreement between the experimental and the numerical results which account for the variable porosity effects. The agreement is both quantitative as well as qualitative as can be seen from the slopes of the lines in Fig. 3. Furthermore, the Nusselt number increases almost linearly with an increase in the Reynolds number based on pore diameter. The discrepancies between the theoretical and the experimental results are attributed to the expected variations in the effective thermal conductivity as well as the small oscillations of the porosity distribution with the distance from the solid boundary. It is recommended that these variations of the thermal conductivity be analyzed in future studies. Figures 4 and 5 are the numerical results for the temperature profiles and the Nusselt numbers corresponding to one of the experimental runs (Re_p = 228). The temperature profiles are presented at ξ = 0.3. Figure 4 compares the temperature distribution which accounts for all the effects, with the temperature distribution based on modified Darcy's Law. Figure 5 compares the Nusselt number corresponding to the two cases shown in Fig. 4. The velocity profiles and the momentum boundary layer thicknesses for variable porosity media are discussed in detail in [11].

Figure 6 presents the experimental and numerical results for the 8-mm beads. Again, it can be seen that there is a good agreement between the theoretical and experimental results. Figures 7 and 8 are the numerical results for the temperature profiles and the Nusselt numbers corresponding to one of the experimental runs (Re_p = 802). The temperature profiles are presented at ξ = 0.3. Figure 8 compares the Nusselt number corresponding to the two cases shown in Fig. 7. Figures 3 and 6 reveal that the average Nusselt number increases with an increase in the Reynolds number Re_p. This is because increasing Re_p leads to an increase in the convected energy compared to that by conduction, causing a thinner thermal boundary layer. This thinner boundary layer creates a larger flux at the boundary leading to an increase in the average Nusselt number for an increase in Re_p. Furthermore, from Figs. 3 and 6, it can be seen that the experimental data are in much better agreement with numerical results which account for the variable porosity effects, the external boundary, and the inertial forces.

The purpose of the present work was to show the importance of variable porosity on flow and heat transfer in variable porosity media. This was done through an experimental and numerical investigation. The experimental results were found to be in good agreement with the theoretical results. A comparison between the experimental and numerical results clearly indicates that the variable porosity effects must be accounted for.

References

1 Burns, P. J., and Tien, C. L., "Natural Convection in Porous Media Bounded by Concentric Spheres and Horizontal Cylinders," *Int. J. Heat Mass Transfer*, Vol. 22, 1979, pp. 929-939.

2 Vafai, K., and Tien, C. L., "Boundary and Inertia Effects on Flow and Heat Transfer in Porous Media," *Int. J. Heat Mass Transfer*, Vol. 24, 1981, pp. 195-203.

3 Vafai, K., and Tien, C. L., "Boundary and Inertia Effects on Convective Mass Transfer in Porous Media," *Int. J. Heat Mass Transfer*, Vol. 25, 1982, pp. 1183-1190.

4 Schwartz, C. E., and Smith, J. M., "Flow Distribution in Packed Beds," *Ind. Eng. Ch.*, Vol. 45, 1958, pp. 1209-1218.

5 Schertz, W. M., and Bischoff, K. B., "Thermal and Material Transport in Non-Isothermal Packed Beds," *AIChE J.*, Vol. 15, 1969, pp. 597-604.

6 Benenati, R. F., and Brosilow, C. B., "Void Fraction Distribution in Packed Beds," *AIChE J.*, Vol. 8, 1962, pp. 359-361.

7 Chandrasekhara, B. C., and Vortmeyer, D., "Flow Model for Velocity Distribution in Fixed Porous Beds Under Isothermal Conditions," *Th. Fluid Dynamics*, Vol. 12, 1979, pp. 105-111.

8 Denloye, A. O. O., and Botterill, J. S. M., "Heat Transfer in Flowing Packed Beds," *Ch. Eng. Sc.*, Vol. 32, 1977, pp. 461-465.

9 Schlunder, E. U., "Transport Phenomenon in Packed Bed Reactors," *Ch. Reaction Eng. Reviews*, 1978, pp. 110-161.

10 Whitaker, S., "Advances in Theory of Fluid Motion in Porous Media," *Ind. Engng. Chem.*, Vol. 61, 1969, pp. 14-28.

11 Vafai, K., "Convective Flow and Heat Transfer in Variable Porosity Media," J. of Fluid Mech., Vol. 147, 1984, pp. 233-259.

12 Tien, C. L., and Vafai, K., "Statistical Bounds for the Effective Thermal Conductivity of Microsphere and Fibrous Insulation," *Prog. Ast. Aero.*, Vol. 65, 1979, pp. 135-148.

13 Ergun, S., "Fluid Flow Through Packed Columns," *Ch. Eng. Prog.*, Vol. 48, 1952, pp. 89-94.

Exact Solutions for Radiative Heat Transfer in Box-Shaped Furnaces

N. Selçuk
Department of Chemical Engineering,
Middle East Technical University,
Ankara, Turkey

Exact expressions for the distributions of the components of radiative flux density and the radiative energy source term in terms of wall and medium temperature distributions have been formulated for an emitting-absorbing medium of constant properties bounded by black walls of a box-shaped enclosure. The accuracy of numerical solutions has been tested on an idealized enclosure for which exact analytical solution of the expressions is possible and shown to have good accuracy. The exact expressions have then been solved numerically for an enclosure problem based on data reported previously on a large-scale experimental furnace. The principal feature of the data is highly nonuniform medium and wall temperature distributions which are typical of the conditions encountered in industrial furnaces. These data have been chosen because of their practical importance and the nonavailability of exact solutions for such data. The resulting exact solutions have been given in tabular form and are intended to serve in the future as standards for testing the accuracy of the approximate predictions produced using various three-dimensional flux models.

1 Introduction

The most accurate procedures available for mathematical modeling of radiation fields within enclosures are the zone [1–3] and Monte-Carlo [4, 5] methods, both of which have been extensively developed and tested [3, 6, 7] for enclosures for which complete knowledge of the flow and concentration fields was available. Utilizing this information, the radiation model was used to predict temperature and radiative flux density distributions, which were then compared with measured values. However, these radiation models have not been extensively used as part of a complete prediction procedure. One reason for this is that, in the complete prediction procedure, the flow, concentration, and reaction fields are mathematically modeled by simultaneous partial differential equations. The equations modeling the radiation field are not differential in form, and, hence, their numerical solution in conjunction with the differential equations is neither convenient nor simple. In addition, the arithmetical labor and machine storage capacity required by these radiation models puts the complete modeling procedure utilizing them beyond the capacity of many computers.

In order to overcome these disadvantages, flux models [8–14] have been widely employed as alternative, albeit intrinsically less accurate, procedures to the zone or Monte-Carlo methods in complete prediction procedures. Flux models of radiation fields take the form of partial differential equations, which can conveniently and economically be solved simultaneously with the equations representing flow and reaction.

Previously published multidimensional evaluations of the accuracy of flux models of radiation fields have taken two forms: (*i*) The flux model has been employed as part of a complete prediction procedure [8–10] and predicted temperature and radiative heat flux distributions have been compared with experimentally determined values. This procedure suffers from two disadvantages: Discrepancies between predicted and measured values may be partly due to errors in the experimentally determined data; even if the experimentally determined data are correct, it is impossible to decide whether discrepancies in the predicted temperature and radiative flux distributions are attributable directly to the flux model employed or to inaccuracies in the models used for the prediction of flow, reaction, etc. (*ii*) The flux model has been tested in isolation from the modeling of other physical processes by using a prescribed radiative energy source term distribution, and comparing predicted temperature and radiative heat flux distributions with values predicted using the zone or Monte-Carlo methods [11, 14]. However, the radiative energy source term has been taken to have identical values at all points within the enclosed medium [11, 14]. Although such uniform distributions are computationally convenient they do not even approximately represent the extremely nonuniform distributions which are likely to be encountered in the operating furnaces and combustors for which the flux model is to be employed. This procedure for the evaluation of the accuracy of a flux model suffers from two major disadvantages: (*a*) Even if acceptably accurate predictions are obtained for the uniform source term distributions, there is no certainty that similarly accurate predictions will be produced for the highly nonuniform distributions in practical enclosures. (*b*) In the complete prediction procedure, the iterative sequence of solution of the equations is as follows: At the end of any cycle of the iterative solution, the enclosed medium and surface temperature distributions are known. These distributions are then used as input data for the radiation model employed, the output data from the use of the model being radiative flux density vector and radiative energy source term distributions. These newly produced flux and source term distributions are then used for the second part of the iterative cycle (i.e., the modeling of the flow and reaction fields), the output, and completion of the cycle, being a new set of values for the medium and surface temperature distributions. With this sequence of iterative solution in mind, it is obvious that when testing a radiation model which is intended for use in a complete prediction procedure, the input data provided should be complete temperature distributions, and the predicted and tested quantities should be the radiative flux density and radiative energy source term distributions.

The specified disadvantages of previous testings of flux models can only be overcome by producing exact solutions for the distributions of radiative flux density and source term in terms of wall and medium temperature distributions typical of an operating box-shaped furnace. Although a few attempts have been reported [15–17] on the exact solutions for multidimensional radiative transfer in Cartesian coordinate configurations, exact solutions for a box-shaped enclosure

Contributed by the Heat Transfer Division for publication in the JOURNAL OF HEAT TRANSFER. Manuscript received by the Heat Transfer Division May 10, 1984.

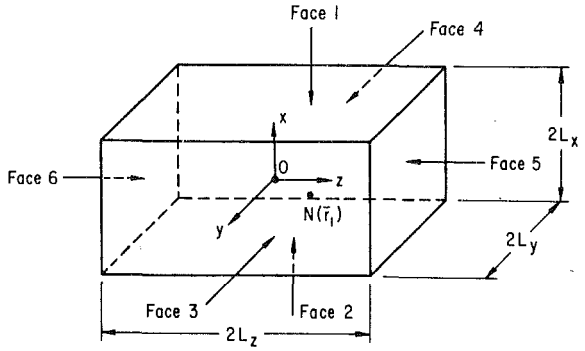

Fig. 1 The rectangular parallelepiped-shaped enclosure

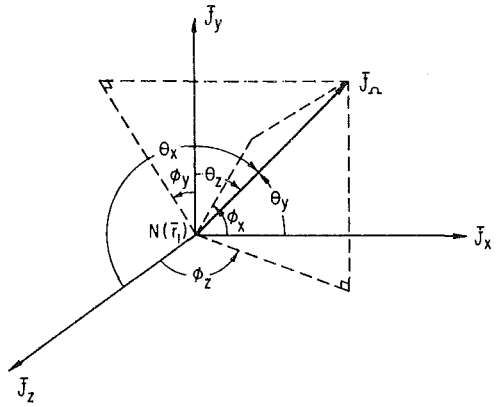

Fig. 2 Polar and azimuthal angles at $N(\bar{r}_1)$

with highly nonuniform medium and wall temperatures encountered in industrial furnaces are not available to date.

Therefore, in this paper, exact expressions for the distributions of components of radiative flux density vector and radiative energy source term in an emitting-absorbing medium bounded by black walls of a box-shaped furnace are formulated. The accuracy of numerical results is tested on an idealized enclosure problem for which exact analytical solution is possible. The exact expressions are then solved numerically for an enclosure problem based on data reported [18] previously on a large-scale experimental furnace with steep temperature gradients and the results are presented in tabular form so that they can be used as a basis for future testing of three-dimensional flux models.

2 Formulation of the Exact Expressions

The physical situation to be considered is that of a rectangular parallelepiped shaped enclosure filled with an absorbing-emitting, nonscattering radiatively grey medium whose absorption coefficient is the same at all points, and of known magnitude. Values of black-body emissive power are assumed to be available at all points within the enclosed medium, and at all points on the interior bounding surfaces of the enclosure. In order to simplify the equations to be solved, all interior bounding surfaces of the enclosure are assumed to be radiatively black.

The enclosure considered is a rectangular parallelepiped of side lengths $2L_x$, $2L_y$, and $2L_z$ in the respective coordinate directions. For convenience the origin of coordinates is taken to be at the center of the enclosure, and the faces of the enclosure are numbered for future identification, as shown in Fig. 1. For the purposes of evaluating the required radiation variables at point $N(\bar{r}_1)$, the total solid angle of 4π steradians surrounding the point is subdivided into six smaller pyramid-shaped solid angle Ω_m ($m = 1$ to 6), each of which is vertically opposite to the solid angle subtended by a face at point N.

The polar and azimuthal angles to be used to define the six solid angles Ω_m ($m = 1$ to 6) are shown in Fig. 2 where $\bar{j}_\Omega$ is a

Nomenclature

a = axial variation of gas temperature
b, c, d, e = azimuthal angles of the f functions in Table 2
d = slope of the axial temperature curve
E = emissive power, Wm^{-2}
f = functions defined in Table 2, gas temperature distribution in the circular cross section
F = function defined by equation (2)
G = total intensity of incident radiation, Wm^{-2}
I = intensity of radiation, $\mathrm{Wm}^{-2}\,\mathrm{sr}^{-1}$
$\bar{j}$ = unit vector in coordinate direction
1 = direction cosine
L = half of the side lengths of the rectangular parallelepiped
$\bar{q}$ = radiative flux density vector, Wm^{-2}
Q = source term for radiative energy, Wm^{-3}
r = radial distance, m
$\bar{r}$ = position vector
R = radius of circular cross section of the furnace, m
s = distance between points $P(\bar{r})$ and $W(\bar{r}_w)$, m
S = distance between points $N(\bar{r}_1)$ and $W(\bar{r}_w)$, m
T = absolute temperature of gas, K
v = distance between point $N(\bar{r}_1)$ and $P(\bar{r})$, m
z' = dimensionless axial distance
α_1-α_4 = azimuthal angles on xy plane
β_1-β_4 = azimuthal angles on yz plane
γ_1-γ_4 = azimuthal angles on zx plane
θ = polar angles between direction Ω and the coordinate axes
τ_o = dimensionless optical thickness
ϕ = azimuthal angles corresponding to the polar angles θ
Ω = pyramid-shaped solid angles
ω = solid angle

Subscripts

b = black body
burner = burner wall
bw = black wall
e = exit
end = end wall
G = gas
i = inlet
1 = lower limit
$m(1,2,\ldots 6)$ = solid angles
max = maximum
0 = reference value
side = side wall
u = upper limit
w = wall
x,y,z = coordinate axes
η = coordinate directions
ξ = coordinate directions
Ω = direction of intensity

Superscripts

~ = dimensionless

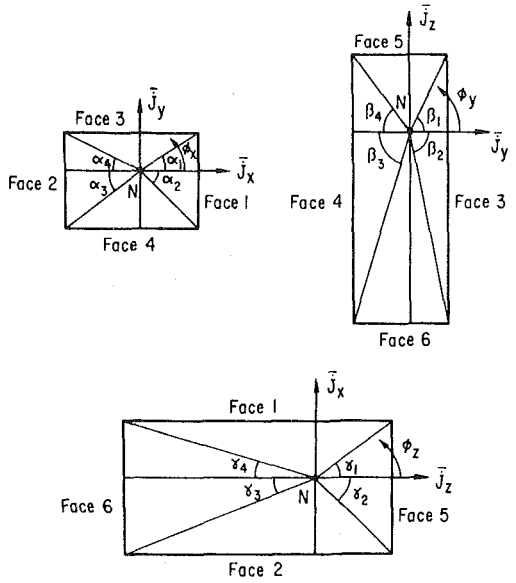

Fig. 3 Azimuthal angles subtended by enclosure faces at $N(x_1, y_1, z_1)$

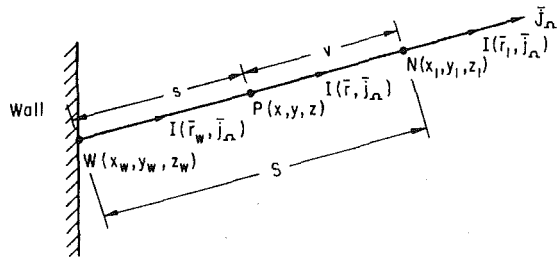

Fig. 4 Geometrical setup for integration of radiant transfer equation

unit vector in direction Ω at point $N(\bar{r}_1)$, $\bar{j}_\xi$ is a unit vector in coordinate direction ξ ($\xi = x, y, z$). ϕ_ξ denotes the azimuthal angle between $\bar{j}_\xi$ and the normal projection of $\bar{j}_\Omega$ onto the plane through N containing $\bar{j}_\xi$ and $\bar{j}_{\text{next }\xi}$, where "next ξ" is decided in the sequence $x \to y \to z \to x$ and θ_ξ represents the corresponding polar angle. $\bar{j}_\Omega$ is related to the unit vectors in the axial directions through the direction cosines 1_x, 1_y, and 1_z.

Comparison of ratios of direction cosines leads to an expression where each polar angle is related to two azimuthal angles by

$$\theta_\xi = F(\phi_{\text{remaining }\xi}, \phi_\xi) \tag{1}$$

where

$$F(a,b) = \tan^{-1}[(\tan a)/(\cos b)] \tag{2}$$

In equation (1), the sequence to be followed in determining the remaining ξ is $x \to z$, $y \to x$, $z \to y$, so that, for example, for $\xi = x$, remaining $\xi = z$.

The azimuthal angles subtended by the six faces of the enclosure at point $N(\bar{r}_1)$ are illustrated in Fig. 3. α_1 to α_4, β_1 to β_4, and γ_1 to γ_4 can all be expressed in terms of the dimensions of the enclosure and the Cartesian coordinates of point N.

Evaluation of the values of the components of the radiative heat flux vector and energy source term at general point N within the enclosure involves the performance of certain angular integrals over the six solid angles Ω_m ($m = 1$ to 6). Before these integrals can be performed it is necessary to specify θ_ξ and ϕ_ξ ranges defining each solid angle. These ranges were worked out for each solid angle in turn and are summarized in Table 1, where $\eta = x$ for $m = 1, 2$, $\eta = y$ for $m = 3, 4$ and $\eta = z$ for $m = 5, 6$.

In order to increase the generality of the exact solution, all physical quantities are expressed in dimensionless forms by

Table 1 Azimuthal and polar angle ranges for all six solid angles

Ω_m	ϕ_η	$(\phi_\eta)_l$	$(\phi_\eta)_u$	θ_η	$(\theta_\eta)_l$	$(\theta_\eta)_u$
Ω_1	ϕ_x	$\pi-\alpha_2$	$\pi+\alpha_1$	θ_x	$F(\gamma_4, \phi_x-\pi)$	$\pi-F(\gamma_1, \phi_x-\pi)$
Ω_2	ϕ_x	$-\alpha_4$	α_3	θ_x	$F(\gamma_3, \phi_x)$	$\pi-F(\gamma_2, \phi_x)$
Ω_3	ϕ_y	$\pi-\beta_2$	$\pi+\beta_1$	θ_y	$F(\alpha_4, \phi_y-\pi)$	$\pi-F(\alpha_1, \phi_y-\pi)$
Ω_4	ϕ_y	$-\beta_4$	β_3	θ_y	$F(\alpha_3, \phi_y)$	$\pi-F(\alpha_2, \phi_y)$
Ω_5	ϕ_z	$\pi-\gamma_2$	$\pi+\gamma_1$	θ_z	$F(\beta_4, \phi_z-\pi)$	$\pi-F(\beta_1, \phi_z-\pi)$
Ω_6	ϕ_z	$-\gamma_4$	γ_3	θ_z	$F(\beta_3, \phi_z)$	$\pi-F(\beta_2, \phi_z)$

defining a reference length (L_0) which is the shortest dimension of the enclosure and a reference temperature (T_0) which is taken to be the maximum temperature of the enclosed medium. With these reference quantities available, temperatures are made dimensionless by dividing them by T_0; intensity and the rest of the radiation variables are made dimensionless by dividing them by the reference intensity (I_0) and reference emissive power (E_0), respectively.

The physical situation to be considered for the integration of the equation of radiant energy transfer is illustrated in Fig. 4. Point $W(x_w, y_w, z_w)$ is found by extending $\bar{j}_\Omega$ through point $N(x_1, y_1, z_1)$ backward until a wall surface is encountered. Point $P(x, y, z)$ is a general point between W and N.

For the situation illustrated in Fig. 4 the equation of radiant energy transfer at point $P(\bar{r})$ in direction $\bar{j}_\Omega$ can be written in dimensionless form as follows:

$$\left(\frac{\partial}{\partial \tilde{s}} + \tau_0\right)\tilde{I}(\bar{r}, \bar{j}_\Omega) = \tau_0 \tilde{I}_b(\bar{r}) \tag{3}$$

where $I(\bar{r}, \bar{j}_\Omega)$ is the intensity of radiation at point $P(\bar{r})$ and in a direction defined by unit vector $\bar{j}_\Omega$. τ_0 is the dimensionless optical thickness of the medium. The "~" sign over any quantity represents the dimensionless form of that quantity. $I_b(\bar{r})$ denotes black-body intensity of the medium at P and s is the distance measured in the direction of $\bar{j}_\Omega$. Equation (3) can be integrated between W and N with respect to s to give

$$\tilde{I}(\bar{r}_1, \bar{j}_\Omega) = e^{-\tau_0 \tilde{S}}\tilde{I}(\bar{r}_w, \bar{j}_\Omega) + \tau_0 \int_{\tilde{v}=0}^{\tilde{v}=\tilde{S}} e^{-\tau_0 \tilde{v}} \tilde{I}_b(\bar{r}) d\tilde{v} \tag{4}$$

where $\tilde{v} = \tilde{S} - \tilde{s}$ (see Fig. 4). In equation (4), the first and second terms on the right-hand side represent the contributions of wall radiation, $\tilde{I}_w(\bar{r}_1, \bar{j}_\Omega)$, and gas radiation between W and N, $\tilde{I}_G(\bar{r}_1, \bar{j}_\Omega)$, to the intensity at N, respectively. With the assumption of black walls, the radiation leaving the wall point is decoupled from the radiation leaving all other points and $\tilde{I}(\bar{r}_w, \bar{j}_\Omega)$ becomes equal to $\tilde{I}_{bw}(\bar{r}_w)$, the black-body intensity corresponding to the temperature of the wall point.

By use of equation (4) with the black-wall assumption the dimensionless intensity $\tilde{I}(\bar{r}_1, \bar{j}_\Omega)$ can be evaluated in any direction $\bar{j}_\Omega$ at point $N(\bar{r}_1)$ by performing the necessary spatial integration using prespecified distributions of $\tilde{I}_b(\bar{r})$ and $\tilde{I}_{bw}(\bar{r}_w)$. By repeating the process for a large number of directions $\bar{j}_\Omega$ at the point N, the angular distribution of intensity at the point becomes available. From this angular distribution the values of the dimensionless radiation variables $\tilde{q}_\xi$ ($\xi = x, y, z$) and $\tilde{Q}$ may be determined by per-

forming the necessary angular integrations of the intensity at the point.

To cover the angular integral involved in the definition of the dimensionless components $\tilde{q}_\xi(\xi = x, y, z)$ of the radiative flux vector, the integral is evaluated successively for the six solid angles Ω_m ($m = 1$ to 6) and the resulting values added to give the final result, that is,

$$\tilde{G}(\bar{r}_1) = \frac{1}{\pi} \sum_{m=1}^{6} \int_{\Omega_m} [\tilde{I}_w(\bar{r}_1, \bar{j}_\Omega) + \tilde{I}_G(\bar{r}_1, \bar{j}_\Omega)] d\omega \tag{6}$$

As a first step in obtaining the value of the radiative energy source term at the general point N, it is first necessary to obtain the value of the total intensity of incident radiation at the same point.

As with $\tilde{q}_\xi$, the dimensionless value of the total intensity $\tilde{G}$ is actually evaluated as the sum of the part values over the six solid angles, that is,

$$\tilde{G}(\bar{r}_1) = \frac{1}{\pi} \sum_{m=1}^{6} \int_{\Omega_m} [\tilde{I}_w(\bar{r}_1, \bar{j}_\Omega) + \tilde{I}_G(\bar{r}_1, \bar{j}_\Omega)] d\omega \tag{6}$$

With the value of $\tilde{G}(\bar{r}_1)$ available $\tilde{Q}(\bar{r}_1)$ may be calculated from

$$\tilde{Q}(\bar{r}_1) = \tau_0 [4\tilde{I}_b(\bar{r}_1) - \tilde{G}(\bar{r}_1)] \tag{7}$$

By using the definitions of 1_ξ and $d\omega$, together with the angle limits for Ω_1 to Ω_6 contained in Table 1, the final forms necessary for the evaluation of the $\tilde{q}_{\xi m}$ and $\tilde{G}_m$ may be expressed as

$$\begin{Bmatrix} \pi\tilde{G}_m(\bar{r}_1) \\ \pi\tilde{q}_{xm}(\bar{r}_1) \\ \pi\tilde{q}_{ym}(\bar{r}_1) \\ \pi\tilde{q}_{zm}(\bar{r}_1) \end{Bmatrix} = \int_{(\phi_\eta)_1}^{(\phi_\eta)_u} \int_{(\theta_\eta)_1}^{(\theta_\eta)_u} \begin{Bmatrix} 1 \\ 1_x \\ 1_y \\ 1_z \end{Bmatrix} [\tilde{I}_{wm}(\bar{r}_1, \theta_\eta, \phi_\eta) + \tilde{I}_{Gm}(\bar{r}_1, \theta_\eta, \phi_\eta)] \sin\theta_\eta d\theta_\eta d\phi_\eta \qquad m = 1,2 \tag{8}$$

$$\begin{Bmatrix} \pi\tilde{G}_m(\bar{r}_1) \\ \pi\tilde{q}_{xm}(\bar{r}_1) \\ \pi\tilde{q}_{ym}(\bar{r}_1) \\ \pi\tilde{q}_{zm}(\bar{r}_1) \end{Bmatrix} = \int_{(\phi_\eta)_1}^{(\phi_\eta)_u} \int_{(\theta_\eta)_1}^{(\theta_\eta)_u} \begin{Bmatrix} 1 \\ 1_x \\ 1_y \\ 1_z \end{Bmatrix} [\tilde{I}_{wm}(\bar{r}_1, \theta_\eta, \phi_\eta) + \tilde{I}_{Gm}(\bar{r}_1, \theta_\eta, \phi_\eta)] \sin\theta_\eta d\theta_\eta d\phi_\eta \qquad m = 3,4 \tag{9}$$

$$\begin{Bmatrix} \pi\tilde{G}_m(\bar{r}_1) \\ \pi\tilde{q}_{xm}(\bar{r}_1) \\ \pi\tilde{q}_{ym}(\bar{r}_1) \\ \pi\tilde{q}_{zm}(\bar{r}_1) \end{Bmatrix} = \int_{(\phi_\eta)_1}^{(\phi_\eta)_u} \int_{(\theta_\eta)_1}^{(\theta_\eta)_u} \begin{Bmatrix} 1 \\ 1_x \\ 1_y \\ 1_z \end{Bmatrix} [\tilde{I}_{wm}(\bar{r}_1, \theta_\eta, \phi_\eta) + \tilde{I}_{Gm}(\bar{r}_1, \theta_\eta, \phi_\eta)] \sin\theta_\eta d\theta_\eta d\phi_\eta \qquad m = 5,6 \tag{10}$$

Table 2 Expressions for the analytical values of components of dimensionless radiative flux density vector and the dimensionless intensity of total incident radiation

Ω_m	b	c	d	e	$\pi\tilde{q}_x$	$\pi\tilde{q}_y$	$\pi\tilde{q}_z$	$\tilde{G}$
Ω_1	α_1	α_2	γ_1	γ_4	$-f_1$	$-f_2$	f_3	f_4
Ω_2	α_3	α_4	γ_2	γ_3	f_1	f_2	f_3	f_4
Ω_3	β_1	β_2	α_1	α_4	f_3	$-f_1$	$-f_2$	f_4
Ω_4	β_3	β_4	α_2	α_3	f_3	f_1	f_2	f_4
Ω_5	γ_1	γ_2	β_1	β_4	$-f_2$	f_3	$-f_1$	f_4
Ω_6	γ_3	γ_4	β_2	β_3	f_2	f_3	f_1	f_4

$$f_1(b,c,d,e) = \frac{1}{2}\{\sin b[\tan^{-1}(\cot d \cos b) + \tan^{-1}(\cot e \cos b)] + \sin c[\tan^{-1}(\cot d \cos c) + \tan^{-1}(\cot e \cos c)] + \cos d[\tan^{-1}(\tan b \sin d) + \tan^{-1}(\tan c \sin d)] + \cos e[\tan^{-1}(\tan b \sin e) + \tan^{-1}(\tan c \sin e)]\}$$

$$f_2(b,c,d,e) = \frac{1}{2}\{\cos c[\tan^{-1}(\cot d \cos c) + \tan^{-1}(\cot e \cos c)] - \cos b[\tan^{-1}(\cot d \cos b) + \tan^{-1}(\cot e \cos b)]\}$$

$$f_3(b,c,d,e) = \frac{1}{2}\{\sin d[\tan^{-1}(\tan b \sin d) + \tan^{-1}(\tan c \sin d)] - \sin e[\tan^{-1}(\tan b \sin e) + \tan^{-1}(\tan c \sin e)]\}$$

$$f_4(b,c,d,e) = \sin^{-1}(\sin b \cos d) + \sin^{-1}(\sin c \cos d) + \sin^{-1}(\sin b \cos e) + \sin^{-1}(\sin c \cos e)$$

3 Testing of the Exact Numerical Solutions

Evaluation of the accuracy of the numerical solution of the triple integrals involved can be achieved by using the computer program to make predictions for an idealized enclosure for which exact analytical solution of the integrals is possible. The idealized situation to be considered is that of a cubical enclosure of side length L, containing a medium of an optical thickness of unity ($\tau_o = 1$) which is in thermal equilibrium with its bounding walls [i.e., $\tilde{I}_b(\bar{r}) = \tilde{I}_{bw}(\bar{r}_w) = 1$].

For the exact analytical solution on the idealized enclosure problem, equations (8), (9), and (10) reduce to the integrals of some trigonometric functions as the sum of the intensities becomes equal to unity. The resulting expressions for the analytical values of $\tilde{q}_x$, $\tilde{q}_y$, $\tilde{q}_z$, and $\tilde{G}$ for all six solid angles are shown in Table 2.

The value of the radiative energy source term $\tilde{Q}(\bar{r}_1)$ may be obtained by using equation (7).

For the exact numerical evaluation of the triple integrals, the simplest numerical integration procedure, Simpson's 1/3 rule, was adopted. In order to assess the effect of fineness of subdivisions on the predicted results, several magnitudes of subdivisions were employed. These were 10, 5, 2.5, and 1 deg

for the angular integrals. For the spatial integrals the number of subdivisions tested were 40 and 80.

Analytical and numerical values of the components of the dimensionless radiative flux density vector and the radiative energy source term have been compared from two points of view: (*i*) the location of the point with respect to the bounding walls, (*ii*) the fineness of subdivisions in angular and spatial integrals of numerical solution necessary to produce good agreement between the analytical and numerical results.

To achieve the former, three points of interest have been chosen: (*i*) a medium point in the center of the enclosure ($\bar{x}=0$, $\bar{y}=0$, $\bar{z}=0$); (*ii*) a medium point adjacent to one wall, to be referred to as a face point ($\bar{x}=1$, $\bar{y}=0$, $\bar{z}=0$); (*iii*) a medium point near a corner of the enclosure ($\bar{x}=0.95$, $\bar{y}=0.95$, $\bar{z}=0.95$). Points (*i*) and (*ii*) represent the grid points resulting from the control volume approach used in complete prediction procedures [19] in which the flux models are used for modeling the radiation field. Point (*iii*) provides a more severe test with regard to the magnitudes of subdivisions required as the size of the interval in space coordinates depends upon the location of the point in the enclosure and the direction which is fixed by the polar and azimuthal angles.

The latter object has been achieved by running the computer program at the points of interest for several subdivisions in θ, ϕ, and $\bar{S}$. Comparison of the analytical and numerical values of all the radiation variables for all medium points of interest has shown that the computer program is logically correct and exact agreement to the fourth figure after the decimal point can be produced for all points if each spatial integral is based on 40 subdivisions and 1-deg subdivisions are employed for the angular integrals.

4 Application to Data on a Large-Scale Experimental Furnace

The experimental furnace under consideration is horizontal, of tunnel type with a square cross section. It is fired horizontally from the center of the left end wall, which is the burner end wall, with a mixture of oil and gas, and with no swirl, and operates at atmospheric pressure. The four side walls are water cooled, and the burner and back end walls are refractory.

4.1 Effect of Symmetries on Calculations. The origin of the space coordinates is taken to be at the center of the rectangular parallelepiped-shaped experimental furnace. The z axis is assumed to run horizontally between the centers of the two end walls, and the x and y coordinates then define position within each square cross section normal to the z axis. As the burner is fired along the z axis, the variation of the gas and wall temperatures about this axis is found symmetrical, and identical in both the x and y directions. For such an enclosure, it is only necessary to calculate the values of the components of the radiative flux density vector and radiative energy source term for 1/8 of the cross section.

4.2 General Form of Gas Temperature Distribution. In the experimental furnace the peak temperature occurs on the axis of symmetry along which the burner is fired. This maximum temperature (T_{max}) is chosen as the reference value T_0, thus producing maximum dimensionless temperature, black-body emissive power and intensity within the enclosure all equal to unity.

Temperature measurements within an experimental furnace are always carried out on a discrete grid of points. However, for numerical evaluation of the exact solution integrals, it is necessary to know the temperature at any point within the enclosed medium or on the interior bounding surface. This can be most conveniently achieved by fitting a general functional form which approximates reasonably to the temperatures at the points of measurement, and also permits prediction of temperature at all intermediate points.

Variation of gas temperature in a furnace of square cross section which is axially fired and symmetrically cooled about the axis of firing can be represented by

$$\tilde{T}_G(x,y,z) = [a(z') - \tilde{T}_e]f(r/R) + \tilde{T}_e \tag{11}$$

where $\tilde{T}_G$ is the dimensionless absolute temperature of the medium, which has a maximum value of unity within the enclosure due to the selection of the maximum gas temperature as the reference temperature T_0. $f(r/R)$ is the functional form employed for the representation of gas temperature in the circular region ($R=L_x=L_y$) tangent to the side walls of the furnace. Outside the circular region the dimensionless gas temperature is assumed to be the same at all points and equal to the exit gas temperature T_e. This assumption is consistent with the real physical situation encountered when the burning jet does not spread rapidly enough to touch the side walls of the enclosure, and recirculation then commences at the back wall because the exit orifice in the wall is smaller than the jet diameter. z' is the dimensionless distance ($=\bar{z}/\bar{L}_z$) and $a(z')$ is the as yet unspecified form accounting for the gas temperature variation along the furnace axis.

4.3 Cross-Sectional Variation of Gas Temperature. Cross-sectional gas temperature distribution can be represented by a bell-shaped curve which satisfies the following conditions

$$\tilde{T}_G = a(z') \quad \text{at} \quad r=0 \tag{12}$$

$$d\tilde{T}_G/dr = 0 \quad \text{at} \quad r=0 \tag{13}$$

$$\tilde{T}_G = \tilde{T}_e \quad \text{at} \quad r=R \tag{14}$$

$$d\tilde{T}_G/dr = 0 \quad \text{at} \quad r=R \tag{15}$$

Equation (13) expresses the fact that the gas temperature reaches a peak on the axis of symmetry of the furnace; equation (14) ensures that the gas temperatures fall to the uniform surrounding temperature T_e at all points on the circumference of the circle of radius R; equation (15) causes the curved profile within the circle to join smoothly on the flat profile outside the circle.

By using equation (11), conditions represented by equations (12–15) can be re-expressed in terms of the unspecified function $f(r/R)$, as shown below

$$f(r/R) = 1 \quad \text{at} \quad r=0 \tag{16}$$

$$\frac{d}{dr}[f(r/R)] = 0 \quad \text{at} \quad r=0 \tag{17}$$

$$f(r/R) = 0 \quad \text{at} \quad r=R \tag{18}$$

$$\frac{d}{dr}[f(r/R)] = 0 \quad \text{at} \quad r=R \tag{19}$$

One possible functional form which can be assumed is a third-order polynomial in (r/R), the coefficients of which can be determined by satisfying the conditions represented by equations (16–19). The resulting relationship for the cross-sectional variation of gas temperature then becomes

$$f(r/R) = 1 - 3(r/R)^2 + 2(r/R)^3 \tag{20}$$

4.4 Axial Variation of Gas Temperature. Gas temperature measured on the furnace axis rises steeply from its inlet value, passes through a maximum, and then decreases continuously toward the exit. Mathematically, this type of variation can be represented by two cubics; one in the range $-1 \leq z' \leq -z'_{max}$, and the other in the range $-z'_{max} \leq z' \leq 1$, z'_{max} denoting the position of the maximum temperature. The coefficients of the former cubic can be determined by satisfying the conditions

$$a = \tilde{T}_i \text{ and } da/dz' = d_i \quad \text{at} \quad z' = -1 \tag{21}$$

$$a = 1 \text{ and } da/dz' = 0 \quad \text{at} \quad z' = -z'_{max} \tag{22}$$

where $\tilde{T}_i$ is the dimensionless axial temperature, and d_i is the

slope of the axial temperature curve at the furnace inlet. If the cubic is made to satisfy the specified conditions, the resulting relationship can be expressed in the form

$$a(z') = 1 + [d_i(1 - z'_{max}) - 3(1 - T_i)]\left(\frac{z' + z'_{max}}{1 - z'_{max}}\right)^2 + [d_i(1 - z'_{max}) - 2(1 - T_i)]\left(\frac{z' + z'_{max}}{1 - z'_{max}}\right)^3 \quad (23)$$

For a furnace in which combustion takes place very rapidly in the neighborhood of the burners, the maximum axial temperature occurs close to the burner wall, and the cubic represented by equation (23) is compressed into a very short z' range. This situation occurs in the experimental furnace considered. It has been found by the present author that the measured temperatures in this region of very rapid variation can be better represented by the cubic if, instead of using the measured inlet slope, the value of d_i is chosen to produce a point of inflection at the peak. That is, if d_i is selected so that

$$\frac{d^2a}{d(z')^2} = 0 \quad \text{at} \quad z' = -z'_{max} \quad (24)$$

Equation (23) is found to satisfy this condition if

$$d_i = 3(1 - \tilde{T}_i)/(1 - z'_{max}) \quad (25)$$

and equation (23) then simplifies to the form

$$a(z') = 1 + (1 - \tilde{T}_i)\left(\frac{z' + z'_{max}}{1 - z'_{max}}\right)^3 \quad \text{for} \quad -1 \leqq z' \leqq -z'_{max} \quad (26)$$

The coefficients of the second cubic are determined by satisfying the conditions

$$a = 1 \quad \text{and} \quad da/dz' = 0 \quad \text{at} \quad z' = -z'_{max} \quad (27)$$

$$a = \tilde{T}_e \quad \text{and} \quad da/dz' = d_e \quad \text{at} \quad z' = 1 \quad (28)$$

where d_e is the slope of the axial temperature curve at the furnace exit. The resulting cubic can be expressed in the form

$$a(z') = 1 - [d_e(1 + z'_{max}) + 3(1 - \tilde{T}_e)]\left(\frac{z' + z'_{max}}{1 + z'_{max}}\right)^2 + [d_e(1 + z'_{max}) + 2(1 - \tilde{T}_e)]\left(\frac{z' + z'_{max}}{1 + z'_{max}}\right)^3$$

$$\text{for} \quad -z'_{max} \leqq z' \leqq 1 \quad (29)$$

By using the data reported [18] for (*i*) the furnace dimensions, (*ii*) the location of the maximum gas temperature, (*iii*) the inlet, exit, and maximum gas temperatures, and (*iv*) the slope of the axial temperature curve at the furnace exit, the temperature of the gases at any point within the enclosure considered can be calculated by using equations (11) and (20), together with either of equations (26) and (29) depending on the z' value of the point under consideration.

4.5 Numerical Data From the Experimental Furnace. In addition to the numerical data required for calculation of gas temperature distribution, input data are also required for the wall temperatures and the absorption coefficient of the enclosed medium. Table 3 shows the complete dimensionless data obtained from the reported work [18] on the experimental furnace and used as input data for the exact solution computer program.

4.6 Solution Procedure. As the problem involves steep gradients in gas temperature distribution, the computer program developed for the evaluation of exact point values of the components of the radiative flux density and of radiative energy source term and tested on an idealized enclosure problem has been retested for the effect of fineness of the

Table 3 Dimensionless data fed to the exact solution program

Dimensions of the furnace	$\tilde{L}_x = 1$, $\tilde{L}_y = 1$, $\tilde{L}_z = 6$
Optical thickness	$\tau_o = 1/6$
Wall black-body intensities	$(\tilde{I}_{bw})_{side} = 0.0020$ $(\tilde{I}_{bw})_{burner} = 0.0574$ $(\tilde{I}_{bw})_{end} = 0.0167$
Gas temperatures	$\tilde{T}_i = 0.1775$ $\tilde{T}_e = 0.6222$ $\tilde{T}_{max} = 1$
Position of the peak	$z'_{max} = 0.8$
Slope of gas temperature distribution at furnace exit	$d_e = -0.220$

Reference values used to make the experimental data dimensionless:

$L_o = 0.48$ m, $T_o = 1673$ K, $E_o = 4.4419 \times 10^5$ Wm^{-2}, $I_o = 1.4139 \times 10^5$ Wm^{-2}sr^{-1}.

Table 4 Exact point values of dimensionless source term in the medium

$\tilde{z}$	-5.75	-5.25	-4.75	-4.25	-3.75	-3.25	-2.75	-2.25
$\tilde{q}(0.25,0.25,\tilde{z})$	0.0493	0.3115	0.3602	0.3567	0.3506	0.3417	0.3302	0.3166
$\tilde{q}(0.75,0.25,\tilde{z})$	0.0667	0.0930	0.0948	0.0939	0.0933	0.0929	0.0925	0.0920
$\tilde{q}(0.75,0.75,\tilde{z})$	0.0734	0.0741	0.0731	0.0725	0.0724	0.0724	0.0726	0.0730
$\tilde{z}$	-1.75	-1.25	-0.75	-0.25	0.25	0.75	1.25	1.75
$\tilde{q}(0.25,0.25,\tilde{z})$	0.3012	0.2846	0.2670	0.2490	0.2308	0.2128	0.1952	0.1783
$\tilde{q}(0.75,0.25,\tilde{z})$	0.0915	0.0910	0.0904	0.0898	0.0890	0.0883	0.0876	0.0867
$\tilde{q}(0.75,0.75,\tilde{z}$	0.0734	0.0739	0.0745	0.0750	0.0757	0.0763	0.0769	0.0776
$\tilde{z}$	2.25	2.75	3.25	3.75	4.25	4.75	5.25	5.75
$\tilde{q}(0.25,0.25,\tilde{z})$	0.1622	0.1471	0.1331	0.1203	0.1087	0.0983	0.0893	0.0824
$\tilde{q}(0.75,0.25,\tilde{z})$	0.0859	0.0850	0.0842	0.0834	0.0826	0.0820	0.0816	0.0818
$\tilde{q}(0.75,0.75,\tilde{z})$	0.0782	0.0788	0.0795	0.0801	0.0807	0.0814	0.0823	0.0834

spatial and angular subdivisions, by running it with the specified input data for finer and finer subdivisions. It has been noted that the accuracy achieved on the idealized enclosure problem was obtainable only at the expense of excessive computing times. Therefore, recourse has been made to a more economical numerical integration procedure, i.e., Gauss–Legendre integration. It has been found that 16-point Gaussian was a compromise between the accuracy and computing time and produced a minimum of five-figure accuracy after the decimal point.

In order that the exact solutions produced can be used for future testing of predictions of various flux models, 1/4 of the larger-scale furnace has been subdivided into $2 \times 2 \times 24$ control volumes in x, y, and z directions, respectively. Exact solutions have been produced for medium grid points which lie at the geometrical center of each control volume and surface grid points which lie in the center of each control volume face in contact with the walls of the enclosure.

5 Results and Discussion

Exact expressions for point values of the dimensionless radiative flux density and the radiative energy source term, formulated in the previous sections, have been solved numerically for $2 \times 2 \times 24$ medium grid points in 1/4 of the large-scale experimental furnace. The point values of the radiation variables have been evaluated by employing 16-point Gaussian spacing for the two angular and one spatial integrals.

Table 5 Exact point values of dimensionless flux densities to the side wall

$\tilde{z}$	-5.75	-5.25	-4.75	-4.25	-3.75	-3.25	-2.75	-2.25
$\tilde{q}_x(1,0.25,\tilde{z})$	0.0642	0.0753	0.0824	0.0850	0.0855	0.0848	0.0834	0.0816
$\tilde{q}_x(1,0.75,\tilde{z})$	0.0530	0.0571	0.0611	0.0630	0.0635	0.0633	0.0625	0.0614
$\tilde{z}$	-1.75	-1.25	-0.75	-.025	0.25	0.75	1.25	1.75
$\tilde{q}_x(1,0.25,\tilde{z})$	0.0795	0.0771	0.0746	0.0719	0.0691	0.0663	0.0636	0.0609
$\tilde{q}_x(1,0.75,\tilde{z})$	0.0601	0.0586	0.0570	0.0553	0.0536	0.0518	0.0500	0.0483
$\tilde{z}$	2.25	2.75	3.25	3.75	4.25	4.75	5.25	5.75
$\tilde{q}_x(1,0.25,\tilde{z})$	0.0583	0.0557	0.0533	0.0510	0.0487	0.0463	0.0433	0.0378
$\tilde{q}_x(1,0.75,\tilde{z})$	0.0466	0.0450	0.0434	0.0418	0.0402	0.0385	0.0362	0.0322

Table 4 shows the exact point values of dimensionless source term evaluated for points ($\tilde{x}=0.25$, $\tilde{y}=0.25$, $\tilde{z}$), ($\tilde{x}=0.75$, $\tilde{y}=0.25$, $\tilde{z}$), and ($\tilde{x}=0.75$, $\tilde{y}=0.75$, $\tilde{z}$). Points ($\tilde{x}=0.25$, $\tilde{y}=0.25$, $\tilde{z}$) represent the points at the center of the row of control volumes nearest to the furnace axis. It can be noted that the exact source term distribution follows the physically expected trend, rising steeply from the burner wall onward, going through a maximum and decreasing continuously toward the exit. The maximum of the source term distribution occurs at the same location as the maximum of temperature distribution. The grid points ($\tilde{x}=0.75$, $\tilde{y}=0.25$, $\tilde{z}$) and ($\tilde{x}=0.75$, $\tilde{y}=0.75$, $\tilde{z}$) represent the medium points nearer to the side wall and near the corner of the furnace respectively. It can be seen that the source term values get lower as the walls are approached and near the corner of the enclosure the source term values are almost the same along the length of the furnace. This is consistent with the uniform temperatures in the medium near the corner of the enclosure.

Exact values of the dimensionless flux density to the side wall in positive x direction have been calculated and are shown in Table 5. Points ($\tilde{x}=1$, $\tilde{y}=0.25$, $\tilde{z}$) and ($\tilde{x}=1$, $\tilde{y}=0.75$, $\tilde{z}$) represent points near the center of the face and near the corner of the face respectively. It can be seen that the source term values get lower as the walls are approached and near the corner of the enclosure the source term values are almost the same along the length of the furnace. This is consistent with the uniform temperatures in the medium near the corner of the enclosure.

Exact values of the dimensionless flux density to the side wall in positive x direction have been calculated and are shown in Table 5. Points ($\tilde{x}=1$, $\tilde{y}=0.25$, $\tilde{z}$) and ($\tilde{x}=1$, $\tilde{y}=0.75$, $\tilde{z}$) represent points near the center of the face and near the corner of the face respectively. It can be noted that exact values increase as the gas temperature rises, and decrease as it falls continuously towards the exit.

To provide a global check of the accuracy of the exact solutions, the total rate of removal of radiative energy through the walls and the total rate of generation of radiative energy within the enclosed medium have been evaluated using the exact values of normal radiative flux density at surface grid points and the radiative energy source term at medium grid points. Total rate of generation and removal of radiative energy were found to be the same and equal to 1.424.

5 Conclusions

Exact expressions for the distributions of the components of radiative flux density vector and the radiative energy source term in terms of wall and medium temperature distributions have been formulated for an emitting-absorbing medium of constant properties bounded by black walls of a box-shaped enclosure. These expressions are in the form of sums of triple integrals with respect to one spatial and two angular coordinates. The accuracy of numerical solutions has been tested on an idealized enclosure for which exact analytical solution of the triple integrals is possible. The idealized situation is that of a cubical enclosure containing a medium of optical thickness of unity in thermal equilibrium with its bounding walls. Good accuracy has been obtained. Exact expressions have then been applied to data previously reported on a box-shaped large-scale experimental furnace. Data are characterized by highly nonuniform gas temperature distribution typical of an operating furnace. Exact solutions obtained are limited to rectangular parallelepiped-shaped enclosures containing a grey medium with steep temperature gradients bounded by black walls and the specific input data utilized.

The use of exact solutions for testing purposes provides a means for assessing the accuracy of predictions of approximate radiation models in isolation from the models of flow and reaction and removes the necessity for building and operating expensive experimental rigs to produce measured values.

In papers to follow, the exact solutions produced will be used as a basis for comparative testing of various previously published flux models.

Acknowledgments

The author wishes to express her thanks to NATO for the financial aid to conduct this research.

References

1 Hottel, H. C., and Cohen, E. S., "Radiant Heat Exchange in a Gas-Filled Enclosure: Allowance for Non-Uniformity of Gas Temperature," *AIChE Journal*, Vol. 4, 1958, pp. 3-14.

2 Hottel, H. C., and Sarofim, A. F., *Radiative Transfer*, McGraw-Hill, New York, 1967.

3 Johnson, T. R., and Beer, J. M., "Radiative Heat Transfer in Furnaces: Further Development of the Zone Method of Analysis," *Proceedings of 14th International Symposium on Combustion*, The Combustion Institute, Pittsburgh, PA, 1973, pp. 639-649.

4 Steward, F. R., and Cannon, P., "The Calculation of Radiative Heat Flux in a Cylindrical Furnace Using the Monte-Carlo Method," *International Journal of Heat and Mass Transfer*, Vol. 14, 1971, pp. 245-262.

5 Steward, F. R., Osuwan, S., and Picot, J. J. C., "Heat Transfer Measurements in a Cylindrical Test Furnace," *Proceedings of 14th International Symposium on Combustion*, The Combustion Institute, Pittsburgh, PA, 1973, pp. 651-660.

6 Steward, F. R., and Osuwan, S., "A Mathematical Simulation of Radiative Heat Transfer in a Cylindrical Test Furnace," *Canadian Journal of Chemical Engineering*, Vol. 50, 1972, pp. 450-455.

7 Arscott, J. A., Gibb, J., and Jenner, R., "The Application of N-E Diffusion Theory and Monte-Carlo Methods to Predict the Heat Transfer Performance of a 500 MW Power Station Boiler from Isothermal Flow Data," *Proceedings of 1st European Combustion Symposium*, Academic Press, London, 1973, pp. 674-679.

8 Lowes, T. M., et al., "Prediction of Radiant Heat Flux Distribution," International Flame Research Foundation, Doc. No. G 02/a/26, 1973.

9 Richter, W., and Quack, R., "A Mathematical Model of a Low Volatile Pulverised Fuel Flame," in: *Heat Transfer in Flames*," edited by N. H. Afgan and J. M. Beer, Scripta, Washington, D.C., 1974, pp. 95-110.

10 Patankar, S. V., and Spalding, D. B., "Simultaneous Predictions of Flow Pattern and Radiation for Three-Dimensional Flames," in: *Heat Transfer in Flames*, edited by N. H. Afgan and J. M. Beer, Scripta, Washington, D.C., 1974, pp. 73-94.

11 Siddall, R. G., and Selcuk, N., "Evaluation of a New Six-Flux Model for Radiative Transfer in Rectangular Enclosures," *Transactions of Institution of Chemical Engineers*, Vol. 57, 1979, pp. 163-169.

12 Selcuk, N., "Evaluation of Multi-Dimensional Flux Models for Radiative Transfer in Combustion Chambers: A Review," AGARD Conference Proceedings No. 353, *Combustion Problems in Turbine Engines*, Specialised Printing Services, Essex, 1984, pp. 28/1-28/10.

13 Selcuk, N., and Siddall, R. G., "A New Moment Model for Radiatively Emitting-Absorbing-Scattering Media in Rectangular Furnaces and Combustors," Vth International Symposium on Combustion Processes, Krakow, Poland, 1977.

14 De Marco, A. G., and Lockwood, F. C., "A New Flux Model for the Calculation of Radiation in Furnaces," *La Rivista dei Combustibli*, Vol. 29, 1975, pp. 184-196.

15 Cheng, P., "Exact-solutions and Differential Approximation for Multidimensional Radiative Transfer in Cartesian Coordinate Configuration," *Progress in Astronautics and Aeronautics*, Vol. 31, 1972, pp. 269-308.

16 Razzaque, M. M., et al., "Finite Element Solution of Radiative Heat Transfer in a Two-Dimensional Rectangular Enclosure with Gray Participating Media," ASME JOURNAL OF HEAT TRANSFER, Vol. 105, 1983, pp. 933-936.

17 Crosbie, A. L., and Schrenker, R. G., "Radiative Transfer in a Two-Dimensional Rectangular Medium Exposed to Diffuse Radiation," *J. Quant. Spectrosc. Radiat. Transfer*, Vol. 31, No. 4, 1984, pp. 339-372.

18 Strömberg, L., "Calculation of Heat Flux Distribution in Furnaces," Ph.D. thesis, Department of Energy Conversion, Chalmers University of Technology, Göteborg, Sweden, 1977.

19 Gosman, A. D., et al., *Heat and Mass Transfer in Recirculating Flows*, Academic Press, London, 1969.

Pool Boiling Heat Transfer in Narrow Horizontal Annular Crevices

Ying-Huei Hung[1]
Associate Professor.
Dept. of Power Mechanical Engineering,
National Tsing Hua University,
Taiwan, Republic of China

Shi-Chune Yao
Professor.
Department of Mechanical Engineering,
Carnegie-Mellon University,
Pittsburgh, PA 15213
Mem. ASME

Experimental results of the pool boiling in horizontal narrow annuli are reported. The effects of fluid properties, pool subcooling, crevice length, and gap size on the boiling behavior and the critical heat flux (CHF) are also studied. The CHF decreases with decreasing gap size or increasing length of the annuli. The lower CHF of narrow crevices may be explained by the thin film evaporation. A semi-empirical correlation is established for the CHF of pool boiling in horizontal confined spaces. This correlation is compared with the CHF data of the present experiment. Satisfactory agreement is obtained.

Introduction

Boiling at the shell side of tube-and-shell heat exchangers, evaporators, and reboilers in the power and chemical processing devices has received substantial attention in the past. Boiling may also occur in the annular crevice between the baffle plate and the heating tube. The boiling phenomena and the critical heat flux in confined vertical annuli with closed bottom have been studied by Yao and Chang [1, 2]. The forced convective boiling in vertical confined annuli has been studied by Hung and Yao [3]. Presently, the boiling phenomena and the critical heat flux of confined annuli at horizontal orientation are studied in this paper.

Saturated pool nucleate boiling on single tubes and horizontal plates has been extensively studied. Interest has been extended to nucleate boiling heat transfer in restricted geometries. Katto and Yokoya [4, 5] and Katto et al. [6] investigated the nucleate pool boiling between two restricted horizontal plates. A movable artificial restriction, which is an optical assembly including an interference plate and a device for observation, was placed above the heated surface. It was found that the CHF decreased with decreasing gap size. At the same heat flux, the wall temperature is invariable while the interference plate is placed comparatively apart from the heated surface (with gap size larger than 2.0 mm), but the wall temperature falls as the gap size is reduced and thereafter rises when the gap size is reduced further. The dryout mechanism is suggested as a phenomenon occurring when there is an imbalance between the consumption of the liquid by evaporation on heated surface and the supply of liquid through the intermittent jetting of vapor.

Improved heat transfer characteristics with the restriction might be attributed to an increase in the heat transfer coefficient due to vaporization from the thin liquid film on the heating surface [4,7] or increased bubble activity [8]. Jensen, Cooper, and Bergles [7] performed experiments of saturated water pool boiling at atmospheric pressure in horizontal annuli utilizing an electrically heated inner surface. Crevice heat transfer coefficients were as much as 230 percent greater than those measured for conventional pool boiling. The increase in the heat transfer was explained by the thin film evaporation. The critical heat flux was found to be directly proportional to the gap size and inversely proportional to the length of annulus. However, Jensen et al. [7] did not report detailed visual observations in the narrow crevice.

As for the visual investigation of pool boiling phenomena, the existing literature is very limited. Ishibashi and Nishikawa [9] studied the saturated pool boiling heat transfer in a vertical narrow annulus with both ends open. They observed that there is a remarkable difference of heat transfer between the coalesced bubble regime and the isolated bubble regime. These regimes were separated by a critical gap size, which varied with fluid properties. The isolated bubble regime was present in larger crevices. Below the critical crevice dimension, the coalesced bubble regime was observed. Yao and Chang [1] presented a series of systematic investigations of pool boiling heat transfer in vertical narrow annuli with closed bottoms. They found that the Bond number is important in characterizing the boiling behavior in confined spaces. However, no systematic visual observations of pool boiling heat transfer in horizontal narrow annuli can be found in open literature.

The objectives of this paper are to establish a systematic data base of pool boiling heat transfer in horizontal annuli with various working fluids and provide the explanation of the physical phenomena; and to develop a correction for the CHF prediction in horizontal annular crevices.

Experimental Apparatus and Procedure

The liquid pool is established in a Pyrex tube of 101.6 mm i.d. and 457.5 mm length with both ends closed. Temperature of the pool is maintained by an immersion heater, which is adjusted by a Variac. The system is kept at atmospheric pressure and monitored by a pressure gauge. The generated vapor in the experiments is released and condensed before flowing back to the equalizer.

A schematic of the test section is shown in Fig. 1. The heated section is a stainless steel 304 seamless tubing with 0.71 mm wall thickness, 25.4 mm o.d., and 101.6 mm heated length. The direct current passing through the heated tube is provided by two d-c power supplies of different capacities.

The hollow quartz cylinders are ground to an o.d. of 63.5 mm with i.d. 26.04, 27.00, and 30.56 mm, respectively, to form different gap sizes with respect to the heated tube with the use of spacers. Both the inside and the outside surfaces of the quartz are polished to a 50-80 finish to permit visual observation of the annular crevice. Four types of annuli are formed in the present experiments. Three of them are 76.2 mm long with the gap sizes of 0.32, 0.80, and 2.58 mm, respectively. The fourth annulus is 25.4 mm long with a gap size of 0.32 mm. Due to the symmetry, a long annulus could also be considered as an approximation of an annular crevice with one end closed at the tube sheet but only half the length.

A pair of J-type stainless-steel-sheathed, ungrounded thermocouples of 0.81 mm diameter are pressed against the

[1]The work was performed when the first author conducted his graduate study in Carnegie-Mellon University.

Contributed by the Heat Transfer Division for publication in the JOURNAL OF HEAT TRANSFER. Manuscript received by the Heat Transfer Division October 3, 1983.

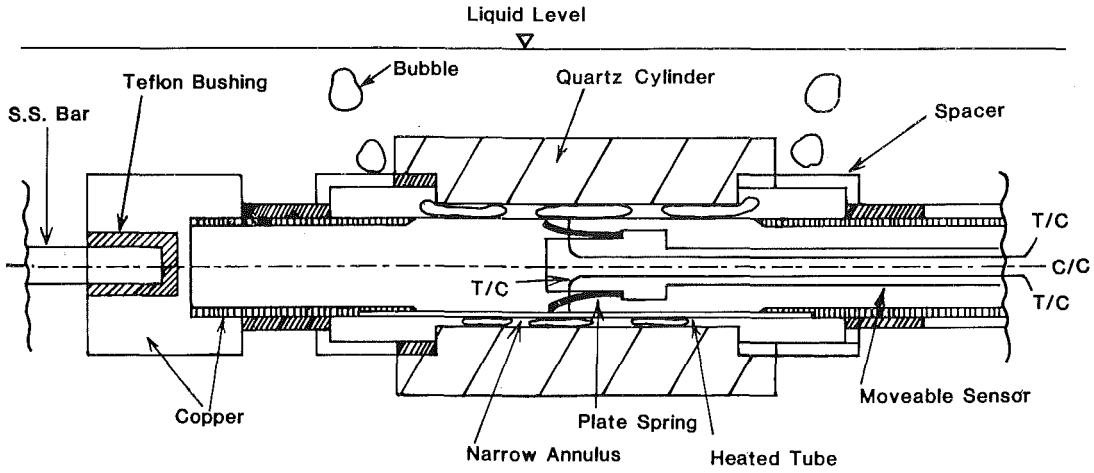

Fig. 1 Schematic of test section

inner wall by plate springs with a force of 2.6N. The location of the thermocouples can be traversed axially or rotated circumferentially. The outer surface temperature of the tube is calculated based upon one-dimensional steady-state heat conduction [10, 11]. The heated surface is polished before each test with a #320 sandpaper. The calibrated thermocouples are recorded by an Accurex Autodata Temperature Logger (model Ten/5) with the accuracy of $\pm 0.1\,^{\circ}C$.

Before each experiment the test section is preheated and preboiled for at least one hour at a low heat flux. The preheating for water test required much longer time than other fluids to remove the entrapped air bubbles. The steady-state data are taken after 3 min for any change of heat flux. When the critical heat flux is reached a temperature excursion occurs. The heating power is terminated before the surface temperature reaches more than 120°C.

Results and Discussion

The experiments are performed with freon-113, acetone, and distilled water at atmospheric pressure. The effects of fluid properties, gap size, crevice length, and subcooling on boiling curves and critical heat flux have been investigated. Circumferential wall temperature distributions are measured. In all the experiments, the dryout starts at the top-center point of the heated tube. This is because at very high heat flux the top-center portion is difficult to rewet by incoming liquid [7, 12]. Therefore, all the data in the present report are measured with the movable thermocouple at the top-center position of the heated tube. In addition to these measurements, a 16 mm color movie series is edited as a record of the observations.

In this section, the characteristics of the boiling curves will be reported in detail. Then the effects of measuring location, crevice length, and pool subcooling will be discussed. The results of line-contact configuration are also presented. Finally, a semi-empirical formula is proposed for critical heat flux predictions.

(a) Characteristics of the Boiling Curves

Single-Phase Natural Convection. The natural convection around a horizontal heated circular cylinder in the range ($10^4 \le Gr \le 3\times 10^8$) was studied by Hermann [13] and Jodlbauer [14]. They concluded that the Nusselt number is proportional to $(Gr)^{1/4}$, where Gr is based on the diameter of cylinder. That is, the heat flux q is proportional to $(T_w - T_a)^{5/4}$. Therefore, the relationship becomes

$$q = C(T_w - T_{sat})^{5/4} \tag{1}$$

The experimental data of single-phase natural convection of a free single tube without restriction in saturated freon-113 before boiling inception is shown as the "open tube" symbols in Fig. 2. The C value in equation (1) is found to be 0.125 for freon-113.

Nomenclature

Bo = Bond number for the gap, defined in equation (2)
C = a constant defined in equation (1)
CHF = critical heat flux
d_i = outside diameter of the heated tube (mm)
$\bar{f}$ = two-phase friction factor
Gr = Grashof number, $\beta_l g(T_w - T_a)d_i^3/\nu_l^2$
g = acceleration of gravity (m/s^2)
L = length of the crevice (mm)
$\dot{m}_g$ = mass flow rate, defined in equation (5) (kg/s)
q = heat flux (kW/m^2)
q_{CHF} = critical heat flux (kW/m^2)
q_{kut} = critical heat flux predicted by Kutateladze's correlation for a horizontal wire, defined in equation (9) (kW/m^2)
r_1 = d_i/δ
T_a = ambient temperature (°C)
T_{sat} = saturated temperature of the fluid (°C)
ΔT_{sat} = $T_w - T_{sat}$ (°C)
T_w = wall temperature of the heated tube (°C)
v_g = vapor velocity at the exit of the crevice (m/s)
w = width of baffle, defined in [7] (mm)
y = coordinate measured in axial direction, defined in Fig. 10(*a*)
α_v = mean void fraction, the range between 0 and 1
β_l = thermal expansion coefficient of liquid ($°C^{-1}$)
δ = gap thickness of the crevice (mm)
λ = latent heat of vaporization (J/kg)
μ_g = viscosity of vapor phase (kg/ms)
μ_l = viscosity of liquid phase (kg/ms)
ν_l = kinematic viscosity of liquid (m^2/s)
θ_p = angle measured from the top of the heated tube (deg)
ρ_l = density of liquid phase (kg/m^3)
ρ_g = density of vapor phase (kg/m^3)
σ = surface tension of liquid phase (N/m)

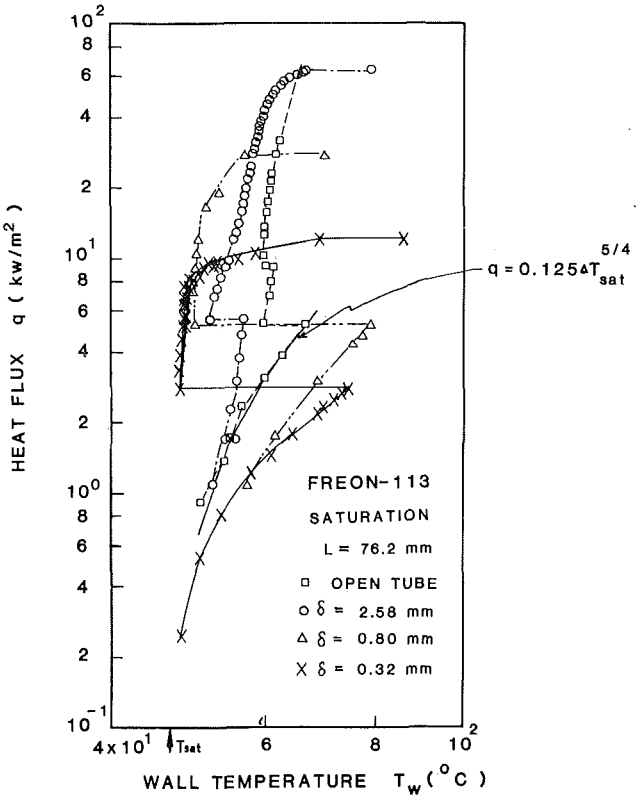

Fig. 2 Boiling curves of freon-113 at saturated condition

Boiling Inception. When heat flux is increased an overshoot of the wall superheat beyond saturation happens before the inception of the boiling. In the present experiment two different kinds of incipient boiling are observed: local incipient boiling which stays at the top of the heated tube, and the overall incipient boiling which propagates simultaneously over the whole tube.

For the tests of freon-113 and acetone with 2.58 mm gap size and open tube, the local incipient boiling occurs first, then the overall boiling happens at a higher heat flux. For the tests using distilled water the phenomenon of local incipient boiling is usually not observed. The stability of the local incipient boiling in horizontal annular crevices could be related to their Bond number, which relates the gap size and the capillary constant (see Table 1).

$$\mathrm{Bo} = \frac{\delta}{[\sigma/g(\rho_l - \rho_g)]^{1/2}} \tag{2}$$

Before the boiling inception, the top portion of the heated tube, where the temperature is comparatively high, will be more likely to initiate the boiling. For the case of $\mathrm{Bo} \geq 1.0$, after boiling inception the bubbles are close to spherical and they flow away easily. When the heat flux is gradually increased, the bubbles may also be initiated at the bottom portion of the tube in which overall boiling occurs.

For the case of $\mathrm{Bo} < 1.0$, the generated bubbles are usually deformed in the gap. This phenomenon is also observed in [1]. During the boiling inception the bubbles expand into the form of isolated-deformed bubbles and propagate in the gap. Then they coalesce over the whole heated surface. Therefore, only the overall boiling inception is observed.

Nucleate Pool Boiling. At nucleate boiling the temperature profile on the tube is found to be rather uniform. The nucleate boiling curves of the experiments are shown in Figs. 3, 4, and 5. At a same heat flux, the wall temperature is decreased with decreasing gap sizes except for the cases of acetone and distilled water with the smallest gap of 0.32 mm. The shaded area in these figures denotes the range of wall temperature oscillations.

The increased heat transfer within the narrow crevices might be attributed to the increased bubbble activity [8] and the vaporization of the thin film on the heated surface [7, 9]. In confined spaces, at a fixed heat flux, the mass of vapor generated is constant so that with decreasing gap size higher vapor velocities are induced. With the increased vapor velocities, the shear stress on the liquid film at the heated surface increases and the liquid film is reduced in thickness. Since the major heat transfer resistance is the heat conduction across the liquid film, the reduced film thickness increases the heat transfer coefficient.

In the present experiments of acetone and distilled water with gap size of 0.32 mm and high heat flux, the wall temperature is higher than that in the cases of gap sizes of 0.80 and 2.38 mm as shown in Figs. 4 and 5. This is because the intermittency of partial dryout and rewetting due to fluid oscillation leads to a wall temperature oscillation (shaded area in figures) and a higher wall temperature. It is interesting to point out that the wall temperature oscillation occurs when the Bond number is less than 0.3 while the bubbles are deformed severely in the crevices. Similar phenomenon has been observed by Katto et al. [4], Jensen et al. [7], and Yao et al. [1].

Critical Heat Flux. The critical heat flux of a tube without restriction is not obtained due to the limitation of the power supply in the experiment. At high heat fluxes, because of the space restriction, numerous coalesced vapor bubbles occur, grow, and spread over the top portion of the heated surface. The top portion of the heated surface is therefore wet by a thin liquid film while the vaporization takes place and liquid can not be supplied easily to the heated surface. The bubbles grow continuously until one of the following two situations occurs: The liquid film underneath the expanding bubble evaporates completely and thereby terminates the driving force for growth, or the bubble grows to such a size that it extends beyond the edge of the restriction. Then the buoyancy causes the bubble to detach from the crevice. Eventually more liquid flows into the crevice and rewets the top portion of the surface. The same cycle starts again. As the heat flux is increased, dry spots begin to appear at the end of the cycle. The vapor flow becomes rather steady with small amount of oscillation imposed upon it. The steady flow is driven by the natural convective type buoyancy of the two-phase mixture in the crevice; the oscillation is related to the bubble detachment at the edge of the crevice. If liquid does not rewet the surface within a certain time, the temperature of the dried portion may become high enough to initiate dryout earlier in the next cycle. Therefore, the CHF occurs. With the fluid circulation retarded when the gap is reduced, rewetting of the heated surface will be more difficult and the CHF becomes lower. The present CHF data at saturated condition are listed in Table 1.

(b) Effect of Measuring Location. Typical boiling curves measured at the top and the bottom positions of the heated tube are compared in Fig. 6. This is the case in which Bond number is less than unity and overall boiling occurs in the gap at the boiling inception. Before the boiling inception the heat transfer at the bottom of the heated tube is higher. At the overall boiling inception, the temperature decrease at the top is more than that at the bottom. After the boiling inception, the heat transfer at the top portion is dominated by thin film evaporation, and the heat transfer coefficient is therefore higher than that at the bottom. As heat flux is further increased, the thin liquid film underneath the squeezed bubbles may dry up easily. Finally, permanent dryout at the top may occur and an early CHF is reached.

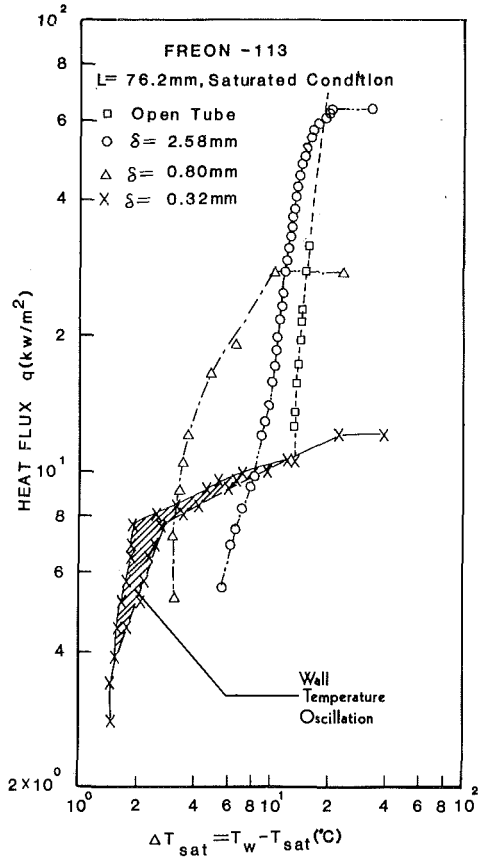

Fig. 3 Nucleate boiling curves of freon-113 (the hatched area indicates oscillation of temperatures, here and in the other figures)

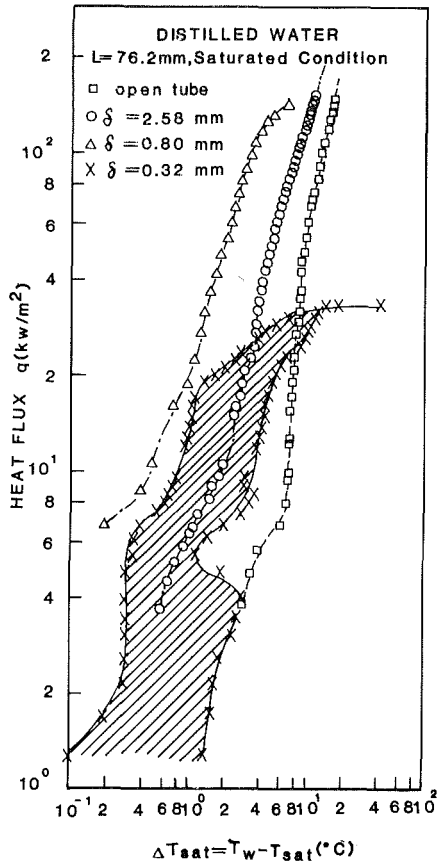

Fig. 5 Nucleate boiling curves of distilled water

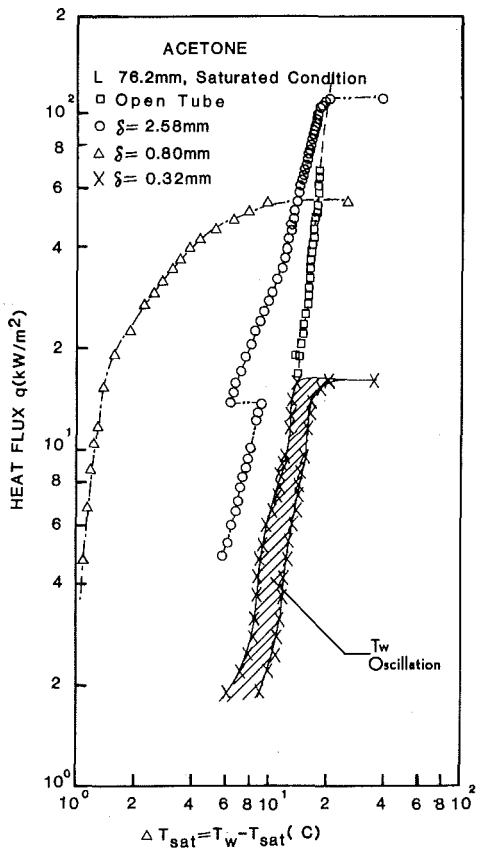

Fig. 4 Nucleate boiling curves of acetone

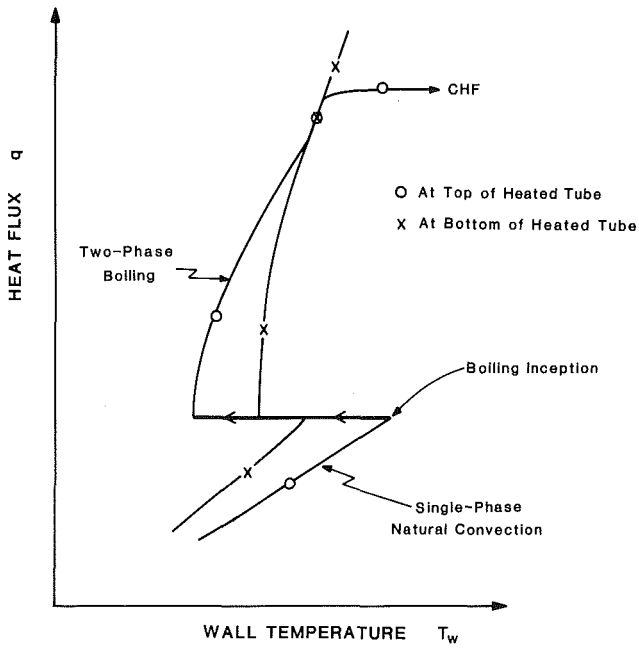

Fig. 6 Typical behavior of the boiling curve

(*c*) **Effect of Crevice Length.** In the experiments of freon-113 with gap size of 0.32 mm, as the length of crevice is decreased from 76.2 mm to 25.4 mm, the overall boiling curve is changed as shown in Fig. 7. The single-phase natural convective heat transfer of long crevice is lower than that of the short crevice due to the higher resistance of the flow. After the boiling inception, the local nucleate boiling heat transfer at the top-center of long crevice length is higher mainly

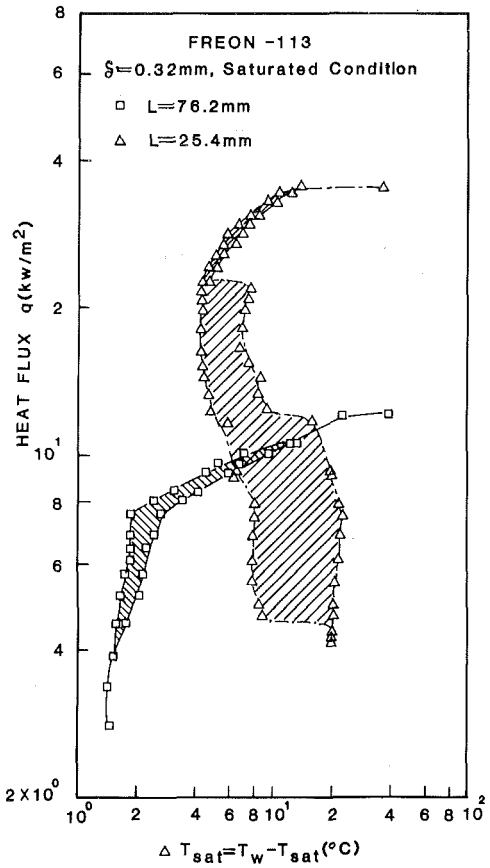

Fig. 7 Boiling curves of $\delta = 0.32$ mm with various crevice lengths

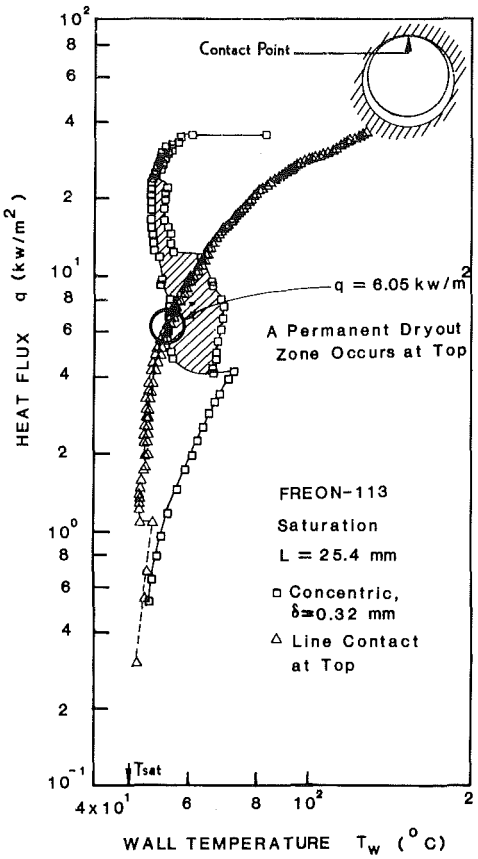

Fig. 9 Boiling curve of line-contact at the top of heated tube

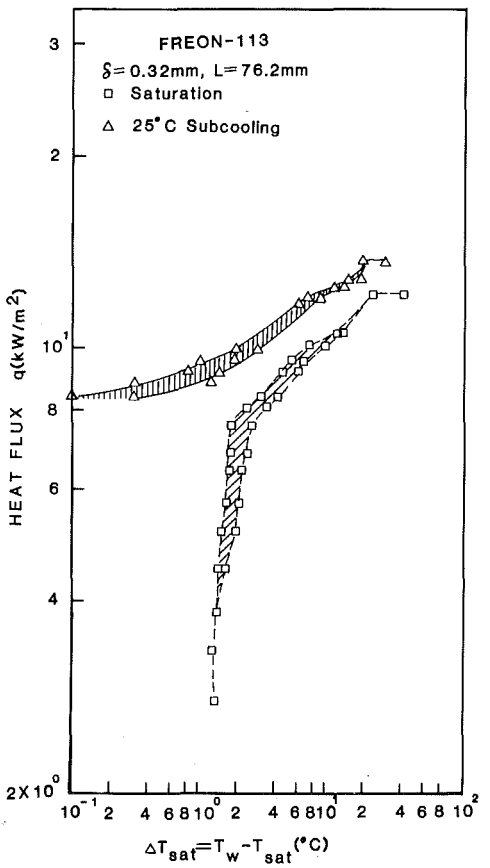

Fig. 8 The effect of pool subcooling on nucleate boiling curve

because the heat transfer at the top is dominated by thin film evaporation. At higher heat flux, it is difficult to rewet the top-center portion of the long crevice, then the CHF of the longer crevice occurs at a lower heat flux. The wall temperature oscillation of the long crevice is much less than that of the short crevice because the long vapor flow passage tends to stabilize the oscillation.

(d) **Effect of Pool Subcooling.** In the subcooled tests, the quasi-steady pool temperature is kept at 25°C subcooling with the crevice gap size of 0.32 mm. The boiling curve in subcooled conditions is compared with that of saturated condition in Fig. 8. As expected, at the same wall superheat, the heat flux is higher for subcooled boiling.

(e) **Boiling Curve of the Line-Contact Configuration.** Figure 9 shows the boiling curve for the configuration of line-contact of the heated tube and the quartz shroud at the top of the eccentric crevice. When heat flux is increased to 6.05 kW/m^2, a permanent dryout zone is observed at the top contacted location. According to the experimental results by Baum and Curlee [15], the occurrence of permanent dryout in some steam generators may lead to local chemical concentration buildup, and the consequent corrosion. As shown in Fig. 9, the heat flux, which leads to permanent dryout when a line-contact occurs, is much less than the CHF of the corresponding situation with concentric configuration of the annulus. On the other hand, due to the significant capillary effect and high flow-resistance near the contact line, the alternate wetting and drying does not occur, and at high heat flux the wall superheat is high but does not lead to an early critical heat flux.

Since the CHF always occur at the top of the annular crevice, when the line-contact at bottom is considered the CHF will be expected to be higher than the concentric annulus condition.

Table 1 The range of Bond number and the CHF data in the present experiments

Tube	O.D. : 25.4 mm Thickness : 0.71 mm Material : Stainless Steel 304 Seamless Tubing
Operating Pressure	1 atm
Pool Temperature	Saturation T_{sat} = 47.6C (F-113), 56.2C (Acetone)

Working Fluid	L (mm)	δ (mm)	Bo	Exp. q_{CHF} (kw/m^2)	Pred. q_{CHF} (kw/m^2) Ref. 7	Pred. q_{CHF} (kw/m^2) Present	% Error Present
Freon-113	76.2	0.32	0.30	12.2	17.5	9.5	-22.5
Freon-113	76.2	0.80	0.74	27.8	36.6	26.2	-5.7
Freon-113	76.2	2.58	2.38	63.7	98.2	63.0	-1.1
Freon-113	25.4	0.32	0.30	35.7	41.5	48.9	37.2
Acetone	76.2	0.32	0.20	16.1	30.8	11.3	-29.6
Acetone	76.2	0.80	0.50	55.0	64.6	35.3	-35.8
Acetone	76.2	2.58	1.60	110.5	173.3	100.3	-9.2
Acetone	25.4	0.32	0.20	94.7	73.2	59.0	-37.7
Distilled Water	76.2	0.32	0.13	33.9	58.4	43.6	28.8

(f) **Semi-empirical CHF Correlation.** A correlation has been developed by Jensen et al. [7] relating the critical heat flux to the geometry of the horizontal tube-baffle crevice and fluid properties. Using a least-square fit, the following empirical equation was obtained

$$\left[\frac{q_{\mathrm{CHF}} L r_1^{\,2}}{4\lambda\mu_g(r_1+1)}\right]\left[\frac{\rho_l-\rho_g}{\rho_g}\right]^{0.78}=2.994\times10^5\left[\frac{\delta}{L}\right]^{-0.213} \tag{3}$$

A comparison of equation (3) with the present CHF data is shown in Table 1. The prediction of equation (3) shows satisfactory agreement with the present data for the small gap of 0.32 mm and the short crevice length of 25.4 mm, but this equation is not adequate for the long crevices. This is because the test conditions in [7] correspond to the cases of the small gap size and short crevice length in the present experiments. In order to predict the CHF in a wide range of the present data, a semi-empirical modeling is established. For this reason, a crude model will be established to lay out the relationship of various parameters.

The schematic of the test section is shown in Fig. 10(*a*). Due to the symmetry, the analysis has only to apply for a quarter portion of the whole annulus. The flow channel for the present analysis is shown in Fig. 10(*b*). The gap size is generally assumed much smaller than the radius of heated tube such that the curvature of the crevice can be neglected. The present model is a simplified representation of a complicated process, and is more realistic when the annular crevice is long. It is also important to point out that although the flow is oscillatory when the crevice is very narrow and the heat flux is low, the flow is usually steady when the CHF is approached (see Figs. 3, 4, 5, etc.). The flow channel of the crevice is split into two flattened regions as shown schematically in Fig. 10(*b*) with the additional assumptions:

1 The flow is driven by the buoyancy in Region I, and balanced by the viscous drag force in Region II. (For long crevices, the viscous effect in Region I could be negligible due to the wide flow passage and low quality and velocity.)

2 The fluid quality at the bottom of the annulus is zero. When the critical heat flux occurs the fluid quality at the upper exit of the annulus is unity.

3 The overall cross-sectional area where the vapor flows out at the top portion of the annulus (Region II) is a constant. In the present study of a fixed tube diameter, it is observed from the movies that the smaller the annular gap the wider Region II. The flow vapor cross section is therefore set as $2a$.

Following assumptions (1) and (2), the balance of the buoyant driving force and the frictional force can be expressed as

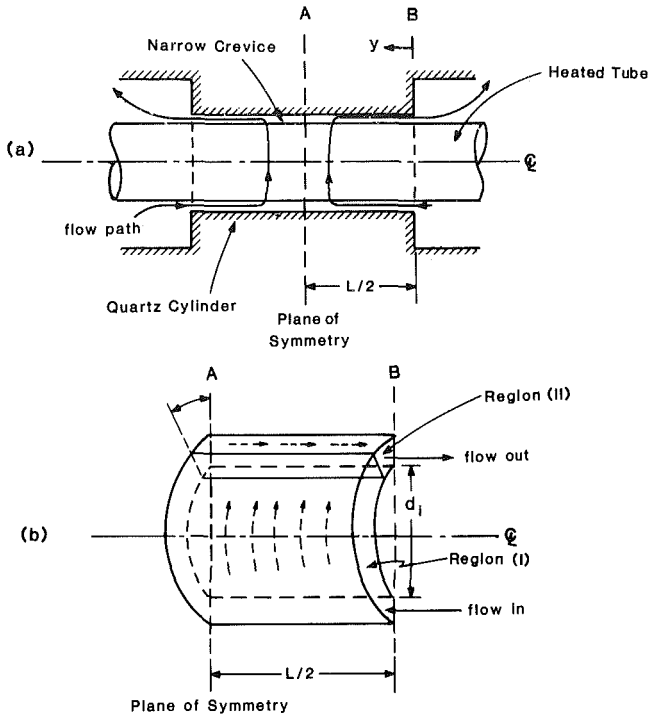

Fig. 10 Schematics of the model for the CHF prediction

$$\alpha_v(\rho_l-\rho_g)gd_i=\bar{f}\left[\frac{L/2}{2\delta}\right]\left[\frac{\rho_g v_g^{\,2}}{2}\right] \tag{4}$$

where α_v is the mean void fraction in Region I. In this analysis, we assume $\alpha_v = 1/2$.

The mass flow rate of the vapor at the exit is

$$\mathring{m}_g=\rho_g v_g a \tag{5}$$

The critical heat flux can be obtained from the conservation of energy, that is

$$\mathring{m}_g\lambda=q_{\mathrm{CHF}}\left(\frac{L}{2}\right)\left(\frac{\pi d_i}{2}\right) \tag{6}$$

The v_g used in equation (5) can be solved from equation (4). The $\mathring{m}_g$ of equation (5) is then used in equation (6). Finally, the predicted CHF q_{CHF} becomes

$$q_{\mathrm{CHF}}=\frac{4a}{\delta d_i\Pi(\bar{f})^{1/2}}\left[(\rho_l-\rho_g)gd_i\rho_g\right]^{1/2}[\delta/L]^{3/2}\lambda \tag{7}$$

This can be converted to

$$q_{\mathrm{CHF}}=F(\bar{f})\left[\mathrm{Bo}^{1/2}\left(\frac{d_i}{L}\right)^{3/2}\right]q_{\mathrm{kut}} \tag{8}$$

where q_{kut} is the critical heat flux predicted by Kutateladze's correlation for a horizontal wire in liquid pool [16]

$$q_{\mathrm{kut}}=K^{1/2}\lambda\rho_g{}^{1/2}[\sigma g(\rho_l-\rho_g)]^{1/4} \tag{9}$$

with the average value of $K^{1/2}$ set at 0.14. Also

$$F(\bar{f})=\frac{4a}{\Pi d_i^2}\left(\frac{1}{K\bar{f}}\right)^{1/2} \tag{10}$$

In the present data base the d_i is fixed. The $F(\bar{f})$ is a function of the two-phase friction factor. The two-phase friction factor $\bar{f}$ is dependent upon ρ_l and ρ_g [17], and it is also affected by Bond number for narrow annuli due to the severe bubble deformation in crevices. Therefore, the function F can be expressed in the nondimensional form

$$F(\bar{f}) = F\left(\frac{\rho_g}{\rho_l}, \text{Bo}\right) \tag{11}$$

The semi-empirical function F was then determined from the best fit to the present data of experiments. That gives

$$F(\bar{f}) = 0.064\left(\frac{\rho_l}{\rho_g}\right)^{0.5}(1 - e^{-1.8\text{Bo}}) \tag{12}$$

Finally, the present semi-empirical correlation is obtained from equations (8), (9), and (12).

Typically, the CHF of the studied crevices are one order of magnitude less than the CHF of open tubes predicted by Kutateladze. The experimental data and the prediction of this semi-empirical formulation have been compared in Table 1. The average error is 23 percent with a maximum error of 38 percent. When the length of crevice is short the error tends to be bigger. This is because the applicability of the model and assumptions is more suitable for a long crevice. It is important to point out that this formulation is semi-empirical. Refinements could be made to the assumptions of the modeling, to further improve the generality of the results.

Conclusions

1 After the overall boiling inception, the boiling heat transfer at the top portion of the heated tube is possibly dominated by thin film evaporation. More effective nucleate boiling heat transfer is observed when the gap of crevices is reduced. The critical heat flux always occurs at the top-center point of the heated tube. The CHF decreases with decreasing gap size or increasing length of the annuli. The mechanism of CHF in confined spaces is related to the dryout of the thin liquid film on the heated surface.

2 Sustained flow oscillation and wall temperature oscillation are observed in the tests of 0.32 mm gap size. This is due to the intermittency of partial dryout and rewetting in narrow crevices.

3 Boiling phenomena of an eccentric annulus with the configuration of line-contact at the top of heated tube are investigated. A permanent dryout zone occurs at the top portion of the heated tube at low heat flux but it does not lead to early burnout due to the significant capillary effects at the contact line.

4 The critical heat flux in the studied crevices is typically one order of magnitude less than that of a free tube. A model has been developed, and a semi-empirical correlation has been established. The comparison between this correlation and the present CHF data has been made with reasonable agreement.

Acknowledgments

The authors are grateful for the support of the Office of Naval Research (N00014-79-C-0623) in performing this study.

References

1 Yao, S. C., and Chang, Y., "Pool Boiling Heat Transfer in Confined Spaces," *Int. J. Heat Mass Transfer*, Vol. 26, No. 6, 1983, pp. 841–848.

2 Yao, S. C., and Chang, Y., "Critical Heat Flux of Vertical Narrow Annuli With Closed Bottoms," ASME JOURNAL OF HEAT TRANSFER, Vol. 105, 1983, pp. 192–195.

3 Hung, Y. H., and Yao, S. C., "Critical Heat Flux of Convective Freon-113 in Very Narrow Annuli," ASME Paper No. 83-HT-10, 21st National Heat Transfer Conference, Seattle, WA, July 24–28, 1983.

4 Katto, Y., and Yokoya, S., "Experimental Study of Nucleate Pool Boiling in Case of Making Interference-Plate Approach to the Heating Surface," *Proc. Third International Heat Transfer Conference*, 1966, pp. 219–227.

5 Katto, Y., and Yokoya, S., "Principle Mechanism of Boiling Crisis in Pool Boiling," *Int. J. Heat Mass Transfer*, Vol. 11, 1968, pp. 993–1002.

6 Katto, Y., Yokoya, S., and Ysunaka, M., "Mechanism of Boiling Crisis and Transition Boiling in Pool Boiling," *Proceedings of the Fourth Int. Heat Transfer Conference*, Vol. 5, B3.2, 1970.

7 Jensen, M. K., Cooper, P. E., and Bergles, A. E., "Boiling Heat Transfer and Dryout in Restricted Annular Geometries," AIChE 16th National Heat Transfer Conference, Paper No. AIChE-14, 1976, pp. 205–213.

8 Plevyak, T. J., "Improved Boiling Heat Transfer With Induced Vapor Bubble Mixing," ASME Paper No. 68-WA/HT-29, 1968.

9 Ishibashi, E., and Nishikawa, K., "Saturated Boiling Heat Transfer in Narrow Space," *Int. J. Heat Mass Transfer*, Vol. 12, 1969, pp. 863–894.

10 Lung, H., Latsch, K., and Rampf, H., "Boiling Heat Transfer to Subcooled Water in Turbulent Annular Flow," *Heat Transfer in Boiling*, Chapter 10, Hemisphere Publishing Corporation, Washington, 1977, pp. 219–235.

11 Hennecke, D. K., and Sparrow, E. M., "Local Heat Sink on a Convectively Cooled Surface—Application to Temperature Measurement Error," *Int. J. Heat Mass Transfer*, Vol. 13, 1970, pp. 287–304.

12 Costello, C. P., and Frea, W. J., "A Salient Nonhydrodynamic Effect on Pool Boiling Burnout of Small Semicylindrical Heaters," *Chemical Engineering Progress Symposium Series*, Vol. 61, No. 57, 1965, pp. 258–268.

13 Hermann, R., "Wärmeübertragung bei frier Strömung am waagerechten Zylinder in zweiatomigen Gasen," *VDI-Forschungsheft*, 1936, p. 379.

14 Jodlbauer, K., "Das Temperatur- und Geschwindigkeitsfeld um ein geheiztes Rohr bei freier Konvektion," *Forschg. Ing.-Wes.*, Vol. 4, 1933, pp. 157–172.

15 Baum, A. J., and Curlee, N. J., Jr., "An Experimental and Analytical Investigation of Dryout and Chemical Concentration in Confined Geometries," ASME Nuclear Eng. Division Conference, San Francisco, August 18–21, 1980.

16 Kutateladze, S. S., "Heat Transfer in Condensation and Boiling," USAEC Report AEC-tr-3770, 1952.

17 Collier, J. G., *Convective Boiling and Condensation*, McGraw-Hill, London, 1972, pp. 28–32.

Axially Varying Vapor Superheats in Convective Film Boiling

D. Evans

S. W. Webb
Mem. ASME

J. C. Chen
Fellow ASME

Institute of Thermo-Fluid Engineering and Science,
Lehigh University,
Bethlehem, PA 18015

Axially varying vapor superheats in convective film boiling have been measured for water flowing in a vertical tube at low to moderate pressures and mass flow rates. Using a slow "reflood" process, measurements of wall temperature and nonequilibrium vapor temperature were obtained as functions of distance from the quench front. With the low quench front velocity, the time required to progapate the front a few millimeters corresponds to many fluid residence times, and the thermal hydraulic data thus obtained are quasi-steady state. These experimental results indicate a zone near the quench front where the vapor generation rate is relatively high, followed by a far zone where the generation rate drops off to a relatively low magnitude. The data obtained agree with the very limited previously reported steady-state data. Comparison with existing heat transfer models shows the models give poor predictions of vapor superheats but reasonable predictions of wall heat fluxes.

Introduction

Convective boiling beyond critical heat flux (CHF) is encountered in such applications as cryogenic systems, metallurgical processing, steam generators, and nuclear reactor loss-of-coolant accidents. In a number of these situations, post-CHF boiling occurs with very high vapor void fractions wherein dispersed two-phase flow occurs in the heated channels. In this regime, termed convective film boiling, the two-phase mixture may exist in a nonequilibrium thermodynamic state with superheated vapor entraining drops or globules of saturated liquid. In this situation, the actual vapor quality is not equal to the thermodynamic equilibrium quality but is related to it by the following equation

$$\frac{X_a}{X_e} = \frac{i_{fg}}{i_v(P,T_v) - i_{ls}} \tag{1}$$

Analysis of this two-phase heat transfer problem requires solution of the vapor continuity and energy equations, which in steady-state, one-dimensional form can be written as

$$G\,dX_a = \Gamma\,dZ \tag{2}$$

$$q''_w P_H dZ = GA\,i_{fg} dX_e \tag{3}$$

In these equations, gamma (Γ) is defined as the volumetric vapor source term representing mass of liquid evaporated per unit time per unit mixture volume.

At the present time, the state of knowledge is lacking in the constitutive relations required to estimate the magnitude of the vapor source term Γ. As noted by many researchers [1-5, 16], the evaporative source intensity results from the simultaneous competitive heat transfer between the hot wall surfaces and the vapor and liquid phases, and between the superheated vapor and liquid phases. Preliminary models for estimating Γ have been proposed, including those of Saha [2] and of Webb and Chen [3]. The assessments of the available gamma models, and the development of improved models, are hampered by a lack of experimental data on the degree of thermodynamic nonequilibrium in convective film boiling.

A number of experiments on convective film boiling have been conducted over the past twenty years. However, due to the extreme difficulty of measuring superheated vapor temperature in the presence of dispersed liquid, only a few attempts to quantify the degree of thermodynamic nonequilibrium have been reported. Mueller [4] and Polomic [5] obtained some limited data at high vapor qualitites in a tube. Hochreiter [6] obtained some indications of vapor superheats in rod bundles, limited primarily to high vapor quality conditions [7]. Recently, Nijhawan et al. [8, 9] successfully used an aspirated thermocouple probe to obtain measurements of vapor superheats at one axial location for convective film boiling in a tube. Gottula et al. [10] extended Nijhawan's technique to obtain simultaneous measurements of vapor superheats at three axial locations for convective film boiling in a tube. Annunziato et al. [11] reported actual flow qualities in convective film boiling by measuring the bulk temperature with exposed thermocouples in low mass flow, atmospheric pressure experiments. To date, the available data base for nonequilibrium flow film boiling is rather sparse, especially with regard to information on the axial variation of nonequilibrium vapor temperatures and flow qualities. Such data are needed for the development of constitutive models for the vapor source term Γ.

Measurements of the axial variation of vapor superheat would ideally be obtained under steady-state conditions downstream from a fixed-critical-heat flux (CHF) location. This of course requires the placement of multiple vapor probes along the axial direction of the heated channel and also requires that the location of the CHF point be held constant with time. This is the approach attempted by Gottula et al. [10]. However, experimental difficulties associated with fixing the location of CHF limit this approach to relatively high vapor quality cases.

The present investigation takes a different experimental approach to obtain information on vapor superheats as a function of axial distance from the CHF quench front. In this approach, starting with the test section in a flow-film-boiling state, the CHF location is permitted to slowly propagate as a quench front up the length of the test section. By restricting the quench front propagation to low velocities, such that the displacement distance of CHF location is negligible during a fluid residence period in the test section, the thermal hydraulic conditions downstream of the CHF location exist in a quasi-steady state. Theoretical analysis of transient convective heat transfer [12, 13] have clearly shown that heat transfer coefficients downstream from an inlet perturbation essentially attain steady-state conditions within one to two fluid residence periods. Therefore, by providing for a minimum of five to ten fluid residence periods in the time that it takes the CHF quench front to propagate a small acceptable distance (of the order of 1 cm), it was possible to obtain quasi-steady-state heat transfer measurements downstream of the CHF

Contributed by the Heat Transfer Division and presented at the 21st National Heat Transfer Conference, Seattle, Washington, July 24-27, 1984. Manuscript received by the Heat Transfer Division September 7, 1983.

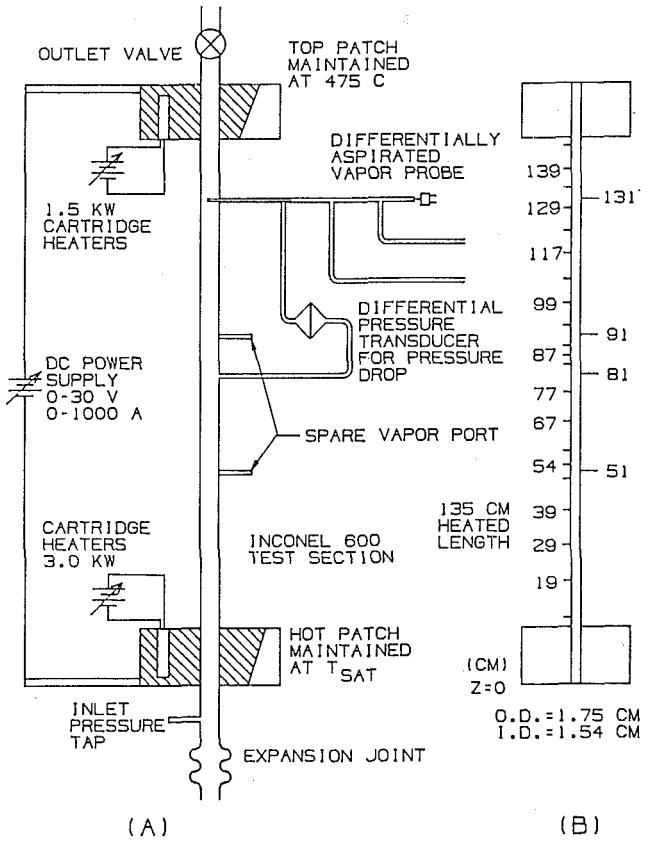

Fig. 1 Single tube post-CHF test section: (*a*) major components; (*b*) thermocouple locations

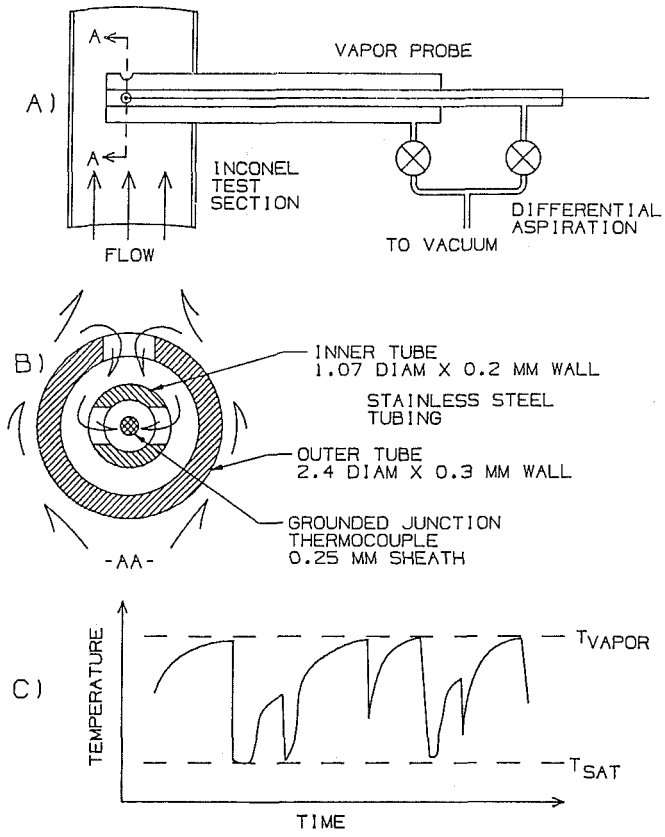

Fig. 2 Differentially aspirated vapor probe for measurement of vapor superheats: (*a*) separation concept; (*b*) construction details; (*c*) typical probe response

location. In this manner, as the quench front approached the fixed single vapor probe station, measurements of wall and vapor superheats were obtained as a function of axial distance from the CHF point.

Experiment

The experiments were carried out in a forced-convection, two-phase flow loop capable of tests with steam and water at pressures up to 5 atmospheres. The tubular test section of 1.54 cm i.d. used for these convective film boiling experiments is illustrated in Fig. 1. A d-c power supply was used to provide direct heat generation in the tube wall over the 135 cm length of the test section (distance between inlet hot patch and outlet hot patch). Thermocouples were attached to the outside surface of the tube wall and pressure taps were provided along the length of the test section as indicated in Fig. 1. At an axial distance of 1.31 m above the bottom of the inlet hot patch, a differentially aspirated vapor probe was installed for measurement of superheated vapor temperatures.

The vapor probe used in these experiments was an improved version of the differentially aspirated probes developed in an earlier effort of this program [8]. As shown in Fig. 2, the double aspiration capability of Nijhawan's probe was maintained while the total probe o.d. was reduced to the present diameter of 2.4 mm. During operation, aspiration through both tubes of the probe provided a torturous path that was effective in separating the vapor and liquid phases and thus permitted measurement of the superheated vapor temperatures between quenches of the sensing thermocouple junction by liquid droplets. A more detailed description of the probe principle is available from [8, 9].

During the experiments, the test section was flooded with argon and preheated to a high superheat temperature (typically 550°C). The inlet hot patch was set for a temperature corresponding to saturation for the anticipated fluid conditions. During this preheating stage, the thermohydraulic conditions were set in the two-phase loop to obtain the desired flow rate, fluid static pressure, and inlet vapor quality. When steady conditions were attained, the film boiling experiment was initiated by introducing the two-phase flow into the test section. After an initial short transient period (typically 5 to 10 s), flow through the test section settled to a steady condition with fixed flow rate, inlet pressure, and inlet vapor quality. As the two-phase flow was maintained through the test section, the CHF quench front gradually propagated upward through the length of the test section. Time-varying records were obtained of the hydraulic parameters, the axial distribution of wall temperatures, wall heat flux, and the vapor superheats at the probe station. In all runs, care was taken to insure that the quench front propagation velocity was

Nomenclature

A = flow area
G = mass flux
i = enthalpy
P = pressure
P_H = heated perimeter
q_w'' = wall heat flux
T = temperature
t = time
X = quality
Z = axial direction

Greek

Γ = vapor source function

Subscripts

a = actual
CHF = critical heat flux
e = equilibrium
fg = phase change
ls = saturated liquid
v = vapor
w = wall

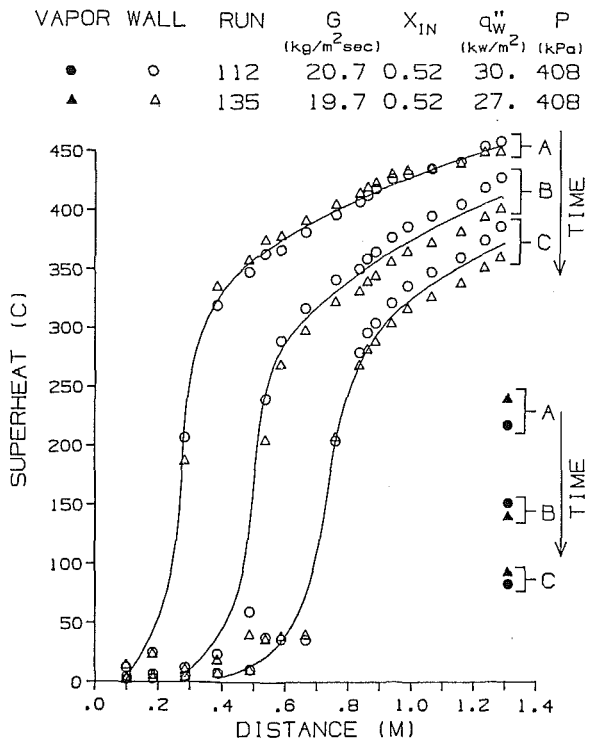

Fig. 3 Wall and vapor superheats versus axial distance

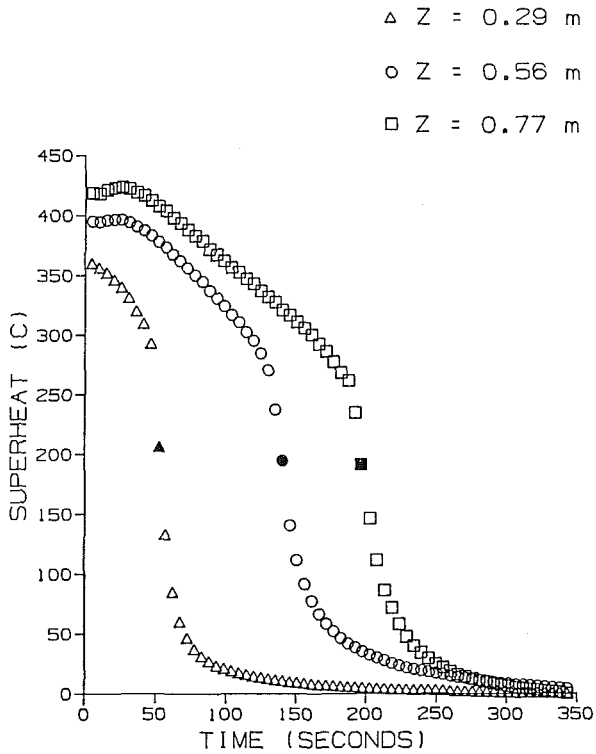

Fig. 4 Wall superheat versus time at three axial locations

sufficiently slow to satisfy the criterion for quasi-steady-state thermal conditions downstream of the quench front as discussed above. Depending on the inlet hydraulic conditions and the test section heat flux, the quench front would typically propagate the length of the test section in a period of 2 to 15 min, corresponding to quench front velocities of 1 cm/s to 1.5 mm/s. During this process, complete scans of measured data quantities were obtained every 5.2 s. All data were logged by a data acquisition system under the control of a PDP-11 computer. The vapor temperature data were recorded continuously on a strip chart.

Over 100 moving quench front experiments were carried out covering the following ranges of parameters:

Mass flux (G)	13 to 85 kg/m^2/s
Pressure (P)	240 to 570 kPa
Inlet vapor quality (X_{in})	0 to 70%
Wall heat flux (q_w'')	18 to 58 kW/m^2

Error estimates indicate the following degrees of uncertainty in the measured experimental variables:

Mass flux (G)	$\pm$(0.4 kg/m^2/s + 1%)
Pressure (P)	$\pm$3 kPa
Inlet vapor quality (X_{in})	$\pm$0.008 (Low X) to $\pm$0.04 (High X)
Wall heat flux (q_w'')	$\pm$3%
Wall temperature (T_w)	$\pm$3°C
Axial position of CHF	$\pm$1 cm
Vapor temperature (T_v)	$\pm$5°C measurement error $\pm$5° to 25°C interpretation error

Vapor temperature was obtained from the vapor probe stripchart recording. Interpretation error increased as the frequency of probe quenches increased. The wall heat flux was determined from a time-dependent energy balance analysis for the Inconel tube. Axial conduction in the tube was determined to be negligible. More details concerning the experimental setup and a compilation of the data are given by Evans, Webb, and Chen [14].

Results and Discussion

Data from two sample runs are shown in Fig. 3. The instantaneous axial distribution of wall superheats and the measured vapor superheat are plotted for three different times (A,B,C) during the history of each run. At any one instant, the wall temperature rises rapidly immediately downstream from the CHF location and attains superheats in the order of 300 to 500°C in the convective film boiling region. With increasing time in each experiment, the CHF location propagates upward in the test section, as indicated by the progression of axial wall temperatures from A to C. The corresponding vapor superheats detected by the vapor probe at a fixed axial location are indicated for each of these three times. Clearly, as the quench front approached the location of the probe station, the measured vapor superheats decreased in magnitude. The two runs plotted in Fig. 3 also give an indication of the experimental duplicability in these tests. As listed in the legend, the test parameters (G, X_{in}, q_w'', P) were similar for the two runs. In the actual test sequence, these two runs were separated by a complete quench of the test section and restart of the experiment. Duplicability of wall superheats in the film boiling regime was of the order of 5 percent (20°C out of 400°C), and the duplicability of vapor superheats was of the order of 10 percent (25°C out of 250°C).

An Eulerian view of the quench experiment can be obtained by plotting the wall superheat at a given axial position versus time, as illustrated in Fig. 4. The heated wall in the convective film boiling regime experienced a normal quench history marked by an initial period of relatively slow precursor cooling until the local superheats decreased to the range of 250 to 350°C. The precursor cooling stage was followed by a period of rapidly decreasing superheat temperatures indicating quenching of the local wall toward the fluid saturation temperature. In these experiments, the CHF quench front was defined as passing a particular thermocouple location when that thermocouple indicates a maximum in the rate of temperature decrease. For each of the

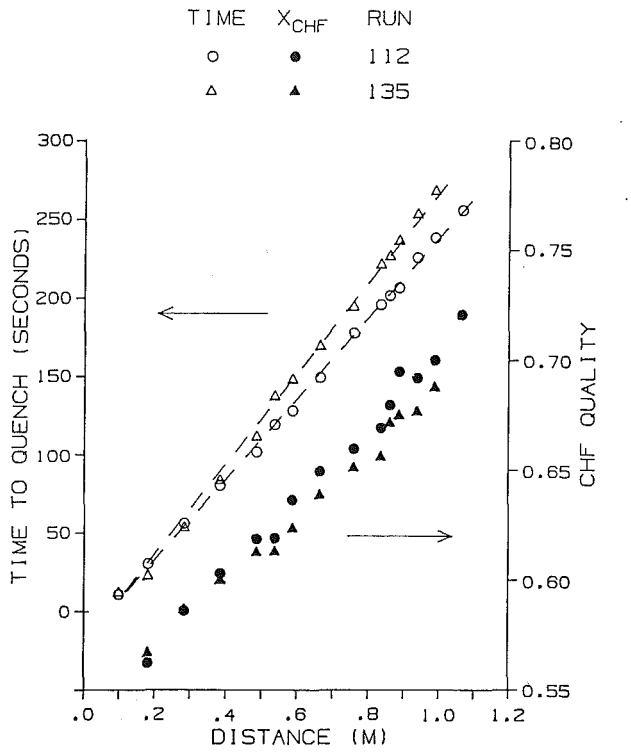

Fig. 5 Time to quench and CHF quality versus axial position

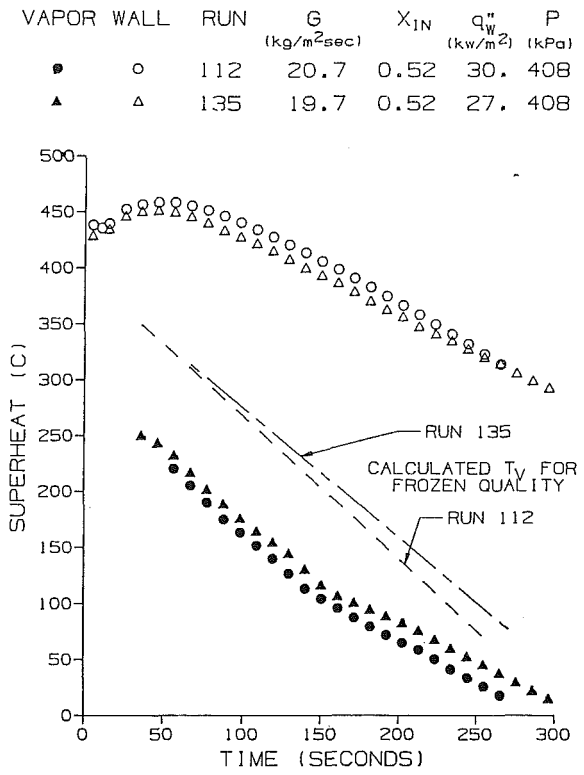

Fig. 6 Wall and vapor superheats versus time at axial location of 1.31 m

three axial positions illustrated in Fig. 4, the time of passage of the quench front is indicated by the dark symbol.

A cross plot of the time to quench at each thermocouple location then provides a clear indication of the propagation of the CHF location along the length of the test section. Results for two runs are shown in Fig. 5. The quench front velocity for each run is essentially constant as indicated by the linear lines through the data points. The slopes of these lines indicate that the quench front velocities for these two runs were approximately 0.4 cm/s.

In each run, the inlet hydraulic conditions, including the inlet vapor quality, were held constant during the quench history. Since net heat flux into the fluid occurs along the length of the test section, the resulting equilibrium vapor quality at the CHF location (X_{CHF}) increased with time as the CHF quench front propagated up the test section. For the two runs illustrated in Fig. 5, the CHF qualities were calculated by heat balance and are indicated in the figure. As the CHF location propagated over a distance of 1 m, the local quality at the CHF location increased from 0.57 to 0.72. The change in vapor quality at the initial and final CHF locations during any one run decreased with decreasing heat flux.

Heat flux from the wall during convective film boiling is commonly understood to be proportional to the difference between wall superheat and vapor superheat. Figure 6 shows a plot of wall and vapor superheats in the vicinity of the vapor probe during the quench history of two runs. Clearly, as the quench approached the measurement station (with increasing time), there is a significant decrease in the wall superheat in spite of the essentially constant wall heat flux. However, there is a corresponidng decrease in the local vapor superheat so that the difference between wall and vapor superheats remained relatively constant, indicating only a minor change in the effective wall heat transfer coefficient. Also plotted on Fig. 6 are curves calculated for the vapor temperature if no further vaporization were to occur beyond the CHF location. Theoretically, this "frozen quality" vapor temperature must be an upper bound for the nonequilibrium vapor superheat. The experimentally measured vapor superheats at the probe

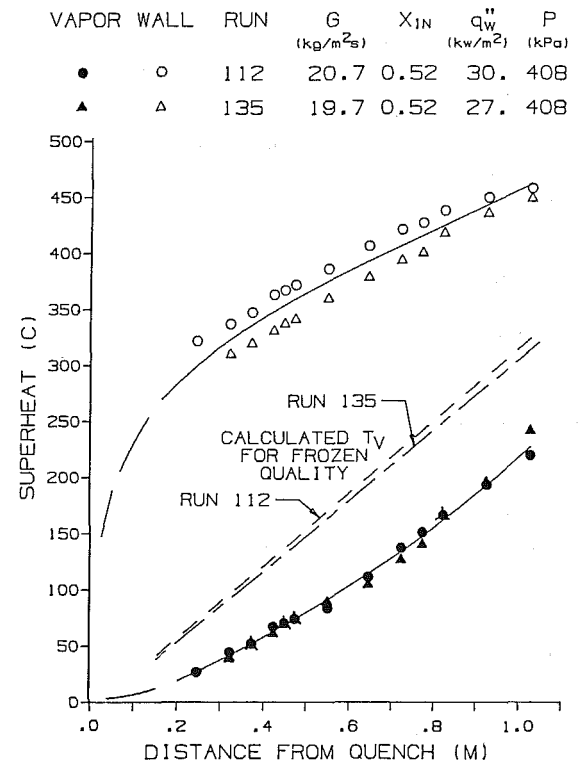

Fig. 7 Wall and vapor superheats at the vapor probe versus distance between the quench front and the vapor probe

station satisfied this thermodynamic limiting condition. Finally, the data shown in Fig. 6 are for two runs with similar test parameters and therefore give an indication of the reproducibility of these experiments.

Combining the results shown in Fig. 6 with the information on the instantaneous quench front location shown in Fig. 5, it is possible to transform the experimental results to obtain

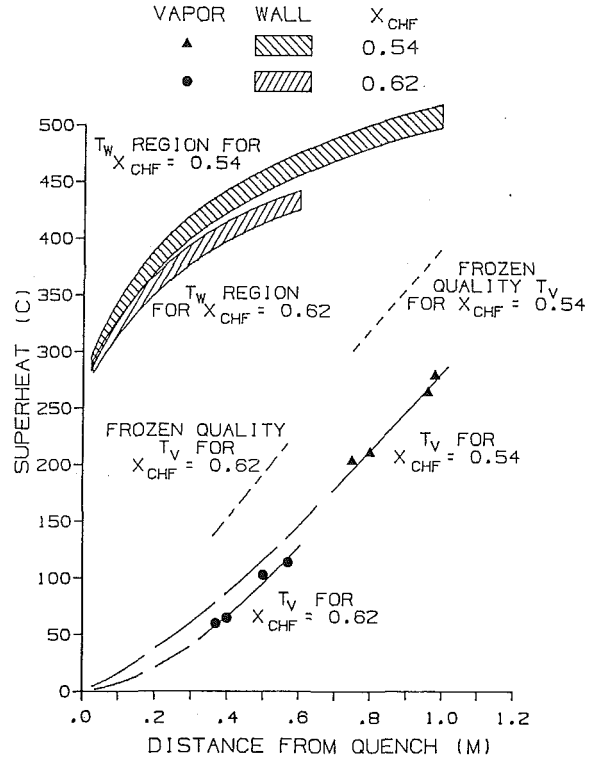

Fig. 8 Wall and vapor superheats versus distance for four different runs at the times when X_{CHF} = 0.54 and X_{CHF} = 0.62

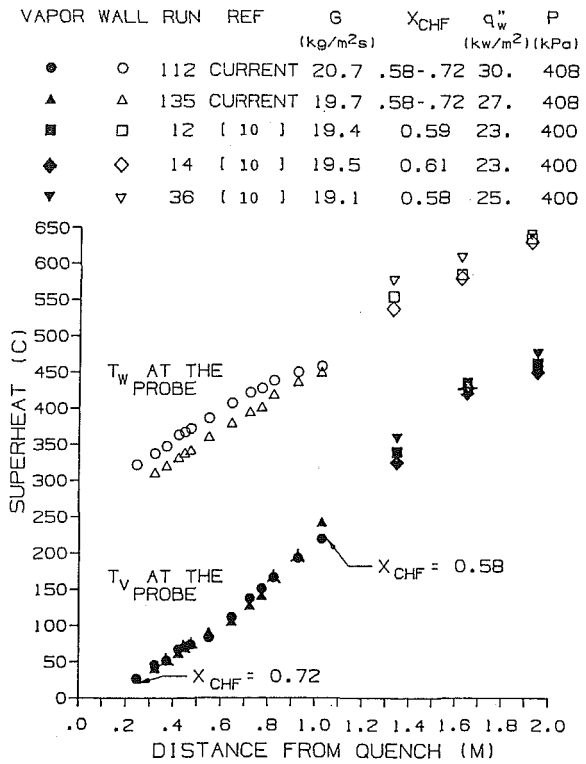

Fig. 9 Wall and vapor superheats versus distance between the quench front and the vapor probe

plots of wall superheats and vapor superheats as a function of distance (ΔZ) from the CHF quench front. As stated in the introduction, this was the principle objective of these experiments. Figure 7 shows such data for the two sample runs, illustrating the fact that this technique of a slowly propagating quench front can be used to obtain measurements of nonequilibrium wall and vapor superheats at various axial distances from the CHF location with use of just a single vapor probe. The data plotted in Fig. 7 show that the wall superheat increased steeply immediately downstream of the CHF location and then leveled off to a slower and more constant rate of increase with increasing axial distance. In contrast, the data on vapor superheats indicate that there was a region (of approximately 0.3 m) downstream from the CHF location where the vapor superheat is fairly small (less than 50°C for these two runs). At greater axial distances, the vapor superheat then increased rapidly and at a rate approximately paralleling that for the wall superheat. Compared to the theoretical "frozen quality" limit, the measured vapor superheats were consistently lower as required by thermodynamic considerations. The behavior illustrated in Fig. 7 for the two sample runs was found to be consistently displayed by all the data obtained in these tests.

The results illustrated in Fig. 7 are particularly significant in two respects. First, the fact that vapor superheats remained small for a significant distance (of the order of 0.3 m) downstream from the CHF location indicates that the vaporization process is relatively efficient in that region near to the CHF front. This implies the existence of a "transition" region immediately downstream from CHF where there is a higher volumetric concentration of liquid in the two-phase mixture than would be expected in established dispersed-film boiling convection. In such a region, both interfacial vapor–liquid heat transfer and liquid–wall heat transfer would be enhanced, leading to enhanced liquid vaporization. It is hypothesized by these authors that this "transition" region corresponds to an engagement length in which the liquid sputtered off from the wall in the region of CHF becomes engaged with the higher velocity vapor. Secondly,

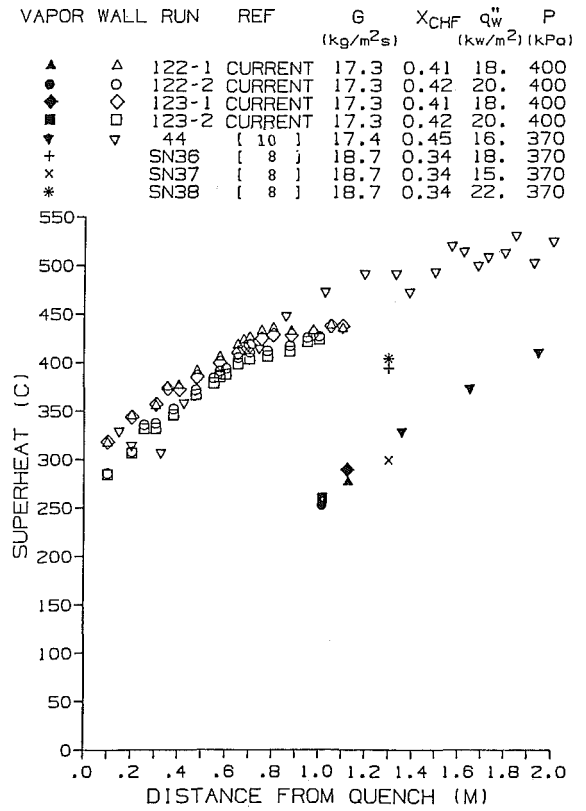

Fig. 10 Wall temperature profile and vapor temperature downstream of the CHF location

the data in Fig. 7 strongly indicate that at greater distances downstream from the CHF location (ΔZ greater than 0.6 m for these tests) the rate of increase in vapor superheat with axial distance approaches the rate calculated for the

theoretical frozen-quality limit. Though the absolute magnitude of the vapor superheat remains below the frozen-quality limit, an equal rate of change (slope of the curves in Fig. 7) implies that the intensity of vaporization in this region becomes small, approaching zero. This is a somewhat unexpected finding. It had commonly been accepted that at greater axial distances where the absolute vapor superheat is high, the vapor to liquid heat transfer would be increased due to the greater temperature driving force. These experimental results appear to indicate that in the established convective film boiling region, beyond the "transition region," the heat transfer between superheated vapor and entrained liquid drops is in fact relatively inefficient. These two observations have important implications for the phenomenological modeling of convective film boiling heat transfer and need to be confirmed by additional experiments.

Figure 8 shows similar transformed axial information results. These data are composites from four different runs selected to give approximately equal vapor quality at the CHF point. This is in contrast to the data shown in Fig. 7, which correspond to results from single runs which had varying vapor qualities at the CHF point. The results plotted in Fig. 8 were obtained from a series of runs with varying inlet qualities which permitted data to be obtained at a moment during the quench history when the vapor qualities at the CHF location were approximately equal. The results are seen to be similar to those displayed in Fig. 7, indicating that the significant findings regarding the nonequilibrium vaporization process as discussed above are pertinent to convective film boiling with fixed vapor quality at the CHF location, as well as to single convective film boiling cases with varying CHF qualities.

An attempt was made to compare these experimental data with the few available measurements from previous studies. Because of the very limited data base, it was not possible to obtain a direct one-on-one comparison with matched parameters. Figure 9 shows a comparison of the data from two runs in this experiment with results recently reported by Gottula et al. [10] at reasonably comparable conditions. The moving quench front data of the present experiments (up to a ΔZ of 1.05 m) are compared to the fixed-quench front data from [10] for ΔZ of 1.35–1.95 m. Though the two separate tests did not overlap in the magnitude of the axial distance, extrapolation between the two sets of experimental data indicates very good agreement in both wall superheats and vapor superheats.

Figure 10 shows an attempt to compare the results with the data of [10], as well as the earlier published results of Nijhawan et al. [8, 9]. It should be noted that due to the difficulty of matching all experimental parameters, the runs from various sources were only of approximate equivalency. Again, excellent agreement was obtained between the moving CHF measurements of the present study with the fixed CHF experiments from [10]. Nijhawan's data [8, 9] bracketed these present results, as would be expected in view of the different ranges of vapor qualities at CHF and the wall heat flux. In general, the agreement between data from the present experiment with the limited published data (as shown in Figs. 9 and 10) indicates reasonable consistency and lends a degree of confidence to the experimental findings.

The experimental data obtained in this investigation have been compared with the predictions of two nonequilibrium convective film boiling models. The CSO correlation [15], which is based on local conditions, and the Saha model [2], which is dependent on axial history, were selected for this evaluation. For the experimental thermal-hydraulic conditions and wall temperatures, the model predictions of wall heat fluxes and vapor superheats were compared with experimental measurements for 510 sets of data. The results are summarized in Table 1.

Table 1 Data-model comparison

	Vapor superheat		Heat flux	
	avg. dev. (%)	std. dev. (%)	avg. dev. (%)	std. dev. (%)
CSO	75	154	19	25
Saha[a]	64	123	16	17

[a]Unable to calculate all the data points—see text for explanation.

$$\text{Average deviation} = \frac{1}{n} \Sigma \text{Error} \times 100$$

$$\text{Standard deviation} = \left\{ \frac{1}{n} \Sigma \text{Error}^2 \right\}^{1/2} \times 100$$

$$\text{Error} = \left| \frac{\text{Measured Value} - \text{Predicted Value}}{\text{Measured Value}} \right|$$

The simpler CSO correlation was able to predict the experimental heat fluxes quite well, with an average deviation and standard deviation of 19 percent and 25 percent, respectively. The vapor superheat comparison, however, shows that the CSO correlation is unable to adequately predict vapor superheats, with average and standard deviations of 75 percent and 154 percent, respectively.

For the more complex Saha correlation, inapplicability of the drift flux model for the void fraction prevented the evaluation of all the data points. Only 61 percent of the data could be calculated. Heat fluxes could be predicted reasonably well, with an average deviation of 16 percent and a standared deviation of 17 percent. The vapor superheats again were not well predicted having an average and standard deviation of 64 percent and 123 percent, respectively. Therefore, while the CSO and Saha correlations can adequately predict the wall heat flux data, the models are not able to match the nonequilibrium vapor conditions.

Summary and Conclusions

An experimental technique using slowly propagating quench fronts was used to obtain measurements of nonequilibrium flow-film boiling conditions as a functions of axial distance from the CHF location. Axial variation of wall superheats was consistent with previous findings, indicating a rapid rise in the region close to the quench front, leveling off to a slower and fairly constant rate of rise further downstream. The new data for vapor superheats indicated a "transition" region immediately downstream from CHF where the two-phase fluid remained close to the equilibrium thermodynamic state. It was hypothesized that the liquid requires a finite axial distance to engage with the faster flowing vapor, and in this engagement region the volumetric presence of liquid is more significant than heretofore understood. This transition region is hypothesized to have relatively efficient vapor-to-liquid and wall-to-liquid heat transfer. At greater distances, the vapor superheat data indicate a relatively ineffective vapor-to-liquid heat transfer process. Thus these experimental findings indicate a zone near the CHF front where the vaporization source intensity (Γ) is relatively high, followed by a far zone where the source intensity drops off to a relatively low magnitude (approaching zero). If these findings are confirmed by future experiments, phenomenological modeling of the nonequilibrium heat transfer process in convective film boiling must account for these two regions of behavior.

References

1 Chen, J. C., "Some Phenomenological Questions in Post-Critical-Heat Flux Heat Transfer," NATO Advanced Research Workshop on Two-Phase Flows and Heat Transfer, Spitzingsee, F. R. Germany, Aug.–Sept. 1982.

2 Saha, P., Shiralkar, B. S., and Dix, G. E., "A Post-Dryout Heat Transfer Model Based on Actual Vapor Generation Rate in Dispersed Droplet Regime," ASME Paper No. 77-HT-80.

3 Webb, S. W., Chen, J. C., and Sundaram, R. K., "Vapor Generation Rate in Nonequilibrium Convective Film Boiling," 7th International Heat Transfer Conference, Munich, 1982.

4 Mueller, R. E., "Film Boiling Heat Transfer Measurements in a Tubular Test Section," EURAEC-1971/GEAP-5423, 1967.

5 Polomik, E. E., "Transition Boiling Heat Transfer Program—Final Summary Report for Feb/63-Oct/67," GEAP-5563, 1967.

6 Hochreiter, L. E., "NRC/Westinghouse/EPRI FLECHT Low Flooding Rate Skew Axial Profile Results," presented at the 5th Water Reactor Safety Information Meeting, Washington, D.C., 1977.

7 Loftus, M. J., et al., "Non-Equilibrium Vapor Temperature Measurements in Rod Bundle and Steam Generator Two-Phase Flows," *Proc. OECD (NEA) CSNI Third Spec. Meet. on Trans. Two-Phase Flow*, Pasadena, Calif., CSNI Report No. 61, 1981.

8 Nijhawan, S., Chen, J. C., Sundaram, R. K., and London, E. J., "Measurements of Vapor Superheat in Post-Critical-Heat-Flux Boiling," ASME JOURNAL OF HEAT TRANSFER, Vol. 102, 1980, pp. 465–570.

9 Nijhawan, S., "Experimental Investigation of Thermal Non-Equilibrium in Post-Dryout Steam-Water Flow," Ph.D. disseration, Lehigh University, 1980.

10 Gottula, R. C., Nelson, R. A., Chen, J. C., Neti, S., and Sundaram, R. K., "Forced Convective Nonequilibrium Post-CHF Heat Transfer Experiments in a Vertical Tube," ASME-JSME Thermal Engineering Conference, Honolulu, Mar. 1983.

11 Annuziato, A., Cumo, M., and Palazzi, G., "Post Dry-out Heat Transfer in Uncovered Core Accidents," ANS 2nd Nuclear Reactor Thermal-Hydraulics Conference, Santa Barbara, Jan. 1983.

12 Sparrow, E. M., and Siegel, R., "Unsteady Turbulent Heat Transfer in Tubes," ASME JOURNAL OF HEAT TRANSFER, Vol. 82, 1960, pp. 170–180.

13 Siegel, R., "Heat Transfer for Laminar Flow in Ducts with Arbitrary Time Variations in Wall Temperature," ASME *Journal of Applied Mechanics*, Vol. 27, 1960, pp. 241–249.

14 Evans, D. G., Webb, S. W., and Chen, J. C., "Measurements of Axially Varying Nonequilibrium in Post-Critical-Heat-Flux Boiling in a Vertical Tube," NUREG/CR-3363, Vols. 1 and 2, June 1983.

15 Chen, J., Ozkaynak, F. T., and Sundaram, R. K., "Vapor Heat Transfer in Post-CHF Region Including the Effect of Thermodynamic Nonequilibrium," *Nucler Engineering and Design*, Vol. 51, 1979, pp. 143–155.

16 Yoder, J. L., and Rohsenow, W. M., "A Solution for Dispersed Flow Heat Transfer Using Equilibrium Fluid Conditions," ASME JOURNAL OF HEAT TRANSFER, Vol. 105, 1983, pp. 10–17.

Reflooding With Steady and Oscillatory Injection: Part I—Flow Regimes, Void Fraction, and Heat Transfer

M. Kawaji

Y.S. Ng

Department of Nuclear Engineering,
University of California,
Berkeley, Calif. 94720

S. Banerjee

Department of Chemical and
Nuclear Engineering,
University of California,
Santa Barbara, Calif. 93106
Mem. ASME

G. Yadigaroglu

Swiss Federal Institute
of Technology,
ETH-Zentrum,
CH-8092 Zürich,
Switzerland
Mem. ASME

Simultaneous void fraction and wall temperature measurements were made during bottom-reflooding of a vertical Inconel tube under both constant and oscillatory injection rates. To support interpretation of these data, flow regime visualization experiments were also conducted by reflooding a heated quartz tube. With constant, high reflooding rates, inverted annular, transition, and dispersed flow regimes exist above the quench front, with typical chordal-average void fractions in the ranges of 10–30 percent, 30–70 percent, and 70–90 percent, respectively. Each regime exhibits different heat transfer rates. With lower injection rates or higher heating rates, annular droplet and dispersed flow regimes appear with void fractions above 80 percent. For reflooding with oscillatory inlet flow and high injection rates, large oscillations are seen in void fraction and wall temperature, indicating periodic changes in the flow regime near the quench front: The regime alternated between inverted annular (during an upstroke) and annular droplet flow (during a downstroke). These flow regimes were observed in the flow visualization experiments to be qualitatively similar to those for the constant injection cases. Heat transfer rates are substantially affected by the flow regime and increase (or decrease) as the void fraction falls (or rises). Compared to the constant-injection tests, increased rates of entrainment were observed during the forced-oscillation tests.

Introduction

During the blowdown phase of a postulated Loss-of-Coolant Accident (LOCA) in a pressurized water reactor (PWR), the reactor core is uncovered and the cladding of the fuel rods experiences rapid temperature excursions due to the redistribution of heat stored in the fuel and decay power production, combined with poor heat transfer. In order to prevent fuel from overheating and eventually failing, emergency core cooling is activated and the accident enters the reflood phase. Complex two-phase flow and heat transfer phenomena take place during this phase of the accident. Since the cladding temperature reaches its peak during reflood, proper understanding of reflood phenomena is necessary to ensure nuclear reactor safety.

Reflooding phenomena have been investigated in the past decade through numerous experimental programs, both large and small in scale. Yadigaroglu [1] reviewed these experiments and summarized the main results.

Depending on the nature of the tests, the experiments can be divided into two categories as *forced reflood tests* and *system effects tests*. In the forced reflood tests, the injection rate to the core is kept constant or variable at a predetermined rate. The main objective of forced reflood tests is to understand two-phase flow and heat transfer phenomena that take place in the core. In the system effects tests, primary loop components relevant to reflooding, such as the downcomer, the core, the upper plenum, and the steam generator are incorporated into the test loop. In some system effects tests, an exit resistance represents the hot-leg, the steam generator, and the pump. Emergency cooling water is injected into the downcomer, and the gravity head due to the water level accumulated there is the driving force pushing coolant into the core. In this manner the dynamics of the entire primary loop are simulated and can be studied.

A systematic study of bottom-reflooding of a vertical tube has been conducted at the University of California, Berkeley over the past several years. The first set of experiments was designed to obtain and analyze data on quench speed and heat transfer during constant-injection reflooding of an Inconel tube (Yu [2], Seban et al. [3]). The quench speed was found to depend on several parameters, including the injection rate, subcooling or quality of the coolant at the quench front, and the local wall temperature. A change in the pattern of flow regimes along the tube, accompanied by a decrease in quench speed, was noted when the coolant reached saturation conditions just below the quench front (QF) [4].

Analytical studies included comparison of the heat transfer data with available heat transfer models (Seban et al. [5]), the development of correlations for heat transfer immediately downstream of the QF [6] and for the QF velocity [2, 5] and of a reflood code based on a Drift Flux model (Arrietta and Yadigaroglu [7, 8]). In addition the data are of value in validating reflood calculations done with computer codes that are meant to predict core behavior in loss of coolant accidents.

For all system effects tests, such as FLECHT-SET, FLECHT-SEASET, LOFT, and JAERI Series 5B tests, violent oscillations are reported [9–13]. As an example, for the FLECHT-SET Series-A tests, the average flooding rate was about 5.6 cm/s, while the peak values of the instantaneous velocity were as high as ±100 to 200 cm/s. The oscillations observed in systems effects tests. In order to isolate the effect of inlet flow oscillations on heat transfer and progressed. Detailed reviews of system effects tests are reported in [1] and [14].

Phenomenological understanding of the actual flow regimes and heat transfer mechanisms in reflooding of a reactor core is further complicated by the effect of these

Contributed by the Heat Transfer Division and presented at the ASME/ANS/AIChE Second International Topical Meeting on Reactor Thermal-Hydraulics, Santa Barbara, California, 1983. Manuscript received by the Heat Transfer Division January 18, 1984.

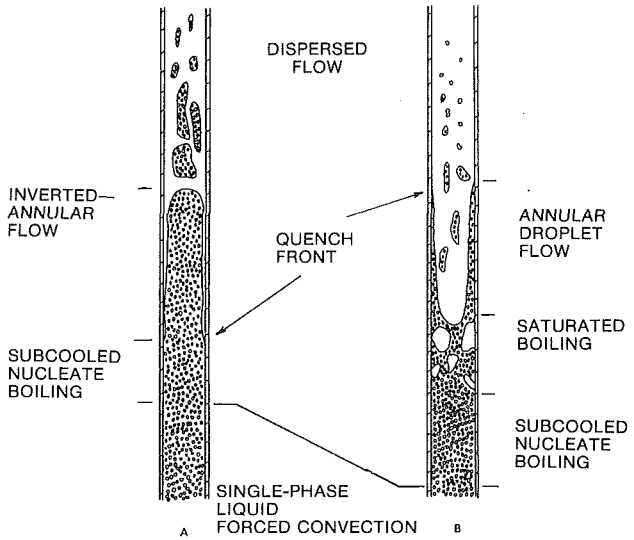

Fig. 1 Flow regimes and heat transfer in reflood: (*A*) fast flooding; (*B*) slow flooding

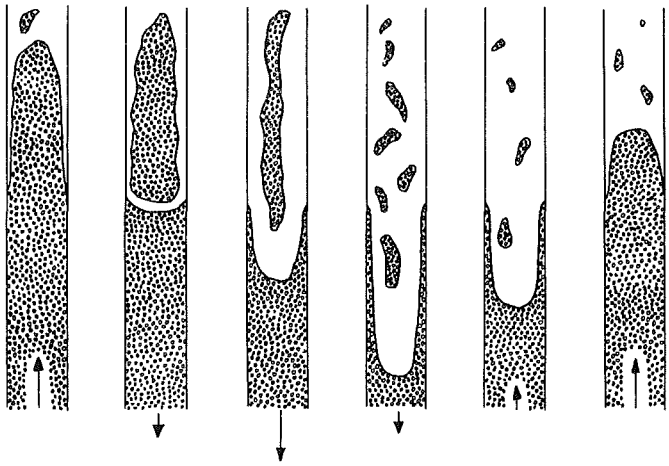

Fig. 2 Flow regime transition in forced-oscillation reflood (arrows indicate inlet velocity)

oscillations observed in systems-effects tests. In order to isolate the effect of inlet flow oscillations on heat transfer and quench speed, controlled forced-oscillation reflood experiments were conducted by superimposing oscillations of constant amplitude and frequency on a constant injection rate [14–16]. The effect of oscillations on the reflooding process was assessed by comparison of the controlled-oscillation reflooding test data with those of the steady constant injection reflooding tests at the same average injection rate.

The benefit of this approach is that the average injection rate is kept at a constant value during oscillatory reflooding. During gravity feed tests, the oscillation amplitude, the period, and the average injection rate vary as the downcomer water level increases. Thus comparison with forced reflood test data is difficult and the effect of the oscillations cannot be systematically examined.

One important parameter that has not been measured in most of the past reflood experiments is void fraction. Simultaneous measurement of void fraction and wall temperatures during reflooding of a metal tube, accompanied by qualitative studies of flow patterns (visualized during quenching of a quartz tube), can elucidate the thermal-hydraulic processes involved and lead to better reflood models. To this end, the results of both quartz and Inconel tube reflood experiments designed to investigate flow regime and heat transfer characteristics under oscillatory as well as constant inlet flow conditions are discussed in the first part of this work. The effect of oscillations on quench front velocity and on the liquid carryover rate is reported in Part II.

The main features of the reflood process observed in the flow visualization experiments are described first before discussing the void fraction and heat transfer data obtained in the Inconel-tube reflooding tests.

Flow Visualization: Reflooding of a Vertical Quartz Tube

In the flow visualization experiments, a vertical 1.5 m quartz tube externally heated with a gas burner over a length of 0.5 m was quenched by injecting subcooled water from the bottom. Flow patterns occurring under both constant and oscillatory inlet flow conditions were recorded with a high-speed movie camera.

Constant Injection Tests. In constant-injection reflood, two distinct flow regimes are possible near the quench front. If the coolant is injected rapidly and remains subcooled at the quench front, inverted annular flow occurs, as sketched in Fig. 1(*A*). A liquid column extends above the quench front, separated from the wall surface by a thin vapor film. Heat transfer rates are expected to be quite high in this region but would decrease significantly with height as the vapor film becomes thicker. Considerable precursory cooling takes place ahead of the quench front; this is believed to account for the relatively high quench speeds observed in this regime.

On the other hand, if the coolant is injected slowly and becomes saturated below the quench front, the flow changes to an annular droplet flow regime, as shown in Fig. 1(*B*). A thin liquid film attaches to the wall between the quench front and the boiling zone. With a short annular flow region, periodic bursts of vapor occur in the boiling zone followed by upward ejection of liquid. While bursts were observed in the flow visualization experiments, no quantitative measurements

Nomenclature

$\hat{A}$ = oscillation amplitude (half-wave)
I = gamma ray intensity
T = temperature
U = velocity
α = void fraction
τ = oscillation period
ω = oscillation frequency

Subscripts

a = area average
c = chordal average
g = tube filled with vapor
f = tube filled with liquid
i = inlet
l = liquid
w = wall

Run conditions (*A-B-C-D-E*) are described in this paper using the following notations:

A = initial wall temperature in °C
B = water supply rate in cm/s
C = water supply temperature in °C
D = superimposed half-oscillation amplitude (peak to peak) in m
E = superimposed oscillation period in seconds

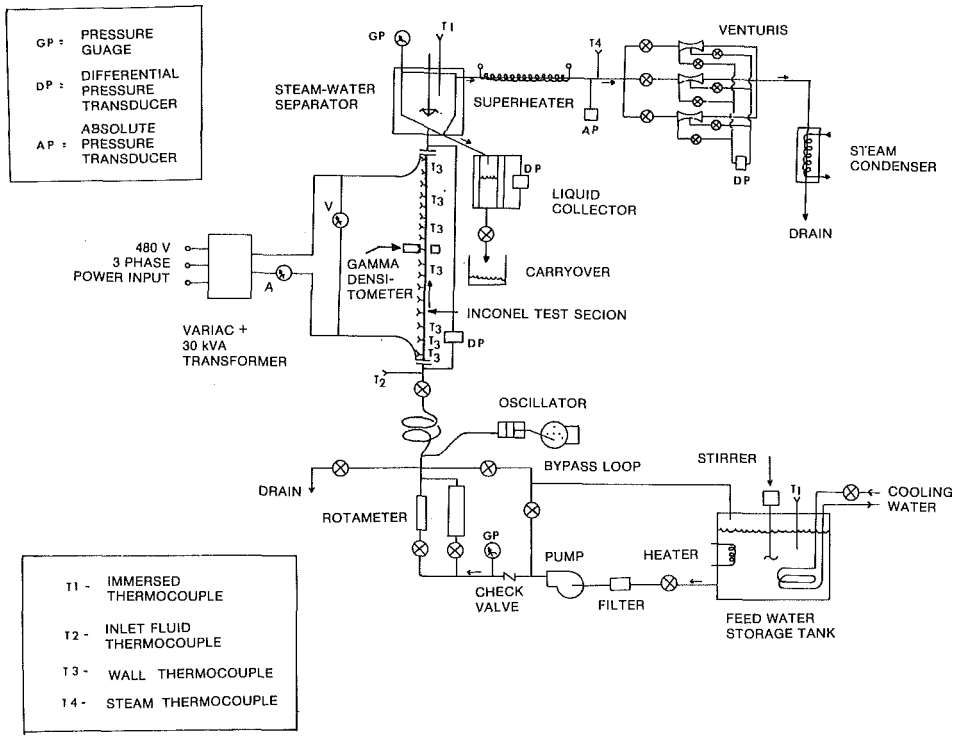

Fig. 3 Schematic of experimental setup

were made. The ejected liquid elongates into filaments that eventually break up into fragments of various sizes and shapes. The filaments and fragments may collide against the wall or with one another and shatter into smaller droplets. Small droplets are entrained by steam and continue to flow upward, but large fragments tend to fall back and accumulate in the boiling zone until another burst of vapor occurs and the process is repeated.

With a longer annular flow region, Ardron and Hall [17] observed waves on the liquid film travelling upward. Whenever the wave crests reach the quench front, sputtering occurs and the quench front advances incrementally. The droplets formed during sputtering are either entrained by vapor or fall down. This appears to be a different mechanism from what we observed for a shorter annular flow region. In either case, the unquenched region is entirely in the dispersed flow regime and the quench rate is much lower than in the inverted annular flow case.

These visual observations and trends were confirmed by a subsequent quantitative analysis of reflooding data [4].

Oscillatory Reflooding Tests. Under oscillatory inlet flow conditions, the flow regime near the quench front alternates between inverted annular flow with a growing liquid column during an upstroke and annular droplet flow during a downstroke. As the flow direction changes from upstroke to downstroke, the liquid column detaches itself near the quench front and continues to flow upward. It elongates, collides against the wall and other liquid fragments, and finally breaks up into fragments of various sizes. Large fragments fall back onto the liquid, but the smaller fragments are entrained and carried upward by the vapor. The sequence of events is sketched in Fig. 2.

Constant and Oscillatory Injection Rate Tests

This qualitative understanding of the flow patterns described above was used in interpreting the data obtained in the Inconel tube reflooding experiments discussed next.

The quantitative data are of value in the development and validation of multifluid reflood models with appropriate constitutive equations for different flow regimes undertaken by the authors of these papers. Here, we will only discuss the main results. The complete data are reported in [14–16].

Following the description of the experimental setup, a flow regime and heat transfer analysis based on the void fraction data is presented first for constant-injection tests and then for forced-oscillation tests.

Experimental Setup

The experimental setup is shown in Fig. 3. The test loop consisted of the test section, the feedwater supply, the oscillator, and an exit carryover measurement system. A gamma densitometer was added for the experiments reported in Part I.

The test section was made of a 3.66-m Inconel tube with 14.3-mm-i.d. and 0.8-mm wall thickness. It was resistance heated by a manually adjustable d-c source. To avoid any ambiguity regarding the calculation of the transient values of the heat flux to the fluid and to facilitate these calculations (as well as the installation of the thermocouples), the test section was left uninsulated. The heated tube was confined, however, within a screen wrapped with aluminum foil to stabilize heat loss to the atmosphere.

For the forced-oscillation tests, an oscillator installed between the test section inlet and the rotameter imposed an oscillatory flow boundary condition. The constant average injection rate was provided by a turbine pump.

The oscillator consisted of a piston-cylinder assembly, a rotating disk and a variable-speed motor. It was capable of providing oscillations with a period τ of 2.0–6.0 s and a half-wave amplitude $\hat{A}$ of 0.15–0.75 m based on the liquid level in the test section. These oscillations were superimposed on the constant injection speed U_l so that the resultant inlet velocity U_i is approximately given by the following equation

$$U_i(t) = U_l + \hat{A}\omega \sin(\omega t) \qquad \text{where } \omega = \frac{2\pi}{\tau} \tag{1}$$

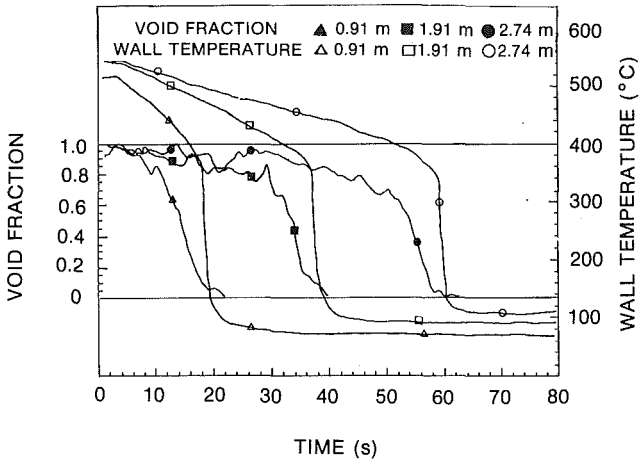

Fig. 4 Void fraction and well temperature histories (constant-injection, high reflooding rate – Run 560-12.7-26-0-0; notation explained in Nomenclature)

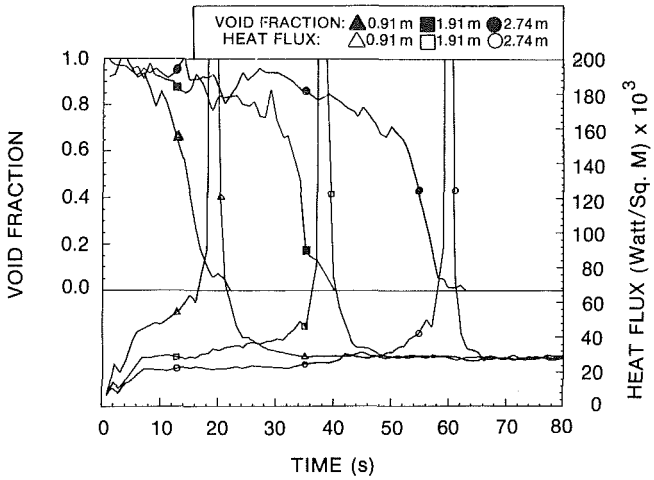

Fig. 5 Void fraction and heat flux histories (constant-injection, high reflooding rate—Run 560-127-25-0-0)

During each run, the amplitude and the period were kept constant.

An unheated section of sufficient length to contain the fluid returning from the heated section during a downstroke was placed immediately upstream of the heated tube, as shown in Fig. 1. This fluid was reinjected into the heated section during the following upstroke. The mixture of superheated steam and water droplets exiting from the test section was first separated by the steam-water separator to measure the carryover rates individually. Water carryover was collected and measured in a liquid collector and steam was passed through a system of venturis and then to a condenser. No detailed measurements of vapor superheat were made at the test section exit. The superheat is expected to depend on wall temperature, reflood rate and liquid inlet temperature among other parameters. For a 530°C initial wall temperature, the few measurements made indicated typical vapor temperatures of ~425°C.

Distilled water stored in the feedwater tank was pumped through rotameters into the test section. Nearly constant average inlet flow rate could be maintained because of a large pressure drop across the rotameter valve and only a slight pressure buildup in the test section during the tests. A detailed description of the test apparatus is available in [14].

The temperature of the test section was measured by gauge-30 (0.254 mm) chromel-alumel thermocouples spot welded on the outside surface at 30 cm intervals. Additional thermocouples were attached at the position of the gamma densitometer beam. Because the tube wall was thin, the difference between the inside and outside surface temperatures of the test section were calculated to be quite small even during the oscillatory tests.

The Gamma Densitometer. In order to measure void fraction and determine the flow regimes, a narrow-beam gamma densitometer was designed and installed. The details of the design and calibration of the densitometer are described by Herschthal et al. [18], and only a brief description will be given here.

The densitometer used a NaI scintillation detector and a 75 mCi Co-57 line source. Since the actual flow regimes were not precisely known, a narrow beam was preferable to a wider beam, as the former minimized errors due to streaming of photons (Schrock [19]). A collimator made of a lead plate with a vertical slit window (0.05 mm × 19.05 mm) was placed between the test section and the detector, allowing only a narrow beam of gamma rays to be detected and counted by a ratemeter. The ratemeter output was continuously monitored on a chart recorder.

For transient measurements, the densitometer response must be faster than the rate of variation of the void fraction, otherwise the dynamic void effects introduce additional error. This was particularly important for forced-oscillation tests, in which flow oscillations of relatively short periods were imposed. With a short integration time, however, the statistical error increases and an optimum integration time must be selected by balancing the statistical and dynamic errors. The integration times used were 1.0 and 0.3 s for constant-injection and forced-oscillation tests, respectively.

With a narrow beam of gamma rays, a limited source strength and short counting periods, the height of the collimator window given above was necessary to obtain adequate counting rates. Because of the finite beam height, the measured void fractions were actually chordal volume-average quantities. However, for simplicity, the terms "chordal-average" and "area-average" are used in this paper to refer to void fractions measured respectively by narrow and wide beam densitometers with a finite beam height.

Experimental Procedure, Test Plan, and Data Reduction

In every test, coolant was initially circulated through the bypass loop at a desired flow rate. The test section was then heated to an initial steady-state temperature at which the electric heat input balanced the external losses. At the start signal, the data acquisition system was turned on and the coolant flow was diverted into the test section by manual opening of the valves. Heating of the test section continued at the same power level, and the data were recorded until nearly the entire test section was quenched and the test was terminated.

In forced-oscillation tests, the oscillator was initially adjusted to provide oscillations of desired amplitude and period. The test was started when the piston reached the fully pulled out position so that the oscillation would begin with an upstroke. This was necessary to prevent the minimum liquid level from falling below the test section inlet.

The thermal-hydraulic parameters measured were: (*i*) test section wall temperature, (*ii*) test section power input, (*iii*) inlet water temperature, (*iv*) inlet water flow rate, (*v*) chordal-average void fraction, (*vi*) pressure drop in the test section, and (*vii*) steam and liquid carryover rates. The sensor outputs were scanned and recorded on a magnetic tape at 1.0-s intervals.

Test Plan. The test matrix shown in Table 1 was chosen to embrace parametric values expected in accident conditions.

Table 1 Matrix of experiments

	Constant-injection tests	Forced-oscillation tests
Initial wall temperature, °C	560, 730	560, 730
Water injection rate, cm/s	2.5, 7.6, 12.7, 17.8	2.5, 7.6, 12.7
Inlet water temperature, °C	25	25
Exit pressure	nearly atmospheric	nearly atmospheric
Oscillation amplitude, m		0.15, 0.45, 0.75
Oscillation period, s		2.0, 4.0

Each test was repeated three times with the gamma densitometer placed at each of the three axial locations: 0.91 m (3 ft), 1.91 m (6 ft), and 2.75 m (9 ft). Reproducibility among the three runs was verified by comparing the quench times at various thermocouple locations.

Data Reduction. For each test, local heat transfer rates to the fluid were calculated from the measured wall temperature, power input, and the calibrated external heat loss data using a heat balance, neglecting axial and radial conduction in the tube wall. Axial and radial temperature gradients were important only at the quench front. Exit carryover rates and liquid inventory in the tube were also calculated and checked by performing an overall mass balance. The detailed data reduction procedure can be found in [2, 14].

The gamma densitometer signals were first smoothed to eliminate statistical fluctuations and then a linear interpolation formula was used to obtain the chordal-average void fractions. Because of the transient nature of the measurement, the void fraction data contain both statistical and dynamic errors. The error analysis for the void fraction calculation is presented in the Appendix.

Flow Patterns and Heat Transfer in Constant-Injection Reflooding

Void fraction data representative of the two flow regimes possible near the quench front, namely inverted annular and annular droplet flow, will be presented and discussed below.

Case of Subcooled Liquid at the Quench Front. When highly subcooled water was injected with sufficient speed so that the coolant would not reach saturation below the quench front, void fraction histories such as those shown in Fig. 4 were obtained. Also shown in this figure are the wall temperature histories obtained at the respective densitometer positions.

At any position, the succession of flow regimes began with single-phase steam flow, soon followed by dispersed droplet flow. The chordal-average void fraction decreased gradually to about 80–70 percent and then showed a sudden decline. The change in slope was clearly observed and is conjectured to indicate a qualitative change in flow regime from dispersed flow to a transient type of flow with large chunks of liquid entrained in steam. This conjecture is supported by visual observations for steady reflooding of a heated quartz tube.

The void fraction then decreased steadily to a value of 20–10 percent and remained above zero for a few seconds until quenching occurred. Quenching was signaled by the sudden drop in the wall temperature. The region of low void fraction prior to quench belonged to the inverted annular flow regime. Again this is supported by visual observation.

In steady, subcooled-flow film-boiling experiments conducted using a hot patch technique, Fung and Groeneveld [20] measured area-average void fractions in inverted annular film boiling using a one-shot type gamma densitometer. They found that the area-average void faction rose steadily with height from about 10 percent near the quench front to above 50 percent where the flow regime was believed to have changed into a dispersed flow. Their experiments were limited to steady film boiling and did not reproduce the very large spike in heat flux observed in the quench front region during reflooding.

Assuming a coaxial cylindrical geometry for the inverted annular flow regime, the area-average void fraction can be estimated from the chordal-average void fraction data using the following relation

$$\alpha_a = 2\alpha_c - \alpha_c^2 \tag{2}$$

For chordal-average void fractions of 10–20 percent, the corresponding area-average void fractions are estimated to be about 19–36 percent, which is consistent with Fung and Groeneveld's data, even though their data are not strictly for reflooding.

The approximate length of a liquid column in the inverted annular flow regime can be calculated from the void fraction history by transforming the time scale to a distance scale using the quench speed obtained from the thermocouple data. For the test shown in Fig. 4, quench speeds were 5.6 cm/s, 4.4 cm/s, and 3.8 cm/s at the times at which the 0.91 m, 1.91 m, and 2.74 m locations were quenched, respectively. Based on visual observations, the liquid column broke up into large chunks at an area-average void fraction of about 50 percent (chordal-average void fraction of about 30 percent). The liquid column heights were thus computed to be about 17 cm, 15 cm, and 13 cm at the three densitometer locations, respectively.

Within the various parameter ranges tested, the liquid column in inverted annular flow was found to extend up to a maximum height of about 30 cm above the quench front. Fung and Groeneveld's data also indicated about the same maximum liquid column height for other inlet water subcooling and injection rates. Above this maximum height, the liquid column is apparently unstable, possibly due to a Kelvin-Helmholtz type instability, and breaks up into large chunks of liquid. This breakup leads to the formation of the transition-flow regime mentioned earlier.

The length of the liquid column was also observed to steadily decrease with quench front elevation. This can be explained if the liquid column breakup is due to the Kelvin-Helmholtz type instability, in which the vapor–liquid interface breaks down at a critical relative velocity between the two phases. As the quench front moves up in elevation, subcooling in the liquid is progressively lost and the vapor generation rate at the quench front and along the liquid column is expected to increase. With increased vapor generation, the vapor velocity would increase with height along the liquid column and a critical relative velocity would be reached at a lower height resulting in a shorter liquid column.

Of great interest to reflood modeling is heat transfer in various flow regimes. Heat flux histories at the three densitometer positions are shown along with the void fraction histories in Fig. 5. The very sharp increase and decrease in heat flux occurs in the region of the quench front. Quantitative measurements of the magnitude of these spikes required very precise axial temperature gradients and could not be made. The heat flux as a function of void fraction for different runs is shown in Fig. 6. Heat transfer rates in the inverted annular and transition flow regimes were found to be much greater than those in the dispersed flow regime.

In the inverted annular flow regime, a rapid decrease in void fraction caused a correspondingly rapid increase in heat flux. This inverse relationship between heat flux and void fraction is further evident in the forced-oscillation test results. In the transition flow plane, the presence of a substantial amount of liquid (much more than in ordinary dispersed flow) in the form of large chunks rather than small droplets is

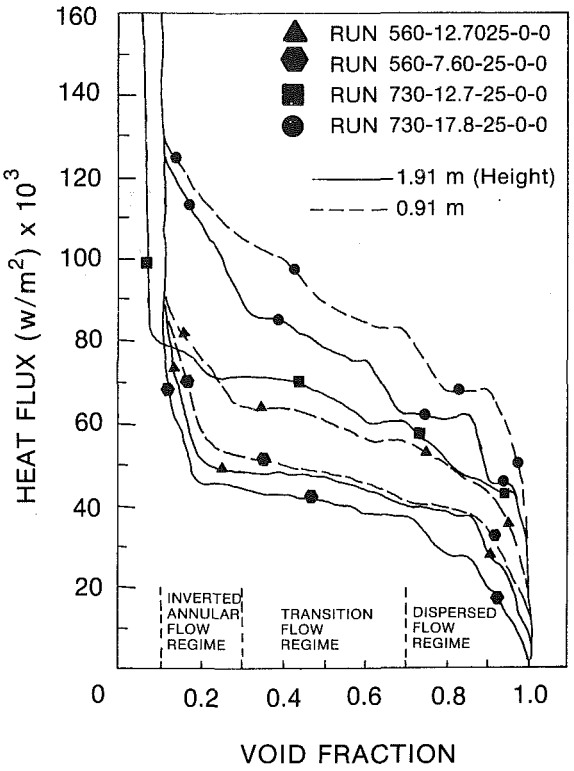

Fig. 6 Heat flux versus void fraction for various runs

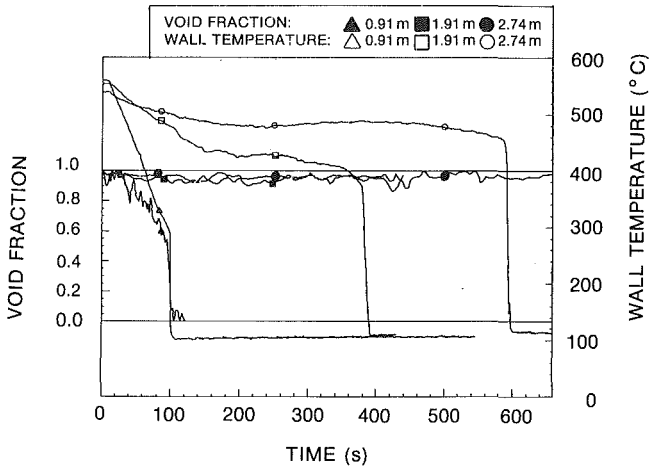

Fig. 7 Void fraction and wall temperature histories (constant-injection, low reflooding rate—Run 560-2.5-25-0-0)

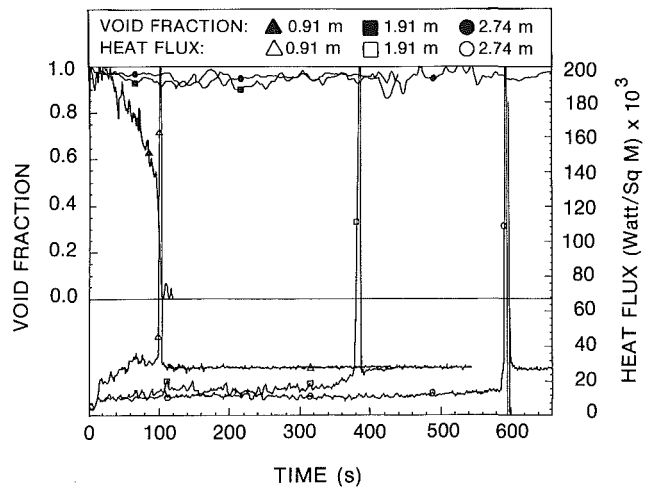

Fig. 8 Void fraction and heat flux histories (constant-injection, low reflooding rate—Run 560-2.5-25-0-0)

responsible for heat transfer rates that are well above the values for dispersed flow film boiling. The visual observations in quartz tube reflooding experiments suggest that an additional heat transfer mechanism such as direct wall–liquid contact which is relatively unimportant in dispersed flow with smaller droplets, may be significant in transition flow due to the greater size of drops and amount of liquid involved.

The region of the transition flow regime was found to be comparable in length to that of the inverted annular flow. In addition, the heat transfer rates within the transition flow regime varied considerably with void fraction for fast injection runs, and their prediction with available dispersed-flow, film-boiling heat transfer models was difficult [5]. Thus development of a transition flow and heat transfer model, to be incorporated into reflood calculations, is necessary.

Case of Saturated Flow at the Quench Front. When the coolant was injected slowly so that it could reach saturation below the quench front, totally different void fraction histories were obtained, as shown in Fig. 7. For the run of Fig. 7, from a simple heat balance neglecting the peak in heat flux at the quench front, the saturation point was calculated to be about 1.0 m above the test section inlet. At the 0.91 m position, the void fraction history was somewhat similar to those of the high injection rate tests. However, the liquid level was only slightly above the quench front.

At the 1.91 m and 2.75 m positions, which are well above the saturation point, void fractions remained at about 90 percent throughout the test. Initially, the flow regime was dispersed flow. Advancement of the quench front had no apparent effect on the void fraction. This indicated that a very thin liquid film advanced upward and quenched the inside surface of the wall, i.e., the flow regime at the quench front was annular. As shown in Fig. 8, the heat flux histories at the 1.91 m and 2.75 m positions do not show any significant increase prior to quench. In other tests, the chordal-average void fractions above the saturation point were in the 80–90 percent range. Qualitatively similar phenomena occurred in the low injection rate flow visualization experiments done in the quartz tube.

Area-average void fractions of 80–90 percent were measured in the annular droplet flow regime by Deruaz and Freitas [21]. They used a neutron scattering technique to measure void fraction profiles along a reflooded tube. Our results could be compared to their data if the phase distribution in this flow regime were precisely known. If the liquid phase is assumed to be mainly in the form of droplets that are homogeneously distributed, then the area-average void fraction should equal the chordal-average value, and our results compare favorably with the measurements of Deruaz and Freitas.

Flow Patterns and Heat Transfer in Forced-Oscillation Reflooding. Two different types of void fraction histories were obtained in forced-oscillation tests. When oscillations were superimposed on a relatively high injection rate, the void fraction histories showed oscillations of large amplitude at all the densitometer positions. The void fraction and wall temperature histories obtained at the 1.91 m position in one of the tests are shown in Fig. 9. The period of void fraction oscillations matched that of the driving oscillation imposed on the inlet flow.

Because of the periodic oscillations in void fraction, local heat transfer rates were affected, resulting in wall temperature oscillations. The heat flux history calculated from the temperature data is shown in Fig. 10. As noted in the previous

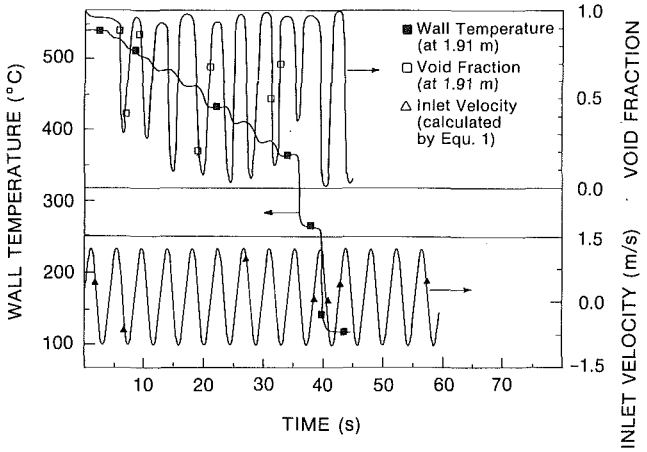

Fig. 9 Void fraction and wall temperature histories (forced-oscillation, high injection rate—Run 560-12.7-25-0.75-4)

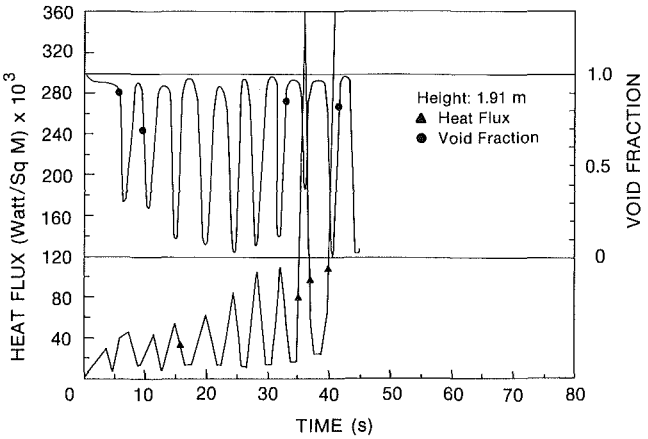

Fig. 10 Void fraction and wall temperature histories (forced-oscillation, high injection rate—Run 560-12.7-25-0.75-4)

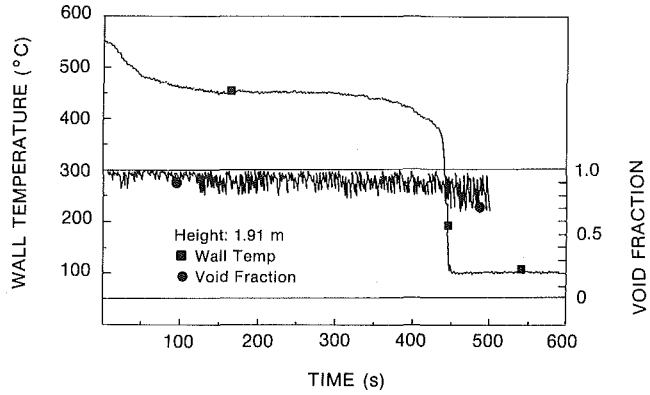

Fig. 11 Void fraction and wall temperature histories (forced-oscillation, low injection rate—Run 560-2.5-25-0.75-4)

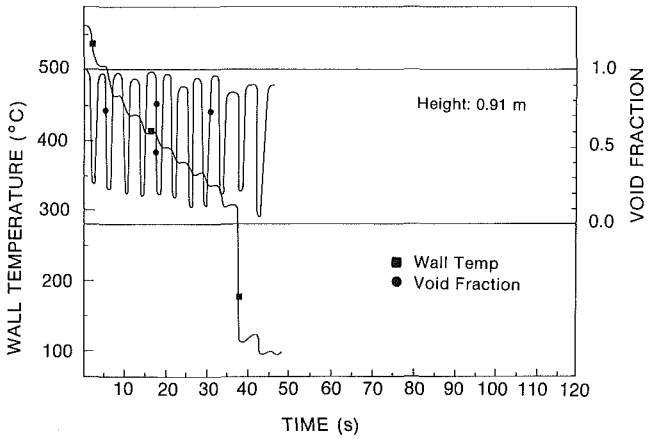

Fig. 12 Void fraction and wall temperature histories (forced-oscillation, low injection rate – Run 560-2.5-25-0.75-4)

section, the heat transfer rate was found to be a strong function of void fraction, and whenever the void fraction rose (or fell), the heat flux decreased (or increased). Substantial changes in void fraction suggest changes in flow regime, e.g., from inverted annular to annular, and so, corresponding changes in heat flux may occur.

The presence of large amplitude oscillations in void fraction reflected the periodic flow regime changes observed in the forced-oscillation, quartz-tube quench experiments. To keep the figures relatively uncluttered, the injection rate is shown only on one figure. Suffice it to say, an inverted annular flow regime existed during the upstroke and an annular droplet flow regime during the downstroke for the higher injection rates.

In forced-oscillation tests with low injection rates, however, the void fraction and wall temperature histories showed insignificant effects arising from the imposed oscillation, as shown in Fig. 11. The void fraction remained high throughout the test, showing only small oscillations due to fluctuations in the droplet flow rate. Therefore, the flow regime below the quench front was probably annular even on the upstroke. Above the quench front, the effects of oscillations further diminished with height and the flow regime was dispersed droplet.

The effect of inlet flow oscillations on the quench speed and the liquid carryover rate is discussed in Part II. Oscillations enhanced quench speed at the beginning but later retarded it in comparison with the constant-injection test results. This effect was more pronounced with oscillations of larger amplitude and shorter period.

The explanation presented is that oscillations increase liquid entrainment because of added inertia and agitation in the liquid flow, in agreement with the liquid column detachment mechanism observed in the flow visualization experiments. These effects are greater with oscillations of larger amplitude and shorter period. At the beginning of a run, more liquid is injected during the upstroke and gets entrained by steam. The increased entrainment rate improves precursory cooling above the quench front and helps in quenching the tube faster. However, the liquid inventory in the tube is depleted faster due to the enhanced entrainment, and the quench speed is later retarded.

The foregoing explanation was supported by the evidence on liquid inventory obtainable from the void fraction data. For example, the void fraction history at the 0.91 m position for a low injection rate test is shown in Fig. 12. The oscillations in void fraction at this position persisted until the end, indicating that the minimum liquid level remained below 0.91 m throughout the test. However, for the corresponding constant-injection case, shown in Fig. 7, single-phase liquid filled the tube at 0.91 m as soon as this height was quenched, and the liquid level stayed above 0.91 m afterwards. Thus, added agitation and inertia of the liquid column caused more liquid entrainment, which led to the reduction in quench speed as discussed above.

The same trend was observed for runs with different boundary conditions. Table 2 shows the time (from initiation of the run) after which the void fraction was always equal to zero for the rest of the run. The no-oscillation cases have apparently higher liquid inventory than the oscillation cases. Thus the results of the void fraction measurements (Table 2) confirm the conclusions from the measurements of Part II in

Table 2 Time required to achieve zero void fraction as a function of elevation

Run[a]	0.91 m height (3 ft)	1.91 m height (6 ft)	2.74 m height (9 ft)
560-12.7-25-0.75-4	32[b]	65	never[c]
560-7.60-25-0.75-4	56	never	never
560-2.50-25-0.75-4	never	never	never
730-7.60-25-0.75-4	never	never	never
560-12.7-25-0.15-4	25	49	64
560-7.60-25-0.15-4	38	75	155
560-12.7-25-0.45-4	27	53	95
560-7.60-25-0.45-4	42	103	never
560-7.60-25-0.75-2	never	never	never
560-2.50-25-0.75-2	never	never	never
730-7.60-25-0.75-2	never	never	never
560-12.7-25-0.45-2	32	55	never
560-7.60-25-0.45-2	42	114	never
730-7.60-25-0.00-0	53	never	never
560-12.7-25.0.00-0	23	41	62
560-7.60-25-0.00-0	32	75	135
560-2.50-25-0.00-0	125	never	never

[a] Notation explained in nomenclature
[b] Indicates that at this location the void fraction is always equal to zero in both upstroke and downstroke after the time shown
[c] Indicates that at this location the void fraction is never equal to zero at downstroke during the whole run

that the oscillations initially increase the amount of liquid carryover.

Conclusion

The flow regime and heat transfer characteristics in constant-injection-rate and forced-oscillation reflooding of a vertical tube have been investigated experimentally. Transient void fraction and wall temperature data were measured at three different heights of the tube under various initial and boundary conditions and analyzed using the information on flow patterns observed in quartz-tube reflooding experiments. The data will be valuable in the development and testing of mechanistic reflood models for LOCA analysis.

In summary, the flow regimes identified above the quench front in constant-injection, high reflooding-rate tests were inverted annular, transition, and dispersed-flow. Chordal-average void fractions of 10–30 percent, 30–70 percent, and 70–90 percent were typical of the three flow regimes, respectively. In constant-injection, low reflooding-rate tests, annular droplet flow and dispersed flow regimes existed below and above the quench front, respectively. The void fractions were above 80 percent in both flow regimes.

In forced-oscillation tests, the flow regime near the quench front alternated periodically between inverted annular and annular droplet flow during the upstroke and downstroke of an oscillation cycle, respectively. Heat transfer rates rose (or fell) whenever the local void fractions decreased (or increased). Oscillations initially increased the rate of liquid carryover through entrainment of the liquid column in inverted annular flow. In low injection rate tests, the effect of oscillations on void fraction and heat transfer rates diminished considerably above the point of coolant saturation.

Acknowledgments

This research was supported by the Electric Power Research Institute. We are indebted to the late Dr. Loren Thompson of EPRI for invaluable discussions.

References

1 Yadigaroglu, G., "The Reflooding Phase of the LOCA in PWRs. Part I: Core Heat Transfer and Fluid Flow," *Nuclear Safety*, Vol. 19, 1978, pp. 20–36.

2 Yu, K. P., "An Experimental Investigation of the Reflooding of a Bare Tubular Test Section," Ph.D. thesis, Department of Nuclear Engineering, University of California, Berkeley, Calif., 1978.

3 Seban, R., Grief, R., Yadigaroglu, G., Elias, E., Yu, K., Abdollahian, D., and Peake, W., "UC-B Reflood Program: Experimental Data Report," EPRI Report NP-743, Apr. 1978.

4 Yadigaroglu, G., and Yu, K.-P., "Flow Regimes and Carryover During Reflooding," paper presented at the European Two-Phase Flow Group Meeting, Zurich, June 14–17, 1984.

5 Seban, R. A., Grief, R., Abdollahian, D., and Peake, W., "Comparison of Experimental and Predicted Heat Transfer for the Data of the UC-B Reflood Experiment," EPRI Report NP-1290, Dec. 1979.

6 Yu, K.-P., and Yadigaroglu, G., "Heat Transfer Immediately Downstream of the Quench Front During Reflooding," ASME Paper No. 79-HT-48, 1979.

7 Arrietta, L., and Yadigaroglu, G., "Analytical Model for Bottom Reflooding Heat Transfer in Light Water Reactors (UCFLOOD Code)," EPRI Report NP-756, 1978.

8 Yadigaroglu, G., and Arrieta, L. A., "Analytical Modeling of Heat Transfer During the Reflooding Phase of the LOCA: The UCLFOOD Code," *Proceedings of the ANS/ASME/NRC International Topical Meeting on Nuclear Reactor Thermal-Hydraulics*, Saratoga Springs, N.Y., October 5–8, 1980, NUREG/CP-0014, Vol. 2, pp. 1173–1195.

9 Blaisdell, J. A., et al., "PWR FLECHT Phase A Report," WCAP-8238, Dec. 1973.

10 Loftus, M. J., et al., "PWR FLECHT-SEASET Unblocked Bundle Forced and Gravity Reflood Task Data Report," EPRI NP-1459 (NUREG/CR-1532), Sept. 1981.

11 Sugimot, J., et al., "Data Report on Series 5 Reflood Experiment," JAERI-M 7450, Jan. 1978.

12 McCreery, G. E., et al., "Thermal-Hydraulic Analysis of Semiscale MOD-1 Reflood Test Series, (Gravity Feed Tests)," TREE-NUREG-1010, Jan. 1977.

13 Riedle, K., et al., "Reflood and Spray Cooling Heat Transfer in PWR and BWR Bundles," ASME Paper No. 76-HT-10, 1976.

14 Oh, S. J., "The Effect of Oscillations During Reflooding of a Tubular Test Section," Ph.D. thesis, Department of Nuclear Engineering, University of California, Berkeley, Calif., 1982.

15 Kawaji, M., and Banerjee, S., "Two-Phase Flow Characteristics During Reflooding of a Hot Vertical Tube," EPRI Report NP-2820, 1983.

16 Ng, Y. S., and Banerjee, S., "Two-Phase Flow Characteristics During Controlled Oscillation Reflooding of a Hot Vertical Tube," EPRI Report NP-2821, 1983.

17 Ardron, K. H., and Hall, P. C., "Measurement of the Size Distribution of Droplets Generated in the Bottom Flooding of a Heated Glass Tube," paper presented at the European Two-Phase Flow Group Meeting, Ispra, Italy, 1979.

18 Herschthal, M., Kawaji, M., and Banerjee, S., "Design and Testing of a Laboratory Gamma-Ray Densitometer for Two Phase Flow," EPRI Report NP-2819, 1983.

19 Schrock, V. E., "Radiation Attenuation Techniques in Two-Phase Flow Measurements," Eleventh National ASME/AIChE Heat Transfer Conference, Minneapolis, 1969, pp. 24–35.

20 Fung, K. K., and Groeneveld, D. C., "Measurement of Void Fraction in Steady-State Subcooled and Low Quality Flow Film Boiling," *International Journal of Multiphase Flow*, Vol. 6, 1980, pp. 357–361.

21 Deruaz, R., and Freitas, R. L., "Void Fraction and Pressure Drop Measurement in a Reflood Single Tube," paper presented at the Third Specialist Meeting on Transient Two-Phase Flow, Pasadena, March 1981.

22 Banerjee, S., and Lahey, R. T., "Advances in Two-Phase Flow Instrumentation," *Advances in Nuclear Science and Technology*, Plenum Press, Vol. 13, 1980.

23 Harms, A. A., and Forrest, F., "Dynamic Effects in Radiation Diagnosis of Fluctuating Voids," *Nuclear Science and Engineering*, Vol. 46, 1971, pp. 408–413.

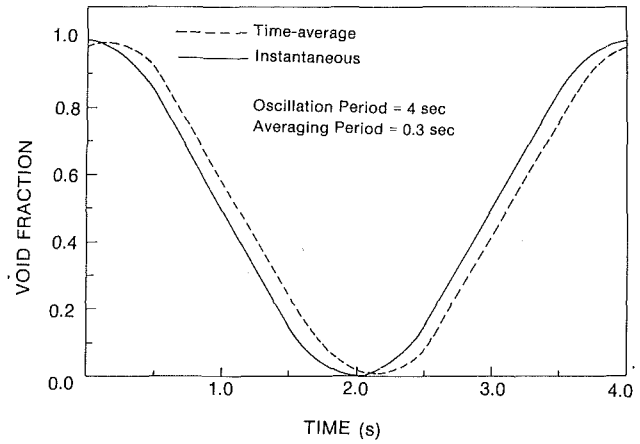

Fig. 13 Dynamic void effects on void measurement

APPENDIX

Void Fraction Measurement Error Analysis

The void fraction data obtained from the gamma densitometer signals contained errors due to the counting statistics, dynamic void effect, and use of a linear instead of a logarithmic interpolation method. A complete error analysis can be found in [15] and [16].

Linear and Log Interpolation Method. For a narrow-beam densitometer, a log interpolation method should be used for void fraction calculation. However, with the densitometer sensitivity, I_g/I_f, of 1.2 and the particular design of the ratemeter and data recorder used, a linear interpolation method was more convenient to use without introducing significant error. Void fractions calculated by the two methods are compared in Table 3.

Statistical Error. The relative error originating from the counting statistics is given by the following equation (Banerjee and Lahey [22]).

$$\frac{\Delta\alpha}{\alpha} = \frac{\Delta I/I}{\alpha \ln(I_g/I_f)} \{1 + (\alpha - 1)^2 + \alpha^2\}^{1/2} \quad \text{(A1)}$$

The statistical fluctuations in the detected gamma ray intensities $\Delta I/I$ were 0.008 and 0.015 for constant-injection and forced-oscillation tests, respectively. Based on these values, the relative error was computed from equation (A1) for various values of void fraction, as shown in Table 4.

Table 3 Void fraction calculation using linear and log interpolation
(Gamma Densitometer Sensitivity = 1.2)

Log	Linear
0.05	0.05
0.10	0.09
0.20	0.19
0.30	0.28
0.40	0.38
0.50	0.48
0.60	0.58
0.70	0.68
0.80	0.79
0.90	0.89

Table 4 Statistical errors

Void fraction	Relative error, $\Delta\alpha/\alpha$	
α	Constant-injection	Forced-oscillation
0.10	0.59	1.11[a]
0.20	0.28	0.53
0.30	0.18	0.34
0.40	0.14	0.25
0.50	0.11	0.20
0.60	0.09	0.17
0.70	0.08	0.15
0.80	0.07	0.13
0.90	0.07	0.12

[a]Means error band larger than measured value

Dynamic Voiding Effect. In the forced-oscillation tests, the void fraction histories showed large-amplitude oscillations. As pointed out by Harms and Forrest [23], the time-averaged void fraction measured by the densitometer is *different from the actual void fraction.*

In order to examine theoretically the dynamic voiding effect, the actual void fraction was assumed to vary with a cosine wave form. The gamma densitometer measured the time-averaged void fraction by averaging the instantaneous value over an integration period. The instantaneous and time-averaged void fraction profiles are shown in Fig. 13 for the integration period of 0.3 s and oscillation period of 4.0 s. The difference between the instantaneous and time-averaged values is the error due to the dynamic void effect.

Overall uncertainties in the void fraction data were estimated to be about ± 0.1 for constant-injection tests and ± 0.2 for forced-oscillation tests.

Measurements and Predictions of the Structure of Evaporating Sprays

A. S. P. Solomon[1]

J-S. Shuen[2]

Q-F. Zhang[3]

G. M. Faeth
Fellow ASME

Department of Mechanical Engineering,
The Pennsylvania State University,
University Park, PA 16802

An experimental and theoretical study of turbulent evaporating sprays is described. Experiments considered round, Freon-11 sprays (Sauter mean diameters of 31 and 58 μm) produced by an air-atomizing injector directed vertically downward in still air. The following structure measurements were made: mean and fluctuating gas velocities, total concentration of Freon-11, drop size and velocity distributions, mean gas temperature, and liquid flux distributions. Three spray models were evaluated using the new measurements: (a) a locally homogeneous flow (LHF) model where interphase transport rates are assumed to be infinitely fast; (b) a deterministic separated flow (DSF) model where finite interphase transport rates are considered but drop-turbulence interactions are ignored; and (c) a stochastic separated flow (SSF) model where effects of finite interphase transport rates and drop-turbulence interactions are considered using random-walk computations for drop motion and transport. The LHF and DSF models performed poorly, since both finite interphase transport rates and drop-turbulence interactions were important for present test conditions. The SSF model gave best agreement between predictions and measurements and appears to be an encouraging approach for treating practical sprays.

Introduction

A theoretical and experimental study of turbulent evaporating sprays injected into still air is described. Objectives were to measure the structure of evaporating sprays, having well-defined initial and boundary conditions, to gain a better understanding of spray transport, and to provide data for evaluation of spray models. Model evaluation was also initiated, considering several current methods.

A recent review by one of us (GMF) describes existing spray measurements and models [1], concluding that additional measurements with well-defined initial and boundary conditions are needed for definitive evaluation of spray models. The present study is part of a systematic investigation of sprays designed to help fill this gap in the literature. The work began with particle-laden jets [2–4] and then considered nonevaporating sprays [5, 6] prior to the present study of evaporating sprays. An earlier study of evaporating sprays was also conducted in this laboratory [7], however, the present study provides additional structure measurements and analysis.

Present experiments yielded measurements of mean and fluctuating gas velocities, mean gas temperatures, drop size and velocity distributions, liquid flux and species concentrations. Three representative spray models were evaluated using the new measurements: (*a*) a locally homogeneous flow (LHF) model, assuming infinitely fast interphase transport rates; (*b*) a deterministic separated flow (DSF) model, allowing for finite interphase transport rates but neglecting effects of turbulence; and (*c*) a stochastic separated flow (SSF) model, where both finite interphase transport rates and effects of turbulence are considered, using random-walk computations for drop motion and transport [1–7].

In the following, experimental and theoretical methods are described first of all. The paper concludes with a description of experimental results and evaluation of the models. The present discussion is brief; more details and a complete tabulation of data appear in [8].

Experimental Methods

Test Apparatus. The test apparatus was similar to the nonevaporating spray study [5]. Freon-11 was injected from an air-atomizing injector into still air; see Table 1 for test conditions and injector specifications. Injection was vertically downward within a screened enclosure (1 m square and 2.5 m high). The injector was traversed to measure profiles of flow properties (two directions using the injector mount and the major traverse direction by moving the entire enclosure). The screened inlet of the exhaust blower system was 1 m below the measurement plane, where its operation had negligible effect on flow properties.

Air flow to the injector, from an oil-free air supply, was metered and controlled with a critical flow orifice and pressure regulator. Freon-11 was fed to the injector from a pressurized tank and metered with a rotameter. Total jet momentum was measured, using earlier methods [7].

Instrumentation. Due to limitations in spatial resolution, structure measurements were only made for $x/d \geqq 50$. Mean and fluctuating gas velocities were measured with a frequency-shifted laser Doppler anemometer (LDA). A single-channel arrangement with several beam orientations provided measurements of various velocity components and the Reynolds stress. Seeding was provided using drops condensed from vacuum pump oil (0.6 μm mean diameter and roughly 3×10^{10} particles/m^3) in the surrounding air. Signals from large drops in the spray were eliminated by setting a low amplitude limit on the burst-counter data processor (maximum drop concentrations were more than an order of magnitude smaller than seeding particle concentrations in any event). Signal rates were high; therefore, the analog output of the burst counter was processed directly to yield time-averages, avoiding velocity bias.

Slide impaction and flash photography were used to measure drop-size distributions. Slide impaction involved

[1]Presently at General Motors Research Laboratories, Warren, MI.

[2]Presently at Sverdrup Technologies, Inc., Cleveland, OH.

[3]Presently Lecturer at the Department of Aero-Engine, Nanjing Aeronautical Institute, Nanjing, The Peoples Republic of China.

Contributed by the Heat Transfer Division for publication in the JOURNAL OF HEAT TRANSFER. Manuscript received by the Heat Transfer Division June 20, 1984.

Table 1 Summary of test conditions[a]

Case	1	2
Injector flow rates, mg/s		
Gas	188	120
Liquid[b]	1450	1894
Loading ratio[c]	7.71	15.78
Jet momentum, mN	105.7	59.7
Initial velocity, m/s	64.5	29.64
Reynolds number[d]	4.1×10^4	3.6×10^4
SMD, μm[e]	30.6	58.1
Spray angle, degrees[f]	27	29

[a] Both flows employ Spraying Systems air-atomizing injector (model 1/4J2050 nozzle, No. 67147 air nozzle, 1.194 mm injector exit diameter). Ambient and injector inlet temperature 300 ± 1 K; ambient pressure, 97 kPa.

[b] Freon-11.

[c] Ratio of injected liquid to gas flow rates.

[d] Assuming LHF with dynamic viscosity of air at NTP.

[e] Area-weighted average SMD measured by slide impaction at x/d = 50.

[f] Determined from concentration measurements at x/d = 50.

briefly exposing a small glass slide coated with magnesium oxide to the flow and measuring the diameters of craters in the coating left by impacting drops [7]. The raw data were corrected for bias, due to changes in probe collection efficiency with size, following Ranz [9]. Typically, 2000 drops were counted at each position to find the local drop size distribution which was processed directly to yield SMD. The slide impactor was also used for liquid flux measurements, similar to past work [7].

Mean gas temperatures were measured with a shielded fine-wire thermocouple, similar to Shearer et al. [1]. This consisted of a 25-μm-dia chromel-alumel, butt-welded thermocouple which was located along the centerline of a 1.6-mm o.d. half-cylindrical shield. The shield was positioned upstream of the thermocouple so that all but the smallest drops (less than 10 μm diameter) impinged on the shield rather than on the thermocouple.

A double-flash shadowphotography method was used for combined measurements of drop size and velocity, similar to McCreath et al. [10]. Several optical configurations, camera optics, and flash intervals were used (see [8] for details). The depth of field was determined as a function of camera optics and drop size so that the drop-size distribution could be corrected for depth-of-field bias [8]. Drop size and velocity distributions were found by measuring 600–800 drops at each location.

Profiles of the total concentration (gas and liquid) of Freon-11 were obtained using a sampling probe (4 mm i.d.) operating at isokinetic conditions (based on the mean gas-phase velocity). The tip of the probe was heated electrically to evaporate Freon-11. The resulting mixture was analyzed using a gas chromatograph.

Uncertainties in mean and fluctuating gas velocities were less than 10 percent and were repeatable within 5 percent. The uncertainty in mean drop velocity was less than 10 percent, but fluctuating drop velocities (particularly for large drops) are only qualitative due to the relatively low number of drops considered. Uncertainties in drop size are ± 25 percent for diameters less than 25 μm, declining to ± 10 percent for larger drops; drops less than 10 μm in diameter were not measured. Conservation checks of the overall flux of Freon-11 suggest uncertainties in concentration measurements less than 15 percent [8]. Past experience with liquid flux determinations by slide impaction, for nonevaporating sprays [5, 6], suggests uncertainties less than 20 percent. Uncertainties in mean gas temperatures are difficult to evaluate due to effects of drop impacts; therefore, these measurements are only qualitative.

Theoretical Methods

General Description. The present LHF model is very similar to earlier work on evaporating sprays in this laboratory [7] and the DSF model is a straightforward simplification of the SSF model; therefore, only the SSF model will be discussed in the following, with changes applying to the other models noted.

Major assumptions for the continuous phase are: axisymmetric and steady (in the mean) flow with no swirl (verified by measurements), boundary layer approximations apply, equal exchange coefficients of all species and heat, buoyancy only affects mean flow, and negligible effects of mean kinetic energy and radiation. The first of these is a condition of the experiments, the remainder are common assumptions for spray analysis [1]. The models employ widely adopted procedures of k-ϵ-g turbulence models for the gas phase, since this approach has provided good structure predictions for constant and variable density single-phase jets, particle-laden jets, and nonevaporating sprays [1–8, 11–13]. Favre (mass weighted)-averaged governing equations are solved, since only a single set of empirical constants is needed for both constant and variable density flows and terms involving density fluctuations are easily accommodated. Effects of buoyancy on turbulence properties were ignored, since this reduces empiricism and has been successful in the past [13].

Nomenclature

a = acceleration of gravity
C_i = parameters in turbulence model
d = injector diameter
d_p = drop diameter
f = mixture fraction
g = square of gas-phase mass fraction or mixture fraction fluctuations
G = liquid mass flux of Freon-11
k = turbulence kinetic energy
L_e = dissipation length scale
m = drop mass
$\dot{m}$ = drop evaporation rate
$P(f)$ = probability density function (PDF) of f
r = radial distance
S_ϕ = source term
$S_{p\phi}$ = drop source term
t = time
t_e = eddy lifetime
u = axial velocity
v = radial velocity
x = axial distance
Y_i = mass fraction of species i
V_j = volume of computational cell j
Δt_p = drop residence time in a computational cell
ϵ = rate of dissipation of turbulence kinetic energy
μ_t = turbulent viscosity
ρ = density
σ_i = turbulent Prandtl/Schmidt number
ϕ = generic property

Subscripts

c = centerline quantity
f = liquid
F = Freon-11
g = vapor
m = average over computational cell
p = drop property
0 = injector exit condition
∞ = ambient condition

Superscripts

$( )''$ = fluctuating quantity
$(\bar{\ })$ = Reynolds (time) average
$(\tilde{\ })$ = Favre (mass weighted) average

Table 2 Source terms in gas-phase governing equations[a]

ϕ	S_ϕ	$S_{p\phi}$
1	0	S_{pm}
$\tilde{u}$	$a(\rho_\infty - \tilde{\rho})$	S_{pu}
Y_{Fg}	0	S_{pm}
k	$\mu_t\left(\frac{\partial \tilde{u}}{\partial r}\right)^2 - \tilde{\rho}\epsilon$	0
ϵ	$\left(C_{\epsilon 1}\mu_t\left(\frac{\partial \tilde{u}}{\partial r}\right)^2 - C_{\epsilon 2}\tilde{\rho}\epsilon\right)(\epsilon/k)$	0
g_{Fg}	$C_{g1}\mu_t\left(\frac{\partial \tilde{Y}_{Fg}}{\partial r}\right)^2 - C_{g2}\tilde{\rho}\, g_{Fg}\epsilon/k$	0

C_μ	$C_{\epsilon 1}$	C_{g1}	$C_{\epsilon 2} = C_{g2}$	σ_k	σ_ϵ	$\sigma_{Y_{Fg}} = \sigma_{g_{Fg}}$
0.09	1.44	2.8	1.87	1.0	1.3	0.7

[a]Form shown is for DSF and SSF calculations. LHF calculations involve setting all $S_{p\phi} = 0$ and denoting $Y_{Fg} = f$ and $g_{Fg} = g$, similar to [7].

The liquid phase was treated by solving Lagrangian equations of motion for trajectories of a statistically significant sample of individual drops and then computing source terms for mass, momentum, and energy due to drops in the governing equations for the gas phase. This involves dividing the drops into n groups (defined by position, diameter, and velocity) at the initial condition, and then computing their subsequent life history in the flow. Difficulties in making measurements near the injector required specification of initial conditions at $x/d = 50$. Downstream of this position, the void fraction was always greater than 99.1 percent and assumptions of dilute sprays could be applied, i.e., the volume of the liquid phase, drop collisions, effects of adjacent drops on drop transport, and direct effects of particle motion on turbulence properties (turbulence modulation [1]) could be ignored with little error. These assumptions are typical of analysis of dilute sprays and are fully discussed elsewhere [1].

Consideration of energy transport within a drop excessively complicates analysis; therefore, the thin-skin approximation was applied, where the bulk liquid remains at its initial condition while only an infinitely thin layer at the surface is heated (or cooled) during evaporation. This approximation provides reasonably good treatment of transient drop effects (comparable to the more widely used uniform drop temperature limit) [1] and has the added advantage that all scalar properties in the gas phase can be specified solely by the mass fraction of vapor (called the state relationships) for present conditions [8]. State relationships are found by simple adiabatic mixing calculations for the state reached when various concentrations of liquid Freon-11 and air at ambient conditions are brought to thermodynamic equilibrium [8].

Gas Phase Formulation. Under present assumptions, the gas phase governing equations for the separated flow models are

$$\frac{\partial}{\partial x}(\tilde{\rho}\tilde{u}\tilde{\phi}) + \frac{1}{r}\frac{\partial}{\partial r}(r\tilde{\rho}\tilde{v}\tilde{\phi}) = \frac{1}{r}\frac{\partial}{\partial r}\left(r\frac{\mu_t}{\sigma_\phi}\frac{\partial \tilde{\phi}}{\partial r}\right) + S_\phi + S_{p\phi} \tag{1}$$

where $\tilde{\phi} = \overline{\rho\phi}/\tilde{\rho}$ is a Favre-averaged quantity. The parameters ϕ, S_ϕ, and $S_{p\phi}$ appearing in equation (1) are summarized in Table 2, along with appropriate empirical constants. Effects of laminar transport are negligible for present flows; therefore, the turbulent viscosity was found from

$$\mu_t = C_\mu \tilde{\rho}\, k^2/\epsilon \tag{2}$$

Interactions between drops and the continuous phase are ignored in the equations for k, ϵ, and g_{Fg} under the dilute spray approximation [1]. The mass and momentum source terms appearing in Table 2 are found by computing the net change of mass and momentum of each drop group i passing through computational cell j, as follows:

$$S_{pmj} = V_j^{-1}\left(\sum_{i=1}^{n} \dot{n}_i (m_{i_{in}} - m_{i_{out}})\right)_j \tag{3}$$

$$S_{puj} = V_j^{-1}\left(\sum_{i=1}^{n} \dot{n}_i ((m_i u_{pi})_{in} - (m_i u_{pi})_{out} + m_{im} a (1 - \rho/\rho_p)\Delta t_p)\right)_j \tag{4}$$

Except for the LHF model, the mass-averaged mean value of any scalar property is found from the state relationships $\phi(Y_{Fg})$ as follows [12, 13]

$$\tilde{\phi} = \int_0^1 \phi(Y_{Fg})\tilde{P}(Y_{Fg})\, dY_{Fg} \tag{5}$$

while $\tilde{\rho}$ is found from

$$\tilde{\rho} = \left(\int_0^1 \frac{1}{\rho(Y_{Fg})}\tilde{P}(Y_{Fg})\, dY_{Fg}\right)^{-1} \tag{6}$$

Following past work [1, 11, 13], $\tilde{P}(Y_{Fg})$ was assumed to be a clipped Gaussian function with most probable value and variance determined by known values of $\tilde{Y}_{Fg}$ and g_{Fg} [8]. Analogous procedures involving f and g apply for the LHF model [13]. Finally, the SSF model requires the time-averaged PDF of Y_{Fg}, $P(Y_{Fg})$, found as follows

$$P(Y_{Fg}) = (\tilde{\rho}/\rho(Y_{Fg}))\tilde{P}(Y_{Fg}) \tag{7}$$

Use of $P(Y_{Fg})$ in an equation analogous to equation (5) yields time-averaged scalar properties.

Calculations for the continuous phase were performed using a modified version of GENMIX [15]. The computational grid was similar to past work [2–7, 13].

Drop Phase. The SSF formulation involves computing drop trajectories as they encounter a random distribution of turbulent eddies, providing simultaneously for drop dispersion by turbulence and effects of turbulent fluctuations on interphase transport. The properties of each eddy and the time of interaction of a drop with a particular eddy were found by extending a method proposed by Gosman and Ioannides [14] and subsequently developed for nonevaporating flows in this laboratory [1–6]. Properties of each eddy are assumed to be uniform and to change randomly from one eddy to the next. The eddy velocity was found by making a random selection from the PDF for velocity assuming an isotropic Gaussian PDF having mean values $\tilde{u}$, $\tilde{v}$,

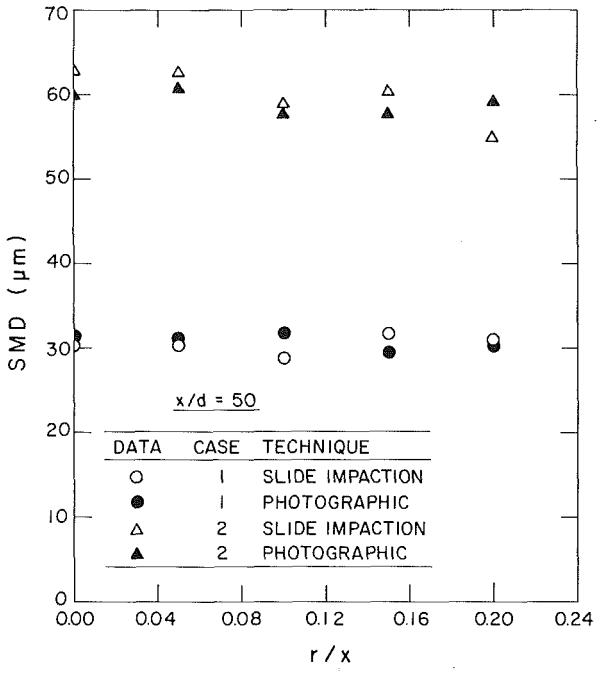

Fig. 1 Radial variation of SMD at $x/d = 50$

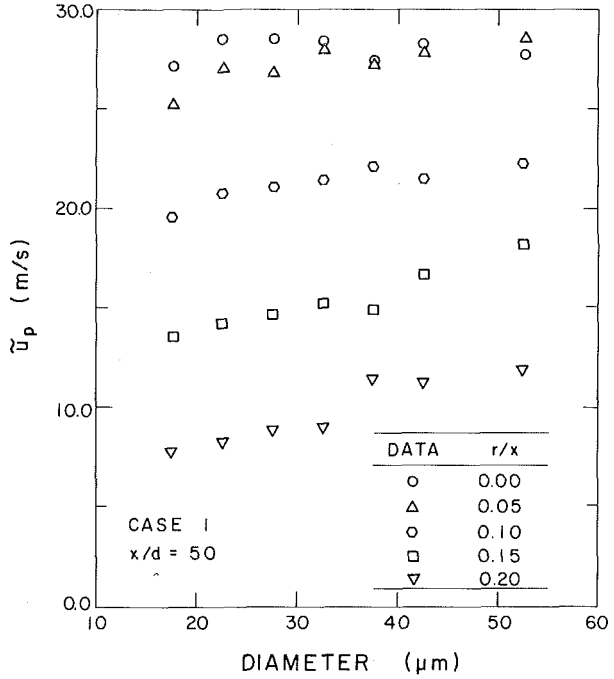

Fig. 2 Mean axial drop velocity as a function of drop size for the case 1 spray at $x/d = 50$

and 0 and standard deviations of $(2k/3)^{1/2}$. This ignores the distinction between Favre and time-averaged velocities (the latter should be sampled), but these differences are small for variable density jets [13] and the approximation avoids additional modeling to find density/velocity fluctuation correlations. Scalar properties of each eddy were found by randomly sampling the time-averaged PDF of Y_{Fg} and obtaining other scalar properties from the state relationships. A drop was assumed to interact with an eddy as long as the time of interaction did not exceed the eddy lifetime t_e or the displacement of the drop through the eddy did not exceed the characteristic eddy size L_e. These quantities were estimated following past practice [1–6], as follows

$$L_e = C_\mu^{3/4} k^{3/2}/\epsilon,\ t_e = L_e/(2k/3)^{1/2} \tag{8}$$

All quantities required for these procedures are available from the continuous-phase solution.

Assumptions for the particle trajectory calculations are typical of analysis of dilute sprays [1, 16]: Interphase transport is assumed to be quasi-steady; since ρ_p/ρ is large, effects of virtual mass, Basset forces, and Magnus forces are neglected with little error; phase equilibrium is assumed at the liquid surface; an empirical expression is used to treat drop drag; and drop heat and mass transfer are treated using stagnant film theory in conjunction with empirical expressions for effects of forced convection. Local ambient properties are taken to be instantaneous eddy properties for the SSF model and local mean properties for the DSF model. The complete formulation is lengthy and space limitations preclude presenting it here (see [1] or [8] for details). Numerical closure was achieved by considering trajectories of 6000 drop groups (SSF model) and 1800 drop groups (DSF model).

Uncertainties in average properties to determine drop transport are a potential source of error. Therefore, the reference condition for average properties was calibrated using measurements of life histories of single Freon-11 drops supported in an air stream [8].

Comparison With Measurements. Time-averaged mean and fluctuating velocities were measured but are compared here with predicted Favre averages (since Favre and time-averaged velocities are nearly the same [13]). The differences between Favre and time-averaged concentrations are generally small [13] and Favre and time-averaged drop properties are identical; therefore, predicted Favre averages are compared with these measurements. Measurements of mean temperatures with a fine-wire thermocouple fall closest to time averages [13]; therefore, predicted time averages are compared with measured mean temperatures.

Results and Discussion

Initial Conditions. Since it is not limited to dilute sprays, LHF predictions were obtained for the entire flow. Initial conditions for LHF calculations were specified at the injector exit, following past practice [7]. Initial conditions for the separated flow calculations were measured at $x/d = 50$. Direct measurements included mean and fluctuating velocities, Reynolds stress and turbulence kinetic energy of the gas phase; mean mass flux, drop-size distribution and mean and fluctuating axial velocities of the liquid phase; and total mean concentration of Freon-11 including both phases. ϵ distributions were computed using the turbulence model, and the mean mass fraction of Freon-11 vapor was found from overall conservation of Freon-11. Profiles of g_{Fg} were not measured directly; therefore, this parameter was estimated using the LHF solution. Fortunately, predictions are not very sensitive to this estimate.

The flash photographs did not provide sufficient resolution to measure mean and fluctuating radial drop velocities. Therefore, mean radial velocity was assumed to increase linearly from the axis to match the spray angle at the edge, while $\tilde{v}_p''^2 = \tilde{u}_p''^2/9$, following past practice [6].

The sensitivity of SSF predictions to initial conditions was assessed by varying each parameter 25 percent while keeping all others constant [8]. Predicted gas properties and SMD were relatively insensitive to input parameters. Predicted mass flux distributions were most sensitive, particularly to initial drop velocities, e.g., $\tilde{G}_c$ at $x/d = 250$ (the most sensitive location) varied 20–25 percent with 25 percent changes in initial values of $\tilde{u}_p$ and $\tilde{v}_p$.

Figure 1 is an illustration of profiles of SMD at $x/d = 50$, showing both slide impaction and photographic

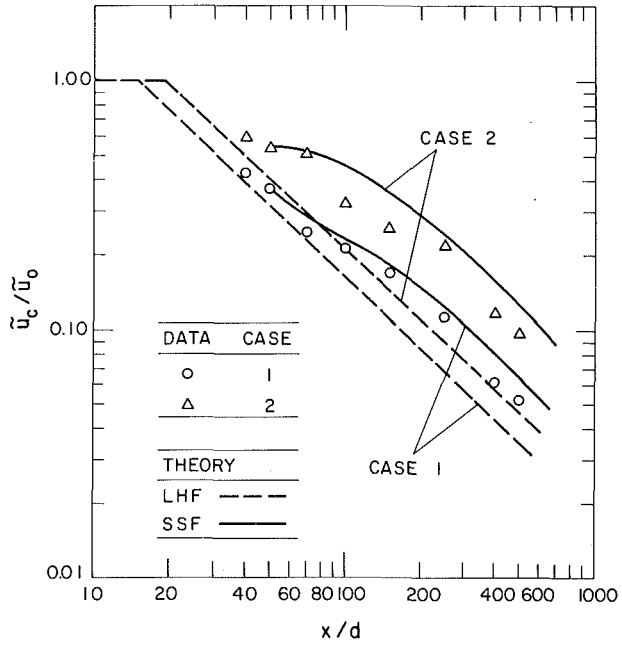

Fig. 3 Predicted and measured mean gas-phase velocity along the spray axis

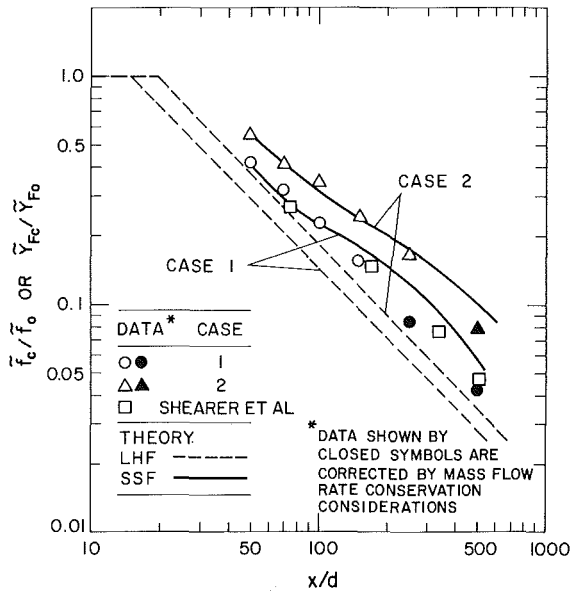

Fig. 4 Predicted and measured mean mixture fraction (LHF) or total Freon-11 concentration (SSF) along the spray axis

measurements. Differences between the two techniques are small, even though slide impaction yields a temporal average while photography yields a spatial average. This is expected since drop velocity is nearly independent of size at this axial location (see Fig. 2). The SMD is nearly invariant over the cross section, similar to nonevaporating sprays for the same location and injector [5, 6].

Mean drop velocity as a function of drop size and radial position at $x/d = 50$ is illustrated in Fig. 2 for the case 1 spray. Drop velocities are nearly independent of size near the axis, but increase with size near the edge of the flow. The case 2 spray and the earlier nonevaporating sprays had similar properties [5, 6, 8].

Centerline Properties. Predicted (LHF and SSF models) and measured mean gas-phase velocities along the axis are illustrated in Fig. 3. The LHF model overestimates the rate of

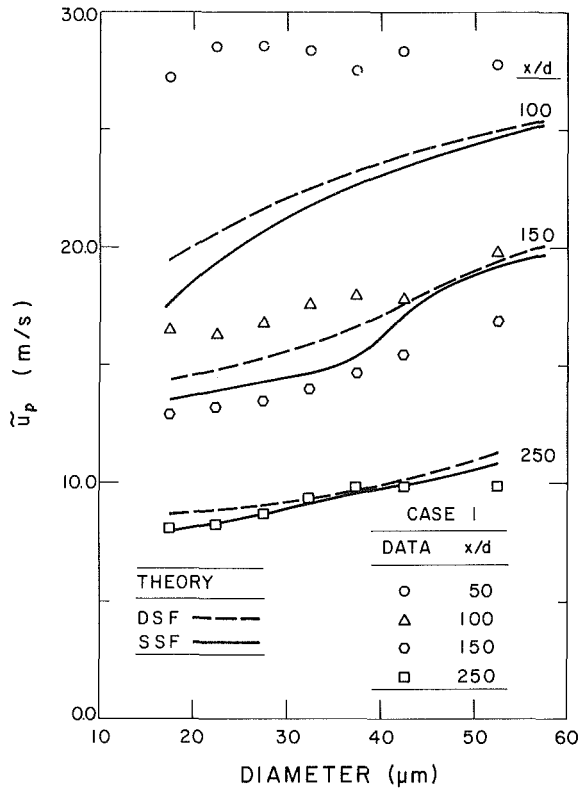

Fig. 5 Predicted and measured mean axial drop velocities along the axis of the case 1 spray

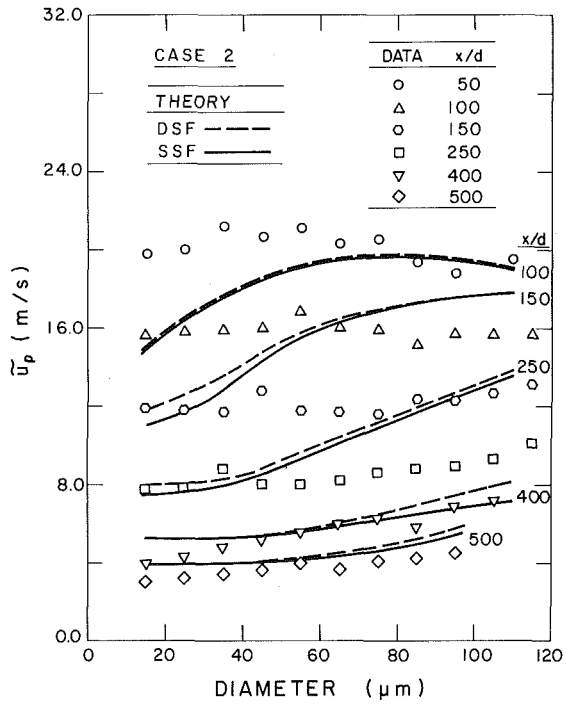

Fig. 6 Predicted and measured mean axial drop velocities along the axis of the case 2 spray

development of the sprays—similar to past findings [1, 7]—with performance deteriorating as the SMD increases. In contrast, the SSF model provides satisfactory predictions for both sprays.

Similar results for mean total mass fraction of Freon-11 (both liquid and gas phases) are shown in Fig. 4. In this case, predicted mean mixture fraction is illustrated for the LHF

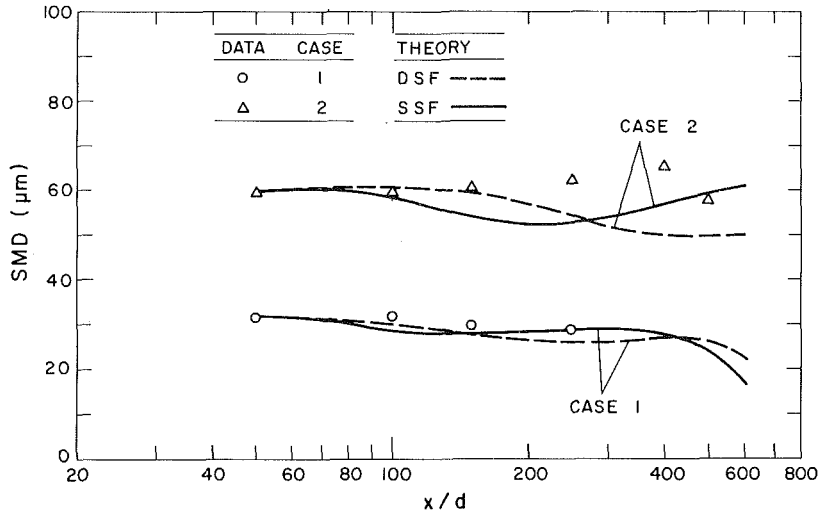

Fig. 7 Predicted and measured SMD along the spray axis

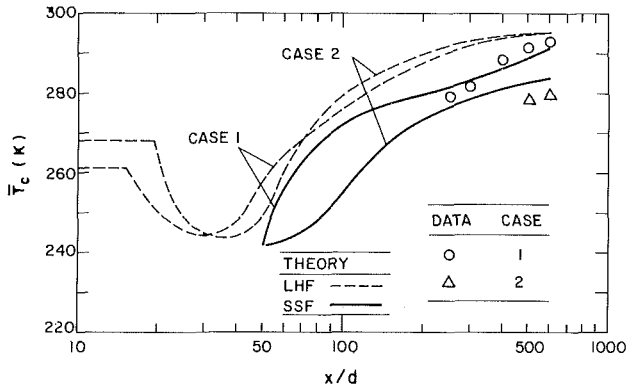

Fig. 8 Predicted and measured mean gas-phase temperature along the spray axis

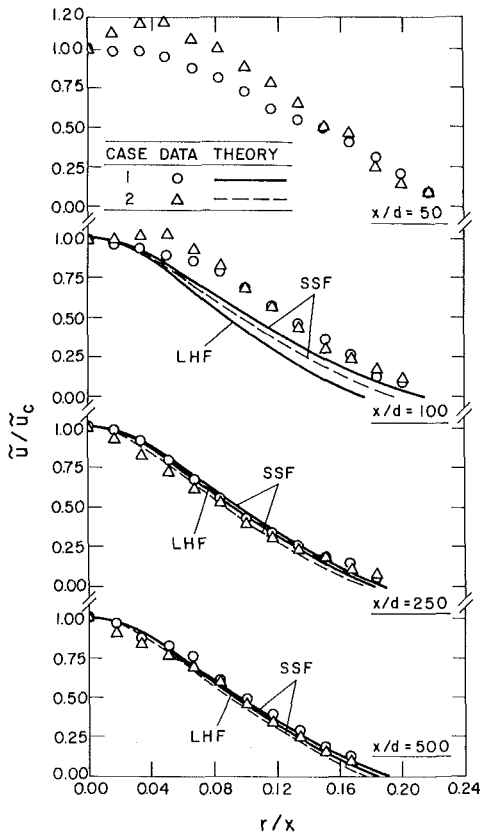

Fig. 9 Predicted and measured radial profiles of mean gas-phase velocity

model, since the two quantities are proportional under the LHF approximation. The data of Shearer et al. [7] for a Freon-11 spray very similar to the present case 1 spray are also shown. The measurements approach LHF predictions only far from the injector, where most drops have evaporated while the SSF model provides good predictions over the range where it was used.

Predicted (DSF and SSF models) and measured mean axial drop velocities are illustrated in Figs. 5 and 6. The SSF model predicts more rapid deceleration than the DSF model for each drop size, due to the nonlinear drop drag law interacting with turbulent fluctuations. Both models provide fair agreement with measurements, particularly at large x/d. Larger errors at x/d near 100 probably result from errors in initial conditions, since initial rates of dispersion are sensitive to estimates of initial velocity fluctuations. LHF predictions (not shown) generally underestimate drop velocities, similar to Fig. 3.

Figure 7 is an illustration of the variation of SMD along the axis. For nonevaporating sprays, turbulent drop dispersion causes the SMD to increase with increasing x/d [6]. For evaporating sprays, however, this is counteracted by drop evaporation; therefore, SMD is relatively constant until the largest drops finally evaporate. Predictions of both models and the measurements are comparable, suggesting that effects of dispersion are less significant for evaporating sprays than for nonevaporating sprays [5, 6].

Figure 8 is an illustration of predictions (LHF and SSF models) and measurements of mean gas-phase temperatures along the axis. Predictions are time averages, which is the best estimate of the thermocouple signal [8]. The poor performance of the LHF model is similar to findings of Shearer et al. [7] and reflects the importance of finite interphase transport rates. In contrast, the SSF model has smaller discrepancies, comparable to experimental uncertainties (particularly effects of drop impingement which would tend to lower measured temperatures).

Radial Profiles. Predicted (LHF and SSF models) and measured radial profiles of mean gas-phase velocity are illustrated in Fig. 9. Radial distances are normalized by distance from the injector, which is the similarity variable for fully developed constant density single-phase jets [1], so that predictions of flow width can be seen directly. Unlike most

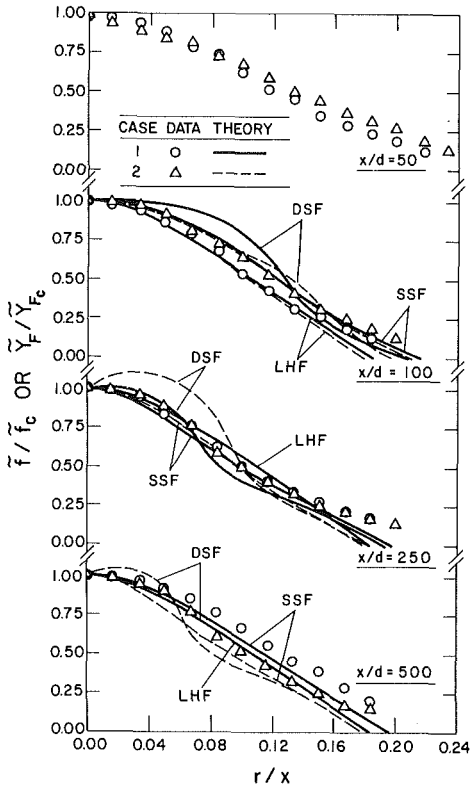

Fig. 10 Predicted and measured radial profiles of mean mixture fraction (LHF) or total Freon-11 concentration (SSF)

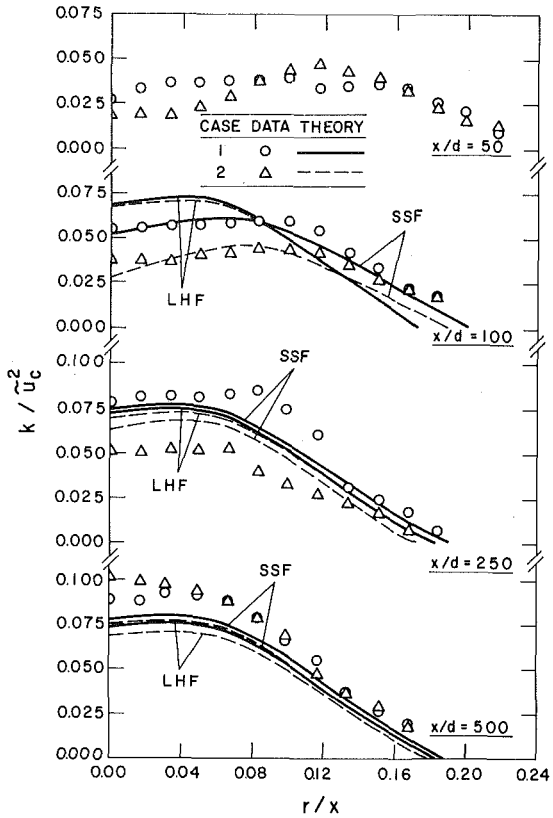

Fig. 11 Predicted and measured radial profiles of gas-phase kinetic energy

particle-laden jets [1], the flow widths of these sprays are greater than LHF predictions due to enhanced dispersion of drops by turbulence. This behavior, however, is less pronounced than in earlier nonevaporating spray tests [5, 6], since drops evaporate quite rapidly as they reach nearly pure air near the edge of the flow (reducing their radial dispersion as drops).

Predicted and measured radial profiles of total (gas and liquid) mean Freon-11 concentration are illustrated in Fig. 10. Predictions of all three models are shown. The DSF model yields a peaked profile, due to neglect of turbulent dispersion of drops, while the LHF and SSF models provide better agreement with measurements. In general, discrepancies between the LHF and DSF models and measurements are smaller than comparable measurements in nonevaporating sprays [5, 6], since Freon-11 vapor tends to dominate the concentration measurement for present test conditions. Turbulent dispersion of drops, however, increases the width of the flow in comparison to single-phase jets [1], an effect which decreases at large x/d where the drops have evaporated.

Figures 11 and 12 are plots of gas-phase turbulence kinetic energy and Reynolds stress. Both these quantities are quadratic, which amplifies discrepancies between predictions and measurements. The comparison between predictions and measurements is reasonably good for the case 1 spray, but poorer for the more heavily loaded case 2 spray. This could be due to turbulence modulation, which was ignored during present calculations. Unusually low values of Reynolds stress are observed for the more heavily loaded case 2 spray at $x/d = 100$ and 250. This could be due to bias of the measurements by drops, since fluctuating radial particle velocities are significantly smaller than radial gas fluctuations in two-phase jets [4].

Conclusions

The present measurements of evaporating spray structure should be useful for evaluation of dilute spray models since

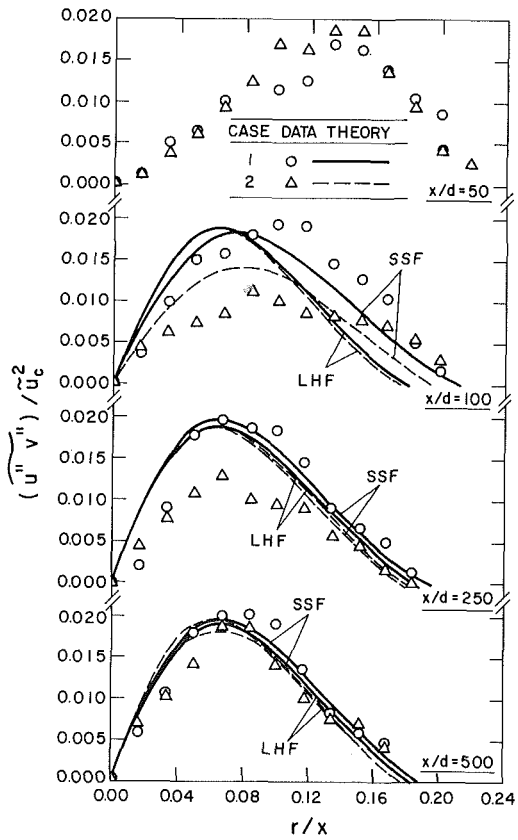

Fig. 12 Predicted and measured radial profiles of Reynolds stress

boundary layer approximations apply, simplifying numerical closure, while initial and boundary conditions are well defined. All measurements are tabulated in [8].

Major conclusions of the study are as follows:

1 The LHF and DSF models did not provide very satisfactory predictions for the test sprays. The DSF model performed poorly due to neglect of drop dispersion by turbulence and nonlinear drag/turbulence interaction. The LHF model performed poorly due to neglect of effects of finite interphase transport rates.

2 The SSF model yielded better predictions than the LHF and DSF models, similar to past experience [1-6], and appears to have potential for practical spray analysis.

3 Specification of initial conditions, i.e., liquid flux, drop sizes, mean and fluctuating drop velocities, etc., is the most critical factor in estimating the structure of dilute sprays, in agreement with Gosman and Ioannides [14].

Acknowledgments

This research was sponsored by the National Aeronautics and Space Administration Grant No. NAG 3-190, under the technical management of R. Tacina of the Lewis Research Center.

References

1 Faeth, G. M., "Evaporation and Combustion of Sprays," *Prog. Energy Combust. Sci.*, Vol. 9, 1983, pp. 1-76.

2 Shuen, J-S., Chen, L-D., and Faeth, G. M., "Evaluation of a Stochastic Model of Particle Dispersion in a Turbulent Round Jet," *AIChE J.*, Vol. 29, 1983, pp. 167-170.

3 Shuen, J-S., Chen, L-D., and Faeth, G. M., "Predictions of the Structure of Turbulent, Particle-Laden Round Jets," *AIAA J.*, Vol. 21, 1983, pp. 1483-1484.

4 Shuen, J-S., Solomon, A. S. P., Zhang, Q-F., and Faeth, G. M., "Structure of Particle-Laden Jets: Predictions and Measurements," *AIAA J.*, in press.

5 Solomon, A. S. P., Shuen, J-S., Zhang, Q-F., and Faeth, G. M., "Structure of Nonevaporating Sprays: I. Near-Injector Conditions and Mean Properties," *AIAA J.*, in press.

6 Solomon, A. S. P., Shuen, J-S., Zhang, Q-F., and Faeth, G. M., "Structure of Nonevaporating Sprays: II. Drop and Turbulence Properties," *AIAA J.*, in press.

7 Shearer, A. J., Tamura, H., and Faeth, G. M., "Evaluation of a Locally Homogeneous Flow Model of Spray Evaporation," *J. of Energy*, Vol. 3, 1979, pp. 271-278.

8 Solomon, A. S. P., "A Theoretical and Experimental Investigation of Turbulent Sprays," Ph.D. Thesis, Department of Mechanical Engineering, The Pennsylvania State University, 1984.

9 Ranz, W. F., "Principles of Inertial Impaction," Engineering Research Bulletin No. 13-66, The Pennsylvania State University, 1956.

10 McCreath, C. G., Roett, M. F., and Chigier, N. A., "A Technique for Measurement of Velocities and Size of Particles in Flames," *J. Phys. E.: Scientific Instruments*, Vol. 5, 1972, pp. 601-604.

11 Lockwood, F. C., and Naguib, A. S., "The Prediction of the Fluctuations in the Properties of Free, Round Jet, Turbulent, Diffusion Flames," *Comb. Flame*, Vol. 24, 1975, pp. 109-124.

12 Bilger, R. W., "Turbulent Jet Diffusion Flames," *Prog. Energy Combust. Sci.*, Vol. 1, 1976, pp. 87-109.

13 Jeng, S. M., and Faeth, G. M., "Species Concentrations and Turbulence Properties in Buoyant Methane Diffusion Flames," ASME JOURNAL OF HEAT TRANSFER, Vol. 106, No. 4, Nov. 1984, pp. 721-727.

14 Gosman, A. D., and Ioannides, E., "Aspects of Computer Simulation of Liquid-Fueled Combustors," AIAA Paper No. 81-0323, 1981.

15 Spalding, D. B., *GENMIX: A General Computer Program for Two-Dimensional Parabolic Phenomena*, Pergamon Press, Oxford, 1978.

16 Faeth, G. M., "Current Status of Droplet and Liquid Combustion," *Prog. Energy Combust. Sci.*, Vol. 3, 1977, pp. 191-224.

Film Condensation Over a Horizontal Cylinder for Combined Gravity and Forced Flow

M. di Marzo
Mechanical Engineering Department,
University of Maryland,
College Park, MD
Assoc. Mem. ASME

M. J. Casarella
Mechanical Engineering Department,
The Catholic University of America,
Washington, D.C.
Assoc. Mem. ASME

The problem of laminar film condensation of a saturated vapor flowing over a cold horizontal cylinder is investigated. A rigorous formulation of the governing equations for the vapor boundary layer and the condensed liquid film, including both the gravity-driven body forces and the imposed pressure gradient caused by the vapor flow, is presented. A generalized transformation of the governing equations allows a wide range of Froude numbers to be investigated. A unique value of the Froude number is defined which allows a distinction between the gravity-dominated flow ($Fr \to 0$) and the forced flow ($Fr \to \infty$) and basically defines the overlap region for the two solution domains. Numerical solutions are obtained in the merging flow regions controlled by both driving forces. The effects of density/viscosity ratio at the liquid-vapor interface, Prandtl number, Jakob number, and Froude number on the heat transfer characteristics are presented.

Introduction

The laminar film condensation of a saturated vapor on a cold surface has been the object of numerous investigations. Nusselt [1] in 1916 developed a very simple but effective analytical model to describe this phenomenon. In 1959 Sparrow [2] applied the boundary layer theory to the formulation of this problem. Since then, advances in the treatment of the boundary layer have allowed the solution of the condensation problem with increasing accuracy. Studies by Chen [3], Koh [4], Shekriladze [5], Fujii [6], and Denny [7] are some of the significant contributions. Recently, substantial advances in the numerical techniques for integrating the boundary layer equations allow the solution to account for most of the factors that influence condensation. Gaddis [8] formulated the governing equations for this problem under the most general conditions. He then proceeded to solve these equations with a series expansion solution. This technique has limitations on its applicability to a wide class of shapes. The present study deals with the set of equations analyzed by Gaddis. A more general approach to the solution and a discussion of the numerical results are pursued. In addition, a more flexible numerical technique is successfully applied to solve the problem for a horizontal circular cylinder as a particular case of the general class of two-dimensional body shapes.

While this paper was being reviewed, an investigation by Honda [9] was submitted to this journal and was recently published. This investigation deals with a similar problem addressing different aspects of it. The numerical technique presented by Honda is unique with respect to the treatment of nonvertical vapor flows. The major thrust of his investigation is the inclusion of the wall temperature distribution obtained by considering the conduction heat transfer in the tube wall. However, the use of the cylindrical coordinate system restricts the solution to circular cylinders.

Formulation of the Governing Equations

A horizontal cylinder is immersed in a flowing stream of pure vapor at its saturation temperature T_s. The vapor free-stream velocity and the gravity field are in the same direction. The cylinder surface temperature T_0 is uniform and lower than T_s; therefore, condensation occurs and a thin film of condensed liquid wets the cylinder surface. The film moves under the combined action of the gravity force and the shear forces at the liquid-vapor interface due to the vapor motion. A representation of the model and the coordinate system is given in Fig. 1. Note that the curvilinear coordinate system has its origin on the liquid-vapor interface and has axes tangential and orthogonal to it. The nondimensional variable θ relates to the coordinate x, being equal to the ratio of x and the fixed characteristic length a, In the particular case of the circular cylinder, θ is also the angle from the vertical symmetry plane.

The rate of condensation of the vapor depends on the effectiveness of the heat removal from the liquid-vapor interface. The heat delivered at the interface by the condensation process is transferred through the liquid film to the cylinder surface and it is also convected downstream by the moving liquid film; therefore, the fluid dynamic and the thermal behavior of the liquid film govern the entire process.

The conservation of mass, momentum, and energy for the steady laminar flow are described by the following equations.

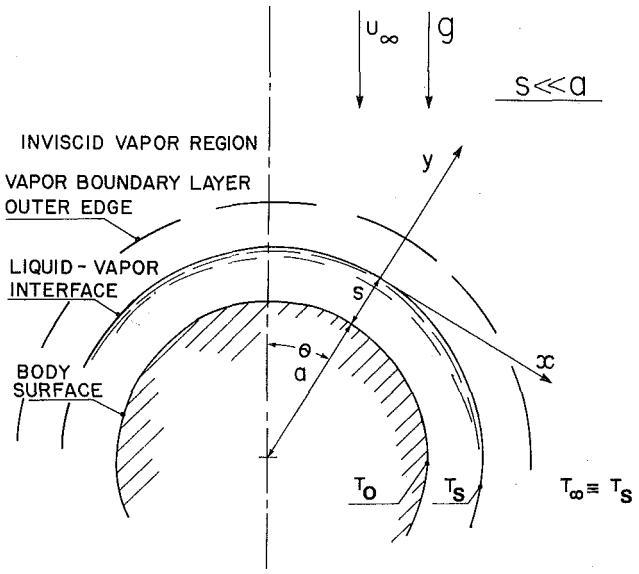

Fig. 1 Model and coordinate system

Contributed by the Heat Transfer Division for publication in the JOURNAL OF HEAT TRANSFER. Manuscript received by the Heat Transfer Division April 26, 1983. Paper No. 83-HT-84.

Vapor boundary layer

$$\frac{\partial u_V}{\partial x} + \frac{\partial v_V}{\partial y} = 0 \tag{1}$$

$$u_V \frac{\partial u_V}{\partial x} + v_V \frac{\partial u_V}{\partial y} = -\frac{1}{\rho_V}\frac{dp}{dx} + \nu_V \frac{\partial^2 u_V}{\partial y^2} \tag{2}$$

Liquid film (treated as a boundary layer)

$$\frac{\partial u_L}{\partial x} + \frac{\partial v_L}{\partial y} = 0 \tag{3}$$

$$u_L \frac{\partial u_L}{\partial x} + v_L \frac{\partial u_L}{\partial y} = -\frac{1}{\rho_L}\frac{dp}{dx} + g\left(1 - \frac{\rho_V}{\rho_L}\right)f + \nu_L \frac{\partial^2 u_L}{\partial y^2} \tag{4}$$

$$u_L \frac{\partial T_L}{\partial x} + v_L \frac{\partial T_L}{\partial y} = \alpha_L \frac{\partial^2 T_L}{\partial y^2} \tag{5}$$

Viscous dissipation, surface tension forces and temperature dependence for the properties have been neglected. The appropriate boundary conditions for this problem are

(*i*) At the cylinder surface ($y = -s$)

$$u_L = 0 \tag{6}$$

$$v_L = 0 \tag{7}$$

$$T_L = T_0 \tag{8}$$

(*ii*) At the liquid-vapor interface ($y = 0$)

$$u_V = u_L \tag{9}$$

$$\rho_V v_V = \rho_L v_L \tag{10}$$

$$\mu_V \frac{\partial u_V}{\partial y} = \mu_L \frac{\partial u_L}{\partial y} \tag{11}$$

$$T_L = T_s \tag{12}$$

(*iii*) At the vapor boundary layer outer edge ($y \to \infty$)

$$u_V = u_e \tag{13}$$

The thickness of the liquid film is determined by a heat balance stating that the heat transferred at the body surface is equal to the heat released at the liquid-vapor interface by the condensation process minus the heat that is convected away by the liquid film. Along with the boundary layer approximation, this balance can be written as

$$k_L \left(\frac{\partial T_L}{\partial y}\right)_{-s} = \frac{d}{dx}\int_{-s}^{0} \rho_L u_L [h_{fg} + c_L (T_s - T_L)]dy \tag{14}$$

By making use of the nondimensional variables θ, z and recalling that the inviscid solution for the pressure gradient gives

$$\frac{dp}{dx} = -\rho_V u_e \frac{du_e}{dx} \tag{15}$$

the conservation laws with their boundary conditions are formulated in terms of the nondimensional stream function ψ and temperature ϕ defined by the relations

$$\frac{\partial \psi}{\partial \theta} = -\frac{va}{\nu} \tag{16}$$

$$\frac{\partial \psi}{\partial z} = \frac{ua}{\nu} \tag{17}$$

$$\phi = \frac{T_s - T}{T_s - T_0} \tag{18}$$

For a detailed discussion refer to [10].

Note that although the momentum and energy equations appear uncoupled, the thickness of the liquid layer implicitly links these equations through the heat balance on the condensed liquid film. In essence, this is a system of three nonlinear partial differential equations coupled through a nonlinear integrodifferential equation.

Scaling Laws and Solution Procedure

In order to solve the system of equations, the following transformation from the physical plane (θ, z) into the transformed plane (θ, η) is introduced

$$\eta = Cz(b/\theta)^{1/2} \tag{19}$$

The constant C and the function $b(\theta)$ are, as yet, undefined. The transformed stream function and temperature become

$$F(\theta,\eta) = (C)^{-1}(b/\theta)^{-1/2}\psi \tag{20}$$

Nomenclature

a = cylinder radius
b = prescribed function, equation (36) or equation (38)
C = prescribed scaling parameter, equation (35) or equation (37)
c = specific heat
F = transformed stream function, equation (20)
f = prescribed shape function, equation (41)
Fr = Froude number = $u_\infty^2/ag(1-\rho_V/\rho_L)$
Fr_c = Froude combined flow (Fig. 2)
G = transformed temperature of the liquid film, equation (21)
g = acceleration of gravity
Gr = Grashof number = $a^3 g(1-\rho_V/\rho_L)/\nu_L^2$
h = heat transfer coefficient: $q = h(T_s - T_0)$
h_{fg} = specific enthalpy of condensation
IR = interfacial ratio = $\mu_V \rho_V / \mu_L \rho_L$
Ja = Jakob number = $c_L(T_s - T_0)/h_{fg}$
k = thermal conductivity
M = driving forces function, equation (34)
Nu = Nusselt number = $h2a/k_L$
p = pressure
Pr = Prandtl number = $\mu_L c_L / k_L$
q = heat flux
Re_L = Reynolds number of the liquid film = $u_\infty a/\nu_L$
Re_V = Reynolds number of the vapor = $u_\infty a/\nu_V$
s = thickness of the liquid film
T = temperature
T_s = fluid saturation temperature
u = velocity component in the x direction
u_e = inviscid flow velocity at the cylinder surface
u_∞ = vapor free-stream velocity
v = velocity in the y direction
w = prescribed function of θ: $w(\theta) = u_e(\theta)/u_\infty$
x = coordinate tangent to the liquid-vapor interface
y = coordinate normal to the liquid-vapor interface
z = nondimensional coordinate: $y = az$
α = thermal diffusivity = $k_L/\rho_L c_L$
η = transformed coodinate of y, equation (19)
θ = nondimensional coordinate: $x = a\theta$
μ = viscosity
ν = kinematic viscosity
ρ = density
ϕ = nondimensional temperature, equation (18)
ψ = nondimensional stream function, equations (16) and (17)

Superscripts

$'$ = differentiation with respect to η

Subscripts

L = liquid film property
V = vapor property
0 = property at the cylinder surface

$$G(\theta,\eta)=\phi \tag{21}$$

By substituting into the governing equations, one obtains

Vapor boundary layer

$$F_V'''+\left(\frac{\theta}{2b}\frac{db}{d\theta}+\frac{1}{2}\right)F_VF_V''-\frac{\theta}{b}\frac{db}{d\theta}(F_V')^2$$

$$=\theta\left(F_V'\frac{\partial F_V'}{\partial\theta}-F_V''\frac{\partial F_V}{\partial\theta}\right)-\frac{(\mathrm{Re})^2}{c^4}\frac{w\theta}{b^2}\frac{dw}{d\theta} \tag{22}$$

Liquid film

$$F_L'''+\left(\frac{\theta}{2b}\frac{db}{d\theta}+\frac{1}{2}\right)F_LF_L''-\frac{\theta}{b}\frac{db}{d\theta}(F_L')^2$$

$$=\theta\left(F_L'\frac{\partial F_L'}{\partial\theta}-F_L''\frac{\partial F_L}{\partial\theta}\right)-M \tag{23}$$

$$C''(\mathrm{Pr})^{-1}+\left(\frac{\theta}{2b}\frac{db}{d\theta}+\frac{1}{2}\right)F_LG'$$

$$=\theta\left(F_L'\frac{\partial G}{\partial\theta}-G'\frac{\partial F_L}{\partial\theta}\right) \tag{24}$$

Heat balance

$$(G')_{-\eta_0}=-\left(\frac{\theta}{2b}\frac{db}{d\theta}+\frac{1}{2}\right)\int_{-\eta_0}^{0}F_L'[(\mathrm{Ja})^{-1}+G]d\eta$$

$$-\theta\frac{d}{d\theta}\int_{-\eta_0}^{0}F_L'[(\mathrm{Ja})^{-1}+G]d\eta \tag{25}$$

The boundary conditions become

(*i*) At the cylinder surface ($\eta=-\eta_0$)

$$F_L=0 \tag{26}$$

$$F_L'=0 \tag{27}$$

$$G=1 \tag{28}$$

(*ii*) At the liquid–vapor interface ($\eta=0$)

$$F_V'=F_L' \tag{29}$$

$$\left(\frac{\theta}{2b}\frac{db}{d\theta}+\frac{1}{2}\right)F_V+\theta\frac{\partial F_V}{\partial\theta}$$

$$=(IR)^{-1/2}\left[\left(\frac{\theta}{2b}\frac{db}{d\theta}+\frac{1}{2}\right)F_L+\theta\frac{\partial F_L}{\partial\theta}\right] \tag{30}$$

$$F_V''=(IR)^{-1/2}F_L'' \tag{31}$$

$$G=0 \tag{32}$$

(*iii*) At the vapor boundary layer outer edge ($\eta\to\infty$)

$$F_V'=\frac{w}{b}\mathrm{Re}_V(C)^{-2} \tag{33}$$

The liquid film is driven by the body forces, the pressure gradient, and the interfacial shear. In the liquid film momentum equation (23) the term M represents the body forces and the pressure gradient and it is written

$$M=\frac{(\mathrm{Re}_L)^2(\rho_V/\rho_L)}{C^4}\frac{w\theta}{b^2}\frac{dw}{d\theta}+\frac{\mathrm{Gr}}{C^4}\frac{f\theta}{b^2} \tag{34}$$

The interfacial shear is introduced by the boundary condition at the liquid–vapor interface.

The constant C and the function $b(\theta)$ in equation (33, 34) are defined in two different forms that are designated as Reynolds scaling and Grashof scaling. For the *Reynolds scaling*, they are written as

$$C=(\mathrm{Re})^{1/2} \tag{35}$$

$$b(\theta)=w(\theta) \tag{36}$$

while for the *Grashof scaling*, they become

$$C=(\mathrm{Gr})^{1/4} \tag{37}$$

$$b(\theta)=f(\theta) \tag{38}$$

Therefore, the function M is respectively

$$M=\frac{\rho_V}{\rho_L}\frac{\theta}{w}\frac{dw}{d\theta}+(\mathrm{Fr})^{-1}\frac{f\theta}{w^2} \quad \text{(Reynolds scaling)} \tag{39}$$

and

$$M=(\mathrm{Fr})\frac{\rho_V}{\rho_L}\frac{w\theta}{f^2}\frac{dw}{d\theta}+\frac{\theta}{f} \quad \text{(Grashof scaling)} \tag{40}$$

Note that the Grashof scaling allows one to solve the problem for gravity-driven flow of the liquid film, that is for values of the Froude number in the low range including zero. The Reynolds scaling, on the other hand, is more adequate for the interfacial shear-dominated flow of the liquid film corresponding to very high values of the Froude number. The two different scalings are needed because equation (39) presents a singularity for Froude number equal to zero, while equation (40) is unbounded for very large values of the Froude number. The merits of using the two scaling laws become apparent when the numerical results are discussed.

The final form of the system of equations (22) to (33) shows that the shape of the body surface is prescribed solely by the functions f and w; thus the analysis could be readily extended to various body configurations by an adequate selection of

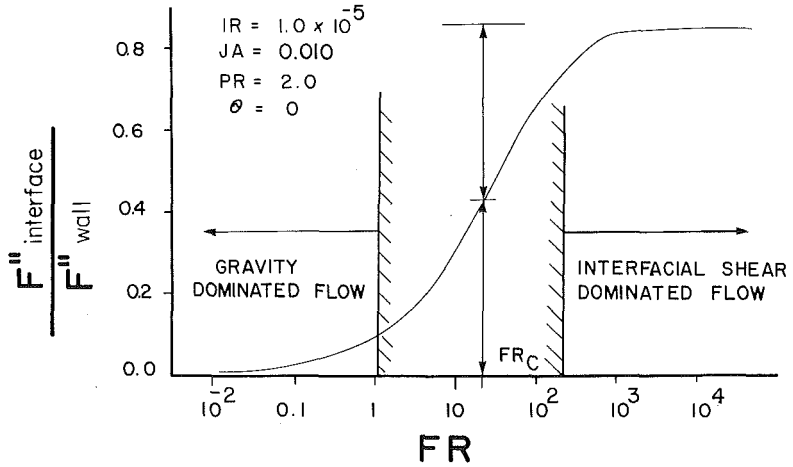

Fig. 2 Ratio of the shear stresses at the liquid-vapor interface and at the cylinder surface as a function of the Froude number

these two functions. In this investigation, the two functions describing a circular cylinder surface are respectively

$$f(\theta) = \sin\theta \tag{41}$$

$$w(\theta) = 2\sin\theta \tag{42}$$

Note that the inviscid solution for the tangential velocity at the cylinder surface w is obtained neglecting the suction effect due to the condensation process and ignoring the presence of the condensed liquid film.

The system of equations is solved by an iteration procedure. A thickness of the liquid layer at the front stagnation point of the cylinder is assumed. The nonlinear momentum equations for the liquid and vapor regions are simultaneously integrated with an iterative linearization scheme. The energy equation for the liquid layer is linear and its solution together with the velocity profile is substituted in the heat balance equation. If the heat balance is not satisfied, a new value for the liquid film thickness is assumed and this procedure is repeated. Once the heat balance equation is satisfied within a given accuracy, the solutions at downstream locations on the body are subsequently computed until separation occurs and the boundary layer model becomes invalid.

At each location on the cylinder, the integration in the η direction is performed with an implicit method developed by Keller [11] and designated as the Box method. The equations are integrated along the θ direction with a finite difference approximation of the first order derivatives. Further details on the numerical techniques are discussed by di Marzo [10].

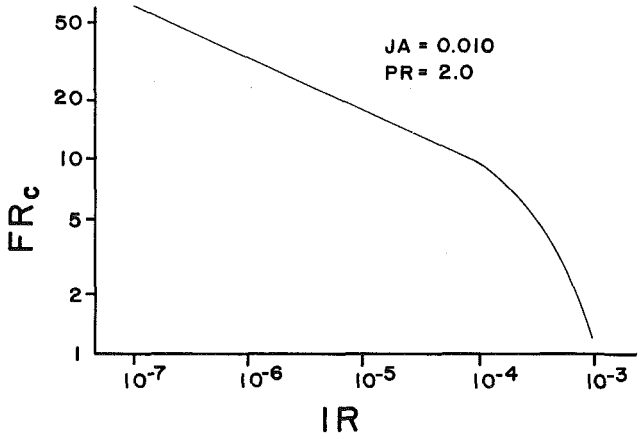

Fig. 3 Froude combined flow as a function of the interfacial ratio

Analysis for Combined Gravity and Forced Flow

The major effort of this investigation is to clearly identify a criterion to merge the solutions obtained from the Grashof and the Reynolds scaling laws. The numerical results overlap in the flow region controlled by both driving forces (gravity and interfacial shear). The results will show that the fluid mechanics of the liquid film is directly responsible for the heat transfer behavior. This consideration allows one to identify a criterion strictly related to the motion of the liquid film. Of all the features one could consider, the ratio of the shear stress at the liquid-vapor interface to the shear stress at the wall is unique because it allows the direct comparison of both the gravity and the shear dominated flows, independently of the scaling law used. Most other parameters, including those associated with the heat transfer, are unbounded in one of the limits of the Froude number.

Figure 2 shows the ratio of the shear forces at the liquid-vapor interface and cylinder surface as a function of the Froude number. In order to later describe the behavior of the various heat transfer parameters in the intermediate flow region, the value of Froude number corresponding to the midpoint of the shear ratio curve, shown in Fig. 2, is defined as the *Froude Combined Flow* (Fr_c). This is the criterion that will separate the two flow domains (gravity/interfacial shear).

Figure 3 illustrates the dependence of Fr_c on the Interfacial Ratio parameter. For low values of IR ($IR < 10^{-4}$) an exponential growth is observed. For high values of the $IR > 10^{-4}$, the value of Fr_c is decreasing rapidly, which means that most of the flow region is dominated by the interfacial shear forces. Figure 4 shows the effect of the thermal driving force (Jakob number) on the value of Fr_c for two Prandtl numbers.

Figure 5 describes the velocity profiles in the liquid layer. As expected, for a high Froude number, the profile is linear, while for zero Froude number the profile is parabolic. These results are in agreement respectively with the Couette flow solution and with the free shear flow of a liquid layer over an inclined plane.

The previous results were for values of Fr_c at the stagnation point. It should be noted that Fr_c is constant in the neighborhood of the stagnation point ($0 \le \theta < 30$ deg for a circular cylinder) and increases thereafter. The consequence of this selection is that Fr_c is biased toward the gravity flow solution. However, this fact is advantageous if one considers that the solution obtained by Nusselt for gravity-dominated flow is reasonably accurate up to that point (see Fig. 6).

Several valid alternative criteria could also be used to separate the flow regimes into two regions where different scaling laws or correlations can predict the heat transfer

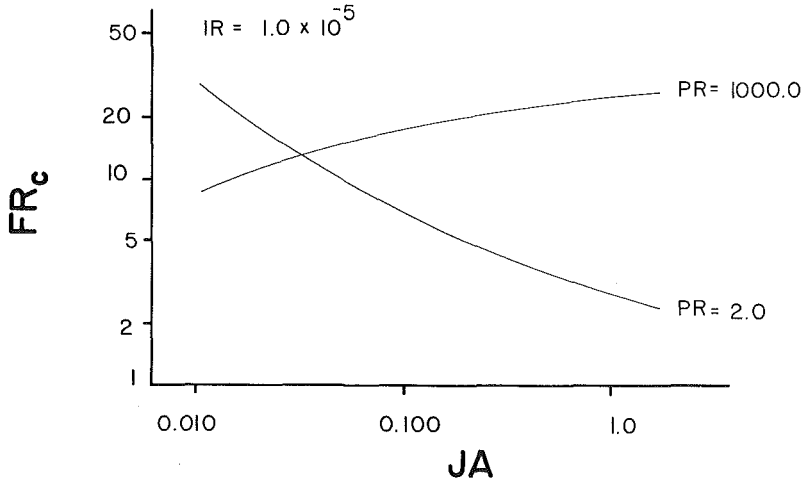

Fig. 4 Froude combined flow as a function of the Jakob number

behavior. The uniqueness of both the shear stress ratio and its selection at the stagnation point allows one to define a criterion based on the "inherent" physical features of the phenomenon.

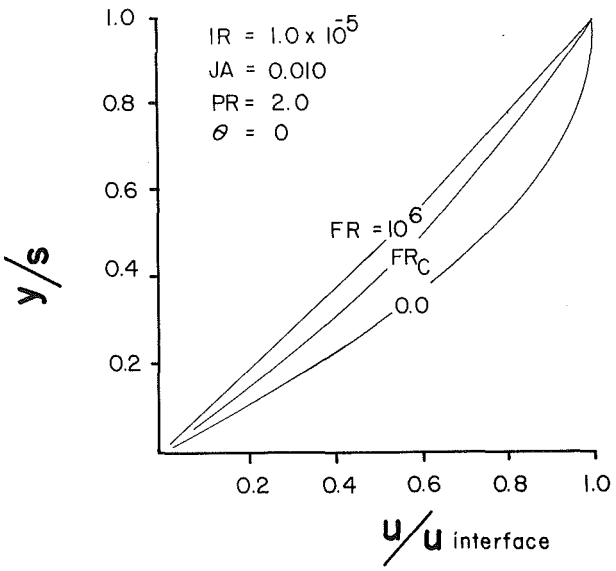

Fig. 5 Liquid film velocity profiles

Numerical Results

The nondimensional parameters governing the condensation process are Froude number, Grashof number, Jakob number, Nusselt number, Prandtl number, Reynolds number, and the ratio of the interfacial properties (density, viscosity). Note that the density and viscosity ratios at the liquid–vapor interface are combined. The results are analyzed with respect to their products identified as the Interfacial Ratio (*IR*). This same parameter was also considered by Koh [4] in the treatment of the forced convection condensation.

Extensive computations indicate that the temperature profile in the liquid film remains linear over a wide range of these governing parameters. The linear temperature profile implies that the Nusselt number at the cylinder surface is equal to the inverse of the nondimensional liquid layer thickness. Therefore, the rate of increase of the thickness of the liquid layer moving along the cylinder is proportional to the decay of the heat transfer coefficient.

In order to compare the results over the range of Froude number, the thickness along the cylinder is normalized with respect to the thickness at the stagnation point. The results are shown in Fig. 7. Note that for the gravity-dominated flow

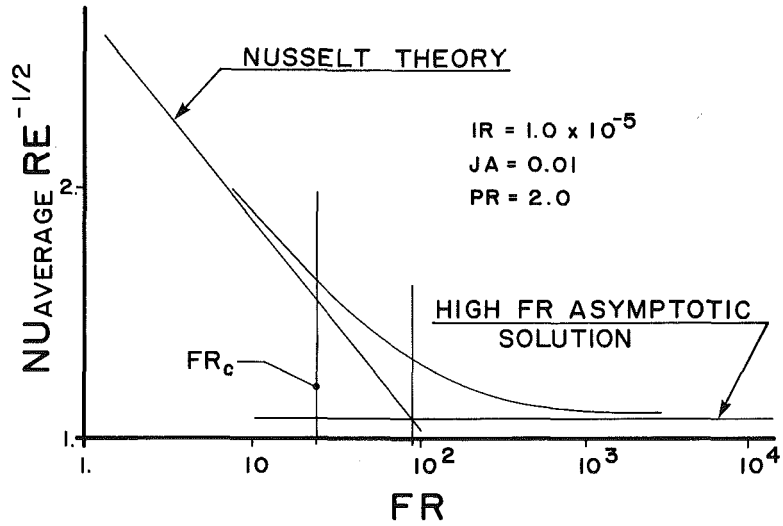

Fig. 6 Froude combined flow with respect to the heat transfer behavior (Reynolds scaling)

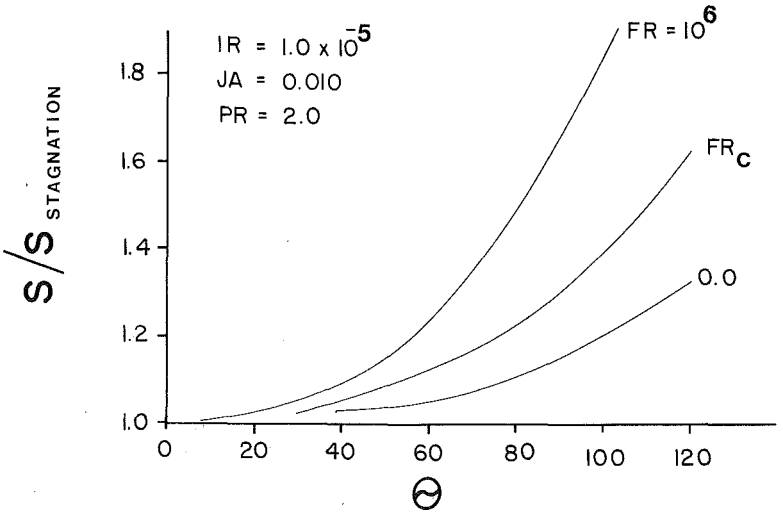

Fig. 7 Liquid film thickness along the cylinder surface

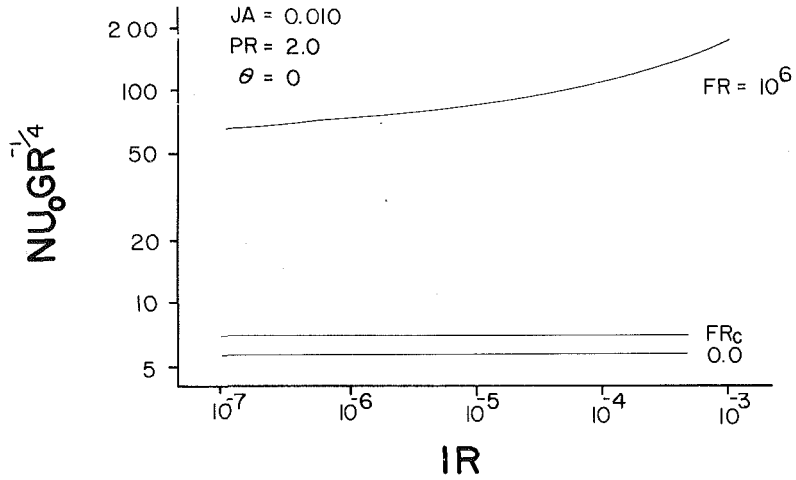

Fig. 8 Heat transfer coefficient at the cylinder stagnation point as a function of the interfacial ratio (Grashof scaling)

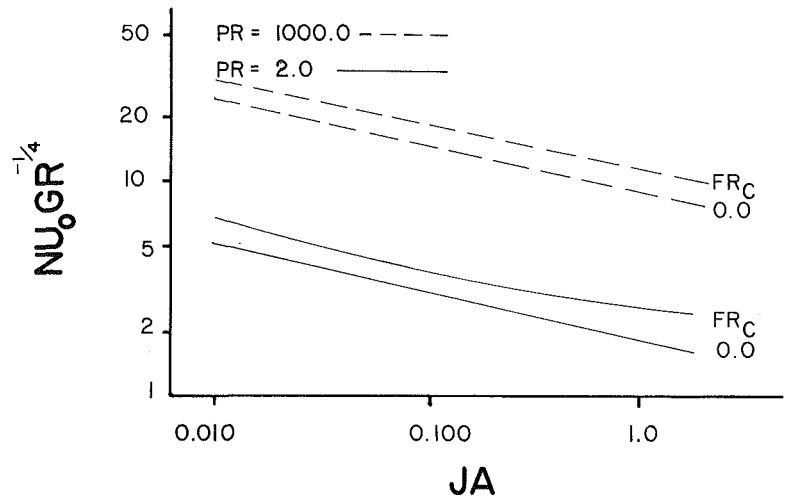

Fig. 9 Heat transfer coefficient at the cylinder stagnation point as a function of the Jakob number (Grashof scaling)

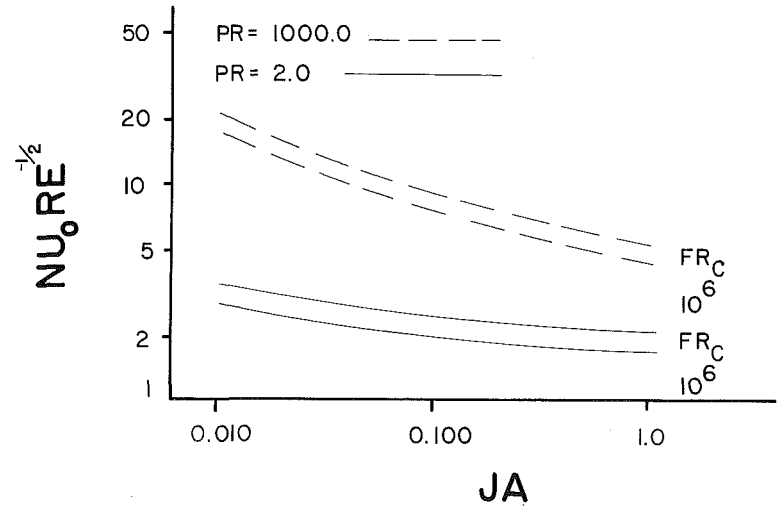

Fig. 10 Heat transfer coefficient at the cylinder stagnation point as a function of the Jakob number (Reynolds scaling)

(Fr = 0), the normalized liquid layer thickness increases gradually along the cylinder; while for the interfacial shear dominated flow (Fr = 10^6), the normalized thickness of the liquid layer increases more rapidly.

The primary objective of this investigation is to describe the heat transfer behavior as a function of the various parameters that appear in the governing equations and boundary conditions.

Figure 8 shows the behavior of the Nusselt number at the front stagnation point of the cylinder as a function of the

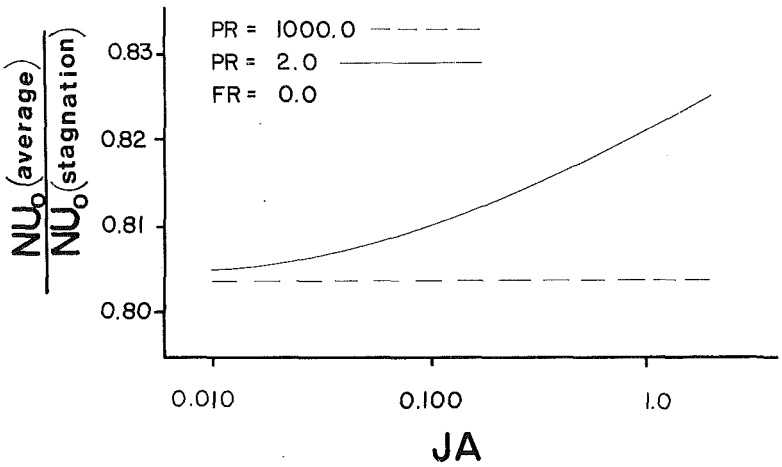

Fig. 11 Ratio of the average and stagnation heat transfer coefficient as a function of the Jakob number

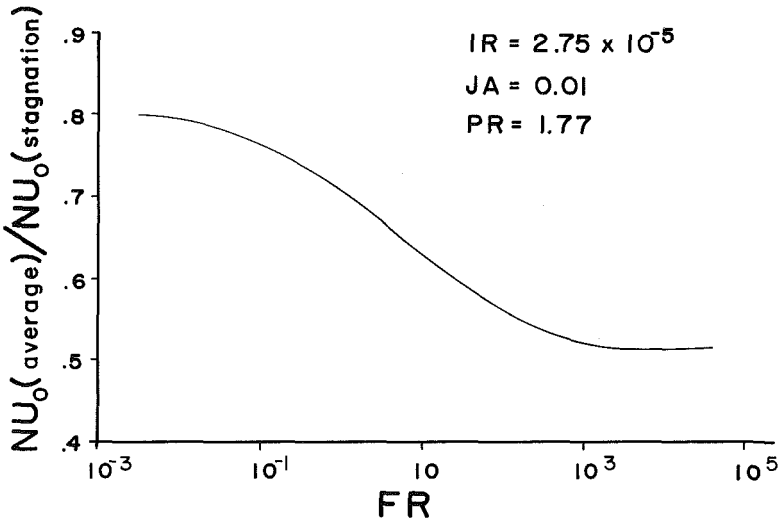

Fig. 12 Ratio of the average and stagnation heat transfer coefficient as a function of the Froude number

Interfacial Ratio for various Froude numbers. Note that for the gravity-driven flow, the parameter *IR* does not influence the heat transfer process. This result becomes apparent if one considers that the interfacial effects have little influence on the flow since the gravitational forces are mainly responsible for the liquid film motion. The Grashof scaling is used in plotting these results and consequently the data tend to a finite limit for Froude number equal to zero.

Figures 9 and 10 illustrate the effects of Jakob number on the heat transfer (Nusselt number for gravity and shear dominated flow, respectively). An important result shown in these figures is that the values of Nusselt number are bounded in the region between two adjacent curves shown in the figures. For example, consider a fluid with a Prandtl number equal to 2. All the solutions are in the region between the two lower curves and, in particular, the solution for Fr_c is coincident in both figures. This result is a clear demonstration of the merits of the two separate scaling laws used in the formulation.

All the heat transfer data presented thus far are at the front stagnation point of the cylinder. In Fig. 11 the average Nusselt number over the whole cylinder surface is related to the value of Nusselt number at stagnation. It can be observed that for very high values of the Prandtl number, one can observe that

$$Nu_{average} = 0.804\, Nu_{stagnation} \tag{43}$$

where the average Nusselt number is obtained by averaging the local Nusselt number over the cylinder surface and neglecting the heat transfer contribution downstream of the flow reversal (separation) point.

The dependence of the Nusselt number on the Froude number is illustrated in Fig. 12. Note that the ratio of the average and stagnation values of the Nusselt number decreases in the combined gravity and interfacial shear flow region. In the high and low Froude number limits, the ratio tends to constant values, as one would expect.

A detailed explanation of the phenomena occurring at the downstream separation location (flow reversal) is presented in the appendix. The implications of these patterns on the heat transfer and the condensation process are discussed.

Comparison With Other Investigations

The numerical accuracy of the computational method is assessed by comparing the computed results with those obtained by Gaddis [8] and by Nusselt [1]. Table 1 presents a comparison of some relevant parameters. The Nusselt number average over the cylinder surface is reported by Gaddis only for the no-flow case (Fr = 0). Therefore, no comparison is possible for the case Fr = 1000.

It is interesting to compare the results of this investigation with those of Shekriladze [5] and Fujii [6]. Consider the case of Ja/Pr→0 and Fr→0. By introducing the current nomenclature, one obtains

Table 1 Comparison of the numerical results

Fluid	Water	Water	Water	Water	Liquid metal	Viscous liquid	Viscous liquid
Froude number	0.0	0.0	1000.0	1000.0	0.0	0.0	1000.0
Jakob number	0.040	0.0020	0.040	0.0020	0.010	1.0	1.0
Prandtl number	1.74	1.74	1.74	1.74	5.0×10^{-3}	100.0	100.0
Density ratio	6.25×10^{-4}	6.25×10^{-4}	6.25×10^{-4}	6.25×10^{-4}	2.94×10^{-4}	0.10	0.10
Viscosity ratio	4.46×10^{-2}	4.46×10^{-2}	4.46×10^{-2}	4.46×10^{-2}	9.19×10^{-3}	1.0	1.0
Thickness of the liquid layer at the stagnation point (s/a)							
Gaddis	4.84×10^{-3}	2.28×10^{-3}	1.59×10^{-3}	7.83×10^{-3}	1.95×10^{-2}	6.85×10^{-3}	1.10×10^{-3}
Present study	4.84×10^{-3}	2.28×10^{-3}	1.56×10^{-3}	7.84×10^{-3}	1.96×10^{-2}	6.86×10^{-3}	1.08×10^{-3}
Nusselt number at the stagnation point							
Nusselt	415	877	–	–	135	286	–
Gaddis	415	877	1264	2553	103	315	1943
Present study	415	877	1290	2551	102	315	1974
Average Nusselt number over the cylinder surface							
Nusselt	333	704	–	–	108	229	–
Gaddis	337	709	–	–	87.4	255	–
Present study	334	705	–	–	83.8	254	–

$$Nu = 1.23Pr^{0.25}Ja^{-0.25}Gr^{0.25} \quad \text{(Shekriladze)} \tag{44}$$

$$Nu = 1.22Pr^{0.25}Ja^{-0.25}Gr^{0.25} \quad \text{(Fujii)} \tag{45}$$

$$Nu = 1.25Pr^{0.25}Ja^{-0.25}Gr^{0.25} \quad \text{(Present investigation)} \tag{46}$$

Consider the case of $Ja/Pr = 5.65\times10^{-3}$ (water vapor at atmospheric pressure, condensing under a temperature difference of $\sim5°C$). Figure 13 offers a comparison of the results. For flow situations characterized by Froude numbers lower than Fr_c, the results obtained by Nusselt are in very good agreement with the findings of the other investigators. At high values of the Froude number ($Fr > Fr_c$), the agreement with Fujii is very good but there are discrepancies with the findings by Shekriladze.

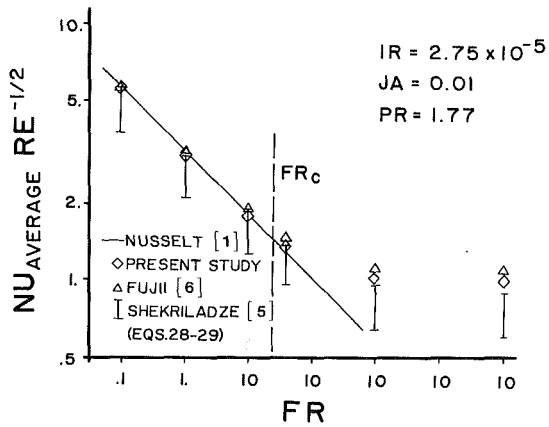

Fig. 13 Average heat transfer coefficient as a function of the Froude number

Summary and Conclusions

The governing equations for the problem of the laminar film condensation of a pure saturated vapor over a two-dimensional, horizontal body are formulated. Two different scaling laws of the transformed governing equations are introduced to investigate the complete range of Froude numbers. The Froude Combined Flow number (Fr_c) is defined to merge the two solution domains and its value is tabulated over a range of the various governing parameters.

The heat transfer coefficient at the cylinder surface is computed over a wide range of Froude, Jakob, and Prandtl numbers, and Interfacial Ratios. The average value of the heat transfer coefficient over the cylinder surface is evaluated. The results of this investigation are compared with other published results over a range of nondimensional parameters.

Acknowledgments

The computations were performed at the University of Maryland and at the Catholic University of America Computer Centers.

References

1 Nusselt, W., "Die Oberflachenkondensation des Wasserdamfes," *Zeitschrift des Vereines Deutscher Ingenieure*, Vol. 60, 1916, pp. 541-546, 569-575.

2 Sparrow, E. M., and Gregg, J. L., "A Boundary-Layer Treatment of Laminar-Film Condensation," ASME JOURNAL OF HEAT TRANSFER, Vol. 81, Feb. 1959, pp. 13-18.

3 Chen, M. M., "Analytical Study of Laminar Film Condensation: Part 1—Flat Plates," ASME JOURNAL OF HEAT TRANSFER, Vol. 83, Feb. 1961, pp. 48-54.

4 Koh, J. C. Y., "Film Condensation in a Forced-Convection Boundary-Layer Flow," *International Journal of Heat and Mass Transfer*, Vol. 5, 1962, pp. 941, 954.

5 Shekriladze, I. G., and Gomelauri, V. I., "Theoretical Study of Laminar Flim Condensation of Flowing Vapor," *International Journal of Heat and Mass Transfer*, Vol. 9, 1966, pp. 581-591.

6 Fujii, T., Uehara, H., and Kurata, C., "Laminar Filmwise Condensation of Flowing Vapor on a Horizontal Cylinder," *International Journal of Heat and Mass Transfer*, Vol. 15, 1972, pp. 235-246.

7 Denny, V. E., and Mills, A. F., "Nonsimilar Solutions for Laminar Film Condensation on a Vertical Surface," *International Journal of Heat and Mass Transfer*, Vol. 12, 1960, pp. 965-979.

8 Gaddis, E.S., "Solution of the Two Phase Boundary-Layer Equations for Laminar Film Condensation of Vapor Flowing Perpendicular to a Horizontal Cylinder," *International Journal of Heat and Mass Transfer*, Vol. 22, 1979, pp. 371-382.

9 Honda, H., and Fujii, T., "Condensation of Flowing Vapor on Horizontal Tube. Numerical Analysis as a Conjugate Heat Transfer Problem," ASME JOURNAL OF HEAT TRANSFER, Vol. 106, 1984, pp. 841, 848.

10 diMarzo, M., "Laminar Film Condensation of a Saturated Vapor Flowing Over a Horizontal Cylindrical Surface," Ph.D. dissertation, Oct. 1982.

11 Keller, H. B., "Numerical Methods in Boundary Layer Theory," *Annual Review of Fluid Mechanics*, Vol. 10, 1978, pp. 417, 433.

APPENDIX

Discussion of the Separation Phenomena

The velocity profiles at the last location on the cylinder where the boundary layer is able to produce meaningful data are sketched in Fig. 14. By meaningful data the authors mean absence of fluctuations in the computational results

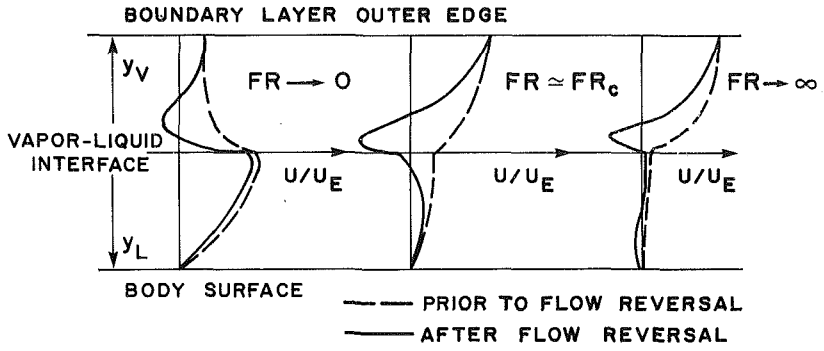

Fig. 14 Qualitative velocity profiles in the proximity of the flow reversal point

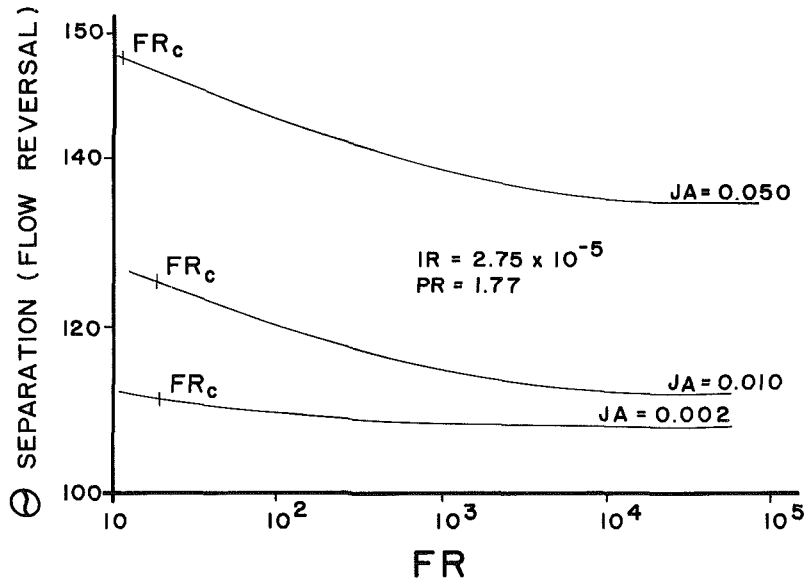

Fig. 15 Separation (flow reversal) point location as a function of the Froude number

(especially the higher order derivatives) that would indicate the onset of instabilities in the numerical computation. The authors postulate separation (flow reversal) to occur approximately at that location. The dashed lines in the figure represent the last meaningful data and the continuous lines represent a reasonable extrapolation of such data (in the adverse pressure gradient region). This behavior of the velocity profiles is well documented by Gaddis and the results of this investigation illustrate similar behavior.

The figure shows that at low Froude number, the depletion of momentum due to the adverse pressure gradient affects the vapor more than the liquid. This is reasonable, because the gravitational forces are responsible for the motion of the liquid and they are far larger than the pressure gradient. At large Froude number, however, the gravitational forces are negligible and flow reversal occurs in the liquid layer.

The implications of these patterns on the heat transfer are very important. At *low Froude number*, the flow reversal occurs in the vapor, and yet the liquid is flowing; there is no increase in the thickness of the liquid layer, nor decaying of the heat transfer. Therefore, one can conclude that ignoring the heat transfer downstream from the flow reversal point is not an accurate assumption. Note that this also means that the classical solution generated by Nusselt, based on no shear at the liquid-vapor interface, is well founded for the gravity-dominated flow region.

At *high Froude number*, flow reversal in the liquid layer means a rapid increase in the film thickness (to satisfy conservation of mass in the liquid); thus an abrupt decrease in the heat transfer is observed. The assumption that the heat transfer is negligible downstream from the flow reversal point is therefore justified. Therefore, separation (flow reversal) is an important issue on the heat transfer performance for Froude numbers greater than Fr_c. To follow up on this conclusion, the data on the location of separation (θ_{sep}) for values of the Froude number higher than Fr_c are presented in Fig. 15 for various condensation rate (Ja number). Note that a higher condensation rate will further delay the flow reversal or separation. This is due to the suction effect caused by the condensation process. The curves indicate that for decreasing Froude numbers (increasing effect of the gravity forces), separation occurs further downstream. This is to be expected because gravity forces prevent the depletion of momentum in the liquid film.

Journal of Heat Transfer

Technical Notes

This section contains shorter technical papers. These shorter papers will be subjected to the same review process as that for full papers.

An Investigation Into the Heat Loss Characteristics of Buried Pipes

G. E. Schneider[1]

Nomenclature

A, B = correlation parameters
Bi = Biot modulus $\equiv hd/k$
d = pipe diameter
D = depth of pipe centerline
f_i = insulated fraction
h = heat transfer coefficient
k = thermal conductivity
L = length of analysis cross section
Q = heat flow rate
R = thermal resistance
S = parameter describing horizontal extent of solution domain
T = temperature
x, y = Cartesian coordinates

Subscripts

a = ambient
f = fluid
g = ground
p = pipe
TOT = total
$1D$ = one-dimensional

Introduction

The understanding and prediction of the heat loss from buried pipes to the earth's surface is an important consideration in pipeline design. This is particularly important where energy transfer to or from the pipe will significantly affect the pumping requirements of the medium carried through the pipe or where such energy transfer will affect the terrestrial environment in the vicinity of the buried pipe. The thermal resistance to heat transfer between the surface of a buried pipe and ground level has been calculated for the case where both the pipe surface and the ground surface are isothermal [1–3], through the use of superposition of line source and sink solutions. A solution for the Dirichlet case is also available based on the solution of the governing differential equation formulated in the bicylinder coordinate system [4]. In order to assess the impact that boundary condition specification has on the thermal resistance, the case in which the ground surface remains isothermal but the pipe surface has a uniform flux boundary prescription has been examined [5, 6]. As noted in [6], however, the solution in [5] is in error since the temperature and the resistance go to zero, for the same heat transfer rate, as the pipe is displaced farther below ground level. This anomaly was rectified in the solution presented in [6].

It is the purpose of this note to examine the problem of heat loss from a pipe buried beneath the earth's surface for which the boundary conditions at both the pipe surface and at the ground surface are convective conditions connecting the pipe and ground to fluid and ambient temperatures, respectively. This specification is more closely representative of the actual conditions under which the heat transfer from the pipe will occur and is the first analysis which applies a boundary condition at the ground surface which is different from the uniform temperature case. A range of values of the parameters describing the convective interaction at both the pipe surface and at the ground surface are examined. The total thermal resistance for the cases studied is provided and a correlation equation is provided for the entire range of parameters considered. In addition, the influence of partial insulation of the upper surface of the pipe on the heat transfer rate to/from the pipe is examined and the results presented. The solutions for which results are reported were obtained from a finite element analysis of the problem and validated independently using a finite difference program written in bicylinder coordinates.

Numerical Solution

The problem of steady-state conduction heat transfer in a medium of uniform thermal conductivity was solved for the problem geometry shown in Fig. 1. The finite element method [7] was employed to determine the temperature distribution within the soil and to thereby determine heat flow rates through the system. Both the inner pipe surface and the ground surface are convectively coupled to their respective fluid temperatures, T_f and T_a. Eight-noded, quadratic, isoparametric, quadrilateral finite elements were used throughout the domain. A Cartesian coordinate system was employed for the basis reference frame while the discretization of the domain was based on the bicylinder coordinate system [4, 6]. To validate the code, and to ascertain the convergence characteristics with mesh refinement, the code was employed to solve several problems for which both Biot moduli approach infinity. In this limit the problem corresponds to a one-dimensional problem in bicylinder coordinates for which the analytical solution is available [4]. While the analytical solution is one dimensional in the bicylinder coordinate system, the problem remains fully two dimensional in the Cartesian frame employed for the domain discretization. Convergence studies indicate an error

[1]Associate Professor, Thermal Engineering Group, Department of Mechanical Engineering, University of Waterloo, Waterloo, Ontario, Canada, Mem. ASME

Contributed by the Heat Transfer Division for publication in the JOURNAL OF HEAT TRANSFER. Manuscript received by the Heat Transfer Division March 29, 1983.

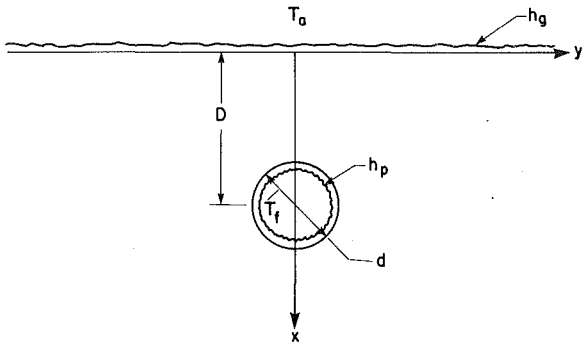

Fig. 1 Problem description

of less than 1 percent for an 8 × 8 element mesh and a 0.11 percent error for a 16 × 16 element mesh. All results presented employed the 16 × 16 element mesh.

In addition to the finite element solutions, further verification of the results to be presented was made through the use of a finite difference code for the identical problem formulation. The finite difference code, however, was written in the bicylinder coordinate system following the general formulation proposed by Schneider et al. [8] for orthogonal curvilinear coordinate systems. The finite difference results, using a 30 × 30 finite difference grid in the bicylinder coordinate system, support all results presented herein. Based on the convergence studies for both the finite difference and finite element solutions, it is suggested that a reasonable estimate of the accuracy of all solutions presented herein would be within 1 percent.

Results

The above-formulated problem was solved for depth-to-diameter ratios of D/d = 1, 2, 5, and 10, for pipe Biot modulus values of Bi_p = 0.1, 1.0, 10.0, and 100.0, and for ground Biot modulus values of Bi_g = 1.0, 2.0, 5.0, 10.0, and 100.0. The results are presented in Table 1 and Fig. 2. To enable engineering calculations to be performed using these data, the results are related to those obtained using a simple addition of one-dimensional component resistances. The nondimensional resistance values and the nondimensional heat flow values given correspond to heat flow from the entire pipe to the entire ground surface, i.e., including both halves of the symmetrical problem.

The actual total resistance of the thermal problem as determined from the numerical solutions is expressed in the nondimensional form

$$R^*_{\mathrm{TOT}} = \left[R^*_{1D} + \frac{1}{\pi \mathrm{Bi}_p} + \frac{1}{S^* \mathrm{Bi}_g}\right] \Big/ [1 - \phi] \tag{1}$$

where

$$R^*_{\mathrm{TOT}} \equiv R_{\mathrm{TOT}} k L \tag{2}$$

$$S^* \equiv 38.20[4(D/d)^2 - 1]^{1/2} \tag{3}$$

and

$$R^*_{1D} = \left(\frac{1}{2\pi}\right) \sinh^{-1}[4(D/d)^2 - 1]^{1/2} \tag{4}$$

and where ϕ is determined by forcing the above right-hand side to equal the numerically computed values for the left-hand side. In the above, S^* is a parameter measuring the nondimensional, i.e., $2y/d$, ground surface width used in the computational domain (the actual ground surface width is infinite), and is sufficiently large that its inverse, together with the assumed values of Bi_g, offers a very small contribution to R^*_{TOT}. The expression given for R^*_{1D} is that corresponding to the one-dimensional, isothermal boundary, analytical solution. The actual numerical results are those presented in Table 1 with the values of Q^* being the inverse of R^*_{TOT}.

Engineering calculations can be made by employing the following correlation equation for ϕ. This is given by

Table 1

D/d	Bi_g	Bi_p	Q^*	R^*_{TOT}	ϕ
1	1	0.1	0.277	3.616	0.0576
		1	1.495	0.669	0.1879
		10	2.686	0.372	0.3108
		100	2.920	0.342	0.3344
	2	.1	0.280	3.567	0.0468
		1	1.616	0.619	0.1347
		10	3.123	0.320	0.2224
		100	3.453	0.290	0.2391
	5	.1	0.283	3.532	0.0387
		1	1.717	0.582	0.0882
		10	3.560	0.281	0.1297
		100	4.011	0.249	0.1345
	10	.1	0.284	3.519	0.0354
		1	1.759	0.568	0.0686
		10	3.765	0.266	0.0854
		100	4.282	0.234	0.0824
	100	.1	0.285	3.506	0.0323
		1	1.802	0.555	0.0485
		10	3.991	0.251	0.0358
		100	4.591	0.218	0.0224
2	1	.1	0.274	3.649	0.0357
		1	1.379	0.725	0.0991
		10	2.312	0.432	0.1512
		100	2.482	0.403	0.1602
	2	.1	0.276	3.618	0.0286
		1	1.438	0.695	0.0651
		10	2.489	0.402	0.0951
		100	2.687	0.372	0.1000
	5	.1	0.278	3.598	0.0238
		1	1.482	0.675	0.0396
		10	2.627	0.381	0.0501
		100	2.849	0.351	0.0513
	10	.1	0.278	3.591	0.0219
		1	1.499	0.667	0.0299
		10	2.681	0.373	0.0325
		100	2.913	0.343	0.0320
	100	.1	0.279	3.584	0.0202
		1	1.514	0.660	0.0206
		10	2.734	0.366	0.0151
		100	2.976	0.336	0.0129
5	1	.1	0.267	3.741	0.0212
		1	1.201	0.833	0.0423
		10	1.846	0.542	0.0569
		100	1.951	0.512	0.0591
	2	.1	0.268	3.727	0.0179
		1	1.221	0.819	0.0277
		10	1.895	0.528	0.0346
		100	2.006	0.499	0.0355
	5	.1	0.269	3.719	0.0158
		1	1.235	0.810	0.0180
		10	1.927	0.519	0.0195
		100	2.042	0.490	0.0195
	10	.1	0.269	3.716	0.0150
		1	1.240	0.807	0.0146
		10	1.939	0.516	0.0141
		100	2.055	0.487	0.0137
	100	.1	0.269	3.713	0.0144
		1	1.244	0.804	0.0114
		10	1.950	0.513	0.0099
		100	2.067	0.484	0.0084
10	1	.1	0.261	3.828	0.0148
		1	1.078	0.928	0.0230
		10	1.567	0.638	0.0281
		100	1.642	0.609	0.0287
	2	.1	0.262	3.821	0.0131
		1	1.086	0.921	0.0159
		10	1.585	0.631	0.0178
		100	1.662	0.602	0.0179
	5	.1	0.262	3.816	0.0120
		1	1.092	0.916	0.0115
		10	1.597	0.626	0.0113
		100	1.675	0.597	0.0110
	10	.1	0.262	3.815	0.0117
		1	1.093	0.915	0.0099
		10	1.601	0.625	0.0090
		100	1.679	0.595	0.0086
	100	.1	0.262	3.813	0.0113
		1	1.095	0.913	0.0085
		10	1.605	0.623	0.0069
		100	1.683	0.594	0.0065

$$\phi = A(D/d)^B \tag{5}$$

where

$$A = \frac{[0.292\ \mathrm{Bi}_p \mathrm{Bi}_g^{-0.6}]^{1.035}}{\mathrm{Bi}_p + 0.478 - 0.261 \log_{10}(\mathrm{Bi}_g)} \tag{6}$$

$$B = \frac{-[\mathrm{Bi}_p \mathrm{Bi}_g^{0.074}]^{1.022}}{\mathrm{Bi}_p + 0.0748 + 0.176 \log_{10}(\mathrm{Bi}_g)} \tag{7}$$

The above correlation equation correlates the numerical data to within 2.5 percent of the resistance values as obtained from the finite element solutions. It is important to note that ϕ approaches zero in this correlation as both the pipe and ground Biot moduli approach infinity, where the one-dimensional solution in fact becomes valid.

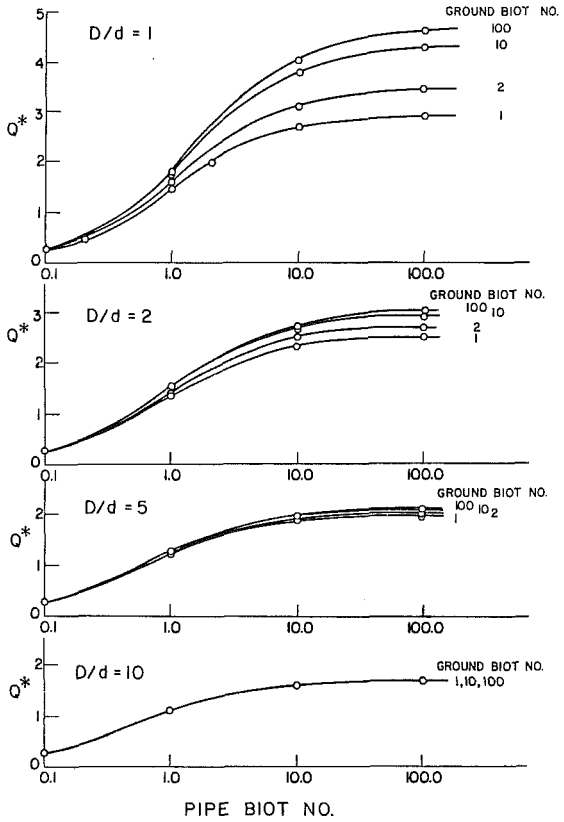

Fig. 2 Heat loss results for D/d = 1, 2, 5, and 10

The results for depth-to-diameter ratios of 1, 2, 5, and 10 are given graphically in Fig. 2. It is seen from the figure that at the smallest value of the pipe Biot modulus the heat loss, and hence resistance, is dominated by the convective layer at the pipe boundary and that the effect of the ground Biot modulus is essentially nonexistent. As the pipe Biot modulus is increased, however, the resistance of the pipe surface layer decreases in dominance and the thermal spreading effect of the ground Biot modulus becomes more apparent. That is, the effect of decreasing the ground Biot modulus is to force the energy transport to be moved to ground locations more distant from the pipe centerline than for higher ground Biot moduli. The effect of this spreading is to increase the ground conductive resistance, and hence increase the total resistance, and to decrease the heat loss from the pipe for the lower Biot modulus cases. As the pipe Biot modulus is increased to higher values, the dependence of the heat loss on the pipe Biot modulus decreases. This corresponds to the approach to the extreme case of an isothermal pipe surface specification for which the dependence on pipe Biot modulus vanishes entirely.

As the depth-to-diameter ratio D/d increases from the top curves of Fig. 2 to the lowermost curve of Fig. 2, it is observed that the influence of the ground Biot modulus decreases markedly, essentially vanishing entirely at D/d = 10. This is a result of the conductive resistance of the soil playing a more dominant role in the overall resistance as the pipe is buried deeper relative to its diameter. For deeply buried pipes, the heat loss from the pipe becomes dependent solely on the conductive, geometric configuration and on the pipe boundary specification.

A second study was undertaken to determine the influence that adding insulation to a portion of the pipe's upper surface would have on the heat loss from the pipe. Selected combinations of D/d = 1, 2, 5, and 10, Bi_p = 10 and 100, and Bi_g = 1, 10, and 100 were examined using the same mesh definition as employed for the previous study. In all cases, conduction circumferentially along the pipe wall was not included and an ideal insulating layer was considered. A typical contour plot of the temperature field corresponding to the top 44 percent of the pipe covered with insulation is

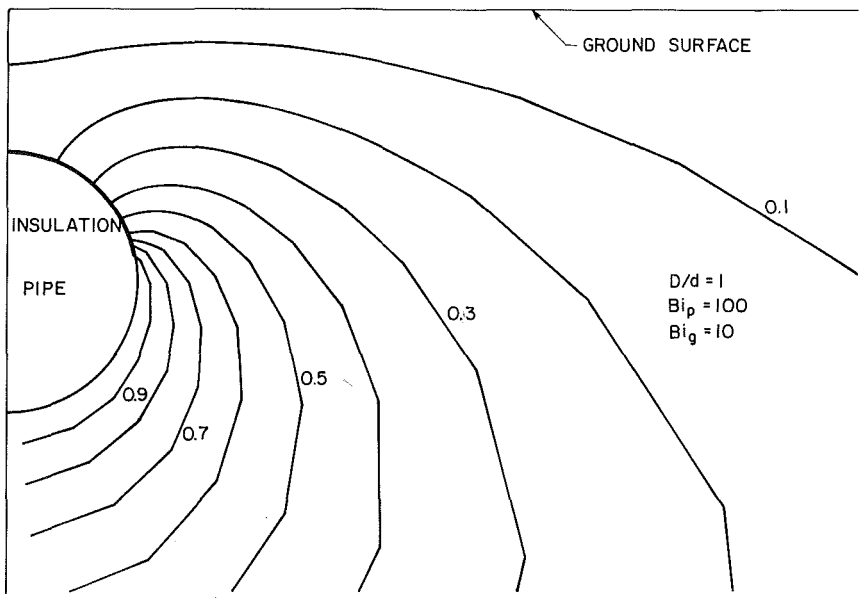

Fig. 3 Contour plot of temperature distribution for partially insulated pipe

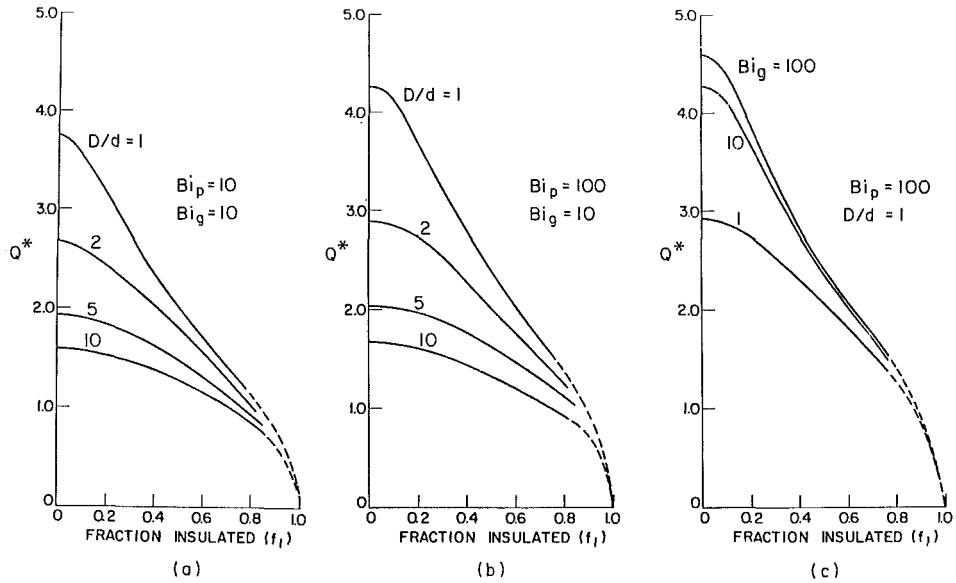

Fig. 4 Partially insulated pipe results

presented in Fig. 3. It is clear from inspection of the figure that the presence of the insulation layer significantly distorts the temperature field and hence the heat flow distribution.

Results for the partially insulated pipe surface are presented in Fig. 4. Figures 4(*a*) and 4(*b*) present the influence of the insulated fraction on the energy loss from the pipe with the depth-to-diameter ratio being the parameter. It is seen that as the pipe is buried deeper relative to its diameter, the influence of insulation addition diminishes. This is a direct result of the more pronounced volumetric influence of the domain configuration which emerges as the pipe is buried further from the surface. For small depth-to-diameter ratios, however, there is a significant rate of energy loss reduction with initial application of insulation, corresponding to the significant influence of insulation on the energy loss to the energy rejection surface which in this case is in close proximity to the pipe. Similar results are presented in Fig. 4(*b*). Figure 4(*c*) presents the dependence of energy loss on the pipe fraction insulated for a shallowly buried pipe and illustrates that largest impact is felt under conditions in which the ground boundary interaction approaches the isothermal limit. As the ground Biot modulus decreases, the impact of insulation addition decreases markedly.

Discussion and Conclusions

The problem of heat loss from a buried pipe has been considered and has included convective film coefficients on both the pipe interior surface and on the exposed ground above the pipe. The present formulation is more representative of expected applications than are those problem specifications which render the problem suitable for solution by classical methods. Numerical results have been presented using both the finite element method and the finite difference method for a wide range of problem parameters. The results of both methods are in strong support of each other.

Results have been presented in both tabular and graphical form for the case where the entire pipe surface is diabatic. Numerical results were presented for depth-to-diameter ratios of 1, 2, 5, and 10 and pipe Biot modulus values of 0.1, 1.0, 10.0, and 100.0. In both the pipe and ground cases the characteristic dimension used in the Biot modulus is the pipe diameter. A correlation of all data has been presented to enable engineering calculations to be performed for the case of a fully diabatic pipe surface.

In addition to the above, numerical results have been provided to determine the influence that partial insulation of the pipe upper surface will have on the heat flow from the pipe. Specific cases examined include depth-to-diameter ratios of 1, 2, 5, and 10 for a ground Biot modulus of 10 and for pipe Biot moduli of 10 and 100. In addition, for a depth-to-diameter ratio of 1, and a pipe Biot modulus of 100, the influence of the ground Biot modulus on heat flow from the pipe for partially insulated pipes has been examined. It was found that the largest influence of partial insulation over the pipe surface was experienced for small depth-to-diameter ratios and for large ground Biot moduli. As the depth-to-diameter ratio is increased, the sensitivity of the heat flow to fraction insulated decreases markedly. While a larger sensitivity is expected for depth-to-diameter ratios less than unity, such installations are unlikely to be encountered in practice.

Acknowledgments

The author wishes to thank the Natural Sciences and Engineering Research Council of Canada and the University of Waterloo for their financial support of this project in the form of an operating grant and a computing research grant, respectively, to the author. The author also expresses appreciation to Mr. K. Knill for performing many of the finite element computations and to Mr. W. Somerville and B. Van den Berg for performing the supporting finite difference calculations.

References

1 Eckert, E. R. G., and Drake, R. M., *Heat and Mass Transfer*, 2nd ed., McGraw-Hill, New York, pp. 60-64.

2 Boelter, L. M. K., Cherry, V. H., Johnson, H. A., and Martinelli, R. C., *Heat Transfer Notes*, McGraw-Hill, New York, 1965, pp. 297-299.

3 Schenck, H., *Heat Transfer Engineering*, Prentice-Hall, 1959, pp. 35-46.

4 Yovanovich, M. M., "A General Expression for Predicting Conduction Shape Factors," AIAA Paper No. 73-121, presented at the AIAA 11th Aerospace Sciences Meeting, Washington, D.C., Jan. 10-12, 1983.

5 Lebedev, N. N., Skalskaya, I. P., and Uflyand, Ya. S., *Problems in Mathematical Physics* (translated from Russian), Prentice-Hall, 1965.

6 Thiyagarajan, R., and Yovanovich, M. M., "Thermal Resistance of a Buried Cylinder with Constant Flux Boundary Condition," ASME JOURNAL OF HEAT TRANSFER, Vol. 96, No. 2, May 1974, pp. 249-250.

7 Schneider, G. E., "Finite Element Formulation of the Heat Conduction Equation in General Orthogonal Curvilinear Coordinates," ASME JOURNAL OF HEAT TRANSFER, Vol. 98, No. 3, Aug. 1976, pp. 525-527.

8 Schneider, G. E., Strong, A. B., and Yovanovich, M. M., "A Physical Approach to the Finite Difference Solution of the Heat Conduction Equation in General Orthogonal Curvilinear Coordinates," ASME Paper No. 75-WA/HT-94, Nov. 1975.

A Direct Analytical Approach for Solving Linear Inverse Heat Conduction Problems

N. M. Alnajem[1] and M. N. Özişik[2]

Introduction

The inverse heat conduction problem is concerned with the determination of the surface conditions (i.e., temperature or heat flux) from the knowledge of the temperature or heat flux measurements taken at the interior point of the solid or at its back surface. In most cases, the inverse analysis leads to the solution of a Fredholm type of integral equation, which is known [1] to have no unique and stable solution, unless some explicit functional form is specified for the applied surface condition. Once an appropriate functional form has been decided upon for the applied surface condition, the analysis can yield a unique answer for the inverse problem.

Various approaches have been reported in the literature for the solution of one-dimensional linear inverse problems [2-11].

Analysis

Consider a slab of thickness L and constant thermal properties, initially at a uniform temperature T_∞. Suddenly, at time $t = 0$, an unknown temperature variation $f(t)$ is applied to the front surface at $x = 0$, while the back surface is either kept insulated or allowed to dissipate heat by convection into a medium at a temperature T_∞ with a heat transfer coefficient h. For generality, we consider convection at the back surface and write a mathematical formulation of the heat transfer problem in dimensionless form as

$$\frac{\partial^2\theta}{\partial X^2} = \frac{\partial\theta}{\partial\tau} \quad \text{for } 0<X<1, \quad \tau>0 \tag{1a}$$

$$\theta(X,\tau) = F(\tau) \quad \text{at } X=0, \quad \tau>0 \tag{1b}$$

$$B\theta + \frac{\partial\theta}{\partial X} = 0 \quad \text{at } X=1, \quad \tau>0 \tag{1c}$$

$$\theta(X,\tau) = 0 \quad \text{for } \tau=0, \quad 0\le X\le 1 \tag{1d}$$

We wish to calculate the applied surface temperature $F(\tau)$ from the temperature measurements taken at the back surface of the slab.

Suppose that the applied surface temperature $F(\tau)$ involves an abrupt change at an unknown time τ_1, and is given in the form

$$F(\tau) = \begin{cases} \displaystyle\sum_{j=0}^{2} \phi_j \tau^j & \tau\le\tau_1 \qquad (2a) \\ \displaystyle\sum_{j=0}^{2} \phi_j \tau_1^j + \sum_{j=0}^{2} \alpha_j\cdot(\tau-\tau_1)^j & \tau>\tau_1 \qquad (2b) \end{cases}$$

where ϕ_j, α_j, and τ_1 are the unknown quantities which are to be determined by the inverse analysis.

The solution is developed in two stages: (a) for times $\tau\le\tau_1$ and (b) for times $\tau>\tau_1$ as described below.

(a) $\tau\le\tau_1$: We set $\theta \equiv U$ for the first stage and the system (1) takes the form

$$\frac{\partial^2 U}{\partial X^2} = \frac{\partial U}{\partial\tau} \quad \text{for } 0<X<1, \quad \tau\le\tau_1 \tag{3a}$$

$$U(X,\tau) = \sum_{j=0}^{2} \phi_j \tau^j \quad \text{at } X=0, \quad \tau\le\tau_1 \tag{3b}$$

$$BU + \frac{\partial U}{\partial X} = 0 \quad \text{at } X=0, \quad \tau\le\tau_1 \tag{3c}$$

$$U(X,\tau) = 0 \quad \text{for } \tau=0, \quad 0\le X\le 1 \tag{3d}$$

(b) $\tau>\tau_1$: For convenience in the analysis we let $\eta=\tau-\tau_1$ and $\theta\equiv V$; then the problem (1) for the second stage takes the form

$$\frac{\partial^2 V}{\partial X^2} = \frac{\partial V}{\partial\eta} \quad \text{for } 0<X<1, \quad \eta>0 \tag{4a}$$

$$V(0,\eta) = U(0,\tau_1) + \sum_{j=0}^{2} \alpha_j \eta^j \quad \text{at } X=0, \quad \eta>0 \tag{4b}$$

$$BV + \frac{\partial V}{\partial X} = 0 \quad \text{at } X=1, \quad \eta>0 \tag{4c}$$

$$V(x,\eta) = U(X,\tau_1) \quad \text{for } \eta=0, \quad 0\le X\le 1 \tag{4d}$$

here, $U(0,\tau_1) = \phi_0 + \tau_1\phi_1 + \phi_2\tau_1^2$.

By utilizing the splitting-up procedure [12], the solution to the problems (3 and 4) is determined as:

$$U(X,\tau) = C_m(X,\tau)\cdot\phi_0 + D_m(X,\tau)\cdot\phi_1 + E_m(X,\tau)\cdot\phi_2 \quad \tau\le\tau_1 \tag{5a}$$

$$V(X,\eta) = F_m(X,\eta,\tau_1)\cdot\phi_0 + G_m(X,\eta,\tau_1)\cdot\phi_1 + H_m(X,\eta,\tau_1)\cdot\phi_2 + P_m(X,\eta,\tau_1)\cdot\alpha_0 + Q_m(X,\eta,\tau_1)\alpha_1 + R_m(X,\eta,\tau_1)\alpha_2 \quad \tau>\tau_1 \tag{5b}$$

where various functions appearing in these equations are defined in the Appendix.

Having established the above rapidly converging direct solutions for the problem, the corresponding inverse analysis of the problem defined by equations (1) can be related to the solutions $U(X,\tau)$ and $V(X,\eta)$ as

$$\theta(X,\tau) = \begin{cases} U(X,\tau) & \text{for } \tau\le\tau_1 \qquad (6a) \\ V(X,\eta) & \text{for } \tau>\tau_1 \qquad (6b) \end{cases}$$

where ϕ_0, ϕ_1, ϕ_2, α_0, α_1, α_2, and τ_1 are the unknown parameters which are to be determined by utilizing the experimental readings of the temperature taken at the back surface. Knowing these coefficients, the applied surface temperature $F(\tau)$ is determined from equations (2). Given $\theta(x,\tau)$, the dimensionless heat flux is computed from its definition

$$Q \equiv -\frac{\partial\theta}{\partial X} \tag{7}$$

To solve the inverse problem, we now make use of the least-square technique in order to minimize the error involved in the computation of these parameters. Let E be the error between the exact temperatures θ_{ei} as computed from equation (6) and the experimental data Y_i, taken at the back surface at times τ_i, $i = 1$ to N. We represent E as

$$E = \sum_{i=1}^{N} (\theta_{ei} - y_i)^2 \tag{8}$$

Note that the solutions (5) for the determination of θ_{ei} involve algebraic equations in which the unknown parameter τ_1, representing the time at which the abrupt change of temperature occurs, appears as a multiplier to other unknown coefficients. Therefore, when θ_{ei} is introduced into equation (8), the resulting system becomes a nonlinear least-square equation. Such a nonlinear system is solved in the following manner:

[1]Mechanical Engineering Department, Box 5969, Kuwait University, Kuwait
[2]Mechanical and Aerospace Engineering Department, Box 7910, North Carolina State University, Raleigh, NC 27695-7910

Contributed by the Heat Transfer Division for publication in the JOURNAL OF HEAT TRANSFER. Manuscript received by the Heat Transfer Division March 23, 1984.

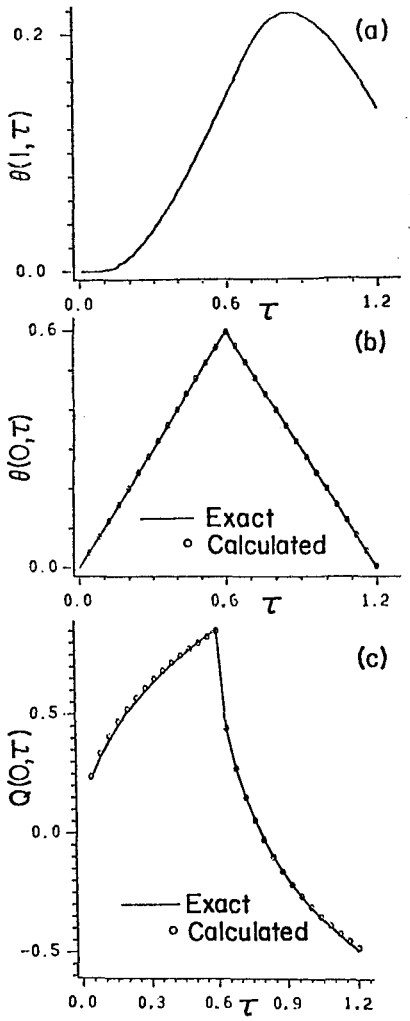

Fig. 1 Applied front surface temperature and heat flux calculated from temperature measurements (generated with a truncation type error) taken at the back surface with $\Delta\tau = 0.01$ intervals: (*a*) measured back surface temperature; (*b*) applied and calculated front surface temperature; and (*c*) applied and calculated front surface heat flux

1 The nonlinear least-square equation (8) is separated into two simpler linear problems by choosing an initial small value for τ_1, say $\tau_1^{(1)}$ as

$$E = \begin{cases} \sum_{i=1}^{M^{(1)}} (U_i - y_i)^2 & \tau \le \tau_1^{(1)} \qquad (9a) \\ \sum_{l=1}^{N} (V_l - y_l)^2 & \tau > \tau_1^{(1)} \qquad (9b) \end{cases}$$

where

(*a*) U and V are defined by equations (5)

(*b*) $M^{(1)} = \dfrac{\tau_1^{(1)}}{\Delta\tau}$ and $\Delta\tau$ (time step) $\equiv 0.01$

(*c*) $l = M^{(1)} + 1$, and N is the total number of readings

(*d*) y_i and y_l are the experimental data taken before and after $\tau_1^{(1)}$, respectively

2 When the least-square errors E in equations (9*a*, *b*) are minimized with respect to the unknown coefficients, one obtains a 3 × 3 symmetrical matrix for each of these equations. When these equations are solved for any given value of τ_1 the corresponding coefficients ϕ_j and α_j are determined. The calculations are started with a sufficient small value of τ_1 and carried out with small increments.

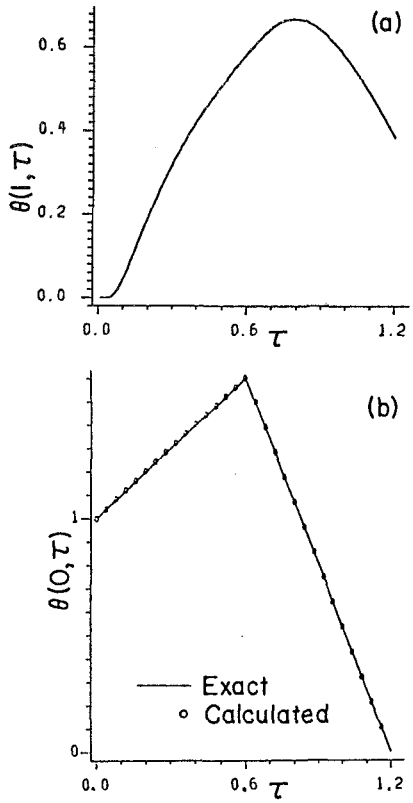

Fig. 2 Applied front surface temperature calculated from temperature measurements (generated with a truncation type error) taken at the back surface with $\Delta\tau = 0.01$ intervals: (*a*) measured back surface temperature; (*b*) applied and calculated front surface temperature

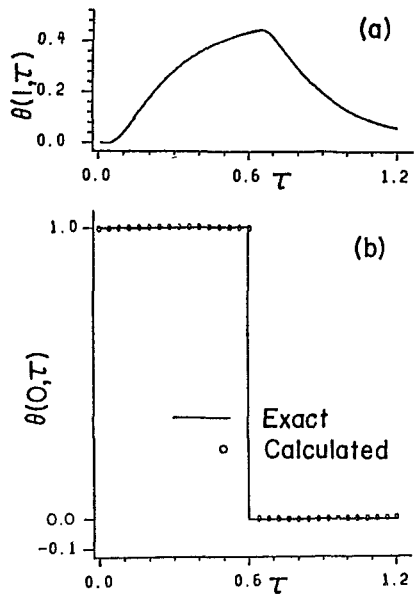

Fig. 3 Applied front surface temperature calculated from temperature measurements (generated with a truncation type error) taken at the back surface with $\Delta\tau = 0.01$ intervals: (*a*) measured back surface temperature; (*b*) applied and calculated front surface temperature

3 For each τ_1, the least-square error E is determined from equations (9) by utilizing the coefficients computed in step 2.

4 The calculations are terminated when the value of τ_1 equals the final time of the temperature measurements.

5 The value of τ_1 corresponding to the smallest value of the least-square error E represents the desired τ_1.

Once the value of τ_1 is established, the coefficients ϕ_j and α_j were determined in step 2 for this particular value of τ_1.

These coefficients represent the desired coefficients for the problem. Knowing the value of τ_1 at which the abrupt change occurs in the surface temperature, and the coefficients ϕ_j and α_j associated with it, the temperature of the front surface is determined from equation (2*a*) for times $\tau \leq \tau_1$ and from equation (2*b*) for times $\tau > \tau_1$ up to the time of the termination of the measurements.

Results and Discussion

To investigate the accuracy of the present method of analysis in predicting the applied surface conditions, we examined several singly applied pulses having shapes such as a triangle, a rectangle, a trapezoid, and a sinusoid.

First we generated the temperature readings from the solution of the appropriate direct problem at the back surface. These temperature readings are taken at extremely small time steps ($\Delta\tau = 0.01$). The use of small time steps is advantageous in that more accurate information can be extracted for the variation of the surface conditions.

Then, we could introduce two different types of random error to the exact measurements which were used as the input data for the inverse analysis. One of them is the truncation at three decimal places of the exact temperatures without rounding off to the nearest third digit. This is similar to that used by Beck [9, 11], and involved very large errors in the input data for early times and the errors become relatively small later on. The other type of error simulation consisted of introducing a ± 5 percent normal independently distributed random error with zero mean and a 99 percent confidence; this type of simulation is similar to that used by Hills et al. [4].

When the inverse study is to be performed by using temperature data taken at the back surface, it is assumed that the boundary condition at that surface is either of the convection type with small Biot number (i.e., $\mathrm{Bi} \equiv 1$) or the surface is insulated. For large Biot number or prescribed back surface temperature conditions, the inverse analysis should be performed with temperature data taken at an interior point of the region.

Figures 1 and 2 show the applied surface conditions in the form of a symmetric triangular and a chopped-off triangular pulse can also be accurately determined either for the temperature or the heat flux from the measurements taken at the back surface subjected to convection with Bi = 1. The truncation type of error is used for the input data for these cases. Figure 3 shows that a rectangular pulse can also readily be predicted with the present method. A sinusoidal-type single pulse from the inaccurate measurements of truncation type taken at the insulated back surface could also be predicted very accurately with the present method.

The present analysis clearly demonstrates that the applied surface conditions involving abrupt changes with time can be effectively accommodated with polynomial representations in time over the entire time domain, and the resulting inverse analysis predicts the surface conditions very accurately. All the previous attempts experienced difficulties in developing analytic solutions applicable over the entire time domain when a polynomial representation was used.

Acknowledgments

This work was supported in part through the National Science Foundation Grant No. MEA-83-13301.

References

1 Tikhonov, A. N., and Arsenin, V. Y., *Solution of Ill-Posed Problems*, Winston, Washington, D.C., 1977.

2 Stolz, G., Jr., "Numerical Solutions to an Inverse Problem of Heat Conduction for Simple Shapes," ASME JOURNAL OF HEAT TRANSFER, Vol. 82, 1960, pp. 20-26.

3 Beck, J. V., "Surface Heat Flux Determination Using an Integral Method," *Nuclear Engineering and Design*, Vol. 7, 1968, pp. 170-178.

4 Hills, R. G., and Mulholland, G. P., "The Accuracy and Resolving Power of One-Dimensional Transient Inverse Heat Conduction Theory as Applied to Discrete and Inaccurate Measurements," *Int. J. Heat Mass Transfer*, Vol. 22, 1979, pp. 1221-1229.

5 Woo, K. C., and Chow, L. C., "Inverse Heat Conduction by Direct Inverse Laplace Transform," *Numerical Heat Transfer*, Vol. 4, 1981, pp. 499-504.

6 Burggraf, O. R., "An Exact Solution of the Inverse Problem in Heat Conduction Theory and Applications," ASME JOURNAL OF HEAT TRANSFER, Vol. 86, 1964, pp. 373-382.

7 Mulholland, G. P., Gupta, B. P., and San Martin, R. L., "Inverse Problem of Heat Conduction in Composite Media," ASME Paper No. 75-WA/HT-83, 1975.

8 Novikov, A., "Solution of the Linear One-Dimensional Inverse Heat-Conduction Problem on the Basis of a Hyperbolic Equation," *Inzh-Fiz Zh*, Vol. 40(6), June 1981, pp. 1093-1098.

9 Beck, J. V., and Wolf, H., "The Nonlinear Inverse Heat Conduction Problem," ASME Paper No. 65-HT-40, 1965.

10 Murio, D. A., "The Modification Method and the Numerical Solution of an Inverse Heat Conduction Problem," *SIAM J. Sci. Stat. Comp.*, Vol. 2, 1981, pp. 17-34.

11 Beck, J. V., "Nonlinear Estimation Applied to the Nonlinear Inverse Heat Conduction Problem, *Int. J. Heat Mass Transfer*, Vol. 13, 1970, pp. 703-716.

12 Mikhailov, M. D., and Özişik, M. N., *Unified Analysis and Solutions of Heat and Mass Diffusion*, Wiley, New York, 1984.

APPENDIX

Definition of the functions appearing in equations (5)

$$C_m \equiv A_0(X) - \sum_{m=1}^{\infty} \frac{\psi_m(X)}{N_m \beta_m} e^{-\beta_m^2 \tau} \tag{A1}$$

$$D_m \equiv A_0(X)\cdot\tau + A_1(X) + \sum_{m=1}^{\infty} \frac{\psi_m(X)}{N_m \beta_m^3} e^{-\beta_m^2 \tau} \tag{A2}$$

$$E_m \equiv A_0(X)\cdot\tau^2 + 2A_1(X)\cdot\tau + A_2(X) - 2\sum_{m=1}^{\infty} \frac{\psi_m(X)}{N_m \beta_m^5} e^{-\beta_m^2 \tau} \tag{A3}$$

$$F_m \equiv C_m \tag{A4}$$

$$G_m \equiv A_0(X)\cdot\tau_1 + \sum_{m=1}^{\infty} \frac{\psi_m(X)}{N_m \beta_m^3} e^{-\beta_m^2 \tau} + \sum_{m=1}^{\infty} \frac{\psi_m(X)}{N_m \beta_m^3} e^{-\beta_m^2 \eta} \tag{A5}$$

$$H_m \equiv A_0(X)\cdot\tau_1^2 - 2\sum_{m=1}^{\infty} \frac{\psi_m}{N_m \beta_m^5} e^{-\beta_m^2 \tau} + 2\tau_1 \sum_{m=1}^{\infty} \frac{\psi_m(X)}{N_m \beta_m^3} e^{-\beta_m^2 \eta} + 2\sum_{m=1}^{\infty} \frac{\psi_m(X)}{N_m \beta_m^5} e^{-\beta_m^2 \eta} \tag{A6}$$

$$P_m \equiv A_0(X) - \sum_{m=1}^{\infty} \frac{\psi_m(X)}{N_m \beta_m} e^{-\beta_m^2 \eta} \tag{A7}$$

$$Q_m \equiv A_0(X)\cdot\eta + A_1(X) + \sum_{m=1}^{\infty} \frac{\psi_m(X)}{N_m \beta_m^3} e^{-\beta_m^2 \eta} \tag{A8}$$

$$R_m \equiv A_0(X)\cdot\eta^2 + 2A_1(X) + A_2(X) - 2\sum_{m=1}^{\infty} \frac{\psi_m(X)}{N_m \beta_m^5} e^{-\beta_m^2 \eta} \tag{A9}$$

where $A_0(X)$, $A_1(X)$, $A_2(X)$, $\psi_m(X)$, N_m, and β_m are defined as

$$A_0(X) \equiv 1 - \frac{BX}{1+B} \tag{A10}$$

$$A_1(X) \equiv -\frac{B^2+3B+3}{3(1+B)^2} X + \frac{X^2}{2} - \frac{BX^3}{6(1+B)} \tag{A11}$$

$$A_2(X) \equiv \frac{2B^3+12B^2+30B+30}{45(1+B)^3} X - \frac{B^2+3B+3}{9(1+B)^2} X^3 + \frac{X^4}{12} - \frac{BX^5}{60(1+B)} \tag{A12}$$

$$\psi_m(X) \equiv \sin \beta_m X \tag{A13}$$

$$\frac{1}{N_m} = 2\frac{\beta_m^2 + B^2}{\beta_m^2 + B^2 + B} \tag{A14}$$

and β_m is the root of

$$\beta_m \cot \beta_m = -B, \quad m = 1,2,3, \ldots . \tag{A15}$$

Determination of Local Heat Transfer Coefficients at the Solid-Liquid Interface by Heat Conduction Analysis of the Solidified Region

K. C. Cheng[1,2] and P. Sabhapathy[1]

Nomenclature

Bi = Biot number = $h_{\text{eff}}(d/2)/k_i$ [7]
$h, h_{n\phi}, h_x$ = local heat transfer coefficient
J = Jacobian of transformation = $x_\xi y_\eta - x_\eta y_\xi$
k = thermal conductivity
M,N = number of grids in the transformed plane
Nu_x = local Nusselt number = $h_x x/k$
n = outward normal at the interface
P,Q = coordinate control functions
R = radial coordinate
R_1 = outside radius of the cylinder
r_2 = dimensionless radial coordinate at the interface = R/R_1
$T, T_c, T_f, T_w, T_\infty$ = temperature, coolant temperature, freezing temperature, wall temperature, and free-stream temperature
x,y = Cartesian coordinates in physical plane
α,β,γ = transformation factors: $\alpha = x_\eta^2 + y_\eta^2$, $\beta = x_\xi x_\eta + y_\xi y_\eta$, $\gamma = x_\xi^2 + y_\xi^2$
δ = local ice thickness
θ_c = cooling temperature ratio = $(T_f - T_c)/(T_\infty - T_f)$
ξ,η = coordinates in the transformed plane
ϕ = angular position measured from forward stagnation point

1 Introduction

When freezing or melting occurs under external or internal, laminar or turbulent conditions involving various geometric shapes, the solid-liquid interface is often irregular and can be oscillatory [1-7]. Thus, in experimental investigations involving solidification processes, it is generally difficult to determine the heat transfer coefficients at the interface by direct measurement of temperature profiles. When the shape of a solidified region can be determined by photographic methods or by direct measurements and the boundary wall temperatures are known at any instant, then the determination of the local heat transfer coefficients at the interface can be reduced to solving a Laplace equation with Dirichlet boundary conditions for the temperature field in the solidified region. One notes that the interface temperature is known to be constant at freezing point temperature and the cooled wall temperatures are either known or can be measured.

For the solution of the Laplace equation with known boundary conditions, one can employ either analytical or numerical methods. The purpose of this note is to show the applicability of the simple method of determining the local heat transfer coefficients at the solid-liquid interface for three ice formation problems involving plane plate in longitudinal flow [1-3], cylinder in crossflow [4, 5], and flow inside a pipe with ice bands [6, 7] reported in the literature.

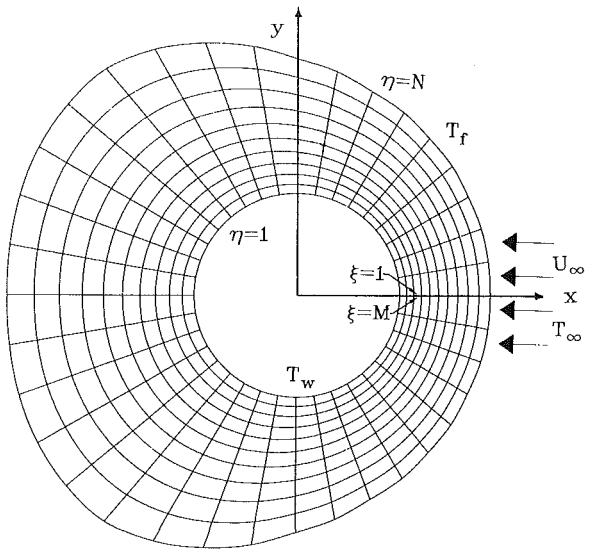

Fig. 1 Physical plane for the solidified region around a cooled cylinder

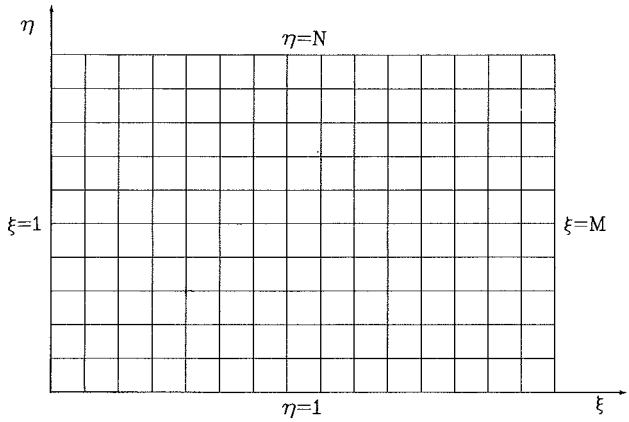

Fig. 2 Transformed plane of the solidified region

2 Analysis

At steady state or quasi-steady state, the local convective heat transfer coefficient at the ice-water interface can be obtained from a heat balance equation at the interface as

$$h(T_\infty - T_f) - k_i \left.\frac{\partial T}{\partial n}\right|_c = 0 \tag{1}$$

where $\partial T/\partial n\,|_c$ is a local temperature gradient for the ice layer at the interface. The temperature gradient $\partial T/\partial n\,|_c$ can be found from the heat conduction analysis of the ice layer. It involves the solution of Laplace equation in an arbitrary geometry. The steady two-dimensional heat conduction equation for the solidified region is

$$\nabla^2 T = 0 \tag{2}$$

where $\nabla^2 = \partial^2/\partial x^2 + \partial^2/\partial x^2$ or $\partial^2/\partial R^2 + \partial/R\partial R + \partial^2/\partial x^2$. The boundary conditions are

$$T = T_f \text{ at interface}$$
$$T = T_w \text{ at cooled wall} \tag{3}$$

Other boundary conditions such as a convective boundary condition at the cooling wall may be specified depending on the particular phase change problem. By using the method of boundary-fitted coordinate systems, the irregular or com-

[1]Department of Mechanical Engineering, University of Alberta, Edmonton, Alberta, Canada
[2]Mem. ASME

Contributed by the Heat Transfer Division for publication in the JOURNAL OF HEAT TRANSFER. Manuscript received by the Heat Transfer Division March 23, 1984.

$$\frac{1}{N_m} = 2\frac{\beta_m^2 + B^2}{\beta_m^2 + B^2 + B} \tag{A14}$$

and β_m is the root of

$$\beta_m \cot \beta_m = -B, \quad m = 1,2,3, \ldots . \tag{A15}$$

Determination of Local Heat Transfer Coefficients at the Solid–Liquid Interface by Heat Conduction Analysis of the Solidified Region

K. C. Cheng[1,2] and P. Sabhapathy[1]

Nomenclature

- Bi = Biot number = $h_{\text{eff}}(d/2)/k_i$ [7]
- $h, h_{n\phi}, h_x$ = local heat transfer coefficient
- J = Jacobian of transformation = $x_\xi y_\eta - x_\eta y_\xi$
- k = thermal conductivity
- M,N = number of grids in the transformed plane
- Nu_x = local Nusselt number = $h_x x/k$
- n = outward normal at the interface
- P,Q = coordinate control functions
- R = radial coordinate
- R_1 = outside radius of the cylinder
- r_2 = dimensionless radial coordinate at the interface = R/R_1
- $T, T_c, T_f, T_w, T_\infty$ = temperature, coolant temperature, freezing temperature, wall temperature, and free-stream temperature
- x,y = Cartesian coordinates in physical plane
- α,β,γ = transformation factors: $\alpha = x_\eta^2 + y_\eta^2$, $\beta = x_\xi x_\eta + y_\xi y_\eta$, $\gamma = x_\xi^2 + y_\xi^2$
- δ = local ice thickness
- θ_c = cooling temperature ratio = $(T_f - T_c)/(T_\infty - T_f)$
- ξ,η = coordinates in the transformed plane
- ϕ = angular position measured from forward stagnation point

1 Introduction

When freezing or melting occurs under external or internal, laminar or turbulent conditions involving various geometric shapes, the solid–liquid interface is often irregular and can be oscillatory [1–7]. Thus, in experimental investigations involving solidification processes, it is generally difficult to determine the heat transfer coefficients at the interface by direct measurement of temperature profiles. When the shape of a solidified region can be determined by photographic methods or by direct measurements and the boundary wall temperatures are known at any instant, then the determination of the local heat transfer coefficients at the interface can be reduced to solving a Laplace equation with Dirichlet boundary conditions for the temperature field in the solidified region. One notes that the interface temperature is known to be constant at freezing point temperature and the cooled wall temperatures are either known or can be measured.

For the solution of the Laplace equation with known boundary conditions, one can employ either analytical or numerical methods. The purpose of this note is to show the applicability of the simple method of determining the local heat transfer coefficients at the solid–liquid interface for three ice formation problems involving plane plate in longitudinal flow [1–3], cylinder in crossflow [4, 5], and flow inside a pipe with ice bands [6, 7] reported in the literature.

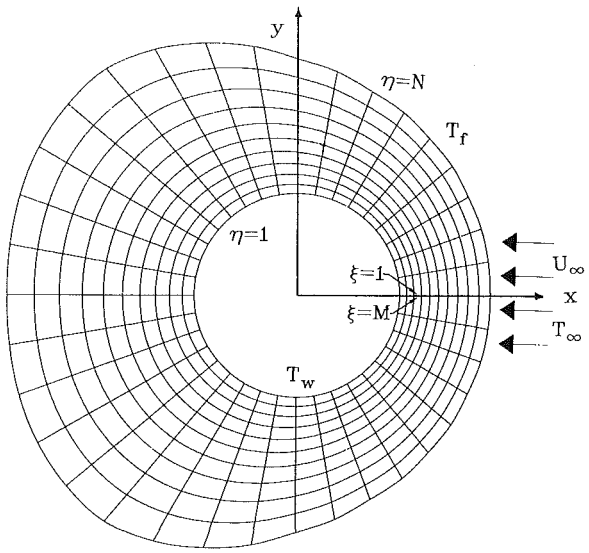

Fig. 1 Physical plane for the solidified region around a cooled cylinder

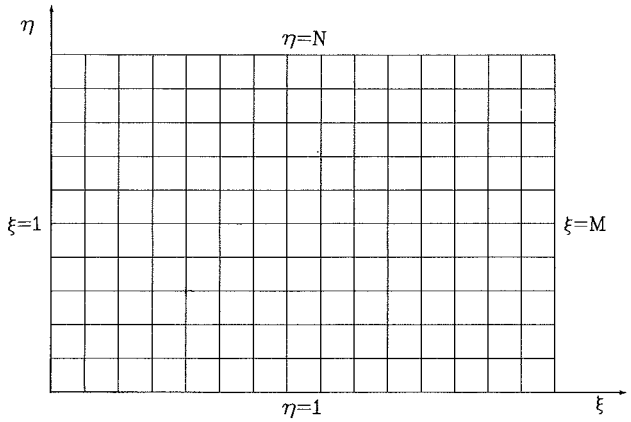

Fig. 2 Transformed plane of the solidified region

2 Analysis

At steady state or quasi-steady state, the local convective heat transfer coefficient at the ice–water interface can be obtained from a heat balance equation at the interface as

$$h(T_\infty - T_f) - k_i \frac{\partial T}{\partial n}\bigg|_c = 0 \tag{1}$$

where $\partial T/\partial n\,|_c$ is a local temperature gradient for the ice layer at the interface. The temperature gradient $\partial T/\partial n\,|_c$ can be found from the heat conduction analysis of the ice layer. It involves the solution of Laplace equation in an arbitrary geometry. The steady two-dimensional heat conduction equation for the solidified region is

$$\nabla^2 T = 0 \tag{2}$$

where $\nabla^2 = \partial^2/\partial x^2 + \partial^2/\partial x^2$ or $\partial^2/\partial R^2 + \partial/R\partial R + \partial^2/\partial x^2$. The boundary conditions are

$$T = T_f \text{ at interface}$$
$$T = T_w \text{ at cooled wall} \tag{3}$$

Other boundary conditions such as a convective boundary condition at the cooling wall may be specified depending on the particular phase change problem. By using the method of boundary-fitted coordinate systems, the irregular or com-

[1]Department of Mechanical Engineering, University of Alberta, Edmonton, Alberta, Canada
[2]Mem. ASME

Contributed by the Heat Transfer Division for publication in the JOURNAL OF HEAT TRANSFER. Manuscript received by the Heat Transfer Division March 23, 1984.

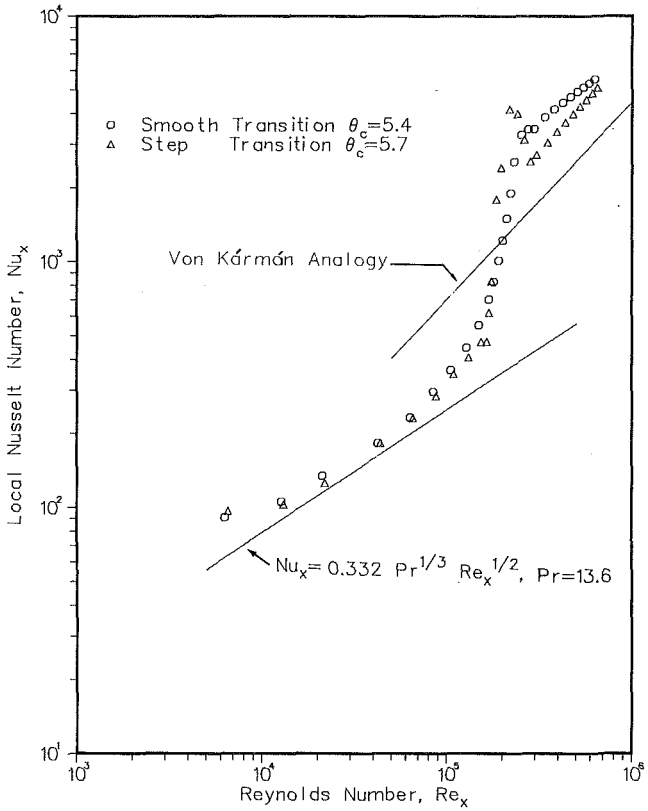

Fig. 3 Variation of local Nusselt number with Reynolds number at the ice-water interface for ice layer on a cooled flat plate

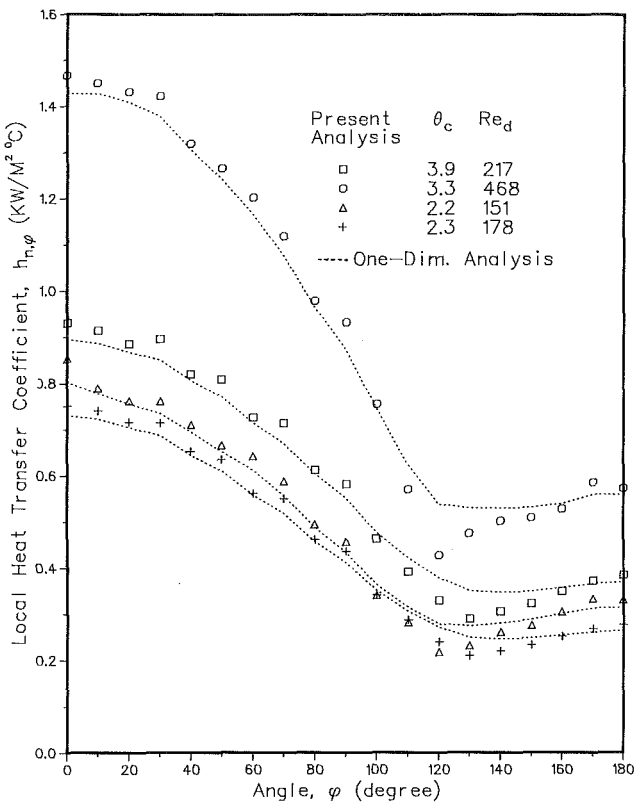

Fig. 4 Variation of local heat transfer coefficient at the ice-water interface with angular position, data from [4]

plicated physical domain for the solidified region such as that shown in Fig. 1 can be transformed into a regular domain such as that shown in Fig. 2. This technique is based on the automatic numerical generation of a curvilinear coordinate system. A detailed account of this method can be found in [8]. When the solidified region is specified by the Cartesian system, the boundary-fitted coordinate system is generated by numerically solving the following system of elliptic equations

$$\alpha x_{\xi\xi} - 2\beta x_{\xi\eta} + \gamma x_{\eta\eta} + J^2(Px_\xi + Qx_\eta) = 0$$
$$\alpha y_{\xi\xi} - 2\beta y_{\xi\eta} + \gamma y_{\eta\eta} + J^2(Py_\xi + Qy_\eta) = 0 \qquad (4)$$

The Dirichlet boundary conditions are prescribed at the boundaries. The coordinate control functions P and Q allow node points to be concentrated in some desired part of the domain such as the layer near the ice-water interface. The equation for the temperature field in the transformed plane becomes

$$\alpha T_{\xi\xi} - 2\beta T_{\xi\eta} + \gamma T_{\eta\eta} + J^2(PT_\xi + QT_\eta) = 0 \qquad (5)$$

The ice-water interface corresponds to $\eta(x,y) = N$ in Fig. 1 and a constant temperature $T = T_f$ is specified there. The other boundary conditions are transformed in a similar manner. Then the finite-difference equations and the boundary conditions are solved using a successive over-relaxation procedure, for example. The temperature derivative in the outward normal direction at the ice-water interface can be shown to be [8]

$$\left.\frac{\partial T}{\partial n}\right|_c = [(\gamma T_\eta - \beta T_\xi)/J(\gamma)^{1/2}]_{\eta=N} \qquad (6)$$

Hence the local heat transfer coefficient at the interface can be found easily.

An approximate solution to the local heat transfer coefficients at the interface can be found from the one-dimensional analysis of the solidified region. For the case of ice formation on a cooled flat plate, the local heat transfer coefficient h can be computed from the following equation

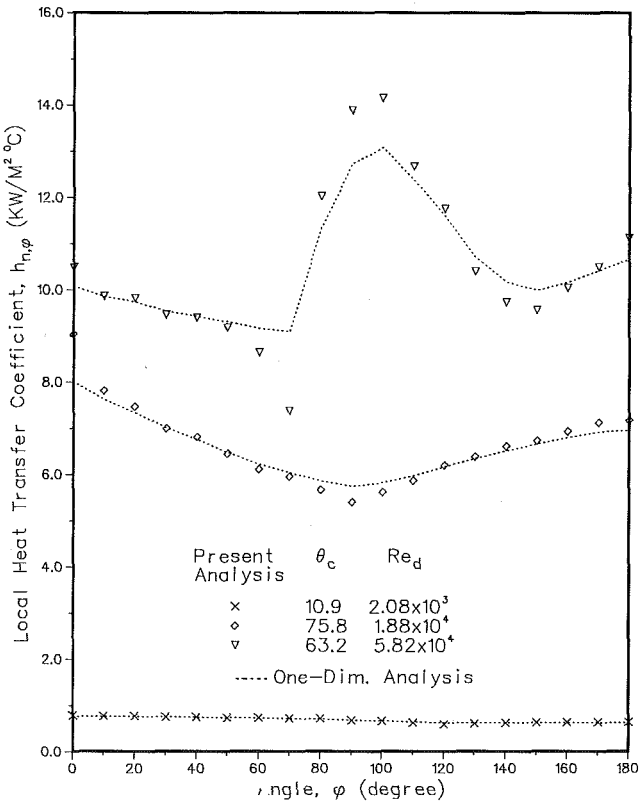

Fig. 5 Variation of local heat transfer coefficient at the ice-water interface with angular position, data from [5]

$$h = \theta_c k_i / \delta \qquad (7)$$

For the case of ice formation outside a cooled cylinder, the expression for the local heat transfer coefficient can be shown to be

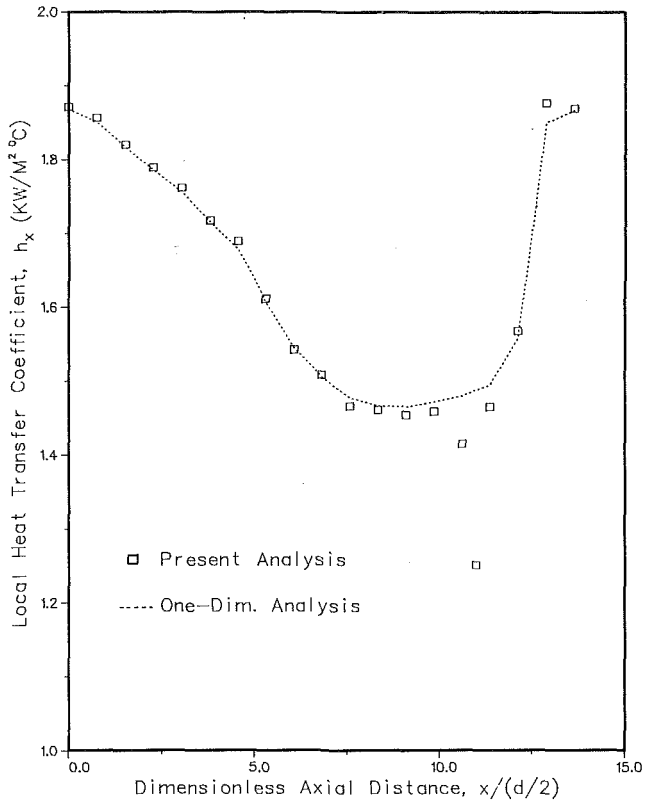

Fig. 6 Local heat transfer coefficients along one wavelength for ice surface waves inside a cooled pipe, data from [7]

$$h = (\theta_c k_i / R_1)/r_2 \ln r_2 \tag{8}$$

For the ice formation inside a cooled pipe, it can be shown that

$$h = (\theta_c k_i / R_1)/r_2 [1/\mathrm{Bi} + \ln(1/r_2)]$$

$$h = (\theta_c k_i / R_1)/r_2 \ln (1/r_2) \text{ for Bi} = \infty \tag{9}$$

For cylindrical geometries, r_2 represents the ice-water interface. The validity of the one-dimensional model can be assessed against the two-dimensional model.

In this study, the square mesh sizes (M, N) were chosen by trial and error, and ($M=25$, $N=11$, 16) for flat plate, ($M=37$, $N=11$, 16) for cylinder, and ($M=20$, $N=11$) for pipe were used to obtain the numerical solution. The convergence criterion used in finding the coordinates was 1×10^{-3} of the maximum value of the coordinate in that particular direction and that for the dimensionless temperature (1 at the interface and 0 at the cooled wall) was also 1×10^{-3}. The maximum difference in the total heat transfer rates at the cooled wall and the interface was found to be less than 0.5 percent in all cases studied.

3 Results and Discussion

3.1 Steady-State Ice Layer on an Isothermally Cooled Flat Plate [2]. The transition from laminar to turbulent flow on a frozen layer formed on an isothermally cooled flat plate placed in a stream of warm water was studied in [1-3]. Due to the interaction between the ice surface and the convective heat transfer, two modes of transition, namely smooth transition and step transition, were observed in the transition flow regime. For both modes, the transition Reynolds number was found to be substantially lower than that for a flow on a flat plate. A typical experimental ice layer profile is given in Fig. 2(*a*) of [2]. The local heat transfer coefficients at the ice-water interface were determined by the analysis of the temperature field in the ice layer and the results are shown in Fig. 3. The local heat transfer coefficient at the interface is higher than that of the classical result particularly in the turbulent flow regime. Also, it is observed that the transition Reynolds number on ice appears to be one order of magnitude lower than that for flow over a flat plate.

For smooth transition, the local heat transfer coefficients from the one-dimensional solution and the two-dimensional solution agree within 1 percent. For the step transition, the two solutions are within 1 percent for Nu_x at all downstream positions except near the points where there is a sudden change in the ice layer thickness. When there is a sudden change in ice layer thickness, the one-dimensional solution is found to overpredict the local Nusselt number at points near a local maximum ice layer thickness and to underpredict at points near a local minimum.

3.2 Steady-State Ice Layer Around an Isothermally Cooled Cylinder in Crossflow [4, 5]. When water freezes over an isothermally cooled cylinder in crossflow, the ice layer form has a complex shape [4, 5]. The local heat transfer coefficients at the interface of the frozen layer were determined by finite difference method in [4] and a collocation method in [5] using the two-dimensional heat conduction equation in cylindrical coordinates for the doubly connected regions. The shapes of the frozen layers were determined by measurements in [4] and by photographs in [5]. For the profiles given in [4] and [5], the local heat transfer coefficients at the interface were determined using a boundary-fitted coordinate method and by one-dimensional analysis. The present two-dimensional solution agrees fairly well with those given in [4] and [5]. As noted earlier, it can be observed in Figs. 4 and 5 that the one-dimensional analysis overpredicts the local heat transfer coefficients where the ice layer thickness is locally maximum and gives fairly accurate results when the ice layer thickness changes smoothly.

3.3 Ice Formation in a Pipe in Transitional and Turbulent Flow Regimes [7]. Freezing of water inside a cooled pipe is of considerable importance in many technical problems such as the blockage of water pipes in cold regions. The ice-band structure in the form of surface waves at the ice-water interface in a cooled pipe was first reported by Gilpin [6, 7] for the Reynolds number range 3.7×10^2 to 1.4×10^4. The local heat transfer coefficients at the ice-water interface for the steady-state ice layer profile shown in Fig. 4(*b*) of [7] were determined by the method of the boundary-fitted coordinate systems and the results are shown in Fig. 6 together with the one-dimensional solution plotted for comparison. As noted in previous cases, the one-dimensional solution predicts higher value for the local heat transfer coefficient at points near the maximum ice layer thickness and agrees fairly well with the two-dimensional analysis when the ice layer thickness changes smoothly. It is noted that the determination of the local heat transfer coefficients by temperature profile measurements would be extremely difficult for this case but the present method can be applied readily.

4 Concluding Remarks

The method of boundary-fitted coordinate systems was applied to a class of steady-state ice formation problems involving simply or doubly connected solidified regions in determining the local heat transfer coefficients at the solid-liquid interface. The method may be useful in studying convective heat transfer problems involving flow separation. It is also shown that the one-dimensional analysis gives fairly accurate results for local heat transfer coefficients at the ice-water interface except at points near a local maximum or minimum ice layer thickness.

Acknowledgments

This work was supported by the Natural Sciences and

Engineering Research Council of Canada through an operating grant.

References

1 Hirata, T., Gilpin, R. R., Cheng, K. C., and Gates, E. M., "The Steady State Ice Layer Profile on a Constant Temperature Plate in a Forced Convection Flow: I. Laminar Regime," *Int. J. Heat and Mass Transfer*, Vol. 22, 1979, pp. 1425-1433.

2 Hirata, T., Gilpin, R. R., and Cheng, K. C., "The Steady State Ice Layer Profile on a Constant Temperature Plate in a Forced Convection Flow: II. The Transition and Turbulent Regimes," *Int. J. Heat and Mass Transfer*, Vol. 22, 1979, pp. 1435-1443.

3 Gilpin, R. R., Hirata, T., and Cheng, K. C., "Wave Formation and Heat Transfer at an Ice-Water Interface in the Presence of a Turbulent Flow," *J. Fluid Mech.*, Vol. 99, 1980, pp. 619-640.

4 Okada, M., Katayama, K., Terasaki, K., Akimoto, M., and Mabune, K., "Freezing Around a Cooled Pipe in Crossflow," *Bulletin of the JSME*, Vol. 21, No. 160, 1978, pp. 1514-1520.

5 Cheng, K. C., Inaba, H., and Gilpin, R. R., "An Experimental Investigation of Ice Formation Around an Isothermally Cooled Cylinder in Crossflow," *J. Heat Transfer*, Vol. 103, 1981, pp. 733-738.

6 Gilpin, R. R., "The Morphology of Ice Structure in a Pipe at or Near Transition Reynolds Numbers," *AIChE Symposium Series 189*, Vol. 75, 1979, pp. 89-94.

7 Gilpin, R. R., "Ice Formation in a Pipe Containing Flows in the Transition and Turbulent Regimes," *J. Heat Transfer*, Vol. 103, 1981, pp. 363-368.

8 Thompson, J. F., "Numerical Solution of Flow Problems Using Boundary-Fitted Coordinate Systems," Von Karman Inst. for Fluid Dynamics, Lecture Series—1978-4, pp. 1-100.

Effect of Crystal Anisotropy on Heat Transfer During Melting and Solidification of a Metal

C. Gau[1] and R. Viskanta[1,2]

Nomenclature

- c = specific heat
- Fo = Fourier number, $\alpha\tau/H^2$
- H = height of the cavity
- Δh_f = latent heat of fusion
- k = thermal conductivity
- Ste = Stefan number, $c_l(T_{wb} - T_f)/\Delta h_f$ for melting and $c_s(T_{wt} - T_f)/\Delta h_f$ for solidification
- s = solid-liquid interface position
- T = temperature
- t = time
- α = thermal diffusivity
- δ = dimensionless interface position, s/H
- θ = dimensionless temperature, $(T - T_f)/(T_{wb} - T_f)$
- τ = dimensionless time, $\tau_l = \mathrm{Fo}_l\mathrm{Ste}_l$ for melting and $\tau_s = \mathrm{Fo}_s\,\mathrm{Ste}_s$ for solidification

Subscripts

- b = refers to bottom plate
- f = refers to fusion
- l = refers to the liquid phase
- s = refers to the solid phase
- t = refers to top plate
- w = refers to wall

Introduction

This paper describes melting and solidification experiments which were performed to determine the effect of crystal anisotropy on solid-liquid phase change heat transfer in the absence of natural convection in the liquid and on the solid-liquid interface morphology. The focus of the paper is on the evolution of the phase-change boundary and comparison of the measured and predicted average interface positions with time. This type of problem, using a pure metal as a phase-change material, is relevant to material processing, solidification of castings, crystal growth, and purification of metals.

A search of archival heat transfer literature failed to reveal experiments or analyses on the type of problem considered here. An up-to-date account of solid-liquid phase-change heat transfer in different materials is available [1], but there have been relatively few studies [2-7] which used metals or metal alloys as the phase-change material. No references could be identified in the literature which used anisotropic materials, i.e., those which have thermal conductivities dependent on the orientation of the crystal axes. The interface position and its morphology during phase transformation is expected to be controlled not only by the thermal conditions in the solid and liquid phases adjacent to the interface but also by the crystallographic effects.

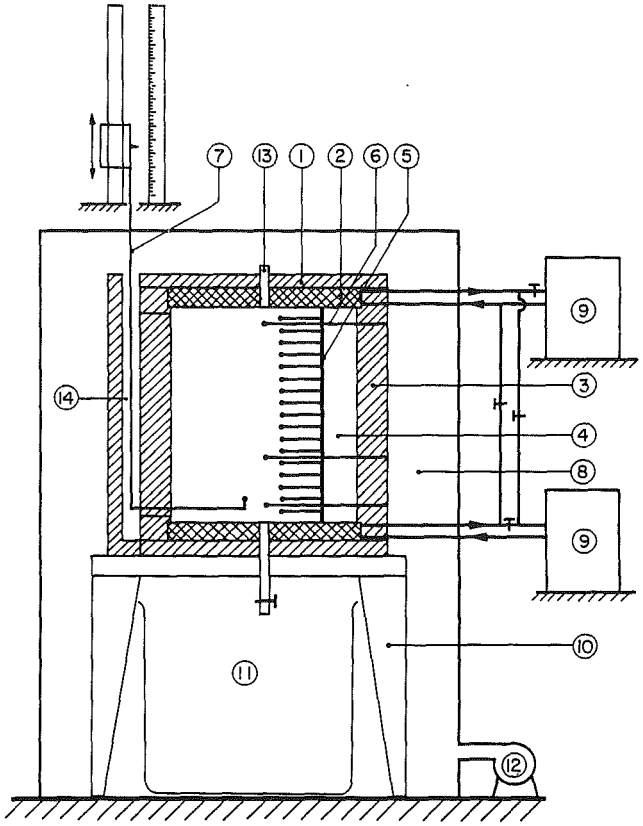

Fig. 1 Schematic diagram of test apparatus: (1) insulation, (2) heat exchanger, (3) Plexiglass wall, (4) phase-change material, (5) thermocouple rack, (6) small diameter thermocouples, (7) L-shaped movable probe, (8) temperature controlled environment, (9) constant temperature bath, (10) support frame, (11) container, (12) heat gun with temperature controller, (13) hole for inserting movable probe, and (14) vertical slot

Experiments

The metal used in the experiments was gallium. It had a purity of 99.6 percent and a fusion temperature of 29.78°C. There were several reasons for selecting gallium. First, pure solid gallium appears in polycrystalline form and each crystal has an orthorhombic structure. Second, the thermophysical properties are reasonably well established [8]. The thermal conductivity of the solid crystal is highly anisotropic and is 40.82 W/m K along the a axis of crystal, 88.47 W/m K along the b axis, and 15.99 W/m K along the c axis [8]. The thermal conductivity of the liquid is still anisotropic but varies only slightly for each of the crystal axes. Third, it has a fusion

[1]School of Mechanical Engineering, Purdue University, West Lafayette, IN 47907

[2]Fellow ASME

Contributed by the Heat Transfer Division for publication in the JOURNAL OF HEAT TRANSFER. Manuscript received by the Heat Transfer Division February 10, 1984.

Engineering Research Council of Canada through an operating grant.

References

1 Hirata, T., Gilpin, R. R., Cheng, K. C., and Gates, E. M., "The Steady State Ice Layer Profile on a Constant Temperature Plate in a Forced Convection Flow: I. Laminar Regime," *Int. J. Heat and Mass Transfer*, Vol. 22, 1979, pp. 1425-1433.

2 Hirata, T., Gilpin, R. R., and Cheng, K. C., "The Steady State Ice Layer Profile on a Constant Temperature Plate in a Forced Convection Flow: II. The Transition and Turbulent Regimes," *Int. J. Heat and Mass Transfer*, Vol. 22, 1979, pp. 1435-1443.

3 Gilpin, R. R., Hirata, T., and Cheng, K. C., "Wave Formation and Heat Transfer at an Ice-Water Interface in the Presence of a Turbulent Flow," *J. Fluid Mech.*, Vol. 99, 1980, pp. 619-640.

4 Okada, M., Katayama, K., Terasaki, K., Akimoto, M., and Mabune, K., "Freezing Around a Cooled Pipe in Crossflow," *Bulletin of the JSME*, Vol. 21, No. 160, 1978, pp. 1514-1520.

5 Cheng, K. C., Inaba, H., and Gilpin, R. R., "An Experimental Investigation of Ice Formation Around an Isothermally Cooled Cylinder in Crossflow," *J. Heat Transfer*, Vol. 103, 1981, pp. 733-738.

6 Gilpin, R. R., "The Morphology of Ice Structure in a Pipe at or Near Transition Reynolds Numbers," *AIChE Symposium Series 189*, Vol. 75, 1979, pp. 89-94.

7 Gilpin, R. R., "Ice Formation in a Pipe Containing Flows in the Transition and Turbulent Regimes," *J. Heat Transfer*, Vol. 103, 1981, pp. 363-368.

8 Thompson, J. F., "Numerical Solution of Flow Problems Using Boundary-Fitted Coordinate Systems," Von Karman Inst. for Fluid Dynamics, Lecture Series—1978-4, pp. 1-100.

Effect of Crystal Anisotropy on Heat Transfer During Melting and Solidification of a Metal

C. Gau[1] and R. Viskanta[1,2]

Nomenclature

- c = specific heat
- Fo = Fourier number, $\alpha\tau/H^2$
- H = height of the cavity
- Δh_f = latent heat of fusion
- k = thermal conductivity
- Ste = Stefan number, $c_l(T_{wb} - T_f)/\Delta h_f$ for melting and $c_s(T_{wt} - T_f)/\Delta h_f$ for solidification
- s = solid-liquid interface position
- T = temperature
- t = time
- α = thermal diffusivity
- δ = dimensionless interface position, s/H
- θ = dimensionless temperature, $(T - T_f)/(T_{wb} - T_f)$
- τ = dimensionless time, $\tau_l = \mathrm{Fo}_l\mathrm{Ste}_l$ for melting and $\tau_s = \mathrm{Fo}_s\,\mathrm{Ste}_s$ for solidification

Subscripts

- b = refers to bottom plate
- f = refers to fusion
- l = refers to the liquid phase
- s = refers to the solid phase
- t = refers to top plate
- w = refers to wall

Introduction

This paper describes melting and solidification experiments which were performed to determine the effect of crystal anisotropy on solid-liquid phase change heat transfer in the absence of natural convection in the liquid and on the solid-liquid interface morphology. The focus of the paper is on the evolution of the phase-change boundary and comparison of the measured and predicted average interface positions with time. This type of problem, using a pure metal as a phase-change material, is relevant to material processing, solidification of castings, crystal growth, and purification of metals.

A search of archival heat transfer literature failed to reveal experiments or analyses on the type of problem considered here. An up-to-date account of solid-liquid phase-change heat transfer in different materials is available [1], but there have been relatively few studies [2-7] which used metals or metal alloys as the phase-change material. No references could be identified in the literature which used anisotropic materials, i.e., those which have thermal conductivities dependent on the orientation of the crystal axes. The interface position and its morphology during phase transformation is expected to be controlled not only by the thermal conditions in the solid and liquid phases adjacent to the interface but also by the crystallographic effects.

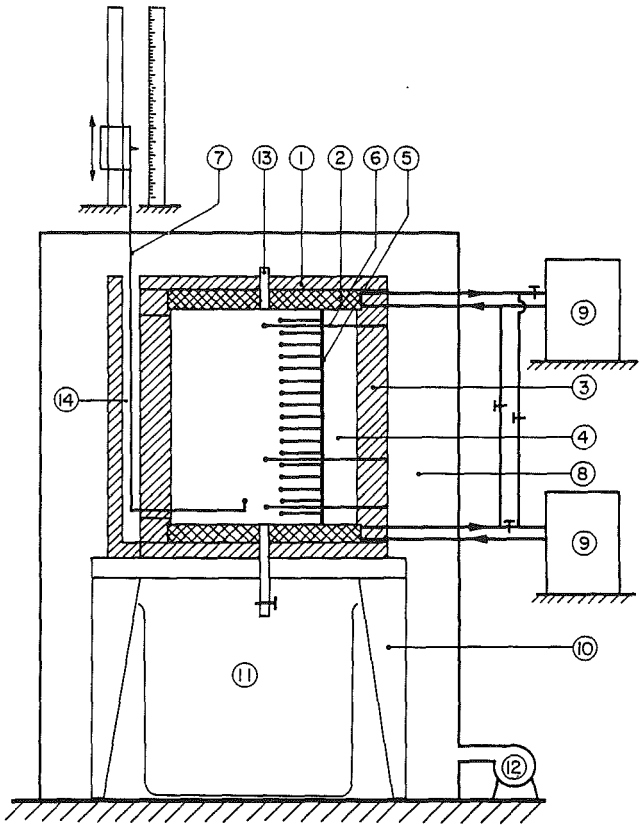

Fig. 1 Schematic diagram of test apparatus: (1) insulation, (2) heat exchanger, (3) Plexiglass wall, (4) phase-change material, (5) thermocouple rack, (6) small diameter thermocouples, (7) L-shaped movable probe, (8) temperature controlled environment, (9) constant temperature bath, (10) support frame, (11) container, (12) heat gun with temperature controller, (13) hole for inserting movable probe, and (14) vertical slot

Experiments

The metal used in the experiments was gallium. It had a purity of 99.6 percent and a fusion temperature of 29.78°C. There were several reasons for selecting gallium. First, pure solid gallium appears in polycrystalline form and each crystal has an orthorhombic structure. Second, the thermophysical properties are reasonably well established [8]. The thermal conductivity of the solid crystal is highly anisotropic and is 40.82 W/m K along the a axis of crystal, 88.47 W/m K along the b axis, and 15.99 W/m K along the c axis [8]. The thermal conductivity of the liquid is still anisotropic but varies only slightly for each of the crystal axes. Third, it has a fusion

[1]School of Mechanical Engineering, Purdue University, West Lafayette, IN 47907

[2]Fellow ASME

Contributed by the Heat Transfer Division for publication in the JOURNAL OF HEAT TRANSFER. Manuscript received by the Heat Transfer Division February 10, 1984.

Fig. 2 Typical solid-liquid interface morphology for solidification of gallium from below: T_{wb} = 5.0°C, T_{wt} = 32.0°C, and t = 8 min

temperature close to the ambient which is conducive for experimentation. Fourth, the metal is important technologically as it is usually combined with other pure elements to form electronic and industrial materials such as semiconductors, laser diodes, solar cells, and magnetic bubble devices. The main disadvantage is that it is very expensive (about one dollar per gram depending on purity).

The melting and solidification experiments were performed in a rectangular test cell that had inside dimensions of 8.89 cm in height, 6.35 cm in width, and 3.81 cm in depth (Fig. 1). The two horizontal walls, which served as the heat source/sink, were made of multipass heat exchangers machined from copper plate. The copper surfaces were plated with a layer of 0.0127-cm-thick chromium for protection against corrosion. All of the vertical walls were made of Lexan (polycarbonate resin): The two vertical sidewalls were 1.27 cm thick Lexan plates to support the cell. For better insulation, the front and back walls had a 0.318-cm air gap between dual plates, 0.318 and 0.635 cm thick, respectively. The entire test cell was covered with removable insulation. A more detailed description of the test cell, instrumentation and test procedure can be found in an earlier paper [7].

Both the pour-out and probing methods were used to determine the solid-liquid interface position. In the pour-out method, the liquid was drained at predetermined times through the sprue on the left side of the test cell. The exposed interface was examined and photographed. The data at succeeding time increments were obtained by repeating the experiment at identical boundary and initial conditions. The probing method involves the use of a probe which was attached to a Vernier caliper and could be moved in the vertical direction.

Analysis

A simple one-dimensional model, which assumes that the solid-liquid interface is planar, was used earlier to predict the average interface position [7]. The model is an extension of the classical Neumann model in that one of the two phases does not have to be semi-infinite in extent. An integral method was used to solve the model equations. The same analysis is used in this note and the details are not included here.

Results and Discussion

Solidification From Below. For the solidification experiments from below the thermocouples located near the top plate and the central region of the test cell did not indicate any oscillations of temperature during the entire phase transformation process. The vertical temperature distribution in the liquid was linear, and therefore the fluid could be considered to be stagnant. Heat conduction was the only mode of energy transfer in the melt. The melt layer near the heat sink was found to be supercooled (by as much as 2.75°C) before solid crystal formation was initiated when the coolant circulation was started through the bottom heat exchanger.

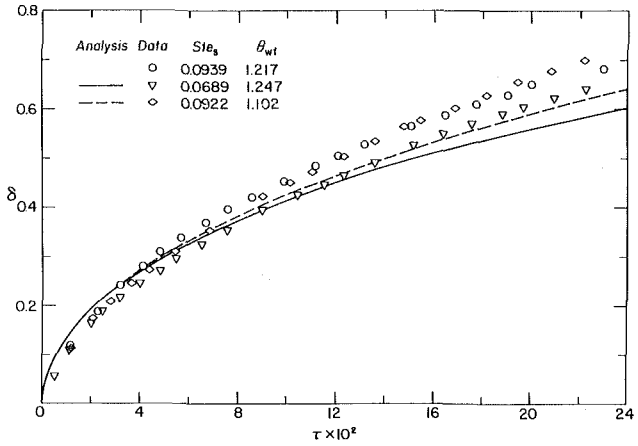

Fig. 3 Comparison of measured and predicted solid liquid interface position during solidification of gallium from below

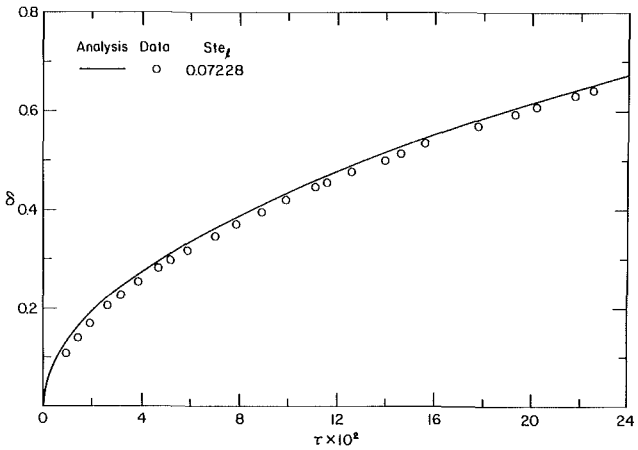

Fig. 4 Comparison of measured and predicted solid-liquid interface positions during melting of gallium from above

After the solid crystal formed, the temperature rose immediately to the fusion temperature and then decreased gradually as the solidification proceeded.

In general, the interface position and shape during phase transformation can be controlled by the thermal conditions in the solid and the liquid phases in the vicinity of the interface and by the crystallographic characteristics. It has been established that the solidification of gallium crystal proceeds by lateral growth or faceted growth because of the relatively high entropy of fusion [9]. Thus, the gallium crystal has a preferred growth direction, and the formation of new planes is controlled by two-dimensional nucleation or a screw dislocation mechanism when deformation occurs. The growth rate of gallium crystal can increase rapidly when dislocations or deformations are introduced into the growing crystal [10]. Visual examinations of the solid-liquid interface shape during experiments with the pour-out method at specific times indicated that the interface shape was irregular and "corrugated" and had the appearance of a regular crystalline structure (Fig. 2). Usually, the region which has a wider and larger facet on the interface has a higher growth rate than the region which has the smaller facet. These are attributed to the combined effect of the previously mentioned growth morphology of solidification front during phase transformation and the highly anisotropic thermal conductivity of the solid crystal.

The probing technique only provided interface position data at one location. Figure 3 shows a comparison between the data obtained at one location and the predictions. It appears likely that the use of test cell cross-section average

interface position for the purpose of comparison would be more reasonable; however, because of unidirectional heat flow the comparisons between the predictions based on the Neumann model and the data obtained with the probing method for the case of one-directional solidification process does become meaningful. The agreement is surprisingly good and each set of experimental data points appears to be very smooth. At later times the measured solidification rates are higher than the predicted ones. This higher growth rate at later times is attributed to the anisotropic thermal conductivity of gallium and possibly the change of the growth mechanism at the interface due to the deformation of the crystal caused by the probe during the measurements. Also, it can be conjectured that the increased surface area afforded by the irregular crystalline structure, relative to a plane surface, should lead to a higher solidification rate. The presence of the structure could not be accounted for in the analysis because of the complexities involved. As predicted, all the data points for the higher Stefan number fall somewhat above the one with the lower Stefan number. The increase in the solidification rate with the Stefan number is expected. Physically, during the solidification process the higher Stefan number implies that more sensible heat is conducted through the solid compared to the latent heat released at the interface, thus increasing the solidification rate.

Melting From Above. For melting experiments from above, the liquid was also found to be stable as the temperature was linear and no oscillations in temperature were detected by thermocouples placed in the vicinity of the heat sink and in the central region of the test cell. The observed interface shape using the pour-out method was found to be very flat. It can therefore be concluded that the anisotropy in the thermal conductivity and the growth morphology of the melting front do not play a significant role in controlling the interface shape macroscopically, and the effect can be neglected during melting. The probing method was then used to measure the interface position during melting from above. The measured data for a typical experiment are compared in Fig. 4 with the predictions based on the Neumann model. The agreement is very good and thus provides further corroborative evidence of the conclusion reached above.

Concluding Remarks

The anisotropy in the thermal conductivity of gallium crystals affects the solid-liquid interface morphology during solidification but not during melting. The large differences in the thermal conductivities of gallium along the axes of the crystal and the associated crystallographic characteristics produce a crystalline structure during solidification. The measured average solid-liquid interface positions were a maximum of about 15 percent higher than the predictions based on the Neumann model using the thermophysical property data published in the literature. This suggests that the crystal anisotropy is not very significant in controlling heat transfer, global motion of the interface, and the rate of solidification of gallium under the experimental conditions studied. During melting the effect of crystal anisotropy on the rate of heat transfer and the solid-liquid interface motion can be neglected.

Acknowledgments

This work was supported by the Heat Transfer Program of the National Science Foundation under Grant No. MEA-8313573.

References

1 Viskanta, R., "Phase-Change Heat Transfer," *Solar Heat Storage; Latent Heat Materials*, Chap. 5, ed. G. A. Lane, CRC Press, Boca Raton, Fla., 1983.

2 Tien, R. H., "Freezing of Semi-Infinite Slab With Time Dependent Surface Temperature—an Extension of Neumann's Solution," *Transactions of the American Institute of Metallurgical Engineers*, Vol. 233, 1965, pp. 1887-1891.

3 Jones, H., "A Comparison of Approximate Analytical Solution of Freezing From a Plane Chill," *Journal of the Institute of Metals*, Vol. 91, 1969, pp. 38-43.

4 Hills, A. W. D., and Moore, M. R., "The Solidification of Pure Metals Under Unidirectional Heat Flow Conditions, I—Solidification With Zero Superheat," *Transactions of the Metallurgical Society*—The American Institute of Metallurgical Engineers, Vol. 245, 1969, pp. 1481-1492.

5 Hills, A. W. D., Malhorta, S. L., and Moore, M. R., "The Solidification of Pure Metals (and Eutectics) Under Unidirectional Heat Flow Conditions. II. Solidification in the Presence of Superheat," *Metallurgical Transactions B*, Vol. 6, 1975, pp. 131-142.

6 Clyne, T. W., and Garcia, A., "Assessment of a New Model for Heat Flow During Unidirectional Solidification of Metals," *International Journal of Heat and Mass Transfer*, Vol. 23, 1980, pp. 773-782.

7 Gau, C., and Viskanta, R., "Melting and Solidification of a Metal System in a Rectangular Cavity," *International Journal of Heat and Mass Transfer*, Vol. 27, 1984, pp. 113-123.

8 Cubberly, W. H., *Metal Handbook Properties and Selection. Nonferrous Alloys and Pure Metals*, 9th ed., American Society of Metals, Metals Park, OH, 1979, pp. 736-737.

9 Jackson, K. A., "Interface Structure," in: *Growth and Perfection of Crystals*, ed. R. H. Doremus et al., Wiley, New York, 1958, pp. 319-324.

10 Alfintsev, G. A., and Ovsienko, D. E., "Growth Mechanism of Gallium Crystals Grown From Melts," *Soviet Physics—Doklady*, Vol. 9, No. 6, 1964, pp. 489-491.

An Analysis of Upward Fire Spread Along Metal Cylinders

T. Hirano,[1] K. Sato,[1] and J. Sato[2]

Introduction

An appropriate assessment of structural metal fire hazards is useful to prevent the accidents caused by burning metal parts of oxygen supply systems or oxygen reservoirs, and for it, an accurate prediction of metal fire spread is indispensable. In our previous study [1], the prediction of metal fire spread in high pressure oxygen was performed on the basis of the results of previous studies. In the analysis, heat release due to chemical reaction between metal and oxygen was assumed to be confined to the oxide-solid metal boundary. However, the results cannot be directly applied to the prediction of fire spread phenomena along metal pieces where the regression is mainly caused by melting. Since such cases are not unusual [2-5], the necessity of a theoretical prediction for them was already pointed out earlier [1]. In the present study, therefore, an analysis of fire spread along metal pieces when chemical reaction occurs in the gas phase, or in the molten metal-oxide mass, has been performed by considering the heat transfer from the molten mass to the solid metal.

Models and Analysis

The present analysis is applicable to the two typical cases shown in Fig. 1. One involves chemical reaction in the gas phase while the other involves chemical reaction in the molten metal-oxide mass. To explore the fundamental characteristics of metal fire spread, upward fire spread, which is more stable than downward spread, is discussed.

The heat for increasing the solid temperature, which must be proportional to the regression rate V, is considered to be transferred through the melting surface B, and the heat flux across the solid surface A is considered negligible [2-5]. Thus, one-dimensional heat transfer is assumed in the solid metal.

The observed high-velocity motion of the molten mass and

[1]Engineering Research Institute, Faculty of Engineering, University of Tokyo, Tokyo, Japan

[2]Research Institute, Ishikawajima-Harima Heavy Industries Co., Ltd., Tokyo, Japan

Contributed by the Heat Transfer Division for publication in the JOURNAL OF HEAT TRANSFER. Manuscript received by the Heat Transfer Division October 10, 1983.

interface position for the purpose of comparison would be more reasonable; however, because of unidirectional heat flow the comparisons between the predictions based on the Neumann model and the data obtained with the probing method for the case of one-directional solidification process does become meaningful. The agreement is surprisingly good and each set of experimental data points appears to be very smooth. At later times the measured solidification rates are higher than the predicted ones. This higher growth rate at later times is attributed to the anisotropic thermal conductivity of gallium and possibly the change of the growth mechanism at the interface due to the deformation of the crystal caused by the probe during the measurements. Also, it can be conjectured that the increased surface area afforded by the irregular crystalline structure, relative to a plane surface, should lead to a higher solidification rate. The presence of the structure could not be accounted for in the analysis because of the complexities involved. As predicted, all the data points for the higher Stefan number fall somewhat above the one with the lower Stefan number. The increase in the solidification rate with the Stefan number is expected. Physically, during the solidification process the higher Stefan number implies that more sensible heat is conducted through the solid compared to the latent heat released at the interface, thus increasing the solidification rate.

Melting From Above. For melting experiments from above, the liquid was also found to be stable as the temperature was linear and no oscillations in temperature were detected by thermocouples placed in the vicinity of the heat sink and in the central region of the test cell. The observed interface shape using the pour-out method was found to be very flat. It can therefore be concluded that the anisotropy in the thermal conductivity and the growth morphology of the melting front do not play a significant role in controlling the interface shape macroscopically, and the effect can be neglected during melting. The probing method was then used to measure the interface position during melting from above. The measured data for a typical experiment are compared in Fig. 4 with the predictions based on the Neumann model. The agreement is very good and thus provides further corroborative evidence of the conclusion reached above.

Concluding Remarks

The anisotropy in the thermal conductivity of gallium crystals affects the solid-liquid interface morphology during solidification but not during melting. The large differences in the thermal conductivities of gallium along the axes of the crystal and the associated crystallographic characteristics produce a crystalline structure during solidification. The measured average solid-liquid interface positions were a maximum of about 15 percent higher than the predictions based on the Neumann model using the thermophysical property data published in the literature. This suggests that the crystal anisotropy is not very significant in controlling heat transfer, global motion of the interface, and the rate of solidification of gallium under the experimental conditions studied. During melting the effect of crystal anisotropy on the rate of heat transfer and the solid-liquid interface motion can be neglected.

Acknowledgments

This work was supported by the Heat Transfer Program of the National Science Foundation under Grant No. MEA-8313573.

References

1 Viskanta, R., "Phase-Change Heat Transfer," *Solar Heat Storage; Latent Heat Materials*, Chap. 5, ed. G. A. Lane, CRC Press, Boca Raton, Fla., 1983.

2 Tien, R. H., "Freezing of Semi-Infinite Slab With Time Dependent Surface Temperature—an Extension of Neumann's Solution," *Transactions of the American Institute of Metallurgical Engineers*, Vol. 233, 1965, pp. 1887-1891.

3 Jones, H., "A Comparison of Approximate Analytical Solution of Freezing From a Plane Chill," *Journal of the Institute of Metals*, Vol. 91, 1969, pp. 38-43.

4 Hills, A. W. D., and Moore, M. R., "The Solidification of Pure Metals Under Unidirectional Heat Flow Conditions, I—Solidification With Zero Superheat," *Transactions of the Metallurgical Society*—The American Institute of Metallurgical Engineers, Vol. 245, 1969, pp. 1481-1492.

5 Hills, A. W. D., Malhorta, S. L., and Moore, M. R., "The Solidification of Pure Metals (and Eutectics) Under Unidirectional Heat Flow Conditions. II. Solidification in the Presence of Superheat," *Metallurgical Transactions B*, Vol. 6, 1975, pp. 131-142.

6 Clyne, T. W., and Garcia, A., "Assessment of a New Model for Heat Flow During Unidirectional Solidification of Metals," *International Journal of Heat and Mass Transfer*, Vol. 23, 1980, pp. 773-782.

7 Gau, C., and Viskanta, R., "Melting and Solidification of a Metal System in a Rectangular Cavity," *International Journal of Heat and Mass Transfer*, Vol. 27, 1984, pp. 113-123.

8 Cubberly, W. H., *Metal Handbook Properties and Selection. Nonferrous Alloys and Pure Metals*, 9th ed., American Society of Metals, Metals Park, OH, 1979, pp. 736-737.

9 Jackson, K. A., "Interface Structure," in: *Growth and Perfection of Crystals*, ed. R. H. Doremus et al., Wiley, New York, 1958, pp. 319-324.

10 Alfintsev, G. A., and Ovsienko, D. E., "Growth Mechanism of Gallium Crystals Grown From Melts," *Soviet Physics—Doklady*, Vol. 9, No. 6, 1964, pp. 489-491.

An Analysis of Upward Fire Spread Along Metal Cylinders

T. Hirano,[1] K. Sato,[1] and J. Sato[2]

Introduction

An appropriate assessment of structural metal fire hazards is useful to prevent the accidents caused by burning metal parts of oxygen supply systems or oxygen reservoirs, and for it, an accurate prediction of metal fire spread is indispensable. In our previous study [1], the prediction of metal fire spread in high pressure oxygen was performed on the basis of the results of previous studies. In the analysis, heat release due to chemical reaction between metal and oxygen was assumed to be confined to the oxide-solid metal boundary. However, the results cannot be directly applied to the prediction of fire spread phenomena along metal pieces where the regression is mainly caused by melting. Since such cases are not unusual [2-5], the necessity of a theoretical prediction for them was already pointed out earlier [1]. In the present study, therefore, an analysis of fire spread along metal pieces when chemical reaction occurs in the gas phase, or in the molten metal-oxide mass, has been performed by considering the heat transfer from the molten mass to the solid metal.

Models and Analysis

The present analysis is applicable to the two typical cases shown in Fig. 1. One involves chemical reaction in the gas phase while the other involves chemical reaction in the molten metal-oxide mass. To explore the fundamental characteristics of metal fire spread, upward fire spread, which is more stable than downward spread, is discussed.

The heat for increasing the solid temperature, which must be proportional to the regression rate V, is considered to be transferred through the melting surface B, and the heat flux across the solid surface A is considered negligible [2-5]. Thus, one-dimensional heat transfer is assumed in the solid metal.

The observed high-velocity motion of the molten mass and

[1]Engineering Research Institute, Faculty of Engineering, University of Tokyo, Tokyo, Japan

[2]Research Institute, Ishikawajima-Harima Heavy Industries Co., Ltd., Tokyo, Japan

Contributed by the Heat Transfer Division for publication in the JOURNAL OF HEAT TRANSFER. Manuscript received by the Heat Transfer Division October 10, 1983.

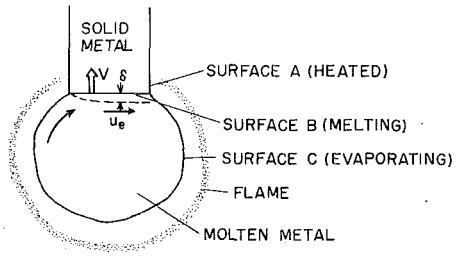

Case I

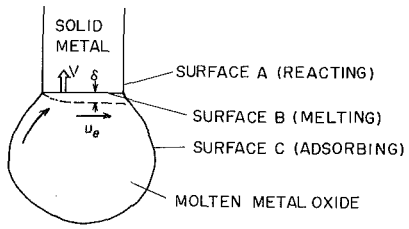

Case II

Fig. 1 Models of upward fire spreading along metal cylinders: Case I: combustion occurs in the gas phase; Case II: combustion occurs in the molten metal-oxide mass

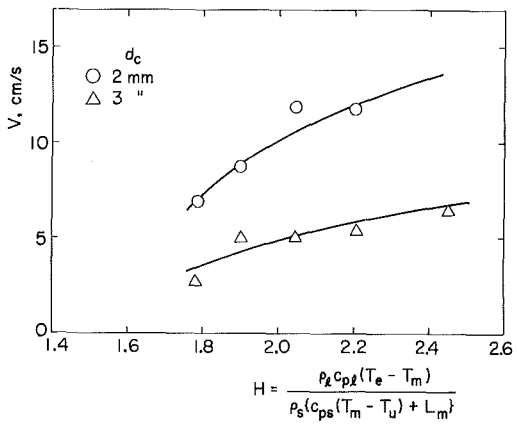

Fig. 2 Dependence of V on H

the dependence of V on the cylinder diameter d_c both imply that the dominant mode of heat transfer from the molten mass to the melting surface B must be convection [3-5]. From the direction of molten mass movement and the dependence of its velocity on cylinder diameter, it can be inferred that the motion is due to the surface tension difference due to the temperature difference near the solid-liquid boundary.

In the present cases, the observed flow velocity is a few tens of cm/s [3] and the Reynolds number $\mathrm{Re} = u_e d_c/\nu$ based on this velocity u_e, the cylinder diameter d_c, and the kinematic viscosity ν of molten mass is $10^2 \sim 10^4$. Thus, a thin boundary layer may be established near the melting surface B in the present cases [6] although the flow from the edge of the molten mass along the melting surface B is unstable with its direction periodically changing [3]. The region of a steep temperature gradient may be limited to this thin boundary layer.

The present analysis is based on the above discussion along with the additional assumptions: that the fire spread is steady and that density ρ_s, thermal conductivity λ_s, and specific heat c_{ps} of the solid metal are constant. For this model, the temperature T at a distance x above surface B can be expressed as [6]

$$T = T_u + (T_m - T_u)\exp\left(\frac{Vx}{\alpha_s}\right) \tag{1}$$

where T_u and T_m are the temperature before ignition and the melting temperature while $\alpha_s = \lambda_s/(c_{ps}\rho_s)$ is the thermal diffusivity.

Table 1 Values used for the calculation of H for aluminum cylinder burning in high pressure oxygen

p_O, MPa		T_e, K	ρ_ℓ, g/cm³
0.3	T_u = 300 K T_m = 933 K ρ_s = 2.7 g/cm³ c_{ps} = 1.05 J/g $c_{p\ell}$ = 1.18 J/g L_m = 397 J/g	2980	2.13
0.5		3120	2.11
1.0		3320	2.09
2.0		3540	2.06
5.0		3880	2.02

Unfortunately, the flow field inside of the molten mass may not be stable. However, assuming relations similar to those which are generally accepted for boundary layers, approximate evaluation of the heat flux to the melting surface B can be obtained. The temperature gradient $(\partial T/\partial x)_{ml}$ at the molten mass side of the melting surface B is given as [6]

$$\left(\frac{\partial T}{\partial x}\right)_{ml} = \frac{a\,\mathrm{Re}^{1/2}}{d_c}(T_e - T_m), \tag{2}$$

where a is a constant and T_e is the temperature at the boundary layer edge.

At the melting surface B, the heat flux from the molten mass is equal to the sum of the heat flux into the solid metal and the heat needed to melt the metal at the rate of $\rho_s V$, i.e.,

$$\lambda_l\left(\frac{\partial T}{\partial x}\right)_{ml} = \lambda_s\left(\frac{\partial T}{\partial x}\right)_{ms} + \rho_s V L_m, \tag{3}$$

where λ_l is the thermal conductivity of molten mass, $(\partial T/\partial x)_{ms}$ is the temperature gradient at the solid side of the melting surface B, and L_m is the latent heat for fusion.

From equations (1-3), the following equation is derived.

$$V = G \cdot H \tag{4}$$

where

$$G = \frac{a\nu}{d_c} \cdot \frac{\mathrm{Re}^{1/2}}{\mathrm{Pr}}, \tag{5}$$

$$H = \left(\frac{\rho_l}{\rho_s}\right)\frac{c_{pl}(T_e - T_m)}{c_{ps}(T_m - T_u) + L_m}, \tag{6}$$

and $\mathrm{Pr} = \mu c_{pl}/\lambda_l$ is the Prandtl number. G and H depend mainly on fluid-dynamic properties of molten mass and thermal characteristics of metal, respectively.

Discussion

Based on experimental conditions for an aluminum cylinder burning in high-pressure oxygen [5], the values of H were calculated. Since endothermic decomposition occurred at the boiling point of a metal oxide, the adiabatic flame temperature for aluminum burning in oxygen is limited to the boiling point of Al_2O_3 [7], which is much higher than the boiling point T_b of aluminum. The fact was confirmed in the previous studies [8, 9]. The observed flame temperature for aluminum burning is almost the same as the boiling point of Al_2O_3, although the radiative heat loss from molten aluminum surface may be appreciable. Before the aluminum mass starts boiling, its temperature must be below T_b but may be very close to it. Thus, T_b was used for T_e. The resulting dependence of V on H is shown in Fig. 2, and the values used to calculate H are shown in Table 1. Data for V when the molten mass is boiling are excluded from Fig. 2 because the molten mass movement similar to that before boiling could not be confirmed to exist.

It is seen that the dependence of V on H decreases as H or V increases. The fire spread rate V causes the mass injection at a velocity $V(\rho_s/\rho_l)$ into the molten mass at the melting

surface B. Thus, the increase of V implies the increase of the injection velocity, which makes $(\partial T/\partial x)_{ml}$ smaller than that without injection [6], i.e., $(\partial T/\partial x)_{ml}$ established by using equation (2) is larger than that for a given value of V. The decrease of the dependence of V on H at a larger value of H or V is attributable to the variation of $(\partial T/\partial x)_{ml}$ with V.

As mentioned in the previous section, the molten mass movement is inferred to be induced by the surface tension difference due to the temperature difference near the liquid-solid phase boundary. Assuming a situation similar to that presented in [10], the following equation can be derived approximately

$$\pi d_c(\gamma_{sm}-\gamma_{se})=b\left(\frac{\pi d_c^2}{4}\right)\mu\frac{u_e \mathrm{Re}^{1/2}}{d_c}=\frac{\pi b}{4}\cdot\frac{\mu^2}{\rho_e}\mathrm{Re}^{3/2}, \tag{7}$$

where γ_{sm} and γ_{se} are the surface tensions near the melting boundary and far from it, respectively, b is a constant, and μ is the dynamic viscosity of the molten mass. Substituting $\mathrm{Re}^{1/2}$ derived from equation (7) into equation (5), the following equation is obtained

$$G=\frac{a}{\mathrm{Pr}b^{1/3}}\left\{\frac{4\mu(\gamma_{sm}-\gamma_{se})}{\rho_e^2 d_c^2}\right\}^{1/3} \tag{8}$$

Since dependence of V on d_c is mainly attributable to that of G on d_c, V is found to be approximately proportional to $d_c^{-2/3}$. This result agrees fairly well with experimental results [2–5]. The effects of viscosity and surface tension can also be inferred from equation (8).

References

1 Hirano, T., Sato, K., Sato, Y., and Sato, J., "Prediction of Metal Fire Spread in High Pressure Oxygen," *Combustion Science and Technology*, Vol. 32, 1983, pp. 137–159.

2 Hirano, T., Sato, Y., Sato, K., and Sato, J., "The Rate Determining Process of Iron Oxidation at Combustion in High Pressure Oxygen," *Oxidation Communications*, Vol. 6, 1984, pp. 113–124.

3 Sato, K., Sato, Y., Tsuno, T., Nakamura, Y., Hirano, T., and Sato, J., "Metal Combustion in High Pressure Oxygen Atmosphere," *Proceedings of the 15th International Congress on High Speed Photography/Photonics*, 1983, pp. 828–832.

4 Sato, J., Sato, K., and Hirano, T., "Fire Spread Mechanisms Along Steel Cylinders in High Pressure Oxygen," *Combustion and Flame*, Vol. 51, 1983, pp. 279–287.

5 Sato, K., Hirano, T., and Sato, J., "Behavior of Fires Spreading Over Structural Metal Pieces in High Pressure Oxygen," *ASME-JSME Thermal Engineering Joint Conference Proceedings*, Vol. 4, 1983, pp. 311–316.

6 Schlichting, H., *Boundary Layer Theory*, 6th ed., translated by J. Kestin, McGraw-Hill, New York, 1968.

7 Grosse, A. V., and Conway, J. B., "Combustion of Metals in Oxygen," *Industrial and Engineering Chemistry*, Vol. 50, 1958, pp. 663–672.

8 Wolfhard, H. G., and Parker, W. G., "Temperature Measurements of Flames Containing Incandescent Particles," *Proc. Phys. Soc. (London)*, Vol. 62B, 1949, pp. 523–529.

9 Cueilleron, J., and Scartazzini, H., "Combustion de l'aluminum dans l'oxygène," *Compt. Rend.*, Vol. 228, 1949, pp. 489–490.

10 Torrance, K. E., and Mahajan, R. L., "Surface Tension Flows Induced by a Moving Thermal Source," *Combustion Science and Technology*, Vol. 10, 1975, pp. 125–136.

Natural Convection of a Radiating Fluid in a Vertical Layer

G. Desrayaud[1] and G. Lauriat[1]

Nomenclature

a = thermal diffusivity
A = aspect ratio (height/width)
D = width $= 2d$
g = acceleration of gravity
n = index of refraction
N = conduction-to-radiation parameter $= \alpha_m \lambda/n^2\,\sigma\,T_m^3$
p = pressure
q_r = radiative heat flux
Ra = Rayleigh number based on $D = g\,\beta\,\Delta T\,D^3/a\nu$
T = temperature
T_m = mean temperature
V = velocity vector
w = z component of the velocity
x,z = coordinates
α_m = mean extinction coefficient
β = coefficient of thermal expansion
γ = vertical temperature gradient $= \frac{1}{2}\frac{\partial\theta}{\partial z}$
ΔT = temperature difference between the side walls
ϵ_i = emissivity of wall i, $i = 1, 2$ at $x = -1, +1$
η = nongrayness factor
λ = thermal conductivity
λ_i = $\epsilon_i/2\,(2-\epsilon_i)$
ν = kinematic viscosity
θ = dimensionless temperature $= T/\Delta T$
θ_m = dimensionless mean temperature $= T_m/\Delta T$
τ_o = optical thickness $= \alpha_m D$

Superscript

$'$ = dimensional quantities

Introduction

The purposes of this note are to assess the validity of a one-dimensional formulation for modeling the interaction of natural convection with radiation in a vertical layer of a participating medium and to show the applicability of a spectral method for solving the governing equations. Indeed, in the perspective of studying the stability of the flow in the various regimes, the first requirement is to find a realistic base flow solution.

In previous works [1, 2], the stability of the conduction regime has been investigated in detail. For this regime, a rather simple base flow solution can be obtained analytically if the radiation part of the problem is linearized. However, it has been shown in recent numerical studies on the interaction in cavities with large but finite aspect ratios [3, 4] that the effects of radiation differ according to the flow regimes. In particular, the flow rate is reduced at low Grashof numbers for fluids having moderate Prandtl numbers and, on the other hand, increased for Grashof numbers greater than a certain value which depends on the extent of the interaction. Consequently, the onset of shear driven instabilities is delayed in the conduction regime while it occurs at lower Grashof numbers for vertical stratifications corresponding to the transition regime. Moreover, a significant loss of the centrosymmetry property, which is characteristic of the nonradiating case, is accomplished for asymmetric radiative boundary conditions and in the convection regime.

From these results, it appears that a base flow solution has to be obtained without using the assumptions of a zero vertical stratification and of the centrosymmetry property. In the present note, a high-order approximate solution for the basic state which verifies qualitatively and quantitatively the abovementioned features of the interaction is developed.

Formulation of the Problem

Consider a free convection flow of a radiating fluid contained in a vertical channel of width $2d$ with the lateral sides being opaque, gray, diffuse, and maintained at different temperatures. The axes z' and x' are chosen to be along and

[1]Laboratoire de Thermique, CNAM, Paris, France

Contributed by the Heat Transfer Division for publication in the JOURNAL OF HEAT TRANSFER. Manuscript received by the Heat Transfer Division January 5, 1984.

surface B. Thus, the increase of V implies the increase of the injection velocity, which makes $(\partial T/\partial x)_{ml}$ smaller than that without injection [6], i.e., $(\partial T/\partial x)_{ml}$ established by using equation (2) is larger than that for a given value of V. The decrease of the dependence of V on H at a larger value of H or V is attributable to the variation of $(\partial T/\partial x)_{ml}$ with V.

As mentioned in the previous section, the molten mass movement is inferred to be induced by the surface tension difference due to the temperature difference near the liquid-solid phase boundary. Assuming a situation similar to that presented in [10], the following equation can be derived approximately

$$\pi d_c(\gamma_{sm}-\gamma_{se})=b\left(\frac{\pi d_c^2}{4}\right)\mu\frac{u_e \mathrm{Re}^{1/2}}{d_c}=\frac{\pi b}{4}\cdot\frac{\mu^2}{\rho_e}\mathrm{Re}^{3/2}, \tag{7}$$

where γ_{sm} and γ_{se} are the surface tensions near the melting boundary and far from it, respectively, b is a constant, and μ is the dynamic viscosity of the molten mass. Substituting $\mathrm{Re}^{1/2}$ derived from equation (7) into equation (5), the following equation is obtained

$$G=\frac{a}{\mathrm{Pr}b^{1/3}}\left\{\frac{4\mu(\gamma_{sm}-\gamma_{se})}{\rho_e^2 d_c^2}\right\}^{1/3} \tag{8}$$

Since dependence of V on d_c is mainly attributable to that of G on d_c, V is found to be approximately proportional to $d_c^{-2/3}$. This result agrees fairly well with experimental results [2–5]. The effects of viscosity and surface tension can also be inferred from equation (8).

References

1 Hirano, T., Sato, K., Sato, Y., and Sato, J., "Prediction of Metal Fire Spread in High Pressure Oxygen," *Combustion Science and Technology*, Vol. 32, 1983, pp. 137–159.

2 Hirano, T., Sato, Y., Sato, K., and Sato, J., "The Rate Determining Process of Iron Oxidation at Combustion in High Pressure Oxygen," *Oxidation Communications*, Vol. 6, 1984, pp. 113–124.

3 Sato, K., Sato, Y., Tsuno, T., Nakamura, Y., Hirano, T., and Sato, J., "Metal Combustion in High Pressure Oxygen Atmosphere," *Proceedings of the 15th International Congress on High Speed Photography/Photonics*, 1983, pp. 828–832.

4 Sato, J., Sato, K., and Hirano, T., "Fire Spread Mechanisms Along Steel Cylinders in High Pressure Oxygen," *Combustion and Flame*, Vol. 51, 1983, pp. 279–287.

5 Sato, K., Hirano, T., and Sato, J., "Behavior of Fires Spreading Over Structural Metal Pieces in High Pressure Oxygen," *ASME-JSME Thermal Engineering Joint Conference Proceedings*, Vol. 4, 1983, pp. 311–316.

6 Schlichting, H., *Boundary Layer Theory*, 6th ed., translated by J. Kestin, McGraw-Hill, New York, 1968.

7 Grosse, A. V., and Conway, J. B., "Combustion of Metals in Oxygen," *Industrial and Engineering Chemistry*, Vol. 50, 1958, pp. 663–672.

8 Wolfhard, H. G., and Parker, W. G., "Temperature Measurements of Flames Containing Incandescent Particles," *Proc. Phys. Soc. (London)*, Vol. 62B, 1949, pp. 523–529.

9 Cueilleron, J., and Scartazzini, H., "Combustion de l'aluminum dans l'oxygène," *Compt. Rend.*, Vol. 228, 1949, pp. 489–490.

10 Torrance, K. E., and Mahajan, R. L., "Surface Tension Flows Induced by a Moving Thermal Source," *Combustion Science and Technology*, Vol. 10, 1975, pp. 125–136.

Natural Convection of a Radiating Fluid in a Vertical Layer

G. Desrayaud[1] and G. Lauriat[1]

Nomenclature

a = thermal diffusivity
A = aspect ratio (height/width)
D = width $= 2d$
g = acceleration of gravity
n = index of refraction
N = conduction-to-radiation parameter $= \alpha_m \lambda/n^2\,\sigma\,T_m^3$
p = pressure
q_r = radiative heat flux
Ra = Rayleigh number based on $D = g\,\beta\,\Delta T\,D^3/a\nu$
T = temperature
T_m = mean temperature
V = velocity vector
w = z component of the velocity
x,z = coordinates
α_m = mean extinction coefficient
β = coefficient of thermal expansion
γ = vertical temperature gradient $= \frac{1}{2}\frac{\partial\theta}{\partial z}$
ΔT = temperature difference between the side walls
ϵ_i = emissivity of wall i, $i = 1, 2$ at $x = -1, +1$
η = nongrayness factor
λ = thermal conductivity
λ_i = $\epsilon_i/2\,(2-\epsilon_i)$
ν = kinematic viscosity
θ = dimensionless temperature $= T/\Delta T$
θ_m = dimensionless mean temperature $= T_m/\Delta T$
τ_o = optical thickness $= \alpha_m D$

Superscript

$'$ = dimensional quantities

Introduction

The purposes of this note are to assess the validity of a one-dimensional formulation for modeling the interaction of natural convection with radiation in a vertical layer of a participating medium and to show the applicability of a spectral method for solving the governing equations. Indeed, in the perspective of studying the stability of the flow in the various regimes, the first requirement is to find a realistic base flow solution.

In previous works [1, 2], the stability of the conduction regime has been investigated in detail. For this regime, a rather simple base flow solution can be obtained analytically if the radiation part of the problem is linearized. However, it has been shown in recent numerical studies on the interaction in cavities with large but finite aspect ratios [3, 4] that the effects of radiation differ according to the flow regimes. In particular, the flow rate is reduced at low Grashof numbers for fluids having moderate Prandtl numbers and, on the other hand, increased for Grashof numbers greater than a certain value which depends on the extent of the interaction. Consequently, the onset of shear driven instabilities is delayed in the conduction regime while it occurs at lower Grashof numbers for vertical stratifications corresponding to the transition regime. Moreover, a significant loss of the centrosymmetry property, which is characteristic of the nonradiating case, is accomplished for asymmetric radiative boundary conditions and in the convection regime.

From these results, it appears that a base flow solution has to be obtained without using the assumptions of a zero vertical stratification and of the centrosymmetry property. In the present note, a high-order approximate solution for the basic state which verifies qualitatively and quantitatively the abovementioned features of the interaction is developed.

Formulation of the Problem

Consider a free convection flow of a radiating fluid contained in a vertical channel of width $2d$ with the lateral sides being opaque, gray, diffuse, and maintained at different temperatures. The axes z' and x' are chosen to be along and

[1]Laboratoire de Thermique, CNAM, Paris, France

Contributed by the Heat Transfer Division for publication in the JOURNAL OF HEAT TRANSFER. Manuscript received by the Heat Transfer Division January 5, 1984.

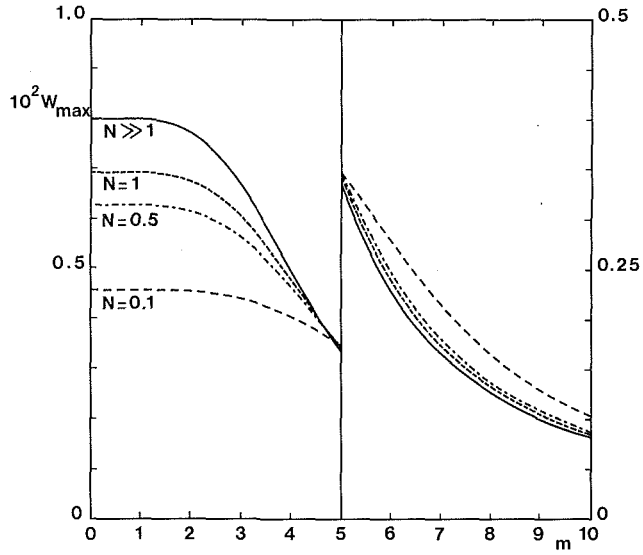

Fig. 1 Variations of the maximum flow velocity with the stratification parameter; $\tau_o = 1, \eta = 1, \epsilon_1 = \epsilon_2 = 1$

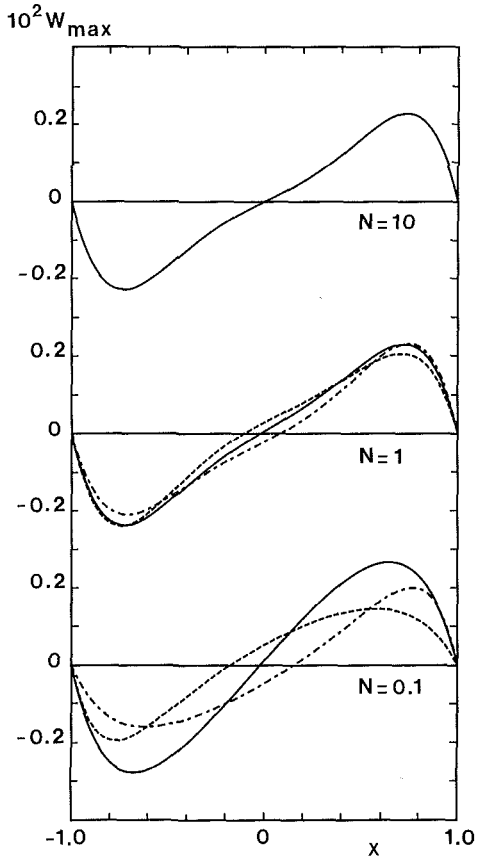

Fig. 2 Vertical velocity profiles for $m = 6$; $\tau_o = 1, \eta = 1$, —$\epsilon_1 = \epsilon_2 = 1$; . . . $\epsilon_1 = 0, \epsilon_2 = 1$; ---$\epsilon_1 = 1, \epsilon_2 = 0$

normal to the plates ($-d \le x' \le +d$; $-\infty < z' < +\infty$). Using the classical assumptions for the convective part of the problem (Boussinesq approximation, constant properties of the fluid) the equations governing the motion of the fluid may be obtained from the one-dimensional form of the general formulation by setting

$$p = p(z') \tag{1}$$

$$V = (0, 0, w'(x')) \tag{2}$$

$$T(x', z') = T(x') + \gamma' z' \tag{3}$$

where γ' is the vertical temperature gradient.

Choosing as in [5] the set $[d, g\beta\Delta T d^2/\nu, \Delta T, \mu/\rho_m g\beta\Delta T d, n^2\sigma T_m^3 \Delta T]$ as scales for length, velocity, temperature, time, and radiative flux respectively, the nondimensional governing equations can be cast in the form

$$\frac{d^3 w(x)}{dx^3} + \frac{d\theta(x)}{dx} = 0 \tag{4}$$

$$\frac{m^4}{4} w(x) - \frac{d^2\theta(x)}{dx^2} + \frac{\tau_o}{2N} \frac{dq_r(x)}{dx} = 0 \tag{5}$$

$$\frac{d^2 q_r(x)}{dx^2} - \frac{3\tau_0^2}{4} q_r(x) - \frac{2\tau_o \eta}{\theta_m^3} \frac{d\theta^4(x)}{dx} = 0 \tag{6}$$

where m is the stratification parameter defined by $m = (1/4\ \mathrm{Ra}\gamma)^{0.25}$. The boundary conditions are

$$w(\pm 1) = 0 \tag{7}$$

$$\theta(\pm 1) = \theta_m \pm 0.5 \tag{8}$$

$$q_r(\pm 1) \pm \frac{2\lambda_i}{\eta\tau_o} \frac{dq_r(\pm 1)}{dx} = 0 \tag{9}$$

In these equations, the pressure has been eliminated by deriving the equation of motion. Consequently, a supplementary condition must be used to insure the closure of the system. In order not to enforce the velocity to be zero at $x = 0$, the third condition applied to the equation of motion is deduced from a mass-flux integral over any cross section

$$\int_{-1}^{+1} w(x)\, dx = 0 \tag{10}$$

The radiation part is solved by the P-1 approximation in order to make quantitative comparisons possible. However, it should be noted that the solution procedure described next allows the transfer equations corresponding to higher approximations (P-3 or P-5) to be solved readily.

Numerical Method

The system of equations (4–10) is solved by the spectral tau method with Chebyshev polynomials used as expansion functions. The solution is then assumed to be expanded as

$$g(x) = \sum_{n=0}^{\infty} g_n T_n(x) \tag{11}$$

where $g(x)$ stands for $w(x)$, $\theta(x)$, and $q_r(x)$. Truncating each of the series to N terms and requiring the residuals to be orthogonal to each expansion function with the usual weight leads to a nonlinear system for the expansion coefficients. Following Gottlieb and Orszag [6], this system can be written as

$$\left.\begin{aligned} & w_n^{(3)} + \theta_n^{(1)} = 0 \\ & \frac{m^4}{4} w_n - \theta_n^{(2)} + \frac{\tau_o}{2N} q_n^{(1)} = 0 \\ & q_n^{(2)} - \frac{3\tau_0^2}{4} q_n - \frac{8\tau_o\eta}{\theta_m^3} \theta_n^3 \theta_n^{(1)} = 0 \end{aligned}\right\} \quad 0 \le n \le N\text{-}2 \tag{12}$$

The expressions of the coefficients $g_n^{(k)}$ are given in [6]. Since the expansion functions don't satisfy the boundary conditions, the system is completed by the following conditions

$$\begin{aligned} & \sum_{n=0}^{N} w_n = 0, \qquad \sum_{n=0}^{N} (-1)^n w_n = 0 \\ & \sum_{n=0}^{N} \theta_n = \theta_m + 0.5, \qquad \sum_{n=0}^{N} (-1)^n \theta_n = \theta_m - 0.5 \\ & \sum_{n=0}^{N} q_n (\pm 1)^n \pm \sum_{n=0}^{N} n^2 q_n (\pm 1)^{n-1} \frac{2\lambda_i}{\eta\tau_o} = 0 \end{aligned} \tag{13}$$

Condition (10) gives $w_o = 0$.

Table 1 Comparisons of the numerical solutions in conduction and boundary layer regimes ($A = 10$, $N = 1$, $\eta = 1$, $\tau_0 = 1$, $\epsilon_1 = \epsilon_2 = 1$); s: spectral solutions; *f.d*: 2-*D* finite difference solutions

-0.50	-0.181	-0.181	-0.666	-0.662	2.62	2.62
-0.40	-0.132	-0.132	-0.587	-0.585	2.69	2.69
-0.30	-0.087	-0.087	-0.468	-0.468	2.74	2.74
-0.20	-0.045	-0.044	-0.320	-0.322	2.79	2.79
-0.10	-0.004	-0.004	-0.154	-0.157	2.82	2.82
0.00	0.035	0.036	0.019	0.016	2.84	2.84
0.10	0.074	0.075	0.191	0.186	2.85	2.85
0.20	0.112	0.113	0.352	0.346	2.85	2.85
0.30	0.151	0.152	0.491	0.483	2.84	2.84
0.40	0.191	0.191	0.599	0.590	2.81	2.81
0.50	0.232	0.233	0.666	0.656	2.77	2.77
0.60	0.276	0.276	0.682	0.671	2.71	2.71
0.70	0.323	0.324	0.636	0.623	2.63	2.63
0.80	0.375	0.375	0.516	0.502	2.52	2.52
0.90	0.433	0.434	0.309	0.311	2.38	2.37
1.00	0.500	0.500	0.000	0.000	2.19	2.21

Ra = 2500; m = 0.754

X	$\Theta - \Theta_m$		W		q_r	
	s	f.d	s	f.d	s	f.d
-1.00	-0.500	-0.500	0.000	0.000	2.09	2.13
-0.90	-0.348	-0.358	-0.170	-0.184	2.26	2.27
-0.80	-0.220	-0.230	-0.247	-0.247	2.36	2.38
-0.70	-0.121	-0.125	-0.263	-0.262	2.39	2.42
-0.60	-0.051	-0.049	-0.243	-0.238	2.38	2.41
-0.50	-0.004	0.000	-0.204	-0.197	2.35	2.38
-0.40	0.022	0.028	-0.158	-0.151	2.30	2.33
-0.30	0.034	0.039	-0.112	-0.107	2.26	2.28
-0.20	0.036	0.041	-0.069	-0.066	2.22	2.25
-0.10	0.031	0.036	-0.029	-0.029	2.21	2.23
0.00	0.024	0.029	0.008	0.006	2.21	2.24
0.10	0.017	0.022	0.045	0.041	2.24	2.26
0.20	0.013	0.018	0.083	0.077	2.29	2.31
0.30	0.014	0.019	0.124	0.116	2.36	2.38
0.40	0.025	0.030	0.165	0.158	2.44	2.46
0.50	0.050	0.056	0.206	0.199	2.53	2.54
0.60	0.092	0.101	0.240	0.235	2.61	2.62
0.70	0.156	0.170	0.255	0.252	2.66	2.66
0.80	0.246	0.264	0.236	0.232	2.67	2.65
0.90	0.362	0.376	0.161	0.168	2.59	2.57
1.00	0.500	0.500	0.000	0.000	2.42	2.44

Ra = 10^5; m = 5.718

The computations were performed in double precision on a VAX 780 computer. For all the cases presented in this paper, the convergence of the tau method was achieved with an absolute precision better than $\epsilon = 10^{-6}$ by retaining a number of terms in the expansions less than $N = 20$. The nonlinear system was solved iteratively until the changes in the expansion coefficients became small enough to satisfy the convergence criterion

$$\max[(w_n,\theta_n,q_n)^{k+1} - (w_n,\theta_n,q_n)^k] \leqq 10^{-9}$$

At this point, it should be noted that to formulate the radiation part in function of the flux instead of the incident radiation allows to divide the number of iterations approximately by four.

Results

The maximum velocities are shown in Fig. 1 for values of the stratification parameter ranging from the conduction regime to the boundary layer regime. The end of the plateau indicates the end of the conduction regime and the boundary layer regime begins at $m \cong 5$ in a nonradiating fluid (it should be noted here that using the scale factors of the stability analyses yields higher dimensionless velocities for low m values). For radiating fluids contained in channels with black sides, the maximum velocities (in absolute values) are located within the cold side and the dashed lines give their variations with m. It may be observed that these curves intersect the one connected to a nonradiating fluid within the transition regime. This result agrees with the numerical solution displayed previously [3]. The velocity profiles in the boundary layer regime are shown in Fig. 2 for various values of the interaction parameter N. The increase of velocities and the loss of the centrosymmetry property mentioned before are also obtained. These effects are accomplished with a reversal in the horizontal temperature gradient at $x = 0$ as pointed out in [3, 4].

For quantitative comparisons with the numerical results, the following precautions must be taken. First, the aspect ratio of the cavity must be sufficient so that the flow in the central part should satisfy the basic assumptions of a one-dimensional formulation, namely, the temperature varies linearly with altitude, the fluid circulates only along the isothermal sides, and the vertical component of the radiative flux is small enough in regard to the horizontal component. A detailed examination of the 2-*D* numerical solutions shows that these conditions can be encountered when the aspect ratio of the cavity is greater than $A = 8$ regardless of the optical thickness and interaction parameter in the range $0.5 \leqq \tau_o \leqq 4$ and $0.1 \leqq N \leqq \infty$. Secondly, comparisons are not always feasible since the flow may become unstable by increasing the aspect ratio and the radiation effect [3]. From a numerical point of view, that means that convergence of the computational method is highly difficult to achieve. In particular, the vertical temperature gradient at cavity midpoint oscillates within a large range and no accurate value of m can be obtained from the numerical modeling. Consequently, quantitative comparisons must be restricted to weak or moderate interactions at any Ra values with $8 \leqq A \leqq 10$ or to stronger interactions in the stable conduction and boundary layer regimes.

Selected results are displayed in Table 1 for the three field variables (θ, w, q_r). The stratification parameters were obtained by solving the 2-*D* conservation equations by a finite difference method on a 101×21 uniform grid system and the convergence was achieved with four significant figures for the temperature gradient at cavity midpoint. It can be seen that the two models agree well quantitatively and it was found that the match between the two solutions is within 10 percent in the range covered by numerical simulations.

In summary, this paper has outlined a high-order approximate solution for the interaction of natural convection with radiation in a vertical fluid layer. This solution has been found in agreement with numerical results presented previously [3] and it is believed that it can be used to depict the basic state in a stability analysis of flows of radiating fluids. Lastly, the power of the spectral methods with Chebyshev polynomials for solving problems with sharp boundary gradients and for finding the base flow solution of a stability problem is emphasized.

References

1 Arpaci, V. S., and Bayazitoğlu, Y., "Thermal Stability of Radiating Fluids: Asymmetric Slot Problem," *Phys. of Fluids*, Vol. 16, 1973, pp. 589-593.

2 Hassab, M. A., and Özisik, M. N., "Effects of Radiation and Convective Boundary Conditions on the Stability of Fluid in an Inclined Slender Slot," *Int. J. Heat Mass Trans.*, Vol. 22, 1979, pp. 1095-1105.

3 Lauriat, G., "Combined Radiation-Convection in Gray Fluids Enclosed in Vertical Cavities," ASME JOURNAL OF HEAT TRANSFER, Vol. 104, 1982, pp. 609-615.

4 Lauriat, G., "Numerical Study of the Interaction of Natural Convection With Radiation in Nongray Gases in Narrow Vertical Cavity," *Proceedings of the 7th International Heat Transfer Conference*, Vol. 2, Paper No. NC 6, 1982, pp. 153-158.

5 Bergholz, R. F., "Instability of Steady Natural Convection in a Vertical Fluid Layer," *Journal of Fluid Mechanics*, Vol. 84, Part 4, 1978, pp. 743-768.

6 Gottlieb, D., and Orszag, S. A., "Numerical Analysis Spectral Methods: Theory and Applications," CBMS-NSF, Conf. Series in Applied Mathematics, 1977.

Analytical Solution for the Heat Transfer Problem of Fluid Flowing Through a Packed Bed of Porous Solids

I. Toovey[1] and J. Dayan[1]

Nomenclature

c, c_f = specific heat of solid and fluid phases, J/kgK
h, h_f = exit and entrance heat transfer coefficients respectively, W/m^{2}K
h_v = effective volumetric heat transfer coefficient between the two phases in the bed, W/m^{3}K
H_1 = $h_f G c_f / k h_v$, nondimensional heat transfer coefficient at the entrance
H_2 = $h G c_f / k h_v$, nondimensional exit heat transfer coefficient
k = thermal conductivity of solid phase, W/mK
K_s = $k h_v / (G c_f)^2$, nondimensional solid phase conductivity
K_1 = $-K_s H_1$
L = length of the packed bed in the flow direction, m
L' = $h_v L / G c_f$, nondimensional length
T = $(T_f - T_i)/(T_{fo} - T_i)$, nondimensional fluid phase temperature
T_f, T_s = fluid and solid phases temperature respectively, K
T_{fo} = oncoming fluid phase temperature, K
T_i = initial temperature, K
t = $h_v \alpha \tau / k$, nondimensional time
x = $h_v z / G c_f$, nondimensional distance from the fluid entry surface
z = distance from fluid-entry surface, m
α = $k/\rho c$, thermal diffusivity of solid phase, m^2/s
α_n = $K_s \beta_n^2$
β_n = eigenvalue found by equation (25)
θ = $(T_s - T_i)/(T_{fo} - T_i)$, nondimensional solid phase temperature
ρ = solid phase density, kg/m^3
τ = time, s

Subscripts

ss = steady state
t = transient

Introduction

An analytical solution is presented for the problem of transient distribution of temperatures in a porous bed through which a fluid, subjected to a temperature step change at the inlet, is flowing. Neglecting the fluid's heat capacity and conductivity while retaining those of the bed's solid material leads to a third-order system having two coupled partial differential equations with interacting boundary conditions at the fluid inlet. The method of solution is based on applying the Green function in a straightforward manner. The system of coupled partial differential equations yields an infinite number of Volterra-type integral equations which are solved by successive integration. The mathematical solution characteristics are analyzed, and a comparison of the present analytical solution to a finite-difference solution is made.

Previous analytical solutions [1-3] have neglected the axial conductivities of both solid and fluid phases. Several numerical solutions that retain the axial conductivity in the solid were also proposed [4-6]. Burch et al. [6] have discussed the applicability of their model, its boundary conditions, and the various associated heat transfer coefficients. A similar problem has been solved for several asymptotic cases employing the perturbation technique [7].

Analysis

Consider the system of a packed bed or a porous medium through which a fluid (gas) is flowing. The system is of length L in the direction of flow and infinite in all other directions. Initially, both solid and fluid are at equilibrium and at constant temperature anywhere in the bed. At time zero the fluid is subjected to a step change in the temperature of the oncoming stream. Due to strong heat interaction between solid and fluid at the entrance to the system, both solid and fluid temperatures at the inlet surface will be affected and changed with time. It is assumed, though, that the outlet end of the system remains at the initial temperature throughout the period studied (infinite heat reservoir). The abovementioned system can be represented by the following set of the nondimensional equations, provided the heat accumulation term and longitudinal conductivity term in the fluid are neglected [6, 7].

$$\frac{\partial T}{\partial x} = \theta - T,\ 0 < x < L',\ t > 0 \tag{1}$$

$$\frac{\partial \theta}{\partial t} = T - \theta + K_s \frac{\partial^2 \theta}{\partial x^2},\ 0 < x < L',\ t > 0 \tag{2}$$

I.C: $t = 0:\ \theta = 0,\ 0 \leqq x \leqq L'$ (3)

B.C's: $x = 0:\ T + K_1 \theta = 1 + K_1,\ t > 0$ (4)

$$x = 0:\ -\frac{\partial \theta}{\partial x} + H_1 \theta = H_1,\ t > 0 \tag{5}$$

$$x = L':\ \frac{\partial \theta}{\partial x} + H_2 \theta = 0,\ t > 0 \tag{6}$$

Equations (1-6) represent a third-order system, whose steady-state solution is known [6].

The transient response, equations (7-12), and its homogeneous boundary conditions are obtainable by substituting $\theta = \theta_{ss} - \theta_t$ and $T = T_{ss} - T_t$ into equations (1-6)

$$\frac{\partial T_t}{\partial x} = \theta_t - T_t,\ 0 < x < L',\ t > 0 \tag{7}$$

$$\frac{\partial \theta_t}{\partial t} = T_t - \theta_t + K_s \frac{\partial^2 \theta_t}{\partial x^2},\ 0 < x < L',\ t > 0 \tag{8}$$

I.C.: $t = 0:\ \theta_t = \theta_{ss}(x),\ 0 \leqq x \leqq L'$ (9)

B.C.'s: $x = 0:\ T_t + K_1 \theta_t = 0,\ t > 0$ (10)

$$x = 0:\ -\frac{\partial \theta_t}{\partial x} + H_1 \theta_t = 0,\ t > 0 \tag{11}$$

$$x = L':\ \frac{\partial \theta_t}{\partial x} + H_2 \theta_t = 0,\ t > 0 \tag{12}$$

Introducing

$$T_t = u \exp[-x] \text{ and } \theta_t = v \exp[-t] \tag{13}$$

into equations (7-12), the transformed system obtained is

$$\frac{\partial u}{\partial x} = e^x \theta_t,\ 0 < x < L',\ t > 0 \tag{14}$$

$$\frac{\partial v}{\partial t} = K_s \frac{\partial^2 v}{\partial x^2} + u e^t e^{-x},\ 0 < x < L',\ t > 0 \tag{15}$$

I.C.: $t = 0:\ v = \theta_{ss}(x),\ 0 \leqq x \leqq L'$ (16)

B.C.'s: $x = 0:\ u + K_1 \theta_t = 0,\ t > 0$ (17)

$$x = 0:\ -\frac{\partial v}{\partial x} + H_1 v = 0,\ t > 0 \tag{18}$$

[1]Faculty of Mechanical Engineering, Technion—Israel Institute of Technology, Haifa, Israel

Contributed by the Heat Transfer Division for publication in the JOURNAL OF HEAT TRANSFER. Manuscript received by the Heat Transfer Division July 18, 1983.

$$x=L': \quad \frac{\partial v}{\partial x}+H_2 v=0, \; t>0 \tag{19}$$

Each of the equations (14) and (15) consists of derivatives of one of the temperatures and a nonderivative term of the other. The latter can be considered as the forcing term in the equation, i.e., an unknown nonhomogeneity. (For convenience, the transient solid temperature θ_f in the fluid equations (14) and (17) has been left untransformed.)

The solution for the transformed solid temperature (transient) v is built around the Green function kernel [8-9]

$$v=\int_0^{L'} G(x,t;x',\tau)\,|_{\tau=0}\theta_{ss}(x')dx' + \int_0^{t} d\tau \int_0^{L'} G(x,t;x',\tau)e^{\tau}e^{-x'}u(x',\tau)dx' \tag{20}$$

where $G(x,t;x',\tau)$ is a Green function related to the solid, needed for the solution of the system (14-19), and is given by

$$G(x,t;x',\tau)=\sum_{n=1}^{\infty} e^{-\alpha_n(t-\tau)}Z_n(x)Z_n(x') \tag{21}$$

$Z_n(x)$ is an orthonormal eigenfunction satisfying equation (22) and defined by equation (23) [10]

$$\int_0^{L'} Z_n(x')Z_m(x')dx'=\begin{cases}1 & \text{for } m=n\\ 0 & \text{for } m\neq n\end{cases} \tag{22}$$

$$Z_n(x)=a_n\cos\beta_n x+b_n\sin\beta_n x \tag{23}$$

where

$$a_n=\frac{\sqrt{2}\,\beta_n}{\left[(\beta_n^2+H_1^2)\left(L'+\dfrac{H_2}{\beta_n^2+H_2^2}\right)+H_1\right]^{1/2}};$$

$$b_n=\frac{\sqrt{2}\,H_1}{\left[(\beta_n^2+H_1^2)\left(L'+\dfrac{H_2}{\beta_n^2+H_2^2}\right)+H_1\right]^{1/2}} \tag{24}$$

The eigenvalues are the positive roots of

$$\tan\beta_n L'=\frac{\beta_n(H_1+H_2)}{\beta_n^2-H_1H_2} \tag{25}$$

Thus, equation (20) consists of series of integrals. It can be shown that the integrands in these series are uniformly convergent. Thus, the order of summation and integration can be exchanged, and the integration can be carried out term by term [11].

The transient solid temperature can be derived from equations (13) and (20)

$$\theta_f=\sum_{n=1}^{\infty}K_{1n}Z_n(x)\left[e^{-(1+\alpha_n)t} + \frac{1}{K_{1n}}\int_0^{t} d\tau e^{-(1+\alpha_n)(t-\tau)}\int_0^{L'}u(x',\tau)e^{-x'}Z_n(x')dx'\right] \tag{26}$$

where $K_{1n}=\int_0^{L'}\theta_{ss}(x')Z_n(x')dx'$; K_{1n} is a Fourier constant for $\theta_{ss}(x)$, i.e.,

$$\theta_{ss}(x)=\sum_{n=1}^{\infty}K_{1n}Z_n(x) \tag{27}$$

The integrand u in equation (26) is not known but the bounds of the integration are known constants, so that θ_f has the following form

$$\theta_f=\sum_{n=1}^{\infty}K_{1n}Z_n(x)F_n(t) \tag{28}$$

where

$$F_n(t)=e^{-(1+\alpha_n)t} + \frac{1}{K_{1n}}\int_0^{t}e^{-(1+\alpha_n)(t-\tau)}d\tau\int_0^{L'}u(x',\tau)e^{-x'}Z_n(x')dx' \tag{29}$$

Integrating equation (14) yields

$$u=\sum_{n=1}^{\infty}K_{1n}f_n(x)F_n(t)+C(t) \tag{30}$$

with

$$f_n(x)=\int^{x}e^{x'}Z_n(x')dx' = e^{x}\left[\frac{(a_n-b_n\beta_n)\cos\beta_n x+(a_n\beta_n+b_n)\sin\beta_n x}{1+\beta_n^2}\right] \tag{31}$$

The function $C(t)$ in equation (30) results from indefinite integration with respect to x', and is dependent on the boundary condition at the system inlet.

Substitution of the inlet boundary condition, equation (17), in equation (30) results in a two-dimensional integral equation of the Fredholm-Volterra type:

$$u=\sum_{n=1}^{\infty}K_{1n}[f_n(x)-f_n(0)-K_1Z_n(0)]F_n(t) \tag{32}$$

Repeated substitution of equation (32) and (29) yields the common convolution-type integral

$$F_n(t)=e^{-(1+\alpha_n)t}+\sum_{m=1}^{\infty}c_{nm}\int_0^{t}e^{-(1+\alpha_n)(t-\tau)}F_m(\tau)\,d\tau \tag{33}$$

where

$$c_{nm}=\frac{K_{1m}}{K_{1n}}\int_0^{L'}[f_m(x')-f_m(0)-K_1Z_m(0)]e^{-x'}Z_n(x')dx' \tag{34}$$

The integrals representing c_{nm} in equation (34) consist of integrals of orthogonal eigenfunction products such as equation (22). It is therefore necessary to employ the orthogonality property, equation (22), and look into two separate cases of c_{nm} before the integration, in order to avoid a zero in the denominator

$$c_{nm}=\begin{cases}\dfrac{K_{1m}}{K_{1n}}\{I_{nm}-[f_m(0)+K_1Z_m(0)]K_{3n}\} & \text{for } m\neq n\\ K_{2n}-[f_n(0)+K_1Z_n(0)]K_{3n} & \text{for } m=n\end{cases} \tag{35}$$

where

$$I_{nm}=\int_0^{L'}Z_n(x')e^{-x'}f_m(x')dx'$$

$$K_{2n}=\int_0^{L'}Z_n(x')e^{-x'}f_n(x')dx' \qquad K_{3n}=\int_0^{L'}Z_n(x')e^{-x'}dx' \tag{36}$$

Equation (33) is a system of infinite number of one-dimensional, coupled, integral equations of the Volterra type, where $F_n(t)$ ($n = 1, 2, \ldots, \infty$) are the unknowns. The general form of $F_n(t)$ is given by

$$F_n(t)=\phi_n(t)+\lambda\sum_{m=1}^{\infty}\int_0^{t}K_{n,m}(t,\tau)F_m(\tau)\,d\tau \tag{37}$$

where $K_{n,m}(t,\tau)=c_{nm}\exp[-(1+\alpha_n)(t-\tau)]$ and $\phi_n(t)=\exp[-(1+\alpha_n)t]$. The method of solution is based on Neumann's series (successive integrations), which is convergent for each λ (for this particular case $\lambda = 1$). The solution for a finite n coupled integral equations [12] can be adapted for the infinite system of equation (33), where

$$F_n(t)=\phi_n(t)+\sum_{p=1}^{\infty}\lambda^p\psi_{n,p}(t) \tag{38}$$

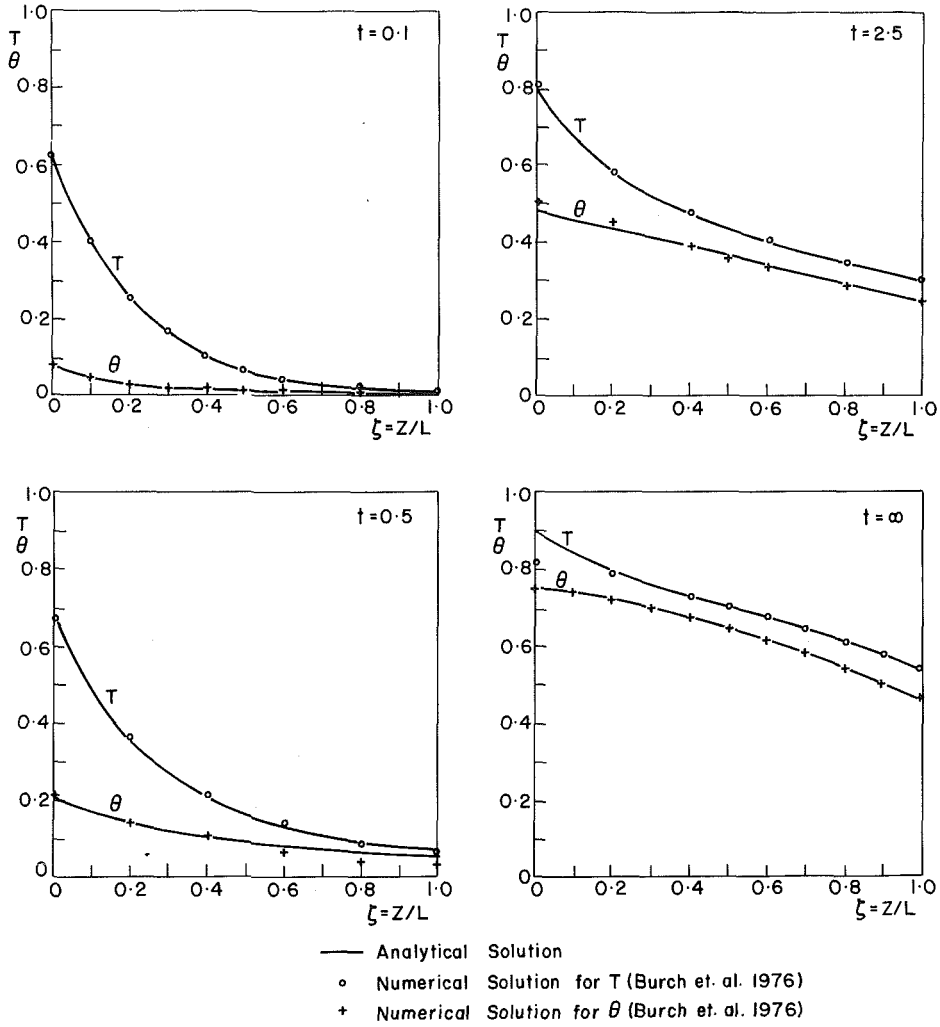

Fig. 1 Comparison of analytic solutions with numerical solutions (finite difference), $H_1 = 0.08$, $H_2 = 0.2$, $K_s = 5$, $L' = 5$ (the corresponding parameters of Burch et al. [6] are $S_t = 0.4$, $H = 1$, $g = 1$, $B = 5$)

Evaluation of the $\psi_{n,p}$ terms can be done by substituting (38) into (33), integrating term by term and equating the coefficients of common powers of λ to zero. Its general form is

$$\psi_{n,p}(t) = \sum_{m=1}^{\infty} \int_0^t K_{n,m}(t,\tau)\psi_{m,p-1}(\tau)\,d\tau \tag{39}$$

Performing the integration of (39), substituting in (38), and rearranging yields

$$F_n(t) = \underbrace{e^{-(1+\alpha_n - c_{nm})t}}_{m=n} + \underbrace{\sum_{m=1}^{\infty} c_{nm} \frac{e^{-(1+\alpha_m)t} - e^{-(1+\alpha_n)t}}{\alpha_n - \alpha_m}}_{m\neq n} + \tag{40}$$

$$+ \underbrace{\sum_{m=1}^{\infty}\sum_{j=1}^{\infty} \frac{c_{nm}c_{mj}}{\alpha_m - \alpha_j}\left[\frac{e^{-(1+\alpha_j)t} - e^{-(1+\alpha_n)t}}{\alpha_n - \alpha_j} + \frac{e^{-(1+\alpha_n)t} - e^{-(1+\alpha_m)t}}{\alpha_n - \alpha_m}\right]}_{m\neq n\neq j} + \ldots$$

Equations (28) and (32) call for summation of an infinite number of terms according to n. However, $F_n(t)$ in these equations is in itself a summation of an infinite number of terms according to m (equation (40)). This is analogous to summing all the terms in an $n \times m$ matrix. All the terms of this matrix (see equation (40)) resulting from Neumann's series contain differences between exponents, except for the main diagonal ($n = m$) terms. Thus, an excellent accuracy for both long and short values of t is obtained by neglecting all of these difference terms ($n \neq m$) and summing only the main diagonal terms. It is surprising that a solution which is based on presentation suitable for long t values is successful for short t as well. It should be noticed, though, that the abovementioned differences of exponent terms are indeed quite small, and thus negligible for these two ranges of t. It is not always negligible for intermediate values of t. However, the number of main diagonal terms which has to be summed for short t values is of course much higher than that for long t.

From (28) and (32), the expressions for the temperatures of the fluid and the solids can be derived. These are:

$$T = T_{ss} - e^{-x}\sum_{n=1}^{\infty} K_{1n}[f_n(x) - f_n(0) - K_1 Z_n(0)]F_n(t) \tag{41}$$

$$\theta = \theta_{ss} - \sum_{n=1}^{\infty} K_{1n} Z_n(x) F_n(t) \tag{42}$$

Results and Discussion

The temperature distribution in both fluid and solid due to step change in the oncoming fluid temperature has been calculated according to equations (41) and (42). The present results are compared with the numerical solution of Burch et al. [6].

Figure 1 shows the temperature distributions T and θ as functions of the normalized location for four different times.

For the shortest time $t = 0.1$ the numerical solution [6] is everywhere identical with the presented analytical solution. For intermediate times ($t = 0.5$–2.5) the agreement is fairly good, and the largest deviation (for the solid temperature) is about 2 percent. For infinite time, the solutions are identical, except for large deviation at the fluid entrance temperature resulting from a probable error in [6]. For the shortest time of $t = 0.1$ (long enough to permit summation of a small number of terms in the series) only ten ($n = 10$) terms were needed. For longer times, the number of terms was even smaller.

In summary, the solution presented is a direct analytical solution based on Green functions and suitable for third-order systems.

In general, the method is suitable for solving higher-order partial differential equations, resulting from coupled phenomena such as heat interaction or diffusion between several phases, with or without sources.

References

1 Schumann, T. E. W., "Heat Transfer: Liquid Flowing Through a Porous Prism," *J. Franklin Inst.*, Vol. 208, 1929, pp. 405–416.

2 Smith, E. M., "General Integral Solution of the Regenerator Transient Test Equations for Zero Longitudinal Conduction," *Int. J. Heat and Fluid Flow*, Vol. 1, No. 2, 1979, pp. 71–75.

3 Spiga, G., and Spiga, M., "A Rigorous Solution to a Heat Transfer Two Phase Model in Porous Media and Packed Beds," *Int. J. Heat Mass Transfer*, Vol. 24, 1981, pp. 355–364.

4 Senshu, T., Hatada, T., and Ishibane, K., "Surface Heat Transfer Coefficients of Fins Used in Air-Cooled Heat Exchangers," *Heat Transfer Japanese Research*, Vol. 8, No. 4, 1979, pp. 16–26.

5 Creswick, F. A., "A Digital Computer Solution of the Equations for Transient Heating of Porous Solid Including the Effects of Longitudinal Conduction," *Industrial Mathematics*, 1957, pp. 61–69.

6 Burch, D. M., Allen, R. W., and Peavy, B. A., "Transient Temperature Distribution Within Porous Slabs Subjected to Sudden Tranpiration Heating," ASME JOURNAL OF HEAT TRANSFER, Vol. 98, 1976, pp. 221–225.

7 Lu, P. C., "Perturbation Solutions of Transient Heat Transfer to a Porous Medium From a Fluid Stream," ASME Paper No. 79-WA/HT-44, 1981.

8 Ozisik, M. N., *Heat Conduction*, Wiley Interscience, New York, 1980.

9 Carslaw, H. S., and Jaeger, J. C., *Conduction of Heat in Solids*, Clarendon Press, Oxford, 1959.

10 Ozisik, M. N., *Boundary Value Problems of Heat Conduction*, International Textbook Co., Scranton, PA, 1968.

11 Tyn, M. U., *Partial Differential Equations of Mathematical Physics*, Elsevier North Holland, 1980.

12 Tricomi, F. G., *Integral Equations*, Interscience, New York, 1970.

A Departure From the Darcy Model in Boundary Layer Natural Convection in a Vertical Porous Layer With Uniform Heat Flux From the Side

D. Poulikakos[1]

Nomenclature

b = constant, equations (2, 4)
B = function in Forschheimer's law, equation (2)
c_p = fluid specific heat at constant pressure
f = local speed, equation (3)
g = gravitational acceleration
G = dimensionless group,

$$\frac{\nu}{K}\left[\frac{k^2}{(g\beta q'')^2 b^3 \alpha H}\right]^{1/5}$$

H = layer height
k = effective thermal conductivity of the porous medium
K = permeability
L = layer length
P = pressure
q'' = uniform wall flux
Ra = Darcy-modified Rayleigh number, $(K g \beta q'' H)/(k\nu\alpha)$
Ra_∞ = large-Reynolds-number-limit Rayleigh number, $(g\beta H^3 q'')/(kb\alpha^2)$
T = temperature
u = horizontal velocity
v = vertical velocity
x = horizontal Cartesian coordinate
y = vertical Cartesian coordinate
α = thermal diffusivity, $k/\rho c_p$
β = coefficient of thermal expansion
δ = boundary layer thickness
μ = viscosity
ν = kinematic viscosity, μ/ρ
ρ = fluid density
ϕ = porosity
Ψ = streamfunction

Superscripts/subscripts

$*$ = dimensionless quantity, equation (8)
$\hat{}$ = dimensionless quantity, equation (21)

1 Introduction

The fundamental problem of buoyancy-induced heat transfer through a porous layer differentially heated in the horizontal direction has direct applications in many engineering areas such as thermal insulation, geothermal systems, and grain storage. A number of studies analyzing this problem model the system as a two-dimensional layer framed by two horizontal adiabatic walls and two vertical isothermal walls. These studies have reported extensive theoretical [1–7], numerical [7–13], and experimental [14–17] results with regard to the flow and heat transfer characteristics of the porous layer.

Recently, the equally important problem of constant heat flux on one [18] or both [19] the side walls of the porous cavity has been investigated. The model in [19], in particular, is more appropriate from the point of view of thermal insulation engineering since isothermal boundaries almost never exist in granular and fibrous vertical insulation layers in buildings. In addition, two fluid-saturated porous reservoirs interacting with each other by exchanging heat by free convection through a vertical wall reach a state closely resembling the uniform flux condition [20].

The present study also focuses on the boundary layer regime in a porous layer subjected to uniform heat fluxes along its vertical boundaries; however, the main purpose of this study is to relax a major assumption which limits the applicability of the results reported in [19]. These results are based on the Darcy flow model [21]; hence, they are valid only in the limit where the Reynolds number based on the volume-

[1]Department of Mechanical Engineering, University of Illinois at Chicago, Chicago, Illinois 60680, Assoc. Mem. ASME.

Contributed by the Heat Transfer Division for publication in the JOURNAL OF HEAT TRANSFER. Manuscript received by the Heat Transfer Division February 24, 1984.

Results and Discussion

The temperature distribution in both fluid and solid due to step change in the oncoming fluid temperature has been calculated according to equations (41) and (42). The present results are compared with the numerical solution of Burch et al. [6].

Figure 1 shows the temperature distributions T and θ as functions of the normalized location for four different times.

For the shortest time $t = 0.1$ the numerical solution [6] is everywhere identical with the presented analytical solution. For intermediate times ($t = 0.5$–2.5) the agreement is fairly good, and the largest deviation (for the solid temperature) is about 2 percent. For infinite time, the solutions are identical, except for large deviation at the fluid entrance temperature resulting from a probable error in [6]. For the shortest time of $t = 0.1$ (long enough to permit summation of a small number of terms in the series) only ten ($n = 10$) terms were needed. For longer times, the number of terms was even smaller.

In summary, the solution presented is a direct analytical solution based on Green functions and suitable for third-order systems.

In general, the method is suitable for solving higher-order partial differential equations, resulting from coupled phenomena such as heat interaction or diffusion between several phases, with or without sources.

References

1 Schumann, T. E. W., "Heat Transfer: Liquid Flowing Through a Porous Prism," *J. Franklin Inst.*, Vol. 208, 1929, pp. 405–416.

2 Smith, E. M., "General Integral Solution of the Regenerator Transient Test Equations for Zero Longitudinal Conduction," *Int. J. Heat and Fluid Flow*, Vol. 1, No. 2, 1979, pp. 71–75.

3 Spiga, G., and Spiga, M., "A Rigorous Solution to a Heat Transfer Two Phase Model in Porous Media and Packed Beds," *Int. J. Heat Mass Transfer*, Vol. 24, 1981, pp. 355–364.

4 Senshu, T., Hatada, T., and Ishibane, K., "Surface Heat Transfer Coefficients of Fins Used in Air-Cooled Heat Exchangers," *Heat Transfer Japanese Research*, Vol. 8, No. 4, 1979, pp. 16–26.

5 Creswick, F. A., "A Digital Computer Solution of the Equations for Transient Heating of Porous Solid Including the Effects of Longitudinal Conduction," *Industrial Mathematics*, 1957, pp. 61–69.

6 Burch, D. M., Allen, R. W., and Peavy, B. A., "Transient Temperature Distribution Within Porous Slabs Subjected to Sudden Tranpiration Heating," ASME JOURNAL OF HEAT TRANSFER, Vol. 98, 1976, pp. 221–225.

7 Lu, P. C., "Perturbation Solutions of Transient Heat Transfer to a Porous Medium From a Fluid Stream," ASME Paper No. 79-WA/HT-44, 1981.

8 Ozisik, M. N., *Heat Conduction*, Wiley Interscience, New York, 1980.

9 Carslaw, H. S., and Jaeger, J. C., *Conduction of Heat in Solids*, Clarendon Press, Oxford, 1959.

10 Ozisik, M. N., *Boundary Value Problems of Heat Conduction*, International Textbook Co., Scranton, PA, 1968.

11 Tyn, M. U., *Partial Differential Equations of Mathematical Physics*, Elsevier North Holland, 1980.

12 Tricomi, F. G., *Integral Equations*, Interscience, New York, 1970.

A Departure From the Darcy Model in Boundary Layer Natural Convection in a Vertical Porous Layer With Uniform Heat Flux From the Side

D. Poulikakos[1]

Nomenclature

b = constant, equations (2, 4)
B = function in Forschheimer's law, equation (2)
c_p = fluid specific heat at constant pressure
f = local speed, equation (3)
g = gravitational acceleration
G = dimensionless group,

$$\frac{\nu}{K}\left[\frac{k^2}{(g\beta q'')^2 b^3 \alpha H}\right]^{1/5}$$

H = layer height
k = effective thermal conductivity of the porous medium
K = permeability
L = layer length
P = pressure
q'' = uniform wall flux
Ra = Darcy-modified Rayleigh number, $(K g \beta q'' H)/(k\nu\alpha)$
Ra_∞ = large-Reynolds-number-limit Rayleigh number, $(g\beta H^3 q'')/(kb\alpha^2)$
T = temperature
u = horizontal velocity
v = vertical velocity
x = horizontal Cartesian coordinate
y = vertical Cartesian coordinate
α = thermal diffusivity, $k/\rho c_p$
β = coefficient of thermal expansion
δ = boundary layer thickness
μ = viscosity
ν = kinematic viscosity, μ/ρ
ρ = fluid density
ϕ = porosity
Ψ = streamfunction

Superscripts/subscripts

$*$ = dimensionless quantity, equation (8)
$\hat{}$ = dimensionless quantity, equation (21)

1 Introduction

The fundamental problem of buoyancy-induced heat transfer through a porous layer differentially heated in the horizontal direction has direct applications in many engineering areas such as thermal insulation, geothermal systems, and grain storage. A number of studies analyzing this problem model the system as a two-dimensional layer framed by two horizontal adiabatic walls and two vertical isothermal walls. These studies have reported extensive theoretical [1–7], numerical [7–13], and experimental [14–17] results with regard to the flow and heat transfer characteristics of the porous layer.

Recently, the equally important problem of constant heat flux on one [18] or both [19] the side walls of the porous cavity has been investigated. The model in [19], in particular, is more appropriate from the point of view of thermal insulation engineering since isothermal boundaries almost never exist in granular and fibrous vertical insulation layers in buildings. In addition, two fluid-saturated porous reservoirs interacting with each other by exchanging heat by free convection through a vertical wall reach a state closely resembling the uniform flux condition [20].

The present study also focuses on the boundary layer regime in a porous layer subjected to uniform heat fluxes along its vertical boundaries; however, the main purpose of this study is to relax a major assumption which limits the applicability of the results reported in [19]. These results are based on the Darcy flow model [21]; hence, they are valid only in the limit where the Reynolds number based on the volume-

[1]Department of Mechanical Engineering, University of Illinois at Chicago, Chicago, Illinois 60680, Assoc. Mem. ASME.

Contributed by the Heat Transfer Division for publication in the JOURNAL OF HEAT TRANSFER. Manuscript received by the Heat Transfer Division February 24, 1984.

averaged velocity and the pore diameter is small (less than 0(1)). The main reason for the wide use of the Darcy model in a plethora of studies [1–13, 19, 20] lies in its simplicity: Since this model is relevant to slow flow applications, it linearizes the momentum equation, thus removing a considerable amount of difficulty in solving the governing equations. The only nonlinear equation for natural convection in a Darcy-porous medium is the energy equation. There is an important reason, however, which makes it necessary to depart from the Darcy flow model, despite its simplicity. Heat transfer through the porous layer is convection-dominated in the boundary layer regime, where the Rayleigh number is very large. In the high Rayleigh number limit ($\mathrm{Ra}\to\infty$) the Darcy flow model is not accurate because the vertical velocity scale increases as $\mathrm{Ra}^{2/3}$ [19]. In other words, as the boundary layer approximations improve, the accuracy of the Darcy model deteriorates. The present study aims at resolving this conflict by formulating the problem in a way appropriate for all values of pore Reynolds number. A similar formulation for boundary layer natural convection from a vertical plate embedded in an infinite porous medium is reported in [22].

2 Theoretical Solution

In the limit of high Reynolds number based on pore diameter, the Darcy momentum equation should be modified to account for inertial effects [21–23]. The resulting expression, including the linear Boussinesq approximation ($\rho=\rho_0[1-\beta(T-T_0)]$) reads

$$\frac{\mu}{K}\left[\frac{\partial}{\partial x}\{B(f)v\}-\frac{\partial}{\partial y}\{B(f)u\}\right]=\rho_0 g\beta\frac{\partial T}{\partial x} \tag{1}$$

where

$$B=1+\frac{bK\rho}{\mu}f \tag{2}$$

$$f=|v|\left[1+\left(\frac{u}{v}\right)^2\right]^{1/2} \tag{3}$$

It is worth noting that in equation (1) the pressure term has been eliminated. The conservation equations for mass and energy are the usual porous medium equations [21]; hence, they are omitted here for brevity. All the symbols in the above equations are defined in the nomenclature.

According to Forschheimer's flow model [21, 23] adopted in equation (1), parameter B (equation 2) defines the boundaries separating three distinct flow regimes in the porous matrix:

a) The Darcy regime, $B=1$, i.e., $(bK\rho/\mu)\,f<<1$; *b*) the non-Darcy regime $B=(bK\rho/\mu)f$, i.e., $(bK\rho/\mu)\,f>>1$; *c*) the intermediate regime, B given by equation (2). The present study focuses on regimes (*b*) and (*c*). Constant b appearing in equation (2) is empirical. For a porous matrix consisting of packed spheres for example, b is given by [24]

$$b=\frac{1.75(1-\phi)}{\phi^3 d} \tag{4}$$

where ϕ is the medium porosity and d the sphere diameter.

The boundary layer problem for the non-Darcy regime is attacked first theoretically, following the approach in [1–3]. Taking into account usual boundary layer scaling arguments [25] we note that the dimensionless *boundary layer* conservation equations are

$$\frac{\partial u_*}{\partial x_*}+\frac{\partial v_*}{\partial y_*}=0 \tag{5}$$

$$\frac{\partial}{\partial x_*}(v_*|v_*|)=\frac{\partial T_*}{\partial x_*} \tag{6}$$

$$u_*\frac{\partial T_*}{\partial x_*}+v_*\frac{\partial T_*}{\partial y_*}=\frac{\partial^2 T_*}{\partial x_*^2} \tag{7}$$

where the dimensionless quantities are defined as follows [22]

$$x_*=\frac{x}{H\mathrm{Ra}_\infty^{-1/5}},\ y_*=\frac{y}{H},\ T_*=\frac{T}{\frac{q''H}{k}\mathrm{Ra}_\infty^{-1/5}},$$

$$u_*=\frac{u}{\frac{\alpha}{H}\mathrm{Ra}_\infty^{1/5}},\ v_*=\frac{v}{\frac{\alpha}{H}\mathrm{Ra}_\infty^{2/5}} \tag{8}$$

The new Rayleigh number Ra_∞ is the appropriate parameter to describe the flow when the traditional Darcy-modified Rayleigh number Ra becomes sufficiently large and the Darcy flow model breaks down. Both Ra_∞ and Ra are defined in the nomenclature.

In the same notation, the uniform heat flux condition reads

$$\frac{\partial T_*}{\partial x_*}=-1 \text{ at } x_*=0 \text{ and } x_*=\frac{L}{H}\mathrm{Ra}_\infty^{1/5} \tag{9}$$

The two horizontal walls are insulated ($\partial T_*/\partial y_*=0$ at $y_*=\pm 1/2$). With regard to the velocity field, all four walls of the layer are assumed impermeable.

The procedure followed for the theoretical solution is described in detail in [1, 2, 4] for layers with isothermal side walls and in [19] for layers with "uniform flux" side walls. Here we present only the final results of the theoretical solution:

(*a*) The flow field in the porous layer consists of a motionless core ($u_{*_c}=v_{*_c}=0$) which is sandwiched by two boundary layers. In addition, the fluid stagnating in the core is linearly stratified

$$T_{*_c}=(2\lambda^3)^{1/2}y_* \tag{10}$$

where λ is a constant given by

$$\lambda=\left(\frac{H}{L}\right)^{1/4}\frac{\mathrm{Ra}_\infty^{1/20}}{6^{1/4}} \tag{11}$$

(*b*) The velocity boundary layers along the two vertical walls are of *constant thickness*. The velocity and temperature distributions in the boundary layer along the left wall are

$$v_*=(2\lambda)^{-1/2}e^{-\lambda x_*},\ T_*=\frac{e^{-2\lambda x_*}}{2\lambda}+(2\lambda^3)^{1/2}y_* \tag{12, 13}$$

Similarly, along the right wall

$$v'_*=-(2\lambda)^{-1/2}e^{-\lambda x'_*},\ T'_*=-\frac{1}{2\lambda}e^{-2\lambda x'_*}+(2\lambda^3)^{1/2}y_* \tag{14, 15}$$

the new coordinate x'_* is the horizontal position measured away from the right wall ($x'=L-x$).

(*c*) Based on equations (12–15) the average temperature difference between the two vertical walls and the volume flowrate through one boundary layer can be evaluated. The latter, in dimensionless form, is identical to the value of the streamfunction in the core region

$$\Delta T_*=[T_*]_{x=0}-[T'_*]_{x'=0}=\left(\frac{L}{H}\right)^{1/4}6^{1/4}\mathrm{Ra}_\infty^{-1/20} \tag{16}$$

$$\Psi_{*_c}=-\int_0^\infty v_* dx_*=-\frac{6^{3/8}}{\sqrt{2}}\left(\frac{L}{H}\right)^{3/8}\mathrm{Ra}_\infty^{-3/40} \tag{17}$$

It is worth noting that the temperature difference between the two driving walls, equation (16), is independent of y_* because the temperature in each vertical layer varies linearly with y_*, in the same manner as the core temperature T_{*_c}. This finding agrees with the results reported for the Darcy regime. However, the wall-to-wall ΔT_* for the non-Darcy regime

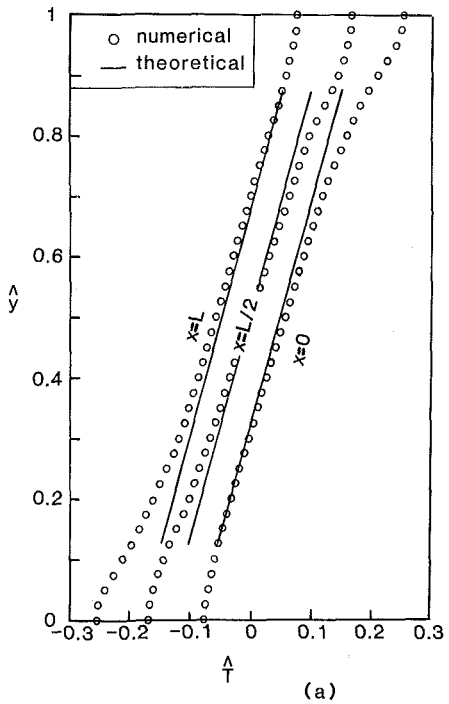

Fig. 1(a) Numerical and theoretical results for the temperature distribution in three vertical planes in the non-Darcy flow limit (H/L = 2, Ra = 5000, G = 0.1)

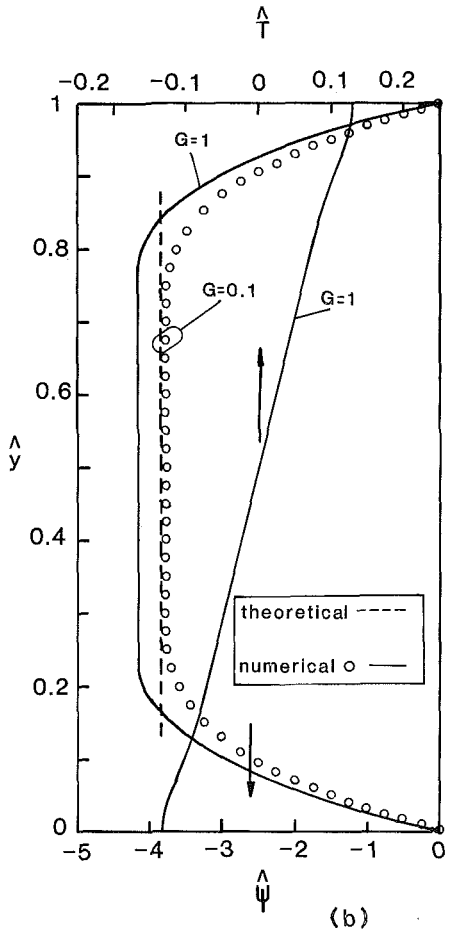

Fig. 1(b) Numerical and theoretical results for the streamfunction variation in the vertical midplane in the non-Darcy flow limit (H/L = 2, Ra = 5000, G = 0.1; the solid lines show numerically obtained streamfunction and temperature variations for the intermediate regime (G = 1)

scales differently with H/L and Ra from the wall-to-wall ΔT_* for the Darcy regime ($\Delta T_* = 2(H/L)^{-1/5}\,\mathrm{Ra}^{-1/15}$ [19]).

3 Numerical Simulations

The numerical simulations presented in this section were performed based on the complete form of the governing equations. Hence, the numerical solution, in addition to checking the theoretical predictions of the previous section, will shed light on the intermediate flow regime which is not amenable to a simple theoretical solution.

The dimensionless governing equations and boundary conditions for the numerical simulations read

$$-G\nabla^2\hat{\Psi} = \mathrm{Ra}_\infty^{-2/5}\left\{\frac{\partial}{\partial\hat{y}}(\hat{f}\hat{u}) - \frac{\partial}{\partial\hat{x}}(\hat{f}\hat{v})\right\} + \mathrm{Ra}_\infty^{3/5}\frac{\partial\hat{T}}{\partial\hat{x}} \tag{18}$$

$$\hat{u}\frac{\partial\hat{T}}{\partial\hat{x}} + \hat{v}\frac{\partial\hat{T}}{\partial\hat{y}} = \nabla^2\hat{T} \tag{19}$$

$$\hat{u} = \hat{\Psi} = 0,\ \frac{\partial\hat{T}}{\partial\hat{x}} = -1 \quad \text{at } \hat{x} = 0, L/H$$
$$\hat{v} = \hat{\Psi} = \frac{\partial\hat{T}}{\partial\hat{y}} = 0 \quad \text{at } \hat{y} = 0,1 \tag{20}$$

The nondimensionalization was carried out according to the following definitions

$$\hat{x} = \frac{x}{H},\ \hat{y} = \frac{y}{H},\ \hat{T} = \frac{T}{q''\dfrac{H}{k}},\ (\hat{u},\hat{v},\hat{f}) = (u,v,f)/(\alpha/H) \tag{21}$$

The dimensionless streamfunction is defined in the usual manner, $\hat{u} = \partial\hat{\Psi}/\partial\hat{y}$, $\hat{v} = -(\partial\hat{\Psi}/\partial\hat{x})$. The new group G appearing in equation (18) describes the departure from the Darcy flow limit as discussed in [22]. $G << 0(1)$ refers to the non-Darcy limit, while the range $G >> 0(1)$ leads back to the Darcy flow model. Values of G of order unity describe the intermediate regime.

The set of equations (18–20) was solved iteratively. Successive relaxation was used to obtain the streamfunction from equation (18). The right-hand side of this equation was known from the previous iteration. Equation (18) was overrelaxed for $G \geq 1$ and underrelaxed for $G < 1$. Typical values of the relaxation parameter are: $\gamma = 1.3$ for $G = 4$, Ra = 5000 and $\gamma = 0.6$ for $G = 0.4$, Ra = 5000. The temperature field was obtained from equation (19) using the power law scheme [26]. The details of the power law scheme are omitted here for brevity, since they can be found in [26]. The process was repeated until convergence was obtained within prescribed error. In the present study we used a uniform grid and the grid fineness $m = 45$, $n = 89$ yielded accurate results throughout the study. Using finer grids led to temperature and streamfunction values within 0.05 percent of the values which resulted from the chosen grid.

Through the numerical simulations the value of the usual Darcy-modified Rayleigh number was held fixed at Ra = 5000, the highest value of Ra that yielded a stable solution. The values of G examined ranged from $G = 0.1$ to $G = 10$. The non-Darcy Rayleigh number Ra_∞ was evaluated from the following relationship which connects Ra, G, and Ra_∞

$$\mathrm{Ra}_\infty = (\mathrm{Ra}\,G)^{5/3} \tag{22}$$

As a result, the values of Ra_∞ used were not always "round." In addition, examining equation (22) leads to the conclusion that decreasing G decreases Ra_∞ unless Ra is increased simultaneously. On the other hand, Ra_∞ should stay as high as possible (boundary layer flow). It was found that $G \approx 0.1$ is the lowest value of G that yields boundary layer flow in the layer for Ra = 5000. As it will be shown next, this value of G is small enough to compare favorably with the theoretical results for the non-Darcy regime ($G \approx 0$).

Figure 1(*a*) shows the temperature distribution along three vertical planes in the porous layer, namely, the two vertical walls and the vertical midplane, for $H/L = 2$, $Ra_\infty = 31{,}498$ in the non-Darcy regime ($G = 0.1$). For most of the porous layer the thermal stratification is indeed linear in y and independent of x. Deviations (as much as 20 percent) from the theoretically predicted pattern occur near the horizontal walls where the numerical solution has to satisfy the "adiabatic" boundary condition. The main characteristic of the theoretically obtained flow field in the non-Darcy regime, namely, the fact that the core region is motionless, is verified in Fig. 1(*b*) which shows the streamfunction profile at $x = L/2$. The flatness of the streamfunction profile away from the horizontal walls indicates that the fluid circulates through two layers parallel to the horizontal boundaries leaving the core region practically motionless. Figure 1(*b*) also shows good quantitative agreement between the numerically and theoretically predicted values of streamfunction in the core. In conclusion, the numerical solution verifies quantitatively and qualitatively the main predictions of the theoretical solution for the non-Darcy regime (G considerably smaller than unity). The solid lines in the same figure provide some insight for the flow and temperature field in the intermediate regime, for they show temperature and streamfunction variations in the vertical, at $x = L/2$, for $G = 1$, $H/L = 2$, $Ra_\infty = 1{,}462{,}009$. This figure reveals that the intermediate regime also possesses a linearly stratified, practically motionless core, along the lines of the Darcy and non-Darcy regimes.

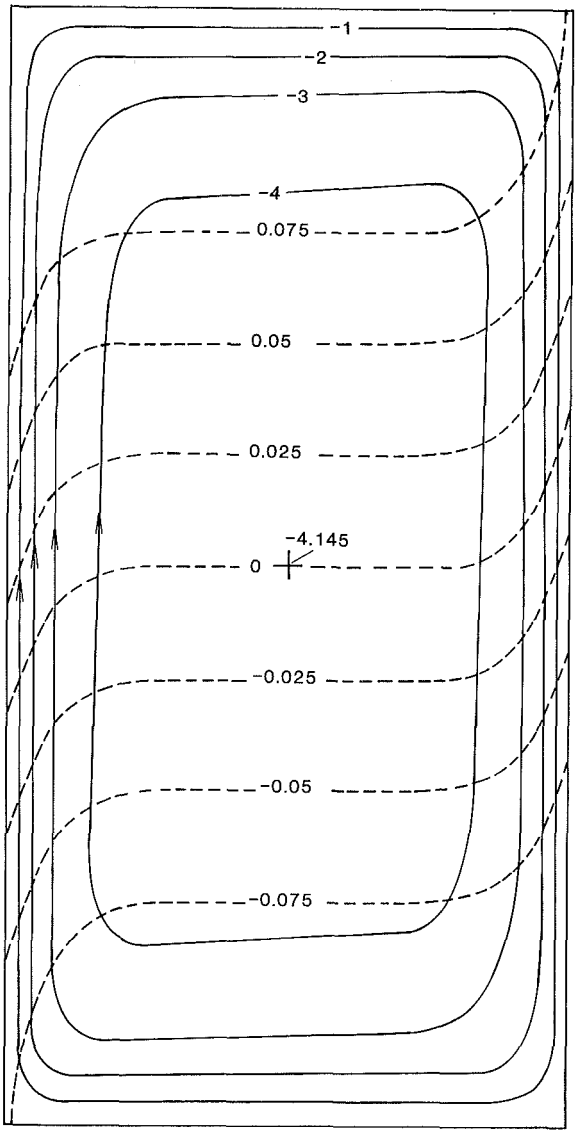

Fig. 2 Streamlines and isotherms: $H/L = 2$, $Ra = 5000$ ($Ra_\infty = 1{,}452{,}009$), $G = 1$

More information regarding the intermediate regime is presented in Fig. 2 ($G = 1$, $H/L = 2$, $Ra_\infty = 1{,}452{,}009$) by means of a representative set of isotherms and streamlines. The flow field consists of a single cell rotating clockwise. The shape of the streamlines indicates the presence of boundary layers along the vertical walls of the porous layer. The boundary layers are also visible in the isotherms (dashed lines) where they sandwich a thermally stratified core. The fact that the streamlines stay parallel to the vertical walls for most of the porous layer and the shape of the isotherms indicate that the thickness of the vertical boundary layers is independent of y everywhere except in the close vicinity of the two horizontal walls. This finding reveals that the theoretical predictions of a constant boundary layer thickness in the non-Darcy regime (section 2) and the Darcy regime [19] extend to the intermediate regime. Streamlines and isotherms obtained for different values of G ($0.1 \le G \le 1$) in the high-Rayleigh-number regime exhibited the same general features as the case illustrated in Fig. 2.

Finally, Fig. 3 shows the effect of G on the wall-to-wall temperature variation. Clearly, the numerically calculated $\Delta\hat{T}$ captures the asymptotic non-Darcy and Darcy limits at low and high values of G, respectively. In addition, the intermediate regime is described by values of $G = 0(1)$.

References

1 Weber, J. W., "The Boundary Layer Regime for Convection in a Vertical Porous Layer," *Int. J. Heat and Mass Transfer*, Vol. 18, 1975, pp. 569–573.

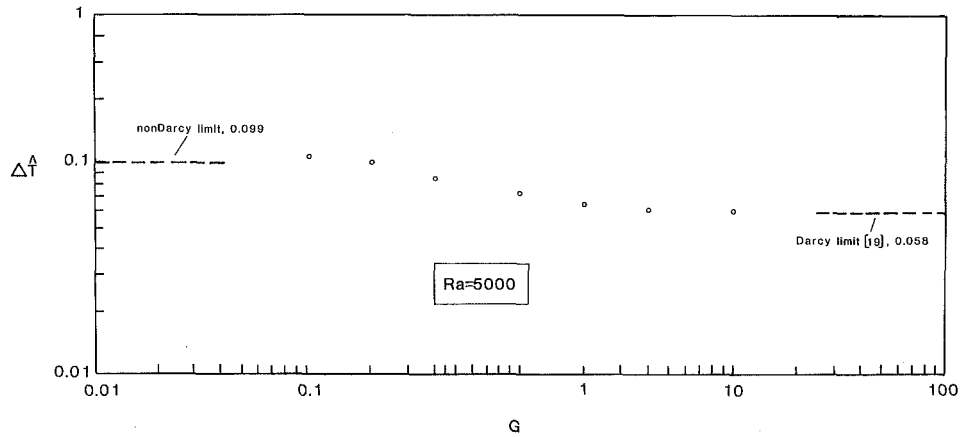

Fig. 3 The wall-to-wall temperature difference at midheight, showing the effect of the Darcy/non-Darcy parameter G

2 Bejan, A., "On the Boundary Layer Regime in a Vertical Enclosure Filled With a Porous Medium," *Lett. Heat Mass Transfer*, Vol. 6, 1979, pp. 93-102.
3 Simpkins, P. G., and Blythe, P. A., "Convection in a Porous Layer," *Int. J. Heat Mass Transfer*, Vol. 23, 1980, pp. 881-887.
4 Blythe, P. A., and Simpkins, P. G., "Convection in a Porous Layer for a Temperature Dependent Viscosity," *Int. J. Heat Mass Transfer*, Vol. 23, 1981, pp. 497-506.
5 Walker, K. L., and Homsy, G. M., "Convection in a Porous Cavity," *J. Fluid Mech.*, Vol. 87, 1978, pp. 449-474.
6 Bejan, A., and Tien, C. L., "Natural Convection in a Horizontal Porous Medium Subjected to an End-to-End Temperature Difference," ASME JOURNAL OF HEAT TRANSFER, Vol. 100, 1978, pp. 191-198.
7 Poulikakos, D., and Bejan, A., "Unsteady Natural Convection in a Porous Layer," *Physics of Fluids*, Vol. 26, 1983, pp. 1183-1191.
8 Chan, B. K. C., Ivey, C. M., and Barry, J. M., "Natural Convection in Enclosed Porous Media With Rectangular Boundaries," ASME JOURNAL OF HEAT TRANSFER, Vol. 92, 1970, pp. 21-27.
9 Bankvall, C. G., "Natural Convection in Vertical Permeable Space," *Wärme und Stoff*, Vol. 7, 1974, pp. 22-30.
10 Burns, P. J., Chow, L. C., and Tien, C. L., "Convection in a Vertical Slot Filled With Porous Insulation," *Int. J. Heat Mass Transfer*, Vol. 20, 1977, pp. 919-926.
11 Hickox, C. E., and Gartling, D. K., "A Numerical Study of Natural Convection in a Horizontal Porous Layer Subjected to an End-to-End Temperature Difference," ASME JOURNAL OF HEAT TRANSFER, Vol. 103, 1981, pp. 797-802.
12 Prasad, V., and Kulacki, F. A., "Convective Heat Transfer in a Rectangular Porous Cavity—Effect of Aspect Ratio on Flow Structure and Heat Transfer," ASME JOURNAL OF HEAT TRANSFER, Vol. 106, 1984, pp. 158-165.
13 Shrialkar, G. S., Haajizadeh, M., and Tien, C. L., "Numerical Study of High Rayleigh Number Convection in a Vertical Porous Enclosure," *Numerical Heat Transfer*, Vol. 6, 1983, pp. 223-234.
14 Schneider, K. J., "Investigation of the Influence of Free Thermal Convection on Heat Transfer Through Granual Material," *Proc. Int. Inst. Refrig.*, Vol. 11, 1963, pp. 247-253.
15 Klarsfeld, S., "Champs de Temperature Associés aux Mouvements de Convection Naturelle dans un Milieu Poreux Limité," *Rev. Gen. Therm.*, Vol. 108, 1970, pp. 1403-1423.
16 Mordchelles-Regnier, G., Micheau, P., Pirovano, A., Jumentier, C., Terpsta, J. S., Lecourt, Y., Cave, P., and Breuille, M., *Recherches Récentes Effectuées en France sur l'Isolation Thermique des Réacteures Nucléaires*, International Atomic Energy Agency, Vienna, 1969, pp. 529-544.
17 Seki, N., Fukusako, S., and Inaba, H., "Heat Transfer in a Confined Rectangular Cavity Packed With Porous Media," *Int. J. Heat and Mass Transfer*, Vol. 21, 1978, pp. 985-989.
18 Prasad, V., and Kulacki, F. A., "Natural Convection in a Porous Cavity With Constant Heat Flux on One Vertical Wall," ASME JOURNAL OF HEAT TRANSFER, Vol. 106, 1984, pp. 152-157.
19 Bejan, A., "The Boundary Layer Regime in a Porous Layer With Uniform Heat Flux From the Side," *Int. J. Heat Mass Transfer*, Vol. 26, 1983, pp. 1339-1345.
20 Bejan, A., and Anderson, R., "Heat Transfer Across a Vertical Impermeable Partition Imbedded in Porous Medium," *Int. J. Heat Mass Transfer*, Vol. 24, 1981, pp. 1237-1245.
21 Cheng, P., "Heat Transfer in Geothermal Systems," *Adv. Heat Transfer*, Vol. 14, 1978, pp. 1-105.
22 Bejan, A., and Poulikakos, D., "The Non-Darcy Regime for Vertical Boundary Layer Convection in a Porous Medium," *Int. J. Heat and Mass Transfer*, Vol. 27, 1984, pp. 717-722.
23 Forshheimer, P. H., *Z. Ver. Dt. Ing.*, Vol. 45, 1901, pp. 1782-1788.
24 Ergun, S., "Flow Through Packed Columns," *Chemical Engin. Progress*, 1982, pp. 89-94.
25 Bejan, A., *Convection Heat Transfer*, Wiley, New York, 1984.
26 Patankar, S., *Numerical Heat Transfer and Fluid Flow*, Hemisphere, New York, 1980.

Mixed Convection Plumes Arising From a Thermal Point Source

K. V. Rao,[1] B. F. Armaly,[1,2] and T. S. Chen[1,2]

Introduction

Plumes arising from a thermal point source are of interest in several engineering applications, e.g., hot-film anemometry, electronic circuitry, and thermal pollution. The limiting case of purely free convection has been studied by Yih [1], Fujii [2], and Mollendorf and Gebhart [3]. The mixed forced and free convection regime was examined by Appalaswamy and Jaluria [4], Afzal [5], and Riley and Drake [6]. Previous analyses which have been employed to study the entire mixed convection regime required one formulation to represent the departure from the pure forced convection and another formulation to represent the departure from the pure free convection. In the present study a new transformation is employed which allows one to examine the entire mixed convection regime via one formulation. The objective of the present study is also to obtain additional results for the velocity and temperature fields for fluids having Prandtl numbers of 0.7, 7, 50, and 100 over the entire mixed convection regime. Equivalent results have not appeared in the literature.

Analysis

The geometry considered in this study is equivalent to a thermal point source that is situated in a flow field with a uniform temperature T_∞ and a uniform upward free-stream velocity u_∞. The boundary layer equations that govern this flow are written in terms of the vertical and radial velocity components u and v, temperature T, the vertical coordinate from the point source x, and the radial distance y from the axis of symmetry, as

$$\frac{\partial(yu)}{\partial x} + \frac{\partial(yv)}{\partial y} = 0 \tag{1}$$

$$u\frac{\partial u}{\partial x} + v\frac{\partial u}{\partial y} = \frac{\nu}{y}\frac{\partial}{\partial y}\left(y\frac{\partial u}{\partial y}\right) + g\beta(T - T_\infty) \tag{2}$$

$$u\frac{\partial T}{\partial x} + v\frac{\partial T}{\partial y} = \frac{\alpha}{y}\frac{\partial}{\partial y}\left(y\frac{\partial T}{\partial y}\right) \tag{3}$$

where g is the gravitational acceleration, β the coefficient of thermal expansion, ν the kinematic viscosity, and α the thermal diffusivity. The boundary conditions are given by

$$v = \frac{\partial u}{\partial y} = \frac{\partial T}{\partial y} = 0 \text{ at } y = 0 \tag{4a}$$

$$u \to u_\infty \text{ and } T \to T_\infty \text{ as } y \to \infty \tag{4b}$$

and the conservation of energy requires

$$Q = 2\pi\rho C_p \int_0^\infty yu(T - T_\infty)dy \tag{5}$$

where Q is the strength of the thermal point source.

In order to facilitate the solution of the above system of equations throughout the entire mixed convection regime, the following transformations are utilized

$$\xi = \mathrm{Re}_x^{1/2}/(\mathrm{Gr}_x^{1/4} + \mathrm{Re}_x^{1/2}), \qquad \eta = \frac{y}{x}(\mathrm{Gr}_x^{1/4} + \mathrm{Re}_x^{1/2}) \tag{6}$$

$$\psi = \nu x F(\eta), \qquad \theta = (T - T_\infty)/T^* \tag{7}$$

where $\mathrm{Gr}_x = g\beta T^* x^3/\nu^2$, $\mathrm{Re}_x = u_\infty x/\nu$, and ψ is the stream function that satisfies the continuity equation (1), with $u = (1/y)(\partial\psi/\partial y)$ and $v = -(1/y)(\partial\psi/\partial x)$, and the equivalent temperature T^* of the thermal point source is given by $T^* = Q/(2\pi\rho C_p \nu x)$. Equations (2-5) can be transformed to the following set of ordinary differential equations

$$\eta^2 F''' - \eta F'' + F' - FF' + \eta FF'' + \eta^3(1 - \xi)^4\theta = 0 \tag{8}$$

$$(\eta\theta')' + \mathrm{Pr}(F\theta)' = 0 \tag{9}$$

with boundary conditions

$$F(0) = F'(0) = \theta'(0) = 0 \text{ at } \eta = 0 \tag{10a}$$

$$\theta(\infty) = 0 \text{ and } \frac{F'}{\eta} = \xi^2 \text{ at } \eta = \infty \tag{10b}$$

and subject to the normalized heat flux condition

[1] Department of Mechanical and Aerospace Engineering, University of Missouri – Rolla, Rolla, MO 65401

[2] Mem. ASME

Contributed by the Heat Transfer Division for publication in the JOURNAL OF HEAT TRANSFER. Manuscript received by the Heat Transfer Division June 5, 1984.

2 Bejan, A., "On the Boundary Layer Regime in a Vertical Enclosure Filled With a Porous Medium," *Lett. Heat Mass Transfer*, Vol. 6, 1979, pp. 93-102.
3 Simpkins, P. G., and Blythe, P. A., "Convection in a Porous Layer," *Int. J. Heat Mass Transfer*, Vol. 23, 1980, pp. 881-887.
4 Blythe, P. A., and Simpkins, P. G., "Convection in a Porous Layer for a Temperature Dependent Viscosity," *Int. J. Heat Mass Transfer*, Vol. 23, 1981, pp. 497-506.
5 Walker, K. L., and Homsy, G. M., "Convection in a Porous Cavity," *J. Fluid Mech.*, Vol. 87, 1978, pp. 449-474.
6 Bejan, A., and Tien, C. L., "Natural Convection in a Horizontal Porous Medium Subjected to an End-to-End Temperature Difference," ASME JOURNAL OF HEAT TRANSFER, Vol. 100, 1978, pp. 191-198.
7 Poulikakos, D., and Bejan, A., "Unsteady Natural Convection in a Porous Layer," *Physics of Fluids*, Vol. 26, 1983, pp. 1183-1191.
8 Chan, B. K. C., Ivey, C. M., and Barry, J. M., "Natural Convection in Enclosed Porous Media With Rectangular Boundaries," ASME JOURNAL OF HEAT TRANSFER, Vol. 92, 1970, pp. 21-27.
9 Bankvall, C. G., "Natural Convection in Vertical Permeable Space," *Wärme und Stoff*, Vol. 7, 1974, pp. 22-30.
10 Burns, P. J., Chow, L. C., and Tien, C. L., "Convection in a Vertical Slot Filled With Porous Insulation," *Int. J. Heat Mass Transfer*, Vol. 20, 1977, pp. 919-926.
11 Hickox, C. E., and Gartling, D. K., "A Numerical Study of Natural Convection in a Horizontal Porous Layer Subjected to an End-to-End Temperature Difference," ASME JOURNAL OF HEAT TRANSFER, Vol. 103, 1981, pp. 797-802.
12 Prasad, V., and Kulacki, F. A., "Convective Heat Transfer in a Rectangular Porous Cavity—Effect of Aspect Ratio on Flow Structure and Heat Transfer," ASME JOURNAL OF HEAT TRANSFER, Vol. 106, 1984, pp. 158-165.
13 Shrialkar, G. S., Haajizadeh, M., and Tien, C. L., "Numerical Study of High Rayleigh Number Convection in a Vertical Porous Enclosure," *Numerical Heat Transfer*, Vol. 6, 1983, pp. 223-234.
14 Schneider, K. J., "Investigation of the Influence of Free Thermal Convection on Heat Transfer Through Granual Material," *Proc. Int. Inst. Refrig.*, Vol. 11, 1963, pp. 247-253.
15 Klarsfeld, S., "Champs de Temperature Associés aux Mouvements de Convection Naturelle dans un Milieu Poreux Limité," *Rev. Gen. Therm.*, Vol. 108, 1970, pp. 1403-1423.
16 Mordchelles-Regnier, G., Micheau, P., Pirovano, A., Jumentier, C., Terpsta, J. S., Lecourt, Y., Cave, P., and Breuille, M., *Recherches Récentes Effectuées en France sur l'Isolation Thermique des Réacteures Nucléaires*, International Atomic Energy Agency, Vienna, 1969, pp. 529-544.
17 Seki, N., Fukusako, S., and Inaba, H., "Heat Transfer in a Confined Rectangular Cavity Packed With Porous Media," *Int. J. Heat and Mass Transfer*, Vol. 21, 1978, pp. 985-989.
18 Prasad, V., and Kulacki, F. A., "Natural Convection in a Porous Cavity With Constant Heat Flux on One Vertical Wall," ASME JOURNAL OF HEAT TRANSFER, Vol. 106, 1984, pp. 152-157.
19 Bejan, A., "The Boundary Layer Regime in a Porous Layer With Uniform Heat Flux From the Side," *Int. J. Heat Mass Transfer*, Vol. 26, 1983, pp. 1339-1345.
20 Bejan, A., and Anderson, R., "Heat Transfer Across a Vertical Impermeable Partition Imbedded in Porous Medium," *Int. J. Heat Mass Transfer*, Vol. 24, 1981, pp. 1237-1245.
21 Cheng, P., "Heat Transfer in Geothermal Systems," *Adv. Heat Transfer*, Vol. 14, 1978, pp. 1-105.
22 Bejan, A., and Poulikakos, D., "The Non-Darcy Regime for Vertical Boundary Layer Convection in a Porous Medium," *Int. J. Heat and Mass Transfer*, Vol. 27, 1984, pp. 717-722.
23 Forshheimer, P. H., *Z. Ver. Dt. Ing.*, Vol. 45, 1901, pp. 1782-1788.
24 Ergun, S., "Flow Through Packed Columns," *Chemical Engin. Progress*, 1982, pp. 89-94.
25 Bejan, A., *Convection Heat Transfer*, Wiley, New York, 1984.
26 Patankar, S., *Numerical Heat Transfer and Fluid Flow*, Hemisphere, New York, 1980.

Mixed Convection Plumes Arising From a Thermal Point Source

K. V. Rao,[1] B. F. Armaly,[1,2] and T. S. Chen[1,2]

Introduction

Plumes arising from a thermal point source are of interest in several engineering applications, e.g., hot-film anemometry, electronic circuitry, and thermal pollution. The limiting case of purely free convection has been studied by Yih [1], Fujii [2], and Mollendorf and Gebhart [3]. The mixed forced and free convection regime was examined by Appalaswamy and Jaluria [4], Afzal [5], and Riley and Drake [6]. Previous analyses which have been employed to study the entire mixed convection regime required one formulation to represent the departure from the pure forced convection and another formulation to represent the departure from the pure free convection. In the present study a new transformation is employed which allows one to examine the entire mixed convection regime via one formulation. The objective of the present study is also to obtain additional results for the velocity and temperature fields for fluids having Prandtl numbers of 0.7, 7, 50, and 100 over the entire mixed convection regime. Equivalent results have not appeared in the literature.

Analysis

The geometry considered in this study is equivalent to a thermal point source that is situated in a flow field with a uniform temperature T_∞ and a uniform upward free-stream velocity u_∞. The boundary layer equations that govern this flow are written in terms of the vertical and radial velocity components u and v, temperature T, the vertical coordinate from the point source x, and the radial distance y from the axis of symmetry, as

$$\frac{\partial(yu)}{\partial x} + \frac{\partial(yv)}{\partial y} = 0 \tag{1}$$

$$u\frac{\partial u}{\partial x} + v\frac{\partial u}{\partial y} = \frac{\nu}{y}\frac{\partial}{\partial y}\left(y\frac{\partial u}{\partial y}\right) + g\beta(T - T_\infty) \tag{2}$$

$$u\frac{\partial T}{\partial x} + v\frac{\partial T}{\partial y} = \frac{\alpha}{y}\frac{\partial}{\partial y}\left(y\frac{\partial T}{\partial y}\right) \tag{3}$$

where g is the gravitational acceleration, β the coefficient of thermal expansion, ν the kinematic viscosity, and α the thermal diffusivity. The boundary conditions are given by

$$v = \frac{\partial u}{\partial y} = \frac{\partial T}{\partial y} = 0 \text{ at } y = 0 \tag{4a}$$

$$u \to u_\infty \text{ and } T \to T_\infty \text{ as } y \to \infty \tag{4b}$$

and the conservation of energy requires

$$Q = 2\pi\rho C_p \int_0^\infty yu(T - T_\infty)dy \tag{5}$$

where Q is the strength of the thermal point source.

In order to facilitate the solution of the above system of equations throughout the entire mixed convection regime, the following transformations are utilized

$$\xi = \mathrm{Re}_x^{1/2}/(\mathrm{Gr}_x^{1/4} + \mathrm{Re}_x^{1/2}), \qquad \eta = \frac{y}{x}(\mathrm{Gr}_x^{1/4} + \mathrm{Re}_x^{1/2}) \tag{6}$$

$$\psi = \nu x F(\eta), \qquad \theta = (T - T_\infty)/T^* \tag{7}$$

where $\mathrm{Gr}_x = g\beta T^* x^3/\nu^2$, $\mathrm{Re}_x = u_\infty x/\nu$, and ψ is the stream function that satisfies the continuity equation (1), with $u = (1/y)(\partial\psi/\partial y)$ and $v = -(1/y)(\partial\psi/\partial x)$, and the equivalent temperature T^* of the thermal point source is given by $T^* = Q/(2\pi\rho C_p \nu x)$. Equations (2-5) can be transformed to the following set of ordinary differential equations

$$\eta^2 F''' - \eta F'' + F' - FF' + \eta FF'' + \eta^3(1 - \xi)^4\theta = 0 \tag{8}$$

$$(\eta\theta')' + \mathrm{Pr}(F\theta)' = 0 \tag{9}$$

with boundary conditions

$$F(0) = F'(0) = \theta'(0) = 0 \text{ at } \eta = 0 \tag{10a}$$

$$\theta(\infty) = 0 \text{ and } \frac{F'}{\eta} = \xi^2 \text{ at } \eta = \infty \tag{10b}$$

and subject to the normalized heat flux condition

[1] Department of Mechanical and Aerospace Engineering, University of Missouri – Rolla, Rolla, MO 65401

[2] Mem. ASME

Contributed by the Heat Transfer Division for publication in the JOURNAL OF HEAT TRANSFER. Manuscript received by the Heat Transfer Division June 5, 1984.

$$\int_0^\infty F'\theta d\eta = 1 \tag{10c}$$

The limiting cases of pure free convection and forced convection plumes correspond to the conditions $\xi = 0$ and $\xi = 1$, respectively. Note that a larger mixed convection parameter corresponds to smaller buoyancy effects, i.e., smaller source strength, or higher forced free-stream velocity and vice versa. Equations (8–10) were solved by using a fourth-order Runge-Kutta integration scheme for specified values of the mixed convection parameter $0 \leq \xi \leq 1$. An integration stepsize $\Delta\eta$ of 0.01 and a convergence criterion of 10^{-4} at the edge of the boundary layer η_∞ were used in the computations.

Results and Discussion

Velocity and temperature distributions in the axisymmetric plume above a thermal point source were obtained for fluids having Prandtl numbers of 0.7, 7, 50, and 100 over the entire mixed convection regime $0 \leq \xi \leq 1$. The predicted results compare very well with the limited range of published values [4–6]. The axial velocity distribution $u/u_\infty = F'/\eta\xi^2$ is presented in Fig. 1 as a function of the nondimensional radial distance $\eta\xi = (y/x)\mathrm{Re}_x^{1/2}$. As expected, the velocity is maximum at the centerline of the plume and it approaches the free-stream velocity at the edge of the boundary layer. The centerline velocity increases but the plume radius decreases as either the mixed convection parameter decreases (i.e., as the buoyancy effect increases) or the Prandtl number increases. The influence of the source strength and of the Prandtl number on the axial velocity distribution diminishes as the magnitude of the mixed convection parameter increases (i.e., as the free-stream velocity increases).

The magnitude of $F''(0)$ is presented in Table 1 as a function of the mixed convection parameter. This quantity is proportional to the axial velocity at the centerline of the plume which is given by $u(0)/u_\infty = F''(0)/\xi^2$ when $\xi \neq 0$ and by $u(0) = (\nu/x)\,\mathrm{Gr}_x^{1/2}F''(0)$ when $\xi = 0$. Fluids with higher Prandtl numbers will experience a higher dimensionless centerline velocity $F''(0)$. The magnitude of $F''(0)$ exhibits a minimum in the range of $0 < \xi < 1$ but the centerline velocity ratio $u(0)/u_\infty$ will always decrease as the mixed convection parameter increases due to the increase in the free-stream velocity.

The radial velocity component, which is given for the case

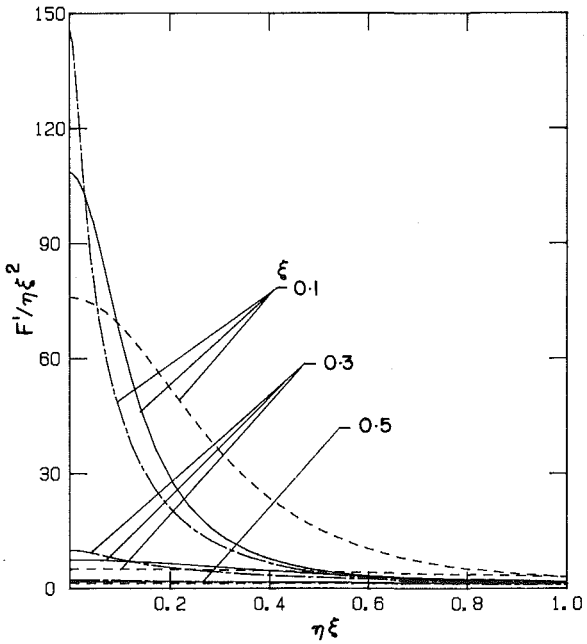

Fig. 1 Axial velocity distribution: ····· Pr = 0.7, —— Pr = 7, – – – Pr = 100

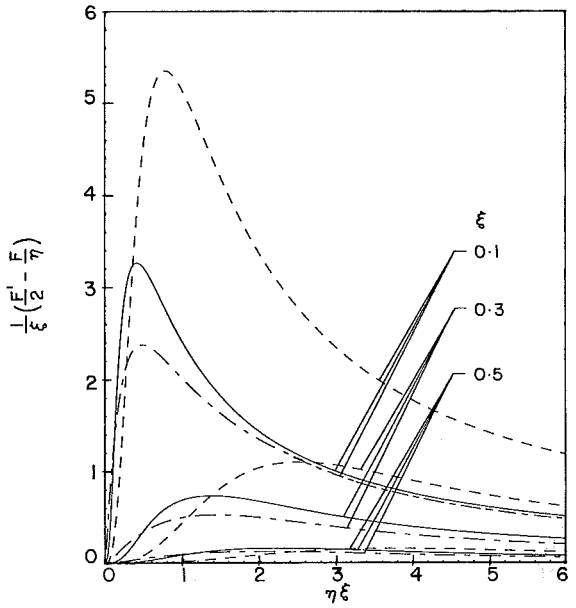

Fig. 2 Radial velocity distribution: ····· Pr = 0.7, —— Pr = 7, – – – Pr = 100

Table 1 Dimensionless centerline velocity and temperature

	Pr = 0.7		Pr = 7.0		Pr = 50		Pr = 100	
ξ	F"(0)	θ(0)	F"(0)	θ(0)	F"(0)	θ(0)	F"(0)	θ(0)
0.0	0.9380	0.4826	1.3370	4.0065	1.6806	26.8778	1.7938	53.1843
0.05	0.8464	0.4821	1.2070	4.0058	1.5170	26.8756	1.6191	53.1784
0.1	0.7593	0.4800	1.0847	4.0029	1.3627	26.8684	1.4546	53.1652
0.15	0.6769	0.4757	0.9702	3.9968	1.2182	26.8554	1.2989	53.1505
0.2	0.5995	0.4685	0.8638	3.9861	1.0837	26.8329	1.1565	53.1035
0.25	0.5281	0.4577	0.7658	3.9686	0.9598	26.7923	1.0235	53.0427
0.3	0.4640	0.4431	0.6770	3.9419	0.8467	26.7285	0.9028	52.9396
0.4	0.3683	0.4051	0.5309	3.8496	0.6566	26.4829	0.6980	52.5636
0.5	0.3389	0.3713	0.4408	3.7065	0.5240	26.0440	0.5524	51.8488
0.6	0.3885	0.3554	0.4317	3.5749	0.4718	25.4754	0.4867	50.8959
0.7	0.4968	0.3510	0.5083	3.5158	0.5174	25.1165	0.5223	50.2300
0.8	0.6410	0.3502	0.6428	3.5020	0.6439	25.0144	0.6453	50.0290
0.9	0.8101	0.3501	0.8101	3.5001	0.8102	25.0006	0.8103	50.0003
0.95	0.9025	0.3501	0.9025	3.5001	0.9025	25.0005	0.9025	50.0000
1.00	1.0000	0.3501	1.0000	3.5001	1.0000	25.0003	1.0000	50.0000

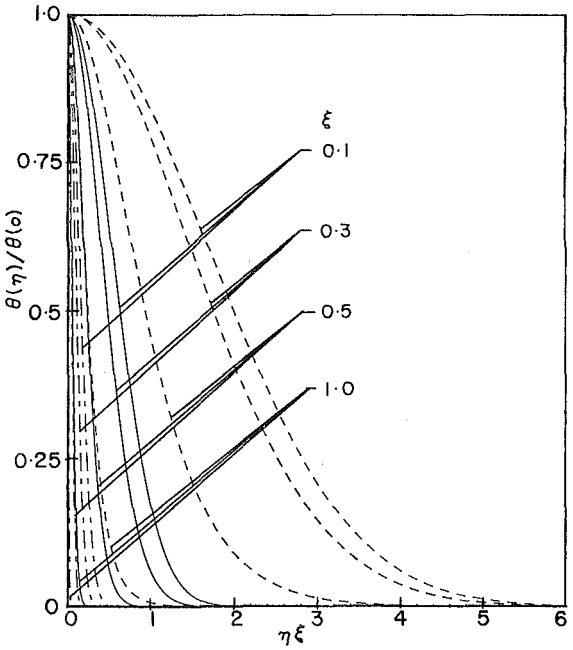

Fig. 3 Temperature ratio distribution: ····· Pr = 0.7, —— Pr = 7, – – – Pr = 100

of $\xi = 0$ by $v = (\nu/x)\,\mathrm{Gr}_x^{1/4}\,(F'/2 - F/\eta)$ and for the case of $\xi \neq 0$ by $v/u_\infty = (F'/2 - F/\eta)/(\xi \mathrm{Re}_x^{1/2})$, increases from its value of zero at the center of the plume to its maximum value, the entrainment, at the edge of the boundary layer. Its magnitude then starts to decrease and it will diminish as the radial distance continues to increase outside the boundary layer. The quantity $(F'/2 - F/\eta)/\xi$ is presented in Fig. 2 as a function of $\eta\xi$ to demonstrate the behavior of the radial velocity component v as a function of the radial position y for a fixed axial position x. The radial velocity increases and the radial distance at which that velocity is maximum decreases as the mixed convection parameter decreases (i.e., higher buoyancy effects). The maximum value of the radial velocity component is equal to the entrainment value at the edge of the boundary layer and this value increases as the Prandtl number decreases.

The centerline temperature varies inversely with the axial distance, i.e., $(T_0 - T_\infty) \sim 1/x$ and its behavior at a fixed axial position is similar to that of $\theta(0)$ (Table 1). The results show that the centerline temperature increases as the Prandtl number increases and decreases as the mixed convection parameter increases (i.e., as the free-stream velocity increases). It is also clear from these results that the centerline temperature becomes almost independent of the forced convection parameter when $\xi \geq 0.7$ and it can be expressed in that range $(0.7 \leq \xi \leq 1.0)$ by $\theta(0) = 0.5\,\mathrm{Pr}$.

The influence of the Prandtl number on the temperature distribution, $\theta = 2\pi k x \mathrm{Pr}(T - T_\infty)/Q$, can be deduced from Fig. 3, where $\theta/\theta_0 = (T - T_\infty)/(T_0 - T_\infty)$ is presented as a function of $\eta\xi$ (where θ_0 is the centerline value). The thermal boundary layer thickness decreases with increasing either the Prandtl number or the mixed convection parameter (i.e., lower buoyancy effects or higher free-stream velocities). Also at a fixed radial and axial distance (i.e., at a fixed $\eta\xi$ value), the temperature ratio θ/θ_0 increases with decreasing either the Prandtl number or the mixed convection parameter (i.e., larger buoyancy effects).

Conclusion

The temperature and velocity distributions of an axisymmetric plume are presented for fluids having Prandtl numbers of 0.7, 7, 50, and 100. The entire mixed convection regime from pure free ($\xi = 0$) to pure forced ($\xi = 1$) convection was covered by utilizing only one set of nonsimilarity variables η and ξ. The centerline velocity and the centerline temperature increase but the plume radii decrease as the Prandtl number increases and as the mixed convection parameter decreases. The entrainment velocity increases as the Prandtl number or the mixed convection parameter decreases. Mixed convection region for this plume can be specified as the region where $0.2 \leq \xi \leq 0.65$. Outside that region, either the pure free or the pure forced convection analysis can be used to estimate the centerline velocity and temperature. Comparison of the present results with the limited range of previously published results [4, 5] for this plume provides a very good agreement.

Acknowledgments

This study was supported in part by a grant from the National Science Foundation (NSF CME 79-19459).

References

1 Yih, C. S., "Free Convection Due to Point Heat Source," *Proc. Ist U.S. Natl. Congr. Appl. Mech.*, 1956, pp. 941-947.

2 Fujii, T., "The Theory of Steady Laminar Natural Convection Above a Horizontal Line Heat Source and a Point Heat Source," *Int. J. Heat Mass Transfer*, Vol. 6, 1963, pp. 597-606.

3 Mollendorf, J. C., and Gebhart, B., "Axisymmetric Natural Convection Flows Resulting From the Combined Buoyancy Effects of Thermal and Mass Diffusion," *Fifth International Heat Transfer Conference*, Tokyo, 1974.

4 Appalaswamy, A. V., and Jaluria, Y., "Axisymmetric Plume Flow in a Vertical Uniform Free Stream," *J. Appl. Mech.*, Vol. 47, 1980, pp. 667-669.

5 Afzal, N., "Mixed Convection in an Axisymmetric Buoyant Plume," *Int. J. Heat Mass Transfer*, Vol. 26, 1983, pp. 381-388.

6 Riley, D. S., and Drake, D. G., "Mixed Convection in an Axisymmetric Buoyant Plume," *J. Mech. Appl. Math.*, Vol. 36, 1983, pp. 42-54.

Experimental Studies on Thermal Performance of a Pebble Bed High-Temperature Heat Exchanger

K. Yoshikawa,[1] H. Kajiyama,[1] T. Okamura,[1] S. Kabashima,[1] H. Yamasaki,[1] S. Shioda,[1] M. Yamada,[2] T. Yokota,[2] M. Ishimura,[2] K. Nakayama,[2] K. Nakamoto,[2] and T. Sasaki[2]

Nomenclature

$A_{gp}(z)$ = heat transfer area between gas and pebble per unit volume $= 6(1-\epsilon)/d_p$, $\mathrm{m}^2/\mathrm{m}^3$

A_{gw} = heat transfer area between gas (or pebble) and insulator per unit volume $= 2/R_0$, $\mathrm{m}^2/\mathrm{m}^3$

$c_g(T_g)$ = specific heat of gas, J/kg K

$c_p(z)$ = specific heat of pebble, J/kg K

$c_w(r)$ = specific heat of insulator, J/kg K

$d_p(z)$ = diameter of pebble, m

$E_g(T_g)$ = emissivity of combustion gas

E_1 = effective emissivity between top of pebble bed and insulator of combustion chamber = 0.5 at 1400°C [1]

E_2 = effective emissivity between pebble and insulator = 0.5 at 1400°C [1]

$G(\tau)$ = inlet gas temperature, K

h_{gp} = heat transfer coefficient between gas and pebble $= h_{gpc} + h_{gpr}$, $\mathrm{W/m^2K}$

h_{gpc} = convective heat transfer coefficient between gas and pebble as a function of film temperature $= (T_g + T_p)/2 =$

[1]Tokyo Institute of Technology, Nagatsuta, Midori-ku, Yokohama, Japan
[2]Toshiba Corporation, Mita, Minato-ku, Tokyo, Japan

Contributed by the Heat Transfer Division for publication in the JOURNAL OF HEAT TRANSFER. Manuscript received by the Heat Transfer Division July 26, 1983.

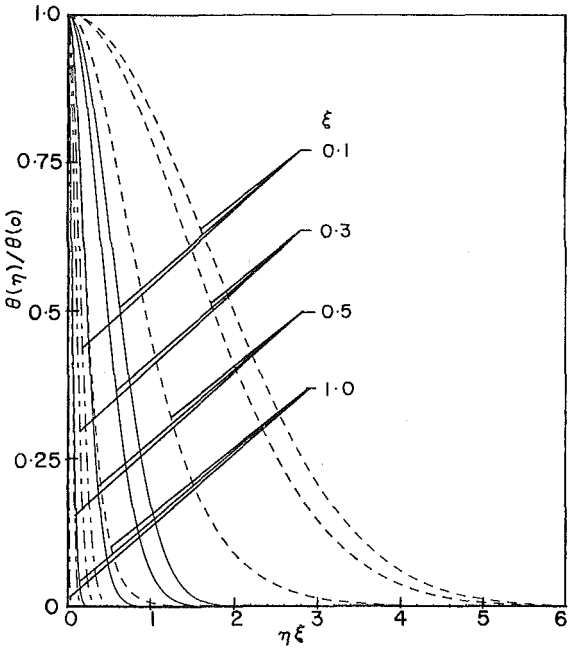

Fig. 3 Temperature ratio distribution: ····· Pr = 0.7, —— Pr = 7, – – – Pr = 100

of $\xi = 0$ by $v = (\nu/x)\,\mathrm{Gr}_x^{1/4}\,(F'/2 - F/\eta)$ and for the case of $\xi \neq 0$ by $v/u_\infty = (F'/2 - F/\eta)/(\xi \mathrm{Re}_x^{1/2})$, increases from its value of zero at the center of the plume to its maximum value, the entrainment, at the edge of the boundary layer. Its magnitude then starts to decrease and it will diminish as the radial distance continues to increase outside the boundary layer. The quantity $(F'/2 - F/\eta)/\xi$ is presented in Fig. 2 as a function of $\eta\xi$ to demonstrate the behavior of the radial velocity component v as a function of the radial position y for a fixed axial position x. The radial velocity increases and the radial distance at which that velocity is maximum decreases as the mixed convection parameter decreases (i.e., higher buoyancy effects). The maximum value of the radial velocity component is equal to the entrainment value at the edge of the boundary layer and this value increases as the Prandtl number decreases.

The centerline temperature varies inversely with the axial distance, i.e., $(T_0 - T_\infty) \sim 1/x$ and its behavior at a fixed axial position is similar to that of $\theta(0)$ (Table 1). The results show that the centerline temperature increases as the Prandtl number increases and decreases as the mixed convection parameter increases (i.e., as the free-stream velocity increases). It is also clear from these results that the centerline temperature becomes almost independent of the forced convection parameter when $\xi \geq 0.7$ and it can be expressed in that range $(0.7 \leq \xi \leq 1.0)$ by $\theta(0) = 0.5\,\mathrm{Pr}$.

The influence of the Prandtl number on the temperature distribution, $\theta = 2\pi k x \mathrm{Pr}(T - T_\infty)/Q$, can be deduced from Fig. 3, where $\theta/\theta_0 = (T - T_\infty)/(T_0 - T_\infty)$ is presented as a function of $\eta\xi$ (where θ_0 is the centerline value). The thermal boundary layer thickness decreases with increasing either the Prandtl number or the mixed convection parameter (i.e., lower buoyancy effects or higher free-stream velocities). Also at a fixed radial and axial distance (i.e., at a fixed $\eta\xi$ value), the temperature ratio θ/θ_0 increases with decreasing either the Prandtl number or the mixed convection parameter (i.e., larger buoyancy effects).

Conclusion

The temperature and velocity distributions of an axisymmetric plume are presented for fluids having Prandtl numbers of 0.7, 7, 50, and 100. The entire mixed convection regime from pure free ($\xi = 0$) to pure forced ($\xi = 1$) convection was covered by utilizing only one set of nonsimilarity variables η and ξ. The centerline velocity and the centerline temperature increase but the plume radii decrease as the Prandtl number increases and as the mixed convection parameter decreases. The entrainment velocity increases as the Prandtl number or the mixed convection parameter decreases. Mixed convection region for this plume can be specified as the region where $0.2 \leq \xi \leq 0.65$. Outside that region, either the pure free or the pure forced convection analysis can be used to estimate the centerline velocity and temperature. Comparison of the present results with the limited range of previously published results [4, 5] for this plume provides a very good agreement.

Acknowledgments

This study was supported in part by a grant from the National Science Foundation (NSF CME 79-19459).

References

1 Yih, C. S., "Free Convection Due to Point Heat Source," *Proc. Ist U.S. Natl. Congr. Appl. Mech.*, 1956, pp. 941-947.

2 Fujii, T., "The Theory of Steady Laminar Natural Convection Above a Horizontal Line Heat Source and a Point Heat Source," *Int. J. Heat Mass Transfer*, Vol. 6, 1963, pp. 597-606.

3 Mollendorf, J. C., and Gebhart, B., "Axisymmetric Natural Convection Flows Resulting From the Combined Buoyancy Effects of Thermal and Mass Diffusion," *Fifth International Heat Transfer Conference*, Tokyo, 1974.

4 Appalaswamy, A. V., and Jaluria, Y., "Axisymmetric Plume Flow in a Vertical Uniform Free Stream," *J. Appl. Mech.*, Vol. 47, 1980, pp. 667-669.

5 Afzal, N., "Mixed Convection in an Axisymmetric Buoyant Plume," *Int. J. Heat Mass Transfer*, Vol. 26, 1983, pp. 381-388.

6 Riley, D. S., and Drake, D. G., "Mixed Convection in an Axisymmetric Buoyant Plume," *J. Mech. Appl. Math.*, Vol. 36, 1983, pp. 42-54.

Experimental Studies on Thermal Performance of a Pebble Bed High-Temperature Heat Exchanger

K. Yoshikawa,[1] H. Kajiyama,[1] T. Okamura,[1] S. Kabashima,[1] H. Yamasaki,[1] S. Shioda,[1] M. Yamada,[2] T. Yokota,[2] M. Ishimura,[2] K. Nakayama,[2] K. Nakamoto,[2] and T. Sasaki[2]

Nomenclature

$A_{gp}(z)$ = heat transfer area between gas and pebble per unit volume $= 6(1-\epsilon)/d_p$, $\mathrm{m}^2/\mathrm{m}^3$

A_{gw} = heat transfer area between gas (or pebble) and insulator per unit volume $= 2/R_0$, $\mathrm{m}^2/\mathrm{m}^3$

$c_g(T_g)$ = specific heat of gas, J/kg K

$c_p(z)$ = specific heat of pebble, J/kg K

$c_w(r)$ = specific heat of insulator, J/kg K

$d_p(z)$ = diameter of pebble, m

$E_g(T_g)$ = emissivity of combustion gas

E_1 = effective emissivity between top of pebble bed and insulator of combustion chamber = 0.5 at 1400°C [1]

E_2 = effective emissivity between pebble and insulator = 0.5 at 1400°C [1]

$G(\tau)$ = inlet gas temperature, K

h_{gp} = heat transfer coefficient between gas and pebble $= h_{gpc} + h_{gpr}$, $\mathrm{W/m^2K}$

h_{gpc} = convective heat transfer coefficient between gas and pebble as a function of film temperature $= (T_g + T_p)/2 =$

[1]Tokyo Institute of Technology, Nagatsuta, Midori-ku, Yokohama, Japan
[2]Toshiba Corporation, Mita, Minato-ku, Tokyo, Japan

Contributed by the Heat Transfer Division for publication in the JOURNAL OF HEAT TRANSFER. Manuscript received by the Heat Transfer Division July 26, 1983.

$\frac{0.255}{\epsilon}\mathrm{Pr}^{1/3}\mathrm{Re}^{2/3}\frac{k_g}{d_p}$ [2], W/m²K

h_{gpr} = radiative heat transfer coefficient between gas and pebble = $\frac{\sigma}{T_g - T_p}(E_g T_g{}^4 - E_g T_p{}^4)$ (combustion gas), W/m²K; = 0 (argon), W/m²K

h_{gw} = heat transfer coefficient between gas and insulator = $h_{gwc} + h_{gwr}$, W/m²K

h_{gwc} = convective heat transfer coefficient between gas and insulator as a function of film temperature = $(T_g + T_w)/2$ =

$0.2\mathrm{Pr}^{1/3}\mathrm{Re}^{0.8}\frac{k_g}{d_p}$ [3], W/m²K

h_{gwr} = radiative heat transfer coefficient between gas and insulator = $\frac{\sigma}{T_g - T_w}(E_g T_g{}^4 - E_g T_w{}^4)$ (combustion gas), W/m²K; = 0 (argon), W/m²K

h_{pc} = radiative heat transfer coefficient between top of pebble bed and insulator of combustion chamber

$= \frac{\sigma E_1}{T_p - T_c}(T_p{}^4 - T_c{}^4)$, W/m²K

h_{pw} = radiative heat transfer coefficient between pebble and insulator

$= \frac{\sigma E_2}{T_p - T_w}(T_p{}^4 - T_w{}^4)$, W/m²K

h_{wa} = free convective heat transfer coefficient between container vessel and atmosphere

$= 1.3\left(\frac{T_w - T_a}{2R_1}\right)^{0.25}$ [4], W/m²K

$k_g(T_g)$ = thermal conductivity of gas, W/m K

$k_p(z)$ = effective thermal conductivity of pebble bed including radiative heat transfer between pebbles [5], W/m K

$k_w(r)$ = thermal conductivity of insulator, W/m K

$\dot{m}(\tau)$ = gas mass flow per unit area, kg/m²s

Pr = Prandtl number

r = radial coordinate, m

R_0 = radius of pebble bed, m

R_1 = radius of container vessel, m

Re = Reynolds number

T_a = room temperature, K

$T_c(\tau)$ = representative temperature of insulator of combustion chamber, K

$T_g(z,\tau)$ = temperature of gas in bed, K

$T_p(z,\tau)$ = temperature of pebble in bed, K

$T_w(r,z,\tau)$ = temperature of insulator, K

z = axial coordinate, m

$= 0$ { at the top of bed during heating; at the bottom of bed during argon blowdown

ϵ = void fraction of bed

$\rho_p(z)$ = density of pebble, kg/m³

$\rho_w(r)$ = density of insulator, kg/m³

σ = Stefan–Boltzmann constant, W/m²K⁴

τ = time, s

Δr = radial differential step of insulator, m

Δz = axial differential step of pebble bed, m

$\Delta\tau$ = differential step of time, s

Introduction

High-temperature pure gases such as air and inert gases are required in many areas, for example, chemical processes, electric power generation (closed cycle MHD and closed cycle gas turbine), and hypersonic windtunnel experiments.

A fossil fuel fired regenerative heat exchanger is capable of heating pure gases over 1500°C. Its operating principle is the same as that of heat exchangers used in blast furnaces with the added evacuation of the heat exchanger before blowing pure gases into it. This evacuation is to realize low impurity contamination levels of pure gases.

In the previous experiment [6], a regenerative heat exchanger with an alumina cored brick bed was tested. The maximum temperatures of cored bricks and argon reached in their experiment are 1621°C and 1482°C, respectively, and the molecular impurity level in argon is less than 100 ppm.

Another choice of a heat storage bed is a pebble bed. A pebble bed-type heat exchanger can be designed to be compact because of a large heat transfer conductance between gas and pebbles. In addition, compared with cored bricks, pebbles are expected to be more resistant against cracking caused by the thermal stress, because their small size and the low thermal conductivity among pebbles realize the uniform distribution of temperature in one pebble. But the pressure loss and dust loading of pure gas passing through a pebble bed may cause some difficulties and almost no investigations have been reported on the selection of pebble material which is appropriate for the use under high temperatures over 1700°C and generates less dust.

Many theoretical works have been done on the thermal analysis of regenerative heat exchangers. But there are few works in which detailed temperature distributions in heat storage beds are measured especially in the high-temperature region above 1500°C and discussions are made about the comparison of measured results and theoretical predictions.

In this study, a pebble bed regenerative heat exchanger for heating argon up to 1700°C is installed and tested. One purpose of the experiments is to select the appropriate pebble material which has high thermal and thermal shock resistances and generates less dust in heated argon. Another purpose is to measure the time changes of the temperature distribution in the pebble bed and to compare them with the results of a heat transfer analysis.

Experimental Facility and Procedure

The system and the specification of the heat exchanger are shown in Fig. 1 and Table 1, respectively. The heat exchanger consists of a burner, a pebble bed, an insulator, and a container vessel. The height and the diameter of the pebble bed are 1.05 m and 0.2 m respectively and it is filled with 20-mm-dia alumina pebbles of which material properties are shown in Table 2. The bed is surrounded by three layered insulating alumina walls with 0.25 m thickness, whose properties are shown in Table 3.

To prevent water condensation inside the container vessel and the pipes during combustion, the vessel and the pipes are heated up to 100°C by electrical heaters, and also heated air (100°C) is blown into the bed for about 20 hr before the start of combustion. This is to avoid water contamination in heated argon. In the burner, propane is combusted with air or oxygen-enriched air. A part of combustion gas flows through the bed from the top to the bottom heating pebbles while the rest of it is bypassed to the argon exhaust pipe directly from the combustion chamber. This is to raise the temperature at the top of the bed as high as possible keeping the temperature at the bottom moderate, because if all the combustion gas flows through the bed of a small height, the temperature at the bottom may become too high to protect pebbles against a strong thermal shock. A typical heating process of the bed is

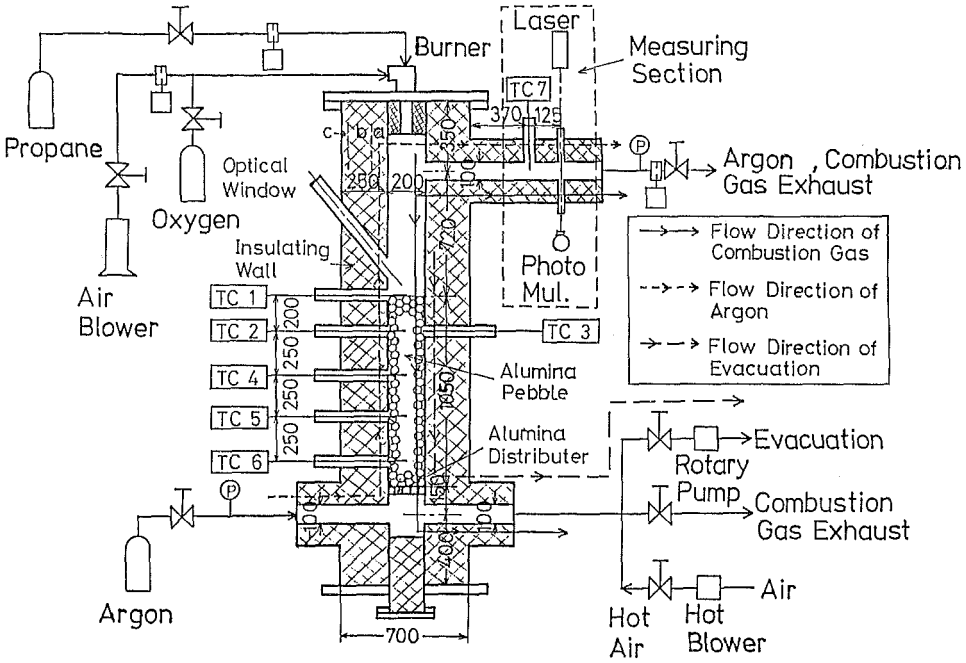

Fig. 1 System of the heat exchanger

Table 1 Specifications of the heat exchanger

Pebble bed diameter	200 mm
Pebble bed height	1050 mm
Pebble weight	67 ∿ 75 kg
Pebble bed void fraction	0.4
Thickness of insulating wall	250 mm
Rated capacity of burner	72.6 kW
Combustion gas mass flow	0.003 ∿ 0.027 kg/s
Argon gas mass flow	0.1 ∿ 0.15 kg/s
Heating time	40 ∿ 60 h
Argon blowing time	60 ∿ 120 s
Pumping speed of the rotary pump	0.05 m^3/s

Table 2 Material properties of the pebble

Name	T-162	HD	SSA-995
Maker	ALCOA	NIPPON KAGAKU TOGYO	
Fabrication method	Sintered alpha alumina	Isostatically pressed sintered alpha alumina	
Diameter (mm)	20	20	20
Alumina purity (%)	99.5	90	99.5
Apparent porosity (%)	3.0	0	0
Specific gravity	3.6 ~ 3.8	3.6	3.9
Specific heat (kJ/kg K)	1.3	1.3	1.3
Thermal conductivity (W/m K)	1.6	6.7	8.4

Table 3 Material properties of the insulating wall

Layer number	a	b	c
Name	CORANDEX-E3	TOLITE-HA-S	F.F #150 BOARD
Maker	TOSHIBA CERAMICS		
Thickness (mm)	100	140	10
Alumina purity (%)	99.1	99.1	72.0
Apparent porosity (%)	20.0	57.1	
Specific gravity	3.15	1.48	0.3
Specific heat (kJ/kgK)	1.3	1.3	1.3
Thermal conductivity (W/mK)	3.1	0.9	0.08

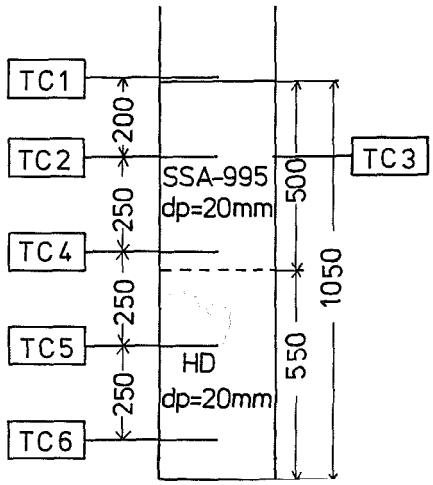

Fig. 2 Location of thermocouples and configuration of packed pebbles in the bed (run 10)

shown in Fig. 3 in which we show the combustion gas mass flow through the bed as Main. After stopping the burner, the container vessel is evacuated by a rotary pump. Then cold argon is injected into the bed from the bottom to the top for about 1 ~ 2 minutes. After that, combustion starts again to reheat the bed for several hours for the next argon blowdown.

Thus the whole operation process consists of five different periods: the preheating, the heating, the evacuation, the argon blowdown, and the reheating.

Temperature distribution in the pebble bed is measured by thermocouples TC1 ~ TC6 inserted in the bed. The location of thermocouples and a typical configuration of packed pebbles in the bed is shown in Fig. 2. The temperature of the heated argon is estimated from the data measured with the thermocouple TC7 located at the exit of the heat exchanger by correcting for radiative losses to walls. Dust loading of the

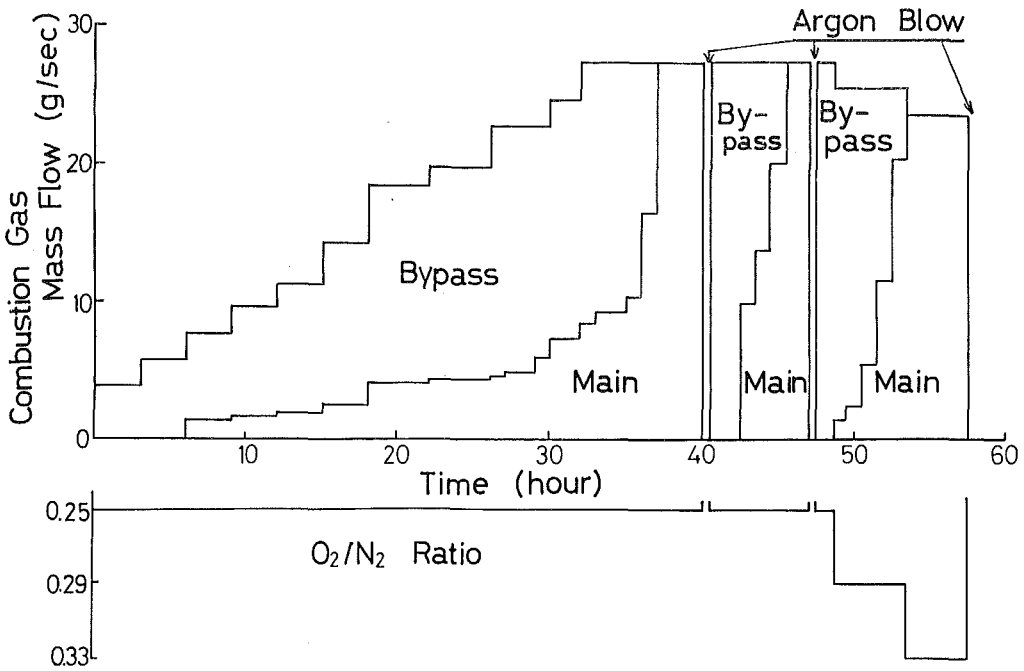

Fig. 3 Heating process of the heat exchanger (run 10)

heated argon is observed by detecting the fluctuation of the intensity of He-Ne laser beam which is transmitted through the argon flow. The optical system is shown in Fig. 1.

Heat Transfer Analysis

A heat transfer analysis has been done to explain the changes of the temperature distribution in the bed during the heating and the argon blowdown periods. The basic equations for the heat transfer between the gases, the pebbles and the insulator are

$$-\dot{m}c_g \frac{\partial T_g}{\partial z} = A_{gp}h_{gp}(T_g - T_p) + A_{gw}h_{gw}(T_g - (T_w)_{r=R_0}) \quad (1)$$

$$(1-\epsilon)\rho_p c_p \frac{\partial T_p}{\partial \tau} = A_{gp}h_{gp}(T_g - T_p) - A_{gw}h_{pw}(T_p - (T_w)_{r=R_0}) + k_p \frac{\partial^2 T_p}{\partial z^2} \quad (2)$$

$$\frac{\partial T_w}{\partial \tau} = \frac{k_w}{\rho_w c_w}\left(\frac{\partial^2 T_w}{\partial r^2} + \frac{1}{r}\frac{\partial T_w}{\partial r}\right) \quad (3)$$

where we neglect radial heat conduction in the bed and axial heat conduction in the insulator. Equation (1) shows the energy balance for the gas including heat transfer between the gas and the pebbles and between the gas and the insulator. In this equation, the $\partial T_g/\partial \tau$ term is neglected because it is small compared with the $\partial T_g/\partial z$ term. In equation (2) of energy balance for the pebbles, the effects of heat transfer between the pebbles and the gas and between the pebbles and the insulator together with axial heat conduction in the bed are included. Equation (3) gives the effect of transient radial heat conduction in the insulator.

The boundary conditions assumed are

$$T_g(0,\tau) = G(\tau) \quad (4)$$

for the inlet gas temperature,

$$h_{pc}(T_c - T_p) + k_p \frac{\partial T_p}{\partial z} = 0 \quad \text{(at the top of the bed)} \quad (5)$$

$$\frac{\partial T_p}{\partial z} = 0 \text{ (at the bottom of the bed)} \quad (6)$$

for the pebble temperature,

$$h_{gw}(T_g - T_w) + h_{pw}(T_p - T_w) + k_w \frac{\partial T_w}{\partial r} = 0 \quad (\text{at } r = R_0) \quad (7)$$

for the boundary between the pebble bed and the insulator, and

$$h_{wa}(T_w - T_a) + k_w \frac{\partial T_w}{\partial r} = 0 \,(\text{at } r = R_1) \quad (8)$$

for the outer boundary of the container vessel.

The inlet gas temperature $G(\tau)$ for the argon blowdown period is assumed to be constant ($=23°C$) because cold argon is injected into the bed. For the heating period, $G(\tau)$ and $T_c(\tau)$ are introduced to simplify the complex heat transfer process in the combustion chamber. Their values are assumed so that the measured and the calculated temperature of the pebbles at the top and at the height of 0.85 m are matched.

The initial temperature distribution in the bed for each period is adjusted to the measured one at the beginning of each period. The initial temperature distribution in the insulator is taken to be uniform for the preheating period ($=23°C$). For the other periods, it is taken for the calculated one at the end of the preceding period.

The time change of the combustion gas mass flow through the bed is assumed as that presented in Fig. 3 as Main while the argon mass flow is assumed to be constant ($=0.1$ kg/s).

By applying central difference representation to the first and second derivatives with respect to z and r, and by applying forward difference representation to the first derivative with respect to τ, the differential equations are transformed into a set of algebraic equations and numerically solved. To fulfill the numerical stability criterion given in [7], we put $\Delta r = 0.02$ m, $\Delta z = 0.025$ m, and $\Delta \tau = 30$ s for the heating period, and $\Delta \tau = 0.5$ s for the argon blowdown period.

Results and Discussion

Thermal Performance. Figure 4 shows the time change of the temperature distribution in the bed during the heating

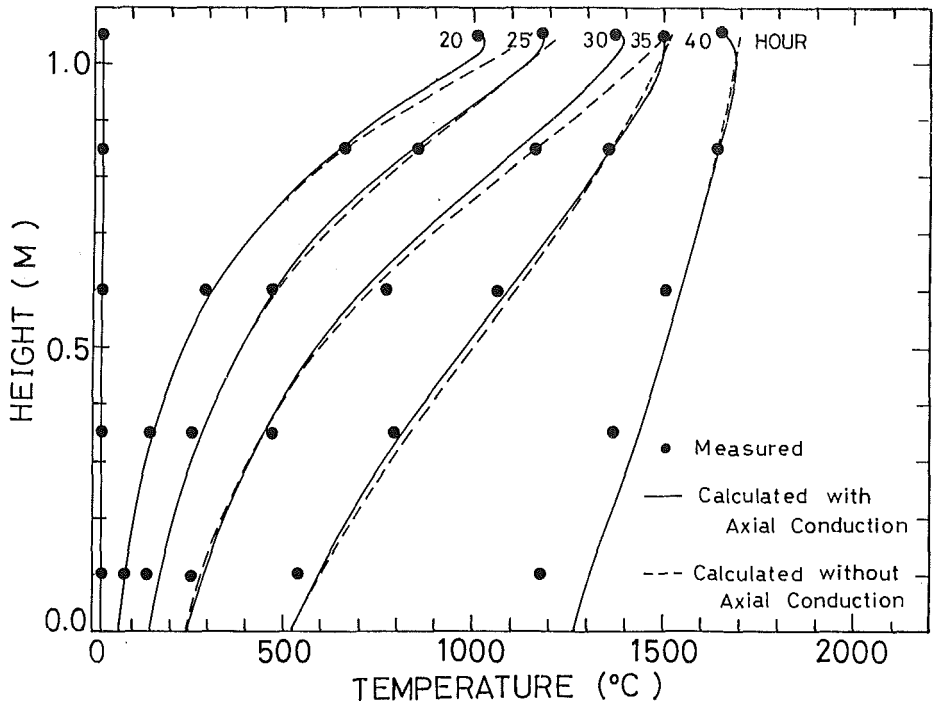

Fig. 4 Time history of temperature distribution in the bed during the heating period (run 10)

period of run 10 whose heating process is shown in Fig. 3. In this heating period, propane is combusted in air without oxygen enrichment, and the final temperature at the top of the bed is 1650°C while the temperature at the bottom is 1100°C. In Fig. 4, to evaluate the effects of the values of $G(\tau)$ and $T_c(\tau)$ on the calculation, the calculated results with and without the axial heat conduction term $k_p \partial^2 T_p / \partial z^2$ in equation (2) are compared with the measured data. In the case of neglecting the axial heat conduction, the boundary condition of equation (5) becomes unnecessary. Thus we can avoid the introduction of $T_c(\tau)$, and we assume the values of $G(\tau)$ only to match the measured and the calculated temperatures of pebbles at the height of 0.85 m. Both calculated results are almost the same except near the top of the bed where the effect of axial heat conduction is large due to radiative heat transfer from the top of the bed to the insulator of the combustion chamber. Therefore, we can say that the values of $G(\tau)$ and $T_c(\tau)$ and the axial heat conduction in the pebble bed have little effect on the heat transfer calculation in the lower part of the bed. The calculated results agree well with the measured ones. The calculated temperature at the bottom of the bed is somewhat higher than the measured one at the final stage of the heating period. The calculated temperature of the insulator rises more rapidly than the measured one, because the heat transfer between the gas (or pebbles) and the insulator occurs only adjacent to the insulator and is overestimated in the present one-dimensional analysis. The higher calculated temperature of the insulator causes a smaller heat loss from the bed to the insulator, resulting in a rapid rise of the calculated temperature at the bottom of the bed in the final stage of heating.

In the second reheating period of run 10, propane is combusted in oxygen-enriched air as shown in Fig. 3 to raise the flame temperature. As a result, the temperature at the top of the bed is increased to 1850°C while the temperature at the bottom remains 1100°C at the end of the second reheating period. Figure 5 shows the measured temperature changes in the bed after stopping combustion together with the calculated one during the argon blowdown following this

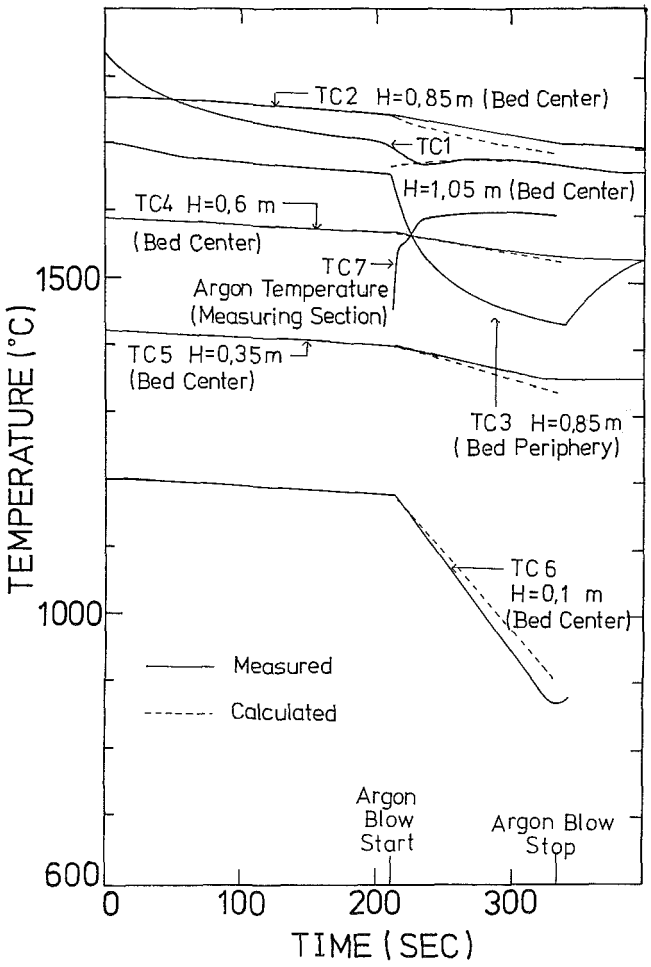

Fig. 5 Temperature changes in the bed and of argon after stopping combustion (the third argon blowdown of run 10)

reheating period. For this argon blowdown period, the calculation correctly predicts the temperature changes in the bed. During this period, the heat transfer between the pebbles and argon is the main heat transfer process and the effect of the heat transfer to the insulator is small, which results in good agreement between the calculation and the measured results. In this argon blowdown, the argon temperature of 1600°C is obtained at the exit of the heat exchanger, which is about 100°C lower than the argon temperature just above the center of the top of the bed. This temperature difference can be explained by the mixing of argon passing through the core and the wall regions of the bed, because the temperature of argon passing through the wall region is much lower than that of argon passing through the core region, as can be seen from the data of TC2 and TC3.

Selection of the Pebble Material

Dust loading in the heated argon flow is observed by detecting the fluctuations of the intensity of the transmitted laser beam caused by dust in argon flow after passing through the pebble bed. As candidates for pebble material, the T-162 pebbles, the HD pebbles, and the SSA-995 pebbles are tested. The T-162 pebbles are commonly used as the heat exchange medium for pebble heaters while the isostatically pressed HD and SSA-995 pebbles are used for grinding medium. In one run, the T-162 pebbles are packed in the whole bed while in another run, as shown in Fig. 2, the SSA-995 pebbles are packed in the upper part of the bed and the HD pebbles are packed in the lower part of the bed. The average fluctuation level in the former run is about 16 percent while that in the latter run is about 2 percent. These results show that an amount of dust in the heated argon is much larger for the T-162 pebbles than for the HD and the SSA-995 pebbles. The latter pebbles have no abrasion, cracking, and melting throughout the bed after ten blowdown cycles (total heating time is about 200 hr). Therefore, the SSA-995 pebbles show high thermal resistance even when they are exposed to high-temperature combustion gas as high as 1900°C, and the HD pebbles show high thermal shock resistance at the bottom of the bed where pebbles are cooled abruptly by the cold argon. Since the SSA-995 pebbles are of higher alumina purity and thus more expensive than the HD pebbles, we can divide the bed into two layers: the SSA-995 pebbles in the upper part of the bed and the HD pebbles in the lower part of the bed.

Conclusions

A pebble bed regenerative heat exchanger for heating argon by propane combustion gas is installed and tested. The maximum temperature at the top of the bed is 1850°C and that of argon at the exit of the heat exchanger is 1600°C. The one-dimensional heat transfer analysis correctly explains the changes of the temperature distribution in the bed during the heating and the argon blowdown periods. The isostatically pressed high-purity alumina pebbles with zero porosity demonstrated good properties as the heat storage material.

Acknowledgments

The authors acknowledge Professor J. F. Louis of the Massachusetts Institute of Technology for improving the English of the paper. The work reported here was partly supported by a Grant-in-Aid from the Ministry of Education, Contract No. 505024, Japan.

References

1 Thomas, H. P., Murray, T. P., and Shepard, R. L., *Temperature—Its Measurement and Control in Science and Industry*, Vol. 4, Instrumental Society of America, Pittsburgh, 1972, p. 299.

2 Handley, D., and Heggs, P. J., "Momentum and Heat Transfer Mechanisms in Regular Shaped Packings," *Transactions of the Institution of Chemical Engineers*, Vol. 46, 1968, pp. T251-T264.

3 Dixon, A. G., and Cresswell, D. L., "Theoretical Prediction of Effective Heat Transfer Parameters in Packed Beds," *AIChE Journal*, Vol. 25, 1979, pp. 663-676.

4 McAdams, W. H., *Heat Transmission*, 3rd ed., McGraw-Hill, New York, 1954, p. 173.

5 Sakae, Y., and Daizo, K., "Studies on Effective Thermal Conductivities in Packed Beds," *Chemical Engineering* (Japan), Vol. 18, 1954, pp. 576-585.

6 Cook, C. S., and Dickinson, K. M., "Argon Contamination Associated With Ceramic Regenerative Heat Exchangers for Closed Cycle MHD," *Proceedings of the 16th Symposium on Engineering Aspects of Magnetohydrodynamics*, 1977, pp. II.4.22-30.

7 Croft, D. R., and Lilley, D. G., *Heat Transfer Calculations Using Finite Difference Equations*, Applied Science Publishers, London, 1977, p. 106.

Transient Response of the Parallel-Flow Heat Exchanger

F. E. Romie[1]

Nomenclature

A_x = cross-sectional flow area, m^2
c = unit heat capacitance of fluid, J/C • kg
E = $(wc)_b/(wc)_a$
hA = convective thermal conductance, W/C
L = flow length of exchanger, m
N = hA/wc
Ntu = defined following equation (3)
p = Laplace parameter
R = $(hA)_b/(hA)_a$
s = Laplace parameter
t = time, s
T = core temperature, °C
u = velocity of fluid in core, m/s
V = defined following equation (3)
wc = capacitance rate of fluid, W/C
WC = thermal capacitance of core, J/C
x = distance from fluid entrance, m
X = x/L
η = $\theta Ntu\,(1+R)/R$
θ = $[(wc)_{\min}/WC]\,(t-x/u_a)$
ν = variable of integration
ρ = fluid density, kg/m^3
τ = fluid temperature, °C
$\bar{\tau}$ = exit fluid temperature, °C

Subscripts

a = refers to stepped fluid
b = refers to unstepped fluid
p = denotes Laplace transform w/r to X
s = denotes Laplace transform w/r to η
∞ = refers to steady-state response

Introduction

The transient response of heat exchangers is required for process control applications. The purpose of this note is to give, for the parallel-flow heat exchanger, the exit fluid temperature histories that are obtained in response to a unit step increase in the entrance temperature of either fluid. The solutions given are restricted to exchangers in which the dwell or residence times of the two fluids are equal or, alternatively, to exchangers in which both fluids are gases.

Differential Equations

The exchanger analyzed, shown schematically in Fig. 1, satisfies the following idealizations.

[1] Palos Verdes Estates, CA 90274, Life Mem. ASME

Contributed by the Heat Transfer Division for publication in the JOURNAL OF HEAT TRANSFER. Manuscript received by the Heat Transfer Division April 26, 1984.

reheating period. For this argon blowdown period, the calculation correctly predicts the temperature changes in the bed. During this period, the heat transfer between the pebbles and argon is the main heat transfer process and the effect of the heat transfer to the insulator is small, which results in good agreement between the calculation and the measured results. In this argon blowdown, the argon temperature of 1600°C is obtained at the exit of the heat exchanger, which is about 100°C lower than the argon temperature just above the center of the top of the bed. This temperature difference can be explained by the mixing of argon passing through the core and the wall regions of the bed, because the temperature of argon passing through the wall region is much lower than that of argon passing through the core region, as can be seen from the data of TC2 and TC3.

Selection of the Pebble Material

Dust loading in the heated argon flow is observed by detecting the fluctuations of the intensity of the transmitted laser beam caused by dust in argon flow after passing through the pebble bed. As candidates for pebble material, the T-162 pebbles, the HD pebbles, and the SSA-995 pebbles are tested. The T-162 pebbles are commonly used as the heat exchange medium for pebble heaters while the isostatically pressed HD and SSA-995 pebbles are used for grinding medium. In one run, the T-162 pebbles are packed in the whole bed while in another run, as shown in Fig. 2, the SSA-995 pebbles are packed in the upper part of the bed and the HD pebbles are packed in the lower part of the bed. The average fluctuation level in the former run is about 16 percent while that in the latter run is about 2 percent. These results show that an amount of dust in the heated argon is much larger for the T-162 pebbles than for the HD and the SSA-995 pebbles. The latter pebbles have no abrasion, cracking, and melting throughout the bed after ten blowdown cycles (total heating time is about 200 hr). Therefore, the SSA-995 pebbles show high thermal resistance even when they are exposed to high-temperature combustion gas as high as 1900°C, and the HD pebbles show high thermal shock resistance at the bottom of the bed where pebbles are cooled abruptly by the cold argon. Since the SSA-995 pebbles are of higher alumina purity and thus more expensive than the HD pebbles, we can divide the bed into two layers: the SSA-995 pebbles in the upper part of the bed and the HD pebbles in the lower part of the bed.

Conclusions

A pebble bed regenerative heat exchanger for heating argon by propane combustion gas is installed and tested. The maximum temperature at the top of the bed is 1850°C and that of argon at the exit of the heat exchanger is 1600°C. The one-dimensional heat transfer analysis correctly explains the changes of the temperature distribution in the bed during the heating and the argon blowdown periods. The isostatically pressed high-purity alumina pebbles with zero porosity demonstrated good properties as the heat storage material.

Acknowledgments

The authors acknowledge Professor J. F. Louis of the Massachusetts Institute of Technology for improving the English of the paper. The work reported here was partly supported by a Grant-in-Aid from the Ministry of Education, Contract No. 505024, Japan.

References

1 Thomas, H. P., Murray, T. P., and Shepard, R. L., *Temperature—Its Measurement and Control in Science and Industry*, Vol. 4, Instrumental Society of America, Pittsburgh, 1972, p. 299.

2 Handley, D., and Heggs, P. J., "Momentum and Heat Transfer Mechanisms in Regular Shaped Packings," *Transactions of the Institution of Chemical Engineers*, Vol. 46, 1968, pp. T251-T264.

3 Dixon, A. G., and Cresswell, D. L., "Theoretical Prediction of Effective Heat Transfer Parameters in Packed Beds," *AIChE Journal*, Vol. 25, 1979, pp. 663-676.

4 McAdams, W. H., *Heat Transmission*, 3rd ed., McGraw-Hill, New York, 1954, p. 173.

5 Sakae, Y., and Daizo, K., "Studies on Effective Thermal Conductivities in Packed Beds," *Chemical Engineering* (Japan), Vol. 18, 1954, pp. 576-585.

6 Cook, C. S., and Dickinson, K. M., "Argon Contamination Associated With Ceramic Regenerative Heat Exchangers for Closed Cycle MHD," *Proceedings of the 16th Symposium on Engineering Aspects of Magnetohydrodynamics*, 1977, pp. II.4.22-30.

7 Croft, D. R., and Lilley, D. G., *Heat Transfer Calculations Using Finite Difference Equations*, Applied Science Publishers, London, 1977, p. 106.

Transient Response of the Parallel-Flow Heat Exchanger

F. E. Romie[1]

Nomenclature

A_x = cross-sectional flow area, m^2
c = unit heat capacitance of fluid, J/C • kg
E = $(wc)_b/(wc)_a$
hA = convective thermal conductance, W/C
L = flow length of exchanger, m
N = hA/wc
Ntu = defined following equation (3)
p = Laplace parameter
R = $(hA)_b/(hA)_a$
s = Laplace parameter
t = time, s
T = core temperature, °C
u = velocity of fluid in core, m/s
V = defined following equation (3)
wc = capacitance rate of fluid, W/C
WC = thermal capacitance of core, J/C
x = distance from fluid entrance, m
X = x/L
η = $\theta Ntu\,(1+R)/R$
θ = $[(wc)_{\min}/WC]\,(t-x/u_a)$
ν = variable of integration
ρ = fluid density, kg/m^3
τ = fluid temperature, °C
$\bar{\tau}$ = exit fluid temperature, °C

Subscripts

a = refers to stepped fluid
b = refers to unstepped fluid
p = denotes Laplace transform w/r to X
s = denotes Laplace transform w/r to η
∞ = refers to steady-state response

Introduction

The transient response of heat exchangers is required for process control applications. The purpose of this note is to give, for the parallel-flow heat exchanger, the exit fluid temperature histories that are obtained in response to a unit step increase in the entrance temperature of either fluid. The solutions given are restricted to exchangers in which the dwell or residence times of the two fluids are equal or, alternatively, to exchangers in which both fluids are gases.

Differential Equations

The exchanger analyzed, shown schematically in Fig. 1, satisfies the following idealizations.

[1] Palos Verdes Estates, CA 90274, Life Mem. ASME

Contributed by the Heat Transfer Division for publication in the JOURNAL OF HEAT TRANSFER. Manuscript received by the Heat Transfer Division April 26, 1984.

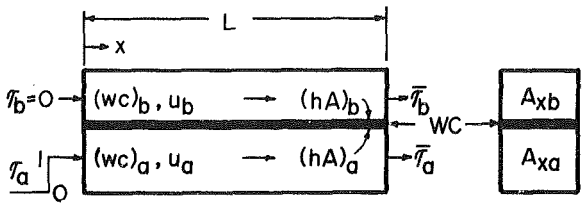

Fig. 1 Schematic of the parallel-flow heat exchanger

1 The capacitance rates $(wc)_a$ and $(wc)_b$ of the two fluids are uniform and constant as are the thermal conductances $(hA)_a$ and $(hA)_b$, the thermal capacitance WC of the exchanger core, and the flow velocities u_a and u_b.

2 No heat is conducted in the axial direction in either the exchanger core or the two fluids.

3 The core wall offers no thermal resistance to flow of heat from one fluid to the other.

4 No heat passes into or through the exchanger shell or shroud.

Three partial differential equations suffice to define the behavior of the exchanger. An energy balance on an elemental length of the exchanger core gives the first equation.

$$WC\frac{\partial T}{\partial t} = (hA)_a(\tau_a - T) + (hA)_b(\tau_b - T) \tag{1}$$

The remaining two equations relate the heat flow from the core element to the change in temperature of the two fluids.

$$(hA)_a(T-\tau_a) = L(A_x\rho c)_a\left[\frac{\partial \tau_a}{\partial t} + u_a\frac{\partial \tau_a}{\partial x}\right] \tag{2}$$

$$(hA)_b(T-\tau_b) = L(A_x\rho c)_b\left[\frac{\partial \tau_b}{\partial t} + u_b\frac{\partial \tau_b}{\partial x}\right] \tag{3}$$

These three equations will be written using the following dimensionless variables and parameters.

$$\theta = (t - x/u_a)[(wc)_{\min}/WC], X = x/L, E = (wc)_b/(wc)_a$$

$$R = (hA)_b/(hA)_a, \frac{1}{Ntu} = (wc)_{\min}\left(\frac{1}{(hA)_a} + \frac{1}{(hA)_b}\right)$$

$$V = [(wc)_{\min}/WC](L/u_b - L/u_a),$$

$$N_a = (hA)_a/(wc)_a, N_b = (hA)_b/(wc)_b$$

The capacitance rate $(wc)_{\min}$ is the lesser of $(wc)_a$ and $(wc)_b$. The parameters N_a and N_b are not independent of Ntu, E, and R. From the definitions of the five parameters,

$$N_a = ENtu(1+R)/R, N_b = Ntu(1+R), (E \le 1) \tag{4}$$

$$N_a = Ntu(1+R)/R, N_b = Ntu(1+R)/E, (E > 1) \tag{5}$$

Introduction of the variable θ requires a change of variable in equations (1), (2), and (3). With the change of variable and the continuity relations, $(wc)_a = (\rho cA_x)_a u_a$ and $(wc)_b = (\rho cA_x)_b u_b$, the equations become,

$$\frac{\partial T}{\partial \theta} = Ntu\frac{(1+R)}{R}(\tau_a - T) + Ntu(1+R)(\tau_b - T) \tag{6}$$

$$N_a(T-\tau_a) = \frac{\partial \tau_a}{\partial X} \tag{7}$$

$$N_b(T-\tau_b) = \frac{\partial \tau_b}{\partial X} + V\frac{\partial \tau_b}{\partial \theta} \tag{8}$$

The solutions of these equations, with $V = 0$, are found for a unit step increase of the inlet temperature of fluid a: $\tau_a = \tau_b = T = 0$ for $\theta < 0$ and $\tau_a\,(x = 0) = 1$ and $\tau_b\,(x = 0) = 0$ for $\theta \ge 0$. The parameter V will be zero if the two flow velocities are equal. If both fluids are gases then, typically, the absolute value of V will be very small ($\lesssim 0.01$) and can be equated to zero whether or not the gas velocities are equal. The times L/u_a and L/u_b for liquids can be generalized (consider only the axial components of u_a and u_b) to the dwell or residence times of an average particle of fluid in the exchanger. Thus in a baffled exchanger replace L/u_a and L/u_b by the dwell times which must be the same for both liquids. Either fluid can be fluid a which is always the stepped fluid.

The value of τ_a at $\theta = 0$ can be found by following the first cross-sectional fluid a lamina which enters at $t = 0$ and $x = 0$ with a temperature of unity and flows through the core with a velocity u_a. This first lamina sees the wall at zero temperature. Therefore its temperature, from equation (7), is exp $(-N_a\,x/L)$. The exit temperature, $\bar{\tau}_a$, of fluid a [$\bar{\tau}_a = \tau_a\,(x = L)$] is thus zero for $t < L/u_a$ ($\theta < 0$) and jumps to exp $(-N_a)$ when $t = L/u_a$ ($\theta = 0$). The time L/u_a is the delay in the response of the fluid a exit temperature. The exit temperature $\bar{\tau}_b$ of fluid b [$\bar{\tau}_b = \tau_b\,(x = L)$] has no discontinuity in its response but does have, with $u_a = u_b$, the same delay time. For gases the delay time L/u_a (and L/u_b) will be found to be small compared to the duration of the transient and can be ignored.

Solution of the Equations

For brevity of notation define $\eta = \theta\,Ntu\,(1 + R)/R$ so that equation (6) simplifies to:

$$\frac{\partial T}{\partial \eta} = (\tau_a - T) + R(\tau_b - T) \tag{9}$$

The Laplace transforms of equations (7), (8), and (9) (with $V = 0$) are taken with respect to η using s as the Laplace parameter. The Laplace transform of the resultant equations is then taken with respect to X using p as the Laplace parameter. The equations so obtained are solved for the double Laplace transforms, τ_{asp} and τ_{bsp}, of τ_a and τ_b.

$$\tau_{asp} = \frac{N_b + p(1+R) + s(p+N_b)}{s[s(p+N_a)(p+N_b) + p(R(p+N_a) + (p+N_b))]} \tag{10}$$

$$\tau_{bsp} = \frac{N_b}{s[s(p+N_a)(p+N_b) + p(R(p+N_a) + (p+N_b))]} \tag{11}$$

The inverse transforms with respect to s can be found using standard Laplace transform tables.

$$\tau_{ap} = \frac{N_b/(1+R) + p}{p\left(p + \dfrac{N_b + N_aR}{1+R}\right)} - G_p - L_p \tag{12}$$

$$\tau_{bp} = \frac{N_b/(1+R)}{p\left(p + \dfrac{N_b + N_aR}{1+R}\right)} - G_p \tag{13}$$

In these two equations

$$G_p = \frac{N_b}{p(p(1+R) + N_aR + N_b)} e^{-\frac{\eta p}{p+N_a}} e^{-\frac{\eta Rp}{p+N_b}} \tag{14}$$

$$L_p = \frac{N_a - N_b}{(p+N_a)(p(1+R) + RN_a + N_b)} e^{-\frac{\eta p}{p+N_a}} e^{-\frac{\eta Rp}{p+N_b}} \tag{15}$$

The inverse transforms G and L of G_p and L_p can be found using Table 1 of [1] and the convolution integral. The following expressions for G and L are for $X = 1$.

$$G = \frac{N_b}{(1+R)} e^{+\frac{\eta R(1+E)}{R-E}} \int_0^1 e^{-\frac{N_b(1+E)\nu}{1+R}} H_0(\eta, N_a(1-\nu)) H_0\left(\frac{\eta R(1+R)}{R-E}, \frac{N_b(R-E)\nu}{1+R}\right) d\nu \tag{16}$$

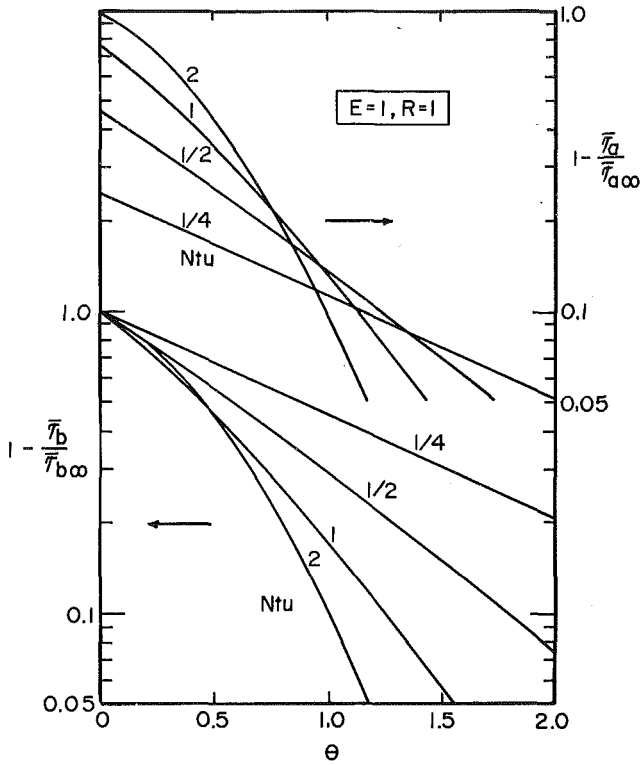

Fig. 2 Complements of the normalized responses

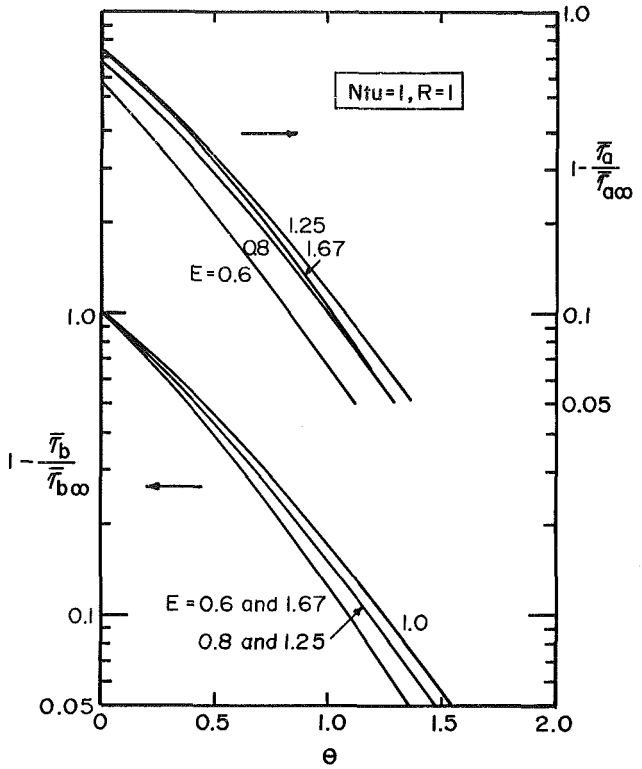

Fig. 3 Complements of the normalized responses

$$L = N_a e^{+\frac{\eta R(1+E)}{E-R}} \left\{ \frac{E-R}{E(1+R)} \int_0^1 e^{-\frac{N_b(1+E)\nu}{1+R}} H_0(\eta R, N_b(1-\nu)) \right.$$

$$H_0\left(\frac{\eta E(1+R)}{E-R}, \frac{N_a(E-R)\nu}{E(1+R)}\right) d\nu$$

$$- \int_0^1 e^{-\frac{N_b(1+E)\nu}{1+R}} H_0(\eta R, N_b(1-\nu)) K_0$$

$$\left.\left(\frac{\eta(1+R)E}{E-R}, \frac{N_a(E-R)\nu}{E(1+R)}\right) d\nu \right\} \tag{17}$$

When $E = R$ or equivalently when $N_a = N_b$, the term L is zero and

$$G = \frac{N_b}{1+R} \int_0^1 H_0(\eta, N_a(1-\nu)) B(\eta R, N_b \nu) d\nu, (E = R) \tag{18}$$

The exit fluid temperature responses are:

$$\bar{\tau}_a = \bar{\tau}_{a\infty} - G - L \tag{19}$$

$$\bar{\tau}_b = \bar{\tau}_{b\infty} - G \tag{20}$$

The terms $\bar{\tau}_{a\infty}$ and $\bar{\tau}_{b\infty}$ are the steady-state responses $(\theta \to \infty)$.

$$\bar{\tau}_{b\infty} = \frac{1 - e^{-\frac{N_b(1+E)}{1+R}}}{1+E} \tag{21}$$

and

$$\bar{\tau}_{a\infty} = 1 - E\bar{\tau}_{b\infty} \tag{22}$$

It can be shown that

$$\bar{\tau}_{b\infty}(Ntu, E) = \frac{1}{E} \bar{\tau}_{b\infty}\left(Ntu, \frac{1}{E}\right) \tag{23}$$

When $E \leq 1$, $\bar{\tau}_{b\infty}$ is the thermal effectiveness of the exchanger.

The functions $H_0(u, v)$, $K_0(u, v)$ and $B(u, v)$ are well known [2, 3, 4].

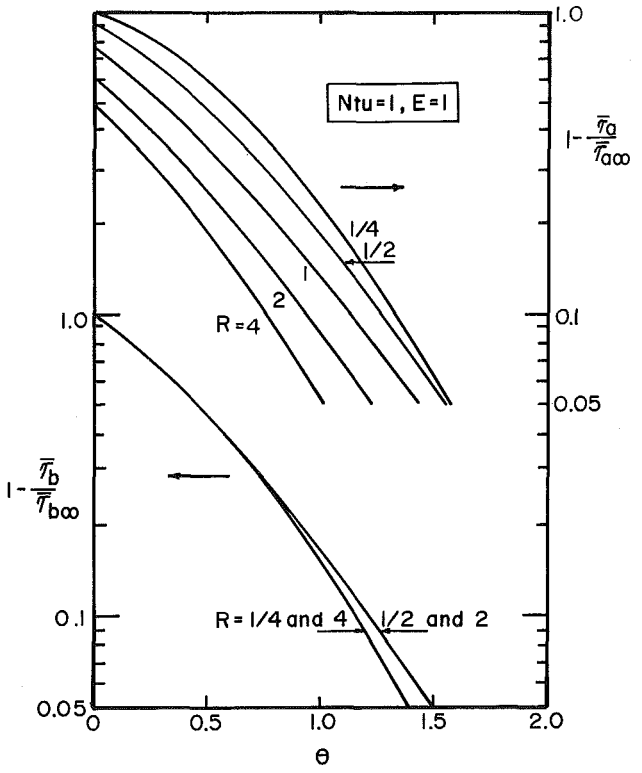

Fig. 4 Complements of the normalized responses

$$K_0(u,v) = \int_0^v e^{-(u+v)} I_0(2\sqrt{uv}) d\nu \tag{24}$$

$$H_0(u, v) - K_0(u,v) = B(u,v) = e^{-(u+v)} I_0(2\sqrt{uv}) \tag{25}$$

I_0 is the modified Bessel function of the first kind, zero order. Numerical values of the functions can be found using their series expansions (see equations A(10) and A(11) of [1]).

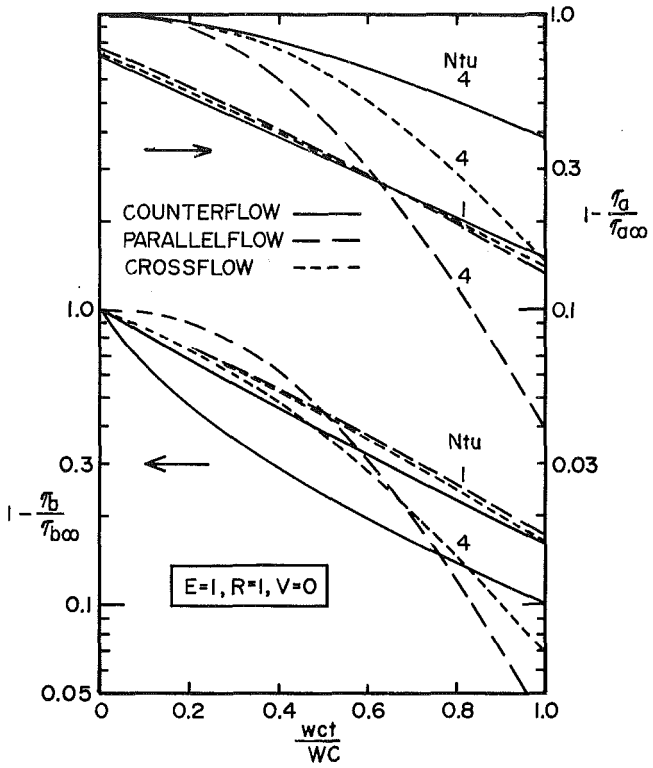

Fig. 5 Effect of exchanger configuration on responses to a unit step change in fluid *a* inlet temperature

Results of Calculation

With $V = 0$, the exit fluid temperature responses $\bar{\tau}_a(\theta)$ and $\bar{\tau}_b(\theta)$ are functions of three parameters: *Ntu*, *E*, and *R*. Figures 2, 3, and 4 show typical responses computed for several values of these parameters. The responses are normalized by dividing them by their final values to give $\bar{\tau}_a/\bar{\tau}_{a\infty}$ and $\bar{\tau}_b/\bar{\tau}_{b\infty}$ which approach unity as θ increases.

The numerical work shows that

$$\frac{\bar{\tau}_b}{\bar{\tau}_{b\infty}}\left(\theta,Ntu,E,R\right) = \frac{\bar{\tau}_b}{\bar{\tau}_{b\infty}}(\theta,Ntu,1/E,1/R) \tag{26}$$

The parameters E and R are reciprocals when first one fluid of an exchanger is stepped (is fluid *a*) and then the other fluid is stepped (is now fluid *a*). Equation (26) thus shows that the normalized response of the unstepped fluid (fluid *b*) will be the same irrespective of which fluid of an exchanger is stepped. Combining equations (23) and (26) gives

$$\bar{\tau}_b(\theta,Ntu,E,R) = \frac{\bar{\tau}_b}{E}(\theta,Ntu,1/E,1/R) \tag{27}$$

This equation indicates that the responses of the unstepped fluids differ only by the factor E when first one fluid of an exchanger is stepped and then the other is stepped. The interpretations of equations (26) and (27) have been found to apply to the counterflow exchanger [5] and the crossflow exchanger [1]. Therefore it seems evident that the interpretations apply to exchangers of all configurations.

For $E = 0$ and for $E = \infty$ the responses, equations (19) and (20), reduce to solutions given by Myers, Mitchell, and Lindeman [6] for exchangers having an infinite capacitance rate fluid (or, equivalently, for exchangers having one fluid at uniform temperature).

Figure 5 compares the responses for gas-to-gas ($V = 0$) counterflow [5], crossflow [1], and parallel-flow heat exchangers with $E = 1$, $R = 1$, and $Ntu = 1$ and 4. The difference between the responses should vanish as *Ntu* becomes small. For $Ntu = 1$, Fig. 5 shows little difference between the responses. For $Ntu = 4$ the responses are quite different with the 90 percent response slowest for the counterflow exchanger and fastest for the parallel-flow exchanger.

References

1 Romie, F. E., "Transient Response of Gas-to-Gas Crossflow Heat Exchangers With Neither Gas Mixed," ASME JOURNAL OF HEAT TRANSFER, Vol. 105, 1983, pp. 563-570.

2 Anzelius, A., "Über Erwärmung Vermittels durchströmender Medien," *Zeitschrift für Angewandte Mathematik und Mechanik*, Vol. 6, 1926, pp. 291-294.

3 Schumann, T. E. W., "Heat Transfer: A Liquid Flowing Through a Porous Prism," *Franklin Institute Journal*, Vol. 208, 1929, pp. 405-416.

4 Klinkenberg, A., "Heat Transfer in Crossflow Heat Exchangers and Packed Beds," *Industrial and Engineering Chemistry*, Vol. 46, 1954, pp. 2285-2289.

5 Romie, F. E., "Transient Response of the Counterflow Heat Exchanger," ASME JOURNAL OF HEAT TRANSFER, Vol. 106, 1984, pp. 620-626.

6 Myers, G. E., Mitchell, J. W., and Lindeman, C. F., "The Transient Response of Heat Exchangers Having an Infinite Capacitance Rate Fluid," ASME JOURNAL OF HEAT TRANSFER, Vol. 92, 1970, pp. 269-275.

Computer Implementation, Accuracy, and Timing of Radiation View Factor Algorithms

A. B. Shapiro[1]

The three-dimensional finite element thermal analysis of enclosure radiation problems requires the calculation of the geometric surface to surface radiation view factor. The geometric view factor between two isothermal, black-body, diffusely emitting and reflecting surfaces (Fig. 1) is

$$F_{IJ} = \frac{1}{A_I}\int_{A_I}\int_{A_J}\frac{\cos\beta_I\cos\beta_J\,dA_I\,dA_J}{\pi r^2} \tag{1}$$

If the two surfaces A_I and A_J are divided into n finite subsurfaces A_i: $i = 1, 2, \ldots, n$ and A_j: $j = 1, 2, \ldots, n$, equation (1) may be approximated by

$$F_{IJ} \simeq \frac{1}{A_I}\sum_{i=1}^{n}\sum_{j=1}^{n}\frac{\cos\beta_i\cos\beta_j\,A_i\,A_j}{\pi r_{ij}^2} \tag{2}$$

This computational scheme is used in the computer codes [1-3] if shadowing surfaces exist.

The area integrals in equation (1) can be transformed to line integrals by using Stokes' theorem [4]. The result is

$$F_{IJ} = \frac{1}{2\pi A_I}\oint_{C_I}\oint_{C_J}(\ln r\,dx_I\,dx_J + \ln r\,dy_I\,dy_J + \ln r\,dz_I\,dz_J) \tag{3}$$

If the two contours C_I and C_J are divided into n finite straight line segments

$$\hat{v}_i\text{: } i = 1,2, \ldots, n \text{ and } \hat{v}_j\text{: } j = 1,2, \ldots, n$$

equation (3) may be approximated by

$$F_{IJ} \simeq \frac{1}{2\pi A_I}\sum_{i=1}^{n}\sum_{j=1}^{n}\ln r_{ij}\,\hat{v}_i\cdot\hat{v}_j \tag{4}$$

Mitalas and Stephenson [5] present a method by which one of the integrals in equation (3) can be integrated analytically. If the surfaces *I* and *J* are quadrilaterals, the result is

[1]University of California, Lawrence Livermore National Laboratory, Livermore, CA 94550

Contributed by the Heat Transfer Division for publication in the JOURNAL OF HEAT TRANSFER. Manuscript received by the Heat Transfer Division May 16, 1984.

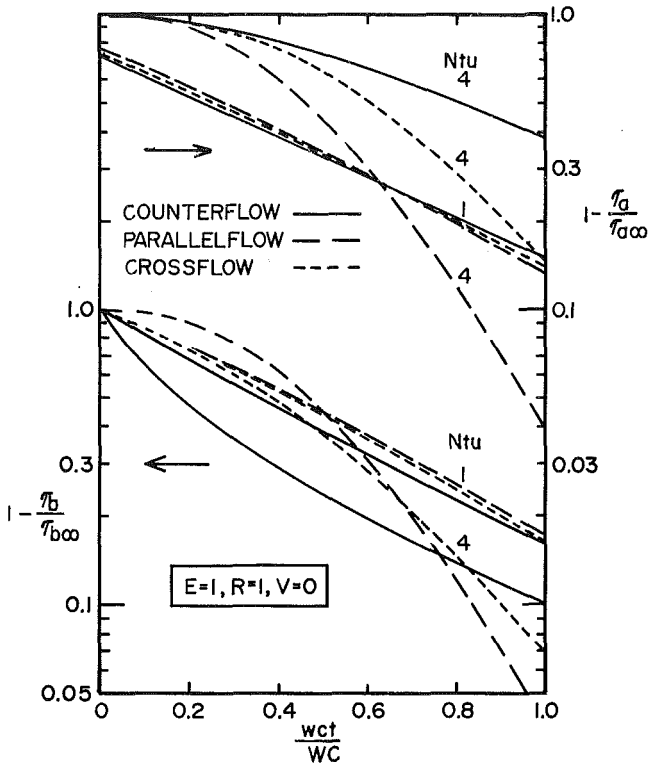

Fig. 5 Effect of exchanger configuration on responses to a unit step change in fluid *a* inlet temperature

Results of Calculation

With $V = 0$, the exit fluid temperature responses $\bar{\tau}_a(\theta)$ and $\bar{\tau}_b(\theta)$ are functions of three parameters: *Ntu*, *E*, and *R*. Figures 2, 3, and 4 show typical responses computed for several values of these parameters. The responses are normalized by dividing them by their final values to give $\bar{\tau}_a/\bar{\tau}_{a\infty}$ and $\bar{\tau}_b/\bar{\tau}_{b\infty}$ which approach unity as θ increases.

The numerical work shows that

$$\frac{\bar{\tau}_b}{\bar{\tau}_{b\infty}}\left(\theta,Ntu,E,R\right) = \frac{\bar{\tau}_b}{\bar{\tau}_{b\infty}}(\theta,Ntu,1/E,1/R) \tag{26}$$

The parameters E and R are reciprocals when first one fluid of an exchanger is stepped (is fluid *a*) and then the other fluid is stepped (is now fluid *a*). Equation (26) thus shows that the normalized response of the unstepped fluid (fluid *b*) will be the same irrespective of which fluid of an exchanger is stepped. Combining equations (23) and (26) gives

$$\bar{\tau}_b(\theta,Ntu,E,R) = \frac{\bar{\tau}_b}{E}(\theta,Ntu,1/E,1/R) \tag{27}$$

This equation indicates that the responses of the unstepped fluids differ only by the factor E when first one fluid of an exchanger is stepped and then the other is stepped. The interpretations of equations (26) and (27) have been found to apply to the counterflow exchanger [5] and the crossflow exchanger [1]. Therefore it seems evident that the interpretations apply to exchangers of all configurations.

For $E = 0$ and for $E = \infty$ the responses, equations (19) and (20), reduce to solutions given by Myers, Mitchell, and Lindeman [6] for exchangers having an infinite capacitance rate fluid (or, equivalently, for exchangers having one fluid at uniform temperature).

Figure 5 compares the responses for gas-to-gas ($V = 0$) counterflow [5], crossflow [1], and parallel-flow heat exchangers with $E = 1$, $R = 1$, and $Ntu = 1$ and 4. The difference between the responses should vanish as *Ntu* becomes small. For $Ntu = 1$, Fig. 5 shows little difference between the responses. For $Ntu = 4$ the responses are quite different with the 90 percent response slowest for the counterflow exchanger and fastest for the parallel-flow exchanger.

References

1 Romie, F. E., "Transient Response of Gas-to-Gas Crossflow Heat Exchangers With Neither Gas Mixed," ASME JOURNAL OF HEAT TRANSFER, Vol. 105, 1983, pp. 563-570.

2 Anzelius, A., "Über Erwärmung Vermittels durchströmender Medien," *Zeitschrift für Angewandte Mathematik und Mechanik*, Vol. 6, 1926, pp. 291-294.

3 Schumann, T. E. W., "Heat Transfer: A Liquid Flowing Through a Porous Prism," *Franklin Institute Journal*, Vol. 208, 1929, pp. 405-416.

4 Klinkenberg, A., "Heat Transfer in Crossflow Heat Exchangers and Packed Beds," *Industrial and Engineering Chemistry*, Vol. 46, 1954, pp. 2285-2289.

5 Romie, F. E., "Transient Response of the Counterflow Heat Exchanger," ASME JOURNAL OF HEAT TRANSFER, Vol. 106, 1984, pp. 620-626.

6 Myers, G. E., Mitchell, J. W., and Lindeman, C. F., "The Transient Response of Heat Exchangers Having an Infinite Capacitance Rate Fluid," ASME JOURNAL OF HEAT TRANSFER, Vol. 92, 1970, pp. 269-275.

Computer Implementation, Accuracy, and Timing of Radiation View Factor Algorithms

A. B. Shapiro[1]

The three-dimensional finite element thermal analysis of enclosure radiation problems requires the calculation of the geometric surface to surface radiation view factor. The geometric view factor between two isothermal, black-body, diffusely emitting and reflecting surfaces (Fig. 1) is

$$F_{IJ} = \frac{1}{A_I}\int_{A_I}\int_{A_J}\frac{\cos\beta_I\cos\beta_J\,dA_I\,dA_J}{\pi r^2} \tag{1}$$

If the two surfaces A_I and A_J are divided into n finite subsurfaces A_i: $i = 1, 2, \ldots, n$ and A_j: $j = 1, 2, \ldots, n$, equation (1) may be approximated by

$$F_{IJ} \simeq \frac{1}{A_I}\sum_{i=1}^{n}\sum_{j=1}^{n}\frac{\cos\beta_i\cos\beta_j\,A_i\,A_j}{\pi r_{ij}^2} \tag{2}$$

This computational scheme is used in the computer codes [1-3] if shadowing surfaces exist.

The area integrals in equation (1) can be transformed to line integrals by using Stokes' theorem [4]. The result is

$$F_{IJ} = \frac{1}{2\pi A_I}\oint_{C_I}\oint_{C_J}(\ln r\,dx_I\,dx_J + \ln r\,dy_I\,dy_J + \ln r\,dz_I\,dz_J) \tag{3}$$

If the two contours C_I and C_J are divided into n finite straight line segments

$$\hat{v}_i: i = 1,2, \ldots, n \text{ and } \hat{v}_j: j = 1,2, \ldots, n$$

equation (3) may be approximated by

$$F_{IJ} \simeq \frac{1}{2\pi A_I}\sum_{i=1}^{n}\sum_{j=1}^{n}\ln r_{ij}\,\hat{v}_i\cdot\hat{v}_j \tag{4}$$

Mitalas and Stephenson [5] present a method by which one of the integrals in equation (3) can be integrated analytically. If the surfaces *I* and *J* are quadrilaterals, the result is

[1]University of California, Lawrence Livermore National Laboratory, Livermore, CA 94550

Contributed by the Heat Transfer Division for publication in the JOURNAL OF HEAT TRANSFER. Manuscript received by the Heat Transfer Division May 16, 1984.

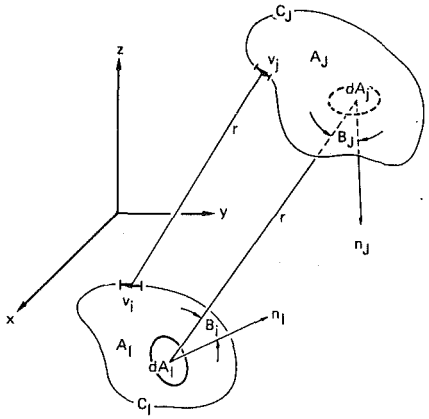

Fig. 1 This sketch illustrates the symbols used in equations (1-4) to calculate the view factor F_{IJ}

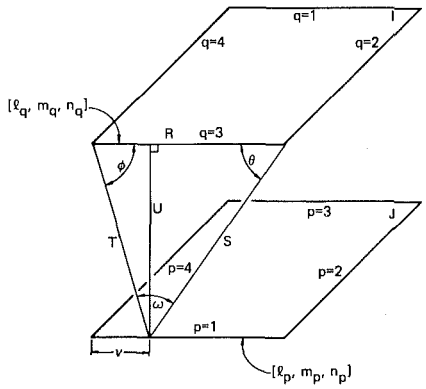

Fig. 2 This sketch illustrates the symbols used in Mitalas and Stephenson's contour integration method, equations (5) and (6), to calculate the view factor F_{IJ}

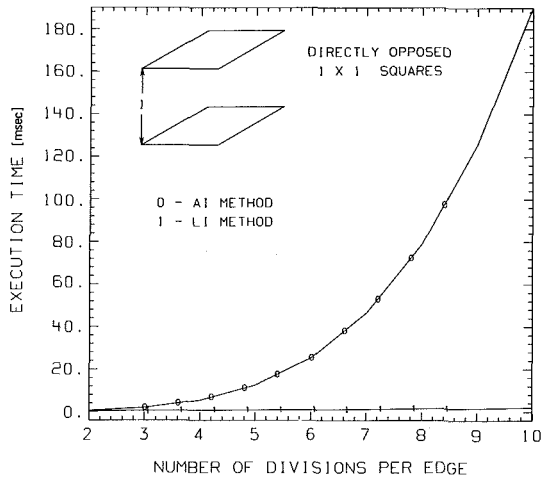

Fig. 3 An operation count showed that $114n^4 + 86n^2$ and $464n^2 + 24n$ operations are required for the *AI* and *LI* methods, respectively; the *LI* method is faster than the *AI* method for $n \geq 2$

$$F_{IJ} = \frac{1}{2\pi A_I} \sum_{p=1}^{4} \sum_{q=1}^{4} \Phi(p,q) \oint_{C_p} [(T \cos\phi \ln T + S \cos\theta \ln S + U\omega - R)dv]_{p,q} \quad (5)$$

where S, T, U, ϕ, and ω are functions of v and

$$\Phi(p,q) = l_p l_q + m_p m_q + n_p n_q \quad (6)$$

The symbols are defined in Fig. 2. Dividing each of the four line segments C_p into n finite straight line segments $\hat{v}_j$: $j = 1, 2, \ldots, n$, equation (5) may be approximated by

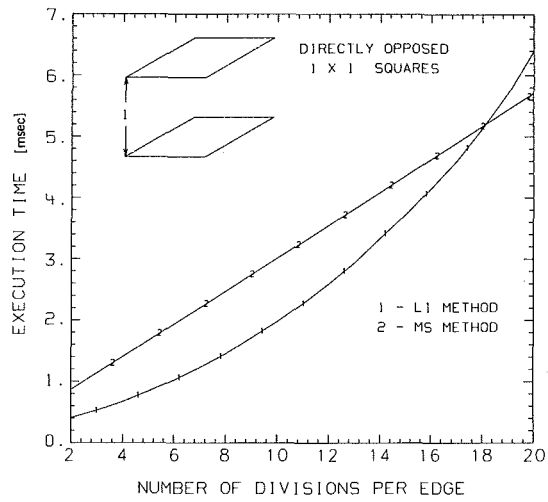

Fig. 4 An operation count showed that $464n^2 + 24n$ and $864n + 288$ operations are required for the *LI* and *MS* methods, respectively; as a result of vectorization of the *LI* method by the CRAY compiler, the *LI* method having more operations is faster than the *MS* method for $n < 18$

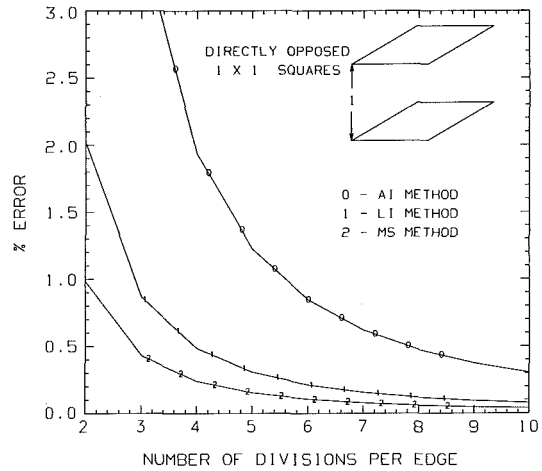

Fig. 5 The line integration methods, *LI* and *MS*, are significantly more accurate than the area integration method *AI*. The *MS* method having one of its line integrals performed analytically is more accurate than the *LI* method.

$$F_{IJ} \simeq \frac{1}{2\pi A_I} \sum_{p=1}^{4} \sum_{q=1}^{4} \Phi(p,q) \sum_{j=1}^{n} [(T \cos\phi \ln T + S \cos\theta \ln S + U\omega - R)|\hat{v}_j|]_{p,q} \quad (7)$$

The computational schemes represented by equations (2), (4), and (7) will subsequently be referred to as the area integration method (*AI*), line integration method (*LI*), and the Mitalas and Stephenson method (*MS*), respectively. The surfaces between which view factors are being calculated are plane quadrilaterals. Methods *LI* and *MS* require a subdivision of the contour of the quadrilateral while method *AI* requires a subdivision of the surface area. Dividing each of the four line segments forming the quadrilateral into n divisions results in a total of $4n$ nodes around the contour and n^2 nodes for the surface area. Operations counts for the three methods are:

AI method	$114n^4 + 86n^2$
LI method	$464n^2 + 24n$
MS method	$864n + 288$

Timing studies (Fig. 3) show that the *LI* method is faster than the *AI* method for $n \geq 2$. Coding of the *LI* method results in FORTRAN DO loops which are vectorized by the CRAY CFT [6] compiler. As a result of vectorization, the *LI* method

having more operations is faster than the *MS* method for $n < 18$. Timing studies for the *LI* and *MS* methods are presented in Fig. 4.

The accuracy of the three methods is compared in Fig. 5. The line integration methods *LI* and *MS* are significantly more accurate than the area integration method *AI*. The *MS* method having one of its line integrals performed analytically is more accurate than the *LI* method. However, based both on accuracy and execution time, Sparrow's *LI* method is superior to the *MS* method for $n \leq 7$.

References

1 Wong, R. L., "User's Manual for CNVUFAC—The General Dynamics Heat Transfer Radiation View Factor Program," University of California, Lawrence Livermore National Laboratory, UCID-17275, 1976.

2 Puccinelli, E. F., "View Factor Computer Program (Program VIEW) User's Manual," Goddard Space Flight Center, Greenbelt, MD, X-324-73-272, 1973.

3 Emery, A. F., "Instructions Manual for the Program SHAPEFACTOR," Sandia National Laboratories, Livermore, CA, SAND80-8027, 1980.

4 Sparrow, E. M., and Cess, R. D., *Radiation Heat Transfer*, McGraw-Hill, New York, 1978.

5 Mitalas, G. P., and Stephenson, D. G., "FORTRAN IV Programs to Calculate Radiant Interchange Factors," National Research Council of Canada, Division of Building Research, Ottawa, Canada, DBR-25, 1966.

6 *CRAY-1 Computer System CFT Reference Manual*, Cray Research Incorporated, Bloomington, MN, publication No. 2240009, 1978.

Radiation Transfer in an Isotropically Scattering Solid Sphere With Space Dependent Albedo, $\omega(r)$

S. T. Thynell[1] and M. N. Özişik[1]

Introduction

There are several studies available in the literature [1-3] that have considered the problem of radiative transfer in an absorbing, emitting, isotropically scattering sphere with a uniform albedo. However, only a limited number of works are available that have considered the effects from a spatially varying albedo [4]; such problems have numerous engineering applications. In such problems, it is of interest to determine the effects of variation of albedo within the medium on the radiative heat transfer.

Analysis

In this work, we solve the problem of radiation transfer in an absorbing, emitting, isotropically scattering, nonhomogeneous sphere, having a reflecting and emitting boundary surface, and energy sources within the medium. For a solid sphere of optical radius R, with constant extinction coefficient β, the mathematical formulation of the problem is written as

$$\mu\frac{\partial I(r,\mu)}{\partial r}+\frac{(1-\mu^2)}{r}\frac{\partial I(r,\mu)}{\partial \mu}+I(r,\mu)$$

$$=Q(r)+\frac{\omega(r)}{2}\int_{-1}^{1} I(r,\mu')d\mu' \qquad (1a)$$

$$\text{for } 0<r<R, -1\leq\mu\leq 1$$

$$I^-(R,-\mu)=(1-\rho_0)f(\mu)+\epsilon\frac{n^2\sigma T^4}{\pi}$$

$$+2\rho_1\int_0^1 I(R,\mu')\mu' d\mu',\ \mu\geq 0 \qquad (1b)$$

Here r is the optical variable, μ is the cosine of the angle between the radial coordinate and the direction of the radiation intensity, and $Q(r)$ is a source term. If the source term is due to the temperature of the medium, it is given by $Q(r)=[1-\omega(r)]n^2\sigma T^4(r)/\pi$, where n is the refractive index of the medium and σ is the Stefan-Boltzmann constant. In addition, the functions $f(\mu)$ and $\epsilon n^2\sigma T^4/\pi$ represent, respectively, radiation intensities of externally incident radiation and emission from the boundary due to its temperature. Here ϵ is the emissivity, and ρ_0 and ρ_1 are the diffuse reflectivities of the outside and inside boundary surfaces, respectively.

We define the incident radiation $I(r)$ as

$$I(r)=\int_{-1}^{1} I(r,\mu)d\mu$$

$$=\int_0^1 I^+(r,\mu)d\mu+\int_0^1 I^-(r,-\mu)d\mu \qquad (2)$$

where $I^+(r,\mu)$ and $I^-(r,-\mu)$ are, respectively, the forward and backward radiation intensities. By solving formally for $I^+(r,\mu)$ and $I^-(r,-\mu)$ in equations (1) and subsequently introducing these quantities into equation (2), we obtain the following integral equation for $I(r)$

$$rI(r)=rB(r)+\int_0^R\left[\frac{\omega(x)}{2}I(x)+Q(x)\right][E_1(|r-x|)$$

$$-E_1(r+x)+\rho_1\xi rD(r)xD(x)]xdx \qquad (3)$$

where $B(r)$, ξ, and $D(r)$ are defined in the Appendix, and $E_n(x)$ denotes the exponential integral function. We now assume that the albedo and the source term are represented by polynomials in the form

$$\omega(r)=\sum_{k=0}^{K}D_k r^k \text{ and } Q(r)=\sum_{l=0}^{L}a_l r^l \text{ for } 0<r<R \qquad (4a,b)$$

where the D_k's and a_l's are known coefficients. To solve this problem, $I(r)$ is represented in a power series

$$I(r)=\sum_{n=0}^{N}C_n r^n \text{ for } 0<r<R \qquad (5)$$

where the C_n's are the unknown expansion coefficients. The Galerkin method [5] is now applied to yield a system of $N+1$ linear algebraic equations for the $N+1$ unknown expansion coefficients C_n, written in a matrix form as

$$[b_{m,n}]\{C_n\}=\{d_m\},\ m,n=0,1,\ldots,N \qquad (6)$$

where the elements of the coefficient matrix $[b_{m,n}]$ and column vector $\{d_m\}$ are computed from

$$b_{m,n}=\frac{R^{m+n+2}}{m+n+2}-\frac{1}{2}\sum_{k=0}^{K}D_k(T_{m,n+k+1}+\rho_1\xi V_m V_{n+k+1}) \qquad (7a)$$

$$d_m=\rho_1\xi R^2K^*V_m$$

$$+2\int_0^R\int_0^1 K[\mu_0(r,\mu)]\cosh(r\mu)e^{-C(R,r,\mu)}d\mu r^{m+1}dr$$

$$+\sum_{l=0}^{L}a_l(T_{m,l+1}+\rho_1\xi V_m V_{l+1}) \qquad (7b)$$

with $T_{i,j}$ and V_i being definite integrals defined in the Appendix and for which analytic expressions are available [6].

Once the C_n's are obtained from equations (6), the forward and backward radiation intensities are determined, respectively, from

[1]Mechanical and Aerospace Engineering Department, North Carolina State University, Raleigh, NC 27695-7910

Contributed by the Heat Transfer Division for publication in the JOURNAL OF HEAT TRANSFER. Manuscript received by the Heat Transfer Division September 5, 1984.

having more operations is faster than the *MS* method for $n < 18$. Timing studies for the *LI* and *MS* methods are presented in Fig. 4.

The accuracy of the three methods is compared in Fig. 5. The line integration methods *LI* and *MS* are significantly more accurate than the area integration method *AI*. The *MS* method having one of its line integrals performed analytically is more accurate than the *LI* method. However, based both on accuracy and execution time, Sparrow's *LI* method is superior to the *MS* method for $n \leq 7$.

References

1 Wong, R. L., "User's Manual for CNVUFAC—The General Dynamics Heat Transfer Radiation View Factor Program," University of California, Lawrence Livermore National Laboratory, UCID-17275, 1976.

2 Puccinelli, E. F., "View Factor Computer Program (Program VIEW) User's Manual," Goddard Space Flight Center, Greenbelt, MD, X-324-73-272, 1973.

3 Emery, A. F., "Instructions Manual for the Program SHAPEFACTOR," Sandia National Laboratories, Livermore, CA, SAND80-8027, 1980.

4 Sparrow, E. M., and Cess, R. D., *Radiation Heat Transfer*, McGraw-Hill, New York, 1978.

5 Mitalas, G. P., and Stephenson, D. G., "FORTRAN IV Programs to Calculate Radiant Interchange Factors," National Research Council of Canada, Division of Building Research, Ottawa, Canada, DBR-25, 1966.

6 *CRAY-1 Computer System CFT Reference Manual*, Cray Research Incorporated, Bloomington, MN, publication No. 2240009, 1978.

Radiation Transfer in an Isotropically Scattering Solid Sphere With Space Dependent Albedo, $\omega(r)$

S. T. Thynell[1] and M. N. Özişik[1]

Introduction

There are several studies available in the literature [1-3] that have considered the problem of radiative transfer in an absorbing, emitting, isotropically scattering sphere with a uniform albedo. However, only a limited number of works are available that have considered the effects from a spatially varying albedo [4]; such problems have numerous engineering applications. In such problems, it is of interest to determine the effects of variation of albedo within the medium on the radiative heat transfer.

Analysis

In this work, we solve the problem of radiation transfer in an absorbing, emitting, isotropically scattering, nonhomogeneous sphere, having a reflecting and emitting boundary surface, and energy sources within the medium. For a solid sphere of optical radius R, with constant extinction coefficient β, the mathematical formulation of the problem is written as

$$\mu\frac{\partial I(r,\mu)}{\partial r}+\frac{(1-\mu^2)}{r}\frac{\partial I(r,\mu)}{\partial \mu}+I(r,\mu)$$

$$=Q(r)+\frac{\omega(r)}{2}\int_{-1}^{1} I(r,\mu')d\mu' \qquad (1a)$$

$$\text{for } 0<r<R, -1\leq\mu\leq 1$$

$$I^-(R,-\mu)=(1-\rho_0)f(\mu)+\epsilon\frac{n^2\sigma T^4}{\pi}$$

$$+2\rho_1\int_0^1 I(R,\mu')\mu' d\mu',\ \mu\geq 0 \qquad (1b)$$

Here r is the optical variable, μ is the cosine of the angle between the radial coordinate and the direction of the radiation intensity, and $Q(r)$ is a source term. If the source term is due to the temperature of the medium, it is given by $Q(r)=[1-\omega(r)]n^2\sigma T^4(r)/\pi$, where n is the refractive index of the medium and σ is the Stefan-Boltzmann constant. In addition, the functions $f(\mu)$ and $\epsilon n^2\sigma T^4/\pi$ represent, respectively, radiation intensities of externally incident radiation and emission from the boundary due to its temperature. Here ϵ is the emissivity, and ρ_0 and ρ_1 are the diffuse reflectivities of the outside and inside boundary surfaces, respectively.

We define the incident radiation $I(r)$ as

$$I(r)=\int_{-1}^{1} I(r,\mu)d\mu$$

$$=\int_0^1 I^+(r,\mu)d\mu+\int_0^1 I^-(r,-\mu)d\mu \qquad (2)$$

where $I^+(r,\mu)$ and $I^-(r,-\mu)$ are, respectively, the forward and backward radiation intensities. By solving formally for $I^+(r,\mu)$ and $I^-(r,-\mu)$ in equations (1) and subsequently introducing these quantities into equation (2), we obtain the following integral equation for $I(r)$

$$rI(r)=rB(r)+\int_0^R\left[\frac{\omega(x)}{2}I(x)+Q(x)\right][E_1(|r-x|)$$

$$-E_1(r+x)+\rho_1\xi rD(r)xD(x)]xdx \qquad (3)$$

where $B(r)$, ξ, and $D(r)$ are defined in the Appendix, and $E_n(x)$ denotes the exponential integral function. We now assume that the albedo and the source term are represented by polynomials in the form

$$\omega(r)=\sum_{k=0}^{K}D_k r^k \text{ and } Q(r)=\sum_{l=0}^{L}a_l r^l \text{ for } 0<r<R \qquad (4a,b)$$

where the D_k's and a_l's are known coefficients. To solve this problem, $I(r)$ is represented in a power series

$$I(r)=\sum_{n=0}^{N}C_n r^n \text{ for } 0<r<R \qquad (5)$$

where the C_n's are the unknown expansion coefficients. The Galerkin method [5] is now applied to yield a system of $N+1$ linear algebraic equations for the $N+1$ unknown expansion coefficients C_n, written in a matrix form as

$$[b_{m,n}]\{C_n\}=\{d_m\},\ m,n=0,1,\ldots,N \qquad (6)$$

where the elements of the coefficient matrix $[b_{m,n}]$ and column vector $\{d_m\}$ are computed from

$$b_{m,n}=\frac{R^{m+n+2}}{m+n+2}-\frac{1}{2}\sum_{k=0}^{K}D_k(T_{m,n+k+1}+\rho_1\xi V_m V_{n+k+1}) \qquad (7a)$$

$$d_m=\rho_1\xi R^2K^*V_m$$

$$+2\int_0^R\int_0^1 K[\mu_0(r,\mu)]\cosh(r\mu)e^{-C(R,r,\mu)}d\mu r^{m+1}dr$$

$$+\sum_{l=0}^{L}a_l(T_{m,l+1}+\rho_1\xi V_m V_{l+1}) \qquad (7b)$$

with $T_{i,j}$ and V_i being definite integrals defined in the Appendix and for which analytic expressions are available [6].

Once the C_n's are obtained from equations (6), the forward and backward radiation intensities are determined, respectively, from

[1]Mechanical and Aerospace Engineering Department, North Carolina State University, Raleigh, NC 27695-7910

Contributed by the Heat Transfer Division for publication in the JOURNAL OF HEAT TRANSFER. Manuscript received by the Heat Transfer Division September 5, 1984.

Table 1 Effects of spatial variation of albedo, $\omega(r)$, on hemispherical reflectivity of a sphere with transparent boundary

ω_{eff}	$\omega(a)$, where $a \equiv r/R$	R = 0.1		R = 1		R = 10	
		Reflec.	NT	Reflec.	NT	Reflec.	NT
	Linear Variation in Albedo						
0.1	2a/15	0.88781	2	0.33999	5	0.03719	16
	0.1	0.88774	2	0.33687	5	0.02944	14
	0.2 - 2a/15	0.88767	3	0.33386	4	0.02194	12
	0.4 - 6a/15	0.88755	3	0.32820	4	0.00765	11
0.5	10a/15	0.93607	3	0.55957	6	0.24825	13
	0.2 + 6a/15	0.93594	3	0.55205	5	0.21454	15
	0.4 + 2a/15	0.93584	2	0.54532	6	0.18431	15
	0.5	0.93580	2	0.54226	6	0.17032	14
	0.6 - 2a/15	0.93576	2	0.53941	4	0.15701	14
	0.8 - 6a/15	0.93569	3	0.53441	5	0.13221	15
	1 - 10a/15	0.93565	3	0.53038	4	0.10955	16
0.9	0.6 + 6a/15	0.98682	2	0.88384	3	0.70960	13
	0.8 + 2a/15	0.98678	2	0.87947	3	0.59381	10
	0.9	0.98677	2	0.87801	4	0.54629	16
	1 - 2a/15	0.98676	2	0.87707	4	0.50431	13
	Quadratic Variation in Albedo						
0.1	$a/30 + a^2/8$	0.88786	3	0.34185	5	0.04283	17
	$0.4 - a/2 + a^2/8$	0.88759	3	0.32982	3	0.01261	9
0.5	$4a/15 + a^2/2$	0.93622	3	0.56871	4	0.30157	13
	$0.4 - 4a/15 + a^2/2$	0.93595	3	0.55292	5	0.22697	16
	$0.6 - 8a/15 + a^2/2$	0.93585	3	0.54619	5	0.19559	15
	$1 - 16a/15 + a^2/2$	0.93571	2	0.53534	4	0.14167	20
0.9	$0.8 + a/30 + a^2/8$	0.98679	2	0.88044	3	0.62703	10
	$1 - 7a/30 + a^2/8$	0.98677	2	0.87755	4	0.53046	11

$$I^+(r,\mu) = I_B(r,\mu)e^{-S_0(r,\mu)} + \frac{1}{2}\sum_{n=0}^{N}\sum_{k=0}^{K} C_n D_k[\lambda_1 X^+_{n+k}(r,\mu) + \lambda_2 {}^*X^+_{n+k}(r,1)] + \sum_{l=0}^{L} a_l[\lambda_1 X^+_l(r,\mu) + \lambda_2 {}^*X^+_l(r,1)],\ \mu \geq 0 \tag{8a}$$

and

$$I^-(r,-\mu) = I_B(r,\mu)e^{-S_0(r,-\mu)} + \frac{1}{2}\sum_{n=0}^{N}\sum_{k=0}^{K} C_n D_k[\lambda_1 X^-_{n+k}(r,\mu) + \lambda_2 {}^*X^-_{n+k}(r,1)] + \sum_{l=0}^{L} a_l[\lambda_1 X^-_l(r,\mu) + \lambda_2 {}^*X^-_l(r,1)],\ \mu \geq 0 \tag{8b}$$

where

$$I_B(r,\mu) = K[\mu_0(r,\mu)] + \rho_1 \xi R^2[K^* + \frac{1}{2}\sum_{n=0}^{N}\sum_{k=0}^{K} C_n D_k {}^*X^+_{n+k}(R) + \sum_{l=0}^{L} a_l {}^*X^+_l(R)]. \tag{9}$$

Here the functions $S_0(r,\mu)$, λ_1, λ_2, $X^+_i(r,\mu)$, ${}^*X^\pm_i(r,\mu)$, ${}^*X^\pm_i(r)$, $K[\mu_0(r,\mu)]$, $\mu_0(r,\mu)$, and K^* are defined in the Appendix.

Knowing the forward and backward radiation intensities, the forward and backward radiation heat fluxes, $q^+(r)$ and $q^-(r)$, are, respectively, determined from

$$\frac{q^+(r)}{2\pi} = Q^+_B(r) + \frac{1}{2}\sum_{n=0}^{N}\sum_{k=0}^{K} C_n D_k {}^*X^+_{n+k}(r) + \sum_{l=0}^{L} a_l {}^*X^+_l(r) \tag{10a}$$

and

$$\frac{q^-(r)}{2\pi} = Q^-_B(r) + \frac{1}{2}\sum_{n=0}^{N}\sum_{k=0}^{K} C_n D_k {}^*X^-_{n+k}(r) + \sum_{l=0}^{L} a_l {}^*X^-_l(r) \tag{10b}$$

where

Table 2 Exit distribution of radiation intensity for a sphere subjected to an isotropic irradiation of unit strength for different $\omega(r)$ and optical radii

R	θ	ω(r) = 2r/3R		ω(r) = 0.5		ω(r) = 1 - 2r/3R	
		$I^+(R,\mu)$	NT	$I^+(R,\mu)$	NT	$I^+(R,\mu)$	NT
0.1	0	0.8766	3	0.9055	3	0.9352	5
	15	0.8883		0.9085		0.9292	
	30	0.9112		0.9173		0.9236	
	45	0.9370		0.9317		0.9264	
	60	0.9610		0.9509		0.9409	
	75	0.9816		0.9741		0.9666	
1	0	0.3405	10	0.4105	9	0.5066	10
	15	0.3696		0.4202		0.4877	
	30	0.4382		0.4511		0.4700	
	45	0.5375		0.5085		0.4818	
	60	0.6615		0.6036		0.5485	
	75	0.8087		0.7557		0.7051	
10	0	0.1890	19	0.1287	16	0.0826	19
	15	0.1929		0.1313		0.0842	
	30	0.2053		0.1396		0.0892	
	45	0.2290		0.1554		0.0986	
	60	0.2700		0.1829		0.1150	
	75	0.3469		0.2380		0.1504	

$$Q^\pm_B(r) = \int_0^1 K[\mu_0(r,\mu)]e^{-S_0(r,\pm\mu)}\mu d\mu + \rho_1 \xi R^2 H^\pm_1(r)[K^* + \frac{1}{2}\sum_{n=0}^{N}\sum_{k=0}^{K} C_n D_k {}^*X^+_{n+k}(R) + \sum_{l=0}^{L} a_l {}^*X^+_l(R)] \tag{11}$$

and the function $H^\pm_1(r)$ is defined in [6].

Finally, the incident radiation is given by

$$rI(r) = rB(r) + \frac{1}{2}\sum_{n=0}^{N}\sum_{k=0}^{K} C_n D_k[T_{n+k+1}(r) + \rho_1 \xi r D(r) V_{n+k+1}] + \sum_{l=0}^{L} a_l[T_{l+1}(r) + \rho_1 \xi r D(r) V_{l+1}] \tag{12}$$

where the function $T_i(r)$ is given in the Appendix. At the origin of the sphere, equation (12) reduces to

$$I(0) = (K_0 + \rho_1 \xi R^2 K^*)2e^{-R} + \sum_{n=0}^{N}\sum_{k=0}^{K} C_n D_k[\Gamma_{n+k+1}(R) + \rho_1 \xi e^{-R} V_{n+k+1}] + 2\sum_{l=0}^{L} a_l[\Gamma_{l+1}(R) + \rho_1 \xi e^{-R} V_{l+1}] \tag{13}$$

where

$$K_0 = \lim_{r\to 0} K[\mu_0(r,\mu)] \text{ and } \Gamma_i(R) = \int_0^R x^{i-1}e^{-x}dx \tag{14a,b}$$

Results and Discussion

To illustrate the application of the previous analysis, we consider a solid sphere subjected to an isotropic incident radiation of unit intensity (i.e., $f(\mu) = 1$).

To examine the error introduced by the assumption of a uniform albedo, we present in Table 1 our converged values of the hemispherical reflectivity for the case of isotropic incident radiation of unit intensity for various spatial distributions of albedo and optical radii. In this table, *NT* represents the number of terms needed to achieve a five-digit accuracy. For comparison purposes, we define the corresponding effective uniform albedo, ω_{eff}, as

$$\omega_{eff} = \int_0^R \omega(r)r^2 dr/(R^3/3) \tag{15}$$

An inspection of Table 1 reveals that for $R \leq 1$, only a small error is involved by assuming a uniform albedo. For example, for $\omega(r) = 0.5$, $\omega(r) = 1-2r/3R$ and $R = 1$, the error is only 2.2 percent. However, for larger optical radii the spatial distribution of albedo has a significant effect on the reflectivity. For example, in the case $R = 10$ the reflectivity is overestimated by 55.5 percent if a uniform albedo $\omega(r) = 0.5$ is used in the calculations instead of an actual variation of albedo $\omega(r) = 1-2r/3R$. The reason for this difference results from the fact that the region near the surface has lower scattering with $\omega(r) = 1-2r/3R$ than for a uniform albedo. As a result, more of the incident radiation is reflected back with the uniform albedo.

Table 2 shows the angular distribution of intensity at the boundary for the case of isotropic incident radiation of unit intensity with no sources within the medium. The results are given for three different spatial variations of albedo in the form $\omega(r) = 2r/3R$, $\omega(r) = 0.5$, and $\omega(r) = 1-2r/3R$, and for three different optical radii $R = 0.1$, 1, and 10. For smaller optical radii (i.e., $R = 0.1$), the results obtained by using the average value of albedo are very close to those including the spatial variation of albedo. On the other hand, with larger optical radii (i.e., $R = 10$), a significant error is involved in the angular distribution of radiation intensity if an average value of albedo is used.

Acknowledgment

This work was supported in part through the National Science Foundation Grant No. MEA 81-10705.

References

1 Heaslet, M. A., and Warming, R. F., "Radiation Flux for a Slab or Sphere," *Journal of Mathematical Analysis and Applications*, Vol. 14, 1966, pp. 359-369.

2 Sobolev, V. V., "Multiple Scattering of Radiation by Free Electrons in a Homogeneous Sphere," *Astrophysics*, Vol. 10, 1974, pp. 113-116.

3 Siewert, C. E., and Grandjean, P., "Three Basic Neutron-Transport Problems in Spherical Geometry," *Nuclear Science and Engineering*, Vol. 70, 1979, pp. 96-98.

4 Simonneau, E., "Radiative Transfer in Atmospheres with Spherical Symmetry—IV. The Non-Conservative Problem," *Journal of Quantitative Spectroscopy and Radiative Transfer*, Vol. 23, 1980, pp. 73-81.

5 Özisik, M. N., and Yener, Y., "The Galerkin Method for Solving Radiation Transfer in Plane-Parallel Participating Media," ASME JOURNAL OF HEAT TRANSFER, Vol. 104, 1982, pp. 351-354.

6 Thynell, S. T., and Özisik, M. N., "Integrals Involving an Exponential Integral Function and Exponentials Arising in the Solution of Radiation Transfer," *Journal of Quantitative Spectroscopy and Radiative Transfer* (in press).

7 LeCaine, J., "A Table of Integrals Involving the Functions $E_n(x)$," MT-131 Atomic Energy Projects, National Research Council of Canada, Chalk River, Ontario, 1945.

APPENDIX

Functions appearing in equations (3, 7-14)

$$B(r) = \rho_1 \xi R^2 K^* D(r) + \int_0^1 K[\mu_0(r,\mu)]\cosh(r\mu) e^{-C(R,r,\mu)} d\mu \tag{A1}$$

$$\xi = 2(1-\rho_1\chi^*)^{-1}/R^2;\ \chi^* = [1-e^{-2R}(1+2R)]/(2R^2) \tag{A2,3}$$

$$K^* = \int_0^1 K(\mu) e^{-2R\mu}\mu d\mu;\ K(\mu) \equiv (1-\rho_0) f(\mu) + \epsilon \frac{n^2\sigma T^4}{\pi} \tag{A4,5}$$

$$D(r) = \left[\frac{(1+R)}{r}\sinh(r) + \cosh(r)\right] e^{-R} + \frac{R^2-r^2}{2r}[E_1(R+r) - E_1(R-r)] \tag{A6}$$

$$\mu_0(r,\mu) = [1-(r/R)^2(1-\mu^2)]^{1/2}; \tag{A7}$$

$$C(R,r,\mu) = [R^2 - r^2(1-\mu^2)]^{1/2} \tag{A8}$$

$$S_0(r,\mu) = r\mu + R\mu_0(r,\mu);\ \lambda_1 = 1,\ \lambda_2 = 0 \text{ for } \mu < 1 \tag{A9,10}$$

$$\lambda_1 = 0,\ \lambda_2 = 1 \text{ for } \mu = 1 \tag{A11}$$

Integrals appearing in equations (7-12)

$$T_{m,n} = \int_0^R \int_0^R [E_1(|r-x|) - E_1(r+x)] x^n dx r^m dr \tag{A12}$$

$$X_n^{\pm}(r,\mu) = \int_{\mp r\mu}^{C(R,r,\mu)} [t^2 + r^2(1-\mu^2)]^{\frac{n}{2}} e^{-t\mp r\mu} dt,\ \mu < 1 \tag{A13}$$

$$^*X_n^{\pm}(r,1) = \pm \int_0^r x^n e^{\mp r \pm x} dx + \int_0^R x^n e^{\mp r - x} dx,\ \mu = 1 \tag{A14}$$

$$^*X_n^{\pm}(r) = \int_0^1 {}^*X_n^{\pm}(r,\mu)\mu d\mu; \tag{A15}$$

$$T_n(r) = \int_0^R [E_1(|r-x|) - E_1(r+x)] x^n dx \tag{A16}$$

Analytic expressions are available in [6] for all of the integrals defined by equations (A12-A16), except for equation (A13) in the cases $n = 1$, 3 and for equation (A15) in the cases n being odd with $r < R$. In the few cases when analytic expressions were not available, we used a 40-point Gaussian quadrature formula for approximating the integrals. We also have

$$V_n = \int_0^R x^n x D(x) dx = \frac{e^{-R}}{2}[\Gamma_{n+2}(R) - (1+R)\Gamma_{n+1}(R)] - \frac{R^2}{2} T_n(R) + \frac{1}{2} T_{n+2}(R) + \frac{1}{2}\sum_{j=1}^{n+2} \frac{(-1)^{j+1}(n+1)! R^{n+2-j}}{(j-1)!(n+2-j)!}\Gamma_j(R) + \frac{1}{2}(1+R)\sum_{j=1}^{n+1} \frac{(-1)^{j+1}(n)! R^{n+1-j}}{(j-1)!(n+1-j)!}\Gamma_j(R) \tag{A17}$$

In addition, by manipulating the formulas given in [7], we obtained the following expressions for $T_{m,n}$ and $T_n(r)$, which were used in the computations for $R = 10$

$$T_{m,n} = m!n!\left\{\frac{(-1)^{n+1}-1}{m+n+2} + [(-1)^m + 1]\sum_{i=0}^{n} \frac{R^{n-i}}{(n-i)!} E_{m+i+3}(R) + [(-1)^n + 1]\sum_{j=0}^{m} \frac{R^{m-j}}{(m-j)!} E_{n+j+3}(R) - \sum_{i=0}^{n}\sum_{j=0}^{m} \frac{R^{m+n-i-j}}{(n-i)!(m-j)!}\left[\frac{(-1)^j}{i+j+2} + E_{i+j+3}(2R)\right]\right\} + n!\sum_{i=0}^{n} \frac{[1+(-1)^i]}{(n-i)!(i+1)} \cdot \frac{R^{m+n+1-i}}{(m+n+1-i)} \tag{A18}$$

and

$$T_n(r) = n!\left\{E_{n+2}(r)[(-1)^{n+1} - 1] + \sum_{i=0}^{n}\left[\frac{[1+(-1)^i] r^{n-i}}{(n-i)!(i+1)} + \frac{R^{n-i}[E_{i+2}(R+r) - E_{i+2}(R-r)]}{(n-i)!}\right]\right\} \tag{A19}$$

Development of the Finite Analytic With Radiation Method

T. F. Smith[1] and S. S. Severin[2]

Introduction

Analyses of systems considering the simultaneous interaction of conduction, convection, and radiation yield a set of nonlinear equations for the system temperature distributions. Any technique based on either analytical or numerical concepts that attempts to reduce these nonlinear effects with a reduction in the effort to obtain accurate solutions becomes attractive. One technique applied to solve fluid flow and convective transfer problems is the finite analytic method (FAM) developed by Chen and co-workers [1]. Results indicate that the FAM is an effective technique in reducing nonlinearities. Concepts associated with the FAM have yet to be applied to systems involving radiant exchange where highly nonlinear effects may be present.

The objective of this study is to develop the FAM to systems involving radiation. The development of the finite analytic with radiation method (FARM) was initiated for a system consisting of an absorbing and emitting gray medium between two infinite, parallel black plates separated by a distance L and maintained at uniform temperatures T_l and T_u. The medium is in local thermodynamic equilibrium and has a refractive index of unity. The medium is stationary, exhibits a constant thermal conductivity k, and has a constant absorption coefficient κ. Conduction normal to the plates is included. Steady-state conditions prevail. One-dimensional temperature profiles for the medium exist normal to the plates. This system was selected for its simplicity and availability of results from other techniques [2–6]. There are presently no restrictions that prevent using the FARM for more complex systems involving real gases [7] with scattering, reflecting boundaries, heat generation, and multidimensional effects. This study attempts to develop the concepts supporting the FARM and to establish the feasibility of the FARM.

Analysis

An energy balance on a differential slab of thickness dy states

$$k\frac{d^2T}{dy^2}=\dot{q}_r \tag{1}$$

where the spatial variable y is measured normal to the plate at T_l and T is the medium temperature at position y. The volumetric net radiant energy leaving $\dot{q}_r$ is given by

$$\dot{q}_r=4\kappa\sigma T^4-\frac{dq_a}{dy} \tag{2}$$

where the second term represents the divergence of the radiative absorption. The Stefan–Boltzmann constant is σ. The boundary conditions are at $y=0$, $T=T_l$ and at $y=L$, $T=T_u$. It is instructive to note that equation (1) also applies to the one-dimensional conduction within a fin where $\dot{q}_r$ is related to the net radiant energy leaving the surface of the fin. The problem can be extended to nongray gases with particles by interpreting κ as the total absorption coefficient and the second term in equation (2) as the total radiant absorption.

In preparation for the FARM, the slab layer is subdivided into M volume zones of thickness Δy_i, where $i=1$ to M with $i=1$ representing the volume zone adjacent to the plate at T_l. The FARM begins by selection of a zone at y_i and the adjacent zones at y_{i-1} and y_{i+1}. For convenience, the $i-1$, i, and $i+1$ zones are referred to as the S, C, and N zones with associated temperatures of T_S, T_C, and T_N. The local spatial variable x is measured from the center of zone C in the direction of zone N. Zone S is at $x=-S$ where S is the distance between zones S and C. Likewise, zone N is at $x=N$ where the distance between zones C and N is N. Two cases, namely, the sink case and the fin case, are examined for acquiring analytical solutions for the local subregion. Equation (1) is applicable to any point x within the subzonal pattern.

For the sink case, $\dot{q}_r$ is assumed to be a constant from zones S to N. Thus, equation (1) is analogous to a plane layer of thickness $S+N$ with a uniform heat sink and boundaries at T_S and T_N [8], and the analytical solution can then be found. Applying the local boundary conditions, setting $x=0$ to yield the temperature at the center of zone C, and returning to the i subscripts give

$$T_i=\frac{T_{i-1}N_i+T_{i+1}S_i}{(N_i+S_i)}-\frac{q_{r,i}}{2k(N_i+S_i)}\{S_iN_i^2+N_iS_i^2\} \tag{3}$$

where values of N_i and S_i depend on the zone spacing. Equation (3) is also the finite difference form of equation (1). Thus, a distinct advantage of the FARM is not realized for the sink case in that it is comparable to analyses utilizing the finite difference method. As shown in equation (3), the net radiant energy term is taken at position y_i.

For the fin case, the emission term is linearized [9] by $T^4\approx T_P^3T$ where T_P represents the temperature at zone C from the previous iteration. Substitution of equation (2) with the linearized emission into equation (1) yields

$$\frac{d^2T}{dx^2}-\frac{4\kappa\sigma T_p^3}{k}T=-\frac{1}{k}\frac{dq_a}{dy} \tag{4}$$

which is analogous to the one-dimensional fin equation [8] with heat generation as given by the right-hand term. This heat generation term is assumed constant within the interval of $-S\le x\le N$. The following dimensionless quantities are introduced

$$\eta=\frac{y}{L};\ \theta=\frac{T}{T_u};\ \bar{N}=\frac{k\kappa}{4\sigma T_u^3};\ \tau_0=\kappa L;\ Q=\frac{q}{4\tau_0\sigma T_u^4};$$

$$\bar{Q}_a=\frac{dQ_a}{d\eta} \tag{5}$$

where $\bar{N}$ is the conduction to radiation parameter, τ_0 is the optical depth based on the plate spacing, and Q is the dimensionless heat flux. The analytical solution is obtained in terms of T_S and T_N and applied at $x=0$ to yield the dimensionless temperature as given by

$$\theta_i\frac{\theta_{i-1}\sinh B_iN_i^*+\theta_{i+1}\sinh B_iS_i^*}{\sinh B_i(S_i^*+N_i^*)}-\frac{1}{\theta_{p,i}^3}\bar{Q}_{a,i}\left\{\frac{\sinh B_iN_i^*+\sinh B_iS_i^*}{\sinh B_i(S_i^*+N_i^*)}-1\right\} \tag{6}$$

where $i=1$ to M and $B_i=\tau_0\theta_{p,i}^{3/2}/\bar{N}^{1/2}$. Values for the dimensionless distances N_i^* and S_i^* can be inserted once the zonal pattern is specified. It should be noted that B must be updated for each iteration since it contains a temperature from the previous iteration.

For the zonal analysis [9], the absorbed radiant flux is

$$\bar{Q}_{a,i}=\frac{1}{4\tau_0\Delta\eta_i}\left[s_lg_i\theta_l^4+s_ug_i+\sum_{j=1}^{M}g_jg_i\theta_j^4\right] \tag{7}$$

[1]Professor, Department of Mechanical Engineering, The University of Iowa, Iowa City, IA 52242, Mem. ASME

[2]Research Assistant, Department of Mechanical Engineering, The University of Iowa, Iowa City, IA 52242, Student Mem. ASME

Contributed by the Heat Transfer Division for publication in the JOURNAL OF HEAT TRANSFER. Manuscript received by the Heat Transfer Division September 24, 1984.

where *sg* and *gg* denote the dimensionless direct exchange areas for surface-to-volume and volume-to-volume radiant exchanges and depend on the optical depth.

The conductive transfer for the lower plate is evaluated from the temperature gradient as found by differentiation of the local analytical solution and is given by

$$Q_l^c = -\frac{\bar{N}^{1/2}\theta_{p,1}^{3/2}}{\tau_0}\left[\frac{\theta_l \cosh B_1(S_1^*+N_1^*)-\theta_2}{\sinh B_1(S_1^*+N_1^*)} - \frac{\bar{Q}_{a,1}}{\Delta\eta_1\theta_{p,1}^3}\left\{\frac{\cosh B_1(S_1^*+N_1^*)-1}{\sinh B_1(S_1^*+N_1^*)}\right\}\right] \tag{8}$$

More accurate results are obtained by using the analytical expression for the temperature gradient than a finite difference form. The conductive wall heat flux contains the absorbed radiant energy term for zone 1. The dimensionless radiative transfer for the lower plate is

$$Q_l^r = \frac{1}{4\tau_0}\left[\theta_l^4 - s_u s_l - \sum_{i=1}^{M} g_i s_l \theta_i^4\right] \tag{9}$$

where *ss* and *gs* denote the dimensionless direct exchange areas for surface-to-surface and volume-to-surface radiant exchanges. The conductive and radiative heat fluxes are added to yield the total heat transfer for the lower plate. Similar heat flux expressions are applicable for the upper plate.

Equation (6) represents a system of simultaneous linear algebraic equations when the radiation terms are assumed known. These equations are rearranged into a tridiagonal coefficient matrix and are solved by an iteration scheme [7]. Within the iteration scheme, the new temperatures were adjusted using a relaxation factor α as follows: $\theta_i = \theta_{p,i} + \alpha(\theta_{n,i} - \theta_{p,i})$ where the subscript n denotes the new temperatures as evaluated from equation (6).

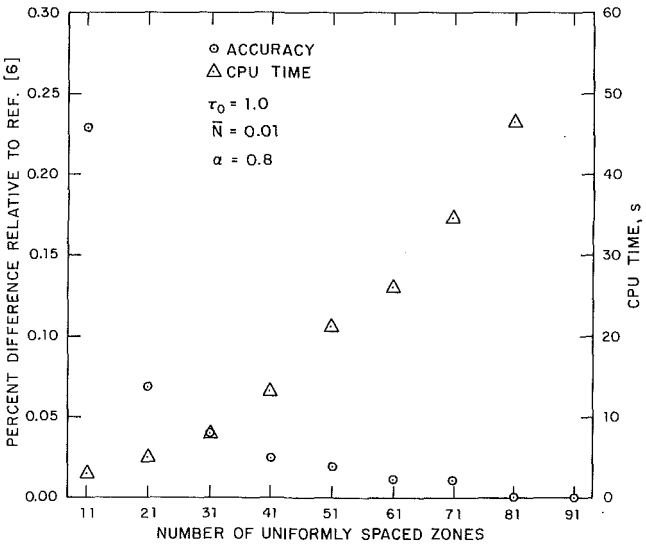

Fig. 1 Influence of number of zones on accuracy and computational times

Results and Discussion

In order to verify that the FARM produces accurate results, a uniform zone spacing with the number of zones set at 51 was selected for the initial comparisons. Results for θ for several combinations of $\bar{N}$, θ_l, and θ_u were verified by comparing them to results of other investigations. In all cases, the present temperature results mirrored those previously presented. Wall heat fluxes were also compared to those reported previously and were found to exhibit a greater sensitivity than the temperatures to the values of the parameters. Thus, attention is directed to a comparison of wall heat fluxes. Emphasis is placed here on the lower wall heat flux. For the system under study, the lower and upper wall heat fluxes should be equal. The differences between the wall heat fluxes evaluated using the sink and fin cases are less than 1.4 and 0.2 percent, respectively. For the sink results, the conductive wall heat fluxes were computed with a finite difference expression for the temperature gradient. These differences, particularly for the fin case, are acceptable.

Results for Q_l for the sink and fin cases are displayed in Table 1 where $\theta_l = 0.5$ and $\theta_u = 1.0$. Several results for the sink case, particularly when radiation dominates, diverged even when $\alpha = 0.1$ was used. Smaller values of α may produce convergence but were not selected since the number of iterations and computational times become excessive. Also shown in Table 1 are results from other studies [2, 5, 6, 9]. The percent difference between the various results and those of Crosbie and Viskanta are given in parentheses. For $\bar{N} = 0$, the zone method and FARM use $\bar{N} = 0.00001$, which may contribute to a portion of the cited errors for the pure radiation cases. The fin case errors are comparable to or in most cases smaller than those for the sink case. In view of this finding as well as the difficulty of achieving convergence for small values of $\bar{N}$, future reference to the FARM implies the fin case and results for the sink case are not examined further.

Table 1 Comparative results of dimensionless wall heat flux

τ_0	$\bar{N}$	Crosbie & Viskanta [2]	Ratzel & Howell [5]	Enoch, Ozil, & Birkebak [6]	Zone [9]	FARM Sink	FARM Fin
0.1	10.0	200.88	200.89 (0.00)	201.11 (0.11)	200.87 (0.00)	200.88 (-)	200.88 (-)
	1.0	20.880	20.89 (0.05)	20.91 (0.14)	20.880 (-)	20.879 (0.00)	20.880 (-)
	0.1	2.8799	2.889 (0.32)	2.88 (0.00)	2.8799 (-)	2.8792(0.02)	2.8800(0.00)
	0.01	1.0799	1.088 (0.75)		1.08 (0.01)	1.0791(0.07)	1.0799 (-)
	0*	0.8585	0.8641(0.65)		0.8616(0.26)	Diverged	0.8618(0.38)
1.0	10.0	20.572	20.58 (0.04)	20.590 (0.09)	20.572 (-)	20.570 (0.01)	20.572 (-)
	1.0	2.5724	2.580 (0.30)	2.5720(0.02)	2.5724 (-)	2.5697(0.08)	2.5724 (-)
	0.1	0.7694	0.7758(0.83)	0.7648(0.60)	0.7693(0.01)	0.7663(0.40)	0.7695(0.01)
	0.01	0.5675	0.5716(0.72)		0.5673(0.04)	Diverged	0.5676(0.02)
	0*	0.5188	0.5210(0.42)		0.5192(0.07)	Diverged	0.5201(0.25)
10.0	10.0	2.1146	2.1150(0.02)	2.1120(0.12)	2.1156(0.05)	2.1142(0.02)	2.1157(0.05)
	1.0	0.3150	0.3150 (-)	0.3100(1.59)	0.3160(0.32)	0.3141(0.29)	0.3161(0.39)
	0.1	0.1335	0.1336(0.07)		0.1343(0.60)	0.1308(2.02)	0.1348(0.97)
	0.01	0.1131	0.1132(0.09)		0.1137(0.53)	Diverged	0.1147(1.41)
	0*	0.1095	0.1096(0.09)		0.1104(0.82)	Diverged	0.1109(1.28)

† Values cited are $q/\sigma T_u^4$

* FARM and zone use 0.00001

The FARM results are in error by less than 1.5 percent, which occurs when $\tau_0 = 10.0$ and $\bar{N} = 0.01$. Furthermore, except for the Ratzel and Howell results and the zone results at $\tau_0 = 10.0$, the FARM yields smaller errors than those from the other cited studies.

The FARM results were also compared to the finite-element technique of Fernandes et al. [4]. For $\tau_0 = 1.0$ and $\bar{N} = 0.05$ Fernandes reported the heat flux to be 0.670 and 0.6647 for Crosbie and Viskanta. These values vary by 0.80 percent. The FARM gives 0.6648 for this heat flux or a 0.02 percent difference with [2]. On the basis of these comparisons, it appears that the FARM is an attractive solution scheme.

The computational time of a solution scheme is also of importance when evaluating a numerical technique. A comparison of the FARM with the results of Chawla and Chan [3] was also made. Chawla and Chan cited a 3.9 percent error with Crosbie and Viskanta when $\tau_0 = 10.0$ and $\bar{N} = 0.01$ using the recommended number of intervals. It is also of interest to note that Chawla and Chan reported an IBM 370/195 Central Processing Unit (CPU) time of 396 s to compute all the results for the five values of $\bar{N}$ as cited in Table 1 when $\tau_0 = 10.0$. Starting with a linear temperature profile for each of the five values of $\bar{N}$ with $\tau_0 = 10.0$, the CPU time on a PRIME 850 computer system is 117 s for the FARM when the optimum values of α as discussed later are used. It has been noted that the IBM system is 6.25 times faster than the PRIME for a FORTRAN benchmark program [10]. For the system under study, the FARM is considerably faster than the method developed by Chawla and Chan.

A parameter that influences the accuracy, computer storage requirements, and computational times is the number of zones. To examine the effects of this parameter, the percent errors of wall heat fluxes from the FARM relative to those of Crosbie and Viskanta [2] are shown in Fig. 1 as a function of M for $\tau_0 = 1.0$ and $\bar{N} = 0.01$. The FARM results for 11 zones vary from those of Crosbie and Viskanta by 0.23 percent. A rapid improvement in accuracy is seen for $M = 31$. A further increase to 81 zones yields "exact" results. The usage of more zones increases the CPU time as depicted in Fig. 1. These results are based on using the pure conduction temperature profile as the initial profile. It is observed that a larger number of zones results in a disproportionately higher CPU time without a significant improvement in accuracy. The improvement in accuracy from 11 to 31 zones is accomplished at the expense of increasing the CPU time by only 5 s.

In addition to M, the spacing of the zones may influence the findings since it may be advantageous to place more zones near the walls where larger temperature gradients are observed. Several nonuniform zone spacings were examined. For the present time, there appears to be no advantage in using nonuniform zone spacing.

The ranges of α over which convergence is achieved are illustrated in Table 2. These results are based on a uniform zone spacing with $M = 51$. Results for values of $\alpha < 0.1$ were not acquired in view of the excessive number of iterations. For values of α greater than those reported, divergence of the iteration scheme occurs. It is of interest to note that overrelaxation where $\alpha > 1$ is possible when radiation effects are weak. In addition, the optimum value of α that yields the minimum number of iterations is displayed along with the number of iterations. The optimum value of α occurs toward the upper limit of the range and is not the largest possible value in the range. A sharp increase in the number of iterations occurs at the end of the range before divergence actually occurs. This behavior has also been reported by Shen et al. [9]. In general, the FARM displays a generous range for the relaxation factor and is a stable solution technique. Only when radiation dominates does the range tend to be limited. These characteristics are common in problems of high nonlinearity.

Table 2 Results for relaxation factor

τ_0	$\bar{N}$	Relaxation Factor Range	Optimum Relaxation Factor	Optimum Number of Iterations
0.1	10.0	0.1 to 1.90	1.00	2
	1.0	0.1 to 1.90	1.00	2
	0.1	0.1 to 1.90	1.00	3
	0.01	0.1 to 1.70	0.90	4
	0.00001	0.1 to 0.60	0.45	4
1.0	10.0	0.1 to 1.90	1.00	2
	1.0	0.1 to 1.90	1.00	4
	0.1	0.1 to 1.50	0.85	5
	0.01	0.1 to 0.92	0.60	10
	0.00001	0.1 to 0.55	0.39	11
10.0	10.0	0.1 to 1.90	1.25	4
	1.0	0.1 to 1.80	1.50	16
	0.1	0.1 to 1.20	1.11	51
	0.01	0.1 to 0.74	0.72	95
	0.00001	0.1 to 0.54	0.53	134

Conclusions

The finite analytic with radiation method that combines analytical solutions for a subregion with a numerical scheme has been developed for a system where conductive and radiative heat transfer occur simultaneously. Results from the method were acquired and compared to available values in order to establish the accuracy of the method. These comparisons illustrated that the method yields accurate results and produces results within acceptable computational times. The method is an attractive solution scheme and should be considered for systems similar to that studied here and examined for its appropriateness to more complex systems.

References

1 Chen, C. J., and Yoon, Y. H., "Finite Analytic Numerical Solution Axisymmetric Navier-Stokes and Energy Equation," ASME JOURNAL OF HEAT TRANSFER, Vol. 105, No. 3, Aug. 1983, pp. 639-645.

2 Crosbie, A. L., and Viskanta, R., "Interaction of Heat Transfer by Conduction and Radiation in a Nongray Planar Medium," *Wärme- und Stoffübertragung*, Vol. 4, 1971, pp. 205-212.

3 Chawla, T. C., and Chan, S. H., "Solution of Radiation-Conduction Problems With Collocation Method Using B-Splines as Approximating Functions," *Int. J. Heat Mass Transfer*, Vol. 22, 1979, pp. 1657-1667.

4 Fernandes, R., Francis, J., and Reddy, J. N., "A Finite-Element Approach to Combined Conductive and Radiative Heat Transfer in a Planar Medium," *Heat Transfer and Thermal Control*, Progress in Astronautics and Aeronautics, Vol. 78, edited by A. L. Crosbie, AIAA, 1981, pp. 92-109.

5 Ratzel, A. C., and Howell, J. R., "Heat Transfer by Conduction and Radiation in One-Dimensional Planar Medium Using the Differential Approximation," ASME JOURNAL OF HEAT TRANSFER, Vol. 104, 1982, pp. 388-391.

6 Enoch, I. E., Ozil, E., and Birkebak, R. C., "Polynomial Approximation Solution of Heat Transfer by Conduction and Radiation in a One-Dimensional Absorbing, Emitting, and Scattering Medium," *Numerical Heat Transfer*, Vol. 5, 1982, pp. 353-358.

7 Severin, S. S., "Development of the Finite Analytic With Radiation Method for a Plane Layer," M.S. thesis, Department of Mechanical Engineering, The University of Iowa, Iowa City, IA, 1984.

8 Incropera, F. P., and DeWitt, D. P., *Fundamentals of Heat Transfer*, Wiley, New York, 1981.

9 Shen, Z. F., Smith, T. F., and Hix, P., "Linearization of the Radiation Terms for Improved Convergence by Use of the Zone Method," *Numerical Heat Transfer*, Vol. 6, 1983, pp. 377-382.

10 Pruess, R. R., Weeg Computing Center, The University of Iowa, Iowa City, IA, personal communication, 1984.

Journal of Heat Transfer

Discussion

An Experimental Study of Mixed, Forced, and Free Convection Heat Transfer From a Horizontal Flat Plate to Air[1]

M. C. Smith[2] and D. A. Haines.[3] The paper by Wang described experiments in which a flat plate was heated nonuniformly across the width of a wind tunnel, although the data were treated as though the heating were uniform. A description of the experiments noted that a central heater, with a width of 40 percent of the channel width, was supplemented by two guard heaters that were used to minimize the transverse heat transfer. Transverse temperature details were not given. Ordinarily this procedure is satisfactory for convective heat transfer, and a number of studies have produced acceptable results. Wang indicated that his data could be used to verify theoretical criteria that determine the conditions marking the onset of longitudinal vortex rolls in a horizontal Blasius flow. These criteria, developed by Wu and Cheng [14], apply to a flat plate heated uniformly and isothermally from below or cooled isothermally from above.

This discussion is prompted by some recent findings of the authors [15] investigating differential heating on a horizontal surface. Our results indicate that vortices resulting from differential heating do not appear to have the same structure as those produced above a uniformly heated surface, e.g., Gilpin et al. [16]. In our study we performed experiments in which a wind tunnel floor with test-section dimensions of 23 cm by 76 cm (height × width) contained a 2.5-cm-wide and 50-cm-long heating ribbon that was oriented parallel to the airflow. The ribbon was heated to a temperature of about 250°C with air speeds ranging from 0.2 to 3.6 m/s. A hot wire, coated with light oil to generate smoke, was oriented normal to the airflow, 5 cm upstream of the ribbon's leading edge and 0.1 cm above the tunnel floor.

A mixed convection flow resulted as indicated by the smoke. Figure 12 shows a typical cross section illuminated through a vertical opening in the tunnel wall and photographed by a downstream camera. This section was 15 cm downstream of the ribbon's leading edge. The vertical smoke plume was located above the ribbon centerline. The vortex pair resulted as the vorticity in the tunnel floor boundary layer was rotated to a downstream direction due to the buoyant forces. A significant inflow to the centerline of the ribbon occurred from the adjacent flow. (With no ribbon heating, the flow was characterized by a stable smoke pattern stretching across the width of the tunnel floor.)

The vortex pair was evident for all wind speeds and also over higher and lower ribbon temperatures. It is evident that

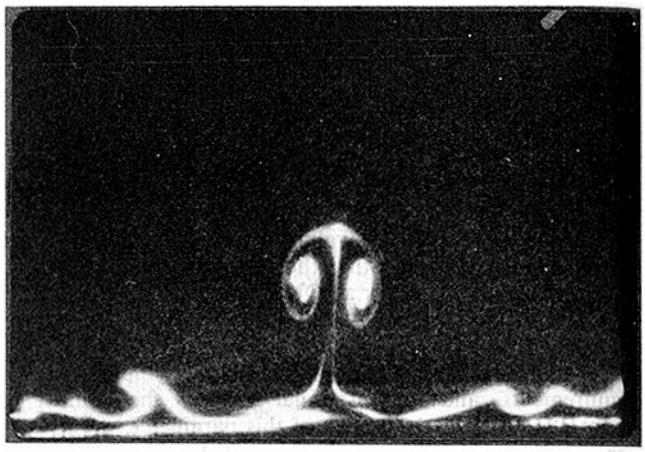

Fig. 1 Airflow over a heated metal ribbon generating a buoyant plume and vortex pair

the vortex structure occurs over a range of mixed convection flows and appears different from that considered by Wu and Cheng [14] and Gilpin et al. [16]. Pertinent questions about the vortices are those of circumstance, i.e., under what conditions of Grashof number, Reynolds number, and transverse temperature variation will this type of downstream vortex pair develop? Also, how drastically will heat transfer and/or surface temperature distributions be affected by the vortices? Of course, the velocity profile of the boundary layer, and particularly the boundary layer vorticity, add another factor.

The authors feel that Wang's data, based on the experiment description, are interpreted validly under conditions of uniform heating. However, questions about vortex type posed in this discussion may be germane to mixed flow experiments and will depend upon the uniformity of plate heating. Thus, at least in some instances, it appears important to describe transverse temperature characteristics of the heated surface and possible effects on the overlying vortex structure.

References

14 Wu, R. S., and Cheng, K. C., "Thermal Instability of Blasius Flow Along Horizontal Plates," *International Journal of Heat and Mass Transfer*, Vol. 19, 1976, pp. 907-913.

15 Haines, D. A., and Smith, M. C., "Wind Tunnel Generation of Horizontal Roll Vortices Over a Differentially Heated Surface," *Nature*, Vol. 306, No. 5941, 1983, pp. 351-352.

16 Gilpin, R. R., Imura, H., and Cheng, K. C., "Experiments on the Onset of Longitudinal Vortices in Horizontal Blasius Flow Heated From Below," ASME JOURNAL OF HEAT TRANSFER, Vol. 100, 1978, pp. 71-77.

Author's Closure

The flat plate in my experiment is heated electrically, and usually it can be treated as constant flux heating. Although

[1] By X. A. Wang, published in the February 1982 issue of the JOURNAL OF HEAT TRANSFER, Vol. 104, No. 1, pp. 139-144.

[2] Mechanical Engineering Department, Michigan State University, E. Lansing, MI 48823

[3] North Central Forest Experiment Station, USDA Forest Service, E. Lansing, MI 48823

the temperature of the plate was not uniform in the longitudinal direction, it was fairly uniform in the transverse direction because of the use of two guard heaters. Two thermocouples were used to measure the transverse temperature differences at two cross sections of the plate as described in the author's paper. The transverse temperature differences were less than 2°C for most of the tests.

The experiment described by Smith and Haines is performed by differential heating of a wind tunnel floor, and it appears to differ from the case of a Blasius flow calculated by Wu and Cheng. Therefore, it is not unexpected that the results of Smith and Haines differ from mine and those of Gilpin et al.

Heat Transfer to Separated Flow Regions From a Rectangular Prism in a Cross Stream[1]

G. Rajen.[2] In a comprehensive and well-documented paper, McCormick, Lessmann, and Test have presented some interesting experimental results for the heat transfer to separated flow regions from a rectangular prism in a cross stream. In their work, they attempt to collapse pressure distributions and heat transfer in separated regions for various bodies onto universal curves.

The constant pressure region in the results of McCormick et al. is about 60 percent of the reattachment length, while for other cases [17, 18, 19] it is about 45 percent.

McCormick et al. explain this as an Aspect Ratio effect. However, another explanation is also possible. It is well known that in regions of laminar separation and subsequent reattachment, the laminar separated layer undergoes transition to turbulence and then reattaches. The length of the constant pressure region in the separated zone corresponds to the length to transition of the laminar separated layer; this length to transition is easily affected by nonadiabatic wall conditions.

The pressure distributions in [17, 18, 19] were for bodies which were at the temperature of the free stream. The body used in the tests of McCormick et al. had a wall-to-free stream absolute temperature ratio of 1.04.

As has been shown by Macha and Shafa [20], in tests on a heated cylinder, nonadiabatic wall conditions can significantly affect separated regions. A theory proposed by Demetriades et al. [21] to predict the length to transition of a laminar separated layer takes into account a possible temperature difference between the dividing stream line and the free stream. This theory is very effective in explaining the results of Macha and Shafa [20], as shown by Rajen [22].

If L_1 is the length to transition of a laminar separated layer with the wall at the temperature of the free stream T_1, and if L_2 is the length to transition for a wall temperature T_2 (different from T_1), the theory of Demetriades et al. gives

$$L_2/L_1 = (T_2/T_1)^{2(n+1)} \tag{2}$$

where n is the exponent in the temperature viscosity law. Assuming the ratio T_2/T_1 to be equal to 1.04 (as in the tests of McCormick et al.), with $n = 1$, gives

$$L_2/L_1 = 1.16 \tag{3}$$

in other words, a 16 percent increase in the length to transition of the laminar separated layer. Thus, the greater length of the constant pressure region in the results of McCormick et al. could well be because of the nonadiabatic wall conditions of their model, and not entirely an Aspect Ratio effect.

References

17 Sam, R. G., Lessmann, R. C., and Test, F. L., "An Experimental Study of Flow Over a Rectangular Body," ASME *Journal of Fluids Engineering*, Vol. 101, Dec. 1979, pp. 443-448.

18 Ota, T., and Itasaka, M., "A Separated and Reattached Flow on a Blunt Flat Plate," ASME *Journal of Fluid Mechanics*, Vol. 98, Mar. 1976, pp. 79-86.

19 Ota, T., "An Axisymmetric Separated and Reattached Flow on a Longitudinal Blunt and Circular Cylinder," ASME *Journal of Applied Mechanics*, Vol. 42, June 1975, pp. 311-315.

20 Macha, J. M., and Shafa, K. S., "Influence of Non-Adiabatic Wall Conditions on the Cross-Flow Around a Circular Cylinder," ASME Paper No. 84-FE-5, 1984.

21 Demetriades, A., Ortwerth, P. J., and Moeny, W. M., "Laminar-Turbulent Transition in Free Shear Layers," *AIAA Journal*, Vol. 19, 1981, pp. 1091-1092.

22 Rajen, G., "Possible Effects of Non-Adiabatic Wall Conditions on Short Separation Bubbles" (to be published).

Authors' Closure

The authors assume that the discussion primarily refers to Fig. 8 of the paper about which the paper states, "The scaled pressure data . . . show the constant pressure region varies from 60 percent of the reattachment length . . . to about 45 percent." The paper implies this could be due to aspect ratio but the discussion says it might be due to nonadiabatic wall effects.

Some of the points in Fig. 8 come from [2] of the paper and the original data behind this reference include pressure coefficients for heated and unheated cases at zero degree angle of attack. The plot from [2] in Fig. 8 is for the unheated case. If the data for the heated case (absolute temperature ratio = 1.04) were plotted in Fig. 8, the constant pressure region might be slightly longer than for the unheated case but not beyond possible experimental error.

The lengthening of the constant pressure region due to nonadiabatic wall effects depends on a statement in the discussion: "The length of the constant pressure region in the separated zone corresponds to the length to transition of the laminar separated layer." The discussor makes no attempt to support this statement.

The length of the constant pressure region may be a function of many things and the discussor is correct in pointing out that one of the things might be nonadiabatic wall effects. However, the evidence at this point does not appear to be conclusive.

Local Heat Transfer Downstream of an Abrupt Expansion in a Circular Channel With Constant Wall Heat Flux[1]

J. K. Eaton.[2] Professor Baughn and his co-workers have presented a very interesting and useful set of heat transfer measurements for the axisymmetric sudden expansion flow. Their unique measurement technique has revealed the presence of a local minimum in the heat transfer coefficient occurring about 1 step height downstream of the expansion. They noted that the Nusselt number at this point is still greater than the fully developed value and attributed the augmentation to a high level of turbulent transport.

[1] By D. C. McCormick, R. C. Lessmann, and F. L. Test, published in the May 1984 issue of the JOURNAL OF HEAT TRANSFER, Vol. 106, No. 2, pp. 276-283.

[2] Graduate Student, Dept. of Mechanical and Aerospace Engineering, University of Delaware; Student Member ASME

[1] By J. W. Baughn, M. A. Hoffman, R. K. Takahashi, and B. E. Launder, published in the November 1984 issue of ASME JOURNAL OF HEAT TRANSFER, Vol. 106, No. 4, pp. 789-796.

[2] Assistant Professor, Department of Mechanical Engineering, Stanford University, Stanford, CA 94305, Assoc. Mem. ASME.

the temperature of the plate was not uniform in the longitudinal direction, it was fairly uniform in the transverse direction because of the use of two guard heaters. Two thermocouples were used to measure the transverse temperature differences at two cross sections of the plate as described in the author's paper. The transverse temperature differences were less than 2°C for most of the tests.

The experiment described by Smith and Haines is performed by differential heating of a wind tunnel floor, and it appears to differ from the case of a Blasius flow calculated by Wu and Cheng. Therefore, it is not unexpected that the results of Smith and Haines differ from mine and those of Gilpin et al.

Heat Transfer to Separated Flow Regions From a Rectangular Prism in a Cross Stream[1]

G. Rajen.[2] In a comprehensive and well-documented paper, McCormick, Lessmann, and Test have presented some interesting experimental results for the heat transfer to separated flow regions from a rectangular prism in a cross stream. In their work, they attempt to collapse pressure distributions and heat transfer in separated regions for various bodies onto universal curves.

The constant pressure region in the results of McCormick et al. is about 60 percent of the reattachment length, while for other cases [17, 18, 19] it is about 45 percent.

McCormick et al. explain this as an Aspect Ratio effect. However, another explanation is also possible. It is well known that in regions of laminar separation and subsequent reattachment, the laminar separated layer undergoes transition to turbulence and then reattaches. The length of the constant pressure region in the separated zone corresponds to the length to transition of the laminar separated layer; this length to transition is easily affected by nonadiabatic wall conditions.

The pressure distributions in [17, 18, 19] were for bodies which were at the temperature of the free stream. The body used in the tests of McCormick et al. had a wall-to-free stream absolute temperature ratio of 1.04.

As has been shown by Macha and Shafa [20], in tests on a heated cylinder, nonadiabatic wall conditions can significantly affect separated regions. A theory proposed by Demetriades et al. [21] to predict the length to transition of a laminar separated layer takes into account a possible temperature difference between the dividing stream line and the free stream. This theory is very effective in explaining the results of Macha and Shafa [20], as shown by Rajen [22].

If L_1 is the length to transition of a laminar separated layer with the wall at the temperature of the free stream T_1, and if L_2 is the length to transition for a wall temperature T_2 (different from T_1), the theory of Demetriades et al. gives

$$L_2/L_1 = (T_2/T_1)^{2(n+1)} \tag{2}$$

where n is the exponent in the temperature viscosity law. Assuming the ratio T_2/T_1 to be equal to 1.04 (as in the tests of McCormick et al.), with $n = 1$, gives

$$L_2/L_1 = 1.16 \tag{3}$$

in other words, a 16 percent increase in the length to transition of the laminar separated layer. Thus, the greater length of the constant pressure region in the results of McCormick et al. could well be because of the nonadiabatic wall conditions of their model, and not entirely an Aspect Ratio effect.

References

17 Sam, R. G., Lessmann, R. C., and Test, F. L., "An Experimental Study of Flow Over a Rectangular Body," ASME *Journal of Fluids Engineering*, Vol. 101, Dec. 1979, pp. 443-448.

18 Ota, T., and Itasaka, M., "A Separated and Reattached Flow on a Blunt Flat Plate," ASME *Journal of Fluid Mechanics*, Vol. 98, Mar. 1976, pp. 79-86.

19 Ota, T., "An Axisymmetric Separated and Reattached Flow on a Longitudinal Blunt and Circular Cylinder," ASME *Journal of Applied Mechanics*, Vol. 42, June 1975, pp. 311-315.

20 Macha, J. M., and Shafa, K. S., "Influence of Non-Adiabatic Wall Conditions on the Cross-Flow Around a Circular Cylinder," ASME Paper No. 84-FE-5, 1984.

21 Demetriades, A., Ortwerth, P. J., and Moeny, W. M., "Laminar-Turbulent Transition in Free Shear Layers," *AIAA Journal*, Vol. 19, 1981, pp. 1091-1092.

22 Rajen, G., "Possible Effects of Non-Adiabatic Wall Conditions on Short Separation Bubbles" (to be published).

Authors' Closure

The authors assume that the discussion primarily refers to Fig. 8 of the paper about which the paper states, "The scaled pressure data . . . show the constant pressure region varies from 60 percent of the reattachment length . . . to about 45 percent." The paper implies this could be due to aspect ratio but the discussion says it might be due to nonadiabatic wall effects.

Some of the points in Fig. 8 come from [2] of the paper and the original data behind this reference include pressure coefficients for heated and unheated cases at zero degree angle of attack. The plot from [2] in Fig. 8 is for the unheated case. If the data for the heated case (absolute temperature ratio = 1.04) were plotted in Fig. 8, the constant pressure region might be slightly longer than for the unheated case but not beyond possible experimental error.

The lengthening of the constant pressure region due to nonadiabatic wall effects depends on a statement in the discussion: "The length of the constant pressure region in the separated zone corresponds to the length to transition of the laminar separated layer." The discussor makes no attempt to support this statement.

The length of the constant pressure region may be a function of many things and the discussor is correct in pointing out that one of the things might be nonadiabatic wall effects. However, the evidence at this point does not appear to be conclusive.

Local Heat Transfer Downstream of an Abrupt Expansion in a Circular Channel With Constant Wall Heat Flux[1]

J. K. Eaton.[2] Professor Baughn and his co-workers have presented a very interesting and useful set of heat transfer measurements for the axisymmetric sudden expansion flow. Their unique measurement technique has revealed the presence of a local minimum in the heat transfer coefficient occurring about 1 step height downstream of the expansion. They noted that the Nusselt number at this point is still greater than the fully developed value and attributed the augmentation to a high level of turbulent transport.

[1] By D. C. McCormick, R. C. Lessmann, and F. L. Test, published in the May 1984 issue of the JOURNAL OF HEAT TRANSFER, Vol. 106, No. 2, pp. 276-283.

[2] Graduate Student, Dept. of Mechanical and Aerospace Engineering, University of Delaware; Student Member ASME

[1] By J. W. Baughn, M. A. Hoffman, R. K. Takahashi, and B. E. Launder, published in the November 1984 issue of ASME JOURNAL OF HEAT TRANSFER, Vol. 106, No. 4, pp. 789-796.

[2] Assistant Professor, Department of Mechanical Engineering, Stanford University, Stanford, CA 94305, Assoc. Mem. ASME.